Compound Semiconductor Electronics and Photonics

Symposium held April 8-10, 1996, San Francisco, California, U.S.A.

EDITORS:

R.J. Shul
Sandia National Laboratories
Albuquerque, New Mexico, U.S.A.

S.J. Pearton
University of Florida
Gainesville, Florida, U.S.A.

F. Ren
Lucent Technologies, Bell Laboratories
Murray Hill, New Jersey, U.S.A.

C.-S. Wu
Texas Instruments
Dallas, Texas, U.S.A.

1996 1125 128

Single article reprints from this publication are available through University Microfilms Inc., 300 North Zeeb Road, Ann Arbor, Michigan 48106

CODEN: MRSPDH

REPORT DOCUMENTATION PAGE

Form Approved
OMB NO. 0704-0188

Public reporting burden for this collection of information is estimated to average 1 hour per response, including the time for reviewing instructions, searching existing data sources, gathering and maintaining the data needed, and completing and reviewing the collection of information. Send comment regarding this burden estimates or any other aspect of this collection of information, including suggestions for reducing this burden, to Washington Headquarters Services, Directorate for information Operations and Reports, 1215 Jefferson Davis Highway, Suite 1204, Arlington, VA 22202-4302, and to the Office of Management and Budget, Paperwork Reduction Project (0704-0188), Washington, DC 20503.

1. AGENCY USE ONLY (Leave blank)	2. REPORT DATE	3. REPORT TYPE AND DATES COVERED
	Nov 96	Final 1 April 96 – 31 Mar 97

4. TITLE AND SUBTITLE

Compound Semiconductor Electronics and Photonics

5. FUNDING NUMBERS

DAAH04-96-1-0084

6. AUTHOR(S)

Robert H. Pachavis   (principal investigator)

7. PERFORMING ORGANIZATION NAMES(S) AND ADDRESS(ES)

Materials Research Society
Pittsburgh, PA   15237

8. PERFORMING ORGANIZATION REPORT NUMBER

9. SPONSORING / MONITORING AGENCY NAME(S) AND ADDRESS(ES)

U.S. Army Research Office
P.O. Box 12211
Research Triangle Park,, NC 27709-2211

10. SPONSORING / MONITORING AGENCY REPORT NUMBER

ARO 35710.1-MS-CF

11. SUPPLEMENTARY NOTES

The views, opinions and/or findings contained in this report are those of the author(s) and should not be construed as an official Department of the Army position, policy or decision, unless so designated by other documentation.

12a. DISTRIBUTION / AVAILABILITY STATEMENT

Approved for public release; distribution unlimited.

12 b. DISTRIBUTION CODE

13. ABSTRACT (Maximum 200 words)

These proceedings are the permanent record of Symposium C, entitled "Compound Semiconductor Electronics and Photonics," which was part of the 1996 MRS Spring Meeting held in San Francisco, California, April 8–12, 1996.

The outstanding success of the symposium was due in part to the efforts of the following people: the authors and speakers who presented their technical work at the meeting and composed the papers in this proceedings; the symposium organizers, who put together the program and saw that it ran smoothly; the session chairpersons (C.R. Abernathy, R.J. Shul, F.R. Shepherd, E.A. Beam, III, J.C. Zolper, J.R. Flemish, S.J. Pearton, F. Ren, K.D. Choquette and A.G. Baca); the staff of the Materials Research Society, who provided the organization for the symposium; and most importantly the sponsors listed below, whose financial backing enabled the organizers to cover the meeting expenses. The editors of these proceedings extend our sincere appreciation to all who contributed to the success of the symposium.

14. SUBJECT TERMS

15. NUMBER IF PAGES

16. PRICE CODE

17. SECURITY CLASSIFICATION OR REPORT	18. SECURITY CLASSIFICATION OF THIS PAGE	19. SECURITY CLASSIFICATION OF ABSTRACT	20. LIMITATION OF ABSTRACT
UNCLASSIFIED	UNCLASSIFIED	UNCLASSIFIED	UL

DTIC QUALITY INSPECTED 3

DISCLAIMER NOTICE

THIS DOCUMENT IS BEST
QUALITY AVAILABLE. THE
COPY FURNISHED TO DTIC
CONTAINED A SIGNIFICANT
NUMBER OF PAGES WHICH DO
NOT REPRODUCE LEGIBLY.

CONTENTS

*Invited Paper

*Invited Paper

*Invited Paper

*Invited Paper

*Invited Paper

x

PREFACE

This proceedings volume is the record from a Materials Research Society symposium covering a wide range of activity in the III-V compound semiconductor electronics and photonics arena. In particular, processing modules such as wet and dry etching, ohmic and Schottky contact formation, ion implantation, annealing and dielectric deposition, along with the performance of completed devices such as long- and short-wavelength laser diodes, VCSELs, QWIPs, heterostructure field effect transistors and heterostructure bipolar transistors are discussed. Summaries of these topics were provided by invited review papers, while contributed and poster papers described work in progress.

The previous trend of industry downsizing and consolidation was again obvious. The compound semiconductor research area has decreased in recent years with AT&T, IBM, Tektronix and others reducing their efforts due to cost and competitiveness issues. Attention is focused on manufacturability, reliability and cost, rather than ultimate performance as in years past. Some issues, such as poor reproducibility of ohmic contacts, lack of a high-quality insulator and the influence of point and line defects remain, probably never to be overcome. A strong effort has been made on high-resolution dry etching techniques in recent years, with both electron cyclotron resonance and inductively coupled plasma sources proving capable of highly anisotropic etching with low surface damage.

There was much interest in the wide bandgap nitrides, GaN, AlN, InN, and their alloys. The commercial availability of blue- and green-light-emitting diodes based on the InGaN/AlGaN system, and the recent announcement of pulsed operation of a laser diode have stimulated interest in the growth, characterization and processing of these materials. Potential applications in high-temperature/high-power electronics appear promising because of the good transport properties of the nitrides.

The symposium was well attended, with a lively and informative poster session. The III-V community continues to produce good science and novel high-performance devices.

<div align="right">

R.J. Shul
S.J. Pearton
F. Ren
C.-S. Wu

June 1996

</div>

ACKNOWLEDGMENTS

MATERIALS RESEARCH SOCIETY SYMPOSIUM PROCEEDINGS

MATERIALS RESEARCH SOCIETY SYMPOSIUM PROCEEDINGS

Part I

Growth and Characterization

GAS-SOURCE MOLECULAR BEAM EPITAXY OF ELECTRONIC DEVICES

E.A. BEAM III, B. BRAR, T.P.E. BROEKAERT, H.F. CHAU, W. LIU and A.C. SEABAUGH
Texas Instruments Incorporated, Corporate R&D/Technology, P.O. Box 655936, M/S 147,
Dallas, TX 75265 USA

ABSTRACT

Gas-source molecular beam epitaxy (GSMBE) has been developed into a useful tool for the growth of both optical and electronic device structures. In this paper, we report on the use of tertiarybutylarsine (TBA) and tertiarybutylphosphine (TBP) in GSMBE for the growth of electronic device structures with state-of-the-art performance. Device structures based on both the $In_{0.48}Ga_{0.52}P/GaAs$ and $In_{0.53}Ga_{0.47}As/InP$ lattice matched materials systems are described. The GSMBE system is based on the use of elemental Group-III sources and employs thermal crackers for precracking TBA and TBP. Dopant sources include both elemental (Sn and Be) and vapor (CBr_4 and $SiBr_4$) sources. Device structures fabricated in the $In_{0.48}Ga_{0.52}P/GaAs$ materials system include single- and double- heterojunction bipolar transistors (SHBTs and DHBTs). Device structures fabricated in the $In_{0.53}Ga_{0.47}As/InP$ materials system include SHBTs, DHBTs, heterojunction field effect transistors (HFETs), and both planar and lateral resonant tunneling diodes (RTDs.) Vertically integrated HFET and multi-RTD heterostructures for high speed logic/memory are also described.

1. INTRODUCTION

Gas-source molecular beam epitaxy is an important epitaxial growth technique for the fabrication of device structures incorporating both As- and P- based alloys. This technique is based on the use of conventional elemental sources for the group-III growth constituents (In, Ga and Al), and gas/vapor sources for the group-Vs [1]. Dopant sources have been predominantly elemental sources, but gas/vapor sources are receiving increasing use. To date, most implementations of GSMBE have relied on arsine and phosphine for the As and P source constituents. The chemical species required for growth are obtained by thermally cracking these sources in low pressure cracking cells using a tantalum catalyst. These sources have been used very successfully for the growth of a wide variety of devices structures [2], however, they are highly toxic and require extensive safety precautions for their use. We have based our approach on the exclusive use of organometallic group-V sources [3]. These sources include tertiarybutylarsine (TBA) as the arsenic precursor and tertiarybutylphosphine (TBP) as the phosphorus precursor. Although, these substances are still toxic, their low vapor pressure enables them to be handled more safely. We have demonstrated that these sources can be used effectively over a six year time period to produce device structures comparable to the best reported using hydride-based GSMBE and conventional solid-source MBE [4].

3

2. GSMBE HARDWARE AND SOURCES

Details of the growth system have been described previously [3,4]. Briefly, our GSMBE system has been constructed from a Perkin-Elmer 425B MBE system with the addition of a turbomolecular vacuum pump. Elemental In, Ga and Al are evaporated using conventional effusion cells. Dopant sources include elemental Be and Sn, and vapor sources CBr_4 and $SiBr_4$. The CBr_4 and $SiBr_4$ dopant sources are delivered to the reactor from external bubblers using pressure based flow control techniques [5]. The TBA and TBP precursors are precracked using separate low-pressure cracker cells constructed with tantalum baffles which act as catalysts. We have studied the thermal cracking of TBA and TBP using our cracker cell design and a modulated beam mass spectroscopy (MBMS) apparatus [3]. The use of the modulated beam technique was important for distinguishing between constituents in the reactor background from the organometallic decomposition products in the direct beam. For TBP, cracker cell temperatures greater than 600°C resulted in P_2 as the dominant species detected in the direct beam. The mass spectra of the organic species corresponded exactly with isobutene. The cracking behavior of TBA was qualitatively very similar to that of TBP, with a slightly higher temperature (~50°C) required for complete cracking. The efficiency of the cracker cells degrades with time due to tantalum hydride formation, but the cells can be regenerated by annealing at 900°C for several minutes. We generally perform this anneal between each growth run, and have used the same tantalum baffles for a year or more. Annealing the cells at temperatures greater than 1000°C results in tantalum carbide formation which permanently degrades the catalytic action of the cell.

3. InGaP/GaAs MATERIALS AND DEVICES

The organic decomposition products produced from the thermal cracking of TBA result in GaAs layers with typical p-type background doping densities of 1×10^{16} cm^{-3}. This background doping is sufficiently low that the controlled n-type doping of GaAs to 2×10^{16} cm^{-3} can be readily accomplished. The GaAs epi-layers are free of oval defects despite the use of elemental Ga, suggesting that the As source has a significant influence on the formation of these defects. InGaP layers lattice matched to GaAs exhibit a room temperature bandgap energy of 1.89 eV, suggesting that the InGaP is disordered. Transmission electron microscopy has been used to corroborate this result [6]. Additional details of the growth and doping of GaAs and InGaP with this system have been described previously [4].

The use of InGaP lattice matched to GaAs is very attractive as a replacement for AlGaAs in heterojunction bipolar transistor structures. We have investigated the use of this material for both single- and double-heterojunction bipolar transistors (SHBTs & DHBTs).

The generic device structure for a SHBT includes a 50-100 nm n-type InGaP emitter layer doped to 5×10^{17} cm^{-3} with Sn, a 50-100 nm p-type GaAs base layer doped to $5\text{-}30 \times 10^{18}$ cm^{-3} with Be, and a 500-1000 nm n-type GaAs collector layer doped to $2\text{-}5 \times 10^{16}$ cm^{-3} with Sn. In addition, heavily doped n-type GaAs layers are provided for making the emitter and collector contacts. Figure 1a presents results from deep level transient spectroscopy (DLTS) experiments of the

4
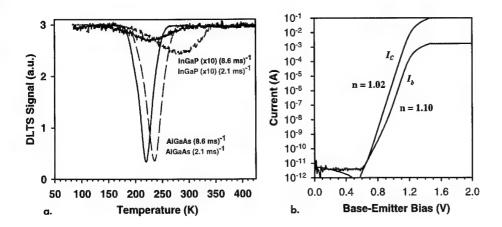
Figure 1   (a) DLTS signals from the emitter- base junction of a MOMBE grown InGaP/GaAs SHBT and a MOCVD grown AlGaAs/GaAs SHBT, and (b) Gummel plot from the InGaP/GaAs SHBT (100 x 100 μm^2 device).

emitter-base junction from a InGaP/GaAs SHBT grown by GSMBE and compares results from a similar AlGaAs/GaAs SHBT grown by MOCVD [6]. The considerably lower trap density in the InGaP emitter device results in substantially less base-emitter space charge recombination, resulting in consistent current gain over a wide range of collector current density. This result is evident in the Gummel plot in Figure 1b showing near ideal characteristics with the base current ideality factor being unity over roughly 5 decades of collector current.
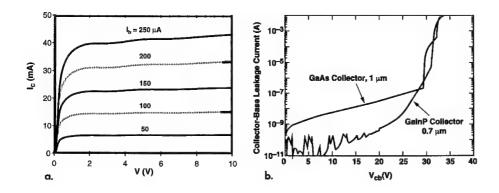
Figure 2   (a) Common-emitter I-V characteristics for InGaP/GaAs DHBT and (b) reverse bias breakdown characteristics for this device and a InGaP/GaAs SHBT device with a 1 μm thick GaAs collector.

5

Another use of InGaP in the HBT structure is as a replacement for GaAs in the collector layer. The higher bandgap energy should result in a higher breakdown voltage for a fixed layer thickness and reduced leakage current. We have examined this possibility by fabricating DHBT devices with the same generic structure as described above, but with a 700 nm n-type InGaP collector layer doped to 3×10^{16} cm^{-3}. In addition, a 20 nm undoped GaAs setback layer is inserted between the base and collector in order to minimize the effective barrier for carriers transporting from the base to the collector. Figs. 2a and 2b show the common-emitter I-V characteristics and reverse breakdown characteristics obtained with this device structure. A small offset voltage of 57 mV is obtained, and the low saturation voltage ($V_{cc} < 2$ V) demonstrates the importance of the collector-base junction design. The reverse bias characteristics indicate a reverse breakdown voltage greater than 30 V. For comparison Fig. 2b also includes the reverse characteristics for a SHBT device with the 1000 nm GaAs collector layer. A similar breakdown voltage is obtained with the 143% thicker GaAs collector. However, the leakage current is nearly two orders of magnitude lower for the InGaP collector structure. These reverse characteristics demonstrate the potential advantages of this material for power applications.

4. InGaAs/InP MATERIALS AND DEVICES

The background dopings of InP, $In_{0.53}Ga_{0.47}As$ and $In_{0.52}Al_{0.48}As$ grown with TBP and TBA are n-type with carrier concentrations typically less than 5×10^{15} cm^{-3}. The optimum growth temperatures with respect to background doping and surface morphology for these materials are 480 C, 450 C and 500 C respectively. The n-type doping of these materials is accomplished using silicon tetrabromide. This dopant source has been found to be nearly ideal for application
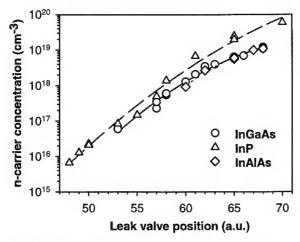
Figure 3   Net electron concentrations versus leak-valve setting for SiBr$_4$ doped InP, $In_{0.53}Ga_{0.47}As$ and $In_{0.52}Al_{0.48}As$

to GSMBE and/or chemical beam epitaxy (CBE) [5,7]. This dopant source is controlled using an indexed variable-rate leak valve, with remarkably good reproducibility. Figure 3 presents a summary of the carrier concentrations vs. leak valve setting (arbitrary units) for these three materials. Carrier concentrations greater than 6×10^{19} cm^{-3} are obtained for InP, while the concentrations appear to saturate at slightly greater than 1×10^{19} cm^{-3} for InGaAs and InAlAs. P-type doping of InGaAs is accomplished using beryllium or carbon tetrabromide. The CBr$_4$ source is controlled using a pressure-based mass flow controller without the use of a carrier gas. We have obtained hole carrier concentrations as high as 9×19^{19} cm^{-3} using this source [5].

4.1 Heterojunction Bipolar Transistors

We have used GSMBE to produce a wide variety of device structures based on the InGaAs/InP materials system. This growth technique is particularly attractive for this system versus MOCVD due to the flexibility of dopant species and the ability to reproducibly grow very thin, abrupt heterostructures. The growth of high performance InP-based power DHBT structures is particularly challenging for several reasons: the base layer must be heavily doped and maintained with a sharp profile; it is necessary to transition the n-type doping from very high levels in the sub-collector to controlled low levels in the collector; and the base-collector junction generally requires a complex composition grading and/or spike doping profile in order to minimize the effective barrier for carriers transporting from the base to the collector [8,9]. Our generic layer structure for the DHBT consists of the following: a 500 nm n-InP sub-collector layer doped to 3×10^{19} cm^{-3} with Si, a 800 nm n-InP collector layer doped to 2×10^{16} cm^{-3} with Si, a ~ 57 nm undoped InGaAs/InP chirped superlattice, a 90 nm p-InGaAs base layer doped to 4×10^{19} cm^{-3} with Be or C, a 100 nm InP emitter layer doped to 5×10^{17} cm^{-3} with Si, and a 150 nm n-InGaAs emitter contact layer doped to 1×10^{19} cm^{-3} with Si.

a. b.
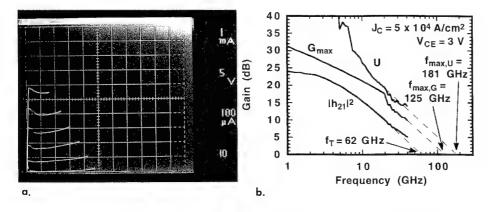
Figure 4 (a) Measured common-emitter I-V characteristics of a 2 x 10 μm^2 InP/InGaAs
      DHBT and (b) frequency dependence of the current gain (h_{21}) and unilateral
      power gain (U).

Figure 4a presents the common emitter I-V characteristics obtained for a device with this structure for which the base is doped with Be. Comparable results have also been obtained using carbon doping [10]. The high breakdown voltage (24 V) illustrated by these I-V characteristics demonstrates the high quality of the InP collector material and the ability to transition the carrier concentration from the sub-collector to collector to the 1×10^{16} cm^{-3} level. Previously, we have found that it is difficult to make this abrupt transition when tin is used as the n-type dopant due to surface segregation and redistribution [4]. The use of SiBr$_4$ as the n-type dopant source has eliminated this problem; however, we found it necessary to add additional cryopaneling to our growth chamber to eliminate a memory effect associated with re-evaporation of SiBr$_4$ from warm surfaces with direct line-of-sight to the substrate. Other desirable features indicated by these I-V characteristics include a small offset voltage V_{CE} of 70 mV and a V_{CE} saturation voltage of about 1.0 V at 5×10^4 A/cm^2. The small dip in the I-V characteristics is due to small changes in the transmission coefficient with bias voltage in the chirped superlattice. Figure 4b presents the high-frequency characteristics obtained for this device structure. The current-gain cutoff frequency f_T and maximum oscillation frequency f_{max} are 62 and 181 GHz respectively. This value of f_{max} is the highest ever reported for an InP-based DHBT with a open-base breakdown voltage BV_{CEO} greater than 8 V. Devices of similar structure have shown a maximum output power density of 2.34 W/mm and a peak power-added-efficiency of 35.5 % at 30 GHz [11].

4.2 Heterojunction Field Effect Transistors

The growth of high-performance InAlAs/InGaAs/InP heterojunction field effect transistors (HFETs) by conventional solid-source MBE (SSMBE) is well established [12,13]. These structures require high purity intrinsic layers for the channel and buffer layers, abrupt
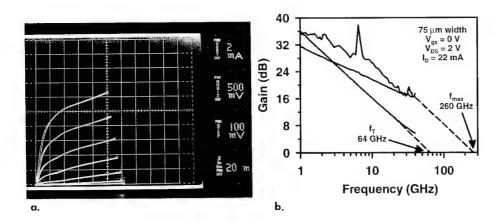
Figure 5 (a) Measured I-V characteristics for a InAlAs/InGaAs HFET grown by GSMBE and (b) the frequency dependence of the current gain (h_{21}) and maximum available gain (MAG.)
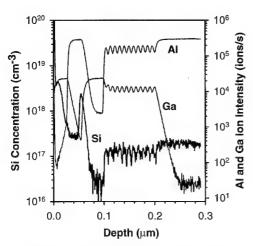
Figure 6 SIMS depth profile of Si, Al and Ga
constituents from an HFET structure
described in the text.

heterointerfaces, and an abrupt doping profile for the modulation doped layer. We have applied
our GSMBE approach for the growth of these device structures with comparable results to
SSMBE grown devices.

Our generic structure for the HFET includes the following: a 120 nm undoped InAlAs buffer
layer; a 10-period undoped InGaAs/InAlAs (4/4 nm) superlattice buffer; a 40 nm undoped
InGaAs channel layer; a 2 nm undoped InAlAs spacer layer; a 3 nm n-InAlAs modulation doping
layer doped to $6-9 \times 10^{18}$ cm^{-3} with Si; a 20 nm undoped InAlAs layer and a 20 nm n-InGaAs cap
layer doped to 5×10^{18} cm^{-3} with Si. Figure 5a and 5b presents the I-V characteristics and on-
wafer S-parameter measurements obtained for a 0.25 µm gate length device with this layer
structure. A transconductance of 720 mS/mm and f_{max} of 260 GHz is obtained. These numbers
are comparable to similar devices grown by SSMBE in our laboratory and reported by others
[12,13]. These results are very encouraging since a high background of organic species exists in
the GSMBE reactor during growth as a byproduct of the decomposition of TBA. These results
demonstrate that very little carbon is incorporated in InGaAs and InAlAs from this intrinsic
source. Figure 6 presents a SIMS depth profile through a similar structure. This Si profile has
been normalized using a GaAs doping standard and may account for the lower than expected Si
concentration $(8 \times 10^{18}$ cm$^{-3})$ in the modulation doped layer. Despite the lack of the InAlAs
standard, the Si signal qualitatively demonstrates that the SiBr$_4$ dopant source is quite capable of
producing the abrupt doping profile needed for the modulation doping layer in this device.

4.3 Resonant Tunneling Diodes and Vertical Integration with HFETs

The co-integration of resonant tunneling diodes (RTDs) with transistors is attractive for
future high-speed, high-density circuit designs. The unique characteristics of these devices

enables more logic per transistor than with just conventional transistors. GSMBE is ideally suited as a growth technique for these structures due to the layer thickness precision required for the RTDs, the low temperatures required for the producing highly mismatched pseudomorphic layers and the ability to grow As- and P-based heterostructures. We have previously reported on the integration of RTDs with InP-based double-heterojunction bipolar transistors [14] and demonstrated integrated XNOR, XOR and full adder circuits using this approach [15,16]. These circuits, operating at room temperature, use fewer transistors (~1/2) than conventional ECL transistor logic.

An integrated process for fabricating stacked RTDs on InP-based InAlAs/InGaAs heterostructure field-effect transistors (RTD/HFET) is desired for several compact and high speed linear and mixed-signal circuits. Growth and processing of a three-stack RTD on the source of an InAlAs/InGaAs HFET has now been demonstrated. The structure was fabricated by first growing the HFET structure described in the previous section, followed by a stack of three pseudomorphic RTDs, each with the following layer sequences: 12/40/12 nm of n-InGaAs doped to $1x10^{18}/1x10^{19}/1x10^{18}$ cm^{-3} followed by 2/1/2/1/2 nm of n-AlAs/InGaAs/InAs/InGaAs/AlAs doped to $1x10^{18}$ cm^{-3}. A 3-nm n-InP layer was inserted between the HFET and the 3-RTD for use as an etch stop to facilitate contacts to the HFET device. With the stacked RTD located on the source of the HFET transistor, the device occupies and area comparable to the footprint of the transistor alone. Figure 7 presents an SEM image of the completed device structure. Note that the HFET, the 3-stack RTD or the integrated 3RTD/HFET can be contacted.
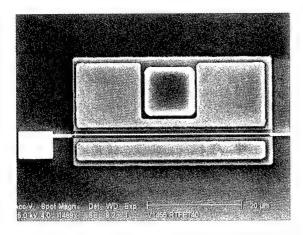
Figure 7 SEM image of the completed 3RTD/HFET structure.

Figure 8 presents the measured current-voltage plot of the dc transfer characteristic of the integrated 3RTD/HFET with the bias conditions given in the inset. The RTDs are 3x3 μm2 in size, and the HFET has a gate length of 0.25 μm with a gate width of 28 μm. The three peaks in
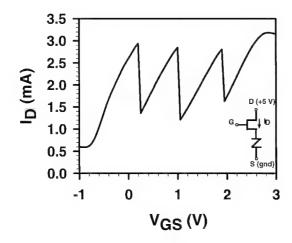
Figure 8 Measured transfer characteristics of a vertically-integrated 3-stack
resonant tunneling diode and heterojunction field effect transistor. The
inset shows the bias conditions for the measurement.

the drain current of the HFET correspond to the sequential switching of each of the three RTDs
in the stack. Note that a gate voltage of -1 V corresponds to a gate/drain bias of -6 V, indicating
a respectably high reverse-breakdown in the HFETs.

4.4 Lateral Resonant Tunneling Diodes

In order to increase the packing density of resonant tunneling devices for circuit applications
it is desirable to implement them in a lateral planar geometry. The fabrication of such lateral
resonant tunneling diodes (LRTDs) is complicated by both the precision lithography required to
define features with lateral dimensions on a scale where quantum effects are possible, and the
need for multiple epitaxial growth steps on these finely patterned wafers to produce the
heterostructures.   GSMBE and/or CBE are the most favorable epitaxial growth techniques for
this application due to the low growth temperatures employed and the ability to grow thin layers
with precision.

We have used GSMBE to demonstrate a planar integrated lateral double barrier
heterostructure exhibiting negative differential resistance for the first time [17]. The device
structure was grown in two steps. The first step consists of a 30 nm undoped InGaAs layer
followed by a 5 nm undoped InP cap layer. The wafer is removed from the GSMBE reactor and
a double line pattern with 15 to 20 nm linewidths and 30 to 40 nm line-to-line edge separation is
defined in photoresist using a novel fabrication procedure which allows the patterning of two
lines within the exposure of a single electron beam line [18]. An Ar+/Cl2 ion beam assisted etch
is used to transfer the pattern into the sample and through the InGaAs channel. The sample is
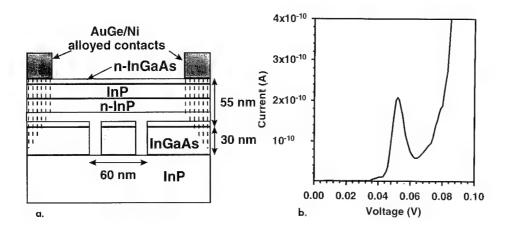
Figure 9 (a) Schematic cross section of the lateral double barrier heterostructure
device and (b) the measured I-V characteristics of the LRTD at 4.2 K.

carefully cleaned using solvents, an O_2 plasma clean and an HF acid dip prior to reloading into the GSMBE reactor. The remaining oxide on the sample is then desorbed in the reactor under a As flux (from precracked TBA) at a temperature of 540°C for 1 min. The structure is then completed with the growth of 5 nm of undoped InP, 20 nm of n-InP doped to 1×10^{18} cm^{-3} with Si, 20 nm of undoped InP and 5 nm of n-InGaAs doped to 5×10^{18} cm^{-3} with Si. A low growth rate of 0.5 μm/hr and a rapid substrate rotation rate (> 1 Hz) are used to facilitate the filling of the etched features. Ohmic contacts to the device are made using AuGeNi metalization followed by an anneal. A schematic cross-section of the complete LRTD structure is depicted in Fig. 9a. Figure 9b presents the I-V characteristics measured for one of these LRTD devices. A peak-to-valley current ratio as high as 3.5 has been obtained at 4.2 K. The small conduction band offset (0.25 eV) available in this material system and the lateral dimensions currently achieved limits the device to low temperature operation. Additional details regarding the electrical characterization of these devices are reported elsewhere [17,19].

5. CONCLUSIONS

The routine GSMBE growth of high performance heterojunction bipolar, field effect and resonant tunneling device structures has been demonstrated using organometallic replacements for arsine and phosphine. The use of thermally cracked TBA and TBP results in high quality epitaxial materials for both the $In_{0.48}Ga_{0.52}P/GaAs$ and $In_{0.53}Ga_{0.47}As/InP$ lattice matched materials systems. In addition, the routine use of CBr$_4$ and SiBr$_4$ vapor source dopants for these device structures has been demonstrated. Device results obtained using these sources are comparable, and in some cases superior, to those reported using hydride-based GSMBE, MOCVD and/or conventional MBE.

ACKNOWLEDGEMENTS

REFERENCES

1. M.B. Panish, J. Electrochem. Soc. **127**, p. 2729 (1980).
2. M.B. Panish and H. Temkin, Gas Source Molecular Beam Epitaxy: Growth and Properties of Phosphorus Containing III-V Heterostructures, Springer-Verlag, New York (1993).
3. E.A. Beam III, T.S. Henderson, A.C. Seabaugh and J.Y. Yang, J. Crystal Growth **116**, p. 436 (1992).
4. E.A. Beam III, H.F. Chau, T.S. Henderson, W. Liu and A.C. Seabaugh, J. Crystal Growth **136**, p. 1 (1994).
5. E.A. Beam III and H.F. Chau, accepted for publication in J. Crystal Growth 1996.
6. W. Liu, E.A. Beam III, T.S. Kim and A. Khatibzadeh, Int. J. High Speed Electronics and Systems, **5**, p. 411 (1994).
7. S.L. Jackson, S. Thomas, M.T. Fresina, D.A. Ahmari, J.E. Baker and G.E. Stillman, Proc. 6th Int. Conf. Indium Phosphide and Related Materials (1994) p. 57.
8. P.M. Asbeck, C.W. Farley, M.F. Chang, K.C. Wang and W.J. Ho, Proc 2nd Int. Conf. Indium Phosphide and Related Materials (1990) p. 2.
9. E. Tokumitsu, A.G. Dentai, C.H. Joyner and S. Chandrasekhar, Appl. Phys. Lett. **57**, p. 2841 (1990).
10. H.F. Chau and E.A. Beam III, unpublished.
11. H.F. Chau, H.Q. Tserng and E.A. Beam III, IEEE Microwave and Guided Wave Lett. **6**, p.129 (1996).
12. S.R. Bahl, J.A del Alamo, J. Dickmann and S. Schildberg, IEEE Trans. Electron Dev. **42**, p. 15 (1995).
13. U. Auer, R. Reuter, C. Heedt, H. Kunzel, W. Prost and F.J. Tegude, Proc 6th Int. Conf. Indium Phosphide and Related Materials (1994) p. 443.
14. A.C. Seabaugh, E.A. Beam III, A.H. Taddiken, J.N. Randall and Y.C. Kao, IEEE Electron Device Lett. **14**, p. 472 (1993).
15. A.C. Seabaugh, A.H. Taddiken, E.A. Beam III, J.N. Randall, Y.C. Kao and B. Newell, Electronics Lett. **29**, p. 1802 (1993).
16. A.C. Seabaugh, A.H. Taddiken, E.A. Beam III, J.N. Randall, Y.C. Kao and B. Newell, IEDM Tech. Dig. (1993) p. 419.
17. T.P.E. Broekaert, J.N. Randall, E.A. Beam III, G. Frazier, D. Jovanovic, B.L. Newell and B.D. Smith, 53rd Dev. Res. Conf. Digest (1995) p. 56.
18. J.N. Randall and B.L. Newell, J. Vac. Sci. Technol. **B12**, p. 3631 (1994).
19. T.P.E. Broekaert, J.N. Randall, E.A. Beam III, D. Jovanovic and B.D. Smith, to be published.

SELECTIVE-AREA EPITAXY AND IN-SITU ETCHING OF GaAs USING TRIS-DIMETHYLAMINOARSENIC BY CHEMICAL BEAM EPITAXY

N. Y. LI, and C. W. TU
ECE Department, University of California, San Diego, La Jolla, CA 92093-0407,
nli@sdcc3.ucsd.edu

ABSTRACT

In this study, we shall first report selective-area epitaxy (SAE) of GaAs by chemical beam epitaxy (CBE) using tris-dimethylaminoarsenic (TDMAAs), a safer alternative source to arsine (AsH_3), as the group V source. With triethylgallium (TEGa) and TDMAAs, true selectivity of GaAs can be achieved at a growth temperature of 470°C, which is much lower than the 600°C in the case of using TEGa and arsenic (As_4) or AsH_3. Secondly, we apply SAE of carbon-doped AlGaAs/GaAs to a heterojunction bipolar transistor (HBT) with a regrown external base, which exhibits a better device performance. Finally, the etching effect and the etched/regrown interface of GaAs using TDMAAs will be discussed.

INTRODUCTION

SAE of GaAs has been extensively studied by organometallic vapor phase epitaxy (OMVPE), metalorganic molecular beam epitaxy (MOMBE) and CBE for optoelectronic and electronic device applications [1,2], but in most cases, the extremely toxic gas source, AsH_3, is used. For safety considerations, a less hazardous and lower vapor pressure alternative that does not need precracking is highly desirable to replace AsH_3[3]. TDMAAs, with As directly bonded to N, is a promising alternative, which has been used in MOMBE [4], CBE [5], and MOCVD [6] recently. Since there are no As-H bonds, one can expect TDMAAs to be less toxic than AsH_3. Furthermore, TDMAAs source is in liquid form with a vapor pressure of 1.35 Torr [7] at room temperature, so the dispersion of TDMAAs is much slower than the release from a high-pressure cylinder of AsH_3.

For regrowth applications, two important issues should be considered to avoid degrading the regrown devices. One is that the oxide desorption and growth temperature of GaAs must be kept low but reasonable (400~550°C) to minimize the effect of dopant outdiffusion. The other is that the interface-state density of a regrown interface must be as low as possible; therefore, in-situ etching of GaAs prior to regrowth is necessary to obtain a clean etched/regrown interface. Our previous results show that the GaAs oxide layer can be removed efficiently at a low substrate temperature of 450°C under an uncracked TDMAAs flux [8]. The As-limited growth rate using TDMAAs is almost constant in the substrate temperature range of 370 to 465°C.

Recently, Asahi et al. discovered that TDMAAs has an etching effect on GaAs at substrate temperatures greater than 500°C [9]. The purpose of this work is therefore to investigate the SAE and in-situ etching of GaAs using TDMAAs to improve the microwave performance of HBTs. To achieve this goal, heavily carbon-doped (Al)GaAs external base layers are selectively regrown on an emitter-up HBT to reduce the base resistance (R_B) [11]. Two factors are expected to limit R_B. One is the coupling between the intrinsic and external base layers, so the growth behavior and profile of (Al)GaAs:C should be studied and optimized
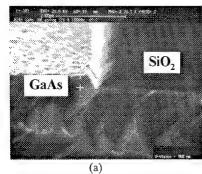
first. The other is the quality of the regrown interface between the intrinsic and external base layers. The presence of a high density of interface defects would result in carrier trapping and considerable resistance in the regrown interface. In-situ etching of GaAs using TDMAAs prior to regrowth should be helpful to reduce the interface-state density, so the TDMAAs etched/regrown interface of GaAs will be studied. In this paper, we first discuss SAE of (Al)GaAs:C for HBTs without in-situ etching. Then we investigate the effect of in-situ etching on the interface-state density.

EXPERIMENT

In this study experiments were performed in a modified Perkin-Elmer 425B CBE system, equipped with solid Ga, As_4, and gas lines for triethylgallium (TEGa), trimethylaluminum (TMAl), TDMAAs, diiodomethane (CI_2H_2), carbon-tetrabromide (CBr_4), and disilane (Si_2H_6). Details of this modified CBE system has been described elsewhere [8]. TEGa and TMAl are used as group-III precursors for the SAE of (Al)GaAs. TDMAAs is used as both SAE and etching source of GaAs. CI_2H_2 and CBr_4 are used as p-type carbon-doping sources for MBE-, MOMBE-, and CBE-grown GaAs:C. Here the V/III incorporation ratios are determined by the group III- and group V-induced oscillations of reflection high-energy electron diffraction (RHEED). The surface morphology, selectivity, and cross-section images of (Al)GaAs using TDMAAs are examined with a scanning electron microscope (SEM). Van der pauw Hall measurement is used to characterize the electrical property of carbon-doped (Al)GaAs epilayers. Capacitance-voltage (C-V) measurement is applied to evaluate the quality of etched/regrown GaAs interfaces .

RESULTS

1. SAE of (Al)GaAs:C using TDMAAs

(a)   (b)
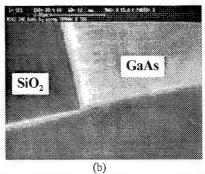
Fig. 1   SEM photographs for GaAs selective area growth: (a) using uncracked TDMAAs at 470-565°C, and (b) using cracked TDMAAs at 470-540°C.

Fig. 1 shows SEM photographs for (a) a selective GaAs epitaxial layer grown in the substrate temperature range of 470 to 565°C with a growth rate of 0.6 μm/hr using TEGa and uncracked TDMAAs. When the substrate temperature is lower than 470°C, a nonselective-

area growth of GaAs is observed. Furuhata et al. [12] and Bove et al. [1] reported that true selectivity of GaAs was achieved at a substrate temperature above 600°C using TEGa and As_4 by MOMBE and between 580 and 620°C using TEGa and AsH_3 by CBE, respectively. In our work, true selectivity of GaAs epitaxial layers with a growth rate of 0.6 μm/h can be achieved at a growth temperature as low as 470°C, indicating that TDMAAs is suitable for regrowth applications at a lower growth temperature. It should be mentioned here that true SAE of $Al_{0.25}Ga_{0.75}As$ layers with a growth rate of 0.5 μm/h can be also achieved at a substrate temperature between 470 and 530°C. At a growth temperature higher than 540°C, aluminum droplets appear on the SiO_2 surface, resulting in non-selective area growth.

The surface morphology of the regrown GaAs layer on the opening, however, is always rippled. This textured surface morphology is independent of V/III incorporation ratios between 1.8 to 4.4 in this growth temperature range, but a smooth surface morphology of regrown GaAs, shown in Fig. 1(b) can be achieved by cracking TDMAAs at 350°C. Recently we found that uncracked TDMAAs can etch GaAs with an etch rate of 0.3 μm/hr at 650°C [12], which agrees well with Villaflor et al.'s result [13], but no etching effect is observed when cracked TDMAAs is used. Therefore, we think this rough surface morphology observed in the regrown GaAs layer is attributed to the etching effect from uncracked TDMAAs.
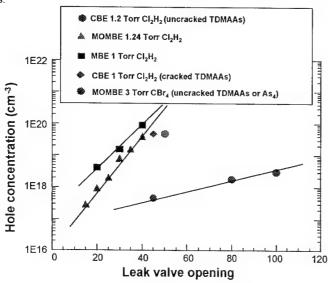
Fig. 2 Hole concentration of carbon-doped GaAs samples grown by MBE, MOMBE, and CBE using Cl_2H_2 and CBr_4 as a function of the leak valve setting.

Fig. 2 shows that the carbon incorporation efficiency using Cl_2H_2 is very low in the CBE-grown GaAs, compared to MBE- and MOMBE-grown GaAs. The highest hole concentration obtainable is only 3×10^{18} cm^{-3} at a leak valve setting of 100, but it can be increased by two orders of magnitude by thermally cracking TDMAAs at 350°C. The highest hole concentration achieved so far is 6.6×10^{19} cm^{-3}. When CBr_4 is used as a doping source,

however, the carbon incorporation efficiency in GaAs using uncracked TDMAAs is almost the same as using As_4. Further work needs to be done to clarify this difference between Cl_2H_2 and CBr_4.

2. Regrown external base of a novel HBT structure

Since we have demonstrated that true SAE of (Al)GaAs:C layers can be achieved at a lower substrate temperature between 470 and 530°C, we apply such SAE in regrowth of external base layers to improve the performance of HBTs. To achieve a complete coupling between the regrown external-base layers and the intrinsic-base layer of an HBT, lateral growth is highly desirable. Details about the SAE growth behavior of (Al)GaAs in the vicinity of the mask edges has been reported and optimized [15]. The V/III ratio for the growth of (Al)GaAs is chose to be near unity to result in a (311) A facet growth which can fill the undercut of the SiO_2 mask. Fig. 3 shows an SEM photograph and a schematic cross section of the SAE GaAs/$Al_{0.25}Ga_{0.75}As$:C layers in an undercut groove of a patterned GaAs substrate. This test sample has the same profile of a patterned HBT structure for regrowth. It shows that the lateral coupling between the GaAs substrate and GaAs/$Al_{0.25}Ga_{0.75}As$:C layers is quite good. Based on these results, GaAs/$Al_{0.25}Ga_{0.75}As$:C ($p \geq 4 \times 10^{19}$ cm^{-3}) external base layers with a thickness of 2800 Å are regrown on a patterned OMVPE-grown HBT structure. The base sheet resistance of the original and the regrown HBT are 350 and 132 $\Omega/\square$, respectively. Due to its wide energy bandgap, the regrown $Al_{0.25}Ga_{0.75}As$:C layer is a barrier layer for a better confinement of minority carriers. It also passivates the base, resulting in a lower surface recombination current, and a higher current gain than the original HBT [15].
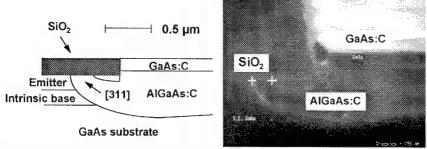
Fig. 3 An SEM photograph and a schematic cross-section of the SAE $Al_{0.25}Ga_{0.75}As$/GaAs:C layers grown in an undercut groove.

3. Etched/regrown GaAs interfaces

Since TDMAAs has an etching effect on GaAs, we shall investigate the etched/regrown interface of GaAs using TDMAAs. C-V measurement is performed on Au/n-GaAs Schottky diodes to study quantitatively etched/regrown interfaces of GaAs with different sample preparations described as below. First, a 0.5 μm-thick n-type GaAs (n=4×10^{17} cm^{-3}) buffer layer is grown on a (100) n^+ Si-doped GaAs substrate (n=2-4×10^{18} cm^{-3}) at 510°C using TEGa, As_4 and Si_2H_6. This sample is then taken out of the CBE chamber and exposed to air

for one day. It is then divided into three samples, labeled A, B, and C. Sample C is etched 200Å ex-situ by reactive-ion etching before being mounted on a Mo block and then loaded into the CBE chamber with samples A and B. Prior to regrowth, sample A is exposed to TDMAAs alone and samples B and C are exposed to As_4 at 600°C to desorb the oxide layers. After oxide desorption sample A is etched in-situ about 65Å by TDMAAs (10 minutes exposure at 600°C). Here, the etched depth is estimated from another etching study of TDMAAs on a patterned GaAs substrate with a SiO_2 mask [10]. A 0.15 μm-thick n-GaAs ($n=3x10^{17}$ cm^{-3}) is regrown subsequently on these three samples and the etched/regrown interfaces are formed. Finally a 1500Å-thick Au is evaporated to form the Schottky contact.
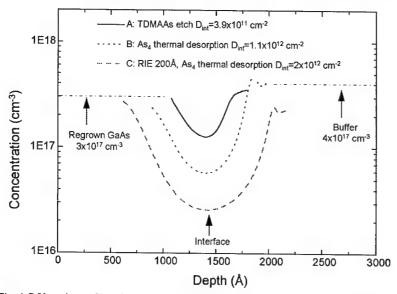
Fig. 4 C-V carrier profiles of three etched/regrown samples with different sample preparations.

Fig. 4 shows C-V carrier concentration profiles around the etched/regrown interfaces of samples A, B, and C. It is quite clear that the carrier depletion across the interface depends strongly on the sample preparation prior to regrowth. The interface-state densities (D_{int}) are estimated by integrating the carrier profiles, and they are $3.9x10^{11}$, $1.1x10^{12}$, and $2x10^{12}$ cm^{-2} for samples A, B, and C, respectively. Sample A has the lowest D_{int} among these three samples, indicating a clean interface can be achieved by the in-situ etching process using TDMAAs. Our preliminary result reported here, however, is higher than the best result reported by Mui et al. [16] using an in-situ Cl_2 etching process ($D_{int} \geq 0.86x10^{11}$ cm^{-2}). We believe this discrepancy is due to our in-situ TDMAAs etching process being not optimized. Further experiments with different in-situ etching/regrowth conditions are under investigation.

CONCLUSIONS

We have successfully achieved true selectivity of heavily carbon-doped CBE-grown (Al)GaAs layers at a growth temperature as low as 470°C using TEGa, TMAl, TDMAAs, and Cl_2H_2 as the carbon-doping source. A higher carbon incorporation efficiency and smooth surface morphology of GaAs:C layers can be obtained by thermally cracking TDMAAs at 350°C. An HBT with selectively regrown carbon-doped GaAs/$Al_{0.25}Ga_{0.75}$As external base layers is successfully fabricated. Compared to the original HBT structure, the device exhibits at least a 62% improvement in the base sheet resistance and a much higher DC current gain. The interface state density of the etched/regrown interface can be reduced when TDMAAs is applied to etch the GaAs surface prior to regrowth. Our results indicate that TDMAAs is a suitable alternative for both SAE and in-situ etching source in CBE for high-quality regrown devices.

ACKNOWLEDGMENTS

REFERENCES

1. P. Bove, K. Ono, K. Joshin, H. Tanaka, K. Kasai and J. Komeno, J. Crystal Growth **136** , p.261 (1994).
2. G. Mörsch, J. Gräber, M. Kamp, M. Hollfelder and H. Lüth, J. Crystal Growth **136**, p. 256 (1994).
3. D. A. Bohling, C. R. Abernathy, and K. F. Jensen, J. Crystal Growth **136**, p.118 (1994).
4. C. R. Abernathy, P. W. Wisk, D. A. Bohling, and G. T. Muhr, Appl. Phys. Lett. **60**, p.2421 (1992).
5. H. K. Dong, N. Y. Li, C. W. Tu, M. Geva, and W. C. Mitchel, J. Electron. Mater. **24**, p.69 (1994).
6. G. Zimmermann, H. Protzmann, T. Marschner, O. Zsebök, W. Stolz, E. O. Göbel, P. Gimmnich, J. Lorberth, T. Filz, P. Kurpas, and W. Richter, J. Cryst. Growth **129**, p.37 (1993).
7. H. Weingarten and W. A. White, J. Am. Chem. Soc. **850**, p.88 (1960).
8. H. K. Dong, N. Y. Li, W. S. Wong, and C. W. Tu, submitted to J. Vac. Sci. Technol. (1996).
9. H. Asahi, X. F. Liu, K. Inoue, D. Marx, K. Asami, K. Miki, and S. Gonda, J. Cryst. Growth **145**, p.668 (1994).
10. N. Y. Li, Y. M. Hsin, W. G. Bi, P. M. Asbeck, and C. W. Tu, unpublished.
11. K. Mitani, H. Masuda, K. Mochizuki and C. Kusano, IEEE Electron Device Lett. **EDL-13**, p.209 (1992).
12. N. Furuhata and A. Okamoto, J. Crystal Growth **112**, p.1 (1991).
13. H. K. Dong, N. Y. Li, W. S. Wong, and C. W. Tu, submitted to J. Vac. Sci. Technol. (1996).
14. A. B. Villaflor, H. Asahi, D. Marx, K. Miki, K. Yamamoto, S. Gonda, J. Cryst. Growth **150**, p.638 (1995).
15. N. Y. Li, H. K. Dong, Y. M. Hsin, T. Nakamura, P. M. Asbeck, and C. W. Tu, J. Vac. Sci. Technol. **B13** , p.664 (1995).
16. D. S. L. Mui, T. A. Strand, B. J. Thibeault, L. A. Coldren, P. M. Petroff and E. L. Hu, Inst. Phys. Conf. Ser. **141**, p.291 (1995).

INTRINSIC N-TYPE MODULATION DOPING IN InP-BASED HETEROSTRUCTURES

W.M. CHEN,* I.A. BUYANOVA,* A. BUYANOV,* W.G. BI** AND C.W. TU**
* Department of Physics and Measurement Technology, Linköping University, S-581 83 Linköping, SWEDEN, wmc@ifm.liu.se
** Department of Electrical and Computer Engineering, University of California, La Jolla, CA 92093-0407, USA

ABSTRACT

We propose and demonstrate a new doping approach, i.e. intrinsic doping, for n-type modulation doping in InP-based heterostructures. Instead of the conventional method of n-type doping by shallow donor impurities, grown-in intrinsic defects are utilized to provide the required doping without external doping sources. The success of this approach is clearly demonstrated by our results from InGaAs/InP heterostructures, where the required n-type doping in the InP barriers is provided by P_{In} antisites, preferably introduced during off-stoichiometric growth of InP at low temperatures (LT-InP) by gas source molecular beam epitaxy. A two-dimensional electron gas (2DEG) is shown to be formed near the InGaAs/InP heterointerface as a result of electron transfer from the LT-InP to the InGaAs active layer, from studies of Shubnikov-de Haas oscillations and photoluminescence. The concentration of the 2DEG is determined to be as high as 1.15×10^{12} cm^{-2}, where two subbands of the 2DEG are readily occupied.

INTRODUCTION

Selective or modulation doping represents one of the essential steps in fabrication of modern quantum structures and devices based on InP-based heterostructures, which are now well recognized as being among the most promising electronic material systems for applications in optoelectronics and high frequency electronics. Such doping has traditionally been done by extrinsic doping, i.e. by incorporating shallow impurity donor or acceptor dopants in the structures via diffusion or ion implantation or in situ incorporation during growth of the host crystal. There are, however, still many problems remaining, such as thermal instability, interdiffusion, implantation damage, memory effects, configurational metastability, etc. [1-3]. There will most likely be more problems emerging during the course of future development in growth and processing technology. These problems are and will be found to be unacceptable for certain devices, in particular those modern devices of lower dimensionality and of submicron or nanometer size, where a high precision of doping and interface profiles is crucial. A large international effort has therefore been devoted to seek for both a better control of the existing doping processes and a better doping mechanism. Most of the research work reported so far on this issue have, however, been largely limited to the extrinsic doping concept.

In contrast, we propose in this work a new and different approach for n-type modulation doping in InP-based heterostructures, where intrinsic defects are utilized to provide the required doping without an external doping source. The success of such an intrinsic doping concept is clearly evident from our results obtained from InGaAs/InP HEMT structures, where all the layers were intentionally undoped and were grown at a normal growth temperature 480 °C except for the top InP layer which was grown at 265 °C by gas source molecular beam epitaxy (GS-MBE). A two-dimensional electron gas (2DEG) was formed near the InGaAs/InP heterointerface as a result of electron transfer from the LT-InP to the InGaAs active layer, and was observed by studies of Shubnikov-de Haas (SdH) oscillations and photoluminescence (PL).

The SdH studies reveal a high concentration of the 2DEG, up to about 1.15×10^{12} cm^{-2}, where two subbands of the 2DEG are readily occupied. For comparison reference samples with identical structures were grown, entirely at 480 °C, where the 2DEG concentration (due to residual doping) was shown to be an order of magnitude lower.

The mechanism responsible for the n-type modulation doping by using GS-MBE LT-InP can be understood from our earlier studies of LT-InP epilayers [4-6]. In those studies, the free electron concentration of the LT-InP films was found to monotonically increase with decreasing growth temperatures. At 265 °C a saturation electron concentration of ~3x10^{18} cm^{-3} is reached when the LT-InP exhibits a metallic n-type conduction. The reason for this high n-type conductivity was shown to be due to the abundant presence of P_{In} antisites, which are deep double donors. The high electron concentration is provided by the auto-ionization of the P_{In} antisites via its first ionization stage, i.e. the (0/+) level, which is located at E_c+0.12 eV resonant with the conduction band [4-6]. In this work, such unique properties of LT-InP are for the first time employed to provide modulation doping in InP-based heterostructures and, to our knowledge, in any semiconductors in general.

EXPERIMENTAL

The lattice-matched In$_{0.53}$Ga$_{0.47}$As/InP heterostructures studied in this work were grown by GS-MBE, on semi-insulating Fe-doped InP substrate. The design of the structures is shown in Fig.1. The entire structures were intentionally undoped and were grown at a normal temperature of 480 °C except the top InP layer which was grown at 265 °C. These samples will be referred below as InGaAs/LT-InP structures. A reference sample was also grown with an identical structure except that the top InP layer was in this case grown at 480°C. Studies of SdH oscillations and PL were performed with the aid of a 5T magneto-optical system.

(a) GROWTH TEMPERATURE

(b) DESIGN OF THE STRUCTURES

LT-InP 500 Å	InP 100 Å	InGaAs 400 Å	InP 5000 Å	SI-InP

(c) ENERGY BAND DIAGRAM
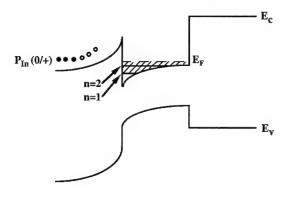
Fig.1 (a) The growth temperature of the InGaAs/LT-InP heterostructure (the solid curve) and of the reference sample (the dashed curve). (b) The design of the InGaAs/InP heterostructures studied in this work. (c) A schematic picture of the energy band diagram for the InGaAs/LT-InP structure. For simplicity only two subbands of the 2DEG are drawn in the figure. The filling of the 2DEG is depicted by the shaded region.

Lithographically defined Hall bars with six In ohmic contacts were fabricated on the samples for electrical SdH measurements. Hall effect measurements were done at 0.2 T, with the Van-der-Pauw geometry. All transport data were taken by a low-amplitude dc-current (1-5 μA) technique. PL, excited at 2 mW by the 6328 Å line of a He-Ne laser, was spectrally dispersed by a grating monochromator and was collected by a cooled Ge-detector.

RESULTS AND DISCUSSION

In Fig.1 we first show schematic pictures of the InGaAs/LT-InP structure together with a growth temperature ramp and a corresponding energy band diagram. Due to electron transfer from the LT-InP barrier to the InGaAs active layer, a notch potential is formed near the heterointerface where the 2DEG is confined (Fig.1(c)). For simplicity only two subbands of the 2DEG are drawn in the figure. The filling of the 2DEG is depicted by the shaded region. A chart of growth temperature for the reference sample is also shown in Fig.1(a) as the dashed curve for easy reference.

Now we shall first show that electronic properties of the InGaAs/LT-InP structure are markedly different from those of the reference sample. Then we shall provide experimental evidence that this difference is a direct consequence of a 2DEG formed in the InGaAs channel due to the intrinsic doping in the LT-InP.

The SdH oscillation spectrum taken at 1.5 K from the InGaAs/LT-InP structure is shown by the upper curve in Fig.2, with the external magnetic field normal to the heterointerface plane. An angular dependence study of the SdH oscillations clearly elucidates the 2D character of the free carriers (a 2DEG to be shown below) where the period of the SdH oscillations obeys a cosine relation of the relative angle between the magnetic field and the direction normal to the conducting layer. It can clearly be seen that there are more than one period of the magneto-resistance oscillations vs. reciprocal magnetic field. A detailed analysis of the SdH oscillations
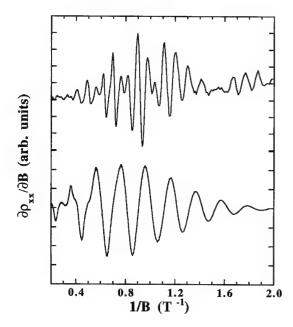
Fig.2 SdH oscillation spectra taken at 1.5 K in dark from the InGaAs/LT-InP structure (the upper curve) and the reference sample (the lower curve), with the external magnetic field normal to the heterointerface plane. The additional structure at low reciprocal magnetic fields is due to spin splittings.
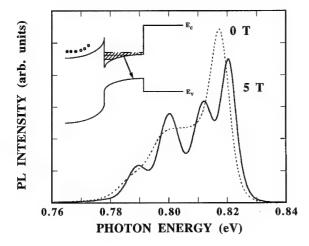
Fig.3 PL spectra at 1.5 K obtained from the InGaAs/LT-InP structure, at zero magnetic field (the dashed curve) and 5 T (the solid curve). In the insert, the arrow across the InGaAs bandgap indicates the PL transition between the 2DEG and photo-excited holes upon optical excitation.

reveals that two subbands of the 2DEG are readily occupied. The sheet concentrations of the first and second subbands of the 2DEG are determined to be $n_1 = 6.75 \times 10^{11}$ cm^{-2} and $n_2 = 4.75 \times 10^{11}$ cm^{-2}, respectively, yielding a total sheet concentration of 1.15×10^{12} cm^{-2}. This is deduced from an analysis of the period in reciprocal magnetic field $\Delta(1/B) = 2e/hn_i$, with the aid of Fourier transformation of the SdH data. Here n_i denotes the sheet concentration of free carriers for the ith subband, e is the electron charge and h is the Planck's constant.

The SdH spectrum from the reference sample, taken under the same experimental conditions, is shown by the lower curve in Fig.2 for comparison. Only a single and much larger period of the magneto-resistance oscillations is observed, reflecting a much lower carrier concentration (due to the residual doping). A detailed analysis of the SdH data reveals the concentration in the reference sample to be 2.37×10^{11} cm^{-2}, where only one subband is partially occupied. This value is about an order of magnitude lower as compared to the 2DEG density in the InGaAs/LT-InP structures discussed above. The much higher concentration of the 2DEG in the InGaAs/LT-InP structure can thus be directly attributed to the presence of the LT-InP in the structure, since the only difference between the two samples is the growth temperature of the top InP layer.

There are in principle two parallel conducting channels, i.e. the LT-InP barrier and the InGaAs active layer, which can possibly contribute to the magneto-transport measurements of the 2DEG. A possible contribution from the LT-InP layer can, however, be safely ruled out based on the following experimental facts. Firstly, the electron mobility $\mu_e \approx 1.3 \times 10^4$ cm^2/Vs obtained by the Hall measurements is much higher than $\mu_e \approx 5 \times 10^2$ cm^2/Vs determined independently for the LT-InP layer grown at the same temperature (i.e. 265 °C).

Further support is given by PL studies of the InGaAs/LT-InP structure. In Fig.3 we show PL spectra obtained from the structure at 0 T and 5 T. Optically detected quantum oscillations identical to the SdH oscillations (the upper curve in Fig.2) were observed by detecting this PL emission at the highest photon energy, indicating that the PL emission originates from the same 2DEG which give rise to the electrical SdH oscillations. The splitting of the PL emission in the magnetic field (Fig.3) therefore represents the Landau level splitting of the monitored 2DEG. The electron mass value $m_e^* \approx 0.05m_0$, determined from the Landau level splitting observed in the PL experiments (Fig.3), differs from the electron mass value $m_e^* = 0.07m_0$ in InP but lies

well within the range $m_e^* \approx (0.04\text{-}0.06)m_0$ of the electron effective mass determined for $In_{0.53}Ga_{0.47}As$ [7]. In addition, the photon energy of the PL emission at around 0.8 eV (Fig.3) is consistent with the bandgap of $In_{0.53}Ga_{0.47}As$. The PL spectrum resembles that observed in similar InGaAs/InP and InGaAs/AlInAs HEMT structures [8,9], where the conventional shallow donors were employed to achieve n-type modulation doping, and was attributed to the recombination between the 2DEG and the photo-excited holes in the InGaAs layer (see the insert in Fig.3).

All the experimental facts given above lead to the conclusion that the SdH oscillations shown in Fig.2 (the upper curve) arise from a dense 2DEG in the InGaAs active layer, formed as a result of electron transfer from the LT-InP barrier.

The unique features of the intrinsic doping approach proposed in this work provide many advantages over the conventional doping by shallow impurity dopants. First of all, no external doping source is needed to be installed in the growth chamber, which implies a reduced risk of side effects such as contamination and memory effects. In addition, a much higher efficiency in the electron transfer from the doped region to the active layer is expected for deep resonant donors such as the P_{In} antisites. This results from a much higher position of the corresponding donor level, well above the bottom of the conduction band, in contrast to the usual case of shallow impurities when the donor level is slightly below the bottom of the conduction band. The obvious disadvantage is the extreme and perhaps inconvenient growth conditions at low temperatures and the growth temperature interruption. Further investigations are now in progress to understand detailed physical properties connected to the intrinsic doping in InP-based heterostructures and to explore a full potential in device applications as an alternative doping mechanism.

SUMMARY

We have proposed a novel modulation doping approach in InP-based heterostructures by employing intrinsic defects such as the P_{In} antisites, without invoking an external doping source. The success of this approach is clearly demonstrated by our results from the InGaAs/LT-InP heterostructures, where the required n-type doping in the InP barriers is efficiently provided by the P_{In} antisites preferably introduced during off-stoichiometric growth of LT-InP by GS-MBE. The formation of the resulting 2DEG (as high as 1.15×10^{12} cm^{-2}) near the InGaAs/InP heterointerface, due to electron transfer from the intrinsically doped InP barrier, is evident from studies of SdH oscillations and PL. Though it has only been demonstrated for InGaAs/InP heterostructures, the principle of the intrinsic doping concept is in fact rather general and can be extended to applications in other electronic material systems.

ACKNOWLEDGEMENTS

REFERENCES

1. P. Müller, T. Bachmann, E. Wendler and W. Wesch, J. Appl. Phys. **75**, 3814 (1994).

2. S.L. Jackson, M.T. Fresina, J.E. Baker and G.E. Stillman, Appl. Phys. Lett. **64**, 2867 (1994).

3. J.A. Wolk, W. Walukiewicz, M.L.W. Thewalt and E.E. Haller, Phys. Rev. Lett. **68**, 3619 (1992).

4. B.W. Liang, P.Z. Lee, D.W. Shih and C.W. Tu, Appl. Phys. Lett. **60**, 2014 (1992).

5. P. Dreszer, W.M. Chen, K. Seendripu, J.A. Wolk, W. Walukiewicz, B.W. Liang, C.W. Tu and E.R. Weber, Phys. Rev. **B47**, 4111 (1993).

6. W.M. Chen, P. Dreszer, A. Prasad, A. Kurpiewski, W. Walukiewicz, E.R. Weber, E. Sörman, B.Monemar, B.W. Liang and C.W. Tu, J. Appl. Phys. **76**, 600 (1994).

7. C.K. Sarkar, R.J. Nicholas, J.C. Portal, M. Razeghi, J. Chevrier and J. Massies, J. Phys. **C18**, 2667 (1985).

8. D.G. Hayes, M.S. Skolnick, D.M. Whittaker, P.E. Simmonds, L.L. Taylor, S.J. Bass and L. Eaves, Phys. Rev. **B44**, 3436 (1991).

9. Yong-Hang Zhang, De-Sheng Jiang, R. Cingolani and K. Ploog, Appl. Phys. Lett. **56**, 2195 (1990).

OXYGEN-RELATED DEFECTS IN HIGH PURITY MOVPE AlGaAs

J.M. Ryan, T.F. Kuech, and K.L. Bray
Department of Chemical Engineering, University of Wisconsin, Madison, WI 53706

ABSTRACT

The near-infrared photoluminescence of high purity, nominally undoped MOVPE AlGaAs was investigated as a function of growth temperature, aluminum content and hydrostatic pressure. Two PL bands, observed at ~1.1 eV and ~0.8 eV independent of aluminum content, were attributed to oxygen-related defects based on the correlation of emission intensity and oxygen concentration. Hydrostatic pressure experiments, along with the measurement temperature dependence, suggest that the ~0.8 eV band is due to emission from an oxygen-related mid-gap level to a shallow acceptor or the valence band, depending on temperature. A tentative defect model based on the off-center O_{As} defect in bulk GaAs and variations in the number of nearest neighbor aluminum atoms is proposed to explain the two PL bands and the dependence of their relative intensity on aluminum content.

INTRODUCTION

Oxygen is a common impurity in III-V semiconductors. Its behavior has been best characterized in GaP where oxygen is known to enter substitutionally for P and form complexes with cations such as Cd and Zn [1]. In addition to luminescence features associated with the isolated O_P defect, strong red luminescence results from donor-acceptor and bound exciton transitions associated with these complexes.

The incorporation of oxygen in GaAs has been more controversial. The presence of oxygen has long been believed to lead to shallow impurity compensation in bulk GaAs. A definitive picture of the molecular center responsible for the compensation has only recently been developed on the basis of localized vibrational mode studies [1]. These studies indicated that an oxygen concentration of ~10^{15} cm^{-3} is present and that oxygen enters both interstitially and in an off-center substitutional manner on As sites. Temperature dependent LVM studies revealed that the electrically active off-center substitutional oxygen defect has negative U character. Interstitial oxygen is electrically inactive.

In contrast to bulk GaAs, oxygen has not been observed in MOVPE (and MBE) GaAs. Oxygen is undetectable by SIMS even when O_2 or H_2O are deliberately introduced in the MOVPE growth ambient of GaAs [2]. Significant levels of oxygen, however, are observed in MOVPE AlGaAs [3]. The appreciable oxygen incorporation found in AlGaAs can be attributed to the strong bonding between aluminum and oxygen. Trace amounts of O_2 or H_2O in the growth environment and the presence of aluminum alkoxides in typical aluminum precursors are the most common sources of oxygen. Oxygen has generally been viewed as an undesirable impurity in AlGaAs and other III-V materials because of its tendency to compensate shallow donors and reduce luminescence efficiency. As a result, much attention has been focused on developing MOVPE growth techniques for minimizing oxygen incorporation.

Recently, however, there has been substantial interest in intentional oxygen doping of MOVPE materials. This interest is due to the semi-insulating and fast carrier trapping properties that result from the oxygen-related deep levels. Most of the intentional oxygen doping work has

27

considered MOVPE GaAs and has involved the use of aluminum alkoxide oxygen doping sources. Controlled oxygen doping at concentrations ranging from $\sim 10^{15}$ cm^{-3} to $\sim 10^{20}$ cm^{-3} has been demonstrated and it has been shown that significant concentrations of aluminum are co-incorporated. Characterization studies have indicated that multiple oxygen-related deep levels are present in these materials and that both electrically active and inactive oxygen is present [4,5].

In order to better understand and control the nature of oxygen-related defects, it is important to develop a clear picture of the electronic defect levels and molecular configurations of oxygen in MOVPE GaAs. The crucial role of aluminum in promoting the incorporation of oxygen suggests that analogies should exist between the defect structure of oxygen-doped GaAs and nominally undoped AlGaAs that contains unintentional oxygen. In this paper, we present the results of near-infrared photoluminescence (NIR-PL) studies of high purity MOVPE AlGaAs. We show that two NIR PL bands are attributable to oxygen and have intensities that vary with growth temperature and alloy content. A tentative model of the oxygen-related defect centers responsible for the PL bands is presented. Temperature and pressure dependent PL studies are used to gain insight into the electronic assignment of the two PL transitions.

EXPERIMENT

The preparation and bandedge PL of the samples used in this study have been previously described in detail [3]. High purity, nominally undoped samples of $Al_xGa_{1-x}As$ (x = 0.05, 0.30, 0.45, and 0.75) were grown in a conventional horizontal, low pressure (78 Torr) reactor.

$(CH_3)_3Ga$, $(CH_3)_3Al$, and AsH_3 were used as growth precursors with H_2 as the carrier gas. The layers were grown on semi-insulating Cr-doped GaAs substrates oriented along the <100> direction tilted $2°$ towards the nearest <110> azimuth. The V/III ratio was 80 and the growth rate for all layers was nominally 0.05 μm/min. The aluminum content, growth temperatures, SIMS oxygen concentration and electrical characteristics of the samples used in this ivestigation are summarized in Table 1.

NIR-PL was excited using the 514 nm line of an argon ion laser (2 W/cm^2) and detected by a 1 m. monochromator equipped with a photomultiplier tube,

Table I. The growth conditions, oxygen concentration and C-V results for the samples used in this investigation.

Composition	Growth Temperature (°C)	N_A-$N_D{}^a$ C-V Measurement (10^{16} cm^{-3})	[O] (10^{17} cm^{-3})^{b,c}
$Al_{0.05}Ga_{0.95}As$	600	0.4 (n-type)	4.5 (c)
	650	0.7 (n-type)	3.0 (c)
	700	1.0 (n-type)	0.9 (b)
	750	1.0 (n-type)	0.5 (c)
$Al_{0.30}Ga_{0.70}As$	600	0.4	15.0 (b)
	650	0.3	9.0 (b)
	700	0.7	3.0 (b)
	750	0.4	1.5 (b)
$Al_{0.45}Ga_{0.55}As$	600	1.0	35.0 (c)
	650	1.0	20.0 (c)
	700	4.0	6.0 (b)
	800	2.0	1.0 (c)
$Al_{0.75}Ga_{0.25}As$	600	depleted	300.0 (c)
	650	depleted	150.0 (c)
	700	20.0	100.0 (c)
	800	40.0	20.0 (c)

a) Samples are p-type unless noted.
b) SIMS data from reference 3
c) Extrapolation of trends obtained from SIMS data in reference 3

Ge-detector or PbS detector. An overall detection range of 0.45 to 2.4 eV was used in the study. Spectra measured with the Ge or PbS detectors were obtained using conventional lock-in amplifier techniques. The samples were mounted in a variable temperature closed cycle refrigerator capable of providing tempertures ranging from 12 - 300 K. High pressure PL measurements were obtained by pressurizing samples in a diamond anvil pressure cell using a 4:1 ethanol:methanol pressure fluid and a ruby pressure calibrant. All spectra have been corrected for system response.

RESULTS AND DISCUSSION

Low Temperature Near-Infrared Photoluminescence of MOVPE AlGaAs

Two NIR-PL bands, near 0.8 eV and 1.1 eV, are observed in MOVPE AlGaAs. Since the two bands are not observed in MOVPE GaAs and oxygen is one of the principal impurities present in AlGaAs, but not in GaAs; we attribute the bands to the unintentional oxygen present in AlGaAs. Other studies have also attributed the ~0.8 eV PL band in MOVPE AlGaAs to an oxygen-related defect [6,7]. The overall and relative intensities of the two oxygen-related NIR-PL bands varied with growth temperature and alloy composition. Figure 1 shows the evolution of the 12 K PL spectrum with growth temperature for $Al_{0.75}Ga_{0.25}As$. At low growth temperatures, both NIR bands were observed and had comparable intensities. As the growth temperature was increased, the intensities of both bands decreased and eventually quenched. The ~1.1 eV band was observed to quench at a lower growth temperature than the ~0.8 eV band. Note that the overall decrease in NIR-PL intensity correlates with the decrease in oxygen concentration with growth temperature indicated in Table 1. Similar effects were observed in the other alloy compositions at slightly different growth temperatures. We generally found that the quenching of the ~1.1 eV band relative to the ~0.8 eV band and the overall quenching of
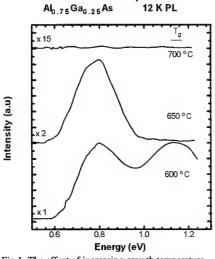
Fig 1. The effect of increasing growth temperature on the NIR-PL of $Al_{0.75}Ga_{0.25}As$ is shown.
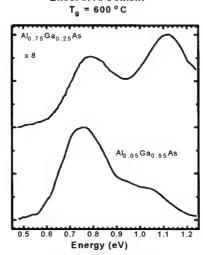
Fig. 2 The effect of increasing Al content on the NIR-PL of AlGaAs is shown.

29

oxygen-related NIR PL occurred at lower growth temperatures as the aluminum content was increased.

The relative intensities of the two oxygen-related NIR PL bands also varied with alloy composition. Figure 2 shows 12 K NIR spectra of samples of $Al_{0.05}Ga_{0.95}As$ and $Al_{0.75}Ga_{0.25}As$ grown at 600 °C. The figure illustrates the general trend observed in the study that the ~1.1 eV band gains intensity relative to the ~0.8 eV band as the aluminum content was increased at a given growth temperature.

Tentative Molecular Model of Oxygen-Related Defect Centers

Unambiguous identification of molecular centers responsible for deep levels in semiconductors is a challenging problem and it is normally difficult to be definitive. We present a preliminary model that appears to be consistent with work completed to date, but which we cannot definitively prove at this time. On-going studies will seek to further clarify the model.

The system with defects possibly analogous to the oxygen-related defects in MOVPE AlGaAs is bulk oxygen-doped GaAs. An electrically inactive interstitial oxygen defect and an electrically active off-center substitutional (oc-O_{As}) defect have recently been identified [1]. The latter defect configuration, shown in Figure 3a, consists of a bridging Ga-O-Ga bond and a molecular Ga-Ga bond. The Ga-Ga bond is thought to be responsible for the electrical activity of the defect [1].

The required presence of Al for oxygen incorporation in MOVPE material indicates that the strong Al-O bond acts as a driving force for oxygen incorporation. The very similar lattice constants of GaAs and AlGaAs lead us to believe that the molecular configuration of oxygen will be similar in the two systems. Accordingly, we propose that oxygen introduces the off-center defect configuration illustrated in Figure 3b into MOVPE AlGaAs. The defect consists of an off-center oxygen with a variable number of nearest neighbor Al atoms. Since aluminum is essential for oxygen incorporation, it is highly likely that at least one nearest neighbor aluminum is associated with the defect. We further propose that distinct defect centers which differ in the number of nearest neighbor Al atoms are responsible for the two NIR PL bands observed in MOVPE AlGaAs.

If we work within the context of this model, the data suggest that we can be more specific about the number of nearest neighbor Al atoms associated with the defects that lead to each of the NIR PL bands. If one applies a random alloy model to $Al_{0.75}Ga_{0.25}As$, one finds 0.4% of the As sites have the OGa_4 configuration, 4.7% are $OAlGa_3$, 21.1% are OAl_2Ga_2, 42.2% are OAl_3Ga and 31.6% are OAl_4. If one of the nearest neighbors is constrained to be Al, the probabilities shift to 0% OGa_4, 1.6% $OAlGa_3$, 14.1% OAl_2Ga_2, 42.2% OAl_3Ga, and 42.2% OAl_4. These results suggest that at least two, and probably three and four, nearest neighbor Al are associated with the oxygen-related defects responsible for the two NIR PL bands in $Al_{0.75}Ga_{0.25}As$.

The similar energy and shape of the two PL bands over the series of samples suggests that the same defect centers are present in all of the samples and that the concentration, not the identity, of the defect centers vary with growth conditions and alloy composition. This statement necessarily implies a strong (non-random) preference of oxygen for nearest neighbor Al atoms in low Al alloy compositions. Since the ~1.1 eV band gains relative to the ~0.8 eV band as the Al composition increases, we suggest that the center responsible for the ~1.1 eV band has one more nearest neighbor Al than the center responsible for the ~0.8 eV band.

We emphasize that the above considerations are tentative and further work is needed to clarify the molecular defect configurations responsible for the two NIR PL bands. Our model, for example, does not consider the possibility of multiple charge states of a single defect configuration as the origin of the two NIR PL bands. It is interesting to note, however, that a preliminary NIR PL spectrum of n-type $Al_{0.30}Ga_{0.70}As$ ([Si] = 6 x 10^{16} cm^{-3}) is very similar to the spectrum obtained from p-type $Al_{0.30}Ga_{0.70}As$ in this study.
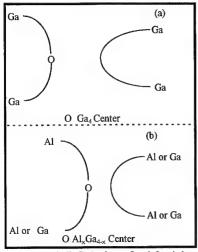
Fig. 3 (a) In bulk GaAs the oc O_{As} defect is known to be electrically active. (b) We propose that similar defect structures are electrically active in MOVPE AlGaAs.
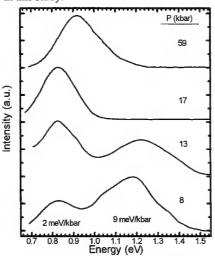
Fig 4. The effect of hydrostatic pressure on the NIR-PL in $Al_{0.30}Ga_{0.70}As$ is shown.

Effect of Pressure on Near-Infrared Photoluminescence

We have completed preliminary high pressure NIR PL studies of $Al_{0.05}Ga_{0.95}As$ and $Al_{0.30}Ga_{0.70}As$ at 40 K. The results for $Al_{0.30}Ga_{0.70}As$ are shown in Figure 4. The ~1.1 eV PL band shifted significantly to higher energy with pressure and quenched between 13 and 17 kbar, a pressure range which coincides with the crossover of $Al_{0.30}Ga_{0.70}As$ to indirect behavior. The band also appeared to broaden and change shape as pressure was applied. This may be evidence that multiple transitions contribute to the ~1.1 eV PL band. The ~0.8 eV PL band showed a much smaller shift with pressure and was still observed at 59 kbar, the highest pressure of the study. No unusual behavior was observed for this band as the sample passed through the direct-indirect crossover.

Assignment of the Near-Infrared Photoluminescence

The data obtained to date permit us to speculate on the electronic origin of the ~0.8 eV PL band. The insensitivity of the energy of the band to alloy composition and the small pressure shift indicate that the transition responsible for the band does not originate in the conduction band. Two other possibilities are viable: a mid-gap defect to valence band transition or an internal transition of the defect center. The variation of the ~0.8 eV band in $Al_{0.05}Ga_{0.95}As$ with temperature (not shown) indicates a constant peak energy of 0.775 eV below 100 K, followed

31

by a gradual increase to a constant value of 0.803 eV above 175 K. The ~28 meV difference in peak energy in the high and low temperature regimes is very close to the ionization energy of carbon, the principal shallow impurity in our samples. Consequently, the data suggest that at low temperature the ~0.8 eV band is due to a transition from a mid-gap defect level to a neutral carbon acceptor level. As the temperature is increased and carbon ionizes, the transition occurs from the mid-gap defect level to the valence band. Although this assignment is tentative, it is difficult to explain the temperature dependence with an assignment based on an internal transition.

At this time, we are not sure of the assignment of the ~1.1 eV PL band. The band shows the unusual behavior of shifting strongly to higher energy with pressure, but showing no shift in energy with alloy composition. Further work is needed to understand this result.

CONCLUSIONS

We have observed two broad oxygen-related deep level near-infrared photoluminescence bands (peak energies ~0.8 and ~1.1 eV) in nominally undoped MOVPE $Al_xGa_{1-x}As$. We found that the energies of the two bands were insensitive to growth temperature (600 - 750 °C) and alloy composition (x = 0.05, 0.30, 0.45, 0.75). The intensities of both bands decreased with increasing growth temperature and correlated with the oxygen concentration of the samples. The ~1.1 eV band quenched at a lower growth temperature than the ~0.8 eV band for all alloy compositions. A tentative defect model based on analogy to the off-center, substitutional OGa_4 defect in bulk GaAs was proposed. In the model, off-center OAl_xGa_{4-x} centers were proposed. The variation of the relative intensity of the two PL bands with growth conditions suggests that OAl_3Ga and OAl_4 centers are responsible for the ~0.8 and ~1.1 eV PL bands, respectively. Temperature and pressure dependent PL studies suggest that the ~0.8 eV PL band is due to a transition from a mid-gap oxygen defect level to carbon acceptors (low T) or the valence band (high T).

ACKNOWLEDGEMENTS

REFERENCES

1. *Deep Centers in Semiconductors*, ed. S.T. Pantelides (Gordon and Breech Science Publishers, 1992).
2. D.W. Kisker, J.N. Miller and G.B. Stringfellow, Appl. Phys. Lett. **40** 615 (1982).
3. T.F. Kuech, R. Potemski, F. Cardone and G. Scilla, J. Electron. Mater. **21** 341 (1992).
4. J.W. Huang, D.F. Gaines, T.F. Kuech, R.M. Potemski and F. Cardone, J. Electron. Mater. **23** 659 (1994).
5. Y. Park and M. Skowronski, J. Appl. Phys. **76** 5813 (1994).
6. M.J. Tsai, M.M. Tashima and P.L. Moon, J. Electron. Mater. **13** 437 (1984).
7. S. Sinha, A.K. Srivastava, S. Banerjee and B.M. Arora, Phys. Rev. B **44** 10941 (1991).

THE GROWTH AND DOPING OF Al(As)Sb BY METAL-ORGANIC CHEMICAL VAPOR DEPOSITION

R. M. Biefeld, A. A. Allerman, and S. R. Kurtz
Sandia National Laboratory, Albuquerque, New Mexico, 87185, USA

ABSTRACT

AlSb and $AlAs_xSb_{1-x}$ epitaxial films grown by metal-organic chemical vapor deposition were successfully doped p- or n-type using diethylzinc or tetraethyltin, respectively. AlSb films were grown at 500 °C and 76 torr using trimethylamine or ethyldimethylamine alane and triethylantimony. We examined the growth of AlAsSb using temperatures of 500 to 600 °C, pressures of 65 to 630 torr, V/III ratios of 1-17, and growth rates of 0.3 to 2.7 µm/hour in a horizontal quartz reactor. SIMS showed C and O levels below 2×10^{18} cm^{-3} and 6×10^{18} cm^{-3} respectively for undoped AlSb. Similar levels of O were found in $AlAs_{0.16}Sb_{0.84}$ films but C levels were an order of magnitude less in undoped and Sn-doped $AlAs_{0.16}Sb_{0.84}$ films. Hall measurements of $AlAs_{0.16}Sb_{0.84}$ showed hole concentrations between 1×10^{17} cm^{-3} to 5×10^{18} cm^{-3} for Zn-doped material and electron concentrations in the low to mid 10^{18} cm^{-3} for Sn-doped material. We have grown pseudomorphic InAs/InAsSb quantum well active regions on AlAsSb cladding layers. Photoluminescence of these layers has been observed up to 300 K.

INTRODUCTION

AlSb and $AlAs_xSb_{1-x}$ are of interest for their potential application in a variety of optoelectronic devices such as infrared detectors, resonant tunneling diodes, and laser diodes.[1-4] We are exploring the synthesis of these materials by metal-organic chemical vapor deposition (MOCVD) for their use as optical confinement materials in 2-6 µm, mid-infrared optoelectronic and heterojunction devices. Emitters in this wavelength range have potential uses as chemical monitors and in infrared countermeasures.[1-4] Although devices using $AlAs_xSb_{1-x}$ have been successfully prepared by molecular beam expitaxy,[2,3] there have been no reports to date of their successful use in devices when prepared by metal-organic chemical vapor deposition (MOCVD). We are aware of two previous reports of the successful growth of $AlAs_xSb_{1-x}$ by MOCVD.[4,5] In one of those reports [5], no mention was made of the electrical quality or the impurity level of the materials. Although there have been several reports by others of the growth of AlSb by MOCVD,[5-9] again very little mention has been made regarding the purity of the materials. It is well known that Al containing materials prepared using MOCVD tend to have larger concentrations of both O and C impurities when compared to the Ga containing analogue.[10,11] The presence of these impurities in Al containing semiconductors is due to the strength of the bond between Al and O or C when compared to the bond strength of Al to P, As, or Sb.[10,11] In this work we have taken an analogous approach to that used for improving the carbon concentration in AlGaAs where trimethylamine alane (TMAA) and triethylgallium (TEGa) were used to prepare high purity AlGaAs by using TMAA or ethyldimethylamine alane (EDMAA) and triethylantimony (TESb) to prepare AlSb by MOCVD.[12,13] Herein we describe the preparation of thin films of n- and p-type AlSb and $AlAs_xSb_{1-x}$ grown on GaAs and InAs substrates as well as the growth of InAsSb/InAs multiple quantum well active regions on top of these cladding layers.

EXPERIMENTAL

This work was carried out in a previously described MOCVD system.[14] TMAA, TESb and 100% arsine were the sources for Al, Sb and As respectively. TEGa was used to grow a 1000Å to 2500Å GaSb cap on all samples to keep the $AlAs_xSb_{1-x}$ layer from oxidizing. Hydrogen was used as the carrier gas at a total flow of 9 slpm. P-type doping was accomplished using 200 sccm to 500 sccm of diethylzinc (DEZn) diluted to 400 ppm in hydrogen. N-type doping was accomplished using tetraethyltin (TESn) held at 18°C to 20°C. The hydrogen flow through the TESn source was typically 20 sccm which was diluted with 350 sccm of hydrogen. Five to 20 sccm of this mixture was introduced into the growth chamber. Semi-insulating epi-ready GaAs and n-type InAs substrates were used for each growth.

AlSb samples 1-2 μm thick were grown at 500°C at either 76 torr or 200 torr with V/III ratios between 4 to 16. The best morphology was achieved at V/III = 15 and was independent of reactor pressure. The surface morphology of each layer was characterized by optical microscopy using Normarski interference contrast. Under this growth condition, the growth rate was 0.4 - 0.5 μm/hr for a group III transport rate of 1×10^{-5} moles of TMAA per minute.

$AlAs_{0.16}Sb_{0.84}$ layers 0.5 - 1 μm thick and lattice-matched to InAs were grown at 500 or 600°C and 76 or 200 torr using a V/III = 3 to 8 and [As]/([As]+[Sb]) = 0.1 to 0.64 in the gas phase. The best morphology was achieved when grown on a previously grown buffer layer of InAs. The growth rate ranged between 0.35 - 2.0 μm/hr for 120 minute growth times. The optimum V/III ratio is lower for AlAsSb grown at 600°C than AlSb grown at 500°C due to the more complete decomposition of TESb at the higher growth temperature.

Secondary ion mass spectroscopy (SIMS) was used to determine C and O impurity levels and dopant concentrations. The SIMS experiments were performed by Charles Evans and Associates, East, using Cs^+ ion bombardment. Five crystal x-ray diffraction (FCXRD) using (004) reflection was used to determine alloy composition. Layer thickness was determined using a groove technique and was cross checked by cross sectional SEM. These techniques usually agreed within a few percent.

Room temperature Hall measurements using the Van der Pauw technique were used to determine the majority carrier type and concentration of $AlAs_xSb_{1-x}$ layers grown on semi-insulating GaAs. Contacts were formed by alloying In/Sn (90:10) or In/Zn (95:5) at 300°C to 340°C in a Ar/H_2 atmosphere.

Capacitance-voltage (C-V) and current-voltage (I-V) measurements using metal Schottky barrier diodes were used to determine the carrier type and concentration of the layers. C-V diodes (10 and 40 mils in diameter) were formed by depositing 700Å to 1000Å of platinum by e-beam evaporation through a shadow mask. C-V and I-V measurements were made using two diodes in series on the epitaxial surface for samples grown on both GaAs and InAs substrates. C-V and I-V measurements were also made on samples grown on InAs substrates using only a single metal diode on the epi-surface and an ohmic back contact. No difference in carrier concentration was observed between the measurement configurations. Electrochemical C-V measurements were made using 0.2M NaOH / 0.1M EDTA electrolyte under various measurement conditions using a Bio-Rad Polaron system.

RESULTS AND DISCUSSION

Previous attempts by others at doping MOCVD grown AlSb, $AlAs_xSb_{1-x}$ alloys n-type have failed and this prohibits their use in bipolar devices. [6-8] The use of the conventional precursors trimethylaluminum (TMAl) and trimethylantimony (TMSb) or triethylantimony

Table I. SIMS and Hall measurements of AlSb and $AlAs_xSb_{1-x}$ grown on GaAs.

| Sample | Material | Growth Conditions (°C/torr) | SIMS | | | Hall |
			Oxygen (10^{17} cm^{-3})	Carbon (10^{17} cm^{-3})	Dopant (10^{17} cm^{-3})	Carriers (10^{17} cm^{-3})
2049	AlSb- N.I.D.[a]	500/200	50	10	.....	.....
2050	AlSb- N.I.D.[a]	500/200	60	20	.....	.....
2100	AlAsSb- N.I.D.[a]	600/76	100	7	.....	p, 0.94
2103	AlAsSb-Sn[b]	600/76	50	2	Sn, 100	n, 23
2107	AlAsSb-Zn[c]	600/76	80	50	Zn, 7	p, 14

a N.I.D. : not intentionally doped.
b N-dopant: TESn @ 20C and 646 torr.
c P- dopant: 400 ppm DEZn in hydrogen.

(TESb) has resulted in material with C and O concentrations exceeding 1×10^{19} cm^{-3}.[9] The surface morphologies were reported as very rough.[6-8] We have used TMAA or EDMAA and TESb to prepare AlSb and $AlAs_xSb_{1-x}$ with C and O concentrations below 1×10^{19} cm^{-3} (see Table I) and we have successfully doped them n-type using TESn.

SIMS and Hall measurements of undoped, Zn, or Sn doped $AlAs_xSb_{1-x}$ layers grown on GaAs are also reported in Table I.   Both C and O levels in the undoped samples are significantly lower than previously reported results and sufficiently low to expect successful n-type doping. The physical concentrations reported were determined from reference standards where known doses of C, O, Sn or Zn were implanted into GaSb substrates. Oxygen levels measured in $AlAs_xSb_{1-x}$ layers are nominally the same regardless of doping or the addition of As. At this point in time it is unclear what the source of the oxygen is in these materials. The oxygen could be coming from contaminants in the source bubblers, background in the reactor or SIMS chamber, or from reaction of the samples with air. The carbon level in undoped and Sn doped $AlAs_{0.16}Sb_{0.84}$ is significantly lower than that found in AlSb. This carbon reduction is consistent with the well known effect of increased AsH_3 effectively reducing the incorporation of C in AlGaAs films. [10,11] The higher level of carbon found in the Zn doped $AlAs_{0.16}Sb_{0.84}$ is most likely related to the DEZn used for doping. It is suspected that the additional carbon is largely responsible for the Hall hole concentration considering the relatively low level of zinc measured by SIMS.

The concentration of Sn (1×10^{19} cm^{-3}) measured in $AlAs_{0.16}Sb_{0.84}$ by SIMS is significantly higher than the carbon and oxygen levels. Hall measurements of sample 2103 showed n-type material with an electron concentration consistent with the Sn concentration measured by SIMS (2.3×10^{18} cm^{-3}). Measurements of undoped $AlAs_{0.16}Sb_{0.84}$ gave hole concentrations of $2\text{-}9 \times 10^{16}$ cm^{-3}. Hall measurements of Sn-doped $AlAs_{0.16}Sb_{0.84}$ grown on GaAs showed n-type material with an electron concentration consistent with dopant flow (Table II). The electron concentration was repeatable for the same dopant flow as for samples 2103 and 2109. However the electron concentration was not repeated in sample 2131 which was grown under the same reactant flows. The difference in doping between 2131 and the previous two runs is believed to be due a change in temperature of the TESb water bath. This suggests that Sn incorporation is dependent on the V/III ratio. When the dopant flow was reduced by half in sample 2132 the electron concentration fell proportionally. The Hall mobility ranged from 100 cm^2/Vs to 300 cm^2/Vs for these samples.

Table II. Hall and C-V measurements of $AlAs_xSb_{1-x}$ grown at 600°C and 76 torr on GaAs.

| Material/ Sample | Dopant Flow[a,b,c] (sccm) | GaSb - Cap | | AlAsSb |
		Doping	CV Carriers ($10^{17} cm^{-3}$)	Hall Carriers ($10^{17} cm^{-3}$)
2100	N.I.D.	N.I.D.	.....	p, 0.94
2105	N.I.D.	N.I.D.	.....	p, 0.23
2103	Sn-350,20,10	Sn	n, 4-6 (on InAs sub.)	n, 23
2109	.. Sn-350,20,10	Sn	n, 4-6	n, 15
2131	Sn-350,20,10	N.I.D.	n, 4-6	n, 51
2132	Sn-350,20,5	N.I.D.	n, 5-6	n, 26
2106	Zn-240	Zn	.....	p, 0.87
2107	Zn-500	Zn	.....	p, 14
2108	Zn-500	Zn	p, 1-3	p, 11

a N.I.D. : not intentionally doped.
b N-dopant: TESn @ 20C and 646 torr, H2 dilution / H2 through TESn bubbler / Mixture into chamber.
c P- dopant: 400 ppm DEZn in hydrogen

Since all of these samples were prepared with a GaSb cap layer it is important to eliminate the possibility that the cap layer is dominating the Hall measurements.   Hall measurements of n- $AlAs_{0.16}Sb_{0.84}$ do not appear to be influenced by the presence of the GaSb cap layer. Changing the GaSb cap thickness from 1000 to 2000 Å did not effect the electron concentration measured by Hall. Also, C-V measurements indicate the electron concentration of the cap layer to be $4-6x10^{17}$ cm^{-3} which is significantly less than the Hall results. C-V measurements (Table II) showed no difference in electron concentrations whether the GaSb cap was intentionally doped (2103 and 2109) or not (2131 and 2132). This is likely due to the thinness of the GaSb cap which causes depletion of most carriers in the GaSb. Finally, I-V measurements of Pt diodes deposited on sample 2109 with the GaSb cap removed by wet etching clearly showed n-type characteristics further indicating n-type doping of $AlAs_{0.16}Sb_{0.84}$ grown on GaAs.

For the growth of Sn-doped n-type AlSb, Polaron and C-V measurements using metal diodes showed good agreement for AlSb (Table III). Both measurements showed n-type AlSb (grown on InAs) with a carrier concentration of $3-7x10^{17}$ cm^{-3}. C-V measurements of the AlSb layer were made by removing the GaSb cap by wet etching prior to metallization. Hall measurements could not be made on any AlSb samples due to poor reproducibility in forming ohmic, metal contacts.

P-type doping of $AlAs_{0.16}Sb_{0.84}$ was easily achieved using DEZn.   The hole concentration measured by Hall was reproducible with dopant flow (Table II).   C-V measurements again show the hole concentration of the GaSb cap to be much less than the Hall measurement indicating that the GaSb cap is not significantly effecting the Hall measurement.

We have grown a previously described pseudomorphic multiple quantum well (MQW) structure which consists of 500Å InAs barriers and 100Å InAsSb wells on the top of the above described AlAsSb cladding layers.[15] The cladding layer is closely lattice-matched to the

Table III.   Polaron and C-V measurements of AlSb grown at 500 ° C and 76 torr on InAs.

| Sample Number | Dopant Flow[a] (sccm) | AlSb | |
		CV Carriers (10^{17} cm^{-3})	Polaron Carriers (10^{17} cm^{-3})
2126	Sn-300,20,10	.....	p, 2-5
2127	Sn-300,20,20	n, 4-7	n, 4

a N-dopant: TESn @ 20C and 646 torr, H_2 dilution / H_2 through TESn bubbler / Mixture into the chamber.
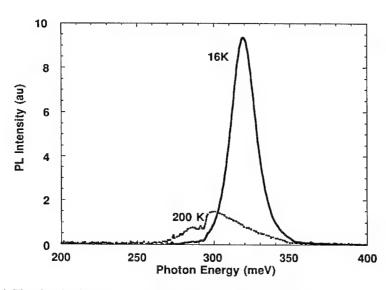
Figure 1. The photoluminescence spectra at 16 and 200 K of an InAsSb/InAs MQW grown on top of an AlAsSb cladding layer.

substrate (Δa/a = 0.001), and the entire active region is pseudomorphic with the substrate and cladding layers. The highly crystalline quality of the MQW active region is confirmed by FCXRD where 7 orders of satellites are observed and in optical characterization where the photoluminescence linewidth was 12 meV at 16 K. The photoluminescence spectra at 14 and 200 K of the MQW are shown in Figure 1 and are similar to the previously reported spectra of the MQW structure used in an injected laser with InPSb cladding layers.[1] Photoluminescence

output from these structures is observed at 300 K and it is of a similar width as that observed for 200 K with a slightly reduced intensity.

In summary, we have demonstrated the growth of low carbon AlSb and $AlAs_{0.16}Sb_{0.84}$ using TMAA or EDMAA, TESb, and AsH_3 by MOCVD. The quality of this material is further evidenced by the demonstration of the first n-type doping of AlSb and $AlAs_{0.16}Sb_{0.84}$ using TESn. Hall measurements show electron concentrations in the low to mid 10^{18} cm^{-3} for Sn doped $AlAs_{0.16}Sb_{0.84}$. Polaron, C-V with metal diodes, and I-V measurements all confirm the n-type measurements by Hall. Polaron and C-V measurements showed Sn-doped AlSb to have an electron concentration of 3-$7x10^{17}$ cm^{-3}. We have grown an InAsSb/InAs MQW active region on top of this AlAsSb layer and observed high quality photoluminescence from it at temperatures up to 300 K. With this demonstration of the growth of n-type AlSb and AlAsSb and high quality active regions by MOCVD, midwave infrared lasers (3-6 μm) using these materials will be prepared by MOCVD in the near future.

ACKNOWLEDGMENTS

REFERENCES

[1] S. R. Kurtz, R. M. Biefeld, L. R. Dawson, K. C. Baucom, and A. J. Howard, Appl. Phys. Lett. **64**, 812 (1994).
[2] H. K. Choi, G. W. Turner, and Z. L. Liau, Appl. Phys. Lett. **65**, 2251 (1994).
[3] Y-H. Zhang, Appl. Phys. Lett. **66**, 118 (1995).
[4] R. M. Biefeld, A. A. Allerman, and M. W. Pelczynski, Appl. Phys. Lett. **68**, 932 (1996).
[5] W. K. Chen, J. Ou, and W-I. Lee, Jpn, J. Appl. Phys. **33**, L402 (1994).
[6] D. S. Cao, Z. M. Fang, and G. B. Stringfellow, J. Crystal Growth, **113**, 441 (1991).
[7] G. J. Bougnot, A. F. Foucaran, M. Marjan, D. Etienne, J. Bougnot, F. M. H. Delannoy, and F. M. Roumanille, J. Crystal Growth, **77**, 400 (1987).
[8] M. Leroux, A. Tromson-Carli, P. Gibart, C. Verie, C. Bernard, and M. C. Schouler, , J. Crystal Growth, **48**, 367 (1980).
[9] C. A. Wang, M. C. Finn, S. Salim, K. F. Jensen, and A. C. Jones, Appl. Phys. Lett. **67**, 1384 (1995).
[10] G. B. Stringfellow, "Organometallic Vapor Phase Epitaxy:Theory and Practice" (Academic Press, Inc., San Diego, CA, 1989).
[11] M. A. Tischler, R. M. Potemski, T. F. Kuech, F. Cardone, M. S. Goorsky, and G. Scilla, J. Crystal Growth, **107**, 268 (1991).
[12] W. S. Hobson, T. D. Harris, C. R. Abernathy, and S. J. Pearton, Appl. Phys. Lett., **58**, 77 (1991).
[13] R. P. Schneider, R. P. Bryan, E. D. Jones, R. M. Biefeld, and G. R. Olbright, J. Crystal Growth, **123**, 487 (1992).
[14] R.M. Biefeld, C.R. Hills and S.R. Lee, J. Crystal Growth, **91**, 515 (1988).
[15] S. R. Kurtz and R. M. Biefeld, Appl. Phys. Lett. **66**, 364 (1995).

STRUCTURAL CHARACTERIZATION OF InAs/(GaIn)Sb SUPERLATTICES FOR IR OPTOELECTRONICS

J. Wagner, J. Schmitz, F. Fuchs, U. Weimar, N. Herres, G. Tränkle, and P. Koidl
Fraunhofer-Institut für Angewandte Festkörperphysik, Tullastrasse 72, D-79108 Freiburg, Germany, wagner@iaf.fhg.de

ABSTRACT

We report on the structural characterization of InAs/(GaIn)Sb superlattices (SL) grown by solid-source molecular-beam epitaxy. SL periodicity and overall structural quality were assessed by high-resolution X-ray diffraction and Raman spectroscopy. Spectroscopic ellipsometry was found to be sensitive to the (GaIn)Sb alloy composition.

INTRODUCTION

There is increasing interest in III/V-antimonide heterostructures for IR optoelectronic devices. Based on InAs/(GaIn)Sb superlattices (SLs) mid- and far-IR photodetectors[1,2] and lasers[3] have been realized. Most of the device structures reported so far were grown by molecular-beam epitaxy (MBE). However, the parameter window for the growth of high-quality InAs/GaSb heterostructures is significantly narrower than that for the growth of, e.g., GaAs/(AlGa)As based structures[4]. Therefore, a fast and efficient non-destructive control of the composition and structural quality of the antimonide heterostructures is required, either in-situ or at least ex-situ immediately after the epitaxial layer growth.

High-resolution X-ray diffraction (HRXRD) in combination with Raman scattering and spectroscopic ellipsometry have been used successfully for the ex-situ structural characterization of InAs/GaSb SLs[5,6]. Among these techniques, Raman scattering and in particular spectroscopic ellipsometry[7] have the potential of being used also as in-situ characterization techniques. The energy of the SL band gap, which determines the cut-off and emission wavelengths of detectors and emitters, respectively, can be conveniently probed by Fourier-transform photoluminescence and photocurrent spectroscopy[8]. In the present study, however, we shall focus on the assessment of the structural properties of MBE grown InAs/(GaIn)Sb SLs using HRXRD in conjunction with Raman spectroscopy and ellipsometry.

EXPERIMENT

InAs/(GaIn)Sb SLs were grown by solid-source MBE on undoped semi-insulating (100) GaAs substrates. Molecular beams of Sb_2 and As_2 were used. Growth of the antimonides started with an AlSb nucleation layer. The InAs/(GaIn)Sb SLs grown at 420°C were then deposited on a 1.1 μm thick strain relaxed GaSb buffer. For further details of sample growth see Refs. 4 and 6. For the present samples the InAs and (GaIn)Sb layer widths were in the 8 to 10 monolayer (ML) range. The nominal composition of the $Ga_{1-x}In_xSb$ layers was either x=0, i.e. binary GaSb, or x=0.25. The shutter sequence for the growth of the InAs/GaSb interfaces (IF) corresponded to the deposition of either 1 ML InSb or 1 ML GaAs, which resulted in the intended formation of InSb- or GaAs-like IF bonds as checked by Raman spectroscopy[6,9]. To calibrate the growth of the (GaIn)Sb, thick strain relaxed layers were
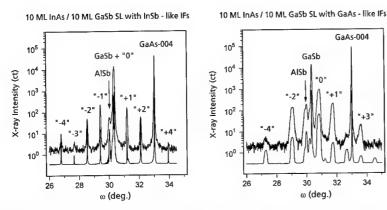
Fig. 1: Measured (upper trace) and simulated (lower trace) HRXRD profiles covering the 004 reflection range of a pair of 10 ML InAs/10 ML GaSb SLs with (left) InSb-like and (right) GaAs-like interfaces.

prepared and their composition was analyzed by HRXRD and Raman spectroscopy. The InAs/(GaIn)Sb SLs were characterized by HRXRD using a set-up described in detail in Ref. 6, Raman spectroscopy of backfolded longitudinal acoustic (LA) phonons[10], and variable angle spectroscopic ellipsometry[11].

RESULTS AND DISCUSSION

Fig. 1 shows HRXRD profiles covering the symmetric 004 reflection range for a pair of 100 period 10 ML InAs/10 ML GaSb SLs grown with either InSb- or GaAs-like IFs. For the SL with InSb-like IFs intense and narrow SL diffraction peaks up to the 4th order are observed indicating a good structural quality of the sample. The 0th order SL peak almost coincides with the diffraction peak from the strain-relaxed GaSb buffer layer, which shows that the lattice parameter of the SL stack along the growth direction is nearly identical to that of the GaSb buffer. Combining this finding with information obtained from HRXRD profiles recorded for asymmetric 115 reflection ranges, the in-plane lattice parameter of the SL was also found to be the same as that for the GaSb buffer. Thus, the SL with InSb-like IFs has a "cubic" metric with negligible residual strain. The 004 HRXRD profile of the SL with GaAs-like IFs exhibits much broader SL diffraction peaks which are shifted towards larger diffraction angles. This peak shift indicates that the average lattice parameter along the growth direction is smaller than that of the GaSb buffer, whereas the in-plane lattice parameter was found to be still that of the buffer layer. Thus, the SL with GaAs-like interfaces is under biaxial in-plane tension. This difference in the strain situation found for InAs/GaSb SLs with different IFs has been attributed to changes in the IF bond length which is much smaller for GaAs- than for InSb-like IFs[6].

Also shown are simulated diffraction profiles which reproduce the peak positions and relative peak widths. To model the peak widths observed for the SLs with GaAs-like IFs an increasing strain relaxation across the SL stack had to be assumed with only the first few
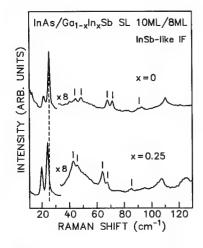
Fig. 2: Room-temperature Raman spectra of 10 ML InAs/8 ML $Ga_{1-x}In_xSb$ SLs with InSb-like IFs and (top) x=0 or (bottom) x=0.25. Higher-order backfolded LA phonon doublets are marked by vertical lines. Optical excitation was at 1.92 eV.

periods closest to the GaSb buffer layer being coherently strained to the in-plane lattice parameter of the buffer layer[6].

Raman spectra covering the frequency region of backfolded LA phonons are shown in Fig. 2 for a pair of 50 period 10 ML InAs/8 ML $Ga_{1-x}In_xSb$ SLs with InSb-like IFs and In contents of x=0 (top) and x=0.25 (bottom). For both SL samples doublets of backfolded LA phonons are resolved up to the 4th order indicating a good and comparable overall structural quality for both types of SLs[10,12]. The frequency of the $\pm m^{th}$ backfolded LA phonon mode is given by[12]

$$\Omega_{\pm m} = (m \, \pi/P_{SL} \pm \Delta k) \, v_{aver}. \tag{1}$$

Here P_{SL} denotes the SL period and v_{aver} is the averaged sound velocity of the SL given by $1/v_{aver} = \alpha/v_{InAs} + (1-\alpha)/v_{GaInSb}$. α is defined as d_{InAs}/P_{SL} with d_{InAs} as the individual InAs layer width; v_{InAs} and v_{GaInSb} are the appropriate sound velocities of bulk InAs and (GaIn)Sb, respectively. Δk is the momentum transferred in the backscattering Raman experiment, which is approximately twice the momentum of the incident photon. The mode frequencies found for binary InAs/GaSb SLs with InSb-like IFs can be well reproduced by Eq. 1 when using the sound velocities of bulk InAs and GaSb[10] of 3.83×10^5 cm/s and 3.97×10^5 cm/s, respectively[13]. For the $InAs/Ga_{0.75}In_{0.25}Sb$ SL sample the LA phonon doublets occur at systematically lower frequencies than for the InAs/GaSb SL. This difference in mode frequencies can only in part be explained by the somewhat larger period of the $InAs/Ga_{0.75}In_{0.25}Sb$ SL determined by HRXRD to be 5.82 nm compared to that of the InAs/GaSb SL for which HRXRD gives a period of 5.47 nm. The remaining difference has to be accounted for by a reduced average sound velocity of 3.75×10^5 cm/s when GaSb is replaced by $Ga_{0.75}In_{0.25}Sb$. This value is somewhat lower than $v_{aver} = 3.83 \times 10^5$ cm/s from a linear interpolation between the sound velocities of bulk GaSb and InSb (3.41×10^5 cm/s, Ref. 14). This apparent reduction is readily explained by alloy scattering, not taken into account in the linear interpolation.

The imaginary part of the pseudodielectric function ϵ_2, derived from room-temperature ellipsometric measurements, is plotted in Fig. 3 for a pair of 100 period 8 ML InAs/10 ML GaSb SLs with either InSb- or GaSb-like IFs. Two critical points are clearly resolved at
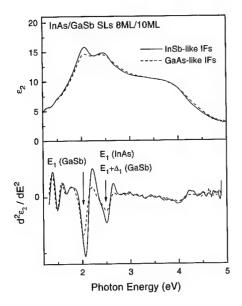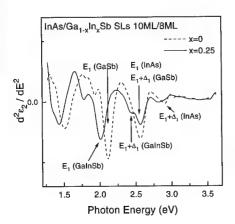
Fig. 3: Imaginary part ϵ_2 of the SL dielectric function (top) and second energy derivatives of ϵ_2 (bottom) for a pair of 8 ML InAs/10 ML GaSb SLs with either InSb-like or GaAs-like IFs.

energies around 2.1 and 2.5 eV. These critical points are marked in the derivative spectra $d^2\epsilon_2/dE^2$ shown in the bottom panel of Fig. 3 as being due to the E_1 interband transition in GaSb and to a superposition of the GaSb $E_1 + \Delta_1$ transition and the E_1 transition in InAs[9]. The oscillatory structure observed in the derivative spectra at photon energies below 1.8 eV is due to interference fringes.

The interband transitions are less well resolved for the SL with GaAs-like IFs than for the SL with InSb-like IFs which reflects the lower structural quality of the SLs with GaAs-like IFs found by HRXRD[6] (see Fig. 1). There are also slight shifts of the critical point energies as a function of the IF bond type, which have been attributed to differences in the strain situation within the SL stack depending on the interfacial bonding[9].

Fig. 4 shows the derivative spectra $d^2\epsilon_2/dE^2$ for a pair of 50 period 10 ML InAs/8 ML $Ga_{1-x}In_xSb$ SLs with InSb-like IFs and x=0 or x=0.25. For the InAs/GaSb SL besides the E_1 transitions of InAs and GaSb and the $E_1 + \Delta_1$ transition of GaSb also the $E_1 + \Delta_1$ transition of InAs is resolved at around 2.8 eV. When GaSb is replaced by $Ga_{0.75}In_{0.25}Sb$ the E_1 transition of (GaIn)Sb shifts to lower energies by 100 meV and the $E_1 + \Delta_1$ transition appears as a seperate shoulder at the low energy side of the E_1 transition of InAs.

The primary reason for the low-energy shift of the E_1 and $E_1 + \Delta_1$ critical points of $Ga_{1-x}In_xSb$ when x is increased from 0 to a nominal value of 0.25, is the composition dependence of the critical point energies. The E_1 and $E_1 + \Delta_1$ gap energies of $Ga_{1-x}In_xSb$ are plotted in Fig. 5 versus the In content x for $0 \leq x \leq 0.33$. The data were obtained by room-temperature ellipsometric measurements on the thick strain relaxed $Ga_{1-x}In_xSb$ reference layers. The decrease in gap energy with increasing x found experimentally is much stronger than expected from a linear interpolation between the corresponding gap energies in GaSb and InSb[15]. This finding indicates a significant bowing in the composition dependence of the E_1 and $E_1 + \Delta_1$ gap energies. An energy down-shift of the E_1 gap of 100 meV as found above for
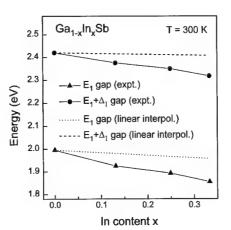
Fig. 4 (left): Second energy derivatives of the imaginary part ϵ_2 of the SL dielectric function for a pair of 10 ML InAs/8 ML $Ga_{1-x}In_xSb$ SLs with InSb-like IFs and In contents x=0 or x=0.25.

Fig. 5 (right): Composition dependence of the E_1 and $E_1+\Delta_1$ band gap energies of $Ga_{1-x}In_xSb$.

the InAs/(GaIn)Sb SL, corresponds to an In content of 0.25. This value is in agreement with the intended In concentration adjusted according to flux calibrations performed using thick (GaIn)Sb reference layers (see Experiment Section).

A second source for shifts in gap energies are strain effects[16]. For GaSb grown pseudomorphically on InAs the by 0.62% smaller lattice parameter of InAs compared to that of GaSb causes a biaxial compressive strain in the GaSb. This strain was found to shift the E_1 and $E_1+\Delta_1$ transitions of GaSb to higher energies by about 14 and 41 meV, respectively. This observation is in agreement with reports on InAs layers compressively strained to the in-plane lattice parameter of InP, for which the $E_1+\Delta_1$ gap was found to shift to higher energies by 0.18 eV whereas the E_1 gap energy showed no detectable shift[17].

Assuming that for the InAs/$Ga_{0.75}In_{0.25}Sb$ SLs the (GaIn)Sb layers are compressively strained to the in-plane lattice parameter of the GaSb buffer corresponding to a lattice mismatch of 1.57%, from the above given strain induced shift of the E_1 gap of GaSb the E_1 gap of (GaIn)Sb is expected to be shifted to higher energies by about 35 meV. Or, in other words, the actual In content is somewhat higher than the value deduced above from the observed E_1 gap shift neglecting strain effects. However, for a quantitative correction, the actual strains in both SLs have to be known. In addition, a more precise value for the strain induced E_1 gap shift in GaSb would be desirable. But even with the present limitation, spectrocopic ellipsometry allows us a control of run-to-run variations in the composition x of InAs/$Ga_{1-x}In_xSb$ SLs.

CONCLUSIONS

InAs/(GaIn)Sb SLs grown by MBE were studied by HRXRD, Raman spectroscopy, and spectroscopic ellipsometry. The overall structural quality and SL periodicity were characterized by X-ray diffraction and Raman scattering by backfolded LA phonons. The SL dielectric function as measured by ellipsometry was found to depend on the overall structural quality and, in particular, on the (GaIn)Sb alloy composition.

REFERENCES

1. D.L. Smith and C. Mailhiot, J. Appl. Phys. **62**, 2545 (1987).
2. D.H. Chow, R.H. Miles, J.N. Schulman, D.A. Collins, and T.C. McGill, Semicond. Sci. Technol. **6**, C47 (1991); M.J. Yang and B.R. Bennett, Electron. Lett. **30**, 1710 (1994).
3. R.H. Miles, D.H. Chow, Y.-H. Zhang, P.D. Brewer, and R.G. Wilson, Appl. Phys. Lett. **66**, 1921 (1995); D.H. Chow, R.H. Miles, T.C. Hasenberg, A.R. Kost, Y.-H. Zhang, H.L. Dunlap, and L. West, Appl. Phys. Lett. **67**, 3700 (1995).
4. J. Schmitz, J. Wagner, F. Fuchs, N. Herres, P. Koidl, and J.D. Ralston, J. Cryst. Growth **150**, 858 (1995).
5. J. Wagner, F. Fuchs, N. Herres, J. Schmitz, and P. Koidl, Proceedings of the 3rd Int. *Symp. on Long Wavelength Infrared Detectors and Arrays: Physics and Applications*, Electrochemical Society Proceedings 95-28, 201 (1995).
6. N. Herres, F. Fuchs, J. Schmitz, K.M. Pavlov, J. Wagner, J.D. Ralston, P. Koidl, C. Gadaleta, and G. Scamarcio, to appear in Phys. Rev. B.
7. See, e.g., D.E. Aspnes, in *Handbook of Optical Constants*, ed. E. Palik (Academic Press, New York, 1985), p. 89.
8. F. Fuchs, N. Herres, J. Schmitz, K.M. Pavlov, J. Wagner, P. Koidl, and J.H. Roslund, Proc. SPIE **2554** (1995), p. 70.
9. D. Behr, J. Wagner, J. Schmitz, N. Herres, J.D. Ralston, P. Koidl, M. Ramsteiner, L. Schrottke, and G. Jungk, Appl. Phys. Lett. **65**, 2972 (1994).
10. J. Wagner, J. Schmitz, N. Herres, J.D. Ralston, and P. Koidl, Appl. Phys. Lett. **66**, 3498 (1995).
11. C.M. Herzinger, P.G. Snyder, B. Johs, and J.A. Woollam, J. Appl. Phys. **77**, 1715 (1995).
12. See, e.g., B. Jusserand and M. Cardona, in *Light Scattering in Solids V*, eds. M. Cardona and G. Güntherodt (Springer, Berlin, 1989), p. 49.
13. M. Yano, H. Furuse, Y. Iwai, K. Yoh, and M. Inoue, J. Cryst. Growth **127**, 807 (1993).
14. J.R. Drabble and A.J. Brammer, Proc. Phys. Soc. **91**, 959 (1967).
15. *Semiconductor Physics of Group IV Elements and III-V Compounds*, edited by O. Madelung, Landolt-Börnstein, New Series, Group III, Vol. 17, Pt. a (Springer, Heidelberg, 1982).
16. F.H. Pollak, in *Semiconductors and Semimetals*, Vol. 32, ed. T.P. Pearsall (Academic Press, New York, 1990), p. 17.
17. C.M. Herzinger, P.G. Snyder, F.G. Celii, Y.-C. Kao, D. Chow, B. Johs, and J.A. Woollam, J. Appl. Phys. **79**, 2663 (1996).

High Quality $In_{1-x}(Ga_x)As_yP_{1-y}$/InP Compressive strained Quantum Well Structures Grown by LP-MOCVD

J. T. Zhu, A. R. Clawson and P. K. L. Yu
ECE Department, University of California, San Diego, La Jolla, CA 92037-0407

ABSTRACT

We report the results of the growth of $InAs_yP_{1-y}$ /InP and $In_{0.86}Ga_{0.14}As_{0.51}P_{0.49}$/$In_{0.86}Ga_{0.14}As_{0.33}P_{0.67}$ compressive strained multiple quantum wells (CSMQW) structures grown by low pressure metalorganic chemical vapor deposition (LP-MOCVD). Our studies showed high quality 1.06 μm $InAs_{0.21}P_{0.79}$/InP CSMQW structure with 6 periods can be obtained when the growth temperature is around 650°C and the pressure in the reactor is about 20 Torr. When the well thickness and composition are tuned for wavelength around 1.30 μm, the quality of this structure degrades. By employing 1.1 μm wavelength, lattice-matched InGaAsP as the barrier layers and setting the growth temperature at 600 °C, high quality 1.30 μm wavelength $In_{0.86}Ga_{0.14}As_{0.51}P_{0.49}$/$In_{0.86}Ga_{0.14}As_{0.33}P_{0.67}$ CSMQW materials with 10 periods can also be obtained. The materials were characterized with high resolution x-ray rocking curves, room and low temperature photoluminescence (PL). The 15K full-width-at-half-maximums (FWHM) of the PL peaks for 1.06 μm $InAs_{0.21}P_{0.79}$/InP and 1.30 μm $In_{0.86}Ga_{0.14}As_{0.51}P_{0.49}$/$In_{0.86}Ga_{0.14}As_{0.33}P_{0.67}$ CSMQW structures are 5.6 meV and 4.97 meV, respectively, which are among the smallest FWHMs reported up to date for these kinds of MOCVD growth materials. Buried heterostructure lasers at 1.3 μm wavelength have been obtained with the CSMQWs as the active layer.

INTRODUCTION

Strained-layer heterostructures of $InAs_yP_{1-y}$ /InP and $In_{1-x}Ga_xAs_yP_{1-y}$/InP are of interest for a variety of optoelectronic device applications. In(Ga)AsP/InP multiple quantum well (MQW) structures can be tailored to emit light in the wavelength range of 1.06 to 1.6 μm by suitable variation of the quantum well composition and width. Previous studies indicate that these strained-layer systems are particularly interesting for applications in ultrahigh speed devices, such as modulators, detectors and lasers[1-4]. The MQW structures with operating wavelength about 1.06 μm and 1.3 μm have drawn much attention because the materials with wavelength of 1.06 μm can be used as the active layer of semiconductor optical amplifiers and the devices with wavelength around 1.30 μm match the lowest dispersion window in single mode fiber. In this article, we report high quality $InAs_yP_{1-y}$/InP and $In_{1-x}Ga_xAs_yP_{1-y}$/$In_{0.86}Ga_{0.14}As_{0.33}P_{0.67}$ compressive strained multiple quantum well structures grown by low pressure metal organic chemical vapor deposition (LP-MOCVD). The materials were characterized using high resolution x-ray diffraction, room and low temperature photoluminescence. Our results show that when $InAs_yP_{1-y}$ well material and InP barrier are used and the thickness of well and barrier layers are about 6 and 20.9 nm, it is easy to get high quality 1.06 μm CSMQW structure of 6 periods with FWHMs of photoluminescence (PL) peaks of 13.1 and 5.6 meV at 300 and 15 K, respectively. However, the quality of this structure degrades as the material composition is tuned toward 1.30 μm operation due to the transfer of arsenic from $InAs_yP_{1-y}$ layer to InP layer and the relaxation of the material with a large strain.

45
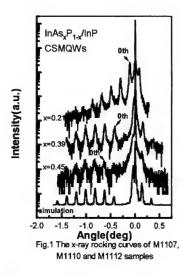
For optical modulator applications, for example, in providing an acceptable optical extinction ratio[5] and for producing a large electric field-induced shift of exciton peak[6], MQWs with thick well layer are required. In order to obtain high quality 1.3 μm CSMQWs, several problems should be considered: 1) the transfer of arsenic between the well and barrier layers, 2) the relaxation of strain in the MQWs, 3) maintaining flat, abrupt interfaces between the well and barrier layers. Our approach is to use 1.1 μm wavelength lattice-matched $In_{0.86}Ga_{0.14}As_{0.33}P_{0.67}$ quaternary as the barrier layers and use $In_{0.86}Ga_{0.14}As_{0.51}P_{0.49}$ as the well layers. Because the well and barrier layers contain the same elements i.e. In, Ga, As and P, and are grown at lower temperature, the diffusion of the atoms between these two layers much decreases and the strain in the material is also reduced. In addition, the change of compositions in well and barrier layers can be achieved by adjusting only the flow rate of arsine, so it is easy to switch the source for the growth of well and barrier layers. With the above ideas, high quality 1.30 μm wavelength CSMQWs with thick well thickness (11 nm) and many periods (10) are obtained. For these CSMQWs, the respective 300 and 15K FWHMs of PL peaks of 24 and 4.97 meV are among the best reported for this kind of material grown by LP-MOCVD and are well comparable to the reported results of $InAs_yP_{1-y}$ /InP MQWs grown by MBE[7].
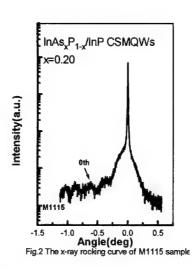
EXPERIMENT

The $InAs_yP_{1-y}$ /InP and $In_{1-x}Ga_xAs_yP_{1-y}$/$In_{1-x}Ga_xAs_zP_{1-z}$ compressive strained multiple quantum well structures were grown on (100) Fe-doped semi-insulating InP substrates in a horizontal LP-MOCVD reactor. The growth temperature and the pressure in the reactor are 650 °C and 20 Torr, respectively. Trimethylindium (TMIn) and triethylgallium (TEGa) are used as group III sources; 10% arsine in hydrogen and 20% phosphine in hydrogen are used as group V sources. Before the substrate is loaded into the reactor, it is etched with the solution H_2SO_4:H_2O_2:H_2O of 8:1:1 for 2 minutes, then rinsed with DI water for a while and dried with nitrogen. The wafer is pre-heated in hydrogen at 120°C for 30 minutes for purging, then heated at 650°C for 10 minutes before growth starts. The mole fraction of TMIn is set at 5×10^{-6} mole/minute to give a growth rate of InP about 25 nm/min. For the $InAs_yP_{1-y}$/InP MQW structure, an InP buffer layer was grown on the substrate, followed by $InAs_yP_{1-y}$ and InP MQW layers. Finally, an InP top layer with a 50 nm thickness was grown. For the $In_{1-x}Ga_xAs_yP_{1-y}$/$In_{1-x}Ga_xAs_zP_{1-z}$ MQW structure, an initial lattice-matched 1.1 μm wavelength $In_{0.86}Ga_{0.14}As_{0.33}P_{0.67}$ was grown as the barrier layer. The compressive strained well layer, $In_{0.86}Ga_{0.14}As_{0.51}P_{0.49}$, was grown using the same flow parameters of TMIn, TEGa, phosphine and arsine as used for the growth of the barrier, except a second arsine line is used to supply the remaining arsine needed for the 1.30 μm bandgap. we need only to control the switching of the second arsine line to either the vent or to the reactor in the growth of barrier layer or well layer. Finally a 50 nm thick InP top layer was grown. .

RESULTS AND DISCUSSION

The MQWs were characterized with high resolution x-ray rocking curve, low and room temperature photoluminescence spectra. Fig.1 shows the x-ray rocking curves of M1107 (λ=1.06 μm), M1110 (λ=1.22 μm) and M1112 (λ=1.30 μm) $InAs_yP_{1-y}$/InP CSMQW samples grown by MOCVD using the growth conditions listed in table 1. Sharp satellite peaks in the x-

Fig.1 The x-ray rocking curves of M1107, M1110 and M1112 samples

Fig.2 The x-ray rocking curve of M1115 sample
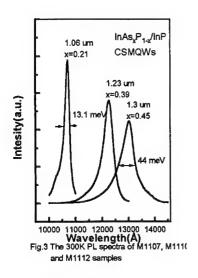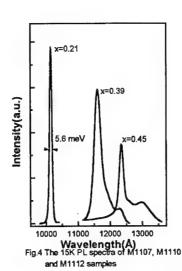
ray rocking curve of the M1107 sample with 6 well layers are observed. In contrast to the M1107 sample, M1110 and M1112 samples with 6 well layers show much broader satellite peaks. There are two possible explanations: 1) the $InAs_yP_{1-y}$ /InP CSMQW materials can be partially relaxed. With increased flow rate of arsine, the arsenic concentration in the $InAs_yP_{1-y}$ well layer increases and the lattice constant of $InAs_yP_{1-y}$ also increases, which enlarges the strain in the structure and causes the material to relax. 2) With increased arsenic concentration in the $InAs_yP_{1-y}$, more arsenic diffuses from the $InAs_yP_{1-y}$ well into the InP barrier. A graded $InAs_yP_{1-y}$ layer may thus form near the interfaces.

Table 1. The growth conditions of the samples

Sample #	Layer	Growth time second	The TMIn	flowrate TEGa	of PH3	sources AsH3 #1	(sccm) AsH3 #2	Thickness (nm)	Periods
M1107	Barrier	50	80		200			20.9	6
	Well	14	80		200	15		6	
M1110	Barrier	50	80		200			20.9	6
	Well	14	80		200	22		6	
M1112	Barrier	50	80		200			20.9	6
	Well	14	80		200	24		6	
M1115	Barrier	50	80		200			20.9	6
	Well	18	80		200	23.4		8	
M1149	Barrier	25	80	29.8	200	5.8		10	10
	Well	28	80	29.8	200	5.8	24	11.3	
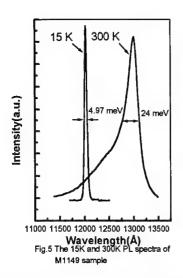
Using a x-ray rocking curve simulation software incorporated with the dynamical x-ray diffraction theory , the arsenic compositions of 0.21, 0.39 and 0.45 in M1107, M1110 and M1112 samples are obtained, the well and the barrier thickness are about 6 and 20.9 nm, respectively. Fig.2 shows the x-ray rocking curve of the M1115 (λ=1.30 μm) sample with well thickness of 8 nm. The absence of satellite peaks indicates that the M1115 sample is much relaxed or the interfaces are very rough. For sample M1107, M1110 and M1112, the corresponding room and low temperature photoluminescence spectra are shown in Fig.3 and Fig.4. For the M1107 sample,

Fig.3 The 300K PL spectra of M1107, M111(
and M1112 samples

Fig.4 The 15K PL spectra of M1107, M1110
and M1112 samples
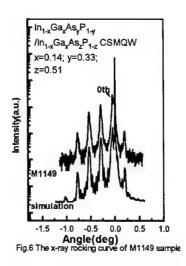
the room temperature FWHM is as narrow as 13.1 meV, indicating high quality of this structure. On the other hand, for M1110 and M1112 samples, the room temperature FWHMs are much broader than that of M1107. Fig.4 shows that a respective small peak appears at long wavelength sides of the low temperature PL curves of M1110 and M1112 samples. The small peaks might be caused by the defect centers generated due to the relaxation of the structures[8].

Fig.5 shows the low and room temperature PL results of sample M1149 of an $In_{0.86}Ga_{0.14}As_{0.51}P_{0.49}$/ $In_{0.86}Ga_{0.14}As_{0.33}P_{0.67}$ MQW structure with 10 periods. As shown, the peak wavelength is 1.3 μm at room temperature for this material and the FWHM of PL peak is 24 meV that is much narrower than the 44.2 meV for the $InAs_yP_{1-y}$ /InP structure grown at 650 °C. For this structure, the 15K FWHM of PL peak is 4.97 meV that is among the narrowest FWHMs reported up to date for such materials grown by MOCVD and it is comparable to the best results for $InAs_yP_{1-y}$ /InP materials grown by MBE system[7]. Fig.6 shows the X-ray rocking curve of M1149. The satellite peaks of this structure are much sharper and stronger than that for M1112 shown in figure 3. Fig.6 also shows the x-ray rocking curve simulation of M1149. From the simulation, the x and y value are determined to be 0.14, 0.33 and 0.14, 0.51 for barrier and well

layers, respectively. The thickness of the well and barrier layer are 11.3 and 10 nm, respectively.

With the 1.3 μm $In_{0.86}Ga_{0.14}As_{0.51}P_{0.49}/In_{0.86}Ga_{0.14}As_{0.33}P_{0.67}/InP$ CSMQWs in the active layer, we have fabricated buried heterostructure lasers. The laser structures were grown with three step MOCVD growth. For three well CSMQW structure lasers, threshold currents of 35 and 70 mA are obtained for active layer width of 3 and 7 μm , respectively.

CONCLUSION

In summary, using LP-MOCVD system, both the $InAs_yP_{1-y}/InP$ and $In_{1-x}Ga_xAs_yP_{1-y}/In_{1-x}Ga_xAs_zP_{1-z}$ CSMQW structures were studied. The results show that high quality 1.06 μm $InAs_{0.21}P_{0.79}/InP$ and 1.3 μm $In_{0.86}Ga_{0.14}As_{0.51}P_{0.49}/In_{0.86}Ga_{0.14}As_{0.33}P_{0.67}$ CSMQW structures   can be grown by LP-MOCVD at 650°C, 600°C and 20 Torr, respectively. Photoluminescence peaks with respective FWHMs as small as 5.6 and 4.97 meV   were observed at 15K. Preliminary results indicate efficient buried heterostructure lasers can be achieved with the CSMQWs at 1.30 μm wavelength.

ACKNOWLEDGMENTS

REFERENCES

1. K. Wakita, I. Kotaka, T. Amano and H. Sugiura, Electronics Letters, 31 P.1,339 (1995).

2. T.K.Woodward, T.-H. Chiu, and T. Sizer,II., Applied physics letters, 60, P. 2846 (1992).

3. J. B. D. Soole, H.P. LeBlanc, N.C. Andreadakis, C. Caneau, R.Bhat, and M.A.Koza, Electronics Letters, 31, P. 1276 (1995).

4. A.Kasukawa, N.Yokouchi, N.Yamanaka, and N.Iwai, Electronics Letters, 31, P.1749 (1995).

5. M.K.Chin, P.K.L. Yu, W.S.C.Chang, IEEE J. Quantum Electron., 27, P. 696 (1991).

6. G. Bastard, E.E. Mendez, L.L.Chang, and L. Esaki, Phys. Rev., B28, P.3241 (1983).

7. W. G. Bi and C.W. Tu, J. Appl. Phys., 78, P. 2889 (1995).

8. M.Nakao, H.Oohashi, H.Sugiura, J. Appl. Phys., 78, P. 3462 (1995).

Part II

Photonics and Processing

SELECTIVE OXIDATION OF BURIED AlGaAs FOR FABRICATION OF VERTICAL-CAVITY LASERS

Kent D. Choquette, K. M. Geib, H. C. Chui, H. Q. Hou, and Robert Hull*

Photonics Research Department   *University of Virginia
Sandia National Laboratories   Department of Materials Science
Albuquerque, NM 87185-0603   Charlottesville, VI 22903-2442
kdchoqu@sandia.gov

Abstract

We discuss the selective conversion of buried layers of AlGaAs to a stable oxide and the implementation of this oxide into high performance vertical-cavity surface emitting lasers (VCSELs). The rate of lateral oxidation is shown to be linear with an Arrhenius temperature dependence. The measured activation energies vary with Al composition, providing a high degree of oxidation selectivity between AlGaAs alloys. Thus buried oxide layers can be selectively fabricated within the VCSEL through small compositional variations in the AlGaAs layers. The oxidation of AlGaAs alloys, as opposed to AlAs, is found to provide robust processing of reliable lasers. The insulating and low refractive index oxide provides enhanced electrical and optical confinement for ultralow threshold currents in oxide-apertured VCSELs.

Introduction

Oxide-apertured vertical-cavity surface emitting lasers (VCSELs) have recently demonstrated record low threshold currents[1,2] and threshold voltages[3] at both infrared and visible[4] wavelengths, as well as record high power conversion efficiencies.[5] These advances arise from the reduction of electrical and optical loss due to efficient current injection into the active region[6] and index-guided optical confinement[7] afforded by the buried oxide converted from AlGaAs.[8] The Al-oxide has also been utilized in the fabrication of a variety of other photonic/microelectronic devices, including edge emitting lasers,[9] optical waveguides,[10] and GaAs metal-oxide-semiconductor field effect transistors.[11] Thus understanding the factors which influence the wet oxidation of AlGaAs is important for the development of robust fabrication techniques for advanced optoelectronic devices.

In this paper we discuss the wet oxidation of AlGaAs, the implementation of the oxide in a monolithic VCSEL, and the resulting performance of oxide-apertured VCSELs. We first examine the influence of temperature and composition on the oxidation rate. The oxidation selectivity with respect to Al content is shown to allow the fabrication of buried oxide layers for confinement within the VCSEL. The use of an oxide formed from AlGaAs, rather than from AlAs, is demonstrated to give robust and reliable VCSELs. Finally, the threshold characteristics of oxide-apertured and ion-implanted VCSELs are compared.

Oxidation of AlGaAs

To develop reproducible fabrication processes, wet oxidation of AlGaAs has been examined as a function of Al composition and process parameters. Samples containing AlGaAs layers are subjected to elevated temperatures (350-500°C) in a steam environment. Specifically, a controlled flow of N_2 gas is bubbled through de-ionized water maintained at 82°C and is passed through a three zone tube furnace. Sufficient gas flow is used to insure a water vapor saturated regime so that the resulting oxidation rates are not reactant limited. The lateral oxidation length at 420°C for buried 84 nm thick $Al_xGa_{1-x}As$ layers with x=1.0, 0.98, and 0.92 are plotted in Fig. 1(a). This figure reveals the lateral oxidation obeys a linear rate without an induction time preceding the onset of oxidation. Using a model of silicon oxidation,[12] the oxidation thickness, d_{ox}, achieved in a time t can be calculated from

$$d_{ox}^2 + Ad_{ox} = Bt \quad (1),$$

where B is related to the diffusion constant of reactants through the oxide and B/A is related to the oxidation reaction rate constant. In the limit of short oxidation times and/or thin oxide thickness, equation (1) yields the reaction rate limited case:

$$d_{ox} = (B/A) t \quad (2).$$
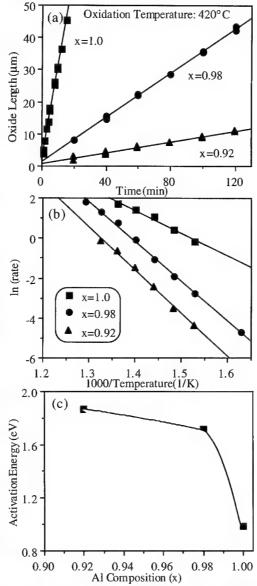
Fig. 1. Wet oxidation of AlGaAs: (a) lateral oxide length; (b) Arrhenius plot of rates; (c) activation energy of oxidation.

For temperatures ranging between 350-500°C linear oxidation rates are observed, which indicate that the lateral oxidation of AlGaAs is rate limited rather than

determined by the diffusion of reactants through the oxide.

The oxidation rate for a specific Al composition depends exponentially on temperature as shown in Fig. 1(b). From this Arrhenius dependence, oxidation activation energies can be calculated and are plotted in Fig. 1(c) for the different AlGaAs alloys. The activation energy for wet oxidation of AlAs is found to be 0.98 eV; in comparison, the wet oxidation activation energy for Si is 1.96 eV.[12] This illustrates the relatively high reactivity of AlAs to oxidation. Notice an increase of the GaAs mole fraction of only 8% nearly doubles the activation energy, producing a value similar to Si. A strong compositional dependence of the oxidation rates follows from the compositional dependence of the activation energies. In fact, the oxidation rate of $Al_xGa_{1-x}As$ for x varying from 1 to 0.8, changes by more than 2 orders of magnitude.[3] Thus a high degree of oxidation selectivity in high Al-containing AlGaAs layers can be obtained with only a minute change in Ga concentration. The oxidation selectivity to Al-content can be exploited for fabrication of buried oxide layers, as described below. However, Fig. 1 also indicates that stringent control of composition and temperature is crucial for attaining a reproducible and selective AlGaAs oxidation processes for device fabrication.

Fabrication of Oxide-Apertured VCSELs

Figure 2 depicts our monolithic VCSEL which employs selective oxidation to produce a buried oxide aperture on each side of the laser active region.[3,13] This oxide-apertured VCSEL structure has several advantages. First, in this monolithic structure we fully exploit low resistance distributed Bragg reflector (DBR) mirror designs (such as parabolic[14] or uniparabolic[15] heterointerface grading in combination with C-doping[16]) in utilizing the entire top mirror to conduct current into the active region. Thus current crowding effects and/or ion implantation damage in the top DBR are avoided. The current apertures immediately surrounding the optical cavity also eliminate sidewall nonradiative recombination present in air-post VCSELs[17] and minimize lateral current spreading outside of the laser cavity. Finally, the smaller refractive index of the oxide layer provides index-guided optical confinement,[7] but in a planar configuration amenable to efficient current flow and heat extraction.
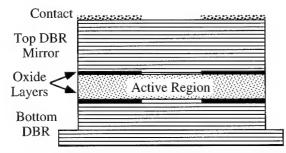
Fig. 2. VCSEL sketch showing the oxidized layers on each side of the active region.
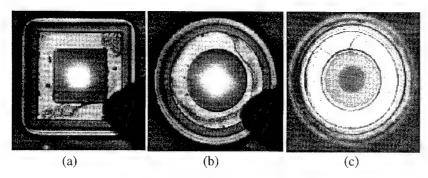
Fig. 3. Top view of VCSELs showing the $Al_xGa_{1-x}As$ current apertures located at the center of the mesas; (a) square mesa emitting light with x=0.98; (b) circular mesa emitting light with x=1.0; (c) circular mesa with x=0.92.

The VCSEL wafers are grown by metalorganic vapor phase epitaxy (MOVPE) in an EMCORE 3200 reactor. This growth technique is especially well suited for selectively oxidized VCSELs due to the complete accessibility of the AlGaAs alloy range, the stringent compositional control, and the high degree of compositional uniformity which can be achieved. The continuous AlGaAs alloy range enables the design of buried oxide layers within the VCSEL by selecting a specific or multiple AlGaAs layer(s) in the VCSEL for oxidation through small variations (≤10%) of the GaAs mole fraction in AlAs. Note that oxidation uniformity requires compositional uniformity. We estimate from our EMCORE oxidation calibration samples that the AlGaAs composition of layers with nominally identical composition vary less than ±0.1%.

Fabrication of oxide-apertured VCSELs[13] begins with the lift-off deposition of a top ring-shaped Ti/Pt/Au p-type contact, and a backside blanket evaporation of a Ge/Au/Ni/Au n-type contact. A silicon nitride mask is deposited on the top surface and patterned to encapsulate the metal contact and form a mesa etch mask. Reactive ion etching employing BCl_3/Cl_2 is used to define the laser mesas, thus forming trenches to expose the mesa sidewalls for oxidation. For the mirror layers not intended for oxidation, we use a GaAs mole fraction of 6 to 8%. The low index layers intended for oxidation adjacent to the optical cavity are adjusted to $Al_{0.98}Ga_{0.02}As$ for an enhanced oxidation rate. The oxidation of VCSELs is typically done at 440°C, producing an oxidation rate of ≈1 μm/min for the $Al_{0.98}Ga_{0.02}As$ layers, which is a factor of 3 or more faster than the surrounding AlGaAs layers. Lastly, the top nitride mask is removed before device testing.

Fig. 3 illustrates top views of oxide-apertured VCSELs. The central regions in the mesa centers correspond to the unoxidized portion of the current aperture which defines the laser cavity. Independent of composition, the current aperture resulting from a square mesa tends to also be square as shown in Fig. 3(a), implying isotropic oxidation. However, for high Al-content layers (x ≥ 0.94) crystallographic dependent oxidation is observed from circular mesas. For example, Fig. 3(b) shows a roughly square aperture results from a circular mesa when oxidizing AlAs. Fig. 3(c) reveals that a circular aperture from a circular

(a)   (b)
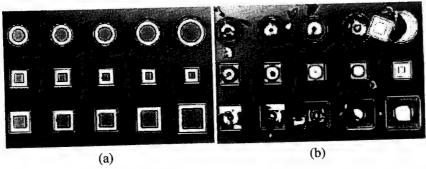
Fig. 4. Top view of VCSEL mesas containing $Al_xGa_{1-x}As$ oxide apertures after rapid thermal annealing to 350°C for 30 sec.; (a) x=0.98; (b) x=1.0.

mesa is regained for an oxide layer composition of x=0.92.

In spite of the crystallographic oxidation, the use of the binary AlAs as the oxidation layer would seem to relax the required compositional control during growth. However, this actually creates new and worse problems. First, the high reactivity of AlAs as seen in Fig. 1 makes control of its oxidation rate problematic. Secondly, structures using oxidized AlAs are mechanically unstable to thermal cycling. Shown in Fig. 4 is a comparison of VCSEL mesas, after rapid thermal annealing to 350°C for 30 seconds, where $Al_{0.98}Ga_{0.02}As$ or AlAs are used in the oxide layers. The mesas containing oxidized AlAs delaminate at the oxide/semiconductor interface, while the mesas with x=0.98 in the oxide layer are unaffected by the anneal. This thermal sensitivity is particularly insidious for post-oxidation VCSEL processing requiring heating to $\approx$100°C or greater, such as for photolithography, polymer planarization, dielectric deposition, etc. Finally and most importantly, VCSELs using AlAs oxide layers have shown obvious degradation over only a few hours of operation.[18,19]

Cross section TEM images (prepared using focused ion beam etching) of oxide-confined VCSELs using $Al_{0.98}Ga_{0.02}As$ and AlAs as the oxide layers are shown in Figs. 5 and 6, respectively. The terminus of the oxide layer is denoted by the vertical arrows in Figs. 5 and 6, with the unoxidized region beyond this point corresponding to the interior of the laser cavity. In Fig. 5 and all other samples that have been examined which employ $Al_{0.98}Ga_{0.02}As$ oxidation layers, no dislocations or other defects are apparent along the oxide/semiconductor interface or near the oxidation terminus. Moreover, evidence of strain is not apparent, as in Fig. 5. However, near the AlAs oxide terminus in Fig. 6 evidence of a strain field is observed (see contrast at arrow). The strain presumably arises from the volume shrinkage in the oxidized AlAs layer: the γ-Al_2O_3 converted from AlAs experiences a volume contraction of >12% as compared to the original AlAs.[20] By comparison, the oxide shrinkage of $Al_{0.92}Ga_{0.08}As$ has been measured to be only 6.7%.[21] Therefore, the dramatic temperature sensitivity of AlAs samples depicted in Fig. 4, the strain observed at the AlAs oxide terminus in Fig. 6, and the degraded laser lifetimes of VCSELs using AlAs are indicative

57
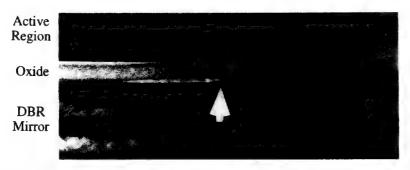
Fig. 5. Cross section TEM image (g=(311)) of a VCSEL with an $Al_{0.98}Ga_{0.02}As$ oxide layer; the arrow denotes the oxide terminus.

Fig. 6. Cross section TEM image (g=(400)) of a VCSEL with an AlAs oxide layer.

of excessive stress in the oxidized structures. To mitigate these adverse effects, the addition of a small amount of Ga to the oxidation layer is found to enable robust oxidation processing and reliable oxide-apertured VCSELs.

Performance of Oxide-Apertured VCSELs

Oxide-apertured VCSELs emitting at 980, 850, 780, and 650 nm have been fabricated and characterized. Shown in Fig. 7 are light-current-voltage curves for 850 and 780 nm devices with 5x5 μm apertures. For many emerging VCSEL applications, such as sources for optical fiber data links, laser printing heads, or free space interconnects, a submilliamp threshold current and an output of ≥ 1 mW is desired. These attributes are depicted in Fig. 7 and have also been demonstrated at 980 nm[3,5,13] and 680 nm[4] using oxide-apertured VCSELs. The improved performance of these VCSELs arises from the enhanced electrical and optical confinement provided by the buried oxide layers.

Figure 8 shows a comparison of oxide-apertured and ion implanted VCSELs fabricated from the same epitaxial wafer. For the latter conventional VCSELs, a deep proton implantation is used to render the material around the laser nonconducting and thus define the laser cavity.[22] For the broad area (>500 μm²)
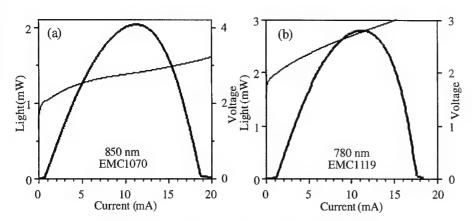
Fig. 7. Characteristics of oxide-apertured VCSELs including output light (heavy curve) and applied voltage (light curve); (a) 850 nm lasing wavelength; (b) 780 nm lasing wavelength.
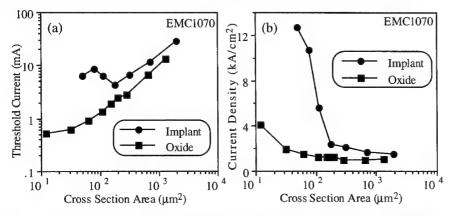
Fig. 8. Threshold properties of 850 nm oxide-apertured VCSELs; (a) threshold current; (b) threshold current density.

lasers in Fig. 8(a), the reduced threshold current of the oxide-confined VCSELs arises due to the improved electrical confinement.[6] Since the insulting oxide layers are located on each side of the active region (see Fig. 2) the charge carriers are efficiently confined and injected into the quantum wells. By comparison, the ion implantation is necessarily located ≈ 0.5 μm above the active region to avoid implantation damage to the quantum wells. Hence significant current spreading outside of the laser cavity occurs, which leads to increased carrier density required for lasing..

Due to the nature of the oxide-apertured VCSELs, extremely small cross section areas approaching 1 μm^2 can be easily fabricated as shown in Fig. 8(a). As a result, threshold currents less than 1 mA are possible for the oxide-apertured VCSELs, as evident in Fig. 8(a) for area $\leq$ 100 μm^2. Notice the

increase of the threshold current observed for implanted VCSELs in Fig. 8(a) with area ≤ 100 μm^2, which is more pronounced in the threshold current density plotted in Fig. 8(b). The increased threshold current for the implanted VCSELs is needed to form a thermal refractive index profile (thermal "lense") necessary to support a transverse optical mode. The monotonic decrease of the threshold currents apparent for the oxide-apertured VCSELs in Fig. 8(a) is due to the concomitant index-guiding of the buried oxide layer.[7] The refractive index changes from 3.0 for the original AlGaAs layer to ≈ 1.6 for the oxide, which induces a significant index difference between the laser cavity and the region surrounding the laser thus providing index-guiding optical confinement. For a given laser cross section area, the smaller threshold current density of the oxide-apertured VCSELs in Fig. 8(b) implies that a smaller modal gain is required for the onset of stimulated emission.[23] This is a manifestation of the reduced loss arising from the more efficient confinement of the charge carriers and photons within the laser cavity for the oxide-apertured VCSELs.

Conclusions

Oxidation of AlGaAs alloys may play an important role in advanced optoelectronic device fabrication. We have shown the lateral oxidation rate of buried AlGaAs layers is dependent on temperature and composition. The linear oxidation rates imply a rate limited reaction, and a strong compositional dependence of the oxidation rates is a consequence of the compositional dependence of the activation energies. The oxidation selectivity which is possible with small variations of Ga content in high Al-containing AlGaAs enables the design of devices with buried oxide layers, but also requires stringent control of the alloy compositions for process reproducibility. Finally, the oxidation of AlGaAs alloys is found to provide a structure with less inherent strain than is obtained using AlAs, resulting in robust device processing of reliable VCSELs.

Utilization of buried oxide layers in VCSELs has been shown to have several advantages. The selectively oxidized structure is suitable for fabrication of small active volume microlasers. The insulating oxide efficiently confines and injects charge carriers into the laser quantum wells, while the reduced refractive index of the oxide transversely confines the laser emission. This enhanced electrical and optical confinement enables ultralow threshold currents. Finally, the selectively oxidized structure has been implemented for VCSELs emitting at 980, 850, 780 and 650 nm, indicating the universality of this structure. High performance oxide-confined VCSELs appropriate for a variety of wavelengths should benefit emerging applications and markets being considered for VCSELs.

Acknowledgments

References

[1]D. L. Huffaker, D. G. Deppe, K. Kumar, and T. J. Rogers, Appl. Phys. Lett. **65**, 97 (1994).

[2]G. M. Yang, M. H. MacDougal, P. D. Dapkus, Electron. Lett. **31**, 886 (1995).

[3]K. D. Choquette, R. P. Schneider, Jr., K. L. Lear, and K. M. Geib, Electron. Lett. **30**, 2043 (1994).

[4]K. D. Choquette, R. P. Schneider, Jr., M. H. Crawford, K. M. Geib, and J. J. Figiel, Electron. Lett. **31**, 1145 (1995).

[5]K. L. Lear, K. D. Choquette, R. P. Schneider, Jr., S. P. Kilcoyne, and K. M. Geib, Electron. Lett. **31**, 208 (1995).

[6]K. D. Choquette, K. L. Lear, R. P. Schneider, Jr., and K. M. Geib, Appl. Phys. Lett. **66**, 3413 (1995).

[7]K. L. Lear, K. D. Choquette, R. P. Schneider, Jr., and S. P. Kilcoyne, Appl. Phys. Lett. **66**, 2616 (1995).

[8]J. M. Dallesasse, N. Holonyak, Jr., A. R. Sugg, T. A. Richard, and N. El-Zein, Appl. Phys. Lett. **57**, 2844 (1990).

[9]J. M. Dallesasse and N. Holonyak, Jr., Appl. Phys. Lett. **58**, 394 (1991).

[10]A. Fiore, V. Berger, E. Rosencher, N. Laurent, S. Theilmann, N. Vodjdani, and J. Nagle, Appl. Phys. Lett. **68**, 1320 (1996).

[11]E. I. Chen, N. Holonyak, Jr., and S. A. Maranowski, Appl. Phys. Lett. **66**, 2688 (1995).

[12]B. E. Deal and A. S. Grove, J. Appl. Phys. **36**, 3770 (1965).

[13]K. D. Choquette, K. L. Lear, R. P. Schneider, Jr., K. M. Geib, J. J. Figiel, and R. Hull, IEEE Photon. Tech. Lett. **7**, 1237 (1995).

[14]R. P. Schneider, Jr., J. A. Lott, M. Hagerott Crawford, and K. D. Choquette, Inter. J. High Speed Electronics and Systems **5**, 625 (1994).

[15]K. L. Lear and R. P. Schneider, Jr., Appl. Phys. Lett. **68**, 605 (1996).

[16]K. L. Lear, R. P. Schneider, Jr., K. D. Choquette, S. P. Kilcoyne, J. J. Figiel, and J. C. Zolper, IEEE Photon. Tech. Lett. **6**, 1053 (1994).

[17]K. D. Choquette, G. Hasnain, Y. H. Wang, J. D. Wynn, R. S. Freund, A. Y. Cho, and R. E. Leibenguth, IEEE Photon. Tech. Lett. **3**, 859 (1991).

[18]D. L Huffaker, J. Shin, and D. G. Deppe, Electron. Lett. **30**, 1946 (1994).

[19]K. D. Choquette, H. Chui, and K. M. Geib, unpublished.

[20]M. H. MacDougal, H. Zhao, P. D. Dapkus, M. Ziari, and W. H. Steier, Electron. Lett. **30**, 1147 (1994).

[21]R. D. Tweston, D. M. Follstaedt, K. D. Choquette, and R. P. Schneider, Jr., submitted to Appl. Phys. Lett. (1996).

[22]Y. H. Lee, B. Tell, K. Brown-Goebeler, J. L. Jewell, and J. V. Hove, Electron. Lett. **26**, 710 (1990).

[23]K. D. Choquette, W. W. Chow, M. Hagerott Crawford, K. M. Geib, and R. P. Schneider, Jr., submitted to Appl. Phys. Lett. (1996).

Long-Wavelength Vertical-Cavity Surface-Emitting Laser Diodes

D.I. Babic[±], V. Jayaraman*, N. M. Margalit, K. Streubel**, M.E.Heimbuch, R.P. Mirin, B.J. Thibeault, J.E. Bowers, E.L. Hu, S.Denbaars

Department of Electrical and Computer Engineering
University of California at Santa Barbara
Santa Barbara, CA 93106

[±]Currently at Hewlett Packard Laboratories
Palo Alto, CA

*Optical Concepts,
Lompoc, CA 93436

**Royal Institute of Technology,
Stockholm, Sweden

Abstract

Long-wavelength (1300/1550 nm) vertical-cavity surface-emitting lasers (VCSELs) have been much more difficult to realize than VCSELs at shorter wavelengths such as 850/980 nm. The primary reason for this has been the low refractive index difference and reflectivity associated with lattice-matched InP/InGaAsP mirrors. A solution to this problem is to "wafer-fuse" high-reflectivity GaAs/AlGaAs mirrors to InP/InGaAsP active regions. This process has led to the first room-temperature continuous-wave (CW) 1.54 µm VCSELs. In this paper, we discuss two device geometries which employ wafer-fused mirrors, both of which lead to CW operation. We also discuss fabrication of WDM arrays using long-wavelength VCSELs.

I. Introduction--VCSEL background

In recent years, the vertical-cavity surface-emitting laser (VCSEL) has emerged as a new coherent light source alongside the conventional in-plane semiconductor laser owing to its compactness, inherent single-longitudinal mode operation, circular beam profile, and low manufacturing cost. The basic structure of a typical 980 nm or 850 nm [1] GaAs-based laser is shown in Fig. 1.1. The resonator is formed between epitaxial multilayer GaAs/AlAs mirrors, and the light emits through an aperture in the top p-contact. A number of other processing methods, such as etched post [2] or lateral oxidation [3] can also be employed and all rely on similar epitaxial growth. State of the art GaAs-based vertical-cavity lasers operate continuously at room-temperature with sub-100 µA threshold currents. The outstanding performance of these lasers greatly relies on their monolithic fabrication process

and the quality of Al(Ga)As/GaAs quarter-wave mirrors, which are presently the highest quality epitaxial mirrors that can be routinely fabricated.
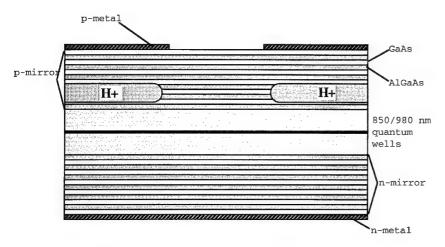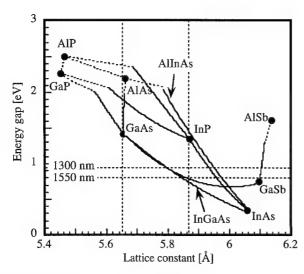
Figure 1.1: Typical 850 nm/ 980 nm VCSEL structure

Long-distance optical fiber transmission systems, however, require sources at 1300 or 1550 nm. The practical realization of VCSELs at these wavelengths has been a difficult process over the last decade due to numerous technological challenges. The most significant problem has been the fabrication of mirrors with sufficiently high reflectivity and adequate electrical and thermal properties. Active layers with bandgap energies in the 1.3 μm to 1.6 μm wavelength range are presently grown using InGaAsP and AlInGaAs lattice-matched to InP, as shown in Fig. 1.2. Following the example of GaAs-based VCSELs shown in Fig. 1.1, the immediate choice for long-wavelength quarter-wave epitaxial mirrors is the InGaAsP/InP or AlInGaAs/InP system lattice-matched to InP. The quaternary alloy is used as the high index and InP as the low index material . The range of refractive index that can be realized by varying the composition of this alloy is relatively small and requires epitaxial growths of thicknesses greater than 10 μm for a single mirror to achieve sufficient reflectivity for vertical-cavity laser operation. The thermal conductivity of the quaternary InGaAsP alloy is an order of magnitude lower than that of InP and therefore laser cavities that use these materials require a careful thermal design involving heat paths around the mirrors for device cooling. This leaves a small margin of error in the design and the fabrication of these lasers. For these reasons, other dielectric and semiconductor mirror options have been investigated for long-wavelength VCSELs. These are described in the next section .

Fig. 1.2: Energy-gap vs. lattice constant for III-V alloys relevant for long-wavelength vertical-cavity laser applications. Vertical lines indicate GaAs and InP substrate lattice constants, while the horizontal lines indicate the energies of the 1300 nm and 1550 nm transitions.

II. Wafer-fused GaAs/AlAs mirrors: Motivation and Properties

For long-wavelength VCSELs, the most common dielectric mirror is Si/SiO_2 (refractive index 3.6/1.46) Owing to the large refractive index ratio these mirrors only require a few periods to achieve high reflectivity. However, their reflectivity is limited by the absorption in amorphous silicon. The thermal conductivity of silicon oxide and amorphous silicon is also quite poor and they can not be used as the bottom, heat transferring mirror in VCSELs. Thermal conduction of these mirrors can be improved by using MgO [4] and silicon carbide. However, one significant disadvantage of all dielectric mirrors is they are electrically insulating. This forces the use of ring contacts, leading to non-uniform injection and current crowding, which degrades device efficiency.

Semiconductor mirrors, on the other hand can be electrically conductive, and generally have better thermal conductivity than dielectric mirrors. Using the process of *wafer fusion*, InGaAsP active layers operating at 1300 nm and 1550 nm can be bonded to epitaxially grown mirrors that are not lattice-matched to InP. Figure 2.1

65
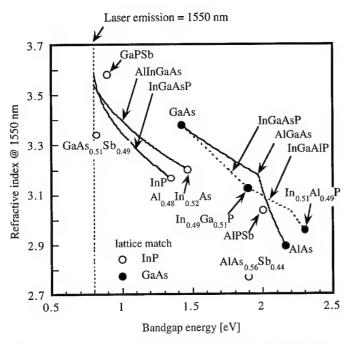
Fig. 2.1: Refractive index as a function of energy gap for material lattice matched to GaAs and InP.

illustrates the options available among semiconductor mirrors for 1.55 μm operation. Figure 2.1 shows the refractive index at 1550 nm as a function of the energy bandgap of the material, and enables a direct comparison between the achievable refractive index values for compatible materials. Evidently, in order to fabricate a semiconductor quarter-wave mirror one uses a wide bandgap material for the lower of the two indexes and a narrow gap material for the higher. In selecting the narrow gap material or alloy composition care must be taken that the lasing wavelength is longer than the wavelength of the absorption edge of the mirror material.

From Fig. 2.1, it is evident that the GaAs/AlAs material system provides high refractive index contrast. This fact, combined with excellent thermal conductivity, and the proven performance of AlGaAs/GaAs mirrors at 980 nm makes them an excellent choice at 1550 nm. Figure 2.2 shows a comparison amongst three mirror combinations: the dielectric Si/SiO_2 combination, the lattice-matched InP/InGaAsP mirror, and the wafer-fused AlAs/GaAs mirror. The dielectric mirror saturates at low reflectivity because amorphous silicon is quite lossy. The other two semiconductor mirrors have been modeled with 10 cm$^-$1 loss, but because the InP/InGaAsP mirror requires a large number of periods, it too

saturates at low reflectivity. The GaAs/AlGaAs system is by far the best choice, and as sections 3 and 4 describe, has produced the best 1.55 μm VCSELs ever.
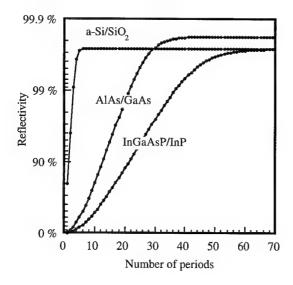
Fig. 2.2: Reflectivity as a function of number of layers for three quarter-wave mirrors used for 1.55 μm vertical-cavity lasers.

III. CW Electrically pumped Double-fused VCSEL Results

Figure 3.1 illustrates a scanning electron micrograph (SEM) of double-fused VCSELs, with an InP/InGaAsP active region and two wafer-fused GaAs/AlGaAs mirrors. The high mirror reflectivity provided by the GaAs/AlAs mirror must be coupled with electrical conductivity and low-free carrier absorption to result in room temperature CW operation. Particularly in the p-type mirror, dopants must be strategically placed in the cavity, with a doping level that is low enough to minimize loss and high enough to minimize electrical resistance. The heterointerfaces in the mirror must also be graded properly to reduce resistance [5].

Careful attention to these issues has resulted in the room-temperature double-fused results shown in Fig. 3.2. Device sizes from 8 μm to 20 μm lase CW, at room temperature, and CW lasing is maintained up to 34 °C [6]. These devices have also been tested in transmission experiments. They maintain a side-mode suppression ratio of 25 dB under 1 Gbit/sec pseudo-random modulation, with a measured bit error rate of $3e^{-12}$ after

transmission through 6.4 km of single-mode fiber. Measured RC-limited bandwidth is 2-3 Ghz. [7]
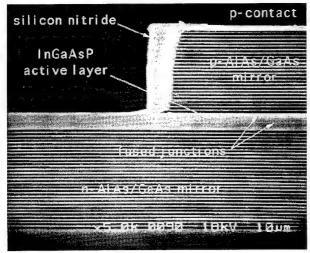
Figure 3.1: SEM of double-fused 1550 nm VCSEL.
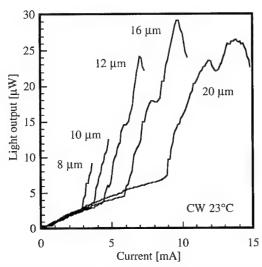
Fig. 3.2: Continuous-wave operation of five sizes of 1.54 μm vertical-cavity lasers.

The double-fused VCSEL results of Fig. 3.2 employ an "etched-post" geometry, which is now known to introduce excess scattering loss. Recent work on 980 nm lasers at Sandia laboratories [3] has demonstrated that an "oxide aperture" geometry introduces much lower loss. The device structure is similar to Fig. 3.1, except now an AlAs layer in the p-mirror close to the active region is oxidized inward from the edge to constrict the current and the optical mode. Applying this to double-fused VCSELs, Margalit et al [8] have obtained the results shown in Fig. 3.3. Threshold current has been reduced to 1.3 mA, and maximum operating temperature increased to 39°C.
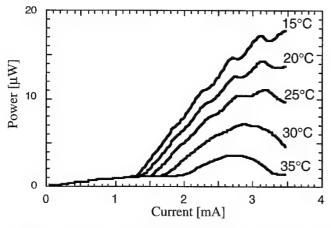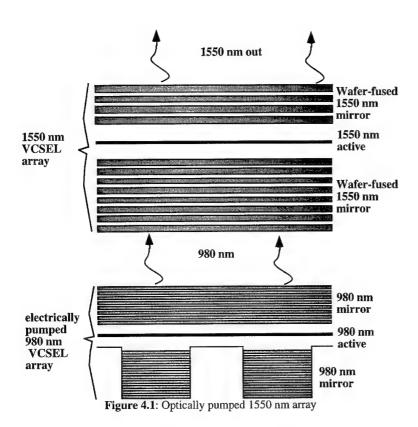
Figure 3.3 - CW L-I vs Temperature for oxidized double-fused device.

IV. CW Optically Pumped Double-Fused VCSEL Results

The double-fused geometry lends itself to another approach to achieving room-temperature CW operation at long-wavelengths. Figure 4.1 shows an approach in which the 1550 nm VCSEL is optically pumped by an underlying 980 nm VCSEL [9]. This "integrated optical pump" scheme retains all the advantages of the VCSEL geometry, such wafer-scale fabrication and testing. Modulation of the long-wavelength radiation is accomplished by modulating the 980 nm pump. The motivation for this approach is to eliminate the need for dopants in the long-wavelength cavity, greatly reducing intracavity losses, and to eliminate resistive heating on the long-wavelength side. It is also possible to use a small diameter pump VCSEL in conjunction with a large mode field in the long-wavelength VCSEL, which could enhance transverse mode control. The absence of resistive heating minimizes thermal lensing.

Figure 4.1: Optically pumped 1550 nm array

One of the reasons this scheme is feasible is that the GaAs/AlAs mirrors of the 1550 nm VCSEL are transparent to the 980 nm radiation, as shown in Fig. 4.2. This allows the pump beam to be coupled efficiently into the long-wavelength VCSEL. It is also true that the 1550 nm VCSEL does not "see" the 980 nm VCSEL mirrors, so stacking the two cavities next to each other does not lead to appreciable coupled-cavity effects.
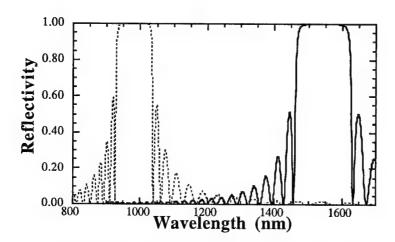
Figure 4.2: 30 period GaAs/AlAs mirrors at 980 nm and 1550 nm.

Also critical to the success of the scheme shown in Fig. 4.1 is designing the long-wavelength cavity with threshold sufficiently low that it can be reached with 980 nm VCSEL power levels.
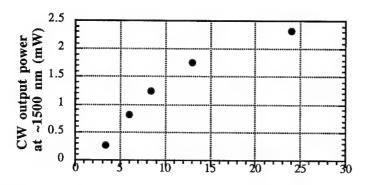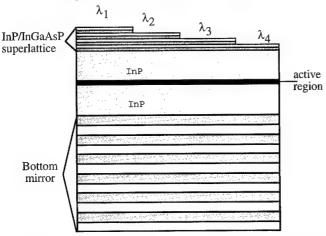
Figure 4.3: CW Power conversion from 935 nm (Ti:Sapphire) to 1500 nm VCSEL. Both power axes are in mW.

The undoped double-fused geometry is inherently low-loss, and further designing the cavity to be optically pumped leads to low optically pumped thresholds. Figure 4.3 shows experimentally measured CW power conversion from 935 nm to 1550 nm using a Ti:Sapphire laser as the pump source, pumping a 1550 nm double-fused VCSEL. Threshold power is 2-3 mW, and maximum output power is approximately 2 mW. These numbers verify qualitatively that wafer fusion does not introduce a large amount of optical loss into the cavity. The pump powers shown on the horizontal axis represent those hitting the long-wavelength active region, and correction has been made for loss through a focusing microscope objective, as well as reflection from a GaAs substrate with no anti-reflection coating. No correction has been made for unabsorbed light. The best 980 nm VCSELs today can deliver nearly 10 mW power for 10 µm device size, so the experiment of Fig. 4.3 indicates that the scheme of Fig. 4.1 is entirely feasible. We choose 10 µm device size because this is comparable to that in single-mode optical fiber.

V. Double-Fused WDM Arrays

Another interesting level of design freedom inherent to the double-fused structure is the possibility of intracavity mode adjustment prior to wafer fusion of the second mirror. Figure 5.1 shows how this can be applied to generate wavelength-division multiplexed (WDM) arrays of long-wavelength VCSELs. Inside the long-wavelength cavity is a superlattice of alternating layers of InP and InGaAsP. Selectively removing layers of this superlattice allows the lasing wavelength to be varied from one device to the next.

Figure 5.1: Intracavity superlattice for WDM arrays. The second GaAs/AlAs mirror is fused to the non-planar top surface.

After this etching has been done, the second mirror can be fused to this stepped surface. Successful fusion to a stepped surface is rather surprising, and the physics of this process

remains to be well understood. Work by Babic [5] has indicated that material tends to move to fill voids during the fusing process, and this apparently aids in obtaining robust wafer fusion over the non-planar surface of Fig. 5.1.

Using the process of Fig. 5.1, the 4-channel WDM array results of Figure 5.2 were obtained.

4-channel WDM VCSEL Array
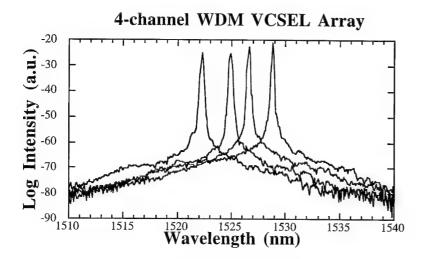
Figure 5.2 Optically pumped WDM array

The channel spacing is approximately 2 nm, and low optically pumped threshold (2-4 mW) is maintained even after fusing to a stepped surface. A number of features remain to be explained, such as the non-uniformity in channel spacing, and correlating the channel spacing with the step height of the intra-cavity etch. Nevertheless, the results of Fig.5.2 suggest that double-fused wavelength-stepped arrays are possible. These hold potential for replacing expensive arrays of distributed feedback (DFB) and distributed Bragg reflector (DBR) lasers in future WDM applications.

VI. Conclusion

Long-wavelength vertical-cavity surface-emitting lasers (VCSELs) have undergone major advancements in the last 2 years due to the introduction of "wafer-fused" GaAs/AlAs mirrors, in conjunction with InGaAsP/InP active regions. Using two wafer-fused mirrors to create a "double-fused" geometry has resulted in the first room-temperature CW devices. Two device structures have been demonstrated. The first uses direct electrical pumping of the double-fused device, and has resulted in 1.3 mA CW threshold. The second uses optical pumping with a shorter wavelength VCSEL, and has demonstrated 1 mW CW output

power with less than 10 mW pump power. We have also demonstrated wafer fusion to stepped surfaces, resulting in a 4-channel WDM array at 1.55 μm.

Acknowledgements

References

1. Morgan, R.A., Hibbs-Brenner, M.K., Walterson, R.A., Lehman, J.A. Marta, T.M., Bounnak, S., Kalweit, E.L., Akinwande, T., and Nohava, J.C., "Producible GaAs-based MOVPE-grown vertical-cavity top-surface emitting lasers with record performance," *Electron. Lett.* , 1995, **31,** (6), pp. 462-464.

2. Geels, R.S., Corzine, S.W., and Coldren, L.A., "InGaAs vertical cavity surface-emitting lasers," *IEEE J. Quantum Electron.* , vol.27, no.6, pp.1359-1367.

3. Lear, K., Choquette, K.D. , Schneider, R.P., Kilcoyne, S.P., and Geib, K.M., "Selectively oxidized vertical-cavity surface-emitting lasers with 50% power conversion efficiency," *Electron. Lett.,* 1995, **31**, (3), pp. 208-209.

4. Baba, T. , Yogo, Y. , Suzuki, K., Koyama, F., and Iga, K., "Near room-temperature continuous-wave lasing characteristics of GaInAsP/InP surface-emitting lasers," *Electron. Lett.,* 1993, **29,** (10), pp. 913-914.

5. Babic, D.I., "Double-fused long-wavelength vertical-cavity lasers," Ph.D. Dissertation, University of California, Santa Barbara, 1995.

6. Babic, D.I., Streubel, K. Mirin, R.P. Margalit, N.M., Bowers, J.E., Hu, E.L., Mars, D.E., Yang, L., and Carey, K.: "Room-temperature continuous-wave operation of 1.54 μm vertical-cavity lasers.," *IEEE Photon. Technol. Lett., 1995,* **7**, (11), pp. 1225-1227.

7. Blixt, P., Babic, D.I., Margalit, N.M., Reynolds, T.E., and Bowers, J.E., "1 Gbit/sec single-mode operation.of vertical-cavity lasers emitting at 1.54 μm," Conference on *Optical Fiber Communication,* (OFC '96), paper TuC4, San Jose, CA Feb. 25-Mar. 1, 1996.

8. Margalit, N.M. Babic, D.I. Streubel, K., Mirin, R.P., Zhang, S. Mars, D.E., Bowers, J.E., and Hu, E.L., "Laterally oxidized long-wavelength CW vertical cavity lasers," Conference on *Optical Fiber Communication,* (OFC '96) post-deadline session, San Jose, CA, Feb. 25-Mar. 1, 1996.

9. Jayaraman, V. and Kilcoyne, M.K. "WDM array using long-wavelength vertical-cavity lasers," *Photonics West* SPIE conference, paper 2690-37, San Jose, CA Jan. 29-Feb. 2, 1996.

STABILIZATION OF TRANSVERSE MODE EMISSION IN VERTICAL-CAVITY SURFACE-EMITTING LASERS BY DEPOSITION OF HIGH REFRACTIVE INDEX AMORPHOUS GaAs

HYO-HOON PARK, BYUENG-SU YOO, HYE YONG CHU AND EL-HANG LEE
Electronics and Telecommunications Research Institute, P.O. Box 106, Yusong,
Taejon, 305-600, Korea, hhpark@utopia.etri.re.kr
MIN SOO PARK, BYUNG TAE AHN, JAE-HEON SHIN AND YONG HEE LEE
Korea Advanced Institute of Science and Technology, Yusong, Taejon, 305-701, Korea

ABSTRACT

We report successful application of a low-temperature-grown amorphous GaAs
(a-GaAs) layer for stabilization of the fundamental transverse mode of InGaAs/GaAs
vertical-cavity surface-emitting lasers. The maximum currents maintaining a stable
fundamental transverse mode were increased by the antiguide effect of a-GaAs with a
high refractive index. For 10-μm- and 15-μm-diameter devices, we attained a stable
single-mode emission over a wide range of current. The antiguiding of transverse
modes in vertical cavity buried in the high refractive cladding layer was calculated
using a two-dimensional beam propagation method.

INTRODUCTION

Vertical-cavity surface-emitting lasers (VCSELs) are considered to be useful light
sources for applications in optical parallel processing, optical communications and
optical interconnections. [1] One of the most imperative issues for these applications is
achieving a stable transverse mode emission at high output power. The requirement of
the high output power needs to increase the maximum laser aperture size maintaining
stable transverse mode emission. In conventional VCSEL index-guided structures,
unstable multi-transverse emission characteristics have been observed even for
relatively small devices of < 10 μm diameter due to strong confinement of high order
transverse modes in the cavity. In gain-guided structure also, stable transverse mode
characteristics have been observed for only the devices with window size of < 10 μm.
[2,3] Recently, several attempts have been made to control the transverse mode in both
index-guided [4] and gain-guided [5] structures. In the work reported by Wu *et al.*, [4] a
buried VCSEL structure with AlGaAs epitaxial layers was employed to stabilize
fundamental transverse mode emission using antiguide effect of the surrounding
AlGaAs layers of relatively high refractive index.

In this work, we report that a VCSEL structure buried in low temperature-
deposited amorphous GaAs (a-GaAs) is very effective in improving the transverse
mode characteristics. Since a-GaAs has high refractive index [6] compared to
crystalline GaAs and AlAs layers composing the cavity and waveguide regions, the a-
GaAs-buried region plays the role of an antiguiding channel. Using this structure, we
could obtain a stable fundamental mode emission for devices of 10 μm diameter.

EXPERIMENTAL

The epitaxial structure was grown by metalorganic chemical vapor deposition technique. The active layers were designed with a periodic gain VCSEL structure having a two-wavelength-thick undoped GaAs cavity and three $In_{0.22}Ga_{0.78}As$ (85Å) quantum wells. The distributed Bragg reflectors (DBR) at the top (p-doped) and the bottom (n-doped) sides respectively consisted of 16 and 23.5 periods of AlAs/GaAs quarter-wave stacks. The detailed laser structure was described in previous reports. [7,8] We fabricated bottom-emitting lasers using chemically-assisted ion beam etching (CAIBE) with chlorine. Ti/Au/Ni metal dots were used as p-contact and mask layers for CAIBE. The laser posts were etched through the active region to the top layer of the bottom mirror, employing *in-situ* monitoring of etch depth using laser reflectometry. [9] After CAIBE, the sample was immediately rinsed with deionized water, and then it was slightly etched using a solution of $H_2SO_4:H_2O_2:H_2O=1:8:1000$ to remove residual chlorine and the ion damaged region on the etched sidewall. The *a*-GaAs layer was deposited by molecular beam epitaxy at 160 °C for 2.5 h under an As/Ga ratio of 20:1. The thickness of *a*-GaAs layer was 2.5 - 3.0 μm. The amorphous state of the GaAs layer was identified from X-ray diffraction measurements. The resistivity of *a*-GaAs layer was higher than 900 Ωcm as determined by I-V measurement for a sample deposited on a semi-insulating GaAs substrate. The refractive index of *a*-GaAs layer was measured to be 3.8 by an ellisometer. Figure 1 shows schematic cross-sectional view of the device. The detailed procedures to fabricate these devices were described in our previous report [10].
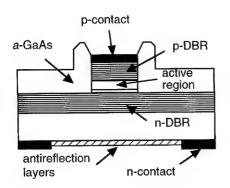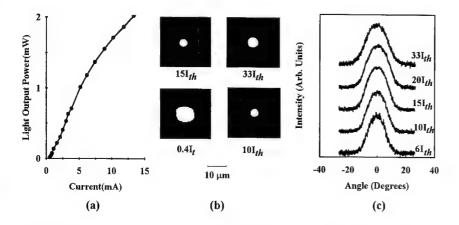
Figure 1. Schematic cross-section of amorphous-GaAs-buried surface-emitting lasers.

DEVICE CHARACTERISTICS

The device characteristics were measured under CW and pulse operation at room temperature without a heat sink. The lasing wavelength was around 990 nm at the threshold. In previous work [10], we reported passivation effect of *a*-GaAs layers on surface defects of etched sidewall of cavity. The threshold currents measured from as-etched circular devices with 15, 20, 25, and 40 μm diameters were 2.5, 4.3, 4.6, and 6.0 mA, respectively. Threshold currents of *a*-GaAs-deposited devices with 15, 20, 25, 30, 35 and 40 μm diameters were 1.3, 2.1, 2.9, 3.4, 4.1 and 5.1 mA. Differential quantum efficiencies as well as threshold currents were significantly improved by the *a*-GaAs deposition.

Figures 2(a), 2(b) and 2(c) show, respectively, L-I curve, near-field and far-field emission patterns of a 10-μm-diameter a-GaAs-buried device measured under pulse operation. The threshold current I_{th} of this device is 0.5 mA and light output power reaches over 2.0 mW. Below threshold, the spontaneous emission is observed over entire device area, as seen in Fig. 2(b) After laser operation, the near-field emission patterns show circularly symmetric and narrow fundamental transverse mode emissions. The fundamental mode emission is stable up to $15I_{th}$ with a constant beam

Figure 2. (a) L-I curve, (b) near-field emission and (c) far-field emission patterns for a 10-μm-diameter amorphous-GaAs-buried device.
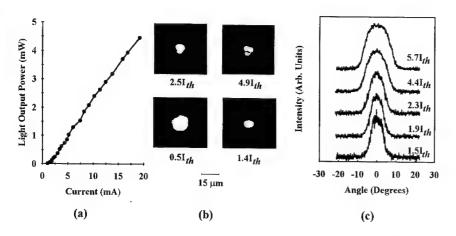
Figure 3. (a) L-I curve, (b) near-field emission and (c) far-field emission patterns for a 15-μm-diameter amorphous-GaAs-buried device.

width. As the current is increased above $15I_{th}$, the near-field patterns develop a slight broadening, but still the fundamental transverse mode is observed to be the dominant emission pattern. Far-field emission patterns, seen in Fig. 2(c), also show stable mode characteristics. Note that the far-field pattern is critical factor for coupling with an optical fiber. The angular spread of the laser mode is rearly constant over all measured current ranges.

Figures 3(a), 3(b) and 3(c) show L-I curve, near-field and far-field emission patterns of a 15-μm-diameter device measured under pulse operation. The threshold current of this device was 1.4 mA. In this device, the fundamental transverse mode is predominantly observed up to the current of around $1.4I_{th}$ and gradually developed next higher order modes with increasing current. The far-field emission patterns show slow increase of the angular spread with gradual transition to multi-transverse modes emission. The air-post devices with a diameter above 7 μm exhibited a rapid transition to multimode emission just above I_{th}. These results suggest that the a-GaAs-buried structure stabilizes the fundamental transverse mode emission quite effectively.

NUMERICAL ANALYSIS

We performed a two-dimensional numerical calculation to investigate the antiguiding effect of the a-GaAs-buried structure. We used a finite difference beam propagation method based on the scalar Helmholz wave equation [11]. Figure 4(a) shows a device model structure that we used for this calculation. The active region was considered as passive uniform media with an effective refractive indexe of n_1(3.523). The refractive index n_2 for DBR mirror region was assumed as an average value, 3.236, for the AlAs/GaAs mirror layers in our device structure. The reflectivity of the top mirror was considered as a unit. In clad, we used the refractive index of 3.8 and the extinction coefficient of 0.06 for the a-GaAs layer, measured by ellisometer.

Figure 4(b) shows the total cavity loss for fundamental and first order transverse modes against device size for various reflectivities of bottom mirror. The total cavity loss is given by the sum of the round trip loss in waveguiding in cavity and the power loss in mirror layers. After several thousand round trips, the profiles of both fundamental and first order modes were determined, respectively, and then the total cavity loss was obtained along with the mirror loss. We found that the total cavity loss of the fundamental and the first order modes increases with decreasing device size, resulting from rapid increase of the round trip loss. As the difference of total cavity loss increases, the first order mode emission can be suppressed effectively. Over the calculated reflectivity ranges, the difference reaches to significant values for the device sizes of 10 μm and less. Therefore, the observation of a stable fundamental mode emission at 10 μm diameter device, seen in Fig. 2, can be attributed to the strong antiguide effect in the a-GaAs-buried structure. In addition, the ratio of total cavity loss of two modes is found to increase with increasing mirror reflectivity, as shown in Fig. 4(b). This indicates that the higher transverse mode emission is suppressed more efficiently with decreased mirror loss. For a mirror reflectivity of 99.8%, the total cavity loss of the first order mode for a 15-μm-size device is 1.2 times that of the fundamental mode. These results suggest that it is possible to achieve a stable single transverse mode emission using the a-GaAs-buried structure up to 15 μm diameter by simply increasing the reflectivity of mirrors.

We also calculated the variation of the antiguiding effect with refractive index of the cladding layer. The round trip loss for fundamental and first order modes rapidly

increased with increasing the refractive index of the clad layer, n_3, above the value of the active region, n_1. However, The round trip losses for these modes are saturated when n_3 reaches near 3.5. This result indicates that the antiguiding effect is not enlarged any more for $n_3 > 3.5$. It has been reported that the properties of a-GaAs is strongly dependent on its composition ratio of As/Ga. With increasing the composition of As in a-GaAs prepared by molecular beam deposition, the refractive index increases from 3.5 to above 4.5, while the resistivity abruptly decreases. [6] Since the antiguiding effect is saturated beyond the refractive index of 3.5, we suggest that the a-GaAs layer with a low As composition may be optimum to achieve both electrical isolation of laser devices and stabilization of the transverse mode.

The high resistivity property of amorphous GaAs can provide an effect on the surface passivation of sidewall of the etched laser post, as reported previously [10]. Furthermore, The low temperature deposition of a-GaAs is performed without thermal damages on the device structure during the process, in particular on top metal mirror layer. Therefore, employing the a-GaAs layer as cladding layer in the VCSEL device structure provides various advantages in improving the device performances and also simplifying the processes.

(a)   (b)
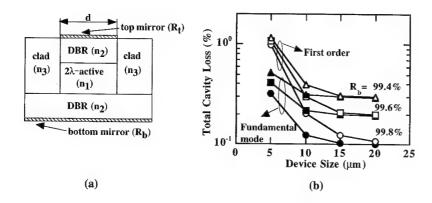
Figure 4. (a) Schematic model and (b) simulated total cavity losses against device size and mirror reflectivity for fundamental and first order transverse modes.

CONCLUSIONS

In conclusion, we have demonstrated that a low-temperature-deposited a-GaAs layer is very effective in stabilizing the fundamental transverse mode of VCSELs. Providing an antiguiding effect with an a-GaAs layer of a high refractive index, we were able to attain stable single transverse mode emission from a 10-μm-diameter device for current level over $20I_{th}$ and from a 15-μm-diameter device for current level over $1.4I_{th}$ under pulse operation.

79

ACKNOWLEDGMENTS

REFERENCES

1. Y.H. Lee, J.L. Jewell, A. Scherer, S.L. McCall, J.P. Harbison, and L.T. Florez, Electron. Lett. **25**, 1377 (1989).
2. C.J. Chang-Hasnain, J.P. Harbison, G. Hasnain, A. C. Von Lehmen, L.T. Florez, and N.G. Stoffel, IEEE J. Quantum Electron. **27**, 1402 (1991).
3. R.A. Morgan, G.D. Guth, M.W. Focht, M.T. Asom, K. Kojima, L.E. Rogers, and S.E. Callis, IEEE Photon. Technol. Lett. **4**, 374 (1993).
4. Y.A. Wu, C.J. Chang-Hasnain, and R. Nabiev, Electron. Lett. **29**, 1861 (1993).
5. D.L. Huffaker, J. Shin, H. Deng, C.C. Lin, D.G. Deppe, and B.G. Streetman, Appl. Phys. Lett. **65**, 2642 (1994).
6. N. Matsumoto and K. Kumabe, Jpn. J. Appl. Phys. **19**, 1583 (1980).
7. B.-S. Yoo, H.-H. Park, and E.-H. Lee, Electron. Lett. **30**, 1060 (1994).
8. H.-H. Park and B.-S. Yoo, ETRI J., **17**, 1 (1995).
9. J.Y. Yoo, J.H. Shin, Y.H. Lee, H.-H. Park, and B.-S. Yoo, Opt. & Quantum Electron. **27**, 421 (1995).
10. H.-H. Park, B.-S. Yoo, M.S. Park, J. Lee, H.G. Lee, E.-H. Lee, J.-H. Shin and Y.H. Lee, Mat. Res. Soc. Symp. Proc. **378**, 1013 (1995).
11. Y.A. Wu, G.S. Li, R.F. Nabiev, K.D. Choquette, C. Caneau, and C.J. Chang-Hasnain, IEEE J. Selected Topics in Quantum Electron. **1**, 629 (1995).

LOW INTERFACE STATE DENSITY OXIDE-GaAs STRUCTURES FABRICATED BY IN-SITU MOLECULAR BEAM EPITAXY

M. PASSLACK * and M. HONG
Bell Laboratories, 600 Mountain Avenue, Murray Hill, New Jersey 07974
* Present address: Motorola Inc., Phoenix Corporate Research Laboratories,
2100 E. Elliot Road, Tempe, AZ 85284, E-mail: a646aa@email.mot.com

ABSTRACT

We have extended the spectrum of molecular-beam epitaxy (MBE) related techniques by introducing in-situ deposition of oxides. The oxide films have been deposited on clean, atomically ordered (100) GaAs wafer surfaces using molecular beams of gallium-, magnesium-, silicon-, or aluminum oxide. Among the fabricated oxide-GaAs heterostructures, Ga_2O_3-GaAs interfaces exhibit unique electronic properties including an interface state density D_{it} in the low 10^{10} cm^{-2}eV^{-1} range and an interface recombination velocity S of 4000 cm/s. The formation of inversion layers in both n- and p-type GaAs has been clearly established. Further, thermodynamic and photochemical stability of excellent electronic interface properties of Ga_2O_3-GaAs structures has been demonstrated.

INTRODUCTION

Low-power components are key to the widespread use of high-performance portable systems. The natural choice for low-power, high speed/frequency devices are technologies using high mobility materials such as GaAs and related compounds [1]. Due to the lack of insulating layers on GaAs based semiconductors providing low interface state density and stable device operation, however, the performance, integration level, and commercial success of both digital and analog GaAs based devices and circuits have been limited. Despite numerous efforts over the last three decades, previously suggested approaches (e.g. [2] - [6]) have been proven to be inadequate for commercial device applications.
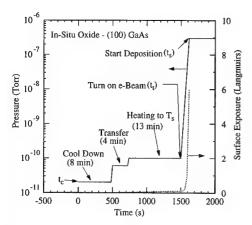
This paper presents an approach to overcome the above described bottlenecks. The first objective of this paper is to demonstrate how the extension of MBE toward in-situ deposition of oxides has provided the required ingredients for the implementation of a stable, low interface state density insulator on GaAs. The second objective is to present and discuss structural and electronic properties of in-situ fabricated oxide-GaAs interfaces with emphasis on the unique electronic properties observed at in-situ fabricated Ga_2O_3-GaAs interfaces.

In order to further illustrate the point at issue, a brief synopsis of fundamental requirements for the implementation of stable, low interface state density insulator on GaAs is given. The first category of requirements can be easily derived from a variety of detailed and comprehensive oxidation studies previously conducted on GaAs. For example, Spicer et al. [7] found that exposure of a clean (110) GaAs surface to more than 100 Langmuirs (1 Langmuir (L) = 10^{-6} Torr sec) of molecular oxygen already induces noticeable Fermi level pinning at the GaAs surface. Since the oxygen surface coverage was typically only a fraction of a monolayer even after an exposure of 10^5 L it was concluded, that Fermi level pinning is indirect, i.e. caused by surface disorder and creation of lattice defects rather than by the electronic structure of the adatom. Similar effects were found for carbon [8]. Other studies focusing on chemical reactions occurring during GaAs oxidation suggested that GaAs oxidation inherently produces thermodynamically unstable oxide-GaAs interfaces via the interfacial reaction $As_2O_3 + 2\,GaAs \rightarrow Ga_2O_3 + 4\,As$. This reaction occurs spontaneously ($\Delta G = -62$ kcal/mol) but slowly even at room temperature (e.g. [9], [10]). Here, Fermi level pinning is ascribed to the formation of As clusters at the interface [11]. Clearly, surface exposure has to be minimized to less than 10 -100 Langmuirs and oxidation must be completely avoided in order to ensure a clean, atomically ordered GaAs surface with low defect density prior to insulator deposition. This requirement may only be met under ultra-high vacuum (UHV) conditions.

The second category concerns the species intentionally deposited on GaAs in order to form the insulating layer. Chemical reactions with the GaAs surface must be excluded and the electronic structure of the deposited molecules must not introduce GaAs gap states. No a priori assumption can be made regarding the latter requirement. Instead, it will be discussed in conjunction with our experimental results later in this paper.

EXPERIMENT

The 2 inch wafers have been fabricated using a multiple-chamber UHV system [12]. The wafer fabrication was comprised of 1.5 μm thick n-type (1.6×10^{16} cm^{-3}) or p-type (4.4×10^{16} cm^{-3}) GaAs epilayers grown by solid source MBE on heavily Si or Zn-doped (100) GaAs substrates, respectively. Subsequently, the freshly grown film with an As-stabilized (2x4) surface was transferred under a vacuum of 6×10^{-11} Torr to another chamber (background pressure = 10^{-10} Torr) for oxide deposition. Figure 1 shows the pressure (solid line) and the corresponding GaAs surface exposure (dashed line) which is typically observed prior to opening the shutter for oxide deposition. The time t_c and t_s is the time of completion of GaAs growth and the time at which the shutter was opened for oxide deposition, respectively. The GaAs surface was exposed to a pressure
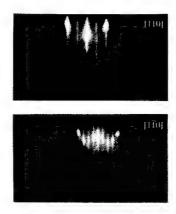
Fig. 1. Pressure (solid line) and surface exposure (dashed line) measured between completion of GaAs epitaxial growth (t_c) and start of oxide deposition (t_s).

Fig. 2. RHEED picture taken at time t_c and t_s. The identical RHEED pictures show a (2x4) reconstructed surface indicating preservation of surface stoichiometry.

not higher than 10^{-10} Torr during the transfer and heating of the substrate to the deposition temperature T_s. For the last two minutes, the e-beam was turned on to heat up the oxide targets. Only then did the GaAs surface begin to experience the pressure from 10^{-10} to 10^{-7} Torr. The pressure rise (predominantly oxygen) was caused by vaporization and thermal dissociation of the oxide targets during e-beam heating. Note that the typical GaAs surface exposure prior to opening the shutter for oxide deposition ($t_c < t < t_s$) was ≤ 10 Langmuirs. Based on typical initial sticking coefficients for oxygen (e.g. [13]), the GaAs surface impurity coverage is estimated at 10^{-5} to 10^{-3}% of a monolayer or 10^8 to 10^{10} surface impurities/cm² prior to deposition.

The preservation of surface periodicity and atomic order has been investigated by in-situ reflection high energy electron diffraction (RHEED) in the time interval $t_c < t < t_s$. RHEED pictures acquired from a (100) GaAs surface at the time t_c and t_s (T_s = 360 °C) are identical, showing a (2x4) reconstructed, As stabilized surface (Fig. 2). Consequently, the surface atomic order and periodicity is not affected by exposure to impurity gases of less than 10 Langmuirs in our experiments and the surface stoichiometry is completely preserved prior to opening the shutter for oxide deposition at time t_s.

Finally, oxide films have been deposited at substrate temperatures T_s ranging from room temperature to ≅ 600 °C using molecular beams of gallium-, magnesium-, silicon-, or aluminum oxide. Single crystal $Gd_3Ga_5O_{12}$ [14], MgO, SiO_2, or Al_2O_3, respectively, were used as source materials and evaporated by an e-beam technique. The use of $Gd_3Ga_5O_{12}$ was motivated by the un-

83

availability of single crystal Ga_2O_3 and had led to the first successful deposition of gallium oxide molecules forming extremely uniform Ga_2O_3 films on GaAs [15].

Reference wafers with identical GaAs epitaxial structure and substrate were also fabricated in the same solid-source III-V chamber using (i) no oxide deposition (bare samples) and (ii) $Al_{0.45}Ga_{0.55}As$ interfaces.

RESULTS AND DISCUSSION

Structural Properties

The chemical composition at in-situ fabricated oxide-GaAs interfaces has been investigated by x-ray photoelectron spectroscopy (XPS). Compositional profiles and the crystallographic structure of the deposited oxide films have been studied by Rutherford backscattering spectrometry (RBS), secondary ion mass spectroscopy (SIMS), transmission electron microscopy (TEM), and RHEED, respectively.

Figure 3 shows measured (solid line) and simulated (dashed line) RBS spectra of (a) gallium, (b) silicon, (c) aluminum, and (d) magnesium oxide films. The ratios of Ga, Si, Al, and Mg with oxygen were determined to 43:55, 33:67, 40:60, and 50:50, respectively. The Si, Al, and MgO films may be oxygen deficient within the error limits of RBS ($\pm 2\%$). Previously published results indicated that the nonstoichiometry of the Ga_2O_3 film is due to incorporation of excess elemental Ga [15]. Further, Ga_2O_3 films using e-beam evaporation of $Gd_3Ga_5O_{12}$ typically exhibit a nonuni-
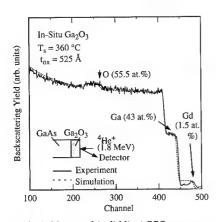
Fig. 3(a). Measured (solid line) RBS spectrum of 525 Å thick Ga_2O_3 film on GaAs substrate. The simulation (dashed line) assumes constant Gd concentration throughout the film.
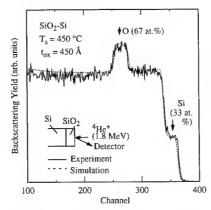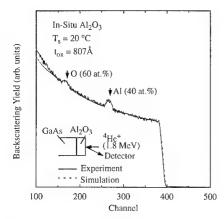
Fig. 3(b). Measured (solid line) and simulated (dashed line) RBS spectrum of a 450 Å thick silicon oxide film on Si.
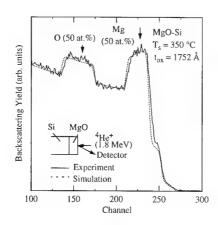
Fig. 3(c). Measured (solid line) and simulated (dashed line) RBS spectrum of a 807 Å thick aluminum oxide film on GaAs.

Fig. 3(d). Measured (solid line) and simulated (dashed line) RBS spectrum of a 1752 Å thick magnesium oxide film on Si.

form Gd distribution characterized by a virtually Gd free interfacial region and a peak in Gd concentration at the surface (see Fig. 3(a)). Our characterization methods (including XPS and SIMS) can not completely exclude the presence of Gd at the interface and possible effects of Gd on electronic interface properties are not known at this time. The presence of Gd in the bulk oxide film, however, may affect electrical measurements conducted on metal-oxide-semiconductor (MOS)

Fig. 4(a). Plan view TEM and the corresponding electron diffraction pattern of a 260 Å thick Ga_2O_3 film in-situ deposited on GaAs at 360 °C.
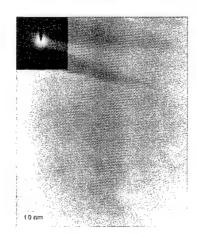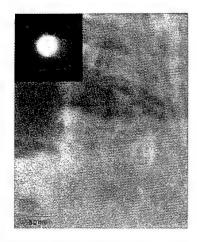
Fig. 4(b). Plan view TEM micrograph and the corresponding electron diffraction pattern of a 400 Å thick SiO_2 film in-situ deposited on GaAs at 410°C.

Fig. 4(c). Plan view TEM micrograph and the cor-
responding electron diffraction pattern of a 807 Å
thick Al₂O₃ film in-situ deposited on GaAs at RT.
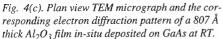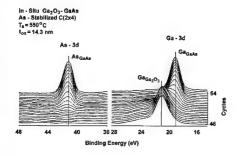
Fig. 4(d). Plan view TEM and the corresponding
electron diffraction pattern of a 285 Å thick MgO
film in-situ deposited on GaAs at 400 °C.

structures to be discussed later. In the following, we will refer to the films as Ga_2O_3, SiO_2, Al_2O_3, and MgO, respectively.

Figure 4 shows the plan view TEM micrographs and the corresponding electron diffraction patterns of (a) Ga_2O_3, (b) SiO_2, (c) Al_2O_3, and (d) MgO films which were in-situ deposited on GaAs. As observed from TEM (and RHEED) studies, SiO_2 films are amorphous. Ga_2O_3 and Al_2O_3 films are amorphous with partial ordering in a completely disordered state for increased deposition temperature. Part of the MgO films, however, is epitaxially grown on GaAs [16] with substrate temperatures around 275 - 400 °C. MgO films grown at lower T_s tend to be randomly oriented poly-crystalline. The insulating film should be preferably of amorphous phase in order to elude problems arising from lattice-mismatched interfaces.

Interfacial As 3d and Ga 3d core level spectra were acquired using a Perkin Elmer 5600 series XPS spectrometer equipped with a monochromatic Al Kα x-ray source. The photon energy was 1486.6 eV. Depth profiling was done in-situ in a UHV chamber (background pressure = 5 x 10^{-10} Torr) by Ar sputtering using an ion gun at 4 keV. The sputtering rate of $\cong$ 3 Å/cycle has been significantly smaller than the estimated photoelectron escape depth of $\cong$ 20 Å [17]. Figure 5 shows typical interfacial depth profiles of Ga and As 3d core levels of in-situ fabricated Ga_2O_3-GaAs structures (a) as deposited and (b) after rapid thermal annealing at 1000 °C for 30 sec. The Ga and As 3d binding energies of $Ga_{Ga_2O_3}$, Ga_{GaAs}, and As_{GaAs} are 21.2, 19.2, and 41.2 eV, respectively, and remain unchanged after temperature stress. The Ga 3d peak gradually shifts from the bulk
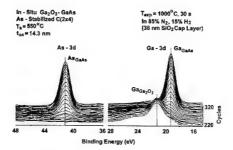
Fig. 5(a). Interfacial depth profile of Ga and As 3d core levels of an as deposited, in-situ fabricated Ga_2O_3 film. Peak energy positions and FWHM exactly correspond to standard values.

Fig. 5(b). Interfacial depth profile of Ga and As 3d core levels of the film in Fig. 5(a) after rapid thermal annealing at 1000 °C for 30 sec.

Ga_2O_3 to the bulk GaAs on a length scale consistent with the electron escape depth. The intermediate Ga_2O_3 peak can easily be fitted as a sum of two components. Chemical reaction products, in particular As_2O_3 (44.6 eV) and As_2O_5 (45.7 eV) are not detectable at both as deposited and temperature stressed Ga_2O_3-GaAs interfaces. Consequently, the chemical reaction As_2O_3 + 2 GaAs $\rightarrow Ga_2O_3$ + 4As resulting in As formation and degradation of electronic interface properties [11] is excluded. The excellent thermodynamic stability is consistent with the predictions based on thermochemical phase diagrams published by Schwartz in 1983 [9] and has important implications for the stability of electronic interface properties to be discussed later. Note that virtually identical, As_xO_y free, interfacial As 3d core level profiles were obtained from in-situ fabricated Al_2O_3- and SiO_2-GaAs structures as well (not shown). A more detailed discussion of XPS spectra acquired from in-situ fabricated oxide-GaAs structures is given in Ref. 18.

Structural interface properties including the absence of chemical reactions and interfacial As_xO_y (and in turn, elemental As) and the crystallographic structure (amorphous) of the majority of the oxide films are virtually identical. However, as will be discussed in the following paragraph, the examined structural interface characteristics do not a priori translate into comparable electronic interface properties.

Electronic Properties

Electronic interface properties including interface state density D_{it} and recombination velocity S have been investigated by capacitance-voltage (C-V), capacitance-time (C-t), conductance voltage (G-V), and steady-state photoluminescence (PL) measurements, respectively.

First, PL measurements at high injection level using an argon ion laser ($\lambda_0 = 514.5$ nm)

have been used to qualitatively characterize the Ga_2O_3-, SiO_2-, Al_2O_3-, MgO-, and $Al_{0.45}Ga_{0.55}As$-GaAs interface as well as the bare sample surface. At high injection level ($\rho > N$), radiative recombination dominates for low nonradiative contributions (internal quantum efficiency $\eta \cong 1$), however, quantum efficiencies close to that of a bare sample ($\eta \ll 1$) are measured for high surface recombination velocity $S \geq 10^6$ cm/s (e.g. [19]). Here, ρ and N are the injected carrier density and the doping concentration, respectively. Figure 6 shows typical PL spectra obtained from oxide- and $Al_{0.45}Ga_{0.55}As$-GaAs interfaces as well as from the bare sample surface (n-type). The excitation power density P_0 is 1100 W/cm^2. Clearly, the results shown in Fig. 6 reveal two distinctively different classes of interfaces where the first group includes Ga_2O_3- and $Al_{0.45}Ga_{0.55}As$-GaAs and the second comprises the other oxides. The latter group exhibits a surface recombination velocity S comparable to that of a bare surface ($\geq 10^7$ cm/s) and a Fermi level pinned at the interface as demonstrated by C-V measurements (not shown). Evidently, the fundamentally different electronic interface properties observed at various in-situ fabricated oxide-GaAs interfaces are due to the specific crystallographic structure associated with the interfacial atoms of GaAs and the deposited oxide molecules. Therefore, we have chosen the term *intrinsic* pinning for our observation of Fermi level pinning at in-situ fabricated SiO_2-, Al_2O_3-, and MgO-GaAs interfaces. In the following, we will focus on the unique electronic interface properties of in-situ fabricated Ga_2O_3-GaAs interfaces.

The interface recombination velocity S has been inferred from thorough studies of the in-
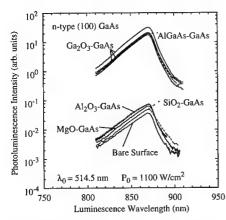
Fig. 6. Measured PL spectra of Ga_2O_3- ($360 \leq T_s \leq 620$ °C), $Al_{0.45}Ga_{0.55}As$-(690 °C), Al_2O_3-, SiO_2- and MgO- ($0 \leq T_s \leq 500$ °C) GaAs structures as well as of a corresponding bare surface.
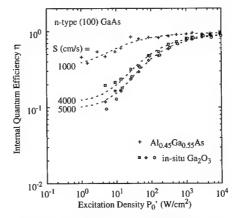
Fig. 7. Measured and calculated efficiency η as a function of P_0' = $T P_0$. Here, T is the optical transmissivity of the samples. For Ga_2O_3, squares, diamonds, and circles are for T_s=360,550,and 620°C.

ternal quantum efficiency η over a wide range of incident light power densities ($1 \le P_0 \le 10^4$ W/cm^2). This technique is based on the relative weight of nonradiative and radiative recombination as a function of P_0 resulting in a unique curve shape of η versus P_0 for a specific S [20].This is demonstrated in Fig. 7 which shows the measured (symbols) and simulated (dashed lines) efficiency η versus P_0 of Ga$_2$O$_3$-GaAs structures and, for comparison purposes, η of an Al$_{0.45}$Ga$_{0.55}$As-GaAs interface as well (n-type). The simulation results have been obtained from calculated PL depth profiles using a selfconsistent, numerical device model for semiconductor heterostructures [20], [21]. Since the PL intensity is not measured in absolute units, the measured curves are rigidly shifted to the calculated ones [22]. The best fit of the simulations to the measurement data has been obtained for S = 4000 - 5000 and 1000 cm/s for Ga$_2$O$_3$- and Al$_{0.45}$Ga$_{0.55}$As-GaAs structures, respectively. Similar results were acquired from p-type structures.
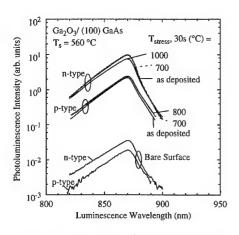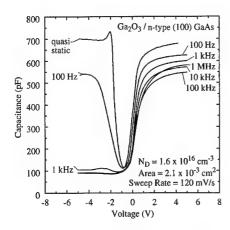
Fig. 8. PL spectra of n- and p-type as deposited and temperature exposed Ga$_2$O$_3$-GaAs structures as well as of the corresponding bare samples.

Additional PL characterizations (P_0 = 1100 W/cm^2) have been performed to demonstrate the thermodynamic stability of electronic properties observed at in-situ fabricated Ga$_2$O$_3$-GaAs interfaces. As indicated in Fig. 8, the PL intensities after rapid thermal annealing for 30 s at 700 or 800 °C are virtually identical to those obtained from the corresponding as deposited samples. These results imply the preservation of excellent electronic interface properties. Further, the PL intensity decreases by only 21% even after temperature exposure of 1000 °C for 30 s ($S \cong 10^4$ cm/s).

MOS structures have been fabricated using a standard shadow mask process. The interface state density D_{it} has been inferred from quasistatic C-V as well as from C-V and G-V measurements at frequencies ranging from 100 Hz to 1 MHz. Figure 9 shows typical C-V characteristics of (a) n-type and (b) p-type Ga$_2$O$_3$-GaAs MOS structures measured in quasistatic mode and at various frequencies between 100 Hz and 1 MHz. The classical operational modes of ideal MOS structures such as (i) inversion, (ii) depletion, and (iii) accumulation are clearly revealed. The frequency dispersion observed in accumulation is attributed to an oxide layer of relatively low resistivity adjacent to the interface (confirmed by G-
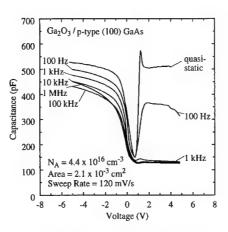
Fig. 9(a). Typical C-V characteristics of n-type samples. The oxide thickness is 462 Å.

Fig. 9(b). Typical C-V characteristics of p-type samples. The oxide thickness is 594 Å.

V measurements) rather than to a high density of interface states near the band edges. The depth dependence of the oxide resistivity may be related to the depth profile of the Gd concentration. A high density of interface states near the band edges can be excluded since (i) integration over the quasistatic capacitance reveals actual operation of the structures in accumulation [23] and (ii) the formation of inversion layers is observed in both n- and p-type sample.
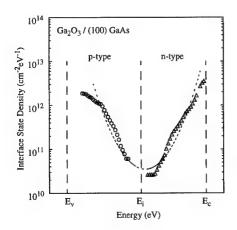
Fig. 10. D_{it} of in-situ fabricated Ga_2O_3 -GaAs structures inferred from C-V measurements on n-type (triangles) and p-type (circles) samples using the quasistatic/high frequency method.

Figure 10 shows typical results obtained for D_{it} as a function of gap energy E using the quasistatic/high frequency C-V technique [24]. The inferred midgap interface state density in the low 10^{10} cm^{-2} eV^{-1} range is consistent with D_{it} values derived from G-V measurements (not shown). However, G-V measurements indicate a considerably wider bottom of the D_{it}-E characteristic [25]. This has also been confirmed by C-t measurements performed in accumulation showing a long term drift of capacitance characterized by time constants

in excess of 1 -10 sec [23]. Clearly, the majority of the states shown in Fig. 10 is ascribed to trapping centers located in the Ga_2O_3 bulk.

CONCLUSIONS

In-situ deposition of oxide molecules has expanded the spectrum of molecular-beam epitaxy related techniques and enabled the fabrication of the first thermodynamically stable, low interface state density insulator-GaAs structures. The excellent electronic interface properties are ascribed to the specific crystallographic structure associated with the interfacial atoms of GaAs and the deposited gallium oxide molecules. The application of our in-situ Ga_2O_3-GaAs technology may pave the way for new device concepts on GaAs and will significantly improve existing GaAs technologies. Field effect device applications will require further improvements of oxide properties, in particular, a reduction in bulk trap density.

ACKNOWLEDGEMENTS

REFERENCES

[1] B. Bernhardt, M. LaMacchia, J. Abrokwah, J. Hallmark, R. Lucero, B. Mathes, B. Crawforth, D. Foster, K. Clauss, S. Emmert, T. Lien, E. Lopez, V. Mazzotta, and W. Ooms, 1995 IEEE GaAs IC Symposium Techn. Dig., (IEEE, Piscataway, NJ, 1995) p. 18.

[2] H. Hasegawa, K.E. Forward, and H.L. Hartnagel, Appl. Phys. Lett. **26**, p. 567 (1975).

[3] J.S. Herman and F.L. Terry, Appl. Phys. Lett. **60**, p. 716 (1992).

[4] C.J. Sandroff, M.S. Hedge, L.A. Farrow, R. Bhat, J.P. Harbison, and C.C. Chang, J.Appl.Phys. **67**, p. 586 (1990).

[5] A. Callegari, P.D. Hoh, D.A. Buchanan, and D. Lacey, Appl. Phys. Lett. **54**, p. 332 (1989).

[6] Z. Wang, M.E. Lin, D. Biswas, B. Mazhari, N. Teraguchi, Z. Fan, X. Gui, and H. Morkoc, Appl. Phys. Lett. **62**, p. 2977 (1993).

[7] W.E. Spicer, I. Lindau, P. Skeath, C.Y. Su, and P. Chye, J. Vac. Sci. Technol. **17**, p.1019 (1980)

[8] J. Saito and K. Kondo, J.Appl.Phys. **67**, p. 6274 (1990).

[9]   G.P. Schwartz,Thin Solid Films **103**, p. 3 (1983).

[10] O. Kubaschewski and C.B. Alcock in Metallurgical Thermochemistry, Pergamon Press, Oxford, 1979.

[11] J.M. Woodall and J.L. Freeouf, J. Vac. Sci. Technol. **19**, p. 794 (1981).

[12] M. Hong, J. Crystal Growth **150**, p. 277 (1995).

[13] R. Ludeke and A. Koma, CRC Crit. Rev. Sol. St. Sci. **5**, p. 259 (1975).

[14] W. Piekarczyk and A. Pajaczkowska, J. Crystal Growth **46**, p. 483 (1979).

[15] M. Passlack, E.F. Schubert, W.S. Hobson, M. Hong, N. Moriya, S.N.G. Chu, K. Konstadinidis, J.P. Mannaerts, M.L. Schnoes, and G.J. Zydzik, J. Appl. Phys. **77**, p. 686 (1995).

[16] K. Hashimoto, D. Fork, and T.H. Geballe, Appl. Phys. Lett. **60**, p. 1199 (1992).

[17] S. Tanuma, C.J. Powell, and D.R. Pen, Surf. Interf. Analys. **17**, p. 911 (1991).

[18] M. Passlack, M. Hong, R.L. Opila, J.P. Mannaerts, and J.R. Kwo, Appl. Surf. Sci., in press, 1996.

[19] O. Brandt, K. Kanamoto, M. Gotoda, T. Isu, and N. Tsukada, Phys. Rev. **B51**, p. 7029 (1995).

[20] M. Passlack, M. Hong, J.P. Mannaerts, S.N.G. Chu, R.L. Opila, and N. Moriya in 1995 IEDM Techn. Dig., (IEEE, Piscataway, NJ, 1995) p. 383.

[21] M.S. Lundstrom and R.J. Schuelke, IEEE Trans. Electr. Dev. **30**, p. 1151 (1983).

[22] O. Brandt, K. Kanamoto, M. Gotoda, T. Isu, and N. Tsukada, Appl. Phys. Lett. **67**, p. 1885 (1995).

[23] M. Passlack, M. Hong, J.P. Mannaerts, Appl. Phys. Lett. **68**, p. 1099 (1996).

[24] E.H. Nicollian and J.R. Brews in MOS Physics and Technology, Wiley, New, 1982, p. 331.

[25] M. Passlack, M. Hong, J.P. Mannaerts, Solid State Electronics, in press, 1996.

ORIENTATION DEPENDENCE OF SURFACE PASSIVATION FOR SEMI-INSULATING GaAs

I.P. KOUTZAROV[1], C.H. EDIRISINGHE[1,2], H.E. RUDA[1,2], L.Z. JEDRAL[1], Q. LIU[1],
J. GUO-PING[1]; H. XIA[3], W. N. LENNARD[3] AND L. RODRIGUEZ-FERNANDEZ[3]
[1] Electronic Materials Group, Department of Metallurgy and Materials Science,
University of Toronto, Toronto, Ontario, Canada M5S 3E4
[2] Department of Electrical and Computer Engineering, University of Toronto, Toronto, Ontario,
Canada, M5S 3E4
[3] Department of Physics and Interface Science Western, The University of Western Ontario,
London, Ontario, Canada N6A 3K7

ABSTRACT

We report on the orientation dependence ((100), (110) and (111)) of photoluminescence (PL), photoreflectance (PR) and Surface Photo-Voltage (SPV) for sulfur passivated bulk semi-insulating (SI) GaAs. Near band gap PL peak intensities (bound-exciton and acceptor-related) were enhanced following $(NH_4)_2S$ or S_2Cl_2 treatment of GaAs for all orientations. The reduction of surface recombination velocity (from PL data) was orientation dependent and especially pronounced for the case of (111)A and (111)B orientations. The effect of thin dielectric layers deposited on S-treated surfaces was also investigated, particularly for (100) and (111)A orientations. SPV data shows a strong increase in the above band gap signal after both S-treatment and dielectric film deposition, which was higher than that measured for only S-treated surfaces. PR data showed an increase in the interfacial electric field following deposition of dielectric film. The results of absolute S-surface coverage measurements using particle-induced X-ray emission measurements were correlated with the optical characteristics.

INTRODUCTION

Non-(100)-oriented semiconductor substrates have recently been exploited for preparing low dimensional structures, while epitaxial growth on such substrates have revealed a variety of interesting device possibilities arising from some unique hetero-interfacial properties [1]. These include, lateral composition modulation, surface segregation and alloy disorder [1-3]. Electronic passivation has often been shown to be an essential prerequisite for fabrication of useful devices [4]. Passivation schemes have involved sulfur-passivation [4] and also organic SAMs, which are formed by chemical grafting of molecules using metal-organic compounds [5]. Self-assembled monolayers (SAM) of alkane thiols grown on GaAs have recently received considerable attention for their potential application in passivation optoelectronic devices [5-7]. These passivants can effectively counter nonradiative recombination at GaAs and other III-V semiconductor surfaces [5-8]. In previous work, we demonstrated that MOCVD-grown n-type and Semi-Insulating (SI) (100) GaAs surfaces can be electronically passivated using siloxane-type SAMs formed from Thio-Silanes (TS) [8]. The focus of this paper is on studying electronic surface passivation of different crystallographic orientations GaAs substrates. Measurements were carried out on these samples before and after deposition of sulfur-siloxane-type SAMs.

EXPERIMENTAL RESULTS

(100), (111) and (110) GaAs samples were cleaned using standard procedures. All substrate preparations were performed in a sealed and pre-evacuated glove-box under continuously flowing dry nitrogen. Native oxides were etched using standard Caros solution buffered to yield a slow etch rate (~30 Å.s^{-1}) followed by a decanting rinse in anhydrous methanol. The samples were then dried under flowing dry N_2. The S-passivation pretreatment was performed using S_2Cl_2 vapors in the same system or $(NH_4)_2S$ standard solution at 60°C. Ultrathin films (~10Å) of TS were synthesized on cleaned, chemically etched and S-passivated surfaces in the absence of water, using anhydrous methanol or toluene under the same conditions. The combination of Caros pre-etching followed by S_2Cl_2 vapour treatment and siloxane SAM deposition is henceforth called "Sulfursiloxane". Photoluminescence (PL) and Photo-Reflectance (PR) measurements were carried out as previously reported with 488 nm Ar$^+$ laser excitation [9], while constant flux Surface Photo-Voltage (SPV) measurement were made under low-level optical excitation [10].

Sulfur coverage was measured using Particle Induced X-Ray Emission (PIXE) in conjunction with Rutherford Backscattering Spectrometry (RBS), including channeling [11]. The specimens were bombarded by 1.8 MeV ^{4}He beam accelerated using a 2.5 MV Van de Graaff generator and characteristic S K_α X-rays were measured. The absolute S coverage was obtained by normalizing the total characteristic X-ray yield with that from a thin self-supporting CdS reference film ($\sim30\mu g/cm^2$). The areal density of S atoms of the CdS film was deduced from RBS measurements. For samples with low S coverage (less than 10^{15} atom/cm^2), channeling techniques were further applied to reduce the Bremsstrahlung, arising from the bulk of the sample. Compared with the "random" geometry, this technique suppresses the intensity of the Bremsstrahlung underneath the S characteristic peak by a factor ~5. This technique is denoted as surface sensitive particle induced X-ray analysis (SPIX). having a sensitivity of 5.0×10^{13} atoms/cm^2.

Table 1. Absolute Coverage Measurements of Sulfur and Siloxane Treated SI GaAs Surfaces.

	Sulfur Coverage			Sulfur Coverage	
Sample and Chemical treatment	[S] (10^{15} cm^{-2})	Sulfur ML	Sample and Chemical treatment	[S] (10^{15} cm^{-2})	Sulfur ML
SI GaAs (100) control	<0.1	<0.16	SI GaAs (100) $(NH_4)_2S$	4.25±0.4	**6.8**
SI GaAs (100) Sulfursiloxane (20°C)	7.27±0.51	**11.6**	SI GaAs (111)A $(NH_4)_2S$	0.98±0.09	**1.36**
SI GaAs (100) Sulfursiloxane (110°C)	2.72±0.19	**4.35**	SI GaAs (110) $(NH_4)_2S$	1.38±0.1	**3.10**
SI GaAs (100) Siloxane only (20°C)	2.07±0.2	**3.31**			

PL of sulfursiloxane treated GaAs (100) measured at 18 K is shown in Fig 1. Temperature (17K-300K) and excitation dependent PL measurements enabled the peaks at ~1.519 eV and 1.498 eV to be identified as due to bound exciton (BE) transitions and those involving carbon acceptors C_{As}, (e°, A), respectively [9]. The BE peak showed an enhancement up to 12 times on

Sulfursiloxane treatment. Fig. 1 also shows that, distinct from (100) and (110) orientations, the PL enhancement of (111)A surfaces are strongly treatment-time dependent.
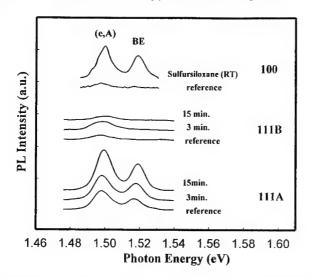
Fig. 1. Dependence of near band gap PL peaks (T=18 K) of GaAs (111)A, (111)B and (100) samples. Treatment times are given for (111)A and B samples.
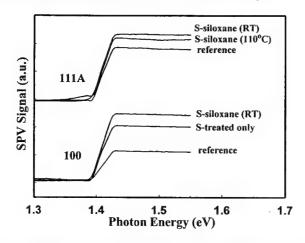
Fig. 2. SPV spectra for (100) and (111)A samples with different treatments.

SPV spectra of S_2Cl_2 treated only and sulfursiloxane treated (111)A surfaces are shown in Fig. 2. The magnitude of the above band gap (ABG) SPV signal and spectral dependence of the surface potential can be used to infer changes in the surface recombination rates. Similar to the PL results, the SPV enhancement for (100) was higher than for (111)A surfaces.
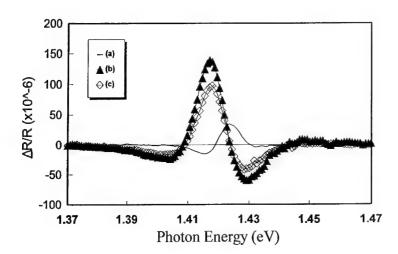
Fig. 3. PR spectra of GaAs (100): **(a)** untreated, **(b)** sulfursiloxane treated at room temperature and **(c)** sulfursiloxane treated at 110°C.

Fig. 3 shows the room-temperature (RT) PR spectra of sulfursiloxane treated (100) samples. These samples exhibit a strong enhancement (up to 10 times) in the amplitude of band gap PR peaks. As the PR lineshape of SI GaAs dose not contain Franz-Keldysh oscillations, only qualitative conclusions regarding the interfacial field could be made by comparison of the PR amplitude from pre- and post-treated surfaces. PR spectra of RT siloxane-type SAMs show a stronger interfacial electric field corresponding to higher S-coverage as shown in Table 1.

DISCUSSION

The intensity of BE to carbon PL varies with the crystallographic orientation, the combination of surface treatments and siloxane deposition conditions (at 20 °C or 110 °C). However the BE peak intensity appear to consistently correlate with the number of sulfur monolayers formed on the GaAs surface as measured by PIXE measurements (e.g., the enhancement ratio of 12.6 for B peak corresponds to 11.6 ML of sulfur for SI GaAs(100) surface after sulfur-siloxane treatments at room temperature as shown in Fig.1 and Table 1). The difference in the total amount of sulfur atoms weakly bonded or in the form of various sulfide compounds for the different surfaces suggests different chemical reactivity rates of each surface and corresponding S overage, correlates with the observed changes in the optical properties of those surfaces.

The surface Fermi level of SI-GaAs is pinned at $E_c - 0.69$ eV due to the large density of surface states [12]. To shift the Fermi level, the interfacial states must be reduced and/or additional charge introduced. Sulfursiloxane and sulfur can result in near surface fixed charges which would cause a significant increase in the interface electric field as evident from PR data. Recent X-ray photoelectron spectroscopy (XPS) data for GaAs (100) shows the presence of Ga-S bonds in the form of Ga_2S_3, below the free sulfur layers [13] which possibly facilitates surface passivation in agreement with our earlier observations for AlGaAs and GaAs [9].

SPV spectra of sulfursiloxane treated GaAs(111), (100) and (110) all show that the ABG signal is higher than untreated surfaces, which is consistent with the results of near band gap PL measurements. In addition, PR results indicate that near surface electric field of GaAs/S/Siloxane interface is also significantly enhanced: a strong electric field in the hetero-interface is probably due to the fixed charge in the thin siloxane layer and weakly bound sulfur present at the surface. S_2Cl_2 molecules contain a S=S double bond and can form atomic chains, with negative charges residing on the terminal atoms of the chain [14]. Hence, the incorporation of further unsaturated sulfur chains (S_2^- or S_4^{2-}) by S_2Cl_2 pre-treatment may provide a larger uncompensated charge density in the disordered sulfur monolayers compared with $(NH_4)_2S$-treatments. The specific chemical nature of S_2Cl_2 molecules as well as the presence of thiol (HS^-) groups from thiosilane can explain the higher observed sulfur coverage values for room temperature treated SI GaAs (100) as compared with that for $(NH_4)_2S$-treatment (see Table 1). PIXE coverage measurements indicate that sulfursiloxane treatments (including S_2Cl_2 pre-treatment) provide a higher sulfur coverage than $(NH_4)_2S$-treatment on all GaAs orientations.

The differences between the Ga- and As-terminated (111) surfaces after sulfur or sulfur-siloxane treatment may be explained as follows. The gallium atom is readily attacked by OH^- ions and is dissolved into solution $((NH_4)_2S + H_2O)$. In anhydrous solution, the reaction with Ga is slower and is dominated by sulfur-related ions such as HS^- from thiosilane. The S-passivation process is slow for (111)A surfaces because of the competitive process between OH^- and S^{-2} ions bonding with Ga atoms. Towards the end, S is dominantly double bonded with Ga and thus cannot be removed either by OH^- or by ambient oxygen under atmospheric conditions. For arsenic in As-terminated (111) surfaces, reaction with sulfur is more efficient than with OH^-. The chemical reaction for As starts with elemental arsenic As^o, which presence was observed by recent XPS data [15] and possibly is weakly bound to the crystalline lattice [16]:

$$As^o + 3h^+ + 4OH^- \rightarrow AsO_2^- + 2H_2O.$$

The reaction continues with accumulation of excess As, since the breaking of Ga-related chemical bonds induces As dimmers (As-As) instead of As-O. As a product of this, As-S bonds are located inside the amorphous passivating overlayer and not on the GaAs surface. Finally, sulfur is irreversibly bound to Ga in a bridge-site configuration (Ga-S-Ga) with a thick disordered overlayer containing excessive As, which could explain the deterioration of the passivation for GaAs (111)B samples.

CONCLUSIONS

Experimental observations relating surface treatment and optical properties were described as a function of GaAs crystallographic orientation. The role of sulfur coverage and interface electric field on surface recombination were discussed.

REFERENCES

1. R.R. LaPierre, B.J. Robinson, and D.A. Thomson, App. Surf. Sci., **90**, 437 (1995).
2. E.S. Snow, B.V. Shanabrook and D. Gammon, Appl. Phys. Lett., **56**, 758 (1990).
3. F.E.G. Guimaraes, D. Lubyshev, V.A. Chitta, P. Basmaji, Mater. Sci. Eng., **B35**, 318 (1995).
4. S. Kamiya, Y. Mori, Y. Takahashi, and K. Ohnaka, Appl. Phys. Lett., **58**, 2595 (1991).
5. J.F. Dorsten, J.E. Maslar, and P.W. Bohn, Appl. Phys. Lett, **66**, 1755 (1995).
6. C.B. Bain, Adv. Mater., **4**, 591 (1992).
7. H. Ohno, M. Motomatsu, W. Mizutani and H. Tokumoto, Extend. Abstr. Intern. Conf. on Solid State Dev. Mater., Yokohama, 49 (1994).
8. I.P. Koutzarov, R. Nicholov and H.E. Ruda, Access in Nanoporous Materials Symposium, East Lansing, Michigan, P-36 (June, 1995); I. P. Koutzarov, H. E. Ruda, L. Z. Jedral, C.H. Edirisinghe, Q. Liu, and R. Nicholov, submitted for publication (1996).
9. I.P. Koutzarov, H.E. Ruda, C.H. Edirisinghe, Q. Liu, L.Z. Jedral, A. Moore, R. Henderson, M. Boudrau, M. Boumerzoug and P. Mascher, SPIE, **2382**, 42 (1995).
10. Q. Liu, H.E. Ruda, I.P. Koutzarov, L.Z. Jedral and G.M. Chen, Mat. Res. Soc. Symp. Proc., Thin Films for Photovoltaic and Related Device Applications, San Francisco, CA (1996)
11. H. Xia, W.N. Lennard, G.R. Massoumi, J.J.J. van Eck, L.L. Huang, W. M. Lau and D. Landheer, Surf. Sci., **324**, 159 (1995).
12. T.P. Chen, Y.C. Liu, S. Fung, and C.D. Beling, J. Appl. Phys., **78**, 4798 (1995).
13. K.S. Butcher, R.J. Egan, T.L. Tansley, D. Alexiev, J. Vac. Sci. Technol., **B 14**, 152 (1996).
14. N. Burford, J. Passmore, and J.C.P. Sanders, in From Atoms to Polymers. Isoelectronic Analogies, J.F. Liebman, A. Greenberg, Eds., (VCH Publishers, Inc., New York), 78 (1989).
15. V.N. Bessolov, A.F. Ivankov, E.V. Konenkova, M.V. Lebedev, and V.S. Strykanov, Semicond., **29**, 1131 (1995).
16. D. Paget, J.E. Bonnet, V.L. Berkovits, P. Chiaradia, J. Avila, Phys. Rev. **B 53**, 4604 (1996).

SURFACE STABILIZATION OF InP USING CdS THIN FILMS

A. DAVIS, H.M. DAUPLAISE, K. VACCARO, B.G. DEMCZYK, G.O. RAMSEYER*,
and J.P. LORENZO
USAF Rome Laboratory, Optical Components Branch, Hanscom Air Force Base, MA 01731
*USAF Rome Laboratory, Reliability Physics Branch, Rome, NY 13441

ABSTRACT

A chemical bath deposition process was used to grow thin (25-200 Å) films of cadmium sulfide on (100) InP from an aqueous solution of ammonium hydroxide, cadmium sulfate, and thiourea at 75-85 °C. Reflection high energy electron diffraction (RHEED) and transmission electron microscopy (TEM) show that ~30 Å films are amorphous, while thicker films exhibit a cubic polycrystalline microstructure, with a preferred orientation in the [110] direction. X-ray photoelectron spectroscopy (XPS) shows the CdS treatment both removes the native oxides of InP and forms a stabilizing layer which protects the substrate from re-oxidation. Quasistatic capacitance-voltage response of MIS capacitors on InP, with a CdS layer between the insulator and substrate, exhibits well defined regions of accumulation, depletion, and inversion, indicating a high-quality interface region. An experimental C_{min}/C_{ox} value of 0.28 was obtained, compared to the theoretical value of 0.07. The density of interface states (D_{it}) was reduced from 10^{12} to 10^{11} $eV^{-1}cm^{-2}$ after CdS treatment when calculated by the high-low method. InP MISFETs fabricated using CdS interlayers showed greatly enhanced device performance over untreated MISFETs.

INTRODUCTION

The optimization of such InP-based devices as photodetectors, transistors, and surface-emitting lasers requires stabilization of the III-V surface to prevent the formation of native oxides and phosphorus vacancies. These surface aberrations are aggravated by elevated temperatures, yielding a surface of poor electrical quality. Numerous attempts have been made to passivate the InP surface and prevent native oxide re-formation by deposition of protective sulfide layers on the III-V surface.[1-3] Recent investigation of the use of thin CdS layers on InP for improved metal-insulator-semiconductor (MIS) devices has shown dramatic improvements in electrical response.[4] The CdS passivation process has been shown to remove InP native oxides and prevent subsequent re-oxidation, yielding an InP surface that is not phosphorus-deficient following dielectric deposition. Here we examine the morphology of the CdS layers, with corresponding chemical and electrical characterization of MIS devices made with those CdS films. This work focuses on the relationship between the structural properties of chemical bath-deposited CdS layers on InP and the resulting MIS electrical response. Studies of film microstructure, by reflection high energy electron diffraction (RHEED) and transmission electron microscopy (TEM); and interfacial chemistry, by x-ray photoelectron spectroscopy (XPS) and Auger electron spectroscopy (AES), will be reported.

EXPERIMENT

We use chemical bath deposition (CBD) to grow CdS on (100) InP based on a technique previously reported for (111) InP.[5] Standard CdS deposition concentrations were 11 M NH_3, 0.028 M thiourea ($CS(NH_2)_2$), and 0.014 M cadmium sulfate ($3 CdSO_4 \cdot 8 H_2O$). A 15 min to 20

min pretreatment in a 12.3 M NH₃, 0.033 M thiourea solution prior to CdS deposition results in improved MIS device performance compared to samples prepared with only an HF etch before CdS deposition.[4] The samples were pretreated at the eventual deposition temperature, then immediately transferred to the growth solution. Deposition times ranged from 1 min to 8 min at 75-85 °C.

RHEED and TEM were used to study the structure and morphology of the as-grown CdS layers. RHEED was performed on an EM-AD stage on a JEOL JEM 100CX Electron Microscope. All samples were oriented to the (110) plane of the InP substrate before measurement. The accelerating voltage was 20 KV. Samples were prepared for TEM by chemo-mechanically thinning, then ion milling, the InP substrate. XPS measurements were done on a Physical Electronics PHI 5100 using non-monochromatic Mg Kα radiation at 1253.6 eV. XPS was used to investigate the chemical states present at the CdS/InP interface following various processing steps. CdS layer thicknesses were estimated from the XPS intensity measurements.[6]

MIS capacitors were fabricated by chemical vapor deposition (CVD) of SiO_2 following CdS treatment, then evaporation of Al front and In back contacts.[7] Capacitance-voltage (C-V) response was measured at 1 MHz and quasistatic. The CdS layers were deposited at standard conditions, followed by deposition of SiO_2. The samples were subsequently annealed overnight at 350 °C in dry nitrogen. Measurements at 1 MHz were made with an HP 4275A multi-frequency LCR meter, and quasistatic measurements were made with a Keithley 595 meter. Leakage current was monitored during the quasistatic measurement and proved to be negligible. All measurements started in accumulation and swept to inversion. Interface-state density (D_{it}) was calculated by the high-low method of Castagné and Vapaille.[8] MISFETs were fabricated from metalorganic chemical vapor deposited epitaxial layers on (100) SI-InP substrates, with an InP ($n = 2 \times 10^{17}$ cm^{-3}) channel. I_D-V_{DS} families were measured on a Hewlett Packard 4142B parameter

(a)   (b)

(c)   (d)
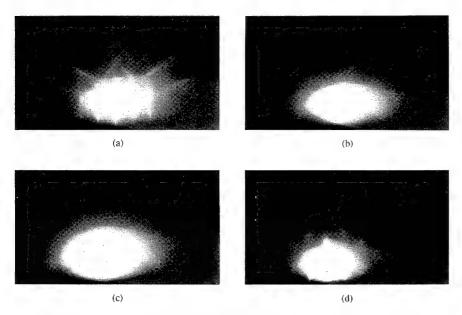
Figure 1. Reflection high energy electron diffraction (RHEED) patterns of CdS layers deposited on (100) InP: (a) HF-etched InP substrate, (b) 20 Å CdS film, (c) 45 Å CdS film, (d) 115 Å CdS film.
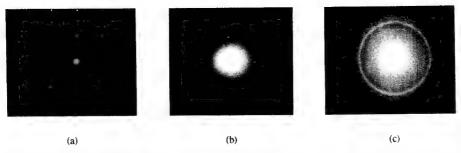
Figure 2. Selected area diffraction (SAD) patterns of CdS deposited on (100) InP: (a) HF-etched InP substrate. (b) 30 Å CdS layer, (c) 200 Å CdS layer. Films were deposited at 75°C following an HF etch of the substrate.
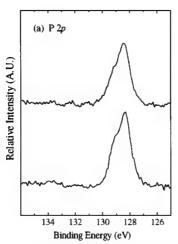
analyzer by continuously sweeping the drain bias, then stepping the gate voltage. MISFETs fabricated with and without CdS under the gate oxide were compared.

RESULTS AND DISCUSSION

Figures 1(a)-1(d) show the RHEED patterns of a (100) InP substrate and CdS films deposited on InP for 1 min, 4 min, and 7 min, respectively. The InP substrate was HF-etched prior to measurement. The CdS layers were grown at 85 °C, as described previously. The substrate shown in Figure 1(a) exhibits a well ordered surface with little native oxide formation and the strong crystalline pattern of a face-centered cubic structure. After a 1 min CdS deposition, the substrate pattern is obscured by a diffuse spot, Figure 1(b), most likely due to an amorphous film. Calculations from XPS data show the CdS layer to be ~20 Å. Following a 4 min deposition, corresponding to ~45 Å of CdS, the RHEED pattern begins to display weak rings, indicating a polycrystalline film, Figure 1(c). Superposed on the ring pattern is a weak spot pattern, suggesting a preferred orientation of certain crystallites in the layer. The periodicity is unexpected, and is believed to be related to surface asperities through which the electron beam undergoes transmission diffraction. After a 7 min deposition, the spots become sharper, as shown in Figure 1(d), indicating a more ordered structure over a larger area of the film.

TEM measurements also suggest amorphous thin CdS films and polycrystalline thicker films. Figure 2(a) shows the selected area diffraction (SAD) pattern from an InP substrate. In addition to the Bragg diffraction spots corresponding to the (100) InP substrate, extra spots in the pattern associated with metallic indium are observed. The metallic In is an artifact of the sample preparation process. The SAD pattern in Figure 2(b) is from an ~30 Å CdS film on HF-etched (100) InP. Both the CdS film and the substrate were included in the selected area aperture. Bragg diffraction spots corresponding to the monocrystalline (100) InP substrate and a diffuse spot corresponding to an amorphous CdS film are readily observed. Figure 2(c) is a SAD pattern of an ~200 Å CdS film on (100) InP. The ring pattern indicates the CdS is cubic, with a preferred orientation in the [110] direction, due to the presence of rings corresponding to the (220) and (440) planes. Froment et al. have previously reported the growth of hexagonal-phase CdS on ($\overline{111}$) InP, but have observed the cubic modification on ($\overline{111}$) InP for cadmium sulfate-to-thiourea ratios equivalent to ours.[9]

The lower traces of Figure 3 show XPS detail scans of an ~30Å CdS layer on InP. The polar angle of analysis was 45°. The In and P scans indicate no native oxides are present and give a P:In ratio near unity. An ~25 Å SiO_2 layer was then deposited on the sample. The In $3d$ and P $2p$
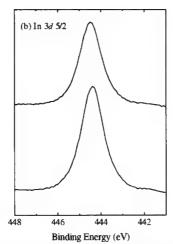
Figure 3. X-ray photoelectron spectroscopy (XPS) detail scans of the (a) P $2p$ and (b) In $3d_{5/2}$ peak regions. The lower scans were taken following deposition of an ~30 Å CdS layer at standard growth conditions. The upper scans were taken following deposition of a thin SiO_2 layer on the same sample.

XPS scans following SiO_2 deposition are shown in the upper traces of Figure 3, and still show no evidence of native oxides on the substrate. The P:In ratio remains near unity after SiO_2 deposition. The measured Cd $3d_{5/2}$ and S $2p$ binding energies of the chemical bath-deposited CdS layers agree well with our measurements of single-crystal CdS. Figure 4 shows the Auger depth profile of an ~35 Å CdS film on n-InP with 500 Å of deposited SiO_2.

Figure 5(a) shows the C-V response of SiO_2/CdS/InP MIS structures with ~20 Å (dashed trace) and ~30 Å (solid trace) CdS interlayers. Negative fixed charge, Q_f, located at the insulator/ semiconductor interface, causes a flatband voltage shift of approximately -22 mV at 1 MHz, corresponding to $Q_f = -2 \times 10^{11}$ cm^{-2} for the ~30 Å CdS sample. Hysteresis of the sample measured at flatband is 57 mV for a bias scanning range from +2 V to -2 V at a sweep rate of 15
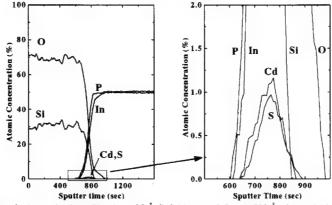
Figure 4. Auger depth profile of an ~35 Å CdS film on n-InP with 500 Å of deposited SiO_2.

102
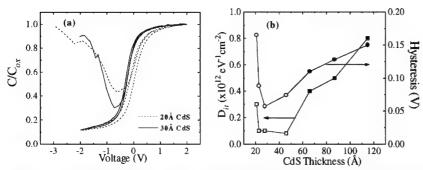
Figure 5. (a) 1 MHz and quasistatic *C-V* data for InP MIS capacitors prepared with 1 min (dashed lines) and 3 min (solid lines) CdS depositions at standard conditions. (b) D_{it} and hysteresis for a number of different CdS interlayer thicknesses. MIS samples denoted by the open symbols have 350 Å of SiO_2, while those denoted by the solid symbols have 500 Å.

mV/sec. Both fixed charge ($Q_f = -3 \times 10^{11}$ cm^{-2}) and hysteresis (165 mV) were higher in the sample with only 20 Å CdS when measured with the same scanning range and sweep rate. The quasistatic data was recorded with 100 mV steps and a 1 sec delay time. The theoretical value of C_{min}/C_{ox} is 0.07 for the quasistatic response. The quasistatic data in Figure 5(a) exhibits C_{min}/C_{ox} values of 0.44 and 0.28 for the 20 and 30 Å CdS interlayers, respectively, with well defined regions of accumulation, depletion, and inversion. Figure 5(b) shows the variation of D_{it} values and hysteresis for MIS samples prepared with CdS interlayers ranging from 20 to 115 Å. An optimum interlayer thickness of ~30 Å is suggested by the plot.

Common-source responses of 4 x 125 µm InP-channel ($n = 2 \times 10^{17}$) MISFETs with ~500 Å SiO_2 are shown in Figures 6(a) and 6(b) for the untreated and CdS-treated samples, respectively. The InP depletion-mode MISFETs without CdS channel treatment typically have high output conductance and poor response to applied gate voltage. The MISFET with CdS treatment exhibits carrier accumulation under positive gate bias, good pinch-off characteristics with negative
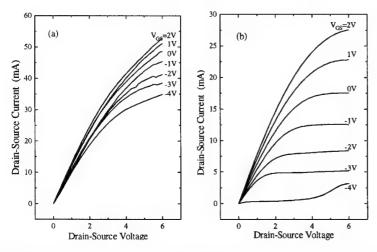
Figure 6. Common-source responses of 4 µm x 125 µm MISFETs: (a) untreated and (b) CdS-treated.

gate bias, low output conductance, and an extrinsic transconductance of 40 mS/mm. The intrinsic value of transconductance for the stated device geometry, doping, active layer, and oxide thickness is approximately 80 mS/mm. Note that neutral-region resistance, contact resistance, and interface-state density can significantly reduce the transconductance. Using calculated values of neutral-region resistance and measured values of contact resistance, the extrinsic transconductance is determined to be 45 mS/mm, implying the interface-state density of the CdS-treated device is not significantly affecting performance.[10] For the CdS-treated device, thinner gate dielectric and lower parasitic resistance will result in additional performance improvements.

CONCLUSIONS

We have deposited thin layers of CdS on (100) n-InP with a chemical bath technique. RHEED and TEM measurements indicated that the films begin growth in either an amorphous or poorly ordered polycrystalline phase. As the films get thicker, the polycrystalline phase becomes dominant, with [110] being the preferred direction of CdS growth on (100) InP. XPS indicated that the deposition process effectively removes existing native oxides on InP and forms a protective layer that maintains a chemically stable surface for subsequent dielectric deposition. Surface analysis also showed that the P:In ratio remains near unity following both CdS treatment and oxide deposition, with no InP native oxide formation detectable. Using CdS as a passivating layer prior to SiO_2 deposition results in dramatic improvements in the electrical response of MIS capacitors. The quasistatic C-V response of CdS-treated MIS capacitors consistently shows well defined regions of accumulation, depletion, and inversion, indicating the Fermi level is not pinned by an excessive density of states. D_{it} values as low as 6×10^{10} $eV^{-1}cm^{-2}$ were found for CdS-treated MIS capacitors. InP depletion-mode MISFETs with CdS interlayers show improved electrical characteristics to those of untreated samples, with a marked reduction in sub-threshold drain current and transconductance virtually unaffected by interface traps.

ACKNOWLEDGMENTS

REFERENCES

[1] C.J. Sandroff, R.N. Nottenburg, J.C. Bischoff, and R. Bhat, *Appl. Phys. Lett.* **51**, 33 (1987).

[2] R. Iyer, R.R. Chang, and D.L. Lile, *Appl. Phys. Lett.* **53**, 134 (1988).

[3] Y. Jeong, S. Jo, B. Lee, and T. Sugano, *IEEE Electron Device Lett.* **16**, 109 (1995).

[4] H.M. Dauplaise, K. Vaccaro, A. Davis, G.O. Ramseyer, and J.P. Lorenzo, accepted by *J. Appl. Phys.*

[5] D. Lincot and R. Ortega-Borges, *Appl. Phys. Lett.* **64**, 569 (1994).

[6] W.M. Lau, S. Lin, X.W. Wu, and S.Ingrey, *J. Vac. Sci. Technol. B* **8**, 848 (1990).

[7] B.R. Bennett, J.P. Lorenzo, K. Vaccaro, and A. Davis, *J. Electrochem. Soc.* **134**, 2517 (1987).

[8] R. Castagné and A. Vapaille, *Surface Sci.* **28**, 157 (1971).

[9] M. Froment, M.C. Bernard, R. Cortes, B. Mokili, and D. Lincot, *J. Electrochem. Soc.* **142**, 2642 (1995).

[10] P.M. Hill, *IEEE Transact. Electron Devices* **ED-32**, 2249 (1985).

Part III

Electronics and Processing

On the investigation of power and reliability performance of pseudomorphic AlGaAs/InGaAs HEMT's

G.P.Li and Y.C.Chou
Department of Electrical and Computer Engineering, University of California, Irvine, CA. 92717
Y.C.Chen, C.S.Wu, K.K.Yu and T.A.Midford
Microelectronics Division, Hughes Aircraft Company, Torrance, CA 90505
Y.Liu and G.J.Sonek
Department of Electrical and Computer Engineering and Beckman Laser Institute and Medical Clinic, University of California, Irvine, CA. 92717
X.Wei and B.J.Tromberg
Department of Physiology and Biophysics, and Beckman Laser Institute and Medical Clinic, University of California, Irvine, CA. 92717

ABSTRACT

In this work, power and reliability performance of pseudomorphic AlGaAs/InGaAs HEMT's are investigated by 2-D device simulation, spatially-resolved electro-luminescence, light emission spectra analysis, and gate current instabilities. A two-dimensional device simulation was used to exploit the off/on state breakdown origins in the power PHEMT's and to explore the physical mechanisms responsible for light emission in both conditions. A correlation between simulated results and light emission spectra highlights the breakdown origins in PHEMT's.

PHEMT's subjected to off-state breakdown stress and on-state hot carrier stress show changes in device characteristics. While gate leakage current, i.e. a surface leakage component associated with the surface passivation layer is reduced by these stresses, a reduction in drain current, transconductance degradation, and an increase in the impact ionization generated gate current are also observed.

Further improvement in off/on state breakdown voltages and device reliability calls for device structure optimization for lower electric field design, surface passivation treatment for lower surface leakage current, and Schottky barrier enhancement for lower gate current.

INTRODUCTION

Microwave monolithic integrated circuits (MMICs) are used in many communication systems, and with the advent of new high frequency applications there is a growing commercial and military requirement for MMICs to operate well into the millimeter wave region. There is current MMIC system design work being carried out in

1. Mobile and cellular communications [1,2],
2. Direct broadcasting from satellites (DBS) and geographical location satellites(GPS, Locstar) [3,4],
3. Military and civil radar systems [5],
4. Fiber optic communication systems [6],
5. Direct line urban links at 23 GHz and higher .

The specification for most microwave systems could be met by a silicon based technology at frequencies around 1 GHz. However, at higher frequencies compound semiconductor technologies are the only ones capable of providing a cost effective totally integrated solution. The advantages over silicon technology are two fold. Firstly, operation frequency at the device level is far superior. Secondly, at the proposed frequencies, the monolithic integration of analog and digital functions cannot be achieved by silicon due to substrate limitations.

The core technologies for implementing the MMIC are the High Electron Mobility Transistor (HEMT) and Heterojunction bipolar transistor (HBT). The HEMT has advantages over other microwave transistors such as Metal-Semiconductor Field-Effect-Transistors (MESFET's) and Heterojunction Bipolar Transistors (HBT's). Its advantages include very high operating frequency, low noise figure, and high gain. Since its inception in the mid-1980s the HEMT has found multi-functional MMIC applications such as Low-Noise Amplifiers (LNAs), Wideband Amplifiers, Power Amplifiers, Mixers and Converters, Oscillators, and Frequency Doublers. Currently, perhaps the greatest avenue of development for the HEMT lies in microwave and millimeter wave power amplification due to the increasing demand of power HEMT's in the design of transceiver. And at millimeter-wave frequencies, HEMT's exhibit power performance (output power, gain and efficiency) unmatched by any other transistor technologies.

There are two major kinds of HEMTs: traditional HEMT's with doped AlGaAs layer; and pseudomorphic AlGaAs/InGaAs HEMT's (PHEMT's) with undoped AlGaAs layer. Since Schottky contact to the undoped layer can reduce the tunneling current to achieve a high breakdown voltage, there has been an increased usage of AlGaAs/InGaAs PHEMT's for MMIC power amplifiers offering high power, gain, and efficiency.

The maximum RF output power available from PHEMT's is typically proportional to the product of the device's breakdown voltage and maximum drain current (Imax). A high Imax can be obtained by increasing the two-dimensional electron gas density (2DEG) in the charge supply layers. However, only a 2DEG density of 2.5×10^{12} to 3.0×10^{12} cm^{-2} has been achieved from the double heterojunction PHEMT's [7]. Furthermore, it is well-known that devices with a higher 2DEG density also leads to a lower breakdown voltage mitigating a broad range of applications using PHEMT power amplifiers. For example, for some ground-based and airborne radar systems, the MMIC amplifiers need to be operated at a high drain voltage (e.g., Vds=7V~10V). Thus, for adequate power performance, a higher breakdown voltage than that is currently available is essential in power PHEMT's development work. Since devices are biased at the high drain voltage, they are operating at high electric field regime. Accordingly, high impact ionization and hot carrier generation at this operation condition may pose a threat on device degradations. Thus, the power and reliability performance of AlGaAs/InGaAs PHEMT's need to be further improved upon to retain the system stability and high power efficiency in microwave/millimeter wave applications.

In this paper, we will firstly resolve the breakdown mechanisms, follow to optimize the PHEMT's device design to increase the breakdown voltage for improving power performance, and secondly investigate device degradation mechanisms to help enhance PHEMT's reliability.

EXPERIMENTS

AlGaAs/InGaAs power PHEMT's with a double-sided silicon planar doping were fabricated for this study as shown in Fig.1. The epitaxial layer structure was grown by molecular beam epitaxy (MBE) on 3-in semi-insulating GaAs substrates as described in [8]. Before starting to process the wafers, epitaxial layers were also characterized by photoluminescence (PL), Secondary ion mass spectroscopy (SIMS), X-ray diffraction technique, Polaron C-V methods, and Van-der Pauw-Hall to ensure all the material parameters, e.g., layer thickness, doping concentration, electron mobility, Al and In compositions, to meet the designed specifications. This double-sided atomic delta-doped layers provide a sheet carrier concentration of ~3×10^{12}cm^{-2} with an electron mobility of ~5500 cm^{2}V^{-1}S^{-1} at 300K. Highly reliable ohmic contacts of Ni/AuGe/Ag/Au were deposited by e-beam evaporation and patterned by conventional lift-off processing [9], producing a contact resistance of about 0.15 Ω-mm. E-beam lithography was used

to define the channel and gate recess patterns to form a T-shaped e-beam deposited Ti/Pt/Au gate (0.3 μm x 125 μm) [10], then followed by nitride deposition for surface passivation using PECVD process. Both channel and gate recesses were etched by wet chemical solutions. The detailed fabrication and device design for achieving a 50% power-added efficiency at X-band were reported elsewhere [11].

   All the devices were mounted in a 24-pin ceramic dual in-line package to perform the measurements. A Leitz inverted microscope with high resolution CCD camera was used to obtain the electro-luminescence(EL) image and spatial resolution. An optical set up was also used to analyze the light emission spectrum. In addition, 2-dimensional device simulation was performed to assist in identifying the device breakdown and degradation mechanisms [12]. A low frequency noise measurement setup was used to to investigate the undesirable gate leakage current mechanisms. To minimize the noise from the power supply and biasing circuit, a battery, metal resistors, and wire wound potentiometers were used to provide the Vgs and Vds during the noise measurement. The gate current noise signal was fed into a low noise transimpedance amplifier, whose low frequency noise was at least 10 dB lower than that from the devices. An HP3563A control systems analyzer was used to acquire the amplified gate current noise spectrum.
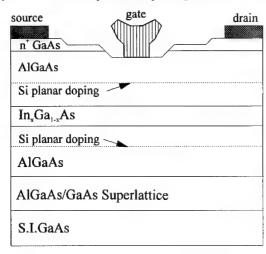
Fig.1 Schematic cross section of a PHEMT device.

RESULTS AND DISCUSSIONS
(1). Off-state breakdown investigation:
   To maximize RF output power in a three-terminal power PHEMT's it is essential to increase the product of maximum channel current (Imax) and drain-source breakdown voltage (BVds) [13]. This can be achieved easier by just increasing the BVds than increasing Imax due to the maximum channel carrier density limitation. It is well known in MESFET's that the drain-source breakdown is limited by the drain avalanche breakdown [14]. However, such a drain-source breakdown mechanism in MESFET's may not be applicable to the planar doped PHEMT's because of the differences in material, doping profiles, device structure, and the electric field distribution [11]. In this section, we show the detailed investigations of drain-source breakdown mechanism.

The drain-source breakdown voltage was measured at a gate bias of -3 V (Channel is at the complete pinchoff condition) and a drain current of 16 mA/mm. Figure 2 shows a typical I-V characteristics of drain-source breakdown in Phase-I PHEMT's with a BVds of about 13 V. Noticeably, the drain current Id is almost equal to the gate current.
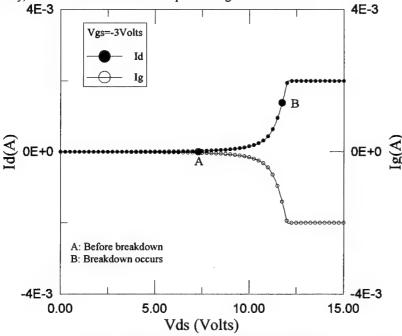
Fig.2 I-V characteristics of drain-source breakdown.

A two-dimensional device simulator was used to further investigate the difference in current flow path inside the device before breakdown (at point A) and right at drain-source breakdown (at point B) as shown in Fig.2. Fig.3 (a) and (b) depict the simulated current flow results at point A and B respectively. Before breakdown, the current flow path is from drain to source and further spreads into the layers underneath the InGaAs channel. This is because the channel carriers are fully depleted with the Schottky gate biased at -3V. As a result of current spreading into the substrate at this operation condition, the material quality of epitaxial layers underneath the InGaAs channel may affect the PHEMT's characteristics [15]. On the other hand, the current flow path at device breakdown is quite different from that of before breakdown. Current is directly flowing from drain to gate illustrating that the three-terminal drain-source breakdown is possibly limited by the gate-drain breakdown. Note that there is no current flowing between drain and source.

It is expected at device breakdown condition that there are plenty of electron-hole pairs generation with carrier energy higher than energy bandgap of the InGaAs channel and AlGaAs top layers, resulting in an electro-luminescence(EL). Since the current flow path is only confined in the gate-drain (G-D) region, one should expect to observe the light emission image coming from the G-D region as shown in Fig.4, which is consistent with the 2-D device simulation result. The spatial distribution of light intensity along the gate length and gate width direction can also be obtained with the help of high resolution CCD camera, thus allowing us to probe the maximum

electric field location and determine the uniformity of electric field distribution. The spatial image of light emission is also compared with the 2-D simulation, showing close match between experimental and simulation results [16]. This method provides an alternative to probe the electric field distribution inside the device, which is valuable for identifying the effects of processing technology (i.e. the gate recess, the channel recess, the surface topology, etc.) on generating the weak spots in breakdown. This in-depth understanding of off-state breakdown will lead to the production yield enhancement.

Before off-state breakdown

(a)   (b)
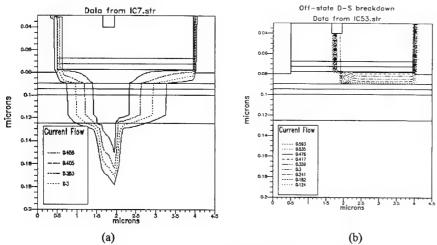
Fig.3 Current flow path. (a):Before breakdown at point A.
(b):Breakdown occurs at point B.

Although EL spectrum has been widely observed on GaAs MESFET's [17] under both open- and pinched-channel operation conditions, there is no detailed investigation on power PHEMT's. Figure 5 shows the light emission intensity versus the emission energy at 300K for device biased at off-state breakdown with different amount of gate current: point 1 (Ig=6.7mA), point 2 (Ig=5.24 mA), point 3 (Ig=4.48mA), and point 4 (Ig=1.6 mA). The spectra show a emission peak centered approximately at 2 eV. The spectrum tail beyond 2.25 eV is a typical Boltzmann distribution, which is a characteristics of hot carrier distribution. Since most of the gate current is the hole current for the gate electrode biased at Vgs=-3V, one would expect that the higher light intensity follows the higher gate current (1>2>3>4) as shown in Fig.5.

The gate-drain breakdown also exhibits a similar EL spectra to that shown in Fig.5, indicating that the drain-source breakdown is indeed limited by the onset of G-D breakdown, analogous to the GaAs MESFET breakdown. Figure 6 shows the temperature dependence of drain-source off-state and gate-drain breakdown in phase-II PHEMT's with routinely demonstrated breakdown voltage greater than 20 V [11]. Clearly, the temperature dependence trend of drain-source breakdown follows the gate-drain breakdown. This further confirms that the drain-source breakdown is essentially dominated by the gate-drain breakdown. Below 300K, the drain source breakdown is controlled by the avalanche breakdown with a positive temperature coefficient of breakdown voltage. On the contrary, breakdown voltage shows a negative temperature coefficient at T>300K because the breakdown is also dependent on the carriers initiating the avalanche breakdown, i.e. the thermionic-emission gate current in this case. The

detailed investigation of temperature dependence of breakdown voltage affected by the process technology, device structure, and material quality will be discussed elsewhere [18].
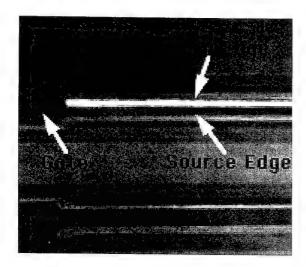
Fig.4 Electro-luminescence at drain-source breakdown.
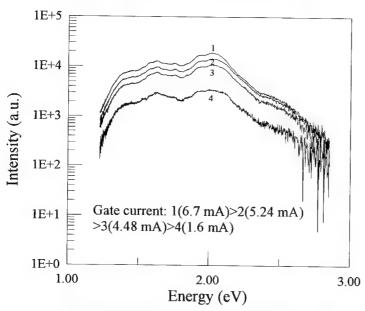
Fig.5 EL spectra at drain-source breakdown (Vgs=-3V, Vds=14V)
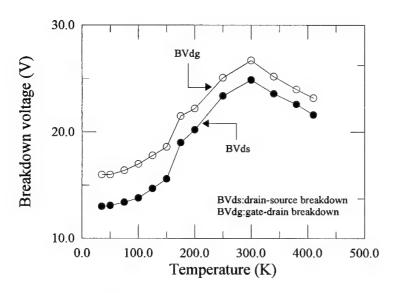
Fig.6 Temperature dependence of drain-source and gate-drain breakdown.

Moreover, 2-D device simulation illustrates the high electric field covering the entire region from InGaAs channel to the n⁺-GaAs capping layer. Consequently, the optimization of device structure can lead to the improvement of breakdown voltage by adjusting the capping layer doping concentration, channel recess depth, total Si planar doping concentration, and channel indium composition as reported by Y.C.Chen et al. [11].

(2). On-state breakdown investigation:

Devices also require high on-state breakdown voltage for the high Vds (Vds=7 V ~10 V) operation in order to deliver high RF output power. Again, the current flow path at Vgs=0V,Vds=7V is shown in Fig.7. It is very clear that the current is confined inside the InGaAs channel between the drain and source. Due to the applied bias at the gate, there is some minor depletion of InGaAs channel carriers underneath the gate. Because of the power dissipation limitation ($\approx$ 4w/mm) due to thermal heating effects on device, we cannot measure the on-state breakdown characteristics. Consequently, devices were biased at high Vds to assess the on-state breakdown mechanisms. Figure 8 shows a typical I-V characteristics of drain and gate current in power PHEMT's. Obviously, the impact ionization effect becomes very pronounced at Vds>7V, thus giving rise to high gate current [19].
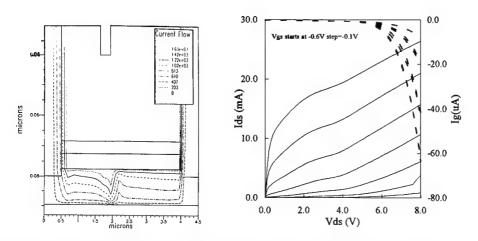
Fig.7 Current flow path at Vgs=0V, Vds=7V.Fig.8 I-V characteristics of Id & Ig at high Vds.

While there are few studies on on-state breakdown owing to impact ionization in PHEMT's [19], its breakdown mechanism is still not clear in high power PHEMT's. As described by C. Canali et al. [19], the excess gate current at Vds>7V is originated from holes generated by impact ionization. If it is the case, one would also expect to observe the electro-luminescence image and its intensity dependence on gate current at on-state breakdown. Figure 9 shows a typical EL image at Vgs=-1V, Vds=9V. The light emission image is flashing out from the entire InGaAs channel region between drain and source, which is different from the drain-source off-state breakdown case. The major emission peak centered around 1.25 eV (close to the InGaAs bandgap) of the EL spectra shown in Fig.10 indicates that the EL is due to band-to-band recombination inside the InGaAs channel. That explains why we do not observe a specific emission region at high Vds. The satellite peak nearby 1.25eV might result from the bound-state interband recombination inside the InGaAs channel. The light intensity is also proportional to the gate current, confirming that Ig is primary hole current. At Ig< 10 μA, the EL image is very vague. The temperature dependence of Ig at Vds=5V-6V was also measured to identify the gate current component. As shown in Fig.11, at Vds=5V, Vgs=-1.3 V, Ig is dominated by impact ionization hole current at T< 200K. In contrast, at T> 200K, Ig is governed by the thermionic-emission current. Obviously, carrier impact ionization rate extracted from Ig/Ids has a strong temperature dependence [20]. The transition point between impact ionization and thermionic-emission is also affected by the applying Vds
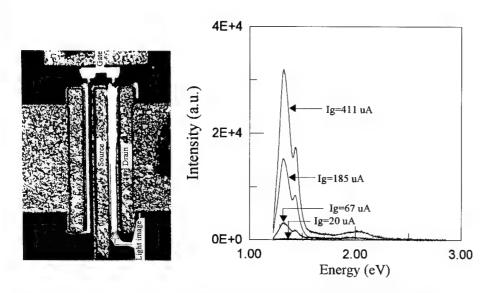
Fig.9 EL image at Vgs=-1V, Vds=9V. Fig.10 EL spectra at Ig=20 μA, 67 μA, 185 μA, and 411μA.
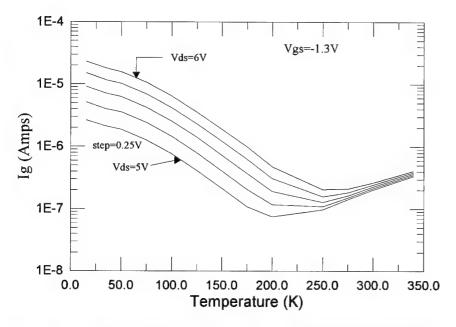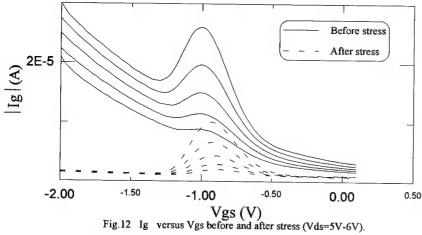
Fig.11 Gate current temperature dependence showing a different trend depending upon the operation temperature range.

(3). The effects of drain-source breakdown and on-state high Vds on gate current:

Since the gate leakage current can increase the stand-by power dissipation and reduce the breakdown voltage, it is essential to alleviate the undesirable gate leakage current. The effects of drain-source breakdown and on-state high Vds stress on the gate leakage current were investigated in detail. While the gate leakage current is drastically reduced after stress as shown in Fig.12, no obvious changes in Ids and Gm are observed. Prior to stress, gate leakage current shows a nearly ideal 1/f noise characteristics with an Ig^2 dependence, suggesting a surface generation-recombination current from the interface between GaAs/AlGaAs surface and passivation layer. After stress, a gate leakage current reduction accompanying with drain-source breakdown improvement can be achieved permanently. The details were reported elsewhere [21].

Fig.12 Ig versus Vgs before and after stress (Vds=5V-6V).

(4). Device reliability

A typical PHEMT's biasing condition at Vgs=-0.75 V , Vds=8V was used to investigate the device reliability. After 100 hours stress at 300K, Ids decrease accompanying with the Gm degradation is shown in Fig.13 and Ig increase is shown in Fig.14. The Ids and Gm degradation indicates that the device degradation is caused by the 2-DEG carrier density reduction, possibly due to the trap generation underneath the gate. The trap might modify the effective electric field, resulting in an increase of Ig as shown in Fig.14. While device exhibits a clear 1/f noise characteristic before stress, it shows an addition of a Lorentzian shape after stress as shown in Fig.15. The Lorentzian shape can be modeled as:

$$S_{IG}(A^2 / Hz) = 4.84x10^{-22} + \frac{7.43x10^{-18}}{f} + \frac{1.53x10^{-20}}{1+(2\pi f)^2 \tau^2}$$

(1)

where $\tau = \dfrac{1}{2\pi f_p}$, fp=1188Hz. The detail will be reported in [22].

116
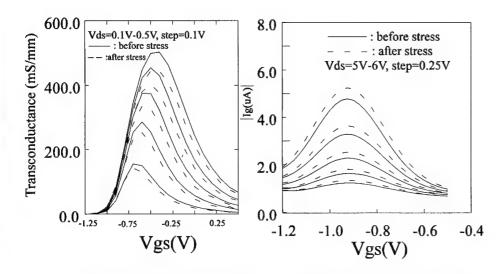
Fig.13 Gm degradation after stress.

Fig.14 Gate current increase after stress.
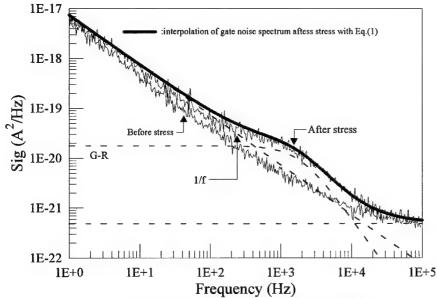
Fig.15 Gate current noise spectra before and after stress.

SUMMARY

Off- and on-state breakdown mechanisms in high power PHEMT's have been investigated in detail by correlating the results from probing current flow paths and electric field distribution in

2-D device simulation, measuring light emission spectrum, and determining temperature dependence of gate leakage current. Both the off-state D-S breakdown and on-state operation at high Vds stresses for short time can alleviate gate leakage current originating from the interface recombination/generation current without adversely affecting the PHEMT's characteristics. However, devices subjected to on-state hot carrier stress for long time give rise to the Ids decrease, Gm degradation, and impact ionization generated gate current increase. Such device characteristics changes after stress also accompany an additional Lorentzian spectrum appearing in gate current noise spectra, possibly related to the trap generation.

REFERENCE

1. M. Chelouche and A. Plattner, Electronics & Communication Engineering Journal., 5, 187(1993).
2. T. Yoshimasu, N. Tanba and S. Hara, IEEE Microwave and Guided Wave Lett., 4, 65(1994).
3. J.M. Merour, 23rd European Microwave Conference Proceedings, 1993, p94
4. M. Shigaki, S. Koike, K. Nogatomo and K. Kobayashi, IEEE Trans. Microwave Theory Tech., 40, 1215(1992).
5. P. Descamps, V. Pauker and JJ. Vindevoghel, 21st European Microwave Conference Proceedings, 1991, p483
6. P.M. Lane, I.Z. Darwazeh, P.M.R.S. Moreira and J.J. O'Reilly, SPIE Proceedings, 1974, 57(1993).
7. C. Gaquiere, D. Theron, B. Bonte and Y.Crosnier, Microwave Optical Tech. Lett., 7, 871(1994).
8. C.S. Wu, F. Ran, S.J. Pearton, M. Hu, C.K. Pao and R.F. Wang, IEEE Trans. Electron Devices, 42, 1419(1995).
9. C.S. Wu, K.K. Yu, M. Hu and H. Kanber, J. Electron Mat., 19, 1265(1990).
10. F. Ren, S.J. Pearton, C.R. Abernathy, C.S. Wu, M. Hu, C.K. Pao, D.C. Wang and C.P. Wen, IEEE Trans. Electron Devices, 39, 2701(1992).
11. Y.C. Chen, C.S. Wu, C.K. Pao, M. Cole, Z. Bardai, L.D. Hou and T.A. Midford, IEEE GaAs IC Symposium Tech. Digest, 1995, p281.
12. Y.C. Chou, G.P. Li, Y.C. Chen, C.S. Wu, T.A. Midford, K.K. Yu and TiC. Cisco, in GaAs Reliability Workshop Tech. Digest, 1995.
13. K. Hikosaka, Y. Hirachi and M. Abe, IEEE Trans. Electron Devices, 33, 583(1986).
14. S.H. Wemple, W.C. Niehausm, H.M.Cox, J.M. Dilorenzo and W.O. Schlosser, IEEE Trans. Electron Devices, 27, 1013(1980).
15. Y.C. Chou, G.P. Li, Y.C. Chen, C.S. Wu, K.K. Yu and T.A. Midford, to be submitted.
16. Y.C. Chou, G.P. Li, Y.C. Chen, C.S. Wu, K.K. Yu and T.A. Midford, to be submitted.
17. R. Yamamoto, A. Higashisaka and F. Hasegawa, IEEE Trans. Electron Devices, 25, 1567(1978).
18 Y.C. Chou, G.P. Li, Y.C. Chen, C.S. Wu, K.K. Yu and T.A. Midford, to be published.
19. C. Tedesco, E. Zanoli, C. Canali, S. Bigliardi, M. Manfredi, D.C. Streit and W.T. Anderson, IEEE Trans. Electron Devices, 40, 1211(1993).
20. Y.C. Chou, G.P. Li, Y.C. Chen, C.S. Wu, K.K. Yu and T.A. Midford, to be submitted
21. Y.C. Chou, G.P. Li, Y.C. Chen, C.S. Wu, K.K. Yu and T.A. Midford, submitted to IEEE Electron Device Lett.,1996.
22. Y.C. Chou, G.P. Li, Y.C. Chen, C.S. Wu, K.K. Yu and T.A. Midford, to be published.

FINITE ELEMENT CALCULATIONS TO OPTIMIZE THE DESIGN OF A STRESSOR FOR STRAINED INDUCED QUANTUM WIRES AND QUANTUM DOTS IN GaAs

K. PINARDI, S. C. JAIN, H. E. MAES
IMEC, Kapeldreef 75, 3001 Leuven, Belgium

ABSTRACT

We have calculated the normalized stress σ_{fxx}/σ_0 (σ_0 is the stress in the large area stressor) in the stressor and σ_{sxx}/σ_0 in the substrate for values of $R_E = E_f/E_s$ (E_f is the Young's modulus of the stressor and E_s is the Young's modulus of the substrate) in the range 0.5 to 1.2. Substrate stresses for 13 stripe stressor samples are also calculated for $R_E = 0.9$ which corresponds to an InGaAs stressor on GaAs with an In concentration of about 25%. It is found that for any given l, the stress at a given depth increases monotonically as h increases (l and h are the halfwidth and thickness of the stressor). The increase is rapid in the beginning for small value of h ($l/h > 2$). It becomes slow for $l/h < 2$ and saturates at $l/h = 0.5$. For large l/h ($l/h > 50$) there are two stress wells in the substrate separated by a barrier. For $l/h = 20$ the two wells merge into one well with a flat bottom. As l/h decreases further the bottom curves downward, and for $l/h < 2$ the shape of the stress distribution curve resembles that of a parabola. The stress σ_{sxx}/σ_0 decays rapidly with distance z from the interface. It is reduced to $1/3$ of its value near the interface at $z \sim h$. It is therefore necessary to construct the active layer close to the interface. Quality of the interface plays a dominant role in the Quantum structures fabricated in this manner. The shape and the strength of the stress well cannot be changed independently in these structures. We have suggested novel stressor designs to remove this limitation.

INTRODUCTION

Strained layers and stripes deposited on semiconductor substrates have been studied extensively in recent years [1 – 3]. Many authors have reported fabrication of Quantum structures in GaAs substrate fabricated by depositing a stressor on its surface [4 – 7]. This method of producing quantum structures has several advantages over the conventional methods [5]. If the lateral confinement of the exciton is obtained by etching, free surface is damaged by the etching process [5]. Patterning by ion implantation requires annealing at high temperatures and is incompatible with low temperature processing. It is difficult to obtain good dimensional resolution, uniformity and low damage of the structure by the conventional methods. In the stressor induced quantum structures some of these difficulties are avoided. Since the quantum structure is buried surface to volume ratio is not large.

In this paper we calculate stress profiles induced by the stressor of different shapes and dimensions with the objective to determine the optimum design of the stressor.

RESULTS

We have studied four types of samples, shown in Fig. 1. In Figs. 1a and 1b the stressors are in the form of stripes and produce Quantum Wires (QWRs) if a Quantum Well (QW) is placed below the interface [5]. In Fig. 1c the stressor is a circular mesa. It produces a Quantum Dot (QD) instead of a QWR. The stresses and the band edges are related through deformation potential (DP) which is different for different materials. However shape of the potential profiles is qualitatively similar to that of the stress profiles [5].

Effect of elastic constants

Finite Element (FE) calculations show that the normalized stresses σ_{xx}/σ_0 in the stressor
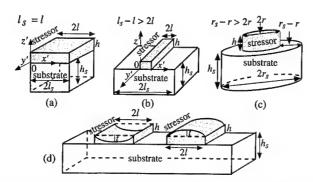
Figure 1: Schematic diagram of (a) α structure with stripe-stressor width $2l$ equal to substrate width $2l_s$, (b) β structure with $\Delta l = l_s - l \geq 2l$, (c) γ structure with a circular mesa stressor with $\Delta r = r_s - r \geq 2r$ and (d) new stressor designs suggested in this paper. Samples are denoted by $\alpha(l, h)$, $\beta(l, h)$, $\gamma(r, h)$ and $\beta(l, h, t)$ in (a), (b), (c) and (d) respectively. Origin of x is not always at the edge of the stripe as shown in this figure.

and in the substrate depend upon the ratio $R_E = E_f/E_s$ where E_f is the Young's modulus of the stressor and E_s is the Young's modulus of the substrate. It does not depend separately on E_f and E_s. Most measurements of stresses are made in the middle of the top layer of the stripe [2, 3]. Moreover FE calculations show that the effect of the change in R_E on the stresses is maximum in the middle of the stressor at $x = l$. We plot in Fig. 2a the stress
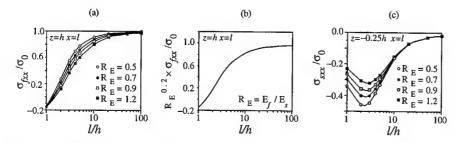
Figure 2: (a) Plot of the normalized stress σ_{fxx}/σ_0 as a function of the ratio l/h for different values of the ratio of Young's modulii shown in the figure. Figure (b) shows the single $R_E^{0.2}\sigma_{fxx}/\sigma_0$ universal curve applicable to all samples with a maximum error of 12% for $30 > l/h > 3$. The error is smaller, it is less than 5%, for values of l/h in the range 4 to 10. (c) Same as (a) but for the substrate stresses.

σ_{fxx}/σ_0 as a function of l/h at $x = l$ in the middle of the surface layer of the stressor for 9 samples and for different values of the ratio R_E. We have shown earlier [2] that stress values depend only on l/h and not on individual values of l and h. This figure shows that the normalized stress is weakly dependent on R_E. This allows us to construct an empirical curve $R_E^{0.2}\sigma_{fxx}/\sigma_0$ versus l/h, shown in Fig. 2b, applicable to samples for all values of R_E in the range 0.5 to 1.2. The values of stress calculated using this curve have a maximum error of 12% for $30 > l/h > 3$. Fig. 2a shows that for $l/h > 30$ the error is smaller if we use $\sigma_{fxx}/\sigma_0 = 1$. FE calculations show (see Fig. 2c) that substrate stresses σ_{sxx}/σ_0 are also weakly dependent on R_E except for $l/h < 3$.
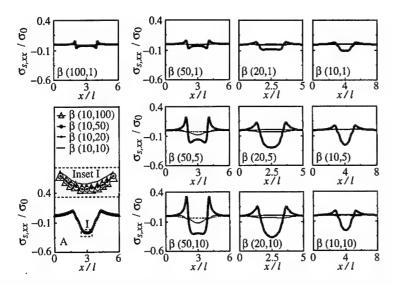
Figure 3: Substrate stresses in 13 samples with dimensions (l, h) given in the figure. Thick lines show the normalized stress at a depth of 2.5 units, thin continuous lines at a depth of 25 units and dashed lines at a depth of 50 units. Fig. A contains data for 3 new samples and also the data for (10,10) sample at a depth of 2.5 units. The inset I in this figure shows the magnified portion in the dotted rectangle. Note that origin of x in this figure is at the edge of the substrate.

Effect of stressor dimensions

We have made FE calculations of the stresses produced by stripe stressors with 13 values of l/h ranging from $l/h = 100$ to $l/h = 0.1$. The value of R_E used in these calculations is 0.9 which corresponds to an In concentration of about 25%. Results of these calculations are shown in Fig. 3. This figure shows that in the (100,1) sample the stress in the middle is practically zero and there are two separated stress wells under the edges of the stripe in agreement with the results reported in [5]. As l decreases, sample (50,1), the depth of the two wells increases and the barrier becomes shallower. In sample (20,1) for $l = 20$ the barrier height becomes practically zero. There is only one stress well with nearly flat bottom. Finally in $l = 10$, sample (10,1), the bottom of the stress well starts curving downward and the shape becomes like that of a parabola. In the samples (50,1), (50,5) and (50,10), l is kept constant at 50 and h increases from 1 through 5 to 10. The large increase in stress with increase in h is prominently seen. Same is true for the (20,1), (20,5) and (20,10) samples and also for the (10,1), (10,5) and (10,10) samples. The increase with h in sample (10,10) is not large. In Fig. 3A, we have plotted the results for very small value of l/h in 4 samples. Halfwidth l is kept constant at 10 and values of h are 10, 20, 50 and 100. The stresses are calculated at a depth of 2.5 units from the interface. Inset shows the magnified view of the curves in the rectangle I. It is seen that the stress has nearly saturated at the value for $l/h = 0.5$. This behaviour can be understood from general considerations. As h increases and l is kept constant the edges of the stripe exert increasingly large force on the substrate and the substrate stress increases. The rate of increase of stress with h decreases as h becomes large because now the top layer is far away from the interface. This behaviour is illustrated in Fig. 4. Edge induced relaxation causes bending and shift of the vertical edge of the stressor which in turn induces stress in the substrate [2]. In (10,10) sample the vertical edge moves away and goes past the position shown by the arrows 2 and 3. With increase in h in sample (10,20), the top of the vertical edge starts moving backwards and now the
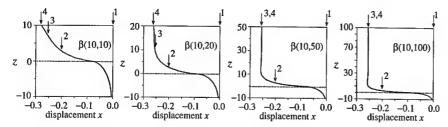
Figure 4: Displacement of the vertical edge of the stripe for four different samples. Arrow 1 at $x = 0$ shows the position of the edge of fully compressed stripe, arrow 2 indicates the position of the edge if the stripe is completely relaxed without any influence of the substrate, arrow 3 gives the position of the edge if it is relaxed in the x direction but not in the y direction, because it is long in the y direction and in this direction it is strained to match the substrate. The edge moves further away from arrow 2 due to Poisson's effect. Arrow 4 is the actual position as calculated by the FE method. The interface is at $z = 0$ shown by the dotted line.

interaction between the edge and the substrate becomes weak. The arrows 3 and 4 become indistinguishable with further increase in h in samples (10,50) and (10,100). Increase in h in this range and beyond has practically no effect on the stress either in the stressor or in the substrate.

Fig. 3 allows us to draw many important conclusions. The shape of the stress curve can be tailored by changing the value l/h. For a constant l the magnitude of the stress at the bottom of the well can be increased by increasing h. Since the energy levels depend on the shape and depth of the potential well (which is similar to the shape of the stress distribution curve) the results of Fig. 3 can be used to optimize the stressor design.

The substrate stress in a (30,10) γ sample is shown in Fig. 5. This stress curve can be
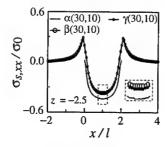
Figure 5: Substrate stresses in an α sample (solid line), in a β sample (○) and in a γ sample (●). Inset shows the magnified curves in the dotted rectangle.

used to fabricate a QD if a QW is placed below the interface. Substrate stresses in a (30,10) β sample and a (30,10) α sample are also shown. Qualitatively the results for α structure are similar to those in the β structure, except that the stress curves are wider and deeper than in the β structure. For the dimension used the stress in the β and γ structures are not very different.

Variation of stresses and strains with depth z

Variation of stresses and strains with reduced depth z/h in two samples (10,10) and (40,10) are plotted in Fig. 6. These curves show that near the interface the components σ_{sxx}/σ_0

122
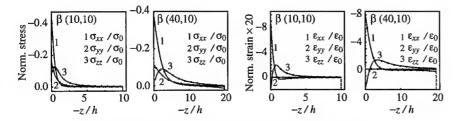
Figure 6: The variation of stresses and strains with depth z

and $\epsilon_{sxx}/\epsilon_0$ are much larger than the other components and they drop by a factor 3 at a depth of the order of h. Therefore in the stressor induced potential wells the active layer is constructed close to the interface. The quality of interface has a large effect on the band structure and the luminescence. This is evident in the measurements of photoluminescence in the stress induced QDs in [6].

NOVEL STRESSOR DESIGNS

We have seen above that the shape of the stress well can be changed by changing the ratio l/h. But a change in l/h also changes strength of the stress. For example in order to have a stress well with a flat bottom l/h must be 20, and to have parabolic shape l/h must be
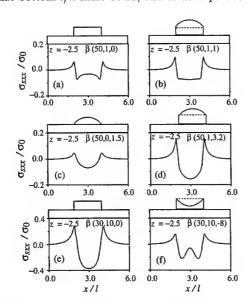
Figure 7: Plot of normalized substrate stresses for different stressor designs given at the top of each figure.

smaller than 2. The strengths of stresses in the two cases are very different. We cannot change the strength and the shape of the stress (or of the potential) well independently. We have therefore investigated novel stressor designs shown earlier in Fig. 1c. The results of

123

our preliminary calculations are shown in Fig. 7. The shapes of the stressors are given in the figure for each sample. Nomenclature used for the stressors is defined in Fig. 1. These new designs provide another degree of freedom through the parameter t defined in Fig. 1c. Now shapes and strengths of the stress curves can be changed independently. We have designed 3 samples in which the value of the maximum stress remains the same but the shapes are (1) two shallow wells, (2) a well with flat bottom and (3) a well with parabolic shape. The results are shown in Figs. 7a, b and c respectively. The maximum stress in these three samples is about the same, the maximum difference being about 7%. We have not attempted to make these stresses exactly equal which can be done by fine tuning of the parameter t. Note also that the new shape of the stress curve shown in Fig. 7f can not be obtained by the conventional stressors with rectangular cross sections.

SUMMARY AND CONCLUSIONS

Using the FE method we have calculated the stress distribution curve for the 13 values of l/h i.e. for 13 different stressor samples. The shape of the normalized stress distribution curve depends weakly on the elastic constants but strongly on the value of l/h. For large l/h, two wells separated by a barrier are observed in the substrate stress in agreement with results reported in [5]. As l/h decreases, the two wells merge into one with a flat bottom. With further decrease in l/h, the bottom curves down and the stress distribution curve becomes similar to that of a parabola. The value of stress also changes with l/h. This value and shape can not be controlled independently. We have suggested novel stressor designs which allow us to control the stress value and shape independently. Multiple Quantum Wells induced by the stressor can also be obtained with the novel stressors.

ACKNOWLEDGEMENTS

References

[1] S. C. Jain, *Germanium–Silicon Strained Layers and Heterostructures*, (Academic Press, Boston 1994).

[2] S. C. Jain, A. H. Harker, A. Atkinson and K. Pinardi, J. Appl. Phys. 78, 1630 (1995).

[3] S. C. Jain, B. Dietrich, H. Richter, A. Atkinson, and A. H. Harker, Phys. Rev. B 52, 6247 (1995).

[4] K. Kash, B. P. Van der Gaag, J. M. Worlock, A. S. Gozdz, J. P. Harbison, and L. T. Florez, *Localization and Confinement of Electrons is Semiconductors* Eds.: F. Kucher, H. Heinrich, and G. Bauer (Springer-Verlag Series in Solid State Sciences,1990) pp 39-50.

[5] K. Kash, D. D. Mahoney, B. P. Van der Gaag, A. S. Gozdz, J. P. Harbison, and L. T. Florez, J. Vac. Sci. Technol. B 10, 2030 (1992). See this paper for references to earlier work of Kash *et al.*

[6] I. H. Tan, R. Mirin, V. Jayaraman, S. Shi, E. Hu, and J. Bowers, Appl. Phys. Lett. 61, 300(1992).

[7] M. Sopanen, H. Lipsanen, and J. Ahopelto, Appl. Phys. Lett. 66, 2364 (1995).

BAND-STRUCTURE ENGINEERING IN NOVEL OPTOELECTRONIC DEVICES

H. Shen and M. Dutta
U. S. Army Research Laboratory, Physical Science Directorate
AMSRL-PS-PB, Fort Monmouth, New Jersey, 07703-5601

ABSTRACT

In this paper we show that unconventionally strained semiconductor heterostructures with unusual band structure exhibit novel and desirable electronic and optical properties not seen in the conventional strained materials. In addition to improving the performance of existing components, unconventional strain may be used to achieve greater functionality in novel optoelectronic devices. We give as examples three such devices that we have conceived and demonstrated, in the two areas of strain, lattice mismatch induced and thermal expansion coefficient mismatch induced. The higher performance and functionality in these devices demonstrate that strain engineered heterostructures are a very promising area for device research and development.

INTRODUCTION

Strain in semiconductor devices was for some time perceived as deleterious to device performance, as it was feared that the excess energy associated with the strain would encourage dislocation formation, the subsequent migration of which would lead to degradation of material quality and concomitantly the device characteristics. Later it was proposed[1] that strain in semiconductors, rather than being detrimental, may in fact offer new functionalities, the advantages of which might far outweigh the disadvantages. Dramatic improvement in strained-layer devices was predicted by theoretical studies.[2-4] Many of the predicted advantages have only recently been demonstrated,[5-7] and the fear of any degradation due to strain has gradually diminished. Now strained-layer structures have been implemented in major applications such as lasers, photodetectors, and bipolar and field-effect transistors. Nevertheless, despite the change of perspective on strain in semiconductor devices, it is mainly utilized to improve the characteristics of an existing device, rather than to offer new applications. For example, incorporation of a compressive (or tensile) strain in a semiconductor laser structure decreases the density of states at the valence band maximum and so reduces the carrier density required to reach threshold. In this paper, we report several novel kinds of strained structures including, but not limited to, 1) delta strained quantum well structures; 2) variable strain quantum well structures; and 3) anisotropically strained quantum well structures. Theses novel structures exhibit new electronic and optical properties not observed previously in conventional strained materials, and thus offer new functionalities. The higher performance and functionality in these devices demonstrate that strained heterostructure engineering is a very promising area for device research and development.

LATTICE MISMATCH INDUCED BIAXIAL STRAIN AND THERMALLY INDUCED ANISOTROPIC STRAIN

For a strained quantum well of lattice constant a_{QW} grown on a substrate with a lattice constant a_S, the strain is given by

$$\varepsilon_{xx}(z) = \varepsilon_{YY}(z) = \frac{a_s - a_{QW}(z)}{a_{QW}(z)}$$

$$\varepsilon_{zz}(z) = -\frac{C_{12}}{C_{11}}[\varepsilon_{xx}(z) + \varepsilon_{YY}(z)] \qquad (1)$$

In most cases the lattice constant a_{QW} and therefore the strain inside the well do not vary. This constraint can be relaxed by grading of the alloy composition inside the QW and thus changing the $a_{QW}(z)$. For example, if $a_{QW}(z)$ varies linearly in the quantum well, it is called a variable strained quantum well, while if $a_{QW}(z)$ has a significant change within a few mono-layers, it is called a delta-strained quantum well.

Although Eq. 1 is valid for strained-layer structures grown on (100) substrates, the lattice mismatch induced strain for any (hhk) orientation is biaxial. Anisotropic in-plane strain ($\varepsilon_{xx} \neq \varepsilon_{yy}$) can only been achieved if a_s in Eq. 1 has a different value for the x and y directions. In our case it is achieved by bonding a MQW thin film at a temperature T_o to a host substrate which has a direction-dependent thermal expansion coefficient ($\alpha_x \neq \alpha_y$). At a temperature $T \neq T_o$, a thermally induced strain of

$$\varepsilon_{xx} = (\alpha_{x,s} - \alpha_{QW})(T - T_o)$$

$$\varepsilon_{YY} = (\alpha_{y,s} - \alpha_{QW})(T - T_o) \qquad (2)$$

is induced, where α_{QW} is the thermal expansion coefficients of the quantum well thin film. An in-plane anisotropic strain breaks the rotation symmetry of the valence band at $k_{//}=0$, mixing the heavy and light hole band in the MQW and creating an anisotropic excitonic absorption.[4]

DELTA-STRAINED QUANTUM WELL

In the delta strained quantum well structure a few monolayers of highly strained material are grown at the center of the quantum well (Fig. 1). The material inserted is chosen such that light hole band is significantly perturbed by the strain while the heavy hole band is not. We have calculated the band structure using the Kohn-Luttinger Hamiltonian including the strain effect. The results indicate that a highly strained layer grown at the
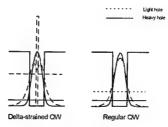
Fig. 1 Illustration of the valence band structure and the lowest heavy- and light-hole wavefunctions of the delta strained quantum well and the regular quantum well.

126

center of a lattice matched QW changes the light-hole wavefunction by further decoupling the heavy- and light- hole bands (see Fig. 1) and altering the valence band dispersion (not shown in this paper) such that the heavy-hole effective mass is reduced. A smaller heavy-hole effective mass is desirable in semiconductor laser applications[8] because it minimizes the carrier density for population inversion while significantly suppressing nonradiative Auger recombination. Although similar results can be achieved with uniformly strained QWs, any improvements are limited due to design compromises between strain and critical layer thickness. The delta-strain approach offers greater design flexibility and enhanced semiconductor laser performance

The samples used in this study were grown by molecular beam epitaxy on InP substrates. A few monolayers of highly strained (2% compressive) InAlGaAs were inserted in the center of a lattice matched InGaAs/InAlAs 80A QW. Two control samples cut from the same wafer and sequentially grown under the same conditions without the delta-strained layer were used as references. One has the same well width as the delta-strained sample, while the other is a 43A InGaAs/InAlAs QW with a uniform compressive strain of 1%.

Shown in Fig. 2 are the room temperature photoluminescence (PL) spectra from the structures. All the samples

Fig. 2 Room temperature photoluminescence spectra from delta strained QW (solid line), unstrained QW (dashed line) and uniformly strained QW (dotted line) .

have room temperature PL at 1.55μm. However, the integrated room temperature PL intensity from the delta-strained QW is more than three times stronger than that from the lattice matched QW. We attribute this enhancement of the integrated room temperature PL intensity to the reduction of non-radiative recombination in the delta-strained QW.

Fig. 3 Integrated PL intensity as a function of temperature. Open circles: delta strained QW; closed circles: unstrained QW

Figure 3 shows the temperature dependence of the integrated PL intensity. Although the integrated PL intensity from the

127

delta-strained QW is more than three times stronger than that from the unstrained QW at room temperature, near 77K the magnitudes approach each other. The integrated PL intensity from the delta-strained QW exhibits a weaker (about 3 times) temperature dependence than the unstrained QW, suggesting that the enhancement of the room temperature PL in a delta-strained QW is due to suppression of the non-radiative process rather than enhancement of the radiative contribution.

VARIABLE-STRAINED QUANTUM WELL

The variable-strain QW structure used in this study consists of a 156A wide $In_xGa_{1-x}As$ well, with the InAs mole fraction x graded nearly linearly from x=0.55 to 0.35. This is incorporated into the i(intrinsic)-region of a $In_{.52}Al_{.48}As$ p-i-n structure (with the p, i, and n layers 5000A, 7500A, and 2500A wide, respectively) nominally lattice matched to InP. Such a linearly varying strain allows the heavy-hole (HH) and light hole (LH) splitting to gradually change from one side of the QW to the other (Fig. 4a). Neglecting the strain-induced coupling between the LH and the spin split-off (s.o.) bands, the HH and LH
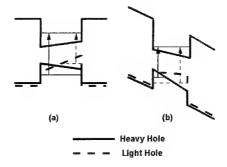
Fig.4. Schematic illustration of the energy bands for a variable-strain quantum well sample; a) without bias, b) with a bias.

Fig. 5 Photocurrent spectra at different biases, dashed lines: light hole; solid lines: heavy hole

band edges in the QW have opposite potential gradients (opposite fields). When a bias is applied to the QW (Fig. 4b), it reduces the field for the LH band, but increases the field for the HH band. Therefore the first heavy hole band (HH1) will have a red shift, while the first light-hole band (LH1) will have a blue shift due to the quantum confined Stark effect (QCSE). As a result, the transition energy (11L) from LH1 subband to the first electron subband (e1) should increase (blue shift), and the transition energy (11H) from HH1 to e1 should decrease (red shift), making the 11H and 11L cross over possible.[9]

Shown in Fig. 5 is the low temperature (10K) photocurrent spectra measured at different biases. The measurement was performed in a waveguide configuration, with the dashed lines representing the TE mode and the solid lines

representing the TM mode. Since the heavy-hole (HH) transition dominates for the TE mode and the light-hole (LH) transition is the only allowed one for the TM mode, the identification of HH and LH transitions is unambiguous. The heavy hole transition displays a strong red shift (30meV) when the bias changes from 0V to 8V, while the light-hole transition exhibits a small blue shift in the bias range 0-3V. Near 3V, the heavy- and light-hole cross each other.

Since the crossing of the 11H and 11L transitions significantly alters the polarization properties of the material, this situation leads to many new opto-electronic device applications such as tunable waveguide polarizers, switches and modulators. Note that in a regular QW the QCSE caused by an electric field can shift HH1 and LH1 bands in the same direction at different rates due to the difference in the effective masses. In contrast, opposing shifts can be realized in a VSQW.

ANISOTROPICALLY STRAINED QUANTUM WELL

The Anisotropically strained quantum well used in this study is composed of a p-i(MQW)-n structure on (100) GaAs. The i region consists of a 150 period, 80 Å GaAs / 60 Å $Al_{0.30}Ga_{0.70}As$ MQW. A 1000 Å AlAs sacrificial etch stop layer was grown beneath the p-i-n structure. The wafer was first thinned to ~ 150 μm. It was then inverted and attached to lithium tantalate ($LiTaO_3$) at 150°C with a thin layer of UV curable optical adhesive. The sample was then held at 150°C for 24 hours. The GaAs substrate was selectively removed using citric acid and the etch stop layer was removed using a 10% buffered HF etchant. Optical and X-ray measurements have shown that this sample was under an anisotropic strain of ~ 0.15% at room temperature. The sample was subsequently fabricated into an array using standard photolithographic techniques. Finally, an identical piece of $LiTaO_3$ was attached to the back of the device substrate, in an orthogonal direction, to compensate for the optical birefringence in $LiTaO_3$.

The thermally induced in-plane anisotropic strain breaks the rotation symmetry of the valence band at $k_{//}=0$, mixing the heavy and light hole band[10] in the MQW and creating an anisotropic excitonic absorption[10]. Application of an electric field to these structures results in tunable polarization rotation and phase retardation, characteristics which make these materials suitable for novel device applications.

The device was tested[11] with normal incident laser light linearly polarized at 45° with respect to the strain axis. To obtain the maximum tunable phase retardation as well as polarization rotation, the operating wavelength (λ) was chosen at 845nm, which is slightly below the
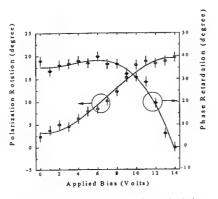
Fig. 6. Relative phase retardation and relative rotation of the polarization of the transmitted light.

heavy-hole exciton peak at a bias of 14V (off state). Fig. 6 shows the relative phase retardation $\Delta\varphi(V)$ and rotation angle $\theta(V)$ of the major axis of the vibrational ellipse of the transmitted light as a function of bias measured at 845nm. The maximum tunable polarization rotation and phase retardation achieved in these experiments were 15° and 37°, respectively.

Shown in Fig. 7 is the emergent light intensity at 845nm as a function of applied bias. The open circles are the tranmitted intensity $I_o(V)$, which exhibits the simple amplitude modulation of a QCSE device. To enhance the contrast ratio a polarizer with an orientation perpendicular to the polarization of the transmitted beam in the off state (14V) was inserted in the beam path, significantly reducing the transmitted light. By decreasing the voltage towards the on-state (0V), the polarization rotation and phase retardation result in an increase in transmission through the polarizer. Shown in Fig. 7 by the solid circles is the transmitted light after the polarizer as a function of bias. A very high contrast ratio of 5000:1 was obtained due to the fact that the intensity of the light in the off-state was greatly attenuated.

Fig.7 Transmitted light intensity as a function of applied bias with (closed circles) and without (open circles) insertion of a polarizer.

Finally, we have examined the manufacturability aspects of the ASQW modulator arrays and compared them with the more commonly used asymmetric Fabry-Perot (ASFP) modulator arrays. In the ASQW modulator, the transmitted light intensity I(V) with the polarizer oriented perpendicular to the transmitted beam is given by:

$$I(V) = I_o(V) \{ \sin^2[\theta(V) - \theta_{off}] + \cos[2\theta(V)]\cos[2\theta_{off}]\sin^2[\frac{\Delta\varphi(V)}{2}] \} \quad (3)$$

where θ_{off} is the polarization rotation angle in the off state, $\theta = \arctan[\exp(-\Delta\alpha d/2)]$, $\Delta\phi = 2\pi\Delta nd/\lambda$, and d is the thickness of the quantum well. . The calculated I(V), represented in Fig. 6 by a line, is in good agreement with the experimental results. In an ASFP reflection modulator, the total reflectivity R_T is related to the front mirror reflectivity R_f, the back mirror reflectivity R_b, the round trip cavity absorption $e^{-2\alpha d}$, and the phase change of the optical beam for a single pass through the cavity $\phi = 2\pi nd/\lambda$. It is given by[12]

$$R_T(V) = \frac{[\sqrt{R_f} - \sqrt{R_b}\, e^{-\alpha d}]^2 + 4\sqrt{R_f R_b}\, e^{-\alpha d}\sin^2(\phi)}{[1 - \sqrt{R_f R_b}\, e^{-\alpha d}]^2 + 4\sqrt{R_f R_b}\, e^{-\alpha d}\sin^2(\phi)} \quad (4)$$

Although in principle the contrast ratio of an ASFP modulator can be as high as an ASQW modulator, the contrast ratio of a ASFP spatial light modulator array is limited because the off-

130

state is extremely sensitive to the total thickness of the QW. For example, in a typical ASFP that has a $\phi = 4\pi$ to 8π, a 1% thickness variation across the array leads to a $\delta\phi$ which varies by 7° to 14°. According to Eq. 4, this corresponds to a maximum contrast ratio of about 16:1. Conversely, the anisotropically strained QW modulator array is less sensitive to any non-uniformities. To achieve maximum contrast in an anisotropically strained QW modulator array, the transmitted light should be linearly polarized ($\Delta\phi=0$) along $\theta_{off} + \pi/2$. Consequently, Eq. 3 implies that one may still obtain a maximum contrast ratio of 3000:1 while assuming the same 1% thickness variation along with an additional 1% variation in the strain.

CONCLUSION

We have presented three unconventional strained semiconductor heterostructures: one possessing delta strain, one possessing strain varying along the growth direction, and finally one possessing a thermally induced in-plane anisotropic strain. We have demonstrated that valence band engineering using unconventional strain is very powerful and results in many novel and desirable electronic and optical properties not seen in conventional strained materials. The higher performance and functionality in these devices demonstrates that strain engineered heterostructures are an extremely promising area for device research and development.

ACKNOWLEDGMENTS

REFERENCES

1. G. C. Osbourn, J. Appl. Phys. 53, 1586, (1982)
2. A. R. Adams, Electron Lett. 22, 249, (1986)
3. E. Yablonovitch and E. O. Kane, J. Lightwave Technol. LT-4, 504 (1986)
4. D. Ahn, S. L. Chuang, IEEE J. Q.E. 30, 350 (1994)
5. D. P. Bour, D. B. Gilbert, K. B. Fabian, J. P. Bednarz, and M. Ettenberg, IEEE Photon Technol. Lett. 2 173 (1990)
6. H. K. Choi and C. A. Wang, Appl. Phys. Lett. 57, 321, (1990)
7. R. L. William, M. Dion, F. Chatenoud, and K. Dzurko, Appl. Phys. Lett. 58, 1816 (1991)
8. E. P. O'Reilly and Alfred R. Adams, IEEE J. of Quantum Electronics, 30, pp. 366-377, 1994
9. Weimin Zhou, H. Shen, J. Pamulapati, P. Cooke and M. Dutta Appl. Phys. Letts. 66 607 (1995)
10. H. Shen, M. Wraback, J. Pamulapati, P. G. Newman, M. Dutta, Y. Lu, and H. C. Kuo, Phys. Rev. B47 13933 (1993)
11. H. Shen, J. Pamulapati, M. Wraback, M. Dutta, H. C. Kuo and Y. Lu, IEEE Photon Technol.Lett. 6, 700 (1994)
12. Kezhong Hu, Li Chen, Anupam Madhukar, Ping Chen, Chris Kyriakakis, Zaheed Karim, and Armand R. Tanguay, Jr., Appl. Phys. Lett., 59, pp. 1664-1666, 1991.

3D ARRAYS OF QUANTUM DOTS FOR LASER APPLICATIONS

N.N. LEDENTSOV*[a], J. BÖHRER[a], D. BIMBERG[a], S.V. ZAITSEV[b], V.M. USTINOV[b],
A.YU. EGOROV[b], A.E. ZHUKOV[b], M.V. MAXIMOV[b], P.S. KOP'EV[b], ZH.I. ALFEROV[b],
A.O. KOSOGOV*[c], U. GÖSELE[c], S.S. RUVIMOV*[d]

[a]Institut für Festkörperphysik, Technische Universität Berlin, Hardenbergstr. 36, D-10623 Berlin, Germany
[b]A.F.Ioffe Physical-Technical Institute, Politekhnicheskaya 26, 194021, St.Petersburg, Russia
[c]Max-Planck-Institut für Mikrostrukturphysik, Weinberg 2, D-06120 Halle, Germany
[d]Lawrence Berkeley Laboratory, University of California, Berkeley, CA 94720,
ruv@mh1.lbl.gov
* on leave from A.F.Ioffe Physical Technical Institute

ABSTRACT

We have fabricated and studied injection lasers based on vertically coupled quantum dots (VECODs). VECODs are self-organized during alternate short-period GaAs-InAs (InGaAs) depositions after InAs (or InGaAs) pyramids are formed on a GaAs (100). The resulting arrangement represents laterally ordered array of nanoscale structures inserted in a GaAs matrix, where each structure is composed of several vertically merging InAs (or InGaAs) parts. VECODs are introduced in the active region of GaAs-AlGaAs double heterostructure laser. The threshold current density remarkably decreases with increase in number of periods (N) of the VECOD (down to 90 A cm-2 at 300K for N=10). The differential efficiency increases with N and the lasing occurs through ground state of quantum dot exciton up to room temperature (λ=1.05 μm).

INTRODUCTION

There is a strong interest in application of quantum dot heterostructures in a new generation of heterostructure diode lasers [1, 2]. Remarkable reduction of the threshold current density and increased temperature stability of threshold current are expected. As it was shown in [3], introduction of dense two-dimensional array of quantum dots in active region of GaAs-AlGaAs double heterostructure laser allows to realize lasing via the ground state of quantum dots (QDs) at low temperatures. Lasing was found to occur near the maximum of quantum dot photoluminescence (PL) spectrum recorded at low excitation densities, and the threshold current density was found to be practically temperature-insensitive in a wide temperature range up to 100-120K [3] in agreement with previous theoretical predictions [1, 2]. At the same time, at elevated temperatures, thermal evaporation of excitons from QDs resulted in a strong decrease in the quantum dot related gain for the same injection current, and, thus, in a remarkable increase in the threshold current density. Lasing energy was found to be close to the wetting layer at 300K [4].

In this work we used the vertically coupled quantum dot structures (VECODs) to improve the lasing characteristics of QD laser and to get additional flexibility in QD laser design. The main objectives to use these structures are:
(i) to increase modal gain (possibly keeping the transparency current the same),
(ii) to increase QD exciton oscillator strength (to decrease radiative lifetime)
(iii) to avoid thermal depopulation of QDs by increasing relative density of QD states compared to GaAs matrix-induced states (to maintain QD exciton lasing up to room temperature)

The authors of Refs. [5, 6] have reported that coherent strained InAs islands formed by Stranski-Krastanow (SK) growth on GaAs (100) substrates maintain after subsequent GaAs deposition their pyramid-like shape. If the InAs islands are completely covered with a sufficiently thick GaAs layer (~100Å), InAs islands formed during the next deposition cycle tend to form vertically correlated structures [7, 8]. However, as both electron and hole wavefunctions are effectively localized inside each quantum dot, this arrangement does not result in a modification of the basic properties of the structures, such as radiative lifetime, energy spectrum, carrier capture and relaxation mechanisms or material gain.

In this paper, to improve the QD injection laser characteristics, we used an island shape transformation effect in SK growth which results in spontaneous formation of laterally-ordered

arrays of structures composed of several vertically merging (InGa)As parts in a GaAs matrix (see [4] and references therein). The samples studied in this work were grown by elemental source molecular beam epitaxy (MBE) by using a Riber-32 MBE machine [4, 6]. The (InGa)As depositions were performed at 480°C and the structures were covered by 10 nm thick GaAs layer at the same temperature. Cladding layers were grown at 600°C to avoid any intermixing of quantum dots. Transmission electron microscopy (TEM) studies were performed by using a high voltage JEOL JEM1000 (1MV) microscope. Calorimetric absorption spectroscopy (CAS) [9] was carried out at T=500 mK. The absorption due to the GaAs substrate has been subtracted from the CAS spectra.

RESULTS

In Fig. 1 we demonstrate plan view (left) and cross-section TEM images of InGaAs-GaAs VECODs formed by six-period 1.2nm $In_{0.5}Ga_{0.5}As$ - 4 nm GaAs deposition. In plan-view TEM image the dots show a rhombic base, with an average size of 20 nm and locally aligned along [010] and [1-10] directions. TEM images of InAs-GaAs VECODs can be found in Ref.2 and references therein.

In Fig. 2 we show typical PL and CAS spectra of InGaAs-GaAs VECOD structure. Formation of VECODs results in a long wavelength shift of the ground state QD exciton emission and absorption as compared to QD structures formed by single-cycle InGaAs-GaAs deposition. One can conclude from Fig. 2, that the QD absorption and PL peaks due to ground QD and excited states coincide in energy, indicating high density of QD-related states.
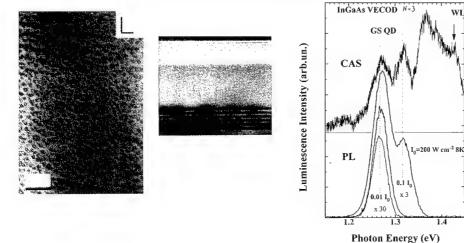
Fig. 1
Vertically coupled InGaAs quantum dots (VECODs) in a GaAs matrix:
left: bright field plan-view transmission electron microscopy (TEM) micrograph under [100] zone axis illumination.
right: cross-section TEM micrograph viewed along [010] direction.

Fig. 2
Upper curve: calorimetric absorption spectrum recorded at 500 mK of the InGaAs-GaAs VECOD structure.
Lower curve: photoluminescence spectrum recorded at 8K for the same structure.
Number of periods: 3.
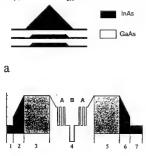
VECODs were introduced in a central GaAs part of GaAs-AlGaAs double heterostructure laser. The schematical representation of the laser structure is given in Fig. 3.

In Fig. 4 we demonstrate the influence of the number of period in VECOD structure on the threshold current density for InGaAs and InAs VECODs [10]. One can conclude that increase in N results in a marked decrease in the threshold current density down to 90A cm^{-2} at 300K for N=10. Even more important: in the latter case, the lasing wavelength is resonant with the ground state PL and absorption peaks indicating that ground QD exciton state is involved in lasing as opposite to the case of single sheet QD structures, where lasing occurs at wavelengths close to one corresponding to wetting layer states (at 933 nm at 300K). We note that the threshold current density (J_{th}) of 90 A cm^{-2} at 300K is a best value for this spectral range (1.05 μm)
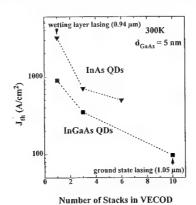
Increase in N for InAs dots from 1 to 3 results in a moderate extension of the high temperature stability range from 80K to 180K, respectively. Characteristic temperature (T_0) in this range equals 350-420K). For InGaAs dots no broadening of the high temperature stability range of J_{th} (20K-180K) was observed for N=3. Further increase in N results in some narrowing of the high J_{th} temperature stability range to about 140K both for InAs and InGaAs dots. The threshold current density, measured in this range decreases with N from about 80A cm^{-2} for N=1 (for long stripes, L>1500 μm, or for totally internally reflecting structures) down to 15 A cm^{-2} (120K, N=10). The most remarkable difference between structures with small and large N (6, 10) is the increase in a T_0 value in a high temperature range in the vicinity of 300K. T_0 near 300K increases from 60K (N=1, 3) to 150K for N=10.

For stripe lasers (W=40 μm) by varying the cavity length one can vary the mirror losses and change the threshold current density of injection laser. Results of this study are presented in Fig. 5. One can see, that even moderate increase in mirror losses at 300K results in a remarkably strong increase in J_{th} for N=1, indicating that both QD and wetting layer (WL) states are strongly saturated. Much more moderate growth in J_{th} occurs for the VECOD structure (N=10, InGaAs). Even less pronounced growth occur for the decoupled InGaAs QDs (N=3, GaAs layer thickness equals 10 nm), but the J_{th} value for the range of small mirror losses is higher in the latter case.

Fig. 3
Schematic diagram of VECOD structure (a) and of the laser structure (b).

1 - Si-doped n$^+$ GaAs buffer layer grown on GaAs n$^+$ substrate; 3, 5 - Al$_{0.3}$Ga$_{0.7}$As cladding layers (1.5 μm) of n (3) and p (5) - type conductivity (5 10^{17}cm^{-3}); 2,6 - (Al,Ga)As graded layers, 7 - GaAs p$^+$ Be-doped contact layer, 4 - active region including VECOD structure confined by two 100 nm - thick undoped GaAs regions (B) and by (Al,Ga)As-GaAs short-period superlattices (100 nm each).

Fig. 4
Dependence of the threshold current density on the number of periods in VECOD structure.

The absolute values of modal gain coefficients are presented in Fig. 6. Structure with decoupled dots and N=3 exhibits higher gain for the same J_{th}, however, for $J_{th} > 2000$ A cm^{-2} the lasing in this structure occurs via the wetting layer (935 nm) resulting in a jump in the gain. Samples with coupled ($d_{GaAs} = 4$ nm) quantum dots exhibit no transition to wetting layer lasing at least up to 4000 A cm^{-2} at 300K.

In Fig. 7 we demonstrate the emission spectrum of VECOD structure. For large N the lasing energy follows the GaAs bandgap dependence with temperature rise, as it is shown in Fig.8. For N=10 the lasing energy coincides with the ground state QD exciton transition energy revealed in PL and absorption spectra. At the same time the maximum of spontaneous emission is shifted towards higher energy by approximately 50 meV at 300K and corresponds to the energy of the excited state of QD exciton in VECOD structure revealed in absorption spectra (see, e.g. Fig.2). The same shift is observed in PL spectra at very high excitation densities. Increase in mirror losses results not only in an increase of the threshold current density, but, also in a shift of the lasing energy towards higher energies. The dependence of the emission wavelength vs. J_{th} is shown in Fig. 9. The results manifest that the QD ground state emission is still very close to the gain saturation regime, and, even for long cavity lengths the lasing occurs via the QD ground state, it can be easily tuned towards excited states. This result agrees with the high energy shift found in the spontaneous emission (see Fig. 8).
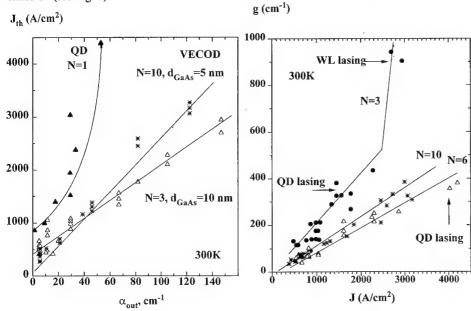
Fig. 5
Threshold current density at 300K as a function mirror losses for different VECOD lasers.

Fig. 6
Gain vs. current density for VECOD lasers at 300K.
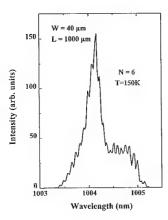
Fig. 7
Lasing spectrum at $J = 1.3 J_{th}$ of VECOD laser.
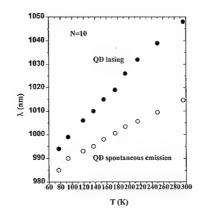
Fig. 8
Lasing wavelength (full circles) as a function of temperature for VECOD laser. Maximum of the spontaneous emission is shown by open circles. T= 300K.
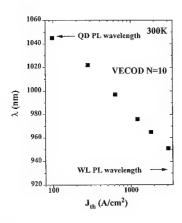
Fig. 9
Lasing energy at 300K as a function of the threshold current density (recorded at different cavity lengths). In the range of high mirror losses excited states of VECODs contribute to lasing.
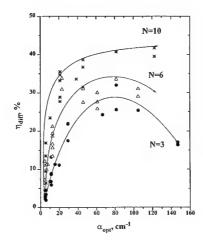
Fig. 10
Differential efficiency of VECOD structures as a function of mirror losses and period of VECOD structure (300K).

On the other hand, as it follows from Fig. 9 for N=10, the emission wavelength do not reach the wetting layer wavelength of 933 nm even at 3000 A cm^{-2}, again in agreement with the results of Figs. 5 and 6. We note that there is a significant density of states in the VECOD structures at energies above the QD ground state energy, as it follows from the absorption spectrum in Fig.2. The gain in the range between the ground state QD and the heavy hole exciton state in the wetting layer are due to transitions between ground state QD electron state and excited hole states, and between ground state QD heavy hole state and electron states in the wetting layer. At high excitation densities, when all electron states in VECODs are populated, most of electrons appear to be concentrated in the wetting layer and nearby GaAs regions.

Fig. 10 demonstrates the dependence of the differential efficiency (η_{diff}) on mirror losses and on N at 300K. Relatively low values of η_{diff} are related to GaAs region in the vicinity of VECODs, grown at low temperature (480°C). One can see, however, that the increase in N increases the differential efficiency. On the other hand, low values of differential efficiency for low mirror losses range, where J_{th} = 90 A cm-2 (N=10), show that only minor part of injected carriers contribute to radiative recombination, and the most of injection current goes to losses due to nonradiative recombination. According to Fig. 10, the real threshold current density in VECOD structure with N=10 can be estimated to be close or smaller than 5 A cm^{-2} at 300K. Further increase in number of periods and optimization of growth conditions will, probably, allow to realize these ultrasmall values of the threshold current densities.

CONCLUSION

-Arrays of coherent vertically-coupled quantum dots can be formed both by InAs-GaAs and InGaAs-GaAs deposition.
-VECOD structures exhibit absorption and luminescence peaks due to QD ground state exciton state at the same energy
-Significant improvements in gain and differential efficiency are realized by using VECODs.
-Ultralow threshold current density of 15 A cm-2 is measured at 120K for N=10.
-The threshold current density of 90 A cm-2 at 300K is observed being the best value for this spectral range (1.05 μm). PL emission maximum and lasing *coincide* in energy.
- The threshold current density corrected to losses due to nonradiatrive recombination is estimated to be close or lower than 5A cm^{-2} at 300K.

ACKNOWLEDGMENTS

REFERENCES
1 Y. Arakawa and H. Sakaki, Appl. Phys. Lett. **40**, 939 (1982)
2 M. Asada, Y. Miyamoto, and Y. Suematsu, IEEE J. Quantum Electronics **22**, 1915 (1995)
3 N. Kirstaedter, N.N. Ledentsov, M. Grundmann, D. Bimberg, U. Richter, S.S. Ruvimov, P. Werner, J. Heydenreich, V.M. Ustinov, M.V. Maximov, P.S. Kop'ev and Zh.I. Alferov, Electronics Letters **30**, 1416 (1994)
4 D. Bimberg, N.N. Ledentsov, M. Grundmann, N. Kirstaedter, O.G. Schmidt, M.H. Mao, V.M. Ustinov, A.Yu. Egorov, A.E. Zhukov, P.S. Kop'ev, Zh.I. Alferov, U. Gösele, and J. Heydenreich, phys. stat. sol. (b) **194**, 159 (1996)
5 Q. Xie, P Chen, A. Madhukar, Appl. Phys. Lett. **65**, 2051 (1994)
6 S.S. Ruvimov, P. Werner, K. Scheerschmidt, U. Gösele, J. Heydenreich, U. Richter, N.N. Ledentsov, M. Grundmann, D. Bimberg, V.M. Ustinov, A.Yu. Egorov, P.S. Kop'ev, and Zh.I. Alferov, Phys.Rev. B **51**, 14766 (1995)
7 L. Goldstein, F. Glas, J.Y. Marzin, M.N. Charasse, and G.Le Roux, Appl. Phys. Lett. **47**, 1099 (1985)
8 Q. Xie, A. Madhukar, P. Chen and N. Kobayashi, Phys. Rev. Lett. **75**, 2542 (1995)
9 A. Juhl and D. Bimberg, J. Appl. Phys. **64**, 303 (1988)
10 S.V. Zaitsev et al., Fizika i Tekn. Poluprovodn. 30, (1996), in print

Synthesis of GaAs Nano-Particles by Digital rf-sputtering

M. Hirasawa, N. Ichikawa, Y. Egashira and H. Komiyama
Department of Chemical Systems Engineering, University of Tokyo,
113, Japan, hirasawa@komiyama.t.u-tokyo.ac.jp

Abstract

Nanometer-sized GaAs particles embedded in SiO_2 were prepared by a digital rf-sputtering method, where GaAs and SiO_2 targets were alternately sputtered in an Ar atmosphere. The GaAs deposition time was kept shorter than the time required to form a continuous layer. Transmission electron microscopy (TEM) observations showed that the sizes of the GaAs particles can be controlled from 2 to 8 nm by changing the sputtering cycle time of the GaAs target. In spite of their small size, the GaAs particles have crystallinity similar to the target material without substrate heating or post annealing. It was also revealed that the mechanism of the particle growth depend on the surface migration of the precursors. The optical absorption spectra of the GaAs particles show a blue shift as large as 1.6 eV, corresponding to strong quantum confinement of electrons and holes.

Introduction

Quantum dots are predicted to have many distinctive optical properties as a result of spatial confinement of electrons and holes, including super-radiant decay[1] and enhancement of nonlinear optical susceptibility.[2,3] Therefore, semiconductor nanometer-sized particles have recently attracted strong interest as new materials for making optical devices with zero-dimension systems. Many kinds of semiconductor particles have been made,[4,5,6,7] using processes such as liquid phase synthesis[8] and a co-sputtering/recrystallization method[9,10]. The difficulty with these methods, however, is that it is difficult to avoid contamination and to control particle size, both of which are critical for making high-quality light-emitting materials. The digital sputtering method proposed in this paper is superior to other methods for making nanometer-sized particles, because of the ability to easily control particle size by changing sputtering cycle times. The proposed method is also free from contamination because the process is carried out under high-vacuum conditions, and because the semiconductor is not dissolved in either a matrix glass or in a solvent.

Experimental Procedure

In this investigation, nanometer-sized GaAs particles were fabricated by digital rf-sputtering, where GaAs and SiO_2 targets were sputtered alternatively in Ar atmosphere.

Fig. 1 is a schematic illustration of sputtering chamber. This is a standard rf (13.56 MHz) planner magnetron sputtering apparatus equipped with an SiO_2 and a semi-insulating GaAs target, each with a diameter of 8 cm. The deposition substrate was a copper grid with a 100Å-thick polymer film. After deposition this substrate was directly used for transmission electron spectroscopy
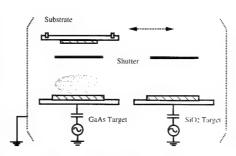
Fig. 1   Schematic illustration
of the sputtering apparatus

139

(TEM) observations. A silica glass substrate was used for optical absorption spectroscopy observations. The substrate was put on a turn table and moved to a position just above each target prior to sputtering. The distance between each target and the substrate was 18 cm. The rf-power put into the SiO_2 and GaAs targets was 100W and 15W, respectively. The flow rate and pressure of Ar gas were 10 sccm and 4.7 mTorr, respectively.

Fig. 2 shows the fabrication sequence of the nanometer-sized GaAs particles. First, an SiO_2 layer was deposited on the substrate by sputtering an SiO_2 target in an Ar atmosphere. Then a GaAs target was sputtered to create nanometer-sized GaAs particles. The sputtering cycle time of the GaAs targets was varied from 30 to 240 s to control the particle size. The SiO_2 target was then sputtered to bury the GaAs particles inside an amorphous SiO_2 film. The deposition periods were controlled by using shutters between the target and the substrate. When one target was sputtered, the plasma on the other target was shut off. This procedure avoided contamination of the GaAs particles by O atoms from the SiO_2 target.
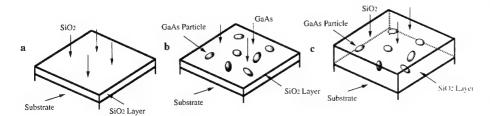
Fig. 2   Schematic fabrication sequence of nanometer-sized GaAs particles

Results and Discussion

Fig. 3 and Fig. 4 show TEM images and size (Feret diameter) distributions, respectively, of GaAs particles prepared by digital sputtering for various GaAs sputtering cycle times. Because the particles are embedded in amorphous SiO_2, the TEM images have poor contrast. The contrast of all the photographs shown here was therefore enhanced through computer processing. The particles had nanometer-scale diameters and grew larger as the sputtering time increased. The mean diameters for the sputtering cycle times of 30, 60, and 90 s were 27, 44, and 77 Å, respectively. Though the particles prepared with 30 s sputtering time of the GaAs target show circular projected image (Fig. 3-1), they tended to become longer as the sputtering time increased (Fig. 3-4), because some particles that were close to each other coalesced as they grew. Further sputtering, for example sputtering cycle times of 240 s, caused all particles to be connected with each other to form a honeycomb like network structure (Fig. 3-5). The lack of small nuclei at long sputtering cycle times indicate that the presence of large particles restricted the further nucleation. This suggests that precursors of GaAs particles migrate on the SiO_2 surface. The number densities of the GaAs particles for the sputtering cycle time of 30 s, 60 s, 90 s were $9.4 \times 10^3 \mu m^{-2}$, $4.4 \times 10^3 \mu m^{-2}$, $1.5 \times 10^3 \mu m^{-2}$, respectively. The decrease of number density of GaAs particles and the increase of distance between neighboring particles reveals that not only adatoms migrate on the amorphous SiO_2 surface, but also GaAs nuclei as large as 30Å in diameter. This implies that the mechanism of nucleation and growth of the GaAs particles strongly depend on the surface migration of adatoms and small nuclei.
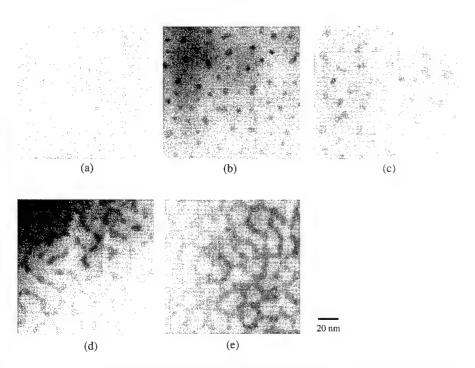
Fig. 3 TEM photographs of GaAs particles doped in silica glass for various GaAs sputtering cycle times: (a) 30 s, (b) 60 s, (c) 90 s, (d) 120 s, (e) 240 s
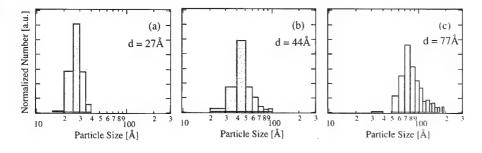
Fig. 4 Size distribution of GaAs paritcles for various GaAs sputtering cycle times: (a) 30 s, (b) 60 s, (c) 90 s
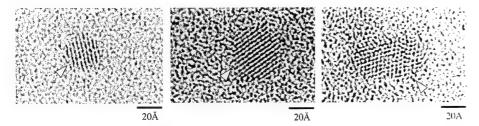
Fig. 5 High magnification TEM images of the GaAsparticles for various
GaAs sputtering times: (a) 30 s, (b) 60 s, (c) 90 s

Fig. 5 shows highly magnified images of the GaAs particles. Though it is generally known that GaAs thin film formed by rf-sputtering is amorphous[11], the particles prepared by digital sputtering are crystalline, even at substrate temperatures as low as 25℃. This is attributed to the high mobility of the GaAs adatoms on the SiO2 surface that enables them to relax to stable structure. The particles show lattice fringes indicative of (111) planes of zinc-blend structures and the observed lattice constant was the same as the GaAs target (3.26 Å), independent of particle size. It is surprising that particles consisting of less than 10 atomic rows retain the structure of the bulk crystal. Particles produced with sputtering cycle times shorter than 60 s consist of a single crystal domain (Fig. 5-1). Polycrystalline particles occurred after further growth (i.e., for sputtering cycle times on the order of 90 s)(Fig. 5-3).

Fig. 6 shows the optical absorption spectra of the GaAs particles. To gain sufficient absorption for observation, the alternate sputtering of GaAs and SiO2 targets was repeated about 20 times. The spectra are standardized against total deposition time of GaAs. The spectra are significantly blue-shifted from the bulk absorption edge of 867 nm, because of the strong quantum confinement. The increase of the energy gap (ΔE) of GaAs particles with mean diameters of 27, 44, and 77 Å are 1.6, 1.2, and 1.1 eV, respectively.

ΔE can be calculated by the following simple model[12],
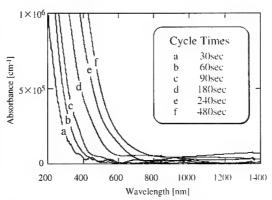
Fig. 6 Optical absorption spectra of the GaAs particles
observed for various GaAs sputtering cycle times

$$\Delta E = \frac{\hbar^2 \pi^2}{2R^2}\left[\frac{1}{m_e^*} + \frac{1}{m_h^*}\right]$$

where $m_e^* = 0.067 m_0$ and $m_h^* = 0.45 m_0$ are the effective mass of electrons and holes, respectively, and R is the radius of the particle. For particle sizes of 27, 44, and 77 Å, the calculated values of ΔE are 3.5, 1.3, and 0.4 eV, respectively. The blue shift observed experimentally therefore shows a weaker dependence on particle size than this analytical model; it is almost three times as large as

the calculated value at a particle size of 77 Å and is half as large at a particle size of 27 Å. One of the most plausible explanations of these differences is the deviation of the particles from a spherical shape, which is assumed in the simple model. We assume the GaAs deposits two-dimensionally on the substrate to form thin particles, because the surface coverage ratio of GaAs particles to the substrate increased linearly with increased sputtering cycle times. If the height of the particles is thin enough to make quantum confinement in the direction normal to the substrate surface stronger than that in the other directions, the particles should indicate a large blue shift and a weak dependence on the particle sizes determined from the projected particle surface area of the two-dimensional TEM image.

We calculate the energy of the fundamental absorption of the thin cylindrical shaped particle (which corresponds to the electronic transition from the highest quantized valence state to the lowest excited state), by solving a wave equation in cylindrical coordinates, using effective mass approximation. The increase of the energy gap (ΔE) is written as

$$\Delta E = \frac{K^2 \hbar^2}{2m^* r^2} + \frac{\pi^2 \hbar^2}{2m^* L^2}$$
$$J_0(\alpha \cdot r) = 0 , \quad K = Min \; \alpha$$

where m* is the reduced effective mass of electron and hole, r and L are the radius and the thickness of the cylinder shaped particles, respectively, and Jo is Bessel function. The results for various values of L are shown with experimental data in Fig. 7. Though these calculations represent weaker dependence on the particle size, they still cannot adequately explain the experimental data, because the 77Å particles would have to be thinner (i.e., L=24 Å) than 44 Å particles (i.e., L=28 Å). Above all, the small blue-shift at a particle size of 27 Å cannot be ascribed to any shape, because the particles would have to have a height much greater than the diameter determined from the projected surface area, and this is not
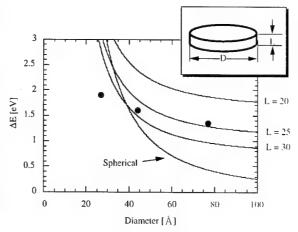
Fig. 7   Calculated ΔE of thin, cylindrical GaAs particles. ● represent experimental data.

plausible. A plausible explanation is that the effective mass of semiconductor particles smaller than about 30 to 40Å is much larger than that of bulk materials, which is used in this calculation. Further research is needed to conclusively determine the differences between measured and calculated size-dependent blue shifts.

Conclusion

Nanometer-sized crystalline particles of GaAs embedded in an amorphous SiO$_2$ matrix

were successfully prepared by a digital rf-sputtering method. The GaAs particle size was controlled by varying the sputtering cycle time of the GaAs target. The decrease of number density of GaAs particles as they grow indicates that adatoms and GaAs nuclei as large as 30Å in diameter migrate on the amorphous SiO_2 surface. High resolution TEM observations show that particles consisting of less than 10 atomic rows retain the structure of the bulk crystal. The experimental result that GaAs particles grow on amorphous SiO_2 indicates that there is no limitation on the matrix crystallinity or lattice orientation for successful crystallization of GaAs nanometer-sized particles. Consequently, digital sputtering can be applied to many combinations of semiconductor and host materials.

Acknowledgement

References

1 E. Hanamura, Phys. Rev. B. **38**, 1228 (1988)
2 T. Takagahara and E. Hanamura, Phys. Rev. Lett. **56**, 2533 (1996)
3 S. Schmitt-Rink, D. A. B. Miller and D. S. Chember, Phys. Rev. B. **35**, 8113 (1987)
4 T. Kawaguchi and S. Miyazima, Jpn. J. Appl. Phys. **32**, L215 (1993)
5 Y. Wang and N. Herron, J. Phys. Chem. **91**, 257 (1987)
6 M. D. Dvorak, B. L. Justus, D. K. Gaskill and D. G. Hendershot, Appl. Phys. Lett. **66**. 804 (1995)
7 P. C. Sercel, W. A. Saunders, H. A. Atwater, K. J. Vahala and R. C. Flagan, Appl. Phys. Lett. **61**. 696 (1992)
8 H. Uchida, C. J. Crutis, P. V. Kamat, K. M. Jones and A. J. Nozik, J. Phys. Chem. **96**. 1156 (1992)
9 Y. Maeda, N. Tsukamoto, Y. Yazawa, Y. Kanemitsu and Y. Masumoto, Appl. Phys. Lett. **59**. 3168 (1991)
10 H. Nasu, J. Matsuoka and K. Kamiya, J. Non-Crystalline Solids **178**, 148 (1994)
11 K. Sedeek, J. Phys. D: Appl. Phys. **26**, 130 (1993)
12 L. Brus, J. Phys. Chem. **90**, 2555 (1986)

LEAD SULPHIDE QUANTUM-SIZED PARTICLES WITH ABSORPTION BAND ONSET IN THE NEAR INFRA RED

J.C. Bhat*†, T. Krishnakumar*, R.R.Nayak‡, O.V. Salata*, J.L. Hutchison‡, P.J. Dobson*
*Department of Engineering Science, University of Oxford, Parks Road, Oxford, OX1 3PJ.
†jerome.bhat@eng.ox.ac.uk
‡Department of Materials Science, University of Oxford, Parks Road, Oxford, OX1 3PH.

ABSTRACT

Lead sulphide nanoparticles were prepared by colloidal techniques and subsequently deposited onto glass slides as uniform, dry films. In so doing, the effective bandgap of the semiconductor was increased from that of the bulk material by the quantum size effect. By varying the growth conditions, it was possible to change the mean particle size from 3nm to 7nm. This size variation was accompanied by (i) a variation in the absorption band onset of the material from $0.7\mu m$ to $1.3\mu m$ and (ii) a change in its colour from red to greyish-brown. No excitonic features were observed. TEM showed that the shape of the particles, as well as their size, was dependent on the growth conditions. Cubic and rod-like particles were grown in aqueous solution. Spherical particles preferable for optoelectronic devices were grown in methanolic/aqueous and aqueous solutions. However, these spherical particles were not as reproducible as the cubic ones.

INTRODUCTION

Small particles of compound semiconductors have been readily prepared by a range of colloidal techniques for the past 20 years or more [1, 2, 3, 4, 5, 6, 7]. Particles prepared by these methods have diameters of a few nanometres and are subject to three-dimensional quantum confinement effects. Considerable widening of the effective bandgap of these materials from those of their respective bulk values ensues. Colloidal dispersions of particles can be produced with initial size distributions as low as $\sigma \approx 10\%$. This size distribution can be further reduced by subsequent heat treatments and size-selective precipitations [2, 8, 9]. Material prepared in this way can exhibit relatively monochromatic luminescence; luminescence peaks having FWHM of the order of 50nm [10, 11] and an individual quantum dot having reported FWHM of 5 Å [12]. Given the relative ease and low cost of fabrication of quantum particles, the idea of incorporating them into device structures is a very attractive one. Optoelectronic devices based on quantum particles have the potential to develop into a technology which seriously rivals that of alloyed or doped semiconductors for engineered bandgap devices.

Nanoparticulate material potentially suitable for infra-red applications has previously been prepared by colloidal techniques. However, little data has been presented on the optical absorption properties of material prepared in this way [1, 13, 14, 15]. In this paper, infra-red absorption data from PbS nanoparticles is presented which demonstrates the suitability of the material for work in this regime. Bulk lead sulphide is a semiconducting material having unusual properties. It has a rock salt crystal structure, each atom having 6-fold co-ordination. Bonding is covalent, but has a high degree of ionicity. PbS has a direct bandgap situated at the L-point. The charge carriers at this point have low effective masses ($\sim 0.08m_e$). It is therefore possible to widen the effective bandgap of the material quite

considerably through the quantum-size effect.

EXPERIMENTAL

Particle Growth

Preparation of the lead sulphide sols was carried out as as follows. $30\mu l$ of 0.1M $Pb(NO_3)_{2\;(aq)}$ solution were added to 30ml of water. $30\mu l$ of 0.1M ethylenediaminetetraacetic acid (EDTA) sodium salt aqueous solution were added to this. The EDTA forms a complex with the Pb^{2+}, slowing the rate of the subsequent reaction [15]. The solution was stirred for several seconds and the pH of the solution was adjusted using $NH_4OH_{(aq)}$. The solution was then exposed to $H_2S_{(g)}$ under gentle stirring. Reactions took several minutes to reach completion. All reactants were obtained from Aldrich. Water was of Analar grade and methanol was of HPLC grade. All other reactants were of the highest available purity.

Optical Absorption Data

Absorption spectra of the colloidal solutions in the visible range were taken using a Philips PU 8749 UV-VIS scanning spectrophotometer. Most common solvents absorb light strongly in the near infra-red. Therefore, in order to measure absorption of the PbS in this region, it was necessary to precipitate the material out of solution. $MgCl_2$ was added to the sol in order to induce flocculation of the nanoparticles. The mixture was transferred to a beaker containing a glass slide at the bottom of it, and the material was allowed to settle onto the slide. The clear, colourless liquid left over was removed and the relatively uniform film of material left on the slide was allowed to air dry. Infra-red illumination of the samples was carried out with a mercury lamp and Bentham M300 monochromator. Second order reflections from the monochromator were filtered out using appropriate Schott colour glass filters. The light was chopped, and focused onto the specimen. Light passing through the specimen was detected using a lead sulphide photodetector and lock-in amplifier.

Other Data

X-ray diffraction was carried out on samples produced by the above procedure. The diffraction patterns obtained confirmed that PbS was the only dominant phase present. No significant diffraction peaks due to $MgCl_2$ were recorded. Transmission electron micrographs (HREM) were used to calculate the average particle size within a given sample. Samples were prepared by taking a portion of the flocculated material, washing it, and redispersing it in water or methanol. A drop of this mixture was then placed on a carbon-coated copper grid which was subsequently dried in a vacuum desiccator.

RESULTS

Size Control of the Quantum Particles

Reactions took between a few minutes and an hour to complete depending on the initial conditions. Increasing the pH of the reaction mixture increased the rate of reaction as well as the particle size as reported in References [1, 15]. The absorption spectra of various PbS

nanocrystal samples is shown in Figure 1. The onset of absorption of the samples have been shifted to significantly shorter wavelengths than that of bulk PbS (3023nm). The initial pH values of samples (b) and (c) are 9.4 and 9.0 respectively. The pH of sample (a) was kept at 9.0 throughout the course of the reaction by repeated and frequent additions of small amounts of $NH_4OH_{(aq)}$. Sample (d) was prepared in an aqueous solution of poly(vinylalcohol) acording to the method of Reference [16].
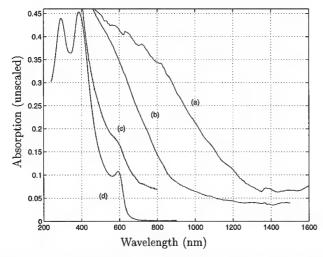
Figure 1: Absorption spectra of PbS quantum dots. Mean particle sizes are (a) 70Å, (b) 50Å, (c)30Å, and (d) 25Å.

The sample characteristics are summarised in Table I. The effective bandgap of the nanocrystals, as calculated from their absorption spectra, are in excellent agreement with Wang et al.'s Hyperbolic Band Model of the size dependence of the effective energy gap of PbS nanocrystallites [17]. Their data is reproduced in Figure 2. Our results are added to this Figure.

Sample	Mean Particle Diameter (Å)	Absorption Onset (nm)	Equivalent Effective Bandgap (eV)	Colour
(a)	70	1380	0.90	greyish-brown
(b)	50	920	1.35	brown
(c)	30	700	1.77	red
(d)	25	590 †	2.10	orange-red

Table I: Properties of PbS Nanocrystals of varying size.
†Position of the first absorption maximum

Nanocrystal Shape

It was found that the nanocrystal shapes could be influenced by adjusting the reaction conditions. Particles grown in aqueous solutions tended to be cubic in shape. Exposure of
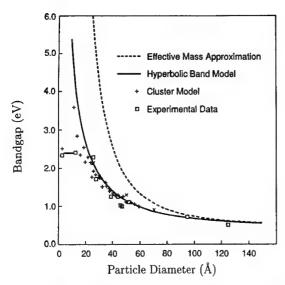
Figure 2: Plot of the effective bandgap of PbS nanocrystallites vs. crystallite size taken from Reference [18]. Our results are added to this as 'x' symbols.

these particles to ultrasound had the effect of rounding-off the cube edges and caused a slight blue-shift in the absorption onset of the material. Particles grown in a 0.1M NaCl$_{(aq)}$ solution tended to be rod-like in shape. Exposure of the colloidal solutions to Group I and Group II salts only after termination of crystal growth did not affect particle shape; material flocculated in this way, washed, and redispersed in fresh water kept its original shape. By substituting methanol for water as the reaction medium it was possible to grow spherical nanocrystallites. However, reactions often precipitated bulk material and reproducibility of results was poor. Carrying out the reactions in an aqueous solution of poly(vinylalcohol) also gave spherical particles. However, it was not possible to extend the absorption of these particles into the infra-red.

DISCUSSION

The shifts in the energy levels of quantum-sized material, ΔE_n, are inversely proportional to the carrier effective masses. For a given size distribution of particles, the distribution of allowed energy levels in quantum-sized PbS is therefore much wider than for other materials such as CdS ($m_h{}^* = 0.8$). Maxima in the absorption spectra of quantum-sized PbS corresponding to the allowed electron-hole transitions in the material will therefore be less evident than in nanoparticles of wider bandgap semiconductors. For this reason, the onset of absorption in samples (a) and (b) is gradual, and no maxima are observed close to this onset.

The absorption spectrum of sample (d) consists of a series of excitonic-like peaks, the first of which occurs at ~590nm. A localised increase in absorption at ~590nm is a feature which is common to many of our samples of quantum-sized PbS of differing mean crystallite sizes.

The feature is evident in the spectra of samples (b) and (c). We therefore believe that the localised increases in absorption observed are due to effects other than that of carrier confinement at the L-point.

Cardona and Greenaway [19] observed minima in the reflectivity spectrum of bulk PbS at 636nm (1.95eV), 350nm (3.54eV), and elsewhere. They attribute these two particular features to electron-hole transitions at minima in the bandgap of PbS in the [110] and [100] reciprocal lattice directions respectively. These transitions are highlighted in Figure 3. We believe that the absorption maxima we are observing in Figure 1 arise from such transitions. We attribute the observed absorption features at 590nm to transitions at the bandgap minimum existing in the [110] direction. The effective masses of the carriers at these wider-bandgap points are much greater than those of carriers at the L-point. Quantum confinement would therefore have a relatively small effect on the positions of the absorption peaks resulting from transitions at these points. This is in keeping with our results as well as with those of Refs. [16, 17, 18, 20]; below a certain size ($\approx$30Å), the bandgap at the L-point becomes so wide that electron-hole transitions at other points in the bandstructure now dominate the absorption spectrum of the material, and there is little variation in the optical absorption of the crystallites. This is evident from the experimental data presented in Figure 2.
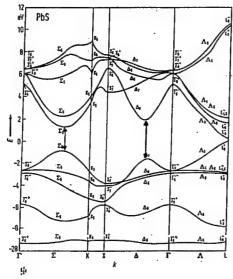
Figure 3: Bandstructure of bulk PbS. Possible electron-hole transitions at positions other than at the L-point are marked out

CONCLUSIONS

We have shown that it is possible to grow PbS nanocrystals suitable for applications in the near infra-red by colloidal techniques. The reasons for the gradual onset of optical absorption of the material, as well as the difficulty in observing absorption peaks due to the allowed electron-hole transitions in the material have been explained. We have gone on to show that

below a particle size of ~ 30Å, variation in the particle size has little effect on the optical absorption of PbS. We have provided an adequate explanation as to why this is.

References

[1] G. Chiu and E. J. Meehan, J. Colloid Interface Sci., **49**, p. 160 (1974)

[2] C. B. Murray, D. J. Norris, and M. G. Bawendi, J. Am. Chem. Soc. **115**, p. 8706 (1993)

[3] A. A. Khosravi, M. Kunu, B. A. Kuruvilla, G. S. Shekhawat, R. P. Gupta, A. K. Sharma, P. D. Vyas, and S. K. Kulkarni, Appl. Phys. Lett. **67**, p. 2506 (1995)

[4] R. Rossetti, R. Hull, J. M. Gibson, L. E. Brus, J. Chem. Phys **83**, p. 1406 (1985)

[5] P. Lianos and J. K. Thomas, Chem. Phys. Lett. **89** p. 2720 (1986)

[6] O. V. Salata, P. J. Dobson, P. J. Hull, and J. L. Hutchison, Adv. Mater. **6**, p. 772 (1994)

[7] T. Gacoin, C. Train, F. Chaput, J.-P. Boilot, P. Aubert, M. Gandais, and Y. Wang, SPIE **1758**, p. 565 (1992)

[8] A. Chemseddine and H. Weller, Ber. Bunsenges. Phys. Chem. **97**, p. 636 (1993)

[9] O. V. Salata, P. J. Dobson, S. Sabesan, P. J. Hull, J. L. Hutchison, Thin Solid Films (in press)

[10] B.O. Dabbousi, M.G. Bawendi, O. Onitsuka, and M.F. Rubner, Appl. Phys. Lett., **66**, p. 1316 (1995)

[11] V. L. Colvin, M. C. Schlamp, and A. P. Alivisatos, Nature **370**, p. 354 (1994)

[12] Y. Nagamune, H. Watabe, M. Nishioka, and Y. Arakawa, Appl. Phys. Lett., **67**, p. 3257 (1995)

[13] E. J. Meehan and D. J. Erdmann, J. Colloid Interface Sci., **62**, p. 8 (1977)

[14] T. Kyprianidou-Leodidou, W. Caseri, and U. W. Suter, J. Phys. Chem. **98**, p. 8992 (1994)

[15] A. D. Uhler and G. R. Helz, J. Crystal Growth **66**, p. 401 (1984)

[16] S. Gallardo, M. Gutierrez, A. Henglein and E. Janata, Ber. Bunsenges., Chem., **93**, p. 1080 (1989)

[17] Y. Wang, A. Suna, W. Mahler and R. Kasowski, J. Chem. Phys., **87**, p. 7315 (1987)

[18] M. T. Nenadovic, M. I. Comor, V. Vasic and O. I. Micic, J. Phys. Chem., **94**, p. 6390 (1990)

[19] M. Cardona and D. L. Greenaway, Physical Review **133** p. A1685 (1964)

[20] J. L. Machol, F. W. Wise, R. Patel, D. B. Tanner, Physica A, **207**, p. 427

Part IV

Wide Bandgap Semiconductors

DRY ETCHING OF SiC FOR ADVANCED DEVICE APPLICATIONS

J. R. FLEMISH, K. XIE AND G. F. McLANE
Army Research Laboratory, Physical Sciences Directorate, Fort Monmouth, NJ 07703

ABSTRACT

In this paper we review and compare most of the published results on dry etching of silicon carbide using various techniques. The vast majority of reports have used RIE methods due to the wide availability of such reactors. Recently, alternative methods of magnetron enhanced RIE (MIE) and electron cyclotron resonance (ECR) plasmas have been demonstrated. MIE has resulted in extremely high etch rates and ECR etching has resulted in smooth, residue-free surfaces with an ability to control the etched profiles.

INTRODUCTION

As the quality of semiconducting, single-crystal 6H- and 4H-SiC improves, there have been continued efforts toward developing commercially viable electronic components from these wide-bandgap semiconductors with a particular focus on high-temperature power device applications. Realization of advanced device structures fabricated from semiconducting SiC requires the ability to etch this material smoothly, controllably and with a minimal amount of damage to the underlying material. For example, SiC power-switching devices which have been envisioned such as vertical MOSFETs [1], MOS-controlled thyristors or insulated-gate bipolar transistors [2] will require the fabrication of active device elements on the sidewalls of etched trenches. These structures need to be free of rough edges and sharp features on both the trench sidewalls and bottoms. The majority of reports on SiC etching have utilized traditional reactive ion etch (RIE) reactors in conjunction with fluorinated gas mixtures. These processes have typically been plagued by the formation of residues which ultimately manifests in rough, micro-masked surfaces. These residues can be minimized or eliminated by addition of H_2 to the gas mixture, albeit at the expense of much lower etch rates [3–5]. Compared to other plasma etching methods RIE exploits the dc self-bias which develops on the substrate to assist in the sputter removal of volatile etch products. High levels of bias, however lead to a greater degree of etch damage caused by energetic ion bombardment. Plasmas in RIE reactors can be magnetically enhanced so that the process can be run at lower pressure and with lower self-bias developing on the substrate for a given plasma power density, resulting in higher etching rates with less ion-damage [6]. Alternative reactor configurations which decouple the sample bias from the plasma power have attracted attention for a number of applications. Examples of these methods include the use of electron cyclotron resonance (ECR) [7] and inductively-coupled plasmas [8]. In this paper we review and compare most of the published results on etching silicon carbide using various techniques and present some new results including (1) profile control using ECR plasmas and (2) fast etching of SiC using magnetron enhanced RIE.

METHODS FOR PLASMA-ASSISTED ETCHING OF SiC

Plasma Etching

The term "plasma etching" is most often interpreted to mean plasma-assisted etching occurring at relatively high pressures (e.g. > several hundred mTorr) with the sample sitting on the grounded electrode of a parallel plate reactor such as shown in Figure 1 [6]. Alternatively, plasma etching may be performed in a barrel reactor or downstream of a microwave or inductively-coupled rf plasma source. Typically in the case of plasma etching only a small sheath potential (10-20 eV) develops on the sample and thus the energy of bombarding ions is relatively low.
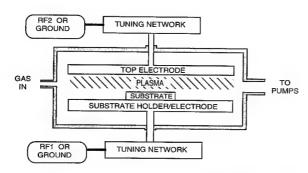
Figure 1. Schematic of rf powered parallel plate reactor for use in plasma etching or RIE.

Early studies showed that sputter-deposited amorphous SiC films could be etched at reasonable rates in plasmas using fluorine-containing gas mixtures and that Al or Cr films could be used as masking materials with a high degree of selectivity [9, 10]. In 1985 Dohmae et al. [10] reported plasma etching of β-SiC using CF_4 and O_2 at pressures of 0.2 to 2.0 Torr where the samples were placed on the grounded electrode in a parallel plate reactor powered at 13.56 MHz. These studies, performed at a pressure of 0.6 Torr and rf power density of 0.50 W/cm^2, showed that a gas composition of 70% O_2 yielded the highest etching rate (17 nm/min). Moreover, the etch rate was found to be proportional to the power density and to decrease sharply with increasing pressure. The morphologies of the etched surfaces were not reported. Using a similar configuration, in 1987 Kelner et al. [12] reported etch rates of 24 nm/min for β-SiC using SF_6 at 0.2 Torr and a power density of 0.18 W/cm^2 indicating that SF_6 was more effective than CF_4 alone for etching SiC. In the latter study the etching rate also increased linearly with power density. However, extremely rough surface morphologies resulted for these conditions. This surface roughness was the result of the micro-masking effect to be discussed in the next section. A similar study reported in 1986 by Palmour et al. [13] used CF_4 and O_2 at 0.5–2.0 Torr with an rf power density at 30 KHz ranging from 0.081-0.326 W/cm^2. They reported that etch rates were in the range of 1–55 nm/min, but that the rates were inconsistent and dark surface layers 20-150 nm thick formed on the SiC surface. Little other work on traditional plasma etching has been reported for SiC.

Recently and in a less traditional manner, plasma etching of 6H-SiC was reported by Luther et al. [14] using a remote microwave (2.54 GHz) plasma. In their remote-plasma arrangement the SiC was placed in a resistance heated furnace downstream from the microwave cavity. The plasma was generated at a power of 400 W and pressure of 1 Torr from a mixture containing 95% Ar with various ratios of NF_3 and O_2. The etching was described as being smooth and nearly isotropic with sloping sidewalls which extended deep underneath the Al masking layer. The etch rate was found to have a strong dependence on both temperature and the ratio of NF_3 to O_2, being a maximum of 220 nm/min in a $NF_3/82\%O_2$ mixture and a temperature of 325-330°C. This rate is approximately ten times greater than those reported for rf-plasmas.

Reactive Ion Etching

The vast majority of reports on SiC etching have since utilized the conventional RIE method using rf (13.56 MHz) power in a parallel-plate reactor of the type shown previously in Figure 1. In contrast to plasma etching, the electrode on which the substrate is placed is powered rather than grounded so that a negative dc self-bias develops on the sample. The dc self-bias coulombically attracts ions from the plasma which assist the etching process through enhanced formation and sputter-removal of volatile etch products. Self-bias dc potentials of hundreds of volts which are potentially damaging to the underlying material are typical for RIE processes.

RIE of β-SiC using CF_4/O_2 mixtures was reported by Palmour et al. [13]. The etch rate was found to be a maximum of approximately 20-24 nm/min in the pressure range of 20–50 mTorr at a power density of 0.55 W/cm^2. At pressures above this range the rate decreased sharply due in part
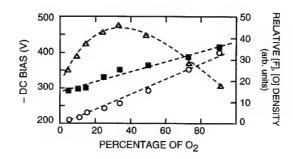
Figure 2. Change in dc bias and relative concentrations of F and O with oxygen addition [ref. 15].

to a reduction in the dc self-bias. At pressures below this range the rate decreased sharply due to the decrease in the density of reactive species in the plasma. In contrast to previous studies the etch rate was not significantly affected by the addition of up to 50% O_2 to the gas mixture. However, similar to previous studies extremely rough surfaces resulted with features described as "sharp columns" and "spikes."

In 1990 Pan and Steckl [15] reported on a comparison of the etching behavior of SiO_2, Si and polycrystalline β-SiC in SF_6/O_2, CHF_3/O_2, and $CBrF_3/O_2$ plasmas at a power density of 0.46 W/cm^2, pressure of 20 mTorr and gas-flow of 20 sccm. Using optical emission spectroscopy they measured the relative concentrations of [F] and [O] reactants as a function of oxygen addition (Figure 2) and detected both CF_x and CO_x products. It was found that the dc self-bias increased linearly from –285V to –400V as O_2 was added and that the highest etch rate of 53.3 nm/min occurred using SF_6 with 35% O_2. The maximum rate corresponded to [F] reaching a maximum value. The etched profiles were found to be more tapered using $CBrF_3/75\%O_2$ and to be more anisotropic using either SF_6/O_2 or CHF_3/O_2. In this study rough etched surfaces were also observed. Under most of their conditions, etching of SiO_2 was slightly faster than SiC, although a slight selectivity (3:2) of $SiC:SiO_2$ could be obtained using a $CBrF_3/O_2$ mixture. In a following section it will be shown that this selectivity can be exploited for profile control.

A comparison of the RIE etch rates of amorphous, polycrystalline β-SiC and single-crystal (100) β-SiC in CF_4/O_2 has been reported by Padiyath et al. in 1991 [16] and is shown in Figure 3. The etch rate of polycrystalline material was found to be much higher than for single-crystal films. This effect was attributed to the large number of high-energy sites associated with dangling bonds at grain boundaries. Moreover, amorphous films which consequently contain significant amounts of hydrogen etched far more rapidly than the crystalline films. This study illustrated the dependence of the etch rate on the degree of crystallinity, but left unanswered the question of whether the etching behavior is different for different polytypes of SiC or for different crystallographic faces of a given polytype. Although no micrographs of the etched materials were presented, the investigators reported that the micro-roughness of the etched films decreased with increasing crystallinity.

Significantly, in 1992 Steckl and Yih [3] reported that the micro-masking effect which led to rough etched surfaces could be eliminated by adding H_2 to the gas mixture for RIE processes using CHF_3/O_2 mixtures. This effect, reproduced using a $CF_4/18\%$ O_2 gas mixture, is illustrated in Figure 4 which shows the resulting surfaces without H_2 (Fig. 4a) and with the addition of 17% H_2 (Fig. 4b). Using Auger electron spectroscopy they found the presence of Al on the rough surfaces which were etched without the H_2 additive, and the absence of Al on the smooth surfaces etched in the presence of H_2. This study ascertained that Al was sputtered from the rf electrode and was redeposited on the SiC surfaces. These Al residues then coalesced and formed micro-clusters which masked the subsequent etching of the underlying SiC. This micro-masking phenomenon was responsible for the resulting surface features which had been previously described as "columnar", "spiked" or "grass-like." Unfortunately, many commercial RIE systems utilize electrodes which are constructed of Al and the addition of H_2 significantly reduces the etch rate.

155

Figure 3. Etch rate comparison of amorphous SiC, poly β-SiC and single-crystal β-SiC [ref. 16].

Figure 4. 6H-SiC etched by RIE with CF_4/18% O_2 (a) without H_2 and (b) with H_2.

Figure 5. 6H-SiC etch rates using (a) various fluorine-containing mixtures and (b) mixtures with the minimum amount of H_2 needed to suppress micromasking [ref. 5].
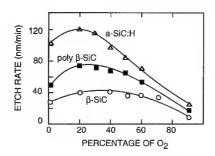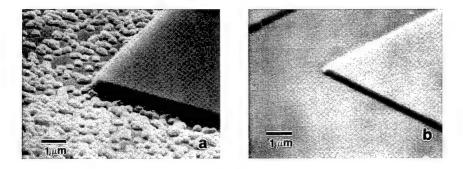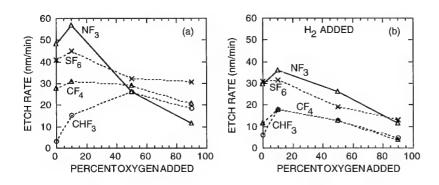
In subsequent papers Yih and Steckl compared the etching behavior of (001) β-SiC and the tendency of residue formation using a variety of gas mixtures and later extended this study to include single crystal (0001) 6H-SiC [4, 5]. Upon the addition of H_2, AlH_x species were detected in the plasma by optical emission spectroscopy, leading to the speculation that the redeposition of sputtered Al was thus prevented by the formation of volatile Al compounds. The data of Yih and Steckl on 6H-SiC has been replotted in Figures 5a and 5b for the cases of no H_2 added and with the minimum amount needed to suppress residue formation, respectively. Here the relative reactivity of these gases and the degree to which O_2 and H_2 addition affect the etch rates is illustrated. Without either additive the reactivity of the gases varied as $NF_3 > SF_6 > CF_4 > CHF_3$. When the minimal amount of H_2 was added the reactivity of the two fluorocarbon gases became comparable as did the reactivities of the SF_6 and NF_3 plasmas. Moreover, when H_2 was added the maxima in the etch rates corresponded to mixtures containing approximately 10% O_2 in each case. It has also been reported that the micro-masking effect can be eliminated with the use of a graphite sheet covering the powered electrode [5]. However, side effects which have been reported include polymeric deposition and flaking within the reactor, contamination of the pumping equipment and mass-loading effects.

By comparison of the aforementioned studies, it appears that under most conditions β-SiC films etched approximately 20-50% faster than 6H-SiC, although accurate experimental comparisons have not been made. It could be speculated that the difference in the etch rates may be due more to differences in the dangling bond densities and thus reactivities of the crystal faces than to the different crystal structures. For example, each atom on a cubic (001) face has two dangling bonds, whereas only one dangling bond exists on a (111) face or similarly on the (0001) face of hexagonal SiC. RIE of (111) β-SiC films has been reported by Wu et al. [21] albeit under conditions where a direct comparison with reports on (001) oriented films cannot be readily made.

Magnetron Ion Etching of SiC

The plasma density can be enhanced and the corresponding dc self-bias reduced with the proper application of magnetic fields inside an RIE reactor as illustrated in Figure 6. This method is often termed magnetron ion etching (MIE) or magnetic field-enhanced RIE (MERIE). In this configuration the permanent magnets confine the electrons in the plasma to cyclodal orbits thereby increasing the ionization cross section [6]. The result is that the MIE system can then sustain relatively denser discharges with lower ion energies (dc self-bias) than RIE and do so at pressures down to 1 mTorr. Importantly, lower ion energy lead to a correspondingly lower degree of damage to the material caused by energetic ion bombardment.

Recently, we have used MIE to etch single crystal (0001) 4H-SiC, using SF_6 both with and without the addition of O_2 and H_2 [18]. In these experiments the samples were mounted on an Al_2O_3-coated, rf-powered (13.56 MHz) electrode, which initially resulted in problematic Al micro-masking effects despite the addition of H_2 to the gas mixture. This effect was eliminated by covering the electrode with a Si wafer coated with indium-tin oxide (ITO) which proved to be fairly impervious to the SF_6 plasma. Figure 7a shows the etching rate and dc self-bias as a function of rf power density at a pressure of 2 mTorr and flow of 5 sccm SF_6. Significantly, for a given power density the etching rate is more than an order of magnitude greater than for the corresponding RIE process and the dc self-bias is nearly four times lower. At the moderate power density of 0.5 W/cm^2 and self-bias of 100V, the observed etch rate of 450 nm/min is to our knowledge the highest reported to date. The etch rate was found to be relatively independent of the addition of oxygen up to 20% O_2, but decreased sharply with further additions as shown in Figure 7b. The rate was fastest at pressures in the range of 2-4 mTorr (Fig 7c). In this case the dc self-bias was not significantly affected by variations in pressure, and varied in the range of 75-80V. The etch rate increased slightly with gas flow rate up to 10 sccm indicating that the supply of SF_6 can be rate-limiting. The anisotropic nature of this process is illustrated in Figure 7d which shows deep (2 μm) trenches etched using a sputtered ITO mask.
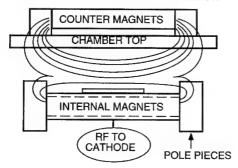
Figure 6. Arrangement of magnets and cathode in MIE reactor.
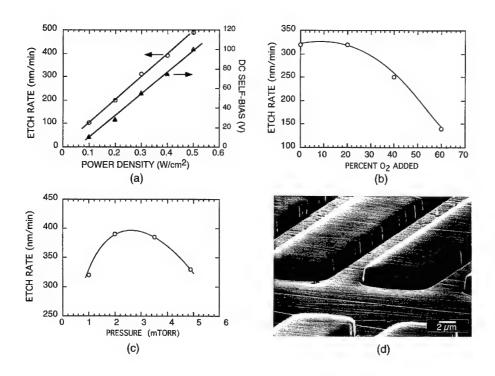
Figure 7.   MIE etch rate as a function of (a) power density (b) oxygen addition (c) pressure
and (d) micrograph of trenched etched in 4H-SiC.

Electron Cyclotron Resonance Plasmas

An excellent review of the principles of ECR and various reactor configurations has been presented by Asmussen [7]. Important advantages of ECR relative to RIE are (1) the sample can be biased independent of the plasma power by applying rf power to the substrate holder and (2) a high density discharge can be generated at lower pressures and is done so in an electrodeless manner. Recently, plasma etching of SiC using ECR has been shown to result in smooth etched surfaces without the formation of micro-masking residues [19]. These studies employed a reactor shown schematically in Figure 8. The multipolar ECR source consisted of six permanent magnets surrounding a six inch diameter microwave (2.45 GHz) cavity constructed of an aluminum alloy. The sample sat approximately 8 cm below the bottom of the ECR source on an electrode which could be rf-powered (13.56 Mz) to provide a desired value of dc bias. The temperature of the electrode could be varied from 20-250°C and operating pressures as low as 1 mTorr were achievable. A 50 sccm $CF_4/18\%$ O_2 mixture at 1-2 mTorr was used to investigate the etching behavior of (0001) Si-face, 6H-SiC. Due to the high reactivity of the ECR plasma it was found that ITO masks endured far better, offered greater selectivity and adhered better to the SiC than Al, Ni or Cr masks. As shown in Figure 9, the etch rate increased linearly with microwave power (a) and nearly so with applied substrate bias (b). Pressure had a strong effect on the rate which decreased steadily with increasing pressure (c) due to the reduced efficiency of the ECR coupling and the reduced gas-phase mean-free-path. The rate of etching was also affected by the proximity of the sample to the plasma source, increasing by a factor of three as the distance is decreased from 8 to 1 cm (Fig. 9d). No significant differences in ECR etch rates had been found for 6H versus 4H polytypes or for different doping types.

A comparison of ECR etching and RIE was performed to assess the degree of etch-induced damage and the tendency of residue formation characteristic of each process [20, 21]. In these experiments samples of n-type 6H-SiC having epilayers with $n=5x10^{15}/cm^3$ were first subjected to a standard RCA cleaning procedure [22]. ECR etching was performed at 600W and 2 mTorr with an imposed dc bias of –20V. The RIE was performed at an rf power density of 0.59 W/cm^2 at 25 mTorr. The same gas flow of 50 sccm of a mixture of $CF_4/18\%O_2$ was used for each case, but in the case of RIE 10 sccm of H_2 was added to prevent the occurrence of micro-masking. Auger electron spectra showed that the ECR etched surfaces and sidewalls were free of any detectable residues containing Al, F, or O. In contrast, the RIE surface composition showed approximately 9% Al and 6% O. Moreover, larger amounts of Al and O were detected on the RIE sidewall along with detectable amounts of F. The reverse-bias I-V characteristics of Pd Schottky diodes fabricated on the etched surfaces showed that leakage currents were 1000 times greater on RIE samples. Furthermore C-V measurements showed a 40% reduction in the donor concentration up to a depth of 0.6 µm in the RIE samples indicative of ion-induced damage. No reduction in donor concentration was measured for the ECR samples, although the reverse bias leakage currents were 100 times higher than for unetched control samples.
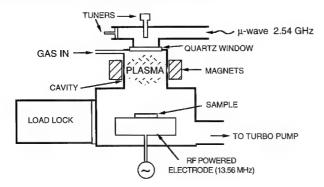
Figure 8. Schematic of microwave ECR plasma reactor with rf biasing capability.

ETCH RATE (nm/min) — 80, 60, 40, 20, 0

100V

20V

200 400 600 800
μ-WAVE POWER (W)

(a)

ETCH RATE (nm/min) — 80, 60, 40, 20, 0

500 W

25 50 75 100
BIAS (-V)

(b)

ETCH RATE (nm/min) — 100, 75, 50, 25, 0

500W
100V

20V
800W

3 6 9 12
PRESSURE (mTorr)

(c)

ETCH RATE (nm/min) — 40, 30, 20, 10, 0

600W
zero bias

2 4 6 8
DIST. FROM ECR CAVITY (cm)

(d)
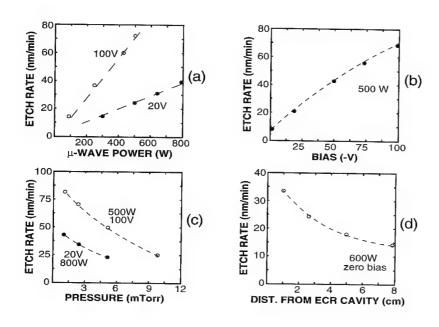
Figure 9.   Etch rate variation of 6H-SiC in $CF_4/18\%O_2$ plasmas with (a) microwave power, (b) applied bias, (c) pressure and (d) sample proximity to ECR source.

PROFILE AND MORPHOLOGY CONTROL WITH ECR ETCHING

In the fabrication of advanced devices from SiC, the profile of the etched sidewall, the morphologies of the etched surfaces and the degree of damage to the underlying SiC are all issues of high concern. For example, fabricating a vertical power-MOSFET where the FET channel is fabricated on the sidewall of an etched trench requires not only smooth surfaces with low damage, but also a tapered transition from the sidewall to the trench bottom to minimize electric field enhancement that would otherwise occur at sharp edges of the gate contact.

In experiments on ECR etching of SiC the level of imposed bias was found to have a strong effect on both the profile and surface morphology [23].   Figure 10 shows the corner of mesa features etched at a high bias of –100V (a) and at a low bias of approximately –8V (b). The ITO masking films were retained on these samples so that the degree of undercutting could be observed. The surface features that result under high bias conditions were found to be relatively smooth both on the etched sidewalls and on the horizontal surfaces. On the other hand, the high bias led to the undesirable consequence of enhanced etching at the base of the sidewalls. This effect, referred to as trenching, results from the deflection of energetic ions at glancing angles off the sidewalls thus enhancing the sputtering component of the etching mechanism in the affected regions [24]. The degree of trenching therefore becomes increasingly more pronounced as the etching proceeds deeper. This effect is also prevalent in RIE and it can be observed in micrographs of etched SiC presented in much of the previously referenced literature. From an applications perspective a profile of this nature is ill suited for device fabrication, if an active element of the device such as the gate of a FET is to be fabricated in or on the etched feature. In contrast, etching with low bias applied to the substrate avoided the trenching effect and led to a more tapered transition from the sidewall to the bottom surface. However, the resulting surface morphology tended to be textured and the sidewalls possessed many jagged edges originating from rough features initially present on the mask edges.
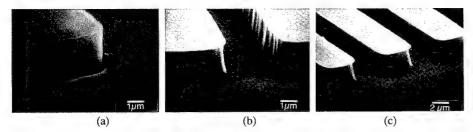
Figure 10. Morphologies of ECR etched samples with (a) –100V shows smooth surfaces and sidewalls with trenching effect, (b) –8V shows rougher surfaces without trenching and (c) two-step bias process to obtain smooth features without trenching.
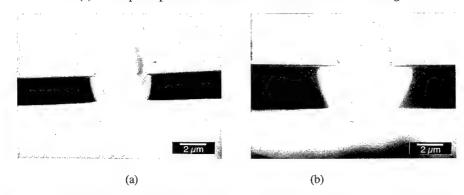
Figure 11. Profiles of 6H-SiC ECR etched with no applied bias have anisotropy of (a) A=0.8 with sample 8cm from ECR source and (b) A=0.5 with sample 1 cm from source.

The consistent appearance of rough features on samples etched at low bias and smooth features on samples etched at high bias suggests that the mask edges can be effectively smoothed by ion-bombardment during the etching process. In light of this speculation, experiments were performed where the samples were subjected initially to a brief high-bias step prior to prolonged etching at lower bias. Figure 10c shows much smoother features which resulted when the sample was etched for 2 min at 100V prior to prolonged etching at –8V. This result shows that a two-step bias process can result in a morphology which is far more suited to the fabrication of a trench device element than are the morphologies which result when a constant level of bias is applied throughout the process.

The effect of the sample proximity to the ECR source on the etching characteristics was investigated. The proximity has indeed been found to affect strongly both the anisotropy and rate of etching. Figure 11 shows the etched profiles as viewed from the corners of adjacent square mesa features with the masking ITO layers still remaining on the structures. In both cases no bias was applied to the substrate. By measuring the vertical etch depth (d) and the lateral etch depth (l), the anisotropy can be quantified as A = (d-l)/d. The anisotropy of etching is approximately 0.8 when the sample is in its normal position of approximately 8 cm from the bottom of the ECR cavity (Fig. 11a). The anisotropy value decreases to approximately 0.5 when the substrate is elevated from its normal position to within approximately 1.5 cm of the ECR source (Fig. 11b). As stated previously, the rate of etching also increased with proximity of the sample to the plasma source. The cause of these effects may be attributed to three important consequences of increased proximity to the source which are; (1) the sample is bombarded by a higher density of reactive species, (2) there is likely a significant degree of sample heating from the plasma and from microwave absorption and (3) the reactive species bombard the sample with a wider angular distribution.
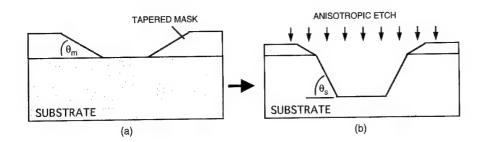
Figure 12.   Diagram of how angled sidewalls are obtained by varying the etch selectivity.

The profile of the etched SiC sidewall can be controlled alternatively by using a thick masking layer of a material which can eroded gradually at the mask edges. One approach is illustrated in Figure 12 where the sloping edges of a mask can be translated to the etched SiC profile with the resulting sidewall angle determined by both the initial slope of the mask edge (θ_m) and the selectivity of etching. Assuming that the etching process is anisotropic, the angle resulting after etching to depths d_s and d_m in the SiC and mask, respectively, will be given by;

$$\tan (\theta_s) = \frac{d_s}{d_m} \tan (\theta_m),$$

where (d_s/d_m) is the selectivity of etching SiC relative to the mask and θ_s is the sidewall angle of the etched SiC relative to the horizontal surface. It is known that SiO_2 films chemically etched in buffered HF solutions will develop an edge taper of approximately 30°. Therefore, by controlling the selectivity of the dry etching process, this method can be applied to SiC using SiO_2 masks. In this case a variation in selectivity from 0.5 to 3.0 will result in a variation in the SiC sidewall from 16° to 60°.

To develop this method, a 0.7 μm layer of SiO_2 was deposited by plasma enhanced chemical vapor deposition onto a 4H-SiC substrate to serve as the masking layer. The SiC was previously oxidized thermally to enhance adhesion of the PECVD film during a densification step whereby the substrate and film were annealed overnight at 1100°C in O_2. The densification was performed to improve the selectivity of etching SiC relative to SiO_2. Experiments were performed to determine the effects of ECR process parameters on the selectivity of etching SiC versus SiO_2. The gas composition (namely the O/F ratio) and sample bias were found to affect the etching selectivity. Figure 13 shows the etching rates of SiC and SiO_2 as a function of the amount of N_2O added to 10 sccm of a gas mixture of $CF_4/18\%O_2$, for conditions of 650 W power, 2 mTorr and applied biases of zero and –50V. Without N_2O the etch rate of SiO_2 was nearly twice that of SiC. However, as N_2O was added the etching became selective in favor of SiC, with the maxima in selectivity occurring at greatly different ratios for the different bias values. Interestingly, at low ratios of O/F an increase in bias favors etching of SiO_2, whereas at high ratios of O/F an increase in bias favors etching of SiC.

In order to test the feasibility of exploiting the etch selectivity for controlling the profile angle, test patterns were defined photolithographically on the SiO_2/SiC samples. Using the photoresist as a mask, the SiO_2 was removed in the exposed regions with a $6NH_4F$:1 HF solution. The chemical etch resulted in a 30° slope to the SiO_2 mask edge as shown in Fig 14a. After removing the resist the sample was etched under conditions of no bias and an O/F ratio of 0.26 which were predicted to yield a selectivity of approximately 1.5 in favor of SiC. The resulting SiC profile corresponding to a 0.6 μm deep etch is shown in Figure 14b after removal of the remaining SiO_2 film. The measured sidewall angle was 48° and (corresponding to a selectivity of 1.7), slightly higher than the 41° angle predicted by a selectivity of 1.5. This result demonstrates the feasibility of this technique which may prove valuable for trench-MOS devices and for edge termination in high voltage devices. Furthermore, this approach may be readily applied to RIE or MIE etching methods.
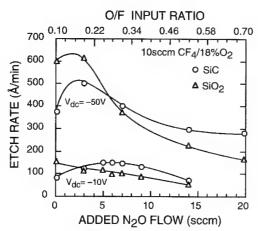
Figure 13.   ECR etch rates of SiC and SiO$_2$ in CF$_4$/18%O$_2$ plasma with addition of N$_2$O.

| (a) | (b) |
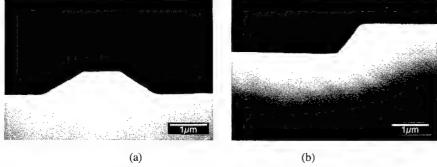
Figure 14.   Profiles of (a) SiO$_2$ chemically etched in BHF using photoresist mask and (b) SiC with angled sidewall etched using tapered SiO$_2$ mask.

SUMMARY

Realization of advanced device structures fabricated from semiconducting SiC requires the ability to etch this material smoothly, controllably and with a minimal amount of damage to the underlying material. In this paper many of the published results on dry etching of silicon carbide using various techniques has been reviewed and compared. The vast majority of reports on SiC etching have utilized traditional reactive ion etch (RIE) reactors in conjunction with fluorinated gas mixtures. These processes have typically been plagued by the formation of micromasking residues. These residues can be minimized or eliminated by addition of H$_2$ to the gas mixture at the expense of lower etch rates. While RIE etch rates are enhanced by the dc self-bias which develops on the substrate, these high levels of bias lead to a greater degree of etch damage. Recently, alternative methods of magnetron enhanced RIE (MIE) and electron cyclotron resonance (ECR) plasma etching have been demonstrated. MIE has resulted in extremely high etch rates and ECR etching has resulted in smooth, residue-free surfaces with an ability to control the etched profiles.

REFERENCES

1. J. W. Palmour, C. H. Carter, Jr., C. E. Weitzel, and K. J. Nordquist, Mat. Res. Soc. Symp. Proc. 339, 133 (1994).

2. M. Ghezzo, personal communications.

3. A. J. Steckl and P. H. Yih, Appl. Phys. Lett. 60, 1966 (1992).

4. P. H. Yih and A. J. Steckl, J. Electrochem. Soc. 140, 1813 (1993).

5. P. H. Yih and A. J. Steckl, J. Electrochem. Soc. 142, 312 (1995).

6. H. W. Lehmann, in Thin Film Processes II, eds. J. L. Vossen and W. Kern (Academic, San Diego, 1991) p. 673.

7. J. Asmussen, J. Vac. Sci. Technol. A7 (3), 883 (1989).

8. P. L. G. Ventzek, T. J. Sommerer, R. J. Hoekstra, and M. J. Kushner, Appl. Phys. Lett. 63, 605 (1993).S. K. Krongelb, IBM Tch. Discl. Bull. 23 (2), 828 (1980).

9. S. K. Krongelb, IBM Tch. Discl. Bull. 23 (2), 828 (1980).

10. C. Y. Chang, Y. K. Fang, C. F. Huang, and B. S. Wu, J. Electrochem. Soc. 132 (2), 418 (1985).

11. S. Dohmae, K. Shibahara, S. Nishino and H. Matsunami, Jap. J. Appl. Phys. 24, L873 (1985).

12. G. Kelner, S. C. Binari, and P. H. Klein, J. Electrochem. Soc. 134 (1), 253 (1987).

13. J. W. Palmour, R. F. Davis, T. M. Wallett, and K. B. Bhasin, "Dry etching of beta SiC in CF_4 and $CF_4 + O_2$ mixtures,"J. Vac. Sci. Technol. A 4, 590 (1986).

14. B. P. Luther, J. Ruzyllo, and D. L. Miller, Appl. Phys. Lett. 63, 171 (1993).

15. W. S. Pan and A. J. Steckl, J. Electrochem. Soc. 137 (1) 212 (1990).

16. R. Padiyath, R. L. Wright, M. I. Chaudhry, and S. V. Babu, Appl. Phys. Lett. 58, 1053 (1991).

17. J. Wu, J. D. Parsons and D.R. Evans, J. Electrochem. Soc. 142 (2), 669 (1995).

18. G. F. McLane and J. R. Flemish, unpublished.

19. J. R. Flemish, K. Xie, and J. H. Zhao, Appl. Phys. Lett. 64, 2315 (1994).

20. J. R. Flemish, K. Xie, W. Buchwald, L. Casas, J. H. Zhao, G. McLane, and M. Dubey, Mat. Res. Soc. Symp. Proc. 339, 145 (1994).

21. K. Xie, J. R. Flemish, J. H. Zhao, W. R. Buchwald and L. Casas, Appl. Phys. Lett. 67, 386 (1995).

22. W. Kern and D.A. Puotinen, RCA Rev. 31, 187 (1970).

23. J. R. Flemish, in Wide Bandgap Semiconductors and Devices, ed. F. Ren (Electrochemical Society, Pennington NJ, 1995) Vol 95-21, 231.

24. C. M. Melliar-Smith and C. J. Mogab, in Thin Film Processes, ed. by J. L. Vossen and W. Kern (Academic, San Diego, 1978) p. 540.

CLEAVED FACETS IN GaN BY WAFER FUSION OF GaN to InP

R. K. SINK *, S. KELLER *, B. P. KELLER *, D. I. BABIĆ *, A. L. HOLMES *,
D. KAPOLNEK *, X. H. WU **, J. S. SPECK **, S. P. DENBAARS *, J. E. BOWERS *
* ECE Dept., University of California, Santa Barbara, California 93106-9560,
  6500kehl@ucsbuxa.ucsb.edu
** Materials Dept., University of California, Santa Barbara, California 93106

ABSTRACT

Basal plane sapphire is a common substrate for the heteroepitaxy of GaN. This presents a challenge for fabrication of cleaved facet GaN lasers because the natural cleavage planes in (0001) α-Al_2O_3 are not perpendicular to the wafer surface. This paper describes a method for achieving perpendicular cleaved facets through wafer fusion that can potentially be used to fabricate GaN based in-plane lasers. We demonstrate successful fusion of GaN to InP without voids or oxide at the interface and fabricate optically flat cleaved GaN facets that are parallel to the crystallographic planes of the host InP. I-V measurements have been performed across the n-N fused interface. These results show that the fused interface exhibits a barrier for electrons passing from the InP to the GaN and ohmic conduction of electrons moving in the opposite direction.

INTRODUCTION

(In,Ga,Al)N in-plane lasers operating in the 300-700 nm range are potentially attractive devices for visible light applications and for high density data storage systems. However, despite the demonstration of blue, green, and yellow high brightness LEDs, electrically pumped lasers have only recently been demonstrated [1]. GaN lasers that have been demonstrated have high thresholds: 100-800 kW/cm^2 at room temperature [2,3]. To reduce the lasing threshold, improved mirrors are necessary. Two promising mirror types for in-plane devices are etched distributed Bragg reflector (DBR) mirrors and etched facet mirrors. Both of these mirror types have difficulties, however. It is difficult with reactive ion etching (RIE) to create facets that are both smooth and perpendicular to the wafer surface [4-6]; so etched facets are difficult to fabricate. In addition, RIE causes surface damage in GaN [7], which is a problem for both DBR and etched facet mirrors. Cleaved facets are another possible mirror choice for GaN based lasers that will likely be easier to fabricate than etched mirrors. With the application of high reflectivity (HR) coatings, these mirrors should offer comparable reflectivities to etched mirrors. Cleaved facet mirrors have been fabricated for GaN grown on SiC [8]. However, cleaved mirrors have not been fabricated for GaN grown on sapphire because the cleavage planes of (0001) sapphire substrates are not perpendicular to the wafer surface. In this letter, we present a method for obtaining cleaved facet mirrors for GaN films grown on sapphire. This method is based on wafer fusion of a (100) InP substrate to epitaxial hexagonal GaN (h-GaN/α-Al_2O_3).

Wafer fusion was first performed over a large area by Liau and Mull in 1991 [9]. Since that time, wafer fusion has been used for many applications because it is a simple method and allows layer structures to be fabricated that can not be achieved by traditional growth methods. Hewlett Packard uses wafer fusion in the production of transparent-substrate AlGaInP/GaP LEDs [10]. Using a double-fused structure, Babic, et al. demonstrated the first long-wavelength vertical-cavity surface-emitting lasers (VCSELs) to operate in continuous-wave (CW) mode at room temperature [11]. Resonant cavity photodetectors and heterojunction avalanche photodetectors based on fusion

have also been reported [12,13]. As illustrated by these examples, the restrictions of material choices due to thermal expansion and lattice mismatch are less stringent for fused interfaces than for heterointerfaces grown by MOCVD or MBE [14]. For both GaN VCSELs and GaN in-plane lasers, these relaxed restrictions will give device designers increased flexibility to choose materials based on optimal thermal or electrical characteristics. Therefore, wafer fusion will potentially solve many of the problems that have prevented an adequate transfer of technology from existing laser material systems to the nitrides.

EXPERIMENT

Material Growth by MOCVD

The GaN films used in this experiment were grown by atmospheric pressure metal-organic chemical vapor deposition (MOCVD) using TMGa and NH_3 sources in a Thomas Swan Ltd. reactor. 19 nm GaN nucleation layers were grown at 600°C on basal plane sapphire substrates before growing a thicker GaN film at 1080°C. GaN film thickness for the samples presented here varied from 1.5 to 2.5 μm. Additional details of the growth process have been reported previously [15]. The InP samples were (100) n-type substrates with no epitaxially grown layers.

Fusion Process and Characterization of Fused Interface

GaN to InP fusion was accomplished by a simple method: The GaN and InP samples, each 8 mm x 8 mm, were cleaned with solvents. Channels 10 μm wide with a period of 150 μm were etched into the InP sample in order to allow gas and liquid to escape from the interface during fusion [16]. The oxide layers from both samples were removed with a 49% HF solution. Before the HF evaporated from the surface, the GaN and InP were pressed together. These samples were then heated to 750°C for 60 minutes. This high temperature allowed for active mass transport of the indium at the InP/GaN interface. This mass transport effectively leveled the surface of the moderately rough GaN to allow a better matching of the InP and GaN surfaces.

After fusion, the sapphire substrate was lapped using a diamond slurry with 15 μm grit to make it thin enough for cleaving (<150 μm). By making a scribe mark on the InP host substrate, turning the fused samples over, and pressing on the sapphire, the GaN and thinned sapphire were forced to cleave parallel to the {110} crystal planes of the InP.

RESULTS

Physical characterization of fused interface

A high quality fused interface resulted from the fusion procedure as shown by plan-view transmission electron microscopy (TEM) as shown in Fig. 1. The InP/GaN fused interface is free of voids and has no oxide layer, which indicate that the two samples are well fused. In addition, the defects formed by the fusion process are contained within a few monolayers of the fused interface, which demonstrates that the wafer fusion preserves the structural integrity of the InP and GaN.
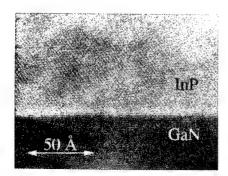
Figure 1. A TEM micrograph of an InP/GaN fused interface is shown. Fusion was performed at 750°C for 60 min.

A scanning electron microscope (SEM) micrograph of the cleaved facet (Fig. 2) provides further proof that the interface is free of voids and therefore well fused. Facets produced in this manner appear to be optically flat when examined by bright-field, dark-field, and Nomarski interference contrast microscopy and by SEM.
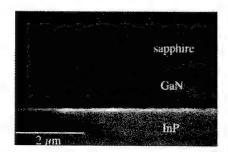
Figure 2. An SEM micrograph of an InP/GaN fused interface that was cleaved after lapping sapphire substrate is shown. The cleave plane from the InP propagates through the GaN and sapphire to produce a smooth cleave plane that can be used for a mirror facet in an in-plane laser or other opto-electronic device.

Electrical characterization of fused interface

Many optoelectronic devices are possible with this technology. Current injection across the fused interface is critically important for most of these devices. To measure the electrical characteristics of the interface, the InP substrate used for the cleaving demonstration was replaced with an epitaxially grown structure, $InP/In_{.53}Ga_{.47}As/InP$, in order to provide an etch stop layer for removing the InP substrate. The epitaxial InP and InGaAs layers were 500 nm and 200 nm thick, respectively, with n type Si doping on the order of 10^{18} cm^{-3} and 10^{19} cm^{-3}. The InP and GaN epitaxial layers were fused using the same process described above. After fusion, the InP substrate was etched away, stopping on the InGaAs etch stop layer. Selected areas of the InGaAs and InP epitaxial layers were then etched away to make contact to the GaN as shown in Fig. 3(a). 200 nm thick aluminum contacts were then evaporated onto the GaN and annealed at 500°C. This was followed by evaporation of Ni, Au/Ge, Ni, Au contacts to InP and a second anneal at 430°C.

167

For the InP contact, the first Ni barrier layer was designed to prevent diffusion of the Ge to the fused interface, thereby preserving the electrical characteristics of the fused interface.

The electrical characteristics of the fused interface were measured using the four point probe type structure (Fig. 3(a)) that was designed to reduce the effects of contact resistance. The pads were 200 μm wide (in the direction perpendicular to current flow) and 170 μm long and were spaced by 20 μm. The resistance along this 20 μm separation was not subtracted from the electrical measurements. Figure 3(b) shows the current-voltage (I-V) characteristic of the fused interface. Electrons moving from the GaN to the InP encounter almost no detectable barrier. Electrons moving from the InP to the GaN encounter a small potential barrier.
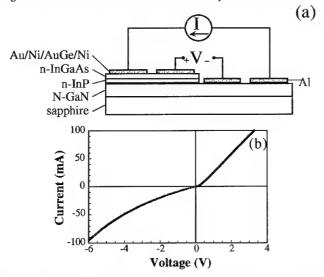
Figure 3(a). The electrical characteristics of the n-InP/N-GaN fused interface were measured using a four point probe structure with 200 μm wide pads separated by 20 μm gaps. (b) The measured current voltage curve shows that electrons can be injected through the interface for small voltage levels. The direction of positive current across the interface is from InP to GaN (i.e. electrons passing from GaN to InP).

The I-V curve measured across fused interfaces is not well understood even in well characterized material pairs such as InP/GaAs. Due to these complicities, calculation of a band diagram from known parameters is difficult, if not impossible. We can calculate some parameters to gain insight into electrical measurements: Based on the differences in electron affinities between GaN and InP, the heterointerface is expected to be a broken gap interface. The band discontinuities based on these differences are given by Eq. 1 and 2. It should be recognized, however, that this method for calculation often does not give accurate band offsets.

$$\Delta E_c = E_c(InP) - E_c(GaN) = 1.9 \text{ eV} \tag{1}$$

$$\Delta E_v = E_v(InP) - E_v(GaN) = 4.2 \text{ eV} \tag{2}$$

If these band offsets are used, we can model the fused interface as a typical broken gap interface, like that of InAs/GaSb. This band structure is shown in Fig. 4. At such an interface with no bias applied, electrons accumulate on one side (in our case, the GaN side) and holes

accumulate on the other side (InP). As a bias is applied, the electrons and holes mix across the interface, which causes a Fermi level gradient. Electron and hole recombination produces current. This explanation of current flow predicts ohmic current flow in both directions. The slight nonlinearity in the negative voltage regime of Fig. 3(b) is not understood. One possible explanation is that this nonlinearity is due to the InGaAs/InP heterointerface.
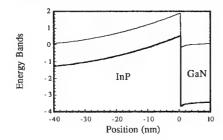
Figure 4. Possible band diagram of fused interface. Band offsets are given by difference in electron affinities. Neglects carrier injection, surface states, strain, and interface impurities.

For fusion of p-InP to p-GaN, hole injection is not predicted to occur in this manner. The large valence band discontinuity is expected to give a barrier that prevents hole injection for low voltages. Therefore, near ohmic injection of holes from p-InP to p-GaN across a fused junction should not occur. A voltage drop of several volts is expected for hole injection.

Transfer of GaN to conductive substrates

Although fusion is not likely to significantly improve p-type contacts for GaN, fusion will possibly ease the fabrication of devices by allowing the transfer of device layers to conductive substrates. By growing a sacrificial liftoff layer on the sapphire substrate, the sapphire substrate can be removed completely from the GaN device layers after fusion. The InP substrate now functions as the substrate for the device. This procedure is shown in Fig. 5. This procedure is expected to have two primary advantages: 1) it is expected to make cleaving easier because the thick sapphire substrate will be removed and 2) backside contacts can be made to the InP substrate, which makes fabrication of many devices, such as in-plane lasers, much simpler.

Figure 5. Removal of sapphire substrate by etching a sacrificial layer grown on the sapphire. This will allow easier cleaving and simpler device designs for in-plane opto-electronic devices.

The InP/InGaAs/InP epitaxial layer structure used for the electrical characterization provided a good measure for the fusion uniformity. After etch removal of the InP substrate, only a thin layer of epitaxial InP/InGaAs remained. In areas that were not well fused, this thin layer cracked and broke away. After etching the substrate, we were therefore able to determine the proportion of sample area that was well fused. For a typical processing run, fusion was achieved over 60-70% of the sample area. The lack of fusion over the other 30-40% of the sample is attributed to increased surface roughness of the GaN in those regions. InGaN samples with an indium mole

fraction of 10-20% were also fused to InP with the idea that the extra indium would facilitate mass transport at the interface. The proportion of area fused was not noticeably improved over the GaN samples, however. We believe that the indium content of the InGaN samples was too low to compensate for the increased roughness of the InGaN samples over the GaN samples.

CONCLUSIONS

In summary, optically flat cleaved GaN facets have been achieved by wafer fusion of GaN to InP. No indications of interface voids or oxide formation were found, which reveals that the samples were well fused. In addition, current injection has been demonstrated across the fused interface at low voltages. Both of these experiments indicate that this method provide a viable means for the fabrication of GaN in-plane lasers. Fusion uniformity has not yet been satisfactory for laser production. This problem is expected to be alleviated by smoother GaN epitaxial layers.

ACKNOWLEDGEMENTS

REFERENCES

1. S. Nakamura, M. Senoh, S. Nagahama, N. Iwasa, T. Yamada, T. Matsushita, H. Kiyoku, and Y. Sugimoto, Jpn. J. Appl. Phys., Part 2, **33**, L74 (1996).
2. X. H. Yang, T. J. Schmidt, W. Shen, J. J. Song, and B. Goldenberg, Appl. Phys. Lett. **66**, 1 (1995).
3. I. Akasaki and H. Amano, Material Research Society (MRS) Symposium Proceedings **339**, 443 (1994).
4. S. J. Pearton, C. R. Abernathy, F. Ren, Appl. Phys. Lett. **64**, 3643 (1994).
5. S. J. Pearton, J. W. Lee, J. D. MacKenzie, C. R. Abernathy, and R. J. Shul, Appl. Phys. Lett. **67**, 2329 (1995).
6. I. Adesida, A. T. Ping, C. Youtsey, T. Dow, M. A. Khan, D. T. Olson, and J. N. Kuznia, Appl. Phys. Lett. **65**, 889 (1994).
7. A. T. Ping, I. Adesida, and M. A. Khan, Appl. Phys. Lett. **67**, 1250 (1995).
8. I. Akasaki and H. Amano, Late News Paper, presented at Topical Workshop on Nitrides, Nagoya, Japan (1995) (unpublished).
9. Z. L. Liau and D. E. Mull, Appl. Phys. Lett. **56**, 737 (1991).
10. F. A. Kish, D. A. Defevere, D. A. Vanderwater, G. R. Trott, Electron. Lett. **30**, 1790 (1994).
11. D. I. Babic, K. Streubel, R. P. Mirin, N. M. Margarlit, J. E. Bowers, E. L. Hu, D. E. Mars, L. Yang, and K. Carey, IEEE Phot. Technol. Lett. **7**, 1225 (1995).
12. I. H. Tan, J. J. Dudley, D. I. Babic, D. A. Cohen, B. D. Young, E. L. Hu, J. E. Bowers, B. I. Miller, U. Koren, and M. G. Young, IEEE Photon. Tech. Lett. **6**, 811 (1994).
13. A. Hawkins, T. Reynolds, D. England, D. Babic, M. Mondry, and J. Bowers, Paper IO2.3, presented at LEOS 8th Annual Meeting, San Francisco, CA, (1995) (unpublished).
14. R. J. Ram, J. J. Dudley, J. E. Bowers, L. Yang, K.Carey, S. J. Rosner, and K. Nauka, J. Appl. Phys. **78**, 4227 (1995).
15. B. P. Keller, S. Keller, D. Kapolnek, M. Kato, H. Masui, S. Imagi, U. K. Mishra, and S. P. DenBaars, Electronics Lett. **31**, 1102 (1995).
16. D. I. Babic, K. Streubel, R. P. Mirin, N. M. Margalit, M. G. Peters, E. L. Hu, J. E. Bowers, to be published in Optical and Quantum Electronics, Special Issue "Optoelectronics based on Indium Phosphide and Related Materials" (May 1996).

STRAIN EFFECTS ON OPTICAL GAIN PROPERTIES OF GaN/AlGaN QUANTUM WELL LASERS

M. SUZUKI and T. UENOYAMA
Central Research Laboratories, Matsushita Electric Industrial Co., Ltd.,
3-4 Hikaridai, Seikacho, Sourakugun, Kyoto 619-02, Japan, suzuki@crl.mei.co.jp

ABSTRACT

Subband structures and optical gains of the strained wurtzite GaN/AlGaN quantum well lasers are theoretically investigated on the basis of k·p theory. First-principles calculations are used for deriving the unknown physical parameters, such as deformation potentials. Neither compressive nor tensile biaxial strains are so effective on the reduction of the threshold carrier density. It is also found that the uniaxial strain in the c-plane is one of the preferable approaches for the efficient improvement of the laser performance.

INTRODUCTION

There is increasing interest in the use of GaN and related materials for the optoelectronic devices in the short wavelength region, due to their wide direct band gaps and physical hardness. At present, high-brightness blue light emitting diodes (LEDs) based on wurtzite (WZ) InGaN/AlGaN heterostructures [1, 2] are commercially available, and very recently the pulse-lasing action of the quantum well (QW) laser diodes (LDs) by a current injection at room temperature was reported for the first time [3]. Furthermore, the recent development of crystal growth techniques made it possible to obtain high quality zincblende (ZB) crystals as well as WZ ones. Although such high quality materials and high luminescent devices have been achieved, many basic aspects of material and device characteristics are almost still unknown.

We have already studied the subband structure and the optical gain of the unstrained WZ GaN/AlGaN QW LDs by the k·p theory [4, 5]. The required physical parameters, such as effective masses, splitting energies and momentum matrix elements, have been theoretically determined with the help of first-principles calculations [6, 7]. As a result, the strong electron affinity and the weak spin-orbit coupling of the nitrogen atom yield very heavy electron and hole effective masses of the group-III nitrides. They play an essential role in causing higher carrier density to realize the population inversion, namely, higher threshold current density than ZB GaAs/AlGaAs QW LDs. In conventional ZB QW LDs, the biaxial strained structures are often used for reducing the threshold current density. However, there is plenty of room for discussing whether the strained QWs are advantageous for the group-III nitrides system, where there is no lattice matched substrate. Therefore, it is very interesting and important to study the strain effects on GaN/AlGaN QW LDs.

In this paper, we investigate the subband structures and the optical gain properties of both compressive and tensile biaxial strained WZ GaN/AlGaN QWs. The uniaxial strain effect in the c-plane is also studied. The relation between the uniaxial strain's direction and the optical polarization is clarified as well.
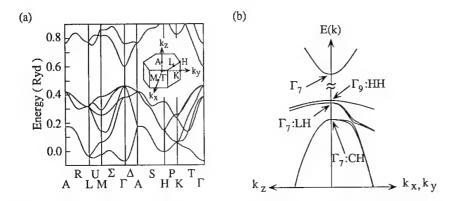
Figure 1: Electronic band structure of wurtzite GaN. (a) Energy dispersion along the symmetry lines. The inset shows the first Brillouin zone. (b) Schematic band structure along the k_z direction and in the k_x-k_y plane near the Γ point.

ELECTRONIC BAND STRUCTURE

In general, the nitrogen atom has such a strong electron affinity that the valence charge densities of the group-III nitrides tend to be well localized. In such a case, a conventional pseudo-potential approach seems to be not adequate. Thus, the electronic band structures of WZ GaN and AlN have been calculated by using a full-potential linearized augmented plane wave (FLAPW) method [8], within the local density functional approximation (LDA) [9]. We use the criteria that $l_{max} = 7$ and $|\mathbf{k} + \mathbf{G}|_{max} = (2\pi/a) \times 3.5$, with $\mathbf{k}$ being a wave vector in the first Brillouin zone (BZ) (see Fig. 1) and $\mathbf{G}$ being a reciprocal lattice vector. The charge densities have been self-consistently determined using 28 meshed $\mathbf{k}$ points in the irreducible BZ. The convergence of the calculated total energies of crystals is less than 1 mRyd. As for the lattice constants of a and c and the internal parameter of u, the experimental values [10, 11] and the ideal value ($u=0.375c$) were used, respectively. In these calculations, the Ga 3d electrons are treated as a part of the valence band states, since they are relatively high in energy even though they might constitute well localized narrow bands. As a matter of fact, our calculated result shows that the Ga 3d states are considerably hybridized with the N 2s states. Thus, the Ga 3d states should not be treated as core states.

At first, we summarize the feature of the electronic structure near the conduction band minimum (CBM) and the valence band maximum (VBM) without a strain. Figure 1 shows (a) the calculated electronic band structure along the symmetry lines and (b) the schematic band structure near the Γ point of WZ GaN. Table 1 shows the calculated effective masses and splitting energies around the CBM and the VBM of WZ GaN and AlN. We label the upper three hole bands as HH (heavy), LH (light) and CH (crystal-field split-off), based on the feature in the k_x-k_y plane, though the effective masses of these three hole bands are not isotropic between the $\mathbf{k}$ directions parallel and perpendicular to the k_z direction, as shown in Fig. 1 and Table 1. According to our calculated results and a group theory, the CBM

172

Table 1: Electron and hole effective masses (m_0) and crystal-field and spin-orbit splitting energies (mRyd) of bulk wurtzite GaN and AlN. m_e, m_{hh}, m_{lh} and m_{ch} denote electron, heavy hole, light hole and crystal-field split-off hole masses, respectively. The superscripts, $\parallel$ and $\perp$, stand for the k_z direction and the k_x direction, respectively. Δ_{cr} and Δ_{so} represent crystal-field and spin-orbit splitting energies, respectively.

	$m_e^{\parallel}$	$m_e^{\perp}$	$m_{hh}^{\parallel}$	$m_{lh}^{\parallel}$	$m_{ch}^{\parallel}$	$m_{hh}^{\perp}$	$m_{lh}^{\perp}$	$m_{ch}^{\perp}$	Δ_{cr}	Δ_{so}
GaN	0.20	0.18	1.76	1.76	0.16	1.61	0.14	1.04	5.3	1.2
AlN	0.33	0.25	3.53	3.53	0.25	10.42	0.24	3.81	-4.3	1.5

and the VBM are almost composed of s- and p-like states, respectively. Furthermore, the lowest conduction band is strongly coupled with the only one hole band due to the weak spin-orbit interaction. Then, the coupled hole band has much lighter mass than the other hole bands.

Here, note that the upper valence band structure in WZ materials is quite different from that in conventional ZB ones. The VBM is split into four-fold (Γ_6) and two-fold (Γ_1) degenerate states by the hexagonal crystal-field, even without the spin-orbit interaction. Considering the spin-orbit interaction, the Γ_6 state is split into two two-fold degenerate states (Γ_9 and Γ_7), and the Γ_1 state has also Γ_7 symmetry. Then, the two Γ_7 levels are also mixed by the spin-orbit interaction. In WZ III-V nitrides, since these six levels are very close to one another due to the weak spin-orbit interaction, we must explicitly treat the upper six valence bands in the analyses of QW devices.

Secondly, we discuss the strain effect on the electronic band structure of WZ bulk. Figure 2 shows the schematic band structure in the k_x-k_y plane around the VBM of bulk WZ GaN, (a) without a strain , (b) with a biaxial strain and (c) with a uniaxial strain in the c-plane. It is found that each energy dispersion of HH, LH and CH bands is almost unchanged even under the strains since the orbital character is dominant because of the
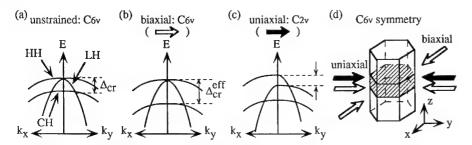

Figure 2: Schematic valence band structures of wurtzite GaN (a) without a strain, (b) with a biaxial strain and (c) with a uniaxial strain. Here, the weak spin-orbit splittings are neglected. (d) the directions of strains in the c-plane.

weak spin-orbit coupling. Under the condition of the compressive (tensile) biaxial strain, the crystal-field splitting energy becomes only effectively large (small) since the symmetry group is still C_{6v}, as well as without the strain. Then, the HH mass is still heavy, and the density of states (DOS) at the VBM is not so reduced. This is very different from ZB crystals, where the HH mass becomes light and the DOS fairly decreases since the T_d symmetry is changed to the D_{2d} one. On the other hand, the uniaxial strain in the c-plane gives the anisotropic energy splitting in the k_x-k_y plane since it causes the symmetry break from C_{6v} to C_{2v}. If the compressive (tensile) uniaxial strain along the y-direction, or the tensile (compressive) one along the x-direction, is induced, the HH band along the k_x-direction as well as the LH band along the k_y-direction moves to higher (lower) energy side. Thus, the DOS at the VBM is largely reduced, compared with the biaxial strain.

k·p THEORY WITH STRAINS

Generally speaking, optical and transport properties are governed by the electronic band structures in close vicinity of the VBM and the CBM. Thus, the k·p theory is not only an appropriate method to describe the electronic structures around the VBM and the CBM, but also a convenient method to analyze the QW devices on the basis of the effective mass approximation. In the analyses of conventional ZB semiconductors, we frequently assume parabolic functions for the conduction bands, and the 4×4 and/or 6×6 Luttinger-Kohn Hamiltonians are used to describe the upper valence bands [12]. In treating the valence bands together with the conduction bands, we often make use of the 8×8 Kane Hamiltonian [13]. For WZ materials, however, we must consider the hexagonal symmetry since the Luttinger-Kohn and Kane Hamiltonians are constructed under the condition of the cubic symmetry. Let us show the k·p and strain Hamiltonians for WZ structure.

We take the following basis functions:

$$|S, \alpha\rangle, \quad |S, \beta\rangle, \quad \frac{1}{\sqrt{2}}|(X + iY), \alpha\rangle, \quad \frac{1}{\sqrt{2}}|(X + iY), \beta\rangle,$$

$$|Z, \alpha\rangle, \quad |Z, \beta\rangle, \quad \frac{1}{\sqrt{2}}|(X - iY), \alpha\rangle, \quad \frac{1}{\sqrt{2}}|(X - iY), \beta\rangle,$$

where $|S\rangle, |X\rangle, |Y\rangle$ and $|Z\rangle$ are the Bloch functions at the Γ point, transforming like atomic s, p_x, p_y and p_z-like functions, respectively, under the operations of the symmetry group C_{6v}. $|\alpha\rangle$ and $|\beta\rangle$ are spin functions corresponding to spin-up and -down, respectively. Then, the Hamiltonian has the following form:

$$\mathbf{H}(\mathbf{k}, \varepsilon) = \begin{pmatrix} \mathbf{H}_{cc} & \mathbf{H}_{cv} \\ \mathbf{H}_{cv}^{\dagger} & \mathbf{H}_{vv} \end{pmatrix}, \tag{1}$$

where $\mathbf{H}_{cc}$ and $\mathbf{H}_{vv}$ are 2×2 and 6×6 matrices for the conduction bands and the valence bands, respectively, without the interaction between them. The interaction with the other bands is treated as the second order perturbation. The interaction between the conduction bands and the valence bands are described by $\mathbf{H}_{cv}$ whose matrix elements are written as

$$\mathbf{H}_{cv} = \begin{pmatrix} Q & 0 & R & 0 & Q^* & 0 \\ 0 & Q & 0 & R & 0 & Q^* \end{pmatrix}, \tag{2}$$

where

$$Q = \frac{1}{\sqrt{2}} P_\perp (k_x + i k_y), \quad R = P_\parallel k_z,$$

$$P_\perp = \frac{\hbar}{m_0} \langle S | p_x | X \rangle, \quad P_\parallel = \frac{\hbar}{m_0} \langle S | p_z | Z \rangle.$$

Note that the dipole matrix elements are related to $P_\parallel$ and $P_\perp$, which are different from each other in WZ structure due to the anisotropy between the directions parallel and perpendicular to the c-axis. According to the first-principles calculation, the values of $P_\parallel^2$ and $P_\perp^2$ for WZ GaN are 0.96 and 1.13 in units of $(\hbar^2/2m_0)\cdot$Ryd, respectively [7]. This means that the anisotropy seems to be not so large in WZ GaN. On the other hand, $P_\parallel^2$ and $P_\perp^2$ can be analytically derived from the 8×8 Hamiltonian [7] as follows:

$$P_\parallel^2 = \frac{\hbar^2}{2m_0} \left(\frac{m_0}{m_e^\parallel} - 1 \right) \frac{(E_g + \Delta_{cr} + \Delta_{so}) E_g + \frac{2}{3} \Delta_{cr} \Delta_{so}}{E_g + \frac{2}{3} \Delta_{so}}, \tag{3}$$

$$P_\perp^2 = \frac{\hbar^2}{2m_0} \left(\frac{m_0}{m_e^\perp} - 1 \right) \frac{(E_g + \Delta_{cr} + \Delta_{so}) E_g + \frac{2}{3} \Delta_{cr} \Delta_{so}}{E_g + \Delta_{cr} + \frac{2}{3} \Delta_{so} + \frac{1}{3} \Delta_{cr} \Delta_{so}/E_g}. \tag{4}$$

These analytical expressions with the observed parameters [14, 15, 16] yield $P_\parallel^2 \sim P_\perp^2 = 1.04 \pm 0.14$ in units of $(\hbar^2/2m_0)\cdot$Ryd. This result is in good agreement with the first-principles result. Therefore, the above relations are reliable and very useful for analyzing the optical properties of WZ materials.

Here, owing to the large band gaps of GaN and AlN, the 8×8 Hamiltonian can be split into the 2×2 Hamiltonian $\mathbf{H}'_{cc}$ for the CBM and 6×6 Hamiltonian $\mathbf{H}'_{vv}$ for the VBM by renormalizing the interaction $\mathbf{H}_{cv}$ within the second order perturbation. The matrix elements of $\mathbf{H}'_{cc}$ and $\mathbf{H}'_{vv}$ are given by

$$\mathbf{H}'_{cc} = \begin{pmatrix} E_c & 0 \\ 0 & E_c \end{pmatrix}, \tag{5}$$

$$\mathbf{H}'_{vv} = \begin{pmatrix} F & 0 & -H^* & 0 & K^* & 0 \\ 0 & G & \sqrt{2}\Delta_3 & -H^* & 0 & K^* \\ -H & \sqrt{2}\Delta_3 & \lambda & 0 & I^* & 0 \\ 0 & -H & 0 & \lambda & \sqrt{2}\Delta_3 & I^* \\ K & 0 & I & \sqrt{2}\Delta_3 & G & 0 \\ 0 & K & 0 & I & 0 & F \end{pmatrix}, \tag{6}$$

where

$$E_c = E_s^0 + \frac{\hbar^2 k_z^2}{2m_e^\parallel} + \frac{\hbar^2 (k_x^2 + k_y^2)}{2m_e^\perp} + a_c (\varepsilon_{xx} + \varepsilon_{yy} + \varepsilon_{zz}),$$

175

Table 2: Valence band parameters A_i $(\hbar^2/2m_0)$ and deformation potentials D_i (Ryd) of bulk wurtzite GaN and AlN. The values are determined by three-dimensionally fitting under the quasi-cubic approximation. The values obtained by fitting along the symmetry lines without the quasi-cubic approximation are also listed in round bracket.

	A_1	A_2	A_3	A_4	A_5	A_6	A_7
GaN	-6.56	-0.91	5.65	-2.83	-3.13	-4.85	0.00
	(-6.27)	(-0.96)	(5.70)	(-2.84)	(-3.18)	(—)	(—)
AlN	-3.95	-0.27	3.68	-1.84	-1.95	-2.92	0.00
	(-4.06)	(-0.26)	(3.78)	(-1.86)	(-2.02)	(—)	(—)

	D_1	D_2	D_3	D_4	D_5	D_6
GaN	-1.13	-0.91	0.22	-0.11	-0.15	-0.27
	(-1.02)	(-1.01)	(0.22)	(-0.12)	(-0.15)	(—)
AlN	-0.95	-0.62	0.33	-0.16	-0.19	-0.30
	(-0.91)	(-0.69)	(0.35)	(-0.15)	(-0.19)	(—)

$$F = \Delta_1 + \Delta_2 + \lambda + \theta, \quad G = \Delta_1 - \Delta_2 + \lambda + \theta,$$

$$H = i(A_6 k_z + iA_7)(k_x + ik_y) + iD_6(\varepsilon_{zx} + i\varepsilon_{yz}),$$

$$I = i(A_6 k_z - iA_7)(k_x + ik_y) + iD_6(\varepsilon_{zx} + i\varepsilon_{yz}),$$

$$K = A_5(k_x^2 - k_y^2 + 2ik_x k_y) + D_5(\varepsilon_{xx} - \varepsilon_{yy} + 2i\varepsilon_{xy}),$$

$$\lambda = E_p^0 + A_1 k_z^2 + A_2(k_x^2 + k_y^2) + D_1 \varepsilon_{zz} + D_2(\varepsilon_{xx} + \varepsilon_{yy}),$$

$$\theta = A_3 k_z^2 + A_4(k_x^2 + k_y^2) + D_3 \varepsilon_{zz} + D_4(\varepsilon_{xx} + \varepsilon_{yy}).$$

E_s^0 and E_p^0 represent the energy level at $\mathbf{k} = 0$ of s- and p-like functions, respectively. Δ_1 corresponds to the crystal-field splitting energy and Δ_2 and Δ_3 to spin-orbit splitting energies. A_i are the valence band parameters, corresponding to the Luttinger parameters in ZB crystals. a_c and D_i are the deformation potentials for the conduction bands and the valence bands, respectively, where ε_{ii} are positive for a tensile strain. In our notation, the energy band gap without a strain is given by

$$E_g = E_s^0 - E_p^0 - \Delta_1 - \Delta_2. \tag{7}$$

We have determined the above unknown valence band parameters A_i and D_i by fitting the first-principles band structures near the BZ center with the $\mathbf{k} \cdot \mathbf{p}$ and strain Hamiltonians
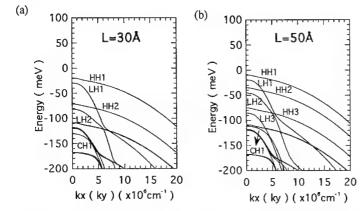
Figure 3: Valence subband structures of the unstrained WZ GaN/Al$_{0.2}$Ga$_{0.8}$N single QWs, with the well lengths L_z being (a) 30 Å and (b) 50 Å.

under the condition of a quasi-cubic approximation [6, 17], which means that the parameters are satisfied with the following relations:

$$A_1 = A_2 + 2A_4, \quad A_3 = -2A_4, \quad \sqrt{2}A_6 = A_3 + 4A_5,$$

$$A_7 = 0, \quad \Delta_{cr} = \Delta_1, \quad \Delta_{so} = 3\Delta_2 = 3\Delta_3. \tag{8}$$

Table 2 shows the obtained values of the parameters for WZ GaN and AlN, compared with the results without the quasi-cubic approximation. The agreement of two kinds of results are fairly well. Thus, the quasi-cubic approximation seems to be good for WZ nitrides, and it is available to decrease the number of independent parameters.

SUBBAND STRUCTURE

For the conduction band states, the subband energy dispersions are nearly parabolic, since the CBM almost consists of s-like states. Thus, the following discussion is limited to the valence subband structure. Assuming that the heterojunction is perpendicular to the c-axis, a wave vector k_z becomes an operator in the k·p Hamiltonian. Furthermore, the well-type potential by the heterojunction must be added to the diagonal terms of the Hamiltonian. Then, we can obtain the subband structure by solving a matrix differential eigenvalue problem [5]. As the required physical parameters, except elastic stiffness constants, we used the theoretical values. As the elastic stiffness constants, the observed values for WZ GaN are adopted [18]. The band offsets and the other parameters in ternary alloys are also determined by the first-principles calculations with the assistance of the virtual crystal approximation [19]. Our calculated valence band offset between GaN and AlN, $\Delta E_v = 0.82$ eV, is in good agreement with the recent observed value of 0.8 ± 0.3 eV, measured by x-ray photoemission spectroscopy (XPS) [20].

At first, we show the valence subband structures of the unstrained WZ GaN/Al$_{0.2}$Ga$_{0.8}$N single QWs in Fig. 3. The valence band offset between GaN and Al$_{0.2}$Ga$_{0.8}$N is about
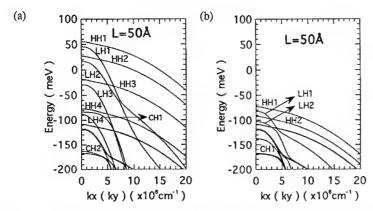
Figure 4: Valence subband structures of the biaxial strained WZ GaN/Al$_{0.2}$Ga$_{0.8}$N single QWs (a) with a compressive strain and (b) with a tensile one. The well lengths L_z are 50 Å.

0.11 eV. Since the Hamiltonian is expanded within the second order of k, the energy dispersions are isotropic in the k_x-k_y plane. In the subband structures, we can also label the energy bands as HH$_i$, LH$_i$ and CH$_i$, as well as in the bulk (see Fig. 1). For any well length, the coupling between HH$_i$ bands and the other bands is weak, and HH$_i$ bands are nearly parabolic. On the other hand, LH$_i$ bands are strongly coupled with CH$_i$ bands with a different parity, through the matrix elements H or I. However, the feature of hole bands, which are typically shown by the above three labels, is almost unchanged even in the QWs since the symmetry group is still C_{6v}, as well as in the bulk. According to our analyses, this character seems to be intrinsic in the WZ III-N QWs, originating from the hexagonal crystal symmetry and the weak spin-orbit coupling of the nitrogen atom. Moreover, it is very different from conventional ZB GaAs/AlGaAs QWs, where the heavy hole mass becomes light and the light hole mass becomes heavy.

Here, the well length dependence of the subband structure is discussed. Roughly speaking, the subband energies at the Γ point are inversely proportional to the bulk's hole masses along the k_z direction and to the square of the well length. This is called the quantum size effect. As for the bulk's masses along the k_z direction, LH band is as heavy as HH band and much heavier than CH band. This is the reason why CH$_i$ bands are more split off from HH$_i$ and LH$_i$ bands in the QWs than in the bulk. In other words, the crystal-field splitting energy Δ_{cr} becomes effectively large due to the quantum size effect. For $L_z = 30$ Å, CH$_1$ band is the only bound state among CH$_i$ bands, and the LH$_2$-CH$_1$ coupling causes the nonparabolicity of LH$_2$ band. For $L_z = 50$ Å, the interval between the same labeled subbands becomes shorter than for $L_z = 30$ Å due to the quantum size effect, then the DOS around the VBM becomes a little larger.

Secondly, we discuss the biaxial strain effect on the subband structures. Figure 4 shows the valence subband structures of the biaxial strained WZ GaN/Al$_{0.2}$Ga$_{0.8}$N single QWs, (a) with a compressive strain and (b) with a tensile strain. The compressive biaxial strain is introduced into the GaN well layer due to the lattice mismatch with the Al$_{0.2}$Ga$_{0.8}$N barrier
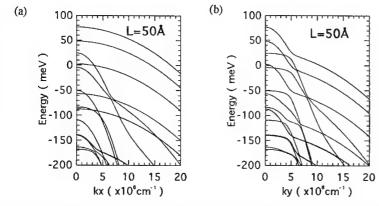
Figure 5: Valence subband structure of the uniaxial strained WZ GaN/Al$_{0.2}$Ga$_{0.8}$N single QWs (a) along the k_x direction and (b) along the k_y one, with the tensile strain along the x-direction. The well length L_z is 50 Å.

layers, and it is 0.5 % in the c-plane. The tensile biaxial strain is virtually induced, and it is also 0.5 %. The main feature of hole bands is the same as in the unstrained QWs. The change by the strains can be qualitatively understood by the well's depth and the strain effect on the bulk. Considering compressive (tensile) biaxial strains, the QWs become deep (shallow) and the number of subbands tends to increase (decrease). For $L_z = 30$ Å, HH$_3$ and LH$_3$ bands also come into the QWs as the bound states. For $L_z = 50$ Å, on the other hand, CH$_2$ band as well as HH$_4$ and LH$_4$ bands comes into the QWs. Then, the LH$_1$-CH$_2$ coupling causes the non-parabolicity of LH$_1$ band as well as LH$_2$ band. For both well lengths, furthermore, the energy difference between HH$_1$ and HH$_2$ bands becomes large (small) due to the deeper (shallower) well's depth, and the energy difference between LH$_i$ and CH$_i$ bands also becomes large (small) due to the biaxial strain effect as well as in the bulk. This is the reason why the DOS around the VBM is smaller (larger) in the compressive (tensile) biaxial strained QWs than in the unstrained QWs. Namely, the compressive (tensile) biaxial strain plays a decreasing (increasing) role in the DOS around the VBM.

Thirdly, the uniaxial strain effect in the c-plane is discussed. Figures 5 shows the valence subband structure of the uniaxial strained WZ GaN/Al$_{0.2}$Ga$_{0.8}$N single QWs. The uniaxial strain is introduced into both the GaN well layer and the Al$_{0.2}$Ga$_{0.8}$N barrier layers, and it is 1.0 % tensile strain along the x-direction (see Fig. 1), where the GaN well layer is lattice matched to the Al$_{0.2}$Ga$_{0.8}$N barrier layers. Each energy dispersion of HH$_i$, LH$_i$ and CH$_i$ bands is the same as in the unstrained QWs. However, the energy splittings between HH$_i$ and LH$_i$ bands are not isotropic in the k_x-k_y plane due to the symmetry lowering from C_{6v} to C_{2v}. The tensile strain along the x-direction makes not only the LH$_i$ bands along the k_y-direction but also the HH$_i$ bands along the k_x-direction moves higher energy side. Therefore, the DOS at the VBM is more effectively reduced than the case of the compressive biaxial strain.
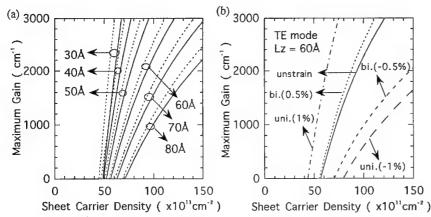
Figure 6: Maximum optical gains of WZ GaN/Al$_{0.2}$Ga$_{0.8}$N single QW LDs. (a) The well length dependence from 30 Å to 80 Å. (b) The strain effects with the well length being 60 Å. The solid, dotted, short-dashed, dash-dotted and long-dashed lines stand for the results without a strain, with ±0.5 % compressive biaxial strains and with ±1.0 % tensile uniaxial strains along the x-direction, respectively.

OPTICAL GAIN

The optical gain of the QW LDs is given by

$$g(\omega) = \frac{2\pi\bar{n}}{c\hbar} \sum_{n,m} \sum_{k_\perp} |\langle c, n, k_\perp | \frac{e}{m_0 c}\vec{A} \cdot \vec{p}|v, m, k_\perp\rangle|^2$$

$$\times \quad \{f_c(E^c_{n,k_\perp}) + f_v(E^v_{m,k_\perp}) - 1\}\delta(\omega - E^c_{n,k_\perp} - E^v_{m,k_\perp}), \tag{9}$$

where $\bar{n}$ denotes the refractive index, m (n) represents the valence (conduction) subband label, and $k_\perp$ is the two-dimensional wave vector in the k_x-k_y plane. Using the calculated subband structures and bulk's momentum matrix elements, we have calculated the optical gains with respect to the interband transition. In WZ bulk nitrides, the hybridization of the CH band with the HH and LH bands is negligible at the VBM, due to $\Delta_{so} \sim 0$. Then, the eigenstates along the k_x (k_y) direction can be approximately expressed as

$$|HH\rangle \sim |Y(X)\rangle, \quad |LH\rangle \sim |X(Y)\rangle, \quad |CH\rangle \sim |Z\rangle.$$

In WZ GaN-based QWs, the CH$_i$ bands are more split off from the HH$_i$ and LH$_i$ bands. Then, the $|Z\rangle$ character, which yields the optical gain for the TM mode, is very small at the VBM. This is the reason why the optical gain for the TE mode is dominant in WZ GaN-based QW LDs. Thus, the following discussion is limited to the TE mode.

Figure 6 shows (a) the well length dependence and (b) the strain effect on the maximum optical gain of WZ GaN/Al$_{0.2}$Ga$_{0.8}$N QW LDs as a function of a sheet carrier density. In the unstrained QWs, as the well length becomes longer than 30 Å, more carrier density might be needed to obtain sufficient optical gain. This is quite obvious from the feature of the subband structure. As the well length becomes longer, the interval between HH$_1$ and

HH$_2$ bands becomes shorter, and the DOS around the VBM becomes larger. This is the reason why it is more difficult to realize the population inversion for longer well length. However, even for $L_z = 30$ Å, the threshold carrier density would be higher than ZB GaAs/AlGaAs LDs. In the compressive biaxial strained QWs, the optical gain property is qualitatively improved for any well length, and the threshold carrier density would become a little lower than in the unstrained QWs. However, the reduction of the threshold carrier density is quantitatively not so effective. On the other hand, the tensile biaxial strain yields qualitatively negative effect for any well length. Therefore, no biaxial strain comes up to our expectations of reducing the threshold carrier density, namely, improving the LDs performance in WZ GaN/AlGaN QWs.

Here, on the analogy of the bulk, if it were possible to introduce a uniaxial strain into the c-plane of WZ QWs, it might cause much larger reduction of the DOS and the threshold carrier density. According to our calculated subband structures, any uniaxial strain in the c-plane reduces the DOS at the VBM due to the anisotropic energy splittings in the k_x-k_y plane. However, considering the optical polarization, the effective uniaxial strain's direction is limited to the following two cases. One is the compressive strain parallel to the optical polarization for the electric field, and the other is the tensile one perpendicular to it. If we induce the tensile (compressive) uniaxial strain along the x-direction (y-direction), LH$_i$ bands along the k_y-direction as well as HH$_i$ bands along the k_x-direction moves to the higher energy side. Then, the orbital component of both LH$_i$ bands along the k_y-direction and HH$_i$ bands along the k_x-direction is almost $|Y\rangle$ character. In other words, such uniaxial strains selectively isolate $|Y\rangle$ band, which is coupled with the TE polarized light. This is the reason why the above two kinds of uniaxial strains cause not ony the reduced DOS at the VBM but also the larger differential optical gain. Therefore, the uniaxial strain in the c-plane is more advantageous for the improvement of the WZ GaN/AlGaN QW LDs performance than the biaxial strain.

CONCLUSIONS

In conclusion, we have theoretically studied the strain effect and the well length dependence on WZ GaN/AlGaN QW LDs. The subband structures and the optical gains, without a strain, with biaxial strains and with uniaxial strains, have been calculated in several well lengths, on the basis of the 8×8 k·p theory. The required physical parameters, such as deformation potentials, have been derived from the first-principles electronic band calculations. In the unstrained QWs, the increase of the well length would make the threshold carrier density higher due to the quantum size effect. In the compressive biaxial strained QWs, the threshold carrier density becomes a little lower for any well length than in the unstrained QWs. However, the reduction is not so effective as conventional GaAs/AlGaAs LDs. On the other hand, the tensile biaxial strain makes the threshold carrier density rather higher. This means that no biaxial strain have remarkable effect on the reduction of the threshold carrier density in WZ GaN-based QW LDs. Furthermore, we clarified the uniaxial strain effect in the c-plane and the relation between the uniaxial strain's direction and the optical polarization. As a result, the use of the uniaxial strain in the c-plane is one of the powerful approaches for reducing the threshold carrier density, namely, improvement of the LDs performance.

ACKNOWLEDGMENTS

REFERENCES

1. S. Nakamura, T. Mukai and M. Senoh, Appl. Phys. Lett. **54** (1994) 1687.

2. I. Akasaki, H. Amano, K. Itoh, N. Koide and K. Manabe, Inst. Phys. Conf. Ser. **129** (1992) 851.

3. S. Nakamura, Jpn. J. Appl. Phys. **35** (1996) L74.

4. S. Kamiyama, K. Ohnaka, M. Suzuki and T. Uenoyama, Jpn. J. Appl. Phys. **34** (1995) L821.

5. T. Uenoyama and M. Suzuki, Appl. Phys. Lett. **67** (1995) 2527.

6. M. Suzuki, T. Uenoyama and A. Yanase, Phys. Rev. B **52** (1995) 8132.

7. M. Suzuki and T. Uenoyama, Jpn. J. Appl. Phys. **35** (1996) 543.

8. E. Wimmer, H. Krakauer, M. Weinert and A. J. Freeman, Phys. Rev. B **24** (1981) 864.

9. O. Gunnarson and B. I. Lundquvist, Phys. Rev. B **13** (1976) 4274.

10. H. P. Maruska and J. J. Tietjen, Appl. Phys. Lett. **15** (1969) 327.

11. W. M. Yim, E. J. Stofko, P. J. Zanzucchi, J. I. Pankove, M. Ettenberg and S. L. Gilbert, J. Appl. Phys. **44** (1973) 292.

12. J. M. Luttinger and W. Kohn, Phys. Rev. **97** (1955) 869.

13. E. O. Kane, J. Phys. Chem. Solids **1** (1957) 249.

14. B. Monemar, Phys. Rev. B **10** (1974) 676.

15. R. Dingle, D. D. Sell, S. E. Stokowski and M. Ilegems, Phys. Rev. B **4** (1971) 1211.

16. A. S. Barker and M. Ilegems, Phys. Rev. B **7** (1973) 743.

17. G. L. Bir and G. E. Pikus, Symmetry and Strain-Induced Effects in Semiconductors, (Wiley, New York, 1974) pp.329.

18. A. U. Sheleg and V. A. Savastenko, Izv. Akad. Nauk SSSR, Neorg. Mater., **15** (1979) 1598.

19. M. Suzuki and T. Uenoyama (unpublished).

20. G. Martin, S. Strite, A. Botchkarev, A. Agarwal, A. Rockett, H. Morkoç, W. R. L. Lambrecht and B. Segall, Appl. Phys. Lett. **65** (1994) 610.

STUDIES OF DEGRADATION IN NICHIA AlGaN/InGaN/GaN BLUE LIGHT EMITTING DIODES UNDER CLOSE TO NORMAL OPERATING CONDITIONS

M. Osiński, D. L. Barton*, C. J. Helms*, P. Perlin, N. H. Berg*, P. Sartori** and B. S. Phillips

Center for High Technology Materials, University of New Mexico, Albuquerque, New Mexico
87131-6081, USA, osinski@chtm.unm.edu

*Sandia National Laboratories, P.O.Box 5800, Albuquerque, New Mexico 87185-1081, USA

**Present address: Ecole Nationale Supérieure des Télécommunications, Paris, France

ABSTRACT

The reliability of devices fabricated in GaN and related alloys, especially under high current densities as would be found in lasers, has yet to be fully characterized. Our previous work [1] investigated the degradation of GaN-based blue light emitting diodes (LEDs) under high pulsed current stress. This work indicated a possible correlation between the high crystal defect density and failures caused by metal migration along these defect tubes. To assess the impact of this data on devices under more normal conditions, several LEDs from both older and more recent production lots were placed in a controlled temperature and current environment for several thousand hours. The test started with a constant 20 mA current for the first 1000 hours and continued for another 1650 hours at various currents up to 70 mA, all at a temperature of 23 °C. During this test, one of the older generation LED's output degraded by more than 50%. Subsequent failure analysis showed that this was caused by a crack which isolated part of the active region from the p-contact. The remaining LEDs were returned to life testing where the temperature was subsequently increased by 5 °C after each 500 hours of testing. The output from one of the newer LEDs dreiven at 70 mA degraded to 55% of its original value after 3600 hours and a second newer LED degraded by a similar amount after 4400 hours. The first failure, LED #16, did not exhibit a significant change in its I-V characteristics indicating that a change in the package transparency was a likely cause for the observed degradation. The second failure, LED #17, did show a noticeable change in its I-V characteristics. This device was subsequently returned to life testing where the degradation process will be monitored for further changes.

INTRODUCTION

Since high brightness blue LEDs have not been available until very recently [2-4], little is known about the basic degradation mechanisms of devices made from group-III nitrides. In the past [1] we subjected these devices to very high current densities as would be encountered in GaN-based lasers. The high current work indicated that the high defect densities in these LEDs may provide a path for metal migration and subsequent device failure. This degradation mechanism, however, may not occur under the normal operating conditions of LEDs. To understand what degradation processes would impact LEDs driven at modest currents and temperatures, an extensive life test is in progress. This work reports on the life test and failure analysis results obtained to date.

LIFE TEST SETUP AND RESULTS

Life test setup

In order to investigate the lifetime of the Nichia LEDs, 20 devices were mounted inside a large environmental chamber which could be maintained at a constant temperature. The light out-

put of each LED was sampled by an optical fiber which was connected to its own photovoltaic detector located outside the chamber. The LED-to-fiber connection was both mechanically stable and light-tight, eliminating intensity variations due to mechanical misalignments and ambient light. The system used a switching device to select a single detector's current, which was fed to a meter for automated reading of each LED's output.

Two separate driving circuits were used in this first life test, one based on op-amps, the other on current-limiting resistors. Each circuit was powered by a supply which maintained a constant output voltage. Currents were held approximately constant through each LED by two different methods. In the op-amp circuit, there was a current feedback loop for each LED which regulated LED drive current. In the resistor circuit, a current limiting resistor was placed in each parallel leg of the circuit to prevent excessive current through any one LED, should any legs become short circuited. The simple resistor circuit is being compared to the more complicated op-amp circuit because life testing of the LEDs also relies on the consistent performance of each circuit component during the test. The op-amp circuit theoretically provides better current regulation, but it may prove to be less reliable during sustained life testing. The test was fully computer controlled, with data automatically gathered every 12 hours or at the operator's request.

For the test, eighteen Nichia NLPB-500 LEDs (numbered 1-18 for the test) were selected from a new, improved batch (4B0001), acquired in April 1995. The test also used two devices (numbered 19 and 20) from batch S403024, acquired a year earlier. Two "improved" devices (labeled A and B) were left untested to serve as controls. The LEDs were placed in cw operation after pre-test power measurements were taken on all 20 devices. Ten LEDs were tested in the resistor circuit and ten in the op-amp circuit.

Test results to date

Figure 1 shows the relative luminous intensity from all 20 devices tested, normalized to their initial readings. The general trend for the 18 newer LEDs was for the output intensity to increase at a faster rate within the first 50-100 h, then at a slower rate over the remainder of the test. The output intensity of the two older LEDs increased within the first 50 h, and then decreased during the remainder of the test.

After the first 1000 hours, the drive currents of the LEDs were increased to try to accelerate the degradation process in some of the devices under test. The previously tested eighteen devices from the new batch were divided into six groups of three. Each group was driven at one of six currents: 20, 30, 40, 50, 60, or 70 mA. Of the two older devices, one (#19) was subjected to a high current of 70 mA, and the other (#20) remained driven at 20 mA. The maximum current level of 70 mA is close to the condition producing a maximum CW output power from the LEDs. The onset of thermal rollover was observed at 80 mA with slightly decreased output. A current of 70 mA was thus expected to be sufficiently high to cause measurable degradation after a few hundred hours.

The relative intensity of one of the older-generation LEDs (#19) dropped to about half of its initial value after approximately 1200 h and the device was removed from the test. In this case, the high current (70 mA) had indeed caused a rapid failure. The remaining devices driven at the same current level, however, have performed much better. After a relatively fast drop in their output (10-15% over the first 750 h), their degradation rate slowed as shown in Figure 1.

The remaining LEDs were returned to life testing where the temperature was subsequently increased by 5 °C after each 500 hours of testing. The output from one of the newer LEDs driven at 70 mA degraded to 55% of its original value after 3600 hours and a second newer LED degraded by a similar amount after 4400 hours. The first failure, LED #16, did not exhibit a significant change in its I-V characteristics indicating that a change in the package transparency was

a likely cause for the observed degradation. The second failure, LED #17, did show a noticeable change in its I-V characteristics. This device was subsequently returned to life testing where the degradation process will be monitored for further changes.

ANALYSIS OF LED #19

In order to determine the cause of the degradation for device #19, a series of I-V measurements were made. The measurements indicated that the junction leakage had increased during the life testing. This data indicated that the light output degradation was not due to a change in contact resistance or a change in the optical transmission of the plastic encapsulation. This data was significant in that the degradation mechanism could be similar to the one identified in the high pulsed current testing done earlier. Figure 2 shows the I-V characteristics of the degraded device #19 and an unstressed LED for comparison. The figure shows that the degraded device has an ohmic leakage path across the junction of about 600 MΩ.
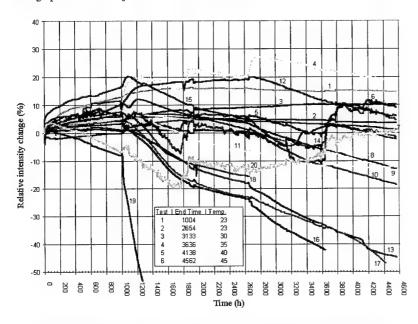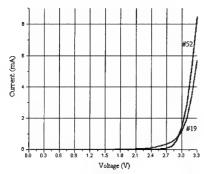

Figure 1 - Relative change in intensity of 20 Nichia blue LEDs subjected to various currents and temperatures for 4562 h.

To identify the cause of the degradation, device #19 was de-encapsulated and prepared for electron beam induced voltage (EBIV) analysis. EBIV analysis differs slightly from the more common EBIC analysis in that the voltage created across the junction by the incident electron beam is used to create the image instead of the current collected across the junction. The EBIV analysis quickly identified that the cause of the light output degradation was a crack in the LED which isolated part of the junction area from the p-contact. With a beam energy of 5 keV, the electron beam interaction volume did not penetrate down to the n-contact. Figure 3 shows the resulting EBIV image which clearly shows that the crack has propagated through the p-contact and the active layer thus isolating part of the LED from the electrical stimulus and reducing its

light output accordingly. We therefore concluded that LED #19 did not degrade in a manner that would be considered typical for operation under close to normal conditions.
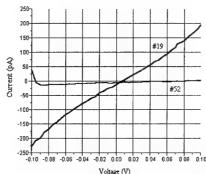

Figure 2 - Forward I-V characteristics (left) and leakage current (right) of the degraded LED (#19) and an unstressed LED (#52) for comparison
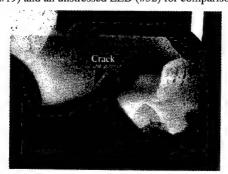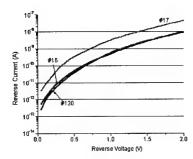

Figure 3 - EBIV image of LED #19 at 5 keV.

ANALYSIS OF LEDs #16 AND 17

In order to identify the process responsible for the degradation in light output measured on LEDs #16 and 17, the first task was to carefully measure the current-voltage characteristics of each device and compare the results to a control LED of the same type. Figures 4-5 show some of the measurements made on the two degraded LEDs along with a control LED. The figures indicate that LED #16 has not undergone a significant change in its I-V characteristics. In fact the I-V data indicates that LED #16 has a lower forward series resistance than the unstressed control device, #120. None of these figures lead us to a degradation mechanism that involves the electrical performance of the LED. The only possibilities for degradation are limited to a change in the radiative versus non-radiative recombination rate or a change in the optical properties of the plastic encapsulation. The former process would involve a 45% loss in radiation from the LED. A careful inspection of LED #16 under a low forward bias (just above the LED's turn-on voltage) revealed no significant non-radiative areas that could account for the loss in light output. The LED showed almost perfectly uniform illumination distribution which is unlike LED #19 described above. These results leave the plastic encapsulation material as the most likely cause for output degradation.
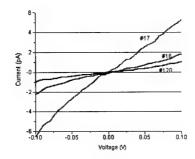
Figure 4 - Reverse I-V characteristics

Figure 5 - Junction leakage measurements

It is commonly known that prolonged exposure to ultraviolet radiation can reduce the optical transparency of many types of plastics. Since band-to-band recombination in the GaN system can produce ultraviolet radiation, a degradation mechanism of this type is reasonable. Figure 6 shows the output spectra for both the older generation, double heterojunction Nichia LED and a newer generation Nichia LED. The spectra were measured at room temperature (295 K) at a forward voltage of 3.5 V. The band-to-band recombination found in the older LED has been suppressed in the newer LED by an increase in the Zn doping concentration in the active InGaN layer [5]. We also know from our previous work [1] that the band-to-band emission component does increase significantly with forward bias indicating that the newer generation LEDs should have a long lifetime at currents less than the 20 mA cw limit in the data sheet, but may have a reduced lifetime by this mechanism at elevated currents.

In order to study the optical transparency of the plastic encapsulation, we have initiated an experiment where we will measure the optical absorption coefficient of the plastic versus wavelength and how this coefficient changes with UV exposure. The experiment will compare plastic from an unstressed LED as well as from degraded LED #16. The plastic samples were removed from the LED in such a manner as to maintain operation of the LED for further study and allow transmission coefficient measurements to be made as a function of position between the region close to the LED and the region at the edge of the package. These results will be published when completed.
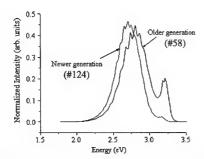

Figure 6 - Output spectra comparing old and newer generation LEDs, measured at 3.5 V.

The I-V data in figures 4-5 show a different degradation mechanism for LED #17. This LED shows a significant difference in its characteristic when compared to both the unstressed and the other degraded LED. Figure 4 indicates that #17 has about an order of magnitude more leak-

age current across the junction than #120 and #16. From Figure 5, calculations of the ohmic leakage paths across the junctions of the three LEDs showed that LED #17 had an order of magnitude lower resistance across the junction (18 GΩ for #17 versus 113 GΩ for #120). Since the degradation of #17 was noticeable but subtle, this LED was subsequently returned to life testing and will continue to be stressed until its output reaches a relative decrease of 90%. Assuming that the same degradation mechanism will continue to adversely affect device performance, the additional degradation will increase the accuracy with which the root cause can be determined.

CONCLUSIONS

The life tests of Nichia blue LEDs completed to date have failed to cause significant degradation on any of the devices operated at currents less than 60 mA. These results indicate that Nichia devices enjoy a remarkable longevity in spite of their high density of defects. As of this report, one of the older technology, double heterostructure Nichia LEDs showed a greater than 50% light output degradation after 1200 hours. Subsequent failure analysis of this LED revealed that a crack had isolated part of the junction and was the cause of the light output degradation. Two of the newer generation LEDs showed a greater than 40% loss in output intensity after 3600 and 4400 hours. Of these LEDs, the earlier failure did not exhibit any significant change in its I-V characteristics indicating that a possible failure mechanism may be related to the plastic encapsulation material. The other LED did show a change in its I-V characteristics. This device was returned to life testing to allow the observed degradation process to continue.

ACKNOWLEDGEMENTS

REFERENCES

1. D. L. Barton, J. Zeller, B. S. Phillips, P.-C. Chiu, S. Askar, D. -S. Lee, M. Osiński, and K. J. Malloy, Proc. 33rd Annual IEEE Int. Rel. Phys. Symp., Las Vegas, NV, pp. 191-199 (1995).
2. S. Nakamura, T. Mukai, and M. Senoh, Appl. Phys. Lett., **64** (13), 1687 (1994).
3. S. Nakamura, J. Cryst. Growth, **145**, 911 (1994).
4. S. Nakamura, J. Appl. Phys., **76** (12), 8189 (1994).
5. S. Nakamura, private communication.

PHOTOLUMINESCENCE STUDY OF CHLORIDE VPE-GROWN GaN

Tetsuzo Ueda*, Masaaki Yuri*, Heon Lee, James S. Harris Jr., and Takaaki Baba*
Solid State Electronics Laboratory, CIS 329, Stanford University, Stanford, CA94305-4075,
*Electronics Research Laboratory, Matsushita Electronics Corporation, Osaka 569, JAPAN

ABSTRACT

We have examined the effect of growth conditions on photoluminescence (PL) characteristics of chloride VPE-grown GaN films. Undoped GaN films are grown on sapphire by a newly developed chloride VPE system which utilizes $GaCl_3$ and NH_3 as source materials.

We find that the spectra depend strongly on the growth temperatures and the corresponding surface morphology. Peaks from excitons and donor-acceptor pairs (D-A pair) recombination are observed for the films with terrace-like flat surfaces grown at between 950°C and 1000°C. A peak due to exciton bound to neutral donors is observed for a growth temperature of 975°C where the acceptor-related peaks are not seen. Decreasing the growth temperature below 950°C causes rough surfaces due to three-dimensional growth , whereas increasing the growth temperature above 1000°C causes cracks or partial pealing off of the film. The films with rough surfaces or crystal failures show broad emission from deep acceptor levels. As a result, residual acceptors are eliminated in the very narrow range of the growth temperature around 975°C. It is also noted that an increase of the V/III ratio during the growth makes the line width of the band-edge peak narrower. The PL results show that a growth temperature around 975°C and high V/III ratio are essential to obtain better crystal quality and reduced concentration of residual acceptors.

INTRODUCTION

III-V nitride materials are promising for application to blue-violet light emitting diodes(LEDs) or laser diodes. Nitride LEDs with a brightness greater than 1 Cd are now commercially available [1]. Furthermore, the first observation of current injection pulsed laser operation at room temperature was recently reported [2]. Pulsed laser action has been observed in spite of an extremely high defect density, around 10^9 cm^{-2}, which could cause the higher threshold current density and prevent continuous laser operation.

Chloride transport vapor phase epitaxy (VPE) is suitable for thick film growth because of its inherent higher growth rate up to 100μm/hr [3-6]. This thick film growth is like bulk formation so that lower defect density might be achieved. Thus, chloride VPE can provide high quality GaN substrates for subsequent metal-organic VPE or molecular beam epitaxy (MBE) to form the device epi-layers, such as double-hetero (DH) structures. So far, the luminescent properties of doped GaN grown by this method have only been investigated for the metal-insulator-semiconductor type LEDs [7-10]. The objectives were to find a suitable dopant as bright luminescent centers and to optimize the doping conditions. In order to examine the crystal quality from the luminescence to produce better GaN substrates, the properties of undoped film are important. There has been no prior study on the effect of the growth conditions on the luminescent properties of undoped GaN films produced by this chloride VPE technique.

In this paper, we investigate the photoluminescence(PL) spectra of chloride VPE grown undoped GaN films obtained under various growth conditions. The effects of growth temperature and ratio of nitrogen source to gallium source, so-called V/III ratio, are examined. The notable feature of our growth system is $GaCl_3$ placed in a cell as a gallium source by which the source supply can be controlled more precisely than the conventional source using Ga metal and HCl gas[11].

EXPERIMENTAL

Undoped GaN films were grown on c-plane sapphire $(Al_2O_3(0001))$ substrates by chloride VPE system using $GaCl_3$ and NH_3 as source materials[11]. Nitrogen is used as a carrier gas. The gallium supply is precisely controlled by the temperature of $GaCl_3$ cell and the flow rate of nitrogen for the cell. The growth of the undoped-GaN was carried out at temperatures from 800°C to 1000°C. The obtained typical growth rate was 5-20μm/hr. The GaN films have hexagonal structure according to the X-ray diffraction measurements. The details of the crystal growth are described elsewhere[11].

The PL was excited by a 10mW He-Cd laser at 325nm. A grating monochromator with a resolution of 0.1nm and a photo-multiplier were used to measure the spectra. The measurement was carried out at room temperature and 77K on 10μm thick films. For the low temperature measurements, the samples are mounted on a copper block cooled by liquid nitrogen.
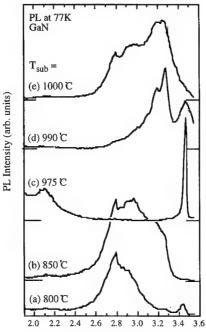
RESULTS AND DISCUSSION

Effect of Growth Temperatures

Fig.1 shows the low temperature PL spectra of undoped-GaN samples grown at various temperatures. Five different types of emission can be identified. The sharp peak at 3.47eV is due to excitons bound to neutral donors [7,8,12]. This peak is called I_2 line and the origin of the residual donor is believed to be N vacancies. Another sharp peak at 3.43eV is due to excitons bound to neutral acceptors [7,8,12]. The peak position of this I_1 line depends on the kind of acceptors and in this study, the residual acceptors are not identified. The set of peaks between 3.0eV and 3.3eV are due to donor-acceptor pair (D-A pair) recombination [12,13]. These peaks consist of the zero-phonon line at 3.26eV and several LO-phonon replicas which were reported in both undoped and doped GaN. In addition, two broad band lower energy emissions were observed. One is at 2.8eV, which is commonly observed as the "blue"-band in Zn- or Cd-doped GaN [7,9,14-16]. The emissions are from deep levels of these acceptors. In this study, such acceptors are not intentionally introduced, thus their origin is unknown. The second band is at 2.1eV, called the "yellow"-band. Pankove et al. reported this band to be related to ion-implantation damage[17]. Ogino et al. suggested this emission was due to the deep acceptor level of carbon [18]. Pankove observed only the "yellow" band, while Ogino observed both the I_2 line and "yellow" band. Since we observed both the "yellow"-band and I_2 line, the origin is likely unintentional carbon doping. We also note that the free exciton peak which should be located at 3.48eV is not observed.

The variation of PL spectra in Fig.1 is strongly correlated with the surface morphology. The surface morphology dependence on growth temperature is shown in Fig.2. At a growth temperature less than 950°C, three dimensional growth occurs with the very rough surfaces. The migration velocity of Ga atoms on the surface is so small at such low temperatures that three dimensional growth occurs from randomly scattered nucleation points. On the contrary, relatively smooth surfaces with terrace structure were obtained for growth between 950°C and 1000°C. This implies that two-dimensional growth occurs in this temperature range. Further increasing the growth temperature causes cracks or partial pealing off of the film. These crystalline failures are due to physical stress between the epi-layer and the substrate.

The flat surface as shown in Fig.2 (b) exhibits the PL with peaks from excitons (I_1 and I_2) and D-A pair recombination. No "blue"-band from deep-acceptor levels is observed. The "yellow"-band at 2.1eV is occasionally observed but is weak and we cannot find any dependence on growth temperature.

Fig.1 Low temperature (77K) PL spectra of GaN films grown at (a) 800°C, (b) 850°C, (c) 975°C. (d) 990°C. (e) 1000°C.

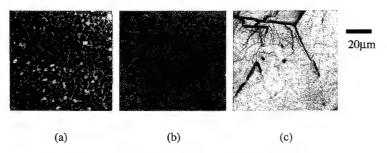(a)   (b)   (c)

Fig.2 Surface morphology of GaN films grown by chloride VPE at (a) 925°C, (b) 975°C, (c) 1000°C.

Thus two-dimensional growth prevents the incorporation of residual acceptors as deep level luminescent centers. In this mid-temperature range, the PL spectra strongly depend on the growth temperature while the terrace-like flat surface is maintained. Fig. 3 shows the detailed PL spectra for films grown in this mid-temperature range. The small difference in growth temperature shown in Fig. 3 causes significant variation in the PL spectra. Only the I_2 line is observed at a growth temperature of 975°C and the acceptor-related I_1 and D-A pair peaks are not seen. Once the growth temperature is increased or decreased from 975°C, the acceptor-related peaks become dominant. This means that the residual acceptors are eliminated for a very narrow range of growth temperature where two-dimensional growth occurs. The best full-width-of half-maximum (FWHM) of the I_2 line is 25 meV at 77K and 9meV at 10K. The best FWHM of the band-edge peak at 3.40eV is 60meV at room temperature.

Samples with a rough surface due to three-dimensional growth at low temperatures show a strong "blue"-band at 2.8eV. A very week I_1 line is also seen. On the other hand, the surface containing cracks or pealing off grown at higher temperatures show a similar "blue" band together with D-A pair recombination. The rough surface and crystal failures both cause deep levels formed by residual acceptors.
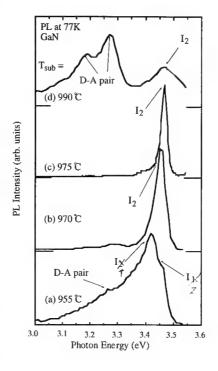

Fig.3 Low temperature (77K) PL spectra of GaN films with terrace-like flat surface grown at (a) 955°C, (b) 970°C, (c) 975°C, (d) 990°C.

Growth at around 975°C is essential to obtain good crystalline quality material without residual acceptors. Since physical cracking and stress appear to create deep level acceptors at higher growth temperature, an appropriate buffer layer which relaxes stress might possibly widen this optimized growth temperature range.

Effect of V/III ratio

Fig. 4 shows the PL spectra for the films grown at various ratios of NH_3 and $GaCl_3$ which is defined as the V/III ratio. The growth was carried out at 975°C so that the effect of the residual acceptors is minimized As shown in Fig. 4, the higher V/III ratio decreases the FWHM of the peak at room temperature. This implies that a higher V/III ratio results in better crystalline quality.
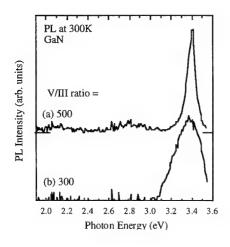
Fig.4 Room temperature PL spectra of GaN films grown at 975°C with V/III ratios of (a) 500 and (b) 300.

CONCLUSION

Photoluminescence of undoped-GaN grown on sapphire by chloride VPE have been investigated for various growth conditions. We observe that the spectra depend strongly on the growth temperatures, apparent growth mode and the corresponding surface morphology. The band-edge peaks from excitons and D-A pair recombination are observed in the terrace-like flat surfaces grown at between 950°C and 1000°C. The strong acceptor-related peaks are eliminated only at around 975°C. Further increasing or decreasing the growth temperature causes rough surfaces which result in "blue"-band emission due to deep acceptor levels. We also find that higher a V/III ratio during the growth reduces the FWHM of the band-edge peak. These PL results suggest that a growth temperature around 975°C and high V/III ratio are essential to obtain the best crystal quality.

ACKNOWLEDGMENTS

REFERENCES

1. S. Nakamura, M. Senoh, N. Iwasa and S. Nagahama, Jpn. J. Appl. Phys. **34**, pp. L797 (1995).
2. S. Nakamura, M. Senoh, S. Nagahama, N. Iwasa, T. Yamada, T. Matsushita, H. Kiyoku and Y. Sugimoto, Jpn. J. Appl. Phys. **35**, pp. L74 (1996).
3. H.P. Maruska and J.J. Tietjen, Appl. Phys. Lett. **15**, pp. 327 (1969).
4. K. Naniwae, S. Itoh, H. Amano, K. Itoh, K. Hiramatsu and I. Akasaki, J. Crystal. Growth **99**, pp. 381 (1990).
5. T. Detchprohm, K. Hiramatsu, H. Amano and I. Akasaki, Appl. Phys. Lett. **61**, pp. 2688 (1992).
6. H. Tsuchiya, T. Okahisa, F. Hasegawa, H. Okumura and S. Yoshida, Jpn. J. Appl. Phys. **33**, pp. 1747 (1994).
7. M. Ilegems, R. Dingle and R.A. Logan, J. Appl. Phys. **43**, pp. 3797 (1972).
8. M. Ilegems and R. Dingle, J. Appl. Phys. **44**, pp. 4234 (1973).
9. J.I. Pankove, J.E. Berkeyheiser and E.A. Miller, J. Appl. Phys. **45**, pp. 1280 (1974).
10. O. Lagerstedt and B. Monemar, J. Appl. Phys. **45**, pp. 2266 (1974).
11. M. Yuri, T. Ueda, H. Lee, K. Itoh, T. Baba ans J.S. Harris Jr., Mat. Res. Soc. Symp. Proc, (1995), to be submitted
12. H.G. Grimmeiss and B. Monemar, J. Appl. Phys. **41**, pp. 4054 (1970).
13. R. Dingle and M. Ilegems, Solid State Commun. **9**, pp. 175 (1971).
14. G. Jacob, M. Boulou and M. Furtado, J. Crystal. Growth **42**, pp. 136 (1977).
15. M. Boulou, M. Furtado, J. Yacob and D. Bois, J. Luminescence **18/19**, pp. 767 (1979).
16. B. Monemar, O. Lagerstedt and H.P. Gislason, J. Appl. Phys. **51**, pp. 625 (1980).
17. J.I. Pankove and J.A. Hutchby, J. Appl. Phys. **47**, pp. 5387 (1976).
18. T. Ogino and M. Aoki, Jpn. J. Appl. Phys. **19**, pp. 2395 (1980).

Vapor Phase Epitaxy of GaN Using Gallium Tri-Chloride and Ammonia

M. Yuri*, T. Ueda*, H. Lee, K. Itoh, T. Baba*, and J.S. Harris, Jr.
Solid State Electronics Lab., CIS 329, Stanford Univ., Stanford, CA 94305-4075
*Electronics Research Lab., Matsushita Electronics Corporation, Osaka 569, Japan

ABSTRACT

GaN films with good crystalline quality are grown on sapphire by atmospheric pressure vapor phase epitaxy using gallium tri-chloride ($GaCl_3$) and ammonia (NH_3). Epitaxial growth is carried out over temperature and V/III-ratio ranges of 800-1000℃ and 100-1000, respectively. Typical growth rate obtained is in the range of 5-20 μm/hr. The films grown below 925℃ typically show three dimensional (island) growth, while above that temperature, continuous films are obtained. Films grown at 975℃ with a V/III ratio > 300 exhibit a smooth surface. XRD analysis shows that the films are single crystal with hexagonal polytype. Strong band-edge photoluminescence is observed with a FWHM of 60 meV at room temperature and 25 meV at 77K. The results indicate that this simple growth technique is effective for growing high quality bulk GaN, which can be used as a substrate for subsequent epitaxy. In order to further improve the surface morphology, a preliminary experiment on GaN growth on a thin GaN buffer layer prepared by gas source MBE is also presented.

INTRODUCTION

The III-V nitride semiconductors have been receiving much attention as they are very promising materials for blue~UV laser diodes. In fact, room temperature pulsed operation of AlGaN/GaN/InGaN laser diodes has been recently demonstrated with the material systems [1].

From the viewpoint of crystal growth, however, lack of lattice-matched substrates has made it difficult to grow high quality GaN. In fact, very high dislocation densities ($>10^9$ cm^{-2}) are commonly observed[2] in GaN films grown on sapphire where the lattice parameter is approximately 14% larger than that of GaN. Furthermore, the large thermal expansion-mismatch between GaN and substrates occasionally causes cracks in the films. In order to circumvent the problem, it is desirable to use un-strained thick GaN as a substrate for the subsequent growth of device structures. While an ideal solution for this would be to use bulk GaN, it is very difficult to obtain large GaN crystals from liquid phase because of the very high equilibrium pressure of nitrogen over the GaN surface [3]. To date, only limited size of such bulk GaN has been obtained [4]. While various substrates which have closer lattice constants to GaN have been explored [5-6], one promising approach is to grow a very thick (over 100μm) GaN film on a lattice-mismatched substrate, most commonly sapphire. For this purpose, hydride vapor phase epitaxy (HVPE) is widely used [7], where NH_3, solid Ga, and HCl are the source materials. Since it is possible to obtain a much higher growth rate with this method than MOCVD or MBE, HVPE is very suitable for preparing thick GaN substrates.

In conventional HVPE, solid Ga placed in the first high-temperature zone reacts with HCl, forming GaCl. GaCl is then transferred to the second high-temperature zone, where the reaction:

$$GaCl(g)+NH_3(g) \rightarrow GaN(s)+HCl(g)+H_2(g) \qquad (1)$$

takes place on the substrate surface. It is therefore necessary to control two high-temperature heating zones; one for Ga metal(~900℃) and the other for substrates (~1000℃). The growth rate depends on these two temperatures as well as the flow rates of HCl and NH_3.

195

We reduced the number of the high-temperature zones from two to one by employing gallium tri-chloride (GaCl$_3$) as the Ga source. Neither solid Ga nor HCl is used in this case. GaCl$_3$ is transferred directly to the hot substrate zone, and reacts with NH$_3$ directly on the substrate surface, producing solid GaN. With this method, only a single high-temperature zone must be controlled. Although the temperature of the GaCl$_3$ needs to be controlled at slightly higher than room temperature to provide a sufficient vapor pressure, doing which is a well-established technique like in MOCVD. Hence this method has potential advantages over conventional HVPE in terms of simplicity of the system and controllability of growth rates.

In this paper, high quality single crystal GaN films are grown on sapphire substrates by chloride VPE. The temperature and III/V ratio dependencies of the crystalline quality are examined and discussed. Room temperature and 77K photoluminescence results are also shown, which indicate the films grown under optimum conditions have good optical properties. Nucleation of GaN on the sapphire substrates is a critical issue and VPE overgrowth of GaN by this method on a gas source MBE (GSMBE)-grown thin GaN is investigated in an attempt to improve surface morphology.

EXPERIMENTAL

Single crystal GaN films are grown on sapphire c-Al$_2$O$_3$ (0001) substrates using the chloride VPE method. The GaCl$_3$ source material (4N+ purity) is kept in a separate quartz vessel at 90℃, where the equilibrium vapor pressure is 19Torr. GaCl$_3$ is then transferred by N$_2$ carrier gas to the substrate region through a nozzle. 100% NH$_3$ is introduced through a separate nozzle in order to prevent pre-reactions with GaCl$_3$ from taking place. The positions of the NH$_3$ and the GaCl$_3$ nozzles are 10mm and 35mm from the substrate, respectively. N$_2$ carrier gas is introduced from the third nozzle placed upstream. The substrate temperature is monitored and controlled by a thermocouple right beneath the quartz substrate holder. The substrate is heated to the growth temperature (T$_g$) under NH$_3$ and N$_2$ flow and held at this temperature for 10 minutes. GaCl$_3$ is then introduced to the reactor to start growth. No low-temperature buffer layer is introduced in the present work. The flow rate ranges of N$_2$(GaCl$_3$ carrier), NH$_3$, and carrier N$_2$ are 0.1~0.3slm, 1.0~2.0slm and 2.0~3.0slm, respectively. The growth is carried out at atmospheric pressure, and the typical growth time is one hour. The V/III ratio is defined by the mole ratio of NH$_3$ to GaCl$_3$, assuming the GaCl$_3$ is fully vaporized in the vessel under the N$_2$ carrier flow.

In order to examine the effect of a buffer layer, a VPE-grown GaN film is formed on a thin GaN layer which is grown on Al$_2$O$_3$ (0001) by GSMBE using dimethyl-hydrazine and solid Ga. The growth temperature for the GSMBE is 750℃, and a 50nm low temperature(550℃) GaN buffer layer is grown prior to the growth of the 0.2μm GaN. A ~10μm thick GaN film is then grown by chloride VPE.

The grown films typically show large non-uniformity across the 10x10mm^2 substrate, especially near the substrate edges due to the nozzle configuration of the present system. We have, however, obtained approximately 5x5mm^2 area of fairly uniform region near the center of each sample. The uniform regions of the films are characterized by optical microscope, cross sectional TEM, X-ray diffraction (XRD), and photoluminescence (PL).

RESULTS AND DISCUSSION

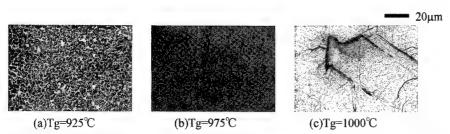Fig. 1 shows the growth temperature dependence of the surface morphology observed

Fig. 1   Typical surface morphology of GaN films for various growth temperatures: (a) 925℃, (b) 975℃, (c) 1000℃. V/III ratio is kept to be 300 for all samples.
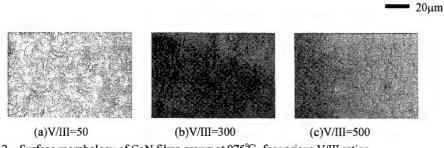

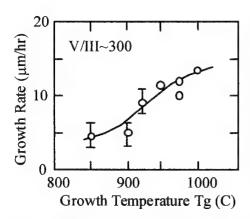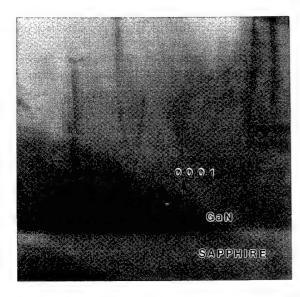Fig. 2   Surface morphology of GaN films grown at 975℃ for various V/III ratios.

Fig. 3   Temperature dependence of the growth rate of GaN. V/III ratio is kept at 300.

through an optical microscope. These samples are grown with a V/III ratio~300, and the thickness of the films are between 10 and 15μm. As shown in the figure, the surfaces typically exhibit 3D island features when T_g is lower than 925℃, while continuous films are obtained above 950℃.   For T_g higher than 1000℃, a high density of cracks and pealing-off are observed. The films with the best surface features are obtained around T_g=975℃. Fig. 2 shows the surface morphology of the films grown at 975℃ for various V/III ratios. No significant change of the surface features is observed over V/III ~ 200, while for V/III ≦ 100, the surface becomes rough, which is similar to the low-temperature grown samples mentioned above.
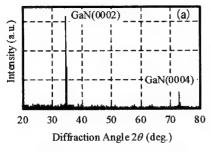
Fig. 3 shows the growth rate as a function of growth temperature. The V/III ratio is kept at 300 for all data shown in this figure. A monotonic increase in growth rate with T_g is observed for the temperature range between 800 and 1000℃. Since the films grown at $T_g <$ 925℃ exhibit

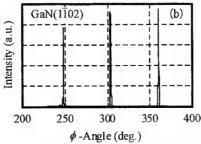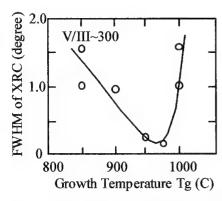Fig. 4   Cross-sectional TEM of the GaN layer grown at 975℃ with V/III ratio of 300.

Fig. 5   XRD patterns of the sample grown at 975℃, V/III=300: (a) 2θ-ω pattern, and (b) ϕ-scan.

3D features, it is hard to define the film thickness precisely.

For a sample grown at 975℃ with V/III = 300, cross sectional TEM is observed as shown in Fig. 4.   The dominant defects in the GaN film are dislocations resulting from the misfit strain induced by the lattice-mismatch between the epilayer and the substrate. The dislocation lines orient themselves irregularly near the interface and then tend to lie close to the [0001] growth direction. Similar behavior of dislocations has been observed in MOCVD-grown GaN with AlN buffer layers [2], although no buffer layer is used prior to the GaN growth in the present samples.
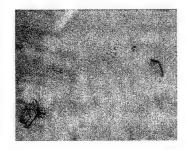
Fig. 5 shows the XRD patterns of the grown film. Only the peaks from hexagonal GaN(0002)-plane at 34.4° and GaN(0004)-plane at 72.7° are observed. Since the thickness of the film is 12μm, no peaks from the Al_2O_3 substrate are detected. Fig. 5(b) gives the in-plane ϕ-scan of the GaN(1$\bar{1}$02) peak. A periodic pattern with a 60-degree spacing is clearly observed, from which it is concluded that the film is single crystal of hexagonal polytype.   Fig. 6 shows

Fig. 6 Growth temperature dependence of the FWHM of X-ray rocking curve of (0002)-GaN. Thickness of the samples ranges between 10 and 15 μm.

Fig. 7 Room temperature (a) and 77K (b) photoluminescence spectra for the sample grown at 975℃ with V/III = 300.

Fig. 8 Surface morphology of chloride VPE-grown sample overgrown on an MBE-prepared 0.2μm-GaN layer. The thickness of the VPE-grown layer is approximately 3μm.

the FWHM of the X-ray rocking curve corresponding to the GaN(0002) peak as a function of the growth temperature. We have obtained a fairly narrow temperature region around 975℃ where the FWHM becomes as small as 0.1 degree. Below this region, the FWHM increases. This is thought to be due to the 3D nature of the growth as described above. For a higher temperature, the FWHM again increases rapidly. We attribute this to the fact that the films are partially pealed off.

Room temperature and 77K PL is performed for the samples. As shown in Fig. 7, strong band edge emission at 3.40eV (RT) and 3.47eV(77K) is dominantly observed for the sample grown at 975℃ with V/III = 300. The FWHMs of the band edge peak at RT and 77K are as small as 60meV and 25meV, respectively, which indicate that the film has good optical properties.   Deep-level related peaks are also seen around 2 eV, which are commonly observed in MOCVD-GaN.   Detailed study of PL will be presented elsewhere.

Although the films grown under optimum conditions showed fairly good crystalline quality in terms of XRD and PL, the surface of the films exhibit terrace-like features as shown in Fig. 1(b), which is not suitable for their use as a substrate for a subsequent growth of device structure. In an attempt to further improve the surface morphology, we carried out chloride VPE of GaN on a thin GaN layer grown on sapphire by GSMBE. T_g and V/III ratio for the chloride VPE growth are 975℃ and 300, respectively, which give the best results as discussed earlier. The resultant surface morphology is shown in Fig. 8, in which it is seen that the surface is improved by introducing the thin GSMBE-grown buffer layer. However, hexagonal features still exist on the surface, which implies that optimization of the buffer layer needs to be done.

CONCLUSIONS

In conclusion, GaN films are epitaxially grown on c-plane sapphire by a simple chloride VPE technique using $GaCl_3$ and NH_3 as the source materials. XRD analysis shows films grown at 975℃ with V/III ratio of 300 have the lowest FWHM of the rocking curve of 0.1 degree. Strong band edge PL is observed for the sample without significant deep-level related long wavelength peaks. The FWHM of the PL peak is 60 meV at room temperature and 25 meV at 77K, which indicates that the film has good optical properties. It is shown that terrace-like features are observed even on the films grown under optimized conditions. A preliminary experiment of growing GaN by this method on a GSMBE-grown thin layer revealed that the surface morphology can be improved by introducing an appropriate buffer layer.

ACKNOWLEDGMENTS

REFERENCES

[1] S. Nakamura, M. Senoh, S. Yamagata, N. Iwasa, T. Yamada, T. Matsushima, H. Kiyoku, and Y. Sugimoto, Jpn. J. Appl. Phys. Part 2, **35**, No. 1B, L74 (1996)
[2] W. Qian, M. Skowronski, M. De Graef, K. Doverspike, L. B. Rowland, and D. K. Gaskill, Appl. Phys. Lett. **66** (10), p.1252 (1995)
[3] J. Karpinski, J. Jun, and S. , J. Crystal Growth, **66**, p.1 (1984)
[4] S. Porowski, J. Jun, M. Bockowski, M. Leszcynski, S. Krukowski, M. Wroblewski, B. Lucznik, and I. Grzegory, Proceedings of the 8th Conference on Semi-Insulating III-V Materials, Warsaw, Poland, 1994, p.61
[5] M. E. Lin, B. Sverdlov, G. L. Zhou, and H. Morokoc, Appl. Phys. Lett., **62**, p.3479 (1993)
[6] A. Kuramata, K. Horino, K. Domen, K. Shinohara, T. Tanahashi, Appl. Phys. Lett., **67**, no.17, p. 2521 (1995)
[7] T. Detchprohm, K. Hiramatsu, K. Itoh, and I. Akasaki, Jpn. J. Appl. Phys, **31**, Part 2, No. 10B, L.1454 (1992)

Part V

Novel Devices and Processing

COMPARISON OF n- AND p-TYPE InGaAs/InP QUANTUM WELL INFRARED PHOTODETECTORS

D.K. Sengupta, J.I. Malin, S.L. Jackson, W. Fang, W. Wu, H.C. Kuo, C. Rowe, S.L. Chuang, K.C. Hsieh, J.R. Tucker, J. W. Lyding, M. Feng, and G.E. Stillman

Department of Electrical and Computer Engineering and Center for Compound Semiconductor Microelectronics, University of Illinois at Urbana-Champaign, Urbana, Il 61801

H.C. Liu
Institute for Microstructural Sciences, National Research Council, Ottawa, Ontario K1A0R6, Canada

ABSTRACT

Over an order of magnitude reduction in dark current was observed for gas-source molecular beam epitaxially (GSMBE) grown, lattice-matched n- and p-type InGaAs/InP quantum-well infrared photodetectors (QWIPs). Peak spectral response at 8.93 and 4.55 μm for n- and p-type QWIPs, respectively, open the possibility of dual-band monolithic integration under identical GSMBE growth conditions.

INTRODUCTION

The processing and epitaxial growth of lattice-matched $In_{0.53}Ga_{0.47}As/InP$ reached maturity as a consequence of applications in optical communications. A four-fold increase in responsivity for n-type InGaAs/InP QWIPs over n-type GaAs/AlGaAs has been reported in the literature [1-2]. In this work, a 30-fold reduction in 77K dark current compared to InGaAs/InP QWIPs reported in the literature is reported. This is attributed to improved InP barrier and interface quality [3]. Furthermore, 4.55 μm detection was observed for novel, narrow well p-type InGaAs/InP QWIPs which, complimented by the high responsivity 8.93 μm n-type InGaAs/InP QWIP, offers the possibility of dual-band monolithically integrated QWIPs [4].

EXPERIMENTAL DETAILS

Epitaxial growth was performed in a modified Perkin-Elmer 430P GSMBE/CBE system. The growth chamber was equipped with a 5000 l/s cryopump and a 2200 l/s turbomolecular pump. Cracked AsH_3 and PH_3 (100%) were used as the group V sources, while elemental solid sources in effusion cells were used for the group III sources. Cracked AsH_3 and PH_3 were injected separately from two independent low-pressure crackers equipped with fast run/vent valves. The switching of AsH_3 and PH_3 was accomplished by the fast run/vent valves in front of each injector. Details of the MBE system and cracker design are reported in Ref. [3]. N- and p-QWIP structure were grown on semi-insulating (001) InP substrates at 500°C. InP was

grown at a rate of 0.59 μm/hr with a PH_3 flow of 2.5 sccm, and latticed-matched $Ga_{0.47}In_{0.53}As$ was grown at 1.05 μm/hr with a AsH_3 flow of 2.5 sccm. Growth chamber pressure with hydride gas flowing was $3X10^{-6}$ Torr as measured by a cold cathode gauge. The pressure reached the gauge baseline value $<10^{-7}$ Torr approximately in 7 seconds after hydride gas flow was switched from the growth chamber into the vent lines. The n-type structure consisted of 20 periods of 60Å Si center doped ($1X10^{18}$ cm^{-3}) $In_{0.53}Ga_{0.47}As$ quantum wells (QWs) and 500Å undoped InP barriers sandwiched between 4000 Å Si doped ($1X10^{18}cm^{-3}$) $Ga_{0.47}In_{0.53}As$ contacts on an InP susbtrate. The p-type structure consisted of 30 periods of 10 Å Be center doped ($3X10^{18}cm^{-3}$) $In_{0.53}Ga_{0.47}As$ quantum wells (QWs) and 500 Å Be doped ($1X10^{17}cm^{-3}$) InP barriers sandwiched between 5000 Å Be doped ($3X10^{18}cm^{-3}$) $In_{0.53}Ga_{0.47}As$ contacts on InP substrate.

Well and barrier widths were confirmed by cross-sectional transmission electron microscopy (TEM). A defect density of $<10^5$ cm^{-2} was observed by plan-view TEM. QW concentration and material quality were confirmed by 77K photoluminescence (PL) and double crystal x-ray diffraction (DCXRD). Cross-sectional scanning tunneling microscopy (STM) was used to charcterize the InGaAs/InP p-type structure with ultra-thin QWs. As shown in Fig. 1, the InGaAs QWs have been measured to be about 4 to 5 monolayers. The InP barriers appear darker than the adjacent InGaAs regions because of the valence band offset. The InGaAs regions also have mottled appearance due to alloy fluctuations. The normal interface (InGaAs grown on InP) is extremely abrupt, while the inverted interface is somewhat rough. Bright spots in the InP barriers are attributed to residual As in the chamber that is incorporated during growth.
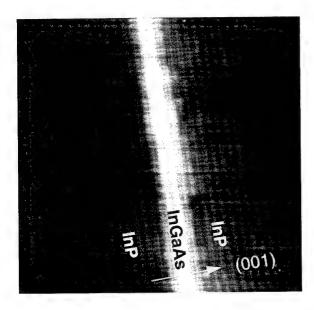

Fig. 1 Cross-sectional scanning tunneling microscopy (STM) of a p-type InGaAs/InP QWIP with about 4 to 5 monolayers within quantum well.

QWIPs were fabricated into 200 μm diameter mesa diodes by chemical etching and either alloyed (400⁰C) Ge/Au/Ni/Au (n-type) or Ti/Pt (p-type) contacts. Devices were polished to 45⁰ (to accommodate selection rules) and indium-bonded to a copper heat sink.

The I-V characteristics (with 300K background and 60 field-of-view) were taken with a HP4145 semiconductor parameter at 82K. The spectral and absolute response at 82K was measured with a Bomem Michelson Interferometer and 1000K blackbody with a filter tuned to the wavelength peak.

RESULTS & DISCUSSION

QWIPs with n-type $In_{0.53}Ga_{0.47}As$ [1] and InP [2] contact layers demonstrated in the literature exhibit different I-V characteristics. Because the InP contact is non-rectifying to the QW active region, the operating voltage is higher (~5-7 V). Our n-type QWIPs (with $In_{0.53}Ga_{0.47}As$ contacts) require the higher biases (~5-7 V), a result of the highly resistive InP barrier layers. The n- and p-type I-V characteristics shown in Fig. 2 demonstrate a three-order of magnitude reduction in dark current at low biases (below 5V) from the QWIP with InP contact layer (the previous $In_{0.53}Ga_{0.47}As$ contact results are at 20K). The sequential resonant tunneling component only obvious for the n-type QWIP at biases > 5V is attributed to the p-type QWIP barrier doping. At operating bias, the dark current is 1mA for both the n-type (-6 V bias) and p-type (-14 V bias) QWIPs. At -6 V bias, the InP QWIP exhibited a 30-fold increase in dark current.

Figs 3 show the spectral response for the n- and p-type QWIP respectively with bias. These QWIPs have a large valence band offset and were designed for the bound-to extended state transition. Hence the n-type QWIP shows a peak response at 8.93 μm whereas the p-type QWIP peaks at 4.55 μm.

At 8.93 μm and -6 V bias, a responsivity of ~ 1A/W is observed from the n-type QWIP which agrees with results in the literature. The improvement over GaAs/AlGaAs QWIPs results from excellent hot electron transport over the InP barriers [1]. As shown in Fig. 4, low responsivities are observed for low biases, and at forward and reverse biases >5V, a sharp increase in responsivity is observed. The phenomena is not nearly as dramatic with the novel p-type QWIP as shown in Fig. 5, however, for which the lower peak responsivity of ~ 15mA/W at -14V is attributed to the heavy hole mass [5]. The more dramatic increase in responsivity with bias for n-type QWIPs results from the onset of sequential resonant tunneling at high biases which is evident in the I-V characteristics [6]. However, despite the lower responsivity in the mid-wavelength infrared (MWIR), the p-type QWIP will benefit from high photon counts.

CONCLUSION

The GSMBE-grown n-type InGaAs/InP QWIP offers responsivity comparable to the GaAs/AlGaAs QWIP and a 30-fold reduction in dark current over previously reported InGaAs/InP QWIPs. Despite its low responsivity, the novel p-type InGaAs/InP QWIP with reduced dark current is capable of normally incident IR illumination [5]. Furthermore, dual-band detection with low dark current (resulting in reduced noise) can be acheived by monolithically integrating n- and p-type InGaAs/InP QWIPs.
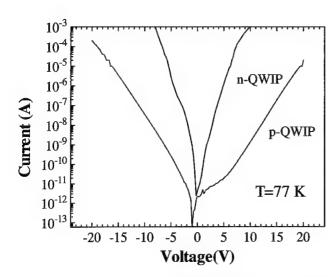
Fig. 2 77 K dark current characteristics with 300K background and 60 field-of-view for n and p-type InGaAs/InP QWIP.
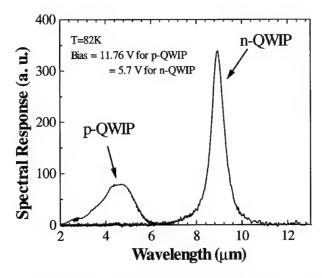

Fig. 3 82K spectral response of n- and p-type InGaAs/InP QWIP.
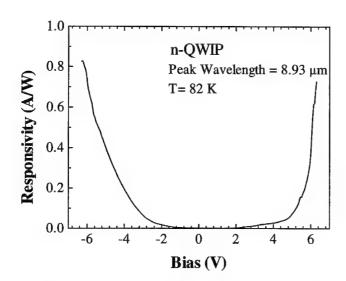
Fig. 4 82K absolute response of a n-type InGaAs/InP QWIP.
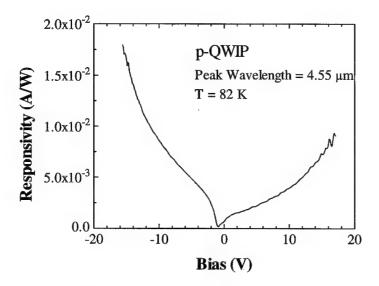
Fig. 5 82K absolute response of a p-type InGaAs/InP QWIP.

ACKNOWLEDGEMENTS

REFERENCES

1. S.D. Gunapala, B.F. Levine, D. Ritter, R. Hamm, and M.B. Panish, Appl. Phys. Lett. **58,** 20224 (1991)

2. J.Y. Andersson, L. Lundqvist, Z. F. Paska, K. Streubel, and J. Wallin, Proc. of SPIE **1762,** 216 (1992)

3. S.L. Jackson, J.N. Baillargeon, A.P. Curtis, X. Liu, J.E. Baker, J.I. Malin, K.C. Hseih, S.G. Bishop, K.Y. Cheng, and G.E. Stillman, J. Vac. Sci. Technol. **B 11,** 1045 (1993).

4. K.L. Tsai, K.H. Cheng, C.P. Lee, K.F. Huang, J.S. Tsang, and H.R. Chen, Appl. Phys. Lett. **62,** 3504 (1993).

5. B.F. Levine, S.D. Gunapala, J.M. Kuo, S.S. Pei, and S. Hui, Appl. Phys. Lett. **59,** 1864 (1991).

6. K.K. Choi, B.F. Levine, C.G. Bethea, J. Walker, and R.J. Malik, Appl. Phys. Lett. **50,** 1814, (1987).

ION IMPLANTATION FOR HIGH PERFORMANCE III-V JFETS AND HFETS

J. C. Zolper, A. G. Baca, M. E. Sherwin*, and J. F. Klem
Sandia National Laboratories, Albuquerque, NM 87185-0603
* present address: Microwave Signal, Inc., 22300 COMSAT Dr., Clarksburg, MD 20871

ABSTRACT

Ion implantation has been an enabling technology for the realization of many high performance electronic devices in III-V semiconductor materials. We report on advances in ion implantation processing technology for application to GaAs JFETs, AlGaAs/GaAs HFETs, and InGaP or InAlP-barrier HFETs. In particular, the GaAs JFET has required the development of shallow p-type implants using Zn or Cd with junction depths down to 35 nm after the activation anneal. Implant activation and ionization issues for AlGaAs will be reported along with those for InGaP and InAlP. A comprehensive treatment of Si-implant doping of AlGaAs is given based on the donor ionization energies and conduction band density-of-states dependence on Al-composition. Si and Si+P implants in InGaP are shown to achieve higher electron concentrations than for similar implants in AlGaAs due to the absence of the deep donor (DX) level. An optimized P co-implantation scheme in InGaP is shown to increase the implanted donor saturation level by 65%.

INTRODUCTION

Ion implantation has been widely used in electronic and photonic devices based on compound semiconductors. Generally, the implantation process serves one of three functions. First, selective area implant doping is used to form low resistance contact regions in Field Effect Transistors (FETs), Heterojunction Bipolar transistors (HBTs), or lasers [1-5]. Selective area doping is also used in FETs to form precisely controlled channel or lightly doped drain (LDD) regions [6]. Second, implantation is employed to form locally high resistance regions for inter-device isolation such as in integrated FET circuits or for current guiding in lasers [7-12]. Third, ion implantation can be used to promote local area inter-diffusion or mixing of the host atoms to alter the local bulk properties of the semiconductor [13].

In this paper we focus on specific examples of using ion implantation for controlled, selective area doping. We begin by highlighting the key features in achieving high performance ion implanted GaAs Junction Field Effect Transistors (JFETs) that rely on shallow, abrupt p-type doping profiles as well as abrupt channel doping. The utility of heavy ion implantation (Zn and Cd) along with the co-implantation of P will be presented.

In a second area of study, we address the issues associated with implant doping of advanced ternary compound semiconductors materials such as AlGaAs, InGaP, and InAlP that are potential barrier layers for heterostructure field effect transistors (HFETs). The ability to selectively dope these barrier layers will enable improved HFET designs. For AlGaAs we report on a comprehensive study of Si implant doping over a wide Al-compositional range from 0 to 70 %. This enables us to separate fundamental donor ionization effects from implant activation phenomena. The results are explained with a ionization energy and density-of-states treatment that will have application to epitaxial doping as well.

For InGaP and InAlP, we report on the donor saturation level versus Si-implant dose and show that this level can be increased in InGaP by an appropriate P co-implantation scheme. The Si donor ionization level in these phosphide materials is also estimated from variable temperature Hall measurements and compared to that of AlGaAs with a similar bandgap.
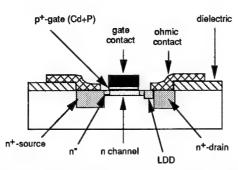
FIG 1. Schematic of all ion implanted, self-aligned, GaAs JFET.

P-TYPE IMPLANTATION DOPING FOR GaAs JFETs

Figure 1 shows a schematic representation of a self-aligned GaAs JFET where all doping is done by ion implantation [5]. This structure overcomes several of the traditional short-comings of non-self-aligned or diffused junction JFETs such as an increased gate-to-source capacitance (C_{GS}) due to the p/n junction gate and gate length broadening during the p^+ gate formation. The attributes of this structure have been well documented elsewhere for devices with gate lengths down to ~0.7 µm [14-16]. To extend this structure to sub-half-micron gate lengths, both the vertical and lateral doping profile must be modified. For the vertical profile, the p^+-gate region must be made very shallow while still maintaining high doping at the surface to insure an ohmic gate contact. The channel profile also becomes more critical at short gate lengths with abrupt doping being required to reduce short channel effects and achieve good carrier confinement. The lateral n-type doping profile must also be modified for short gate operation to minimize hot carrier effects and impact ionization on the drain side of the gate to reduce short channel effects and improve the breakdown voltage. This is accomplished with the use of lightly doped regions on both sides of the gate (n") defined by dielectric sidewall spacers and an additional asymmetric lightly doped region on drain side of the gate (lightly doped drain, LDD). These regions are represented in Fig. 1. In this paper we discuss experimental improvements to the vertical p-type doping profile, in particular, the p^+-gate implant. Optimization of the lateral profile will be presented elsewhere [17].

While initial work on the JFET structure in Fig. 1 employed Mg-implantation to form the p^+-gate region later generations demonstrated the utility of using the a heavier acceptor species such as Zn [15, 18]. That work clearly showed that abrupt, shallow p^+-regions can be formed with Zn-implantation when a P co-implantation is included. The effect of the P co-implantation can be explained via two possible mechanisms, both of which increase the probability of the Zn-ion to occupy the column III sublattice and act as an acceptor [18]. Once the Zn is substitutional on a Ga-site its diffusion coefficient is dramatically reduced compared to the fast diffusing interstitial Zn as exists in an external source Zn-diffusion. The mechanisms both stem from the realization that as-implanted material will consist of both Ga and As vacancies and interstitials due to the radiation damaged introduced in the implantation process. The first possible mechanism is that the P-ion will fill As-vacancies thereby forcing the formation of excess Ga vacancies which the Zn can occupy [19]. Second, the P-ions may tie up interstitial Ga thereby rebuilding the lattice and reducing the competition between the host column III-elements and implanted Zn atoms for occupation of the vacant Ga-sites [20].

The same discussion on the effect of P co-implantation can also be extended to Cd implantation in GaAs. Cd will form still shallower implanted profiles than Zn (for the same energy) due to its heavier mass (120 versus 64 AMU). Figure 2 shows secondary ion mass spectroscopy (SIMS) profiles for the Cd-gate implant (45 keV, $3x10^{14}$ cm^{-2}) either alone or with a P co-implant ($^{62}P_2$: 40 keV, effective ^{31}P dose of $6x10^{14}$ cm^{-2}). The use of P along with Cd is seen to markedly reduce the in-diffusion of Cd. The reduction in diffusion is critical to achieving the required abrupt p/n junction gate. Using a Cd-implanted gate, a p/n junction depth of 35 nm has been demonstrated after the 830 °C activation anneal [16].
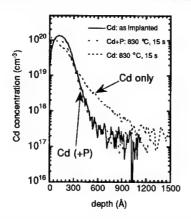

Fig 2. SIMS profiles for Cd as-implanted (45 keV, $3x10^{14}$ cm^{-2}) and annealed (830 °C, 15 s) with and without a P co-implant ($^{62}P_2$: 40 keV, effective P dose of $6x10^{14}$ cm^{-2}). The P co-implantation is seen to dramatically reduce the redistribution of Cd during the anneal.
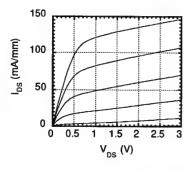
Fig 3: I_{DS} versus V_{DS} for a 0.7 x 50 µm^2 Cd-gate JFET.
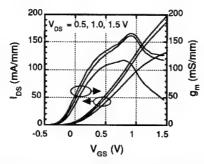
Fig 4: I_{DS} and g_m versus V_{GS} for a 0.7 x 50 µm^2 Cd-gate JFET.

Figure 3 and 4 show the DC performance a 0.7 x 50 µm^2 Cd-gate JFET. A saturation current of 130 mA/mm and transconductance of 165 mS/mm was realized at V_{DS} = 1.5 V and V_{GS} = 1 V. This same device had a unity current cutoff frequency (f_t) of 26 GHz and a maximum oscillation frequency (f_{max}) of 42 Ghz [16]. These frequency metrics are comparable to a similar gate length GaAs MESFET; however, the JFET has a 0.4 to 0.5 V

higher gate turn-on voltage [V_{GS}(on) ~ 1V] than the MESFET [V_{GS}(on) ~ 0.55 V] which will significantly reduce power consumption.

Si-IMPLANTATION IN AlGaAs

500 nm thick undoped AlGaAs layers were grown at 590 °C in a Varian Gen II MBE reactor on semi-insulating (100) GaAs substrates. A 200 nm undoped GaAs buffer was grown prior to the AlGaAs layer and a 5 nm GaAs cap layer was grown on top of the AlGaAs to inhibit oxidation. This MBE system has been used to grow high mobility AlGaAs/GaAs two dimensional electron gas structures with 77 K mobilities in excess of 10^6 cm^2/Vs demonstrating the high quality of the AlGaAs/GaAs material grown in this system [21]. ^{29}Si-implants were performed in a non-channeling direction at an energy of 100 keV at a dose of either 5.6×10^{12} or 2.8×10^{13} cm^{-2}. These doses are in the range used for FET channel and LDD formation or source/drain formation, respectively. Beam currents were kept below 0.1 μA/cm^2 to minimize sample heating and in-situ annealing. The estimated ion peak range is at 100 nm from the surface with a corresponding peak concentration of ~1.8×10^{18} cm^{-3} for the higher dose samples. This concentration level is in the range where Si doping starts to saturate in GaAs [22]. Annealing was performed for 15 s in flowing Ar in a SiC coated graphite susceptor that had been precharged with As [23]. Room temperature and variable temperature (T = 77 to 400 K) Hall measurements were done using Van der Pauw Hall samples with In/Sn contacts alloyed at the corners of each sample at 400 °C for 1 min.

Figure 5 shows n_s versus %AlAs for the samples annealed at 900 °C. This temperature was determined to yield a maximum value of n_s for this implant dose. n_s is seen to be relatively constant for a given dose out to 20% AlAs, dramatically decreases at 35% AlAs, and then increases at the higher Al-fractions (50 and 70% AlAs). The reason for these variations will be discussed in more detail shortly.
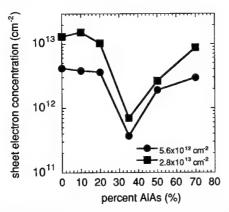

Fig 5. Sheet electron density versus %AlAs for AlGaAs implanted with Si at 100 keV for the two doses shown. The samples were annealed at 900 °C for 15 s.

By doing variable temperature Hall measurements on the high dose sample from Fig. 5, the apparent donor ionization energy (E_d) can be estimated assuming:

$$n_s \propto \exp\left(\frac{-E_d}{kT}\right) \tag{1}$$

The apparent ionization energy levels are listed in Table I, along with η_{eff}. Our values of E_d agree well with those reported for epitaxial Si-doped AlGaAs [24]. The 35 and 50% samples are seen to have similar ionization energy levels near 160 meV while the 70% sample has two levels at 86 and 55 meV. The two levels in the 70% sample correspond to the deep DX level (86 meV) and the hydrogenic donor level (55 meV) corresponding to different local Al and Ga environments about the Si atoms. For the 35 and 50% samples the free electrons all freeze-out into the deep DX level and the shallow donor level is not seen. Since the ionization energies are similar in the 35 and 50% samples, the ionization energy levels alone do not explain the effective activation efficiency dependence on Al-fraction shown in Fig 5. That is, based solely on the ionization energy, the 35 and 50% samples should both have similarly low activation but this is seen not to be the case from Table I.

Table I: Summary of ionization energies and effective activation efficiency of Si-implanted AlGaAs for the two doses studied.

%AlAs	apparent ionization energy, E_d (meV)	$\eta_{eff}{}^a$ $\phi =$ 5.6x10^{12} cm^{-2}	$\eta_{eff}{}^a$ $\phi =$ 2.8x10^{13} cm^{-2}
0	3.2	74.3	46.8
10	4.3	67.9	54.6
20	9.2	64.3	36.8
35	162	6.6	2.5
50	155	34.1	9.5
70	86, 55	52.8	31.1

$^a\eta_{eff} = (n_s/\phi) \times 100$

Figure 6 shows the dependence of the conduction band density-of-states in AlGaAs versus %AlAs based on the expression given below [25]:

$$N_c \equiv 2\left(\frac{2\pi m_{de}kT}{h^2}\right)^{3/2} M_c \qquad (2)$$

where M_c is the number of equivalent minima in the conduction band and m_{de} is the density-of-states effective mass given by

$$m_{de} = (m_e^\Gamma m_e^X m_e^L)^{1/3} \qquad (3)$$

where m_e^Γ, m_e^X, and m_e^L are the effective electron mass in each of the energy bands and vary with Al-composition as follows [26]:

$$m_e^\Gamma = 0.067 + 0.83x \qquad (4a)$$

$$m_e^X = 0.32 - 0.06x \qquad (4b)$$

$$m_e^L = 0.11 + 0.03x \qquad (4c)$$

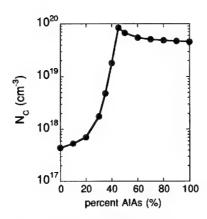Other terms in Eqn 2 have their usual meaning.

Fig 6. Conduction band density-of-states versus %AlAs for AlGaAs calculated using Eqn 2.

The free electron density (n) can then be expressed as:

$$n = N_c \exp\left(\frac{-(E_c - E_f)}{kT}\right) \qquad (5)$$

where E_c is the conduction band minimum energy. The position of the Fermi level (E_f) can be solved for from the following expression for the density of ionized donors:

$$N_d^+ = N_d \left[1 - \frac{1}{1 + \frac{1}{g}\exp\left(\frac{E_d - E_f}{kT}\right)} \right] \qquad (6)$$

assuming the implanted layer thickness is equal to two standard deviations of the profile (t_{imp} = two implant straggles = $2\Delta R_p$) and N_d = (implanted dose)/t_{imp} . g is the electron ground state degeneracy and is equal to 2. E_d is the donor ionization energy listed in Table I. We further assume $N_d \gg N_a$ and take the density of ionized donors to be equal to the measured sheet electron concentration divided by t_{imp}.

Figure 7 is a plot of calculated n from Eqn 5 and measured n ($n=n_s/t_{imp}$) versus %AlAs for the high dose samples at 300 K. The trend of electron concentration versus %AlAs, particularly the pronounced minima at 35% AlAs, is consistent between the calculated values and measured data. However, the lack of absolute agreement between the theory and experiment is up to an order-of-magnitude and has several possible origins. First, as already stated, Eqn 5 is only an approximation that does not account for compensation effects. Second, previous work on epitaxial AlGaAs has shown the difficulty in achieving absolute agreement between a theoretical density-of-states treatment of electron concentrations and the measured Hall concentration even when a full charge balance description is employed that includes acceptor compensation [27]. In that work a difference of an order-of-magnitude was reported between theory and Hall data. The lack of agreement is likely the result of the complex band structure of AlGaAs. Third, the 0, 10 and 20% samples will be degenerately doped since N_c is only ~$7x10^{17}$ cm^{-3} at 20% AlAs. Therefore, Eqn 6 does not yield the correct Fermi level position. Fourth, for implanted material several additional factors can be expected to affect the electron profile. For example, since the electron distribution is not uniform the mobility and compensation ratio is expected to vary throughout the profile. The Hall measurement also will only yield an average value for electron concentration and mobility that

at best can be treated with a two band conduction model but in practice is not readily separated into its component parts. Finally, the defects generated during the implantation process which can act as either compensating acceptors or as scattering centers that degrade the electron mobility are most likely not the same in the different Al composition samples. Therefore, it is not clear that assuming a set compensation ratio over the entire compositional range is valid or useful.
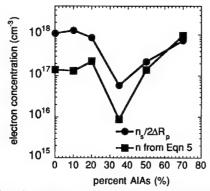

Fig 7. Calculated (based on Eqns 5 and 6) and measured electron concentration versus %AlAs for AlGaAs implanted with Si at an energy of 100 keV and a dose of 2.8×10^{13} cm^{-2}.

Despite the shortcomings to the theory just discussed, the general variation in electron concentration evident in Fig. 5 can be qualitatively explained by the combined ionization energy and density-of-states treatment. We feel this treatment, although not absolute, is the most appropriate approach for explaining the Si-implantation results in AlGaAs.

Si AND Si+P IMPLANTATION IN InGaP AND InAlP

We now turn to Si-implantation doping of InGaP and InAlP. $In_{0.5}Ga_{0.5}P$ and $In_{0.5}Al_{0.5}P$ epitaxial layers lattice matched to GaAs have been employed as replacement materials for AlGaAs in semiconductor lasers, heterojunction bipolar transistors (HBTs), and heterostructure field effect transistors (HFETs) [28-32]. InGaP is of interest because it does not suffer from the deep donor (DX) level associated with Al-containing materials while InAlP (E_g = 2.3 eV for x=0.5) is attractive due to its higher bandgap than $Al_xGa_{1-x}As$, even for x=1 [30,33]. While initial work in these materials focused mostly an laser and HBT applications, recent progress has been made in HFETs [34]. While HFETs are particularly suited to the application of ion implantation doping to reduce the device access resistance, there are a limited number of reports on ion implantation doping of InGaP and InAlP. Ion implantation doping of these materials can be expect to play an enabling role in advanced transistor designs as has been the case for more mature semiconductor technologies based on Si and GaAs. Although n-type ion implantation doping of InGaP [35] and InAlP [36] with Si has been reported, further work is needed to optimize Si-implantation in these materials.

$In_{0.5}Ga_{0.5}P$, $In_{0.5}Al_{0.5}P$, and $In_{0.5}Ga_{0.25}Al_{0.25}P$ layers were grown at 640 °C by metalorganic chemical vapor deposition (MOCVD) on (100) semi-insulating GaAs in an Emcore rotating disk reactor. The source gases were trimethylgallium, trimethlyindium, arsine, and phosphine. X-ray measurements confirmed that the films were lattice matched to the GaAs substrate within 0.22% for InGaP and 0.4% for the Al-containing films. ^{29}Si implants were performed in a nonchanneling direction at 90 keV at one of four doses (1, 5, 10, or 50×10^{13} cm^{-2}). P co-implants were done at 100 keV to overlay the Si-profile and at five multiples of the Si-dose (0, 0.5, 1.0, 1.5, or 2.0). After implantation, samples were annealed

in a SiC coated graphite susceptor in flowing Ar for 15 s at the prescribed temperature ± 5°C. Prior to heating a three cycle pump/purge sequence is employed to reduce background oxygen levels. Room temperature and variable temperature Hall measurements were performed in a van der Pauw configuration with In/Sn or In/Pb contacts alloyed at the corners of the samples at 400 °C for 1 min.

Figure 8 shows the sheet electron concentration (n_s) versus annealing temperature for Si-implanted InGaP at four doses. n_s is seen to reach a maximum value of 1.33×10^{13} cm^{-2} in the range of 850 to 900 °C for a dose of 5×10^{13} cm^{-2} which is consistent with the earlier results of Si-implanted InGaP [35]. At higher doses self compensation starts to occur as Si demonstrates an amphoteric behavior. As will be demonstrated next, this saturation level can be increased by the application of P co-implantation.

Figure 9 shows the sheet electron concentration (n_s) versus annealing temperature for Si-implanted InAlP at three doses (5, 10, or 50×10^{13} cm^{-2}). InGaAlP implanted at a dose of 5×10^{13} cm^{-2} had n_S values after annealing almost identical to the same dose InAlP samples. For the lowest dose the samples were highly resistive for annealing temperatures below 750 °C and then display less than 4% effective activation out to 900 °C. n_S in the higher dose InAlP samples continues to increase out to 900 °C to a maximum of 9.6×10^{12} cm^{-2} but still with an effective activation efficiency of only ~10%. The lack of data for the lowest dose samples below 850 °C results from the difficulty in forming reliable Hall contacts to these high resistance samples.
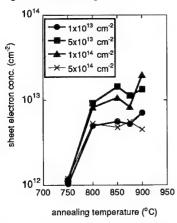

Fig 8. Sheet electron concentration versus annealing temperature for 90 keV Si-implanted InGaP at the doses shown.
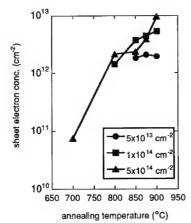
Fig 9. Sheet electron concentration versus annealing temperature for 90 keV Si-implanted InAlP at the doses shown.

Figure 10 shows the change in n_s versus P co-implantation dose normalized to the Si-dose for two Si-doses in InGaP and one dose in InAlP. These samples were all annealed at 900 °C for 15 s. Although n_s of the low dose InGaP samples does not change significantly with P co-implantation over the P-dose range studied, the InGaP material implanted with a dose of 5×10^{13} cm^{-2} demonstrates a dramatic increase in n_s for a P dose of 2.5×10^{13} cm^{-2} (0.5 times the Si-dose) while the InAlP shows an increase for a P-dose 1.5 times the Si-dose. The InAlP sample with 1.5xP has a 35% increase in n_s but this still only corresponds to ~5% effective activation efficiency. The reason for this low activation will be addressed later. The

InGaP sample with 0.5xP has a 65% increase in n_s from the sample without P which corresponds to 44% activation in the co-implant sample. The decrease in n_s at higher P-doses can be explained by local deviation of stoichiometry due to excess P or to the additional implant damage not being completely removed at the higher doses. The increase in n_s at 0.5xP corresponds to a 41% reduction in the sheet resistance from 530 to 310 $\Omega/\square$. Such a reduction will have a dramatic effect on the performance of a FET that incorporates a InGaP barrier layer and Si-implantation doping in the source and drain regions. The improvements seen here for n_s in InGaP are slightly higher than that seen for Si/P implants in GaAs (~50%) [37] and InP (~30%) [38].
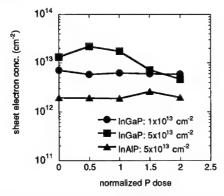

Fig 10. Sheet electron concentration versus P co-implant dose normalized to the Si-implant doses listed for InGaP and InAlP. The samples where annealed at 900 °C for 15 s.

The effect of the P co-implantation can be explained via the same two possible mechanisms discussed above for P co-implants with Zn or Cd with the additional consideration of three host elements. In addition, since the host elements of InGaP and InAlP have significantly different atomic masses, as compared to GaAs where the elements are similar, local stiochiometry variations will exist in the crystal after implantation due to the different amount of recoil of each element. The P-implantation will therefore also help to restore the local crystal stiochiometry.
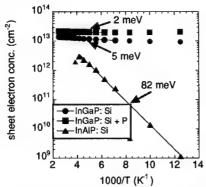

Fig 11. Arrhenius plot of the sheet electron concentration for InGaP implanted with Si-only or with Si+P(0.5xSi) and InAlP implanted with Si-only. The Si dose is 5×10^{13} cm^{-2}. The estimated donor ionization energies are listed on the figure.

Finally, the Si-donor apparent ionization energies were estimated from the Arrhenius plot in Fig. 11 for InGaP and InAlP. Both the InGaP implanted with Si-only and Si+P are seen to have shallow donor levels in the range of 2-5 meV. In contrast, the InAlP sample has an estimated ionization energy level of ~80 meV that will limit the number of ionized donors at room temperature to ~4.5% of the active Si-donors. This means the Si/1.5xP InAlP sample in Fig. 10 has effectively 100% Si-activation on column III sites but with only ~5% ionized donors at room temperature. The results for InGaP are particularly important when compared to Si-implanted AlGaAs with the same energy gap at 35% AlAs. Si-implantation in $Al_{0.35}Ga_{0.64}As$ is limited by the high donor ionization energy (~160 meV) associated with the DX level and relatively low conduction band density-of-state at this composition [39]. Therefore, InGaP is extremely attractive as an alternative to AlGaAs in n-type doped structures whether they are formed by implantation or epitaxially grown due to the shallow donor level. InAlP, on the other hand, will behave more like AlGaAs, although with a somewhat shallower donor level.

CONCLUSION

In conclusion, we have presented results on Cd-implantation in GaAs to achieve very shallow p$^+$-regions for short gate JFETs. Using this approach junction depths of 35 nm have been achieved. A comprehensive study of Si-implantation doping in AlGaAs was also presented with the results explained based on the ionization energy and the conduction band density-of-states dependence on Al-composition. This treatment qualitatively explains why a strong minima is seen at 35% AlAs in the measured electron density. Finally, we have reported on the activation properties of Si-implanted InGaP and InAlP. An optimum dose P co-implantation was shown to increase the donor saturation level by 65% in InGaP and 35% in InAlP. The Si-donor ionization level was shown to be very shallow in InGaP while it is estimated to be ~80 meV in InAlP due to the existence of a DX level. This work improves the understand of ion implantation doping in these materials and will enable continued advances in ion implanted compound semiconductor devices.

REFERENCES

[1] K. Daoud-Ketata, C. Dubon-Chevallier, and C. Besombes, IEEE Trans. Elec. Dev. **8**, 205 (1987).

[2] S. J. Pearton, F. Ren, P. W. Wisk, T. R. Fullowan, R. F. Kopf, J.-M. Kuo, W. S. Hobson, and C. R. Abernathy, J. Appl. Phys. **62**, 698 (1991).

[3] J. P. de Souza and D. K. Sadana, IEEE Trans. Elec. Dev. **39**, 166 (1992).

[4] M. Feng and J. Laskar, IEEE Trans. Elec. Dev. **40**, 9 (1993).

[5] J. C. Zolper, A. G. Baca, R. J. Shul, A. J. Howard, D. J. Rieger, M. E. Sherwin, M. L. Lovejoy, H. P. Hjalmarson, B. L. Draper, J. F. Klem, and V. M. Hietala, IEEE Trans. Elec. Dev, **41**, 1078 (1994).

[6] A. I. Akinwanda, K. L. Tan, C. H. Chen, and P. J. Vold, IEEE Elec. Dev. Lett. **9**, 275 (1988).

[7] D. C. D'Avanzo, IEEE Trans. Elec. Dev. **29**, 1051 (1982).

[8] F. Ren, S. J. Pearton, W. S. Hobson, T. R. Fullowan, J. Lothian, and A. W. Yanof, Appl. Phys. Lett. **56**, 860 (1990).

[9] J. C. Zolper, A. G. Baca, and S. A. Chalmers, Appl. Phys. Lett. **62**, 2536 (1993).

[10] S. J. Pearton, Mat. Sci. Rep. **4**, 313 (1990).

[11] M. Orenstein, N. G. Stoffel, A. C. Von Lehmen, J. P. Harbiunson, and L. T. Florez, Appl. Phys. Lett. **59**, 31 (1991).

[12] K. L. Lear, R. P. Schneider, K. D. Choquette, S. P. Kilcoyne, J. J. Figiel, and J. C. Zolper, IEEE Photonic Tech. Lett. **6**, 1053 (1994).

[13] D. G. Deppe and N. Holonyak, Jr. J. Appl. Phys. **64**, R93 (1988).

[14] J. C. Zolper, M. E. Sherwin, A. G. Baca, R. J. Shul, J. F. Klem, and V. M. Hietala, IEEE Elec. Dev. Lett. **15**, 493 (1994).

[15] M. E. Sherwin, J. C. Zolper, A. G. Baca, R. J. Shul, A. J. Howard, D. J. Rieger, J. F. Klem, and V. M. Hietala, IEEE Elec. Dev. Lett. **15**, 242 (1994).

[16] J. C. Zolper, A. G. Baca, M. E. Sherwin, and R. J. Shul, Elec. Lett. **31**, 923 (1995).

[17] J. C. Zolper, A. G. Baca, V. M. Hietala, R. J. Shul, and M. E. Sherwin, submitted to Device Research Conf. 6/96.

[18] M. E. Sherwin, J. C. Zolper, A. G. Baca, T. J. Drummond, R. J. Shul, A. J. Howard, D. J. Rieger, R. P. Schnieder, and J. F. Klem, J. Elec. Mater. **23**, 809 (1994).

[19] G. Landgren and W. H. van Berlo, J. Appl. Phys. **63**, 2783 (1989).

[20] K. K. Patel and B. J. Sealy, Appl. Phys. Lett. **48**, 1467 (1986).

[21] J. F. Klem, private communication.

[22] S. J. Pearton, J. Mod. Phys. B **7**, 4687 (1993).

[23] S. J. Pearton, A. Katz, and M. Geva, J. Appl. Phys. **68**, 2482 (1990).

[24] N. Chand, T. Henderson, J. Klem, W. T. Masselink, R. Fisher, Y. C. Chang, and H. Morkoç, Phys. Rev. B **30**, 4481 (1984).

[25] S. M. Sze, <u>Physics of Semiconductor Devices</u>, 2nd edition, (John Wiley, New York, NY, 1981) pp. 17- 24.

[26] S. Adachi, J. Appl. Phys. **58**, R1 (1985).

[27] S. P. Svensson and A. W. Swanson, J. Appl. Phys. **59**, 2870 (1986).

[28] H. Asahi, Y. Kawamura, and H. Nagai, J. Appl. Phys. **54**, 6958 (1983).

[29] K. Kobayashi, I. Hino, A. Gomyo, S. Kawata, and T. Suzuki, IEEE J. Quantum Electron. **23**, 704 (1987).

[30] J. H. Quigley, M. J. Hafich, H. Y. Lee, R. E. Stave, and G. Y. Robinson, J. Vac. Sci. Technolo. B **7**, 358 (1989).

[31] D. P. Bour, J. R. Shealy, G. W. Wisks, and W. J. Schaff. Appl. Phys. Lett. **50**, 615 (1987).

[32] J. S. Yuan, M. T. Tsai, C. H. Chen, R. M. Cohen, and G. B. Stringfellow, J. Appl. Phys. **60**, 1346 (1986).

[33] S. Adachi, J. Appl. Phys. **63**, 64 (1988).

[34] K. Wantanabe, F. Hyuga, H. Yamazaki, and T. Nittono, J. Appl. Phys. **78**, 5939 (1995).

[35] S. J. Pearton, J. M. Kuo, F. Ren, A. Katz, and A. P. Perley, Appl. Phys. Lett. **59**, 1467 (1991).

[36] S. J. Pearton, W. S. Hobson, J. M. Kuo, H. S. Luftman, A. Katz, and F. Ren, Appl. Phys. Lett. **60**, 1117 (1992).

[37] F. Hyuga, H. Yamazaki, K. Wanatabe, and J. Osaka, Appl. Phys. Lett. **50**, 1592 (1987).

[38] A. Dodabalapur and B. G. Streetman, J. Elec. Mat. **18**, 65 (1989).

[39] J. C. Zolper, J. F. Klem, A. G. Baca, M. E. Sherwin, M. J. Hafich, and T. J. Drummond, J. Appl. Phys., submitted 2/96.

CHARACTERIZATION OF THE SOLID-PHASE EPITAXIAL GROWTH OF AMORPHIZED GaAs WITH IN-SITU ELECTRON MICROSCOPY

K. B. Belay[*], M. C. Ridgway[*] and D. J. Llewellyn[**]
[*]Department of Electronic Materials Engineering, Research School of Physical Sciences and Engineering, The Australian National University, Canberra, Australia.
[**]Electron Microscope Unit, Research School of Biological Sciences, The Australian National University, Canberra, Australia.

ABSTRACT

The influence of non-stoichiometry on the solid-phase epitaxial growth of amorphized GaAs has been studied with in-situ Transmission Electron Microscopy (TEM). Ion-implantation has been used to produce microscopic non-stoichiometry via Ga and As implants and macroscopic non-stoichiometry via Ga or As implants. It has been demonstrated that amorphous GaAs recrystallizes into a thin single-crystal layer and a thick heavily twinned layer. Video images of the recrystallization process have been quantified for the first time to study the velocity of the crystalline/amorphous (c/a)-interface as a function of depth and ion species. Regrowth rates of the single crystal and twinned layers as functions of non-stoichiometry have been calculated. The phase transformation is rapid in Ga-rich material. In-situ TEM results are consistent with conventional in-situ Time Resolved Reflectivity, ex-situ Rutherford Backscattering Spectroscopy and Channelling measurements and ex-situ TEM.

INTRODUCTION

Considerable work [1,2] has been devoted to the study of the recrystallization processes in ion-implanted semiconductors to investigate the annealing of amorphized layers. In the temperature range of 200-400ºC, the Solid-Phase Epitaxial Growth (SPEG) of GaAs yields recrystallized layers with a high density of implantation induced residual defects [1]. The kinetics of SPEG of GaAs have been previously studied using in-situ Time Resolved Reflectivity (TRR) measurements [1]. The influence of ion dose or alternatively the effect of microscopic and macroscopic non-stoichiometry on the SPEG of GaAs have been discussed in reports preceding the present one [3,4]. Microscopic and macroscopic non-stoichiometry are obtained by implanting Ga and/or As into GaAs, respectively. In microscopic non-stoichiometry, the chemical disorder is localized and the one-to-one ratio of the constituent atoms is maintained in the bulk. In macroscopic non-stoichiometry, the one-to-one ratio of the constituent atoms is not maintained. In the case of Ga-rich non-stoichiometry, the increase in rate of the phase transformation was dramatic. This startling observation inspired us to investigate further the SPEG of GaAs using in-situ Transmission Electron Microscopy (TEM) to complement the conventional approaches namely, in-situ TRR, ex-situ Rutherford Backscattering Spectroscopy and Channelling (RBS/C) and ex-situ TEM. For the present report, the SPEG of amorphized GaAs has been recorded with in-situ TEM using the JEOL 2000 FX at the Australian Nuclear Science and Technology Organization. The dynamic events in the video have been quantified. Pertinent results on the SPEG of the thin specimens appropriate for TEM analysis have been compared with the traditional bulk studies and are shown to be consistent.

EXPERIMENT

To investigate the kinetics of the SPEG of GaAs, undoped semi-insulating liquid-encapsulated Czochralski (100) GaAs substrates were implanted and amorphized as described elsewhere [3]. Cross sectional TEM samples were prepared as follows: 3x1 mm sections were cut across the GaAs samples in the desired [011] orientation for imaging. Pieces were glued together and mechanically polished to a thickness < 200 μm. A disc of 3 mm was cut from the glued pieces. The disc was dimpled on both sides, yielding a thin layer of ~ 20 μm thickness. This was then milled to electron transparency by an ion-beam miller with the sample maintained at ~ -196°C. A double-tilt holder with a hot stage was used to anneal the sample in-situ. The annealing temperature 260°C was attained in two steps. In the first step, it was ramped to 200°C at the rate of ~ 0.7°C/sec. At this temperature the growth rate is negligible. In the second step, the temperature was ramped to 260°C at the rate of ~ 1°C/sec. The dynamic events during the regrowth process were recorded on video. The overall magnification of the image displayed on the video monitor was 3.75×10^5. Image contrast was enhanced by use of a digital edge-filter and the signal-to-noise ratio was enhanced by real-time averaging of ~ 25 video frames. The video recording was reduced to still frames and images were captured and stored using a quick imaging technique. The contrast of this captured image was enhanced further and was analysed quantitatively. Experimental results obtained by in-situ TRR, ex-situ RBS/C and ex-situ TEM [3] were used to verify the consistency of the in-situ TEM results.

RESULTS AND DISCUSSION

The regrown material in the annealed sample consisted of a thin single crystal layer bordered by a thick heavily twinned layer as shown in figure 1 for 190 keV, 1e16 cm^{-2} Ga-implanted GaAs, partially recrystallized at ~ 260°C.
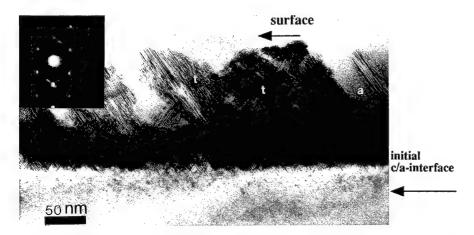

Figure 1: XTEM micrograph of 190 keV, 1e16 cm^{-2} Ga-implanted GaAs partially recrystallized at ~ 260°C. Inset is selected area diffraction pattern. (c= crystalline, a = amorphous, t = microtwins).

Inset is the selected-area diffraction pattern. Stacking faults are indicated by the streaks in the diffraction pattern and microtwins are indicated by the spots displaced one-third of the distance between primary diffracted spots.

In Figure 2 the TRR spectra of microscopic and macroscopic non-stoichiometric amorphous GaAs are shown.
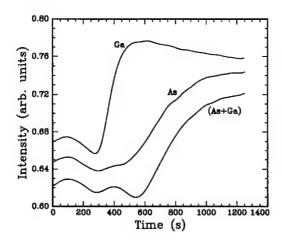

Figure 2: TRR spectra of (190 keV) Ga, (200 keV) As and (190 keV) Ga and (200 keV) As implanted samples to a total dose of 1e16 cm^{-2}, annealed to completion at ~ 260°C.

The intensities of the signals are indicative of the c/a-interface structure. More importantly the Ga-rich material recrystallizes very rapidly. The spectrum of As-rich material is similar to the Ga-and-As implanted GaAs spectrum. This shows that excess As has no influence on the SPEG of GaAs. During the first 100 sec of the regrowth process, the c/a-interface velocity in all samples appears to be the same. This is the regrowth rate of the single-crystal regime as confirmed by RBS/C measurements [3].

Figure 3(a) shows the athermal Ga depth distribution calculated with TRIM [4] and Figure 3(b) shows in-situ TEM data of the interfacial velocity during both single-crystal and twinned regrowth as a function of depth.
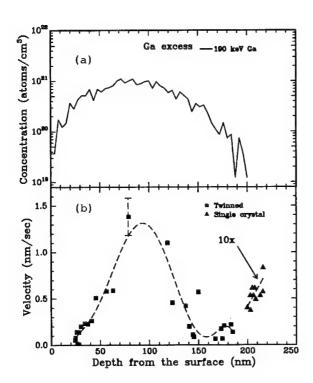

Figure 3: (a) TRIM calculation of the athermal Ga depth distribution. (b) c/a-interface velocity as a function of depth during both single-crystal and twinned regrowth of Ga-rich GaAs.

From this, it can be inferred that the maximum in interfacial velocity during twinned regrowth was at a comparable depth to the maximum in excess Ga concentration. The influence of excess Ga on SPEG of GaAs can be related to the influence of In in Si [2]. It was reported that the excess In as a molten precipitate promotes a rapid amorphous-to-polycrystalline transformation.

The c/a-interface velocity as a function of depth of As-rich material against the athermal As depth distribution is shown in Figure 4. An influence of excess As is not apparent. This is consistent with the TRR spectra in Figure 2.
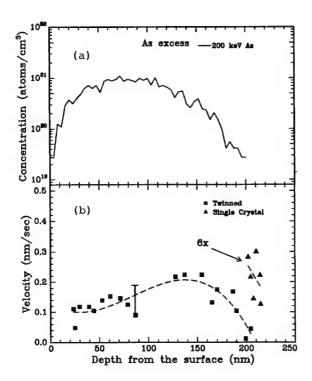

Figure 4: (a) TRIM calculation of the athermal As depth distribution. (b) c/a-interface velocity as a function of depth during both single-crystal and twinned regrowth of As-rich GaAs.

The effect of the recoiled surface oxides or contaminants which were readily adsorbed to the substrate surface maintained at ~ -196°C and ~ 5e-8 torr was observed to be the same in both in-situ TRR and in-situ TEM results. These contaminants significantly retarded the regrowth rate of a thin surface layer of width ~ 30 nm.

From the comparison of the in-situ TRR and in-situ TEM data on the single-crystal growth rate we anticipated that the actual annealing temperature was different from the apparent

temperature 260°C, as measured by the thermocouple. This difference in temperature was due to the imperfect contact between sample and the oven. This is attributed to the geometry of the sample. The actual annealing temperature of each sample was calculated using the Arrhenius temperature dependent equation: $V = V_o(-E_a/kT)$, where $E_a = 1.56$ eV and $V_o = 1.48 \times 10^{14}$ nm/sec [5]. For example the actual annealing temperature for the Ga-rich was 15°C less and for As-rich was 25°C less than the apparent annealing temperature.

CONCLUSION

We have shown that the quantitative results of the in-situ TEM measurements were consistent with the in-situ TRR, ex-situ RBS/C and ex-situ TEM results. It was demonstrated that the amorphous-to-crystalline transformation of Ga-rich GaAs was extremely rapid. We speculate that the excess Ga as a molten precipitate is potentially facilitating the mass transport of atoms at the interface. The velocity of amorphous-to-crystalline transformation of Ga-rich GaAs increases with concentration. Excess As does not influence SPEG of GaAs.

ACKNOWLEDGMENT

REFERENCES

1. C. Licoppe, Y. I. Nissim, C. Meriadec and P. Henoc, J. Appl. Phys. **50** (23), P. 1648 (1987) and references there in.

2. E. Nygren, J. S. Williams, A. Pogany, R. G. Elliman and J. C. McCallum, Mat. Res. Soc. Symp. Proc. Vol. **74**, P.307, (1987) and references there in.

3. K. B. Belay, D. L. Llewellyn and M. C. Ridgway, Mat. Res. Symp. Proc. Vol. **378**, P. 201 (1995). references there in.

4. K. B. Belay, D. L. Llewellyn and M. C. Ridgway, Appl. Phys. Lett. (unpublished) and

5. S. T. Johnson, Ph.D. Thesis (Department of Physics, Melbourne University, Melbourne, Australia) 1989 and references there in.

COMPLEMENTARY HFET TECHNOLOGY FOR LOW-POWER MIXED-MODE APPLICATIONS

A. G. BACA*, M. E. SHERWIN**, J. C. ZOLPER*, D. F. DUBBERT*, V. M. HIETALA*, R. J. SHUL*, L. R. SLOAN*, and M. J. HAFICH*

*Sandia National Laboratories, P. O. Box 5800, Albuquerque, NM 87185-0603 , agbaca@sandia.gov
**Present Address: Microwave Signal, Inc., 22300 COMSAT Drive, Clarksburg, MD 20871

ABSTRACT

Development of a complementary heterostructure field effect transistor (CHFET) technology for low-power, mixed-mode digital-microwave applications is presented. An earlier digital CHFET technology with independently optimizable transistors which operated with 319 ps loaded gate delays at 8.9 fJ is reviewed. Then work demonstrating the applicability of the digital nJFET device as a low-power microwave transistor in a hybrid microwave amplifier without any modification to the digital process is presented. A narrow band amplifier with a $0.7 \times 100 \, \mu m$ nJFET as the active element was designed, constructed, and tested. At 1 mW operating power, the amplifier showed 9.7 dB of gain at 2.15 GHz and a minimum noise figure of 2.5 dB. In addition, next generation CHFET transistors with sub 0.5 μm gate lengths were developed. Cutoff frequencies, f_t of 49 GHz and 11.5 GHz were achieved for n- and p-channel FETs with 0.3 and 0.4 μm gates, respectively. These FETs will enable both digital and microwave circuits with enhanced performance.

INTRODUCTION

Portable electronics provides a large driving force for low power electronic components and continued miniaturization of systems. GaAs complementary logic, known as CHFET when heterostructure field effect transistors are employed, offers the potential for greatly reducing the power consumption of digital integrated circuits while offering high performance [1-6]. Power consumption of complementary logic circuits is much lower than other digital circuits because they consume very little static power. Dynamic power consumption becomes an important concern for high speed circuits because of the relation $P_d = C_L(V_{DD})^2 f$, where P_d is the dynamic power, C_L is the load capacitance, V_{DD} is the power supply voltage, and f is the frequency. An important consideration of all complementary logic technology is that dynamic power is reduced dramatically at lower power supply voltages. The performance of the FETs is also reduced as the power supply voltages drop, pushing technology development of smaller gate length FETs to compensate. As this evolution to lower power supply voltages takes place, compound semiconductor FETs still achieve acceptable performance at low power supply voltages and reasonable gate lengths because of superior electron transport properties, whereas CMOS technology is driven towards very small gate lengths approaching 0.1 μm [7]. At the present time leakage currents in compound semiconductor CHFET technology are not as low as CMOS and preclude its use where VLSI technology is required because they result in high static power consumption. The current niche for CHFET technology is medium size circuits with high speed and low power consumption, especially if radiation hardness is required.

On the other hand, low-power microwave technology is also very important for portable electronics and is only recently receiving attention. Because there is no fundamental circuit approach to reduce power consumption of microwave technology, device biasing and device size are the main approaches to lower operating power and this usually results in some sacrifice in performance [8]. When circuits are biased for low power consumption, the devices may not be fully turned on, and do not operate at maximum gain. Intrinsically high gain devices such as GaAs FETs have margin to sacrifice some gain at lower frequencies, in addition to other

commonly cited microwave advantages of low noise and semi-insulating substrates suitable for low loss monolithic integration.

In this work, we present compatible low power digital and microwave GaAs-based technology suitable for mixed-mode applications where low power, high speed, and system miniaturization are desired. Monolithic integration of digital and microwave functions is generally desirable for performance enhancement, increased reliability, and cost reduction in packaging and system assembly. Applications such as electronic tags can benefit from low power and system miniaturization, especially at higher frequencies, where the antennas can be made smaller.

A complementary logic digital technology with self-aligned JFETs has been described previously [9] and will be briefly reviewed. Then the same digital active n-channel JFET is characterized for low-power microwave operation and is demonstrated in a hybrid microwave circuit. A complete integrated process for monolithic digital and microwave circuits is presented. Finally, higher performance n- and p-channel FETs with shorter gate lengths are demonstrated. These devices form the basis for future technology improvements.

TECHNOLOGY DESCRIPTION

The GaAs complementary logic technology integrates an epitaxial design, p-channel HFET and a fully ion implanted n-channel JFET [9], as illustrated in Fig. 1. This approach permits the independent optimization of the p- and n-channel devices, including the ability to independently set threshold voltages. An all-implanted self-aligned n-channel GaAs JFET allows any epitaxial pHFET design that is temperature compatible with the nJFET. In this way pHFET designs other than the HIGFET can be employed for high performance. Since pHFET performance is approximately 6-8 times worse than nFET performance, even incremental improvements in pHFET design are worthwhile. In our approach, epitaxial doping, material composition, and layer design can all be varied to optimize the p-channel device, since none of these layers will be shared with the n-channel device. A drawback of this approach is that n-channel performance will be sacrificed relative to n-channel HFET designs.

The self-aligned n-channel JFET [10,11] fabricated in the epitaxially grown GaAs buffer allows operation with low gate leakage up to 1 V, which is important in minimizing static power. In addition to the usual benefits of self-aligned processing, the self-aligned JFET also offers important advantages over a conventional JFET as illustrated in Fig. 2. The conventional JFET suffers excess gate capacitance from metal overhang as well as junction broadening. This typically leads to a rf-performance penalty in the conventional JFET compared to MESFETs of the same gate length. The self-aligned JFET with a coincident or slightly undercut junction gate region has shown comparable rf performance to a MESFET of the same gate length with the
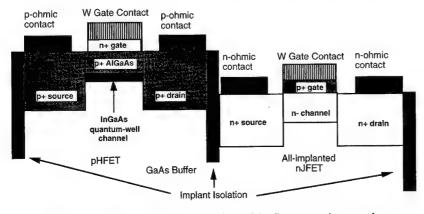

Figure 1. Schematic device cross sections of the first generation complementary nJFET and pHFET devices. These devices are independently optimizable.
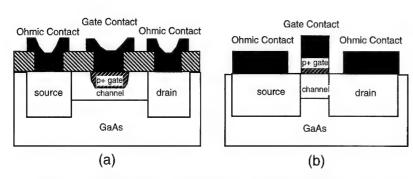
Figure 2. A comparison of non self-aligned (a) and self-aligned (b) JFETs. The self-aligned JFET results in reduced parasitic gate capacitance.

added advantage of a higher gate turn-on voltage [10].

A self-aligned refractory gate process based on tungsten or tungsten silicide gate metal was used to fabricate the complementary circuits. A 13 mask process with the following steps was employed: 1) pHFET active area definition by wet chemical etching, 2) nJFET active area implants (gate, channel, and backside) [11], 3) a thermally stable isolation implant based on oxygen ions [12], 4) gate definition with tungsten or tungsten silicide refractory gate deposition, patterning, reactive ion etch in $SF_6:Ar$ [13-15], and a wet etch to remove the heavily-doped junction-gate semiconductor regions, 5) the n^+ source and drain implants with Si, 6) the p^+ source and drain implants with Zn followed by a capless rapid thermal anneal, 7) the p-ohmic metal definition and alloy using AuBe, 8) n-ohmic metal definition and alloy using GeAuNiAu, 9) first via definition with silicon nitride dielectric, 10) first metal interconnect with TiPtAu, 11) second via with silicon nitride, 12) second metal interconnect with TiPtAu, and 13) passivation with silicon nitride. Minimum feature dimensions of 3 μm lines, 2 μm spaces, 0.7 μm gates, and 1.5 μm vias were verified by scanning electron microscopy. The use of a junction-gate pHFET simplifies the processing of step 4) since the wet etch definition of the junction gates is simultaneous for n- and p-channel FETs. This process sequence is modified for the short gate FETs presented in a later section. It is important to note that for the JFETs the electrical gate is the pn junction region. The metal-semiconductor contact is fabricated to be a non-alloyed ohmic contact to a heavily doped semiconductor region [16], Zn-implanted GaAs for the nJFET and InGaAs:Si for the pHFET.

Both nJFET and pHFETs are enhancement-mode devices. The nJFET shows a maximum transconductance (g_m) of 230 mS/mm. At a 1.0 V gate and drain bias typical of circuit operation, the g_m and I_{DS} are approximately 170 mS/mm and 90 mA/mm, respectively with f_t of 19 GHz, f_{max} of 28 GHz, and a subthreshold slope of 90 mV/decade. Likewise, the pHFET shows a maximum g_m of 43 mS/mm, but g_m of 29 mS/mm and I_{DS} of 20 mA/mm under operating conditions of 1.0 V on gate and drain. The pHFET shows an f_t of 3.5 GHz and poor subthreshold characteristics due to soft turn-on.

The CHFET technology with a self-aligned nJFETs and junction-gated, modulation-doped pHFETs achieved loaded 31-stage ring-oscillator delays of 319 ps/stage at 8.9 fJ with a power supply of 0.8 V [9]. The loading was provided by 200 μm of wire in second metal which was interdigitated with grounded first metal to provide a capacitive load between each stage. Faster gate delays up to 179 ps were obtained higher power supply voltages, but gate current caused an increase in power consumption. The power consumption was predominantly static power caused by a soft turn-on of the pHFET. In this work an improved pHFET design based on a doped GaAs channel will be presented in the section on short gate devices.

MICROWAVE TECHNOLOGY

An nJFET fabricated in the digital CHFET process was evaluated as a microwave device. A narrow-band amplifier was selected as a test vehicle since its successful implementation demonstrates the feasibility of most monolithic microwave integrated circuit (MMIC) functions. The approximate gate length used was 0.8 μm and the gate width was 100 μm. The low power digital applications require low bias voltages ($V_{DS} \approx 1$ V), a small positive gate threshold, and large gate turn-on voltages (>1 V). These design parameters are also ideal for low-power microwave applications. The voltages are very suitable for battery operation on a single cell and the positive gate threshold along with the large positive gate turn-on voltage, eliminates the need for a negative supply as commonly required with MESFETs. Though not explicitly designed for microwave operation, the device's microwave properties are impressive with $f_t > 13$ GHz, $f_{max} > 20$ GHz and a minimum noise figure of about 1.6 dB (with a 12 dB associated gain) all measured at a 1 mW DC bias level.

The transistor was mounted in a standard 100 mil stripline package and measured S-parameters of the packaged part were used for a narrow-band 2.4 GHz microstrip based amplifier design. The amplifier was fabricated on Rogers TMM-10 25 mil thick substrate (see Figure 3) and tests were performed using an HP 8510C network analyzer and an HP 8971 noise figure meter. The measured gain and noise figure are plotted in Figure 4. The amplifier's gain approaches 10 dB at 2.15 GHz. The minimum noise figure was about 2.5 dB and occurred at a frequency higher than the gain's peak. This is not surprising as the amplifier was designed for maximum gain and not minimum noise figure. A minimum noise figure design should achieve a value more consistent with the on-wafer measured value of 1.6 dB.

Because the digital CHFET process was used to fabricate the transistor, addition of MMIC passive elements that are compatible with the digital process will provide a mixed-mode technology. The passive elements needed are: 1) a thin film resistor, 2) thin film capacitors, 3) inductors, 4) tansmission lines, 5) airbridges, and 6) backside vias. The CHFET via process will be used to etch dielectric back to the substrate in the MMIC areas and the CHFET first metal process will be used for capacitor bottom electrodes and the base of transmission lines (including spiral inductors). The following new process steps will provide for the rest of the MMIC passive elements: 1) thin film resistor, 2) capacitor dielectric, 3) capacitor top metal, 4) airbridge post, 5) airbridge, and 6) backside via. A full CHFET-MMIC process will require up to 19 mask levels and is currently being implemented in our laboratory.
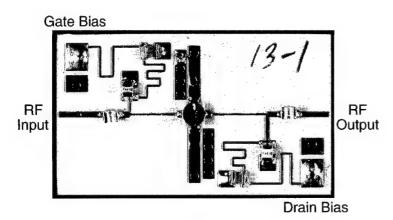

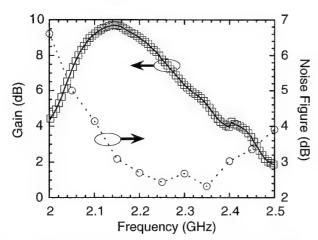Figure 3. Photograph of the narrow-band CHFET amplifier.

Figure 4. Plot of measured gain and noise figure versus frequency. Data is for 1.01 mW DC bias ($V_{ds} = 1.0$ V, $I_{ds} = 1.01$ mA, and $V_{gs} = 0.168$ V).
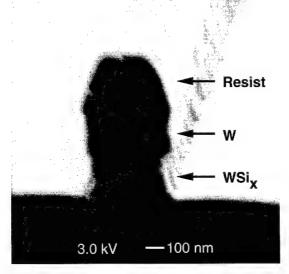

Figure 5. SEM cross-sectional image of a 0.3 μm W/WSi$_x$ bilayer gate taken prior to resist removal.

SHORT GATE CHFET DEVICES

While demonstration of the digital and microwave technologies has been made, performance improvements by reducing the gate length is desired. We have reduced the gates from optically patterned 0.7 μm lengths to the 0.3 - 0.4 μm range by the use of e-beam lithography. Both W and W/WSi$_x$ bilayer gates have been patterned. While the W gates are preferable for the non-alloyed ohmic contacts to JFETs because of its greater conductivity, WSi$_x$ gates make superior
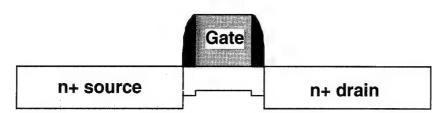
Figure 6. Schematic cross-section of FET sidewalls and implants.

Schottky contacts for $0.4 \leq x \leq 0.5$ [17]. The Schottky contacts are better for conventional pHFET structures (i.e. non JFETs) and for these FETs the W/WSi$_x$ bilayer gate provides both a good Schottky contact and low gate resistance. Good anisotropic profiles with low plasma damage and sub 0.5 μm W/WSi$_x$ bilayer gates have been obtained with negative electron-beam resist and reactive ion etching in a SF$_6$/Ar chemistry [15]. A representative gate profile prior to resist removal is shown in Figure 5. A short gate W process works well with the same conditions as the W/WSi$_x$ bilayer gates. The short gate processes have been used to fabricate self-aligned nJFETs and pHFETs. These devices show promise for even higher performance CHFET circuits.

0.3 μm nJFET

In addition to short gate definition, the process must be designed to address short channel effects as with self-aligned MESFETs. The channel's active region should be made more shallow and steps must be taken to prevent buffer conduction and associated threshold voltage shift from the source and drain implants. The nJFET p$^+$ gate implant was changed from Zn to Cd to maintain a high surface doping level greater than 10^{19} cm^{-2} while moving the pn junction closer to the surface [18]. The channel active region was kept the same with a Si implant energy of 70 KeV along with a C backside confinement implant [11]. The Si dose was adjusted to keep the threshold voltage the same. The lateral short channel effects were addressed by implementing a
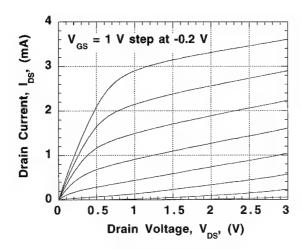

Figure 7. I$_{DS}$-V$_{DS}$ characteristics for a self-aligned 0.3x20 μm nJFET.

232

sidewall process with a shallow 40 KeV SiF implant under a 0.1 μm wide SiN sidewall [19] and a deeper 50 KeV Si implant spaced from the gate by the sidewall in the source and drain regions. The sidewall geometry is shown schematically in Figure 6.

Using this process a high performance 0.3 x 40 μm JFET with W gates was fabricated. The drain I-V characteristics are shown in Figure 7. A maximum transconductance of 265 mS/mm was measured with an f_t of 49 GHz, f_{max} of 58 GHz, and a subthreshold slope of 110 mV/decade, as seen in Figure 8. The f_t increases proportionately with inverse gate length from 0.7 μm to 0.3 μm, indicating that short channel effects have been suppressed. The increase in f_{max} is not proportional to inverse gate length, indicating that high gate resistance is an important factor at these short gate lengths. This nJFET needs a slight threshold voltage shift for enhancement-mode operation.

0.4 μm pHFET

In addition to the new short gate process, the pHFET structure was completely redefined. As mentioned previously, process simplicity was one factor in choosing junction gates for both pFET and nFET, but low pFET performance compels another approach. A doped-channel GaAs/AlGaAs pHFET was chosen for the current work. A 100 Å Be-doped GaAs channel with a 50 Å GaAs spacer, a 150 Å $Al_{0.75}Ga_{0.25}As$ undoped barrier layer, and a 100 Å cap layer form the active layers of the pHFET. This pHFET is still process compatible with the GaAs self-aligned nJFET and is only process compatible with an epitaxial nHFET using stacked layers or small area, selective epitaxial regrowth. The doped channel pHFETs can be adjusted for the desired threshold voltage independently of the nJFET, while maintaining high gate turn-on voltage demonstrated in HIGFETs with high Al mole fraction AlGaAs barriers [20]. Lateral short channel effects are especially severe in compound semiconductor pFETs. They have been
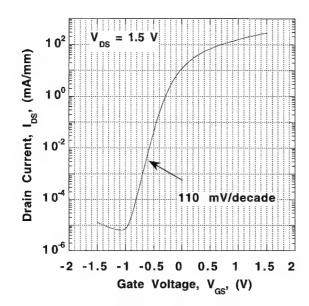

Figure 8. I_{DS}-V_G characteristics at a drain biases of 1.5 V for a self-aligned 0.3x20 μm nJFET.

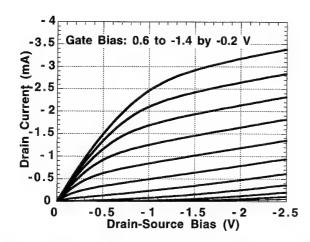Figure 9. I_{DS}-V_{DS} characteristic for a self-aligned 0.4 x 40 μm pHFET.

addressed in this work with a 0.1 μm wide SiN sidewall process using 50 KeV Zn implants under the sidewalls and 125 KeV implants in the source and drain regions.

pHFETs with gate lengths ranging from 1.0 to 0.3 μm was fabricated and characterized. The transistors scaled well down to 0.5 μm gate length. The output conductance and subthreshold slope degraded noticeably at 0.4 μm gate length and severe short channel effects were observed at 0.3 μm. Nevertheless, good rf characteristics were observed down to 0.4 μm gate lengths. Drain I-V characteristics for a 0.4 x 20 μm pHFET are shown in Figure 9. A maximum

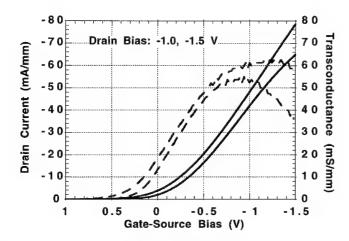Figure 10. I_{DS}-V_G and g_m-V_G characteristics at drain biases of -0.5, -1.0, and -1.5 V for a self-aligned 0.7x20 μm pHFET.

234

transconductance of 62 mS/mm was measured, as seen in Figure 10, with f_t of 11.5 GHz and f_{max} of 13 GHz. The subthreshold slope ranges from 130-170 mV/decade for gate lengths 0.5 μm and longer, as seen in Figure 11. At 0.4 μm gate length the subthreshold slope increases to 310 mV/decade. These subthreshold slopes are still not as good as nJFET values but are clear improvements even at long gate lengths from our previous pHFETs [9]. The transconductance decreases only slightly to 54 mS/mm for operating biases of 1.0 V on gate. A slight threshold voltage adjustment will be necessary to get enhancement-mode operation for use in CHFET circuit designs. These excellent transistor properties will be presented with more extensive DC and rf data in a future publication.

CONCLUSION

CHFET technology development with independently optimizable transistors aimed at high speed, low-power, digital-microwave mixed-mode applications has been described. The first generation digital CHFET technology operated with 319 ps loaded gate delays at 8.9 fJ. The digital nJFET device was used as a low-power microwave transistor in a hybrid microwave amplifier without any modification to the digital process. A narrow band amplifier with a 0.7 x 100 μm nJFET as the active element was designed, constructed, and tested. At 1 mW operating power, the amplifier showed 9.7 dB of gain at 2.15 GHz and a minimum noise figure of 2.5 dB. In addition, next generation CHFET transistors with sub 0.5 μm gate lengths were demonstrated. Cutoff frequencies, f_t of 49 GHz and 11.5 GHz were achieved for n- and p-channel FETs with 0.3 and 0.4 μm gates, respectively. These FETs will enable both digital and microwave circuits with enhanced performance.
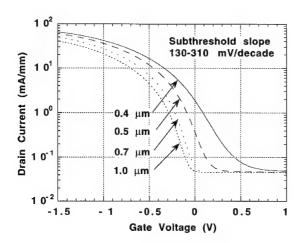
ACKNOWLEDGMENTS

Figure 11. I_{DS}-V_G characteristics at a drain bias -1.0 V for a self-aligned pHFET.

REFERENCES

[1] D. E. Grider, P. P. Ruden, J. C. Nohava, I. R. Mactaggart, J. J. Stronczer, and R. H. Tran, "0.7 Micron Gate Length Complementary $Al_{0.75}Ga_{0.25}As$/GaAs HIGFET Technology for High Speed/Low Power Digital Circuits," *IEDM Technical Digest*, pp. 331-334, 1992.

[2] J. K. Abrokwah, J. H. Huang, W. Ooms, C. Shurboff, J. A. Hallmark, R. Lucero, J. Gilbert, B. Bernhardt, and G. Hansell, "A Manufacturable Complementary GaAs Process," *IEEE GaAs IC Symposium Technical Digest*, pp. 127-130, 1993.

[3] R. A. Kiehl, J. Yates, L. F. Palmateer, S. L. Wright, D. J. Frank, T. N. Jackson, J. F. Degelormo, and A. J. Fleischman, "High-Speed, Low-Voltage, Complementary Heterostructure FET Circuit Technology," *IEEE GaAs IC Symposium Technical Digest*, pp. 101-104, 1991.

[4] K. Matsumoto, M. Ogura, T. Wada, T. Yao, Y. Hayashi, N. Hashizume, M. Kato, N. Fukuhara, H. Hirashima, and T. Miyashita, "Complementary GaAs SIS FET Inverter Using Selective Crystal Regrowth Technique," *IEEE Electron Device Letters*, vol. 7, pp. 182-184, 1986.

[5] T. Mizutani, S. Fujita, and F. Yanagawa, "Complementary Circuit with AlGaAs/GaAs Heterostructure MISFETs Employing High-Mobility Two-Dimensional Electron and Hole Gases," *Electronics Letters*, vol. 21, pp. 1116-1117, 1985.

[6] R. Zuleeg, J. K. Notthoff, and G. L. Troeger, "Double-Implanted GaAs Complementary JFETs," *IEEE Electron Device Letters*, vol. 5, pp. 21-23, 1984.

[7] B. Davari, W. H. Chang, K. E. Petrillo, C. Y. Wong, D. Moy, Y. Taur, M. R. Wordeman, J. Y. C. Sun, C. C. H. Hsu, and M. R. Polcari, " A High-Performance 0.25 μm CMOS Tehcnology: II-Technology," *IEEE Transactions on Electron Devices*, vol. 39., pp. 967-975, 1992.

[8] D. Scherrer, J. Kruse, J. Laskar, M. Feng, M. Wada, C. Takano, and J. Kasahara, "Low-Power Performance of 0.5 μm JFET for Low-Cost MMIC's in Personal Communications," *IEEE Electron Device Letters*, vol. 14, pp. 428-430, 1993.

[9] A. G. Baca, J. C. Zolper, M. E. Sherwin, P. J. Robertson, R. J. Shul, A. J. Howard, D. J. Rieger, and J. F. Klem, "Complementary GaAs Junction-Gated Heterostructure Field Effect Transistor Technology," *IEEE GaAs IC Symposium Technical Digest*, pp. 59-62, 1994.

[10] M. E. Sherwin, J. C. Zolper, A. G. Baca, R. J. Shul, A. J. Howard, D. J. Rieger, J. F. Klem, and V. M. Hietala, "An All Implanted Self-Aligned Enhancement Mode n-JFET with Zn Gates for GaAs Digital Applications," *IEEE Electron Device Letters*, vol. 15, pp. 242-244, 1994.

[11] J. C. Zolper, M. E. Sherwin, A. G. Baca, R. J. Shul, J. F. Klem, and V. M. Hietala, "Enhanced High Frequency Performance in a GaAs, Self-Aligned, n-JFET Using a Carbon Buried p-Implant," *IEEE Electron Device Letters*, vol 15, pp. 493-495, 1994.

[12] J. C. Zolper, A. G. Baca, and S. A. Chalmers, "Thermally Stable Oxygen Implant Isolation of p-type $Al_{0.2}Ga_{0.8}As$," *Applied Physics Letters*, vol. 62, pp. 2536-2538, 1993.

[13] R. J. Shul, D. J. Rieger, A. G. Baca, C. Constantine, and C. Barratt, "Anisotropic Electron Cyclotron Resonance Etching of Tungsten Films on GaAs.," *Electronics Letters*, vol. 30, pp. 84-85, 1994.

[14] R. J. Shul, A. G. Baca, D. J. Rieger, and A. J. Howard, "Anisotropic Etching of WSi Films on GaAs," *Electronics Letters*, vol. 31, pp. 317-318, 1995.

[15] R. J. Shul, M. E. Sherwin, A. G. Baca, J. C. Zolper, and D. J. Rieger, "Short Gate Etching of W/WSi Bilayer Gates," *Electronics Letters,* vol 32, pp. 70-71, 1996.

[16] M. E. Sherwin, J. C. Zolper, A. G. Baca, T. J. Drummond, R. J. Shul, A. J. Howard, D. J. Rieger, R. P. Schneider, and J. F. Klem, "Comparison of Mg and Zn Gate Implants for GaAs n-channel Junction Field Effect Transistors," *Journal of Electronic Materials,* vol. 23, pp. 809-818, 1994.

[17] A. G. Lahav, C. S. Wu, and F. A. Baiocchi, "WSi$_x$ Refractory Metallization for GaAs Metal-Semiconductor Field Effect Transistors," *J. Vac. Sci. Technol.,* vol. B6, pp. 1785-1795.

[18] J. C. Zolper, A. G. Baca, M. E. Sherwin, and R. J. Shul, "High Performance GaAs JFET with a Shallow Implanted Cd-Gate," *Electronics Letters,* vol. 31, pp. 923-924, 1995.

[19] A. G. Baca, A. J. Howard, R. J. Shul, and M. E. Sherwin, "Trenching Observed During Sidewall Formation in GaAs Self-Aligned Refractory Gate FETs," *Electronics Letters,* vol 32, p. 74-75, 1996.

[20] P. P. Ruden, M. Shur, D. K. Arch, R. R. Daniels, D. E. Grider, T. E. Nohava, "Quantum-Well p-Channel AlGaAs/InGaAs/GaAs Field Effect Transistors," *IEEE Trans. Elect. Devices,* vol. 36, pp. 2371-2379, 1989.

237

DAMAGE INTRODUCTION IN InGaP AND AlGaAs BY ELECTRON CYCLOTRON RESONANCE Ar PLASMAS

J. W. Lee, S. J. Pearton, R. R. Stradtmann and C. R. Abernathy
University of Florida, Gainesville FL 32611

W. S. Hobson and F. Ren
Lucent Technologies Bell Laboratories, Murray Hill NJ 07974

ABSTRACT

Changes in sheet resistance of n- and p-type InGaP exposed to Electron Cyclotron Resonance Ar plasmas have been used to measure the introduction of ion-induced damage. P-type material is much more resistant to change in its conductivity than n-type InGaP, indicating that electron traps are the predominant entity produced by the ion bombardment. For short (~1 min.) plasma exposures the ion current is more important than ion energy in producing resistance changes. Annealing of damage in both conductivity types occurs with an activation energy of ~3.4±0.5eV. p^+AlGaAs is found to be much more susceptible than n^+AlGaAs to the introduction of electrically active deep levels during exposure to Electron Cyclotron Resonance Ar plasmas. In both AlGaAs materials the resistivity of thin (~0.5μm) epitaxial layers increases rapidly with both plasma exposure time and the ion energy, while the ion density in the Ar discharge has a much greater influence on p^+AlGaAs than n-type material . These results suggest that the energetic ion bombardment introduces deep hole traps more readily than deep electron traps in AlGaAs and that pnp transistor structures will be more susceptible to plasma damage than comparable npn structures.

INTRODUCTION

The InGaP/GaAs heterostructure is increasingly being used to replace the AlGaAs/GaAs materials system in devices such as heterojuction bipolar transistors (HBTs) and 980nm pump lasers because of the avoidance of problems such as oxidation and DX-centers associated with AlGaAs[1,2]. High etching selectivities for both InGaP over GaAs and vice-versa, have been reported for wet and dry etching[3], whereas there is no selective dry etch for AlGaAs over GaAs. In addition wet etching in the GaAs/AlGaAs system is more complicated.[4,5] By contrast, infinite selectivity for InGaP over GaAs can be obtained in HCl-based solutions,[3] whereas sulfuric or phosphoric acid solutions are selective for GaAs over InGaP.

In dry etching of both InGaP and AlGaAs it has been found that $CH_4/H_2/Ar$ plasma chemistries provide smooth, controlled material removal, with much faster rates for high ion density techniques such as Electron Cyclotron Resonance (ECR). To date there have been no reports concerning comparison of damage introduction into InGaP and AlGaAs during patterning by dry etching. In this paper we detail an investigation into the changes in conductivity induced in both n- and p-type InGaP and AlGaAs during exposure to ECR, and more conventional rf (or "reactive ion etching") discharges. We employ a simple Ar plasma chemistry to simulate the physical bombardment component induced by the materials during $CH_4/H_2/Ar$ dry etching. Van der Pauw Hall measurements were employed to monitor the introduction of deep level states that trap charge carriers in the material and lead to a decrease in conductivity. We find that p-type InGaP is much more resistant to this type of damage than n-type material, and that the degree of

disruption to the electrical properties is strongly dependent on the microwave power (or ion density), the process pressure and the duration of the plasma exposure. Once introduced the damage is tenacious, and requires annealing in the range 750-850°C to remove. For the cases of n- and p-type AlGaAs, over a wide range of plasma conditions we find that n-type AlGaAs is substantially more resistant to damage introduction than p-type material, suggesting that deep donor states are readily induced during Ar ion bombardment than are deep acceptor states, which is opposite to the case of InGaP.

EXPERIMENTAL

Most of the ~0.7 μm thick InGaP was grown by Metal Organic Chemical Vapor Deposition (MOCVD) at 675°C on semi-insulating GaAs substrates oriented 2° off (100) → (111)A. Trimethylindium, triethylgallium and phosphine were used as the growth precursors, while disilane or diethylzinc were employed as n- or p-type dopants, respectively. Doping levels were 3×10^{18} cm^{-3} for n-type and $1 \times 10^{18} cm^{-3}$ for p-type. Some samples were grown by Metal Organic Molecular Beam Epitaxy (MO-MBE) using similar precursors and a growth temperature of 550°C. The layer compositions ($In_{0.51}Ga_{0.49}P$) were measured by both photoluminescence and x-ray diffraction.
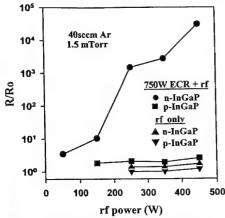
Si-doped $Al_{0.22}Ga_{0.78}As$ was grown on semi-insulating GaAs substrates by Metal Organic Chemical Vapor Deposition at 675°C. Disilane was employed for n-type doping, while triethylaluminium, triethylgallium and AsH_3 was used as precursors.[2] C doped $Al_{0.22}Ga_{0.78}As$ was grown on semi-insulating GaAs substrates by Metal Organic Molecular Beam Epitaxy at 575°C, using trimethylgallium as the carbon source, and trimethylamine alane and AsH_3.[6] The AlAs mole fractions were established from photoluminescence measurements, and the net ionized impurity densities obtained by Hall measurements. Carrier concentration ($p=2.8 \times 10^{19} cm^{-3}$ and $n=10^{18} cm^{-3}$) was calculated for the AlGaAs samples.

Ohmic contacts were placed at the corners of 5×5 mm^2 samples using alloyed HgIn (420°C, 180sec) and the sample sheet resistance obtained from Van der Pauw measurements both before and after exposure to the Ar plasmas. The contact resistance is $\leq 10^{-5} \Omega$ cm^2, and did not change as a function of the etches since the metal protects the semiconductor/contact interface. The discharges were created in a Plasma-Therm SLR 770 system using an Astex 4400 ECR source operating at 0-1000W, with additional rf (13.56MHz) biasing of the sample chuck (0–450W). The process pressure was varied from 1.5 mTorr to 10 mTorr, and the plasma exposure time set at 1–5 minutes. Sheet resistance of the etched samples was obtained using Hall measurements.

RESULTS AND DISCUSSION

Figure 1 shows the ratio of the sample sheet resistance after Ar plasma exposure (1 min) relative to the initial values for both n- and p-type InGaP, as a function of the rf power applied to the He backside-cooled chuck on which the samples sit. For samples exposed only to the RIE-like plasmas (i.e. rf power only) there is little change in the electrical properties of either conductivity type even for the highest power employed (450W). This suggests that for low ion currents the ion energy has little effect on the InGaP, since the dc bias on the samples corresponds to values between −125 and −400V for rf powers between 150 − 450W. When the ion density in the discharge is varied from ~$10^9 cm^{-3}$ for the RIE conditions to ~5×10^{11} cm^{-3} by application of 750W of microwave power to the ECR source, there are correspondingly much different responses of n- and p-type InGaP in terms of damage. The n-type material now shows an increase in resistance

even for very low rf powers (50W) and displays an almost exponential increase with further increases in rf power (essentially, ion energy). By contrast the p-type InGaP is much more resistant to changes in resistance, even though it is more lightly-doped than the n-type material. We assume in analogy with ion implant damage experiments that the resistance increases are due to the introduction of deep level states which trap charge carriers, and since these states are not thermally ionized at room temperature the conductivity is decreased. The results of Figure 1 suggest that creation of electron traps in n-InGaP is much more effective than creation of hole traps in p-type material and therefore the latter is more resistant to ion damage. This would imply that pnp InGaP/GaAs HBTs should be relatively immune to dry etch damage since the emitter mesa step involves a selective etch of GaAs, stopping on p-type InGaP.
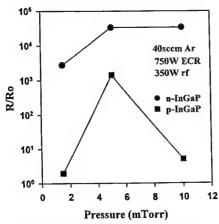

Figure 1. Resistance ratio increase (relative to the initial values Ro) of n- and p-type InGaP exposed to Ar discharge with either 0 or 750W ECR power, as a function of rf power applied to control Ar+ ion energy.

Figure 2. Resistance ratio increase for InGaP exposed to 750W ECR Ar plasmas with 250W of rf power, as a function of exposure time.

The dependence of the resistance increases on plasma exposure time for a 750W ECR Ar discharge with 250W of rf power is shown in Figure 2. It is clear that even relatively short exposures of n-type material lead to rapid degradation of the electrical properties, so that under conditions of both high microwave and rf powers, the over-etch time should be minimized when removing an overlayer from an InGaP film. It should be emphasized that inert gas plasmas create more damage than those involving a chemical component because in the latter case material is being removed at a much faster rate, reducing the apparent damage depth.[7,8] Therefore short over-etch times with low rf powers should be acceptable for device fabrication with real ECR etching processes.

Figure 3 shows the process pressure dependence of resistance increases for high ECR (750W) and rf (350W) powers (1 minute exposures). In p-type InGaP the degradation peaks at ~5 mTorr, where the Ar^+ ion density is a maximum in our system. Under these conditions, whereas at higher pressures the ionization efficiency decreases. In the case of n-InGaP we can not measure resistance increases of more than $\sim 3 \times 10^4$, since the sheet resistance then becomes similar to that of the GaAs substrate. The results in Figure 3 therefore show only a saturation effect at pressures of 5 and 10 mTorr for n-type material.

Once damage is introduced into InGaP, quite high annealing temperatures are required to remove it. We annealed our samples using the proximity method—separate atomic force
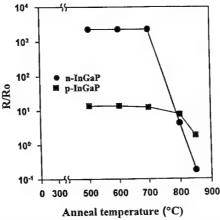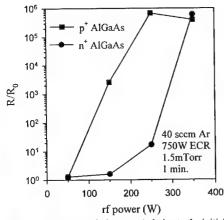
Figure 3. Resistance ratio increase for InGaP exposed to 750W ECR Ar plasmas with 350W of rf power as a function of process pressure.

Figure 4. Annealing temperature dependence (1 min anneals) of damage removal in Ar-plasma exposed InGaP.

microscopy and Auger electron spectroscopy measurements showed the surface retained their initial stoichiometry. Figure 4 shows the damage removal characteristics. In both conductivity types the deep compensating centers anneal between ~750-850°C. For n-type material the conductivity after 850°C annealing is actually higher than in the as-grown samples, indicating improved electron mobilities or increased Si-doping efficiency. Assuming a first order annealing process in which the deep states anneal by short-range diffusion of point defects, then the data in Figure 4 correspond to activation energies for removal of these states of ~3.4±0.5eV in both materials.[9] The fairly wide uncertainty range means we cannot say definitely the activation energy in the same in both materials. The annealing temperatures required to remove the ion-induced damage in InGaP are higher than those in GaAs[10] and emphasizes that one should avoid its introduction rather than rely on subsequent annealing.

Figure 5 shows the ratio of final -to-initial sheet resistances for AlGaAs samples exposed to ECR Ar plasmas for 1min with 750W of microwave power and a process pressure of 1.5mTorr as a function of rf power. Note that the sheet resistance of the p^+AlGaAs begins to increase at lower rf powers, or correspondingly lower ion energies, than does the n^+ material. The Hall measurements showed that the increase in sheet resistance was due almost completely to a reduction in net carrier density, and therefore that the energetic ion bombardment creates deep level traps that remove carriers from the respective bands. This is typical of processes such as implant isolation, where the implantation of chemically inactive ions is used to create highly resistive regions in III-V materials in order to electrically or optically isolate device structures.[11] The results in Figure 5 suggest that p-type AlGaAs is more susceptible to deep level introduction than n-type material and therefore that creation of deep hole traps is more prevalent than formation of deep electron traps . Remarkably, this result is opposite to that obtained in n^+ and p^+ InGaP,[12] where it was found that p-type material was more radiation hard than n-type InGaP. This has implications for devices where ion damage is an issue either during fabrication or subsequent operation (e.g. solar cells or space-borne electronics or detectors). For example npn GaAs/AlGaAs HBTs should be relatively less sensitive to dry etch damage during emitter mesa formation than pnp structures.
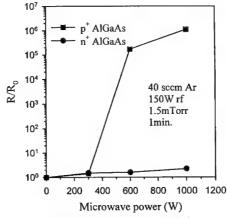
242

Figure 5. Resistance ratio increase (relative to the initial value R_0) of n^+ and p^+ AlGaAs exposed to Ar discharges (1.5 mTorr, 750W microwave power) as a function of rf power applied to control Ar^+ ion energy.

Figure 6. Resistance ratio increase for AlGaAs exposed to 150W rf, 1.5mTorr ECR Ar discharges, as a function of microwave power.

The microwave power dependence of the resistance increases are shown in Figure 6 for fixed rf power (150W). The dramatic difference in sensitivity to introduction of dry etch damage is clear in this data and shows that increasing ion density (i.e. microwave power) at fixed ion energy (i.e. rf power) has little effect on n-type AlGaAs but makes p-type material insulating above ~500W. This data shows that once one is above the ion energy threshold for point defect creation the damage is able to accumulate more rapidly as the ion flux increases, whereas in n-type AlGaAs where the deep acceptor creation rate is low at this ion energy, there is little dependence on ion flux. These types of plasma power (150W rf, 1000W microwave) are fairly typical of III-V etching processes,[13,14] and show that n-type AlGaAs should be relatively insensitive to plasma damage. It is important to remember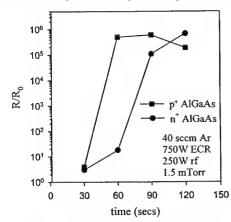 that the changes in p-type materials will be less severe in a real etching process where the damaged material is being removed at a faster rate that in our current experiment.

Figure 7. Resistance ratio increase for AlGaAs exposed to 750W ECR Ar plasmas with 250W of rf power, as a function of exposure time.

The dependence of the resistance increases on plasma exposure time for a 1000W ECR Ar discharge with 250W of rf power is shown in Figure 7. These results are instructive when calculating allowable over-etch times in dry etch processes such as removal of SiO_2 or SiN_x from an AlGaAs layer using a chemistry such as SF_6/Ar. In n-type material the damage builds up rapidly beyond 30 seconds, while again the p-type AlGaAs is even more sensitive. Thus, over-etch times should be minimized when removing an overlayer from either n- or p-type AlGaAs films. Ion-induced damage can be annealed at ~650°C in AlGaAs,[11]

243

but many device processing sequences do not allow for these types of temperatures because of metal contact interactions with the semiconductor or diffusion of dopant impurities.

CONCLUSIONS

In conclusion, we find that n-type InGaP is much more susceptible to ion-induced damage during dry etching than p-type material. For short exposure times (~1 min), the ion current is a more important parameter than ion energy, especially for n-type InGaP. Annealing temperatures above ~800°C are required to remove the plasma-induced damage. Turning to the AlGaAs we find that p-type AlGaAs is much more susceptible to ion -induced damage during dry etching than n-type material. The amount of changes to the electrical conductivity of plasma exposed AlGaAs is strongly dependent on ion energy and exposure time. The results are opposite to those for InGaP.

ACKNOWLEDGMENTS

REFERENCES

1. sec for example, J. M. Kuo, Thin Solid Films **231** 158 (11993).
2. W. S. Hobson, Proc. Mater. Res. Soc. Symp. **300** 75 (1993).
3. J. R. Lothian, J. M. Kuo, F. Ren and S. J. Pearton, J. Electron Mater. **21** 441 (1992).
4. F. Ren, Pro. Mater. Res. Soc. Symp. 300 21 (1993); F. Ren, J. R. Lothian, S. J. Pearton, C. R. Abernathy, P. W. Wisk, T. R. Fullowan, B. Tseng, S. N. G. Chu, Y. K. Chen, C. Yang, S. T. Fu, R. Brozovich, H. H. Lin, C. L. Henning and T. Henry, J. Vac. Sci. Technol. B **12** 2916 (1994).
5. S. A. Merriff and M. Dagenais, J. Electrochem. Soc. **140** 138 (1993).
6. C. R. Abernathy, Mat. Sci. Eng. Rep. **14** 203 (1995).
7. S. W. Pang, J. Electrochem. Soc **133** 784 (1986).
8. K. L. Seaward and N. J. Moll, J. Vac. Sci. Technol. B **10** 46 (1992).
9. S. J. Pearton, J. W. Corbett and M. Stavola, Hydrogen in Crystalline Semiconductors (Springer-Verlag, Heidelberg, 1992).
10. S. J. Pearton, U. K. Charkrabarti and W. S. Hobson, J. Appl. Phys. **66** 2061 (1989).
11. S. J. Pearton, Mat. Sci. Rep. **4** 313 (1990).
12. J. W. Lee, S. J. Pearton, C. R. Abernathy, W. S. Hobson and F. Ren, Appl. Phys. Lett. **67** 3129 (1995).
13. F. Ren, S. J. Pearton, C. R. Abernathy, C. S. Wu, M. Hu, C. K. Pao, D. C. Wang and C. P. Wen, IEEE Trans Electron. Dev. ED-39 2701 (1992).
14. F. Ren. C. R. Abernathy, S. J. Pearton, J. R. Lothian, P. Wisk, T. Fullowan, Y. K. Chen, L. W. Yang, S. Fu, R. Brozovich and H. H. Lin, IEEE Electron Dev. Lett. **14** 332 (1993).

ECR ETCHING OF GaP, GaAs, InP, and InGaAs in Cl$_2$/Ar, Cl$_2$/N$_2$, BCl$_3$/Ar, and BCl$_3$/N$_2$

[*]R. J. Shul, [*]A. G. Baca, [*]D. J. Rieger, [*] H. Hou, [**]S. J. Pearton, and [***]F. Ren

[*] Sandia National Laboratories, Albuquerque, NM 87185-0603
[**] University of Florida, Gainesville, FL 32611
[***] AT&T Bell Laboratories, Murray Hill, NJ 07974

ABSTRACT

Electron cyclotron resonance (ECR) etching of GaP, GaAs, InP, and InGaAs are reported as a function of percent chlorine-containing gas for Cl$_2$/Ar, Cl$_2$/N$_2$, BCl$_3$/Ar, and BCl$_3$/N$_2$ plasma chemistries. GaAs and GaP etch rates were faster than InP and InGaAs, independent of plasma chemistry due to the low volatility of the InCl$_x$ etch products. GaAs and GaP etch rates increased as %Cl$_2$ was increased for Cl$_2$/Ar and Cl$_2$/N$_2$ plasmas. The GaAs and GaP etch rates were much slower in BCl$_3$-based plasmas due to lower concentrations of reactive Cl, however enhanced etch rates were observed in BCl$_3$/N$_2$ at 75% BCl$_3$. Smooth etched surfaces were obtained over a wide range of plasma chemistries.

INTRODUCTION

Plasma etching of InP, GaP, GaAs, and related compound semiconductor materials has significant impact on the fabrication of several photonic and electronic devices. Several different plasma chemistries have been used to etch these materials. The preference has been to etch Ga-containing films in Cl-based plasmas due to the high volatility of the Ga- and group-V-chlorides.[1-4] Etch rates are typically fast, with anisotropic profiles and smooth etch morphologies. CH$_4$/H$_2$-based plasmas have also been used to etch GaAs and AlGaAs, producing smooth anisotropic profiles at much slower etch rates than those obtained in Cl$_2$-based plasmas.[5-8] The preferred plasma chemistry for In-containing materials has been CH$_4$/H$_2$-based due to the formation of volatile InCH$_x$ etch products.[9] Etching In-containing compounds in room temperature Cl$_2$-based plasmas often results in roughened surfaces due to the low volatility of the In-chlorides and the preferential loss of the group-V species. Increasing the temperature to ~150°C improves the etch results due to higher volatilities of In-chlorides.[10, 11] Recently, high etch rates for In-containing materials were reported in ECR generated BCl$_3$/N$_2$ plasmas at 100°C and 1000 W microwave power.[12, 13] As N$_2$ was added to the plasma, the concentration of reactive Cl and Cl ions increased. High etch rates were attributed to increased plasma densities which increased the sputter desorption of non-volatile InCl$_x$ species formed at the surface. Thomas *et al.* have reported InP etch rates exceeding 2500 nm/min in a high-density ECR-generated Cl$_2$ discharge at 25°C.[14] In this paper, we report ECR etching of GaP, GaAs, InP, and InGaAs as a function of Cl-based plasma chemistries at 10°C. Atomic force microscopy (AFM) and scanning electron microscopy (SEM) were used to evaluate surface morphology and etch profile.

EXPERIMENT

The GaP, GaAs, and InP samples etched in this study were semi-insulating, undoped substrates. The InGaAs sample was unintentionally-doped In$_{0.53}$Ga$_{0.47}$As lattice-matched to a semi-insulating InP substrate. The InGaAs was grown at 580°C in a metal organic vapor phase epitaxy (MOVPE) reactor. The samples were patterned using a photoresist mask. The ECR plasma reactor used in this study was a load-locked Plasma-Therm SLR 770 etch system with a low profile Astex 4400 ECR source in which the upper magnet was operated at 165 A. Energetic ion bombardment was provided by superimposing an rf-bias (13.56 MHz) on the sample.

245

Samples were mounted using vacuum grease on an anodized Al carrier that was clamped to the cathode and cooled with He gas. Etch gases were introduced through an annulus into the chamber just below the quartz window. To minimize field divergence and to optimize plasma uniformity and ion density across the chamber, an external secondary collimating magnet was located on the same plane as the sample and was run at 25 A. Plasma uniformity was further enhanced by a series of external permanent rare-earth magnets located between the microwave cavity and the sample. ECR etch parameters held constant in this study were: 10°C electrode temperature, 1 mTorr total pressure, 30 sccm total gas flow, 850 W of applied microwave power, and 150 W rf-power with a corresponding dc-bias of -140 ± 10 V.

Etch rates were calculated from the depth of etched features measured with a Dektak stylus profilometer after removing the photoresist mask. Samples were approximately 1 cm^2 and depth measurements were taken at a minimum of three positions. Error bars for the etch rates represent the uniformity across each sample. Surface morphology, anisotropy, and sidewall undercutting were evaluated with a SEM. The root-mean-square (rms) surface roughness was quantified using a Digital Instruments Dimension 3000 AFM system operating in tapping mode with Si tips.

RESULTS AND DISCUSSIONS

The etch rates for GaP, GaAs, InP, and InGaAs in an ECR generated Cl_2/Ar plasma are shown in Figure 1 as a function of %Cl_2. In general, the GaP and GaAs etch rates increased as the %Cl_2 increased due to higher concentrations of reactive Cl and the strong chemical component of the etch mechanism. The sputter rates for all 4 materials in a pure Ar plasma were typically less than 250 nm/min. Under these conditions the material removal was purely physical. This data agrees with our earlier results[8] but are higher than InP and GaAs sputter rates reported by Pearton *et al.* using an ion milling instrument at -200 to -800 V dc-bias.[15] Faster sputter rates reported in the ECR were due to the generation of higher ion densities (3 to 4 orders of magnitude higher in the ECR). Etch rates for the In-containing materials were much slower than etch rates for Ga-containing materials and were relatively constant, independent of %Cl_2. This was due to the low volatility of the $InCl_x$ etch products. The rms roughness for all samples was quite smooth, independent of the %Cl_2. InP exposed to a pure Ar plasma showed the highest rms roughness, 7.8 nm, as compared
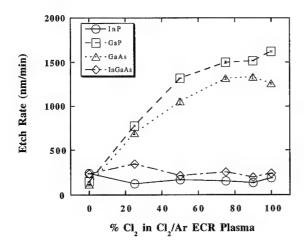

Figure 1. GaP, GaAs, InP, and InGaAs etch rates in an ECR-generated Cl_2/Ar plasma as a function of %Cl_2.

to the InP control which had an rms roughness of 0.28 nm. Pearton *et al.* observed similar behavior during Ar ion milling where the surface morphology of InP was typically rougher than GaAs etched surfaces.[15]

In Figure 2, etch rates are shown as a function of %Cl_2 in an ECR-generated Cl_2/N_2 plasma. Once again, the GaP and GaAs etch rates were faster than InP and InGaAs, however the increase occurred at much higher %Cl_2 than that observed in the Cl_2/Ar plasma. The GaP and GaAs etch rates were slower in the Cl_2/N_2 plasma possibly due to the generation of less reactive Cl in the plasma or the formation of involatile nitride deposits on the semiconductor surface. The InGaAs etch rate reached a maximum value at 50% Cl_2 (~350 nm/min) and then decreased at higher Cl_2 concentrations, whereas the InP etch rate was fairly constant and slow, independent of %Cl_2. The sputter rates were 2 to 3 times slower in pure N_2 as compared to pure Ar due to higher sputtering efficiency of Ar. The rms roughness was less than ~4 nm for all films, independent of %Cl_2.
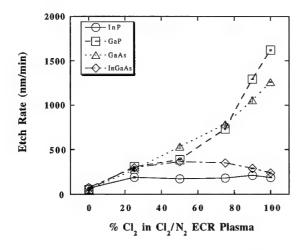

Figure 2. GaP, GaAs, InP, and InGaAs etch rates in an ECR-generated Cl_2/N_2 plasma as a function of %Cl_2.

In Figure 3, etch rates are shown as a function of %BCl_3 in an ECR-generated BCl_3/Ar plasma. The GaP and GaAs etch rates increased with higher %BCl_3, however the etch rates were much slower than those obtained in the Cl_2/Ar plasma due to the generation of less reactive Cl in BCl_3-based plasmas. In this study, etch rates for In-containing materials in BCl_3-based plasmas were comparable to those obtained in Cl_2-based plasmas. The rms roughness for GaP, GaAs, and InGaAs remained smooth independent of %BCl_3, whereas the InP rms roughness increased from ~8 nm in pure Ar to ~45 nm in pure BCl_3. This may be attributed to the preferential loss of P or micromasking effects at higher BCl_3 concentrations.

The dependence of etch rates on %BCl_3 in a BCl_3/N_2 ECR-generated plasma is shown in Figure 4. With the addition of N_2 to the BCl_3 plasma the Ga-containing materials etched at much higher rates at 75% BCl_3. Using optical emission, Ren *et al.* observed increases in the intensity of atomic and molecular chlorine lines when N_2 was introduced into an ECR-generated BCl_3 discharge with a maximum intensity at 75% BCl_3.[12, 13] Nitrogen enhanced the dissociation of BCl_3 resulting in higher concentrations of reactive Cl and Cl ions. This resulted in faster etch rates due to enhanced chemical etching and physical ion bombardment where the sputter desorption of $InCl_x$ etch products improved. This trend was observed for GaP and GaAs etch rates in this study, however the InP and InGaAs etch rates remained relatively constant similar to those obtained in the BCl_3/Ar plasmas. Ren observed an InP etch rate of ~700 nm/min at 850 W applied microwave
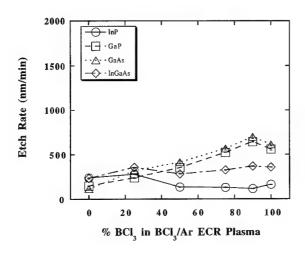
Figure 3. GaP, GaAs, InP, and InGaAs etch rates in an ECR-generated BCl_3/Ar plasma as a function of %BCl_3.
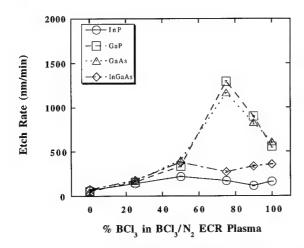

Figure 4. GaP, GaAs, InP, and InGaAs rms roughness in an ECR-generated BCl_3/N_2 plasma as a function of BCl_3 concentration.

power which was almost a factor of 5 faster than that observed in this study. This may be attributed to several differences in plasma conditions as well as the ECR source-to-sample distance which was ~30 cm greater in this report, thereby decreasing the ion density at the sample and the sputter desorption efficiency. Enhanced etch rates were not observed with the addition of N_2 to the Cl_2 plasma implying that N_2 did not liberate more reactive Cl under these plasma conditions.

In Figure 5, SEM micrographs of GaP, GaAs, InP, and InGaAs are shown as etched in an ECR-generated BCl_3/N_2 plasma at 75% BCl_3. The GaP and GaAs etches were anisotropic with
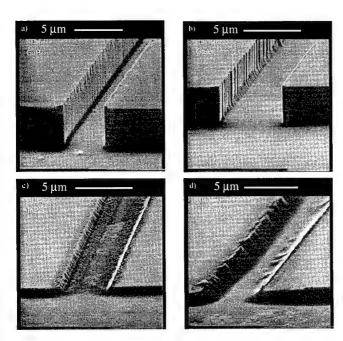
Figure 5. GaP, GaAs, InP and InGaAs SEM micrographs etched in an ECR-generated BCl_3/N_2 at 75% BCl_3.

smooth surface morphologies, however the GaAs showed some vertical striations in the sidewall possibly due to the striations in the mask which were replicated into the GaAs sidewall. There was also a slight "foot" at the base of the GaAs feature possibly due to mask-edge erosion. The InP and InGaAs etch profiles were severely overcut with poor dimensional control.

CONCLUSIONS

In summary, ECR etching of GaP, GaAs, InP, and InGaAs are reported as a function plasma chemistry. Etch rates for GaP and GaAs were faster in Cl_2-based plasmas as compared to BCl_3-based plasmas due to the generation of higher concentrations of reactive Cl. The InP and InGaAs etch rates were relatively slow, independent of plasma chemistry. This was due to the low volatility of $InCl_x$ etch products at $10°C$, poor sputter desorption efficiency at 850 W microwave power, and the large source-to-sample spacing used in this etch system. Surface morphologies showed very smooth pattern transfer for a wide range of plasma conditions for all materials, however InP was more sensitive to changes in the plasma chemistry. Etch profiles were typically anisotropic with smooth sidewalls for GaP and GaAs, whereas the etch profiles were more overcut with poor dimensional control for InP and InGaAs.

ACKNOWLEDGMENTS

REFERENCES

1. S. J. Pearton, F. Ren, A. Katz, J. R. Lothian, T. R. Fullowan, and B. Tseng, J. Vac. Sci. Technol. B **11**, 152 (1993).

2. E. L. Hu and R. E. Howard, Appl. Phys. Lett. **37**, 1022 (1980).

3. R. Cheung, Y. H. Lee, K. Y. Lee, T. P. Smith III, D. P. Kein, S. P. Beaumont, and C. D. W. Wilkinson, J. Vac. Sci. Technol. **B7**, 1462 (1989).

4. S. W. Pang, J. Electrochem. Soc. **133**, 784 (1986).

5. S. J. Pearton, U. K. Chakrabarti, A. P. Perley, and W. S. Hobson, J. Electrochem. Soc. **138**, 1432 (1991).

6. V. J. Law, M. Tewordt, S. G. Ingram, and G. A. C. Jones, J. Vac. Sci. Technol. B **9**, 1449 (1991).

7. J. Werking, J. Schramm, C. Nguyen, E. L. Hu, and H. Kroemer, Appl. Phys. Lett. **58**, 2003 (1991).

8. R. J. Shul, A. J. Howard, C. B. Vartuli, P. A. Barnes, and S. Weng, J. Vac. Sci. Technol. A, accepted.

9. S. J. Pearton, C. R. Abernathy, and F. Ren, Appl. Phys. Lett. **64**, 2294 (1994).

10. C. Constantine, C. Baratt, S. J. Pearton, F. Ren, and J. R. Lothian, Appl. Phys. Lett. **61**, 2899 (1992).

11. C. Constantine, C. Baratt, S. J. Pearton, F. Ren, and J. R. Lothian, Electron. Lett. **28**, 1749 (1992).

12. F. Ren, J. R. Lothian, J. M. Kuo, W. S. Hobson, J. Lopata, J. A. Caballero, S. J. Pearton, and M. W. Cole, J. Vac. Sci. Technol. **B14**, 1 (1995).

13. F. Ren, W. S. Hobson, J. R. Lothian, J. Lopata, J. A. Caballero, S. J. Pearton, and M. W. Cole, Appl. Phys. Lett. **67**, 2497 (1995).

14. S. Thomas III, K. K. Ko, S. W. Pang, J. Vac. Sci. Technol. A **13**, 894 (1995).

15. S. J. Pearton, U. K. Chakrabarti, A. P. Perley, and K. S. Jones, J. Appl. Phys. **68**, 2760 (1990).

Electron Cyclotron Resonance Etching of SiC in SF_6/O_2 And NF_3/O_2 Plasmas

F. Ren, J. M. Grow*, M. Bhaskaran**, J. W. Lee**, C. B. Vartuli**, J. R. Lothian, and J. R. Flemish***

    Lucent Technologies, Bell Laboratories, Murray Hill, NJ
*   New Jersey Institute of Technology, Newark, NJ
**   University of Florida, Gainesville, FL
*** Army Research Laboratory, Fort Monmouth, NJ

Abstract

Etching of β-SiC with electron cyclotron resonance (ECR) system was investigated. Anisotropic and smooth etching of SiC was demonstrated with SF_6/O_2 based discharges. The root-mean-square roughness increases from 35 nm to 56 nm for as deposit and etched sample, respectively. The addition of small amount oxygen enhanced the etch rate of SiC slightly, but further increase of oxygen content reduced the etch rate which resulted   from dilution of F ion and free radical densities. NF_3/O_2 based discharges also showed same trends and produced anisotropicly etching. However, the smoothness is not as good as SF_6/O_2 based discharges.

Introduction

There has been great attention on SiC based devices for high power and high temperature application due to its large energy bandgap and high saturation velocity[1]. In order to achieve good device performance, high quality materials and robust processing techniques are prerequisite. Besides metal contact technologies, patterning of device structure is another critical device fabrication step. Wet chemical etching of SiC was demonstrated with molten salts at elevated temperatures which is not suitable for device fabrication[2]. More recent photo-electrochemical etching was demonstrated[3], however up to date all the devices being demonstrated were used conventional reactive ion etching with CF_4, SF_6, or NF_3 based discharges[4-6]. Lately, electron cyclotron resonance etching was also used to [7]

In this work, we studied of the effects of both ECR and RF power levels on etch rates of SiC as well as the roughness and stoichiometry of etched SiC surfaces. . Optical emission spectroscopy was used to studied the plasma chemistry.

Experimental

The β-SiC were grown by low pressure chemical vapor deposition on <111> Si substrates at ~1000°C. The thickness of the films was 1.2 μm. Sample etchings were attained with a load-locked Plasm-Therm SLR 770 ECR system. The plasma was generated in an ASTEX 4400 low profile microwave power source operating at 2.45 GHz. A manual 3-stub tuner is used to minimize the reflected power. This ECR system also has two set of magnets, the upper one to produce resonance and the lower one positioned concentric to the lower electrode to allow control of incident ion current at the electrode(carrier/sample). This will collimate the divergent lines of flux which emanate from the ECR chamber to improve the flux uniformity across the sample. A microwave power at the range from 200 to 800 W was employed for the SiC etchings

in our studies. Ion energies were controlled by super-imposing a rf biased at 13.56 MHz on the sample plate. In our case, rf bias was set at 0-300 W, corresponding to a dc bias of up to approximately -275V. Samples were placed on a 4" sapphire wafer carrier that was clamped down to the cathode and cooled with He backside cooling. The temperature of lower electrode is controlled via a resistive heater up. The temperature used in the etching was kept at 50 °C. The process pressure was varied from 1 to 10 mTorr2 mtorr. Electronic grade SF_6 or NF_3 with different proportion of O_2 were introduced into the ECR Source through separated mass flow controllers. Sputtered indium-tin-oxide (ITO) layer was used as an etch mask and the patterns were defined with a conventional resist lift-off process. This ITO layer can be selectively removed with HCl solution. Etch rates were measured by stylus profilometry of the resulting features. Optical emission spectroscopy (OES) was performed with a Verity Instruments EP200DAS spectroscopic data acquisition system. The spectral sensitivity range is 100-900 nm and the spectrum were taken from the ECR etching chamber through a sapphire view port which is approximately 10 cm from the sample.

Result And Discussion

Fig. 1 shows the etch rates of SiC as a function of ECR power. The etch rate increases almost linearly with ECR power. This is due higher F ion and free radical densities generated at higher microwave power which is conformed with optical emission spectrum.
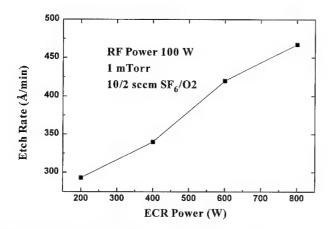

Fig. 1. Etch rates of SiC in SF_6/O_2 (10/2 sccm) discharges as a function of microwave power.

The etch rates also enhance with an addition of small oxygen percentage in the SF_6. There is no increase of F radicals being detected as in the case of CF_4/O_2 based discharges.[8] This enhancement of SiC etching in SF_6/O_2 discharges can results from the volatile CO_x compounds. As Illustrated in Fig. 2, further increases of O_2 proportion will actually decrease the etch rates by diluting the F ion and radical densities.
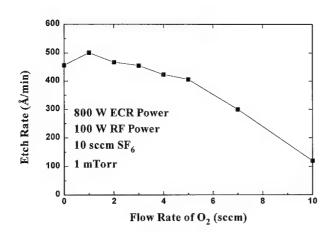
Fig. 2. Dependence of SiC etch rates on O_2 content in SF_6.

For the NF_3/O_2 based discharges, similar trends were observed. Higher microwave power and certain percentage of oxygen raised the SiC etch rates. But, the etch rates of SiC in NF_3/O_2 plasmas were 3-4 times higher than those in SF_6/O_2 plasmas. This is due to NF_3 has low dissociation energy which will produce more reactive F radicals. Fig. 3 shows the SEM of SF_6/O_2 etched SiC sample with ITO removed. Perfect anisotropic etch was demonstrated and excellent morphology was also achieved. This shows the SF_6/O_2 based ECR etching is suitable for device fabrication.
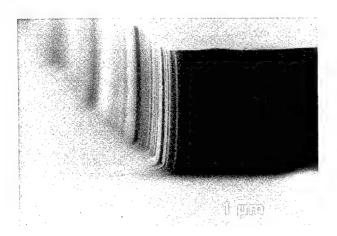

Fig. 3. SEM of SF_6/O_2 based plasma etched SiC.

253

Fig. 4 depicts the AFM scans (5 × 5 μm²) as deposit and etched SiC samples. The root-mean-square (RMS) roughness increased from 35 nm to 56 nm for as deposit and respectively. The high initial RMS roughness was due sample preparation prior to SiC growth.

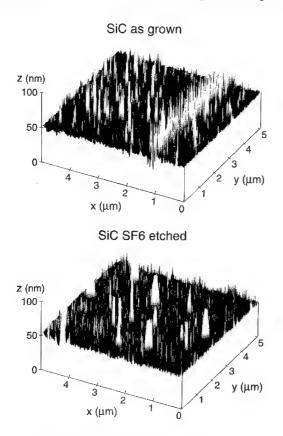SiC as grown

SiC SF6 etched

Fig. 4. AFM scans of as deposit and SF_6/O_2 based plasma etched SiC surface.

In conclusion, anisotropic and smooth etching of SiC has been demonstrated with SF_6/O_2 based discharges in a ECR system. The effects of microwave power and oxygen contents in SF_6 were also investigated. Higher microwave power produces more reactive ions and free radicals resulting in fast etch rates. Adding small amount of oxygen did increase the etch rate of SiC slightly, however further increasing of oxygen will reduce the etch rate significantly due to the dilution of reactive F species.

References

1. Muench and E. Pettenpual, J. Appl. Phys., **48**, 4823 (1977).

2. Marshall, J. W. Faust, and C. E. Ryan, "SiC 1973", p.657, University of South Carolina Press, Columbia (1973).
3. Shor and A. D. Kurtz, J. Electrochem. Soc., **141**, 778 (1994).
4. Yih and A. J. Steckl, J. Electrochem. Soc., **140**, 1813 (1993).
5. Palmour, R. F. Davis, T. M. Wallett, and K. B. Bhasin, J. Vac. Sci. Technol. **A4**, 590 (1986).
6. Wolf and R. Helbig, J. Electrochem. Soc., **143**, 1037 (1996).
7. Flemish, K. Xie, and J. H. Zhao, Appl. Phys. Lett., **64**, 2315 (1994).
8. D. L. Flamm, Solid State Tecnol. **22**, 109 (1979).

INTERACTIONS AT METAL/InP INTERFACES FORMED AT 300K AND 77K

J.W. PALMER*, W.A. ANDERSON*, D.T. HOELZER**, and H. HARDTDEGEN***
* State University of New York at Buffalo, Department of Electrical and Computer Engineering, Center for Electronic and Electro-Optic Materials, 215 Bonner Hall, Buffalo, NY 14260
** NYS College of Ceramics, Alfred University, McMahon Hall, Alfred, NY 14802
*** Institut für Schicht- und Ionentechnik, Forschungszentrum Jülich GmbH, Postfach 1913, D-5170 Jülich, Germany

ABSTRACT

Depositing Pd or Au on n-InP at cryogenic substrate temperatures has previously been found to significantly increase the barrier height of the resulting Schottky diode. Cross-sectional transmission electron microscopy (XTEM) has been performed on Pd/InP and Au/InP interfaces formed at room temperature (RT) and low temperature (LT) to determine the differences responsible for the change in barrier height. In the Pd case, a solid state amorphization which occurs at the interface upon RT metal deposition is nearly eliminated in as-deposited LT Pd/InP diodes. In the Au case, RT deposition results in the initial monolayers of Au entering the InP lattice, while no such effect was observed in the LT Au/InP diodes. It is clear that the LT deposition dramatically reduces the interaction between the metal and substrate, resulting in a greater barrier height. Enhanced barrier height Schottky diodes are crucial to the development of optical and electronic devices on InP. Preliminary results will be discussed on metal-semiconductor-metal (MSM) photodetectors and metal-semiconductor field-effect-transistors (MESFET's) fabricated using the LT process.

INTRODUCTION

InP is an attractive III-V compound semiconductor for use in high-speed field-effect transistors and optical devices. However, conventional Schottky barriers formed on n-InP typically exhibit low barrier heights in the range of 0.4-0.55 eV, hindering the development of these devices. In recent years, researchers have applied numerous techniques to enhance the Schottky barrier height (Φ_B) to n-InP [1,2]. In our laboratory, it was found that depositing Pd or Au on n-InP at liquid nitrogen substrate temperatures resulted in Φ_B near 0.96 eV [3,4]. This report summarizes the structural differences between LT and RT metal/InP interfaces responsible for the enhanced Φ_B observed in LT Schottky diodes. Also, the LT deposition process was applied in the fabrication of InP MSM photodetectors and MESFET's.

EXPERIMENT

Analysis of the metal/InP interfaces was done primarily by XTEM. Bulk samples of Pd/InP and Au/InP were formed at room temperature (RT) and liquid nitrogen temperature (LT). The InP was first cleaned in acetone, methanol, and de-ionized H_2O. It was then etched in $H_2SO_4{:}H_2O_2{:}H_2O$ (3:1:1) for 1 min, HF/H_2O (1:1) for 1 min, rinsed, and dried with N_2 gas. Metal deposition was done by thermal evaporation at a base pressure in the 10^{-8} Torr range. In the LT case, the substrate was cooled to near 77K with liquid nitrogen prior to deposition. Thin-foils for XTEM were then fabricated using a standard procedure of stack construction, slicing, thinning, disc cutting, dimpling and ion milling [5]. The specimens were analyzed by energy dispersion spectroscopy (EDS) using a Scanning Transmission Electron Microscope (UHV-

STEM) operating with a 100 keV accelerating potential and a 10Å spot size. A windowless Si(Li) detector was used to collect the X-ray spectra. Atomic percentage profiles of the interfaces were generated by stepping the spot across the metal/InP interfaces at 25Å intervals and collecting an X-ray spectrum at each point. Standard k-factor analysis [6] was used to calculate the atomic percentages from the EDS data. Imaging and diffraction work was also done using a conventional transmission electron microscope. In this report, only the EDS profiles are presented since they clearly illustrate the essential differences between the LT and RT diodes. Images and electron diffraction patterns have been published elsewhere [7,8].

MSM photodetectors were fabricated on semi-insulating (SI) InP using a LT Pd metallization (Fig 1a). Simple lift-off could not be used for the LT metallization because photoresist cannot withstand the severe thermal stresses present during the deposition. Instead, a bi-layer polyimide/ SiO_2 lift-off mask was used. First, the SI-InP was cleaned and etched as previously described. A polyimide layer, 0.6 μm thick, was then spun on and cured at 170°C, followed by deposition of a SiO_2 layer, 0.1 μm thick, by plasma enhanced chemical vapor deposition (PECVD). Photoresist was then applied and standard lithography was used to pattern the grid lines. Reactive-ion-etching (RIE) in CHF_3 was used to transfer the metallization pattern to the SiO_2, followed by RIE in O_2 which simultaneously patterned the polyimide and removed the photoresist. Immediately prior to LT Pd deposition, the samples were briefly etched in H_2SO_4:H_2O_2:H_2O (2:1:1) followed by HCl:H_2O (1:10) to remove any damage to the InP left by RIE. LT Pd was then deposited as previously described. The bi-layer lift-off mask after LT metal deposition is shown in Fig 1b. Lift-off was done in Shipley 1165 remover, which dissolved the polyimide over a period of several hours. Finally, a SiO anti-reflection coating, 1100Å thick, was deposited to attain near-zero reflection at λ = 840 nm. The photo-response of the detectors was measured using a Ti:Saphire laser operating with λ=840 nm, continuous wave, and a 100 μm FWHM spot size.

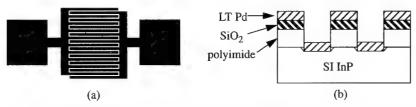Fig 1 - (a) Plan-view sketch of a MSM detector. Line width x line spacing = 3 x 3 μm, total active area = 150 x 180 $μm^2$; (b) Cross section of the structure immediately prior to lift-off.

MESFET's were fabricated using a 3-level process of mesa isolation, ohmic contact formation, and LT Pd gate metallization. The InP mesa-isolation was done by RIE in a H_2/CH_4/ O_2 mixture using a SiO_2 mask [9]. Ohmic contact metallization was done by standard lift-off of Au:Ge/Ni followed by rapid thermal annealing (RTA) at 380°C for 10 sec. The LT Pd gate metallization was done using the bi-layer lift-off mask as previously described. Fig 2 shows a cross-sectional view of an InP MESFET.
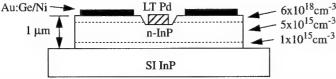

Fig 2 - Cross-sectional view of an InP MESFET. Gate length = 2 μm, gate width = 200 μm.

RESULTS AND DISCUSSION

XTEM of RT and LT Pd/InP

Fig 3a is an atomic compositional profile of RT Pd/InP obtained by EDS. An amorphous layer approximately 180Å thick exists between a polycrystalline Pd layer and the InP substrate. The crystalline nature of the layers was verified by selective area electron diffraction (SAED). The composition of the amorphous layer varies from Pd-rich near the Pd/amorphous interface to InP-rich near the amorphous InP interface. In Fig 3a, distance=0 corresponds to the edge of the InP lattice. This convention will be used in the other compositional profiles as well.

Fig 3b is a compositional profile of LT Pd/InP obtained by EDS. In LT Pd/InP, the thick amorphous interaction layer of RT Pd/InP was not observed. Instead, a thin P-rich amorphous interlayer was present between the Pd polycrystalline layer and the InP substrate. This interlayer was approximately 30Å thick on average, and up to 50Å thick in localized areas. The LT Pd/InP compositional profile also shows a narrow region of excess In present in the Pd polycrystalline layer near the P interlayer. It appears that In had begun diffusing into the Pd, leaving a thin P layer behind at the interface.
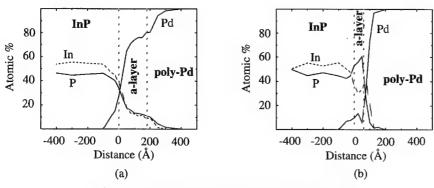

Fig 3 - (a) Compositional profile of RT Pd/InP from EDS;
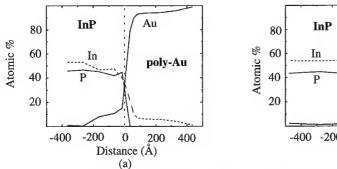*(b) Compositional profile of LT Pd/InP from EDS.*

In RT Pd/InP contacts, a solid state amorphization reaction occurs upon deposition of the Pd. One criterion for a solid-state amorphization reaction is a rapid-diffusivity of one of the species [10]. It has been suggested that diffusion of the more mobile Pd into an InP substrate at low temperatures, at which In and P are relatively immobile, leads to the formation of the amorphous ternary compounds [11]. The thickness of the amorphous layer increases with low-temperature annealing, as the reaction with Pd consumes more and more of the InP substrate. At higher temperatures, In and P can also diffuse, and more stable crystalline phases are eventually formed. One work [12] found that a 130Å thick amorphous interlayer in an as-deposited Pd/InP sample increased to about 600Å thick after annealing at 225°C. Pd_2InP and Pd_5InP crystalline phases were then detected in the interlayer after annealing at temperatures between 225°C and 275°C. At temperatures greater than 400°C, these phases decomposed into PdIn and PdP_2, which were thermodynamically stable in contact with InP. Hence, in the Pd/InP system, an amorphous metastable phase is formed as an intermediate step to the binary crystalline phase formation.

In this work, the 180Å thick amorphous interlayer found in RT Pd/InP is very similar to the results of others. However, depositing Pd at low substrate temperatures prevented this interaction layer from forming. Instead, a P-rich amorphous interlayer was found in LT Pd/InP averaging only 30Å in thickness. A possible explanation is that near 77K, the Pd diffusivity in InP is reduced to the point where the solid state amorphization process cannot occur. However, upon subsequent annealing at 100°C during the XTEM sample preparation, a different thin amorphous layer grew at the interface. We believe that the elimination of the thick amorphous interaction layer is responsible for the high barrier height observed in as-deposited LT Pd/InP diodes.

XTEM of RT and LT Au/InP

Fig 4a is a compositional profile of RT Au/InP obtained by EDS. There is no amorphous interaction layer present, unlike RT Pd/InP. However, there is a significant amount of Au extending over 200Å into the InP lattice and a considerable amount of In throughout the thickness of the RT Au film.

Fig 4b is a compositional profile of LT Au/InP obtained by EDS. The main difference between this profile and that of the RT Au/InP sample was that there appears to be much less Au extending into the InP lattice. The In concentration profile in the bulk Au is similar in both RT and LT Au/InP. Also, both RT and LT Au/InP profiles show a small region of excess P in the InP lattice near the metal-semiconductor interface.
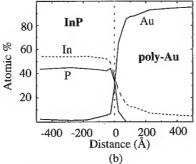

Fig 4 - (a) Compositional profile of RT Pd/InP from EDS;
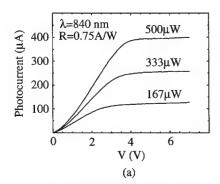(b) Compositional profile of LT Pd/InP from EDS.

The interaction between Au overlayers and InP and its relation to the barrier height of the interface has been the subject of extensive research. Basically, the interaction between Au and InP upon formation of the contact can be split into two stages. First, the initial several monolayers of Au deposited are absorbed into the InP substrate during a standard deposition, leaving various defects in the crystal structure of the semiconductor [13]. In one work [14], it was found that over 17 monolayers of Au were absorbed by the InP before bulk Au appeared on the semiconductor surface. The second stage is that after bulk Au forms, In enters it via a dissociative diffusion process which proceeds very rapidly, even at room temperature [15]. This proceeds until a saturated solid solution of In in Au is achieved. The phosphorous atoms that are released when In enters the Au remain unreacted and occupy non-lattice sites in the metallization near the interface. The diffusion during this stage of the reaction is highly unidirectional in that Au does not further enter the substrate [16].

It appears that the first stage of this process is critical to the formation of the Schottky barrier height in Au/InP contacts. There is significant evidence that low Φ_B values near 0.5 eV for a standard Au deposition on InP are the result of Fermi level pinning due to the crystal defects caused by the absorption of the initial monolayers of Au. It has been observed that the pinned Fermi level matures to its final position in the bandgap after only several mono-layers of metal are deposited [17], before bulk Au ever appears on the InP surface. We believe that the interaction between the metal and semiconductor proceeded in this manner in the RT Au/InP interface of this work. The small tail of Au observed extending into the InP was due to the penetration of the initial monolayers of Au into the InP. However, in the LT Au/InP interface, it appears that the extent to which this first stage of the process occurred was reduced significantly, resulting in a much higher barrier height. The second stage of In diffusing into the Au happened in both the RT and LT samples, resulting in a small atomic percent of In throughout the thickness of the Au films. Such profiles are very similar to previous results [16], and it appears that this stage of the reaction does not dramatically alter the final value of Φ_B.

MSM Photodetectors and MESFET's

Typical illuminated dc characteristics of InP MSM photodetectors fabricated in this work are shown in Fig 5a. The MSM photodetector had a LT Pd metallization on SI InP, as previously described. The dark current of the detector was linear with voltage, and had a value of 30 nA at 6 V. This type of detector is transit-time limited, and the onset of current saturation corresponds to the voltage at which the carrier transit time becomes less then the carrier lifetime. The responsivity (R) of the detector shown is approximately 0.75 A/W, which corresponds to a total quantum efficiency of 1.1. Since approximately half the incident light is blocked because of grid shading, there must be an internal gain of over 2 present in the detector, the cause of which is still under investigation. The R value and saturation characteristic of this detector are superior to those of previous detectors on SI InP using standard RT metallizations [18].

Typical dc characteristics of InP MESFET's having a gate length of 2 μm and a gate width of 200 μm are shown in Fig 5b. The maximum transconductance (g_m) was 42 mS/mm, the barrier height of the gate was 0.83 eV, and the drain current at $V_{gs} = 0$ was $I_{ds} = 3.5$ mA. Most previous efforts to fabricate InP MESFET's have generally used a thin insulator to passivate the gate area, and g_m values around 100 mS/mm have been reported [19]. The reason we have a considerably lower g_m is that our channel doping is 5×10^{15} cm^{-3}, while most others used a channel doping near 1×10^{17} cm^{-3}. Increasing the channel doping should increase g_m in our devices.
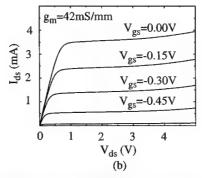

Fig 5 - (a) Illuminated characteristics of MSM photodetectors; (b) MESFET characteristic.

CONCLUSIONS

LT Pd/InP and LT Au/InP interfaces had as-deposited barrier heights over 0.9 eV, compared to barrier heights near 0.5 eV for RT metal/InP interfaces. RT Pd/InP exhibited an amorphous interaction layer 180Å thick containing Pd, P, and Pd, while LT Pd/InP had a P-rich interlayer about 30Å thick on average. RT Au/InP had a significant Au concentration extending over 200Å into the InP lattice, while LT Au/InP did not. The high barrier height observed in both LT Pd/InP and LT Au/InP are related to a significant reduction in the interaction between the metals and InP upon formation of the interfaces. This decrease in the interaction relieves the Fermi level pinning, resulting in higher barrier heights. The LT deposition technique was applied in the fabrication of InP MSM photodetectors and MESFET's. In the photodetectors, a flat saturated regime resulted with R = 0.75 A/W. In the MESFET's, g_m = 42 mS/mm was measured, which can probably be improved by increasing N_D in the channel.

ACKNOWLEDGEMENTS

REFERENCES

1. D.T. Quan and H. Hbib, Solid State Elec. **36**, 339 (1993).
2. A.A. Iliadis, W. Lee, and O.A. Aina, IEEE Elec. Device Lett. **10**, 370 (1989).
3. Z.Q. Shi, R.L.Wallace, and W.A. Anderson, Appl. Phys. Lett. **59**, 446 (1991).
4. Z.Q. Shi and W.A. Anderson, J. Appl. Phys. **70**, 3137 (1991).
5. J.C. Bravman and R. Sinclair, J. Elec. Mic. Technol. **1**, 53 (1984).
6. *Principles of Analytical Electron Microscopy*, edited by D.C. Joy, A.D. Romig, and J.I. Goldstein (Plenum Press, New York and London, 1986), pp. 123-217.
7. J.W. Palmer, W.A. Anderson, D.T. Hoelzer, and M. Thomas, J. Elec. Mater., submitted.
8. J.W. Palmer, W.A. Anderson, and D.T. Hoelzer, Proc. 1994 Fall MRS Meeting **355**.
9. J.W. McNabb, H.G. Craighead, H. Temkin, and R.A. Logan, J. Vac. Sci. Technol. B **9**, 3535 (1991).
10. D.H. Ko and R. Sinclair, J. Appl. Phys. **72**, 2036 (1992).
11. R. Caron-Popowich, J. Washburn, T. Sands, and A.S. Kaplan, J. Appl. Phys. **64**, 4909 (1988).
12. D.G. Ivey, P. Jian, and R. Bruce, J. Elec. Mater. **21**, 831 (1992).
13. R.H. Williams, A. McKinley, G.J. Hughes, V. Montgomery, and I.T. McGovern, J. Vac. Sci. Technol. **21**, 594 (1982).
14. K.A. Stair and Y.W. Chung, Phys. Rev. B **32**, 3904 (1985).
15. N.S. Fatemi and V.G. Weizer, J. Appl. Phys. **67**, 1934 (1990).
16. N.S. Fatemi and V.G. Weizer, J. Appl. Phys. **65**, 2111 (1989).
17. L.J. Brillson, C.F. Brucker, A.D. Katnani, N.G. Stoffel, R. Daniels, and G. Margaritondo, J. Vac. Sci. Technol. **21**, 564 (1982).
18. D. Kuhl, F. Hieronymi, E.H. Bottcher, and D. Bimberg, IEEE Phot. Tech. Lett. **2**, 574 (1990).
19. Y. Robach, M.P. Besland, J. Joseph, G. Hollinger, P. Viktorovitch, P. Ferret, M. Pitaval, A. Falcou, and G. Post, J. Appl. Phys. **71**, 2981 (1992).

INVESTIGATION OF DEEP-LEVEL DEFECTS IN 10 MeV ELECTRONS IRRADIATED SI-GaAs

Fengmei Wu,*Zhouying Zhao and Haifeng Li
Department of Physics, Nanjing University, Nanjing 210093, P. R. China
*Nanjing Electronic Devices Institute, Nanjing 210016, P. R. China

Abstract

The deep-level defects in 10 MeV electron irradiated undoped semi-insulating (SI) LEC GaAs were investigated. The results show that the density of EL2 (Ec-0.83eV) and EL12 (Ec-0.69eV) defects increases and the density of EL6 (Ec-0.39eV) and EL3 (Ec-0.58eV) defects decreases in irradiated SI-GaAs at higher fluence levels. At lower fluences, we observe decrease in density of EL2 and EL12 defects, however, the density of the EL6 and EL3 defects is increased. It could be related mainly to the dissociation of the EL2 and EL12 defects. The influence of 10 MeV electrons irradiation on the resistivity will also be discussed.

Introduction

In the case of bulk Liquid Encapsulated Czochralski (LEC) GaAs substrate, the semi-insulating is realized by the compensation of shallow carbon acceptors by deep donors, EL2 [1]. The EL2 density of bulk materials is in the high levels being over than 10^{16} cm^{-3}, commonly, but in practice the SI-GaAs material with very low densities of carbon and EL2 is desired. The point defects and especially the EL2 defect in electron irradiated GaAs have attracted much attention in the past twenty years [2-5]. However, the density of the induced defects by varying 10 MeV electron irradiation fluence has not been reported so far.

In this work, we investigate the effects of 10 MeV electron irradiation on deep-level defects density using Photo Induced Transient Spectrum (PITS) [6]. We find that the irradiation tends to remove to some extent deep level EL2 at lower fluence levels in undoped SI-GaAs. At higher fluences, the density of EL2 defect increases. The influence of 10MeV electron on the resistivity will also be discussed.

Experiment

Undoped semi-insulating LEC(100) GaAs wafers were small pieces of approximately 4x8 mm^2, which served for PITS measurement. Contacts present an additional possible source of error and great care was taken to achieve ohmic contacts. Indium-contacts were deposited and sintered at 400°C for 15 min. The PITS measurements were then performed with DL 4600 Deep Level Transient Spectroscopy (DLTS) system [7]. The wave length of pulse light is 850 nm, the width 5 ms. 10 MeV electron irradiations were carried out in an accelerator at room temperature. The electron fluence was 10^{14} to 10^{16} cm^{-2}. We used the PITS method to determine the energy level E and current intensity I. The density of these defects is directly proportional to the intensity. Because of the difficulty in separating hole traps and electron traps using PITS method, many workers assume that defects present in n-type GaAs are also present in SI-GaAs.
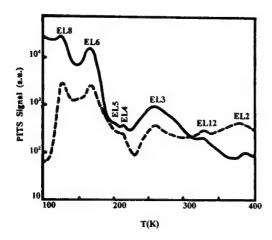
Results and Discussion.

Fig.1   The PITS signal for 10 MeV electron irradiated undoped SI-GaAs.
The window setting was 200 s^{-1}.The electron fluence was 1×10^{14} cm^{-2}
_____ after irradiation,----- before irradiation.

Figure 1 shows the PITS signal for undoped SI-GaAs sample irradiated at 1×10^{14}cm^{-2}.
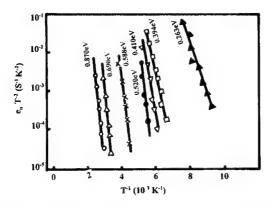Seven peaks can be observed obviously. Figure 2 shows the ln (e_n/T^2) as a function of

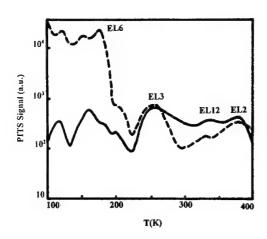Fig.2 Temperature dependence of the electron emissivity e_n

264

Fig.3   The PITS signal for 10 MeV electron irradiated undoped SI-GaAs.
The window setting was 200 s^{-1}. The electron fluence was 1x 10^{15} cm^{-2}
_____ after irradiation, ----- before irradiation.

temperature, where, e_n is electron emissivity. By plotting ln (e_n/T^2) vs 1/T, one obtains a straight line as shown in Fig.2, from which energy level E and the capture cross section σ of these defects can be determined. We have identified the EL2 (Ec-0.870eV), EL12 (Ec-0.690eV), EL3 (Ec-0.588eV), EL6 (Ec-0.394eV), EL4 (Ec-0.520eV), EL5 (Ec-0.410eV) and EL8 (Ec-0.263eV).

Two midgap levels have been reported in unirradiated GaAs by different works [1][8]. We also observed two peaks in PITS signal for unirradiated and irradiated SI-GaAs. Similarly two midgap states, labelled EL2 and EL12 have been reported in unirradiated GaAs through DLTS method [1]. Another group has reported the EL2 defect consisting of two peaks, labelled EL21 and EL22 with energies at Ec-0.74eV and between 0.54 and 0.73eV above the valence band [8].The identity of these two peak is not fully known, and we will call them EL2 and EL12. A broad peak appears at about 250 K, reminiscent of the U trap [9] labelled EL3, but we always could not resolve it sufficiently to measure its energy level. A peak appears at about 150 K which we identified with the EL6 trap [10]. Other two peaks whose energy coincides with EL5 [1] or EL8 [1], we will still call them EL5 or EL8.

Due to the uniformity of SI-GaAs material, the values of the energy levels of EL2, EL12 , EL6 and so on are not identical in different samples. The range of the energy levels for EL2, EL12 and EL6 is (0.77-0.97eV), (0.61-0.81eV) and (0.27-0.40)eV, respectively.

Fig.3 and Fig.4 show the PITS signal for SI-GaAs samples irradiated at 1x10^{15} and 1x10^{16} cm^{-2}, respectively. It is noticeable in Fig.3 and Fig.4 that at higher fluences, the density of EL2 and EL12 defects increases and density of EL6 and EL3 defects decreases; however, for sample irradiated at 1x10^{14} cm^{-2}, the density of EL2 defect decreases and the density of EL6 defect increases. Fig.5 shows the PITS relative intensity I/I$_0$ of EL2, EL12, EL3 and EL6 defects as a function of 10 MeV electrons fluences in undoped SI-GaAs. I$_0$ or I is the intensity of PITS signal
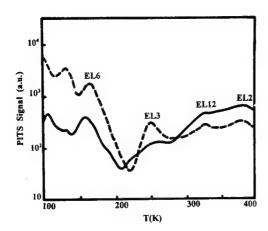
Fig.4 The PITS signal for 10 MeV electron irradiated undoped SI-GaAs.
    The window setting was 200 s^{-1}. The electron fluence was 1x 10^{16} cm^{-2}
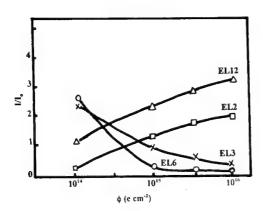   _____ after irradiation, ----- before irradiation.

Fig.5 The relative intensity of PITS signal for EL2, EL12, EL3 and EL6 defects as
    a function of 10MeV electron fluence in undoped SI-GaAs .
    Window setting:200 s^{-1}. Bias voltage:6V.

before and after irradiation, respectively. The PITS intensity of EL2 and EL12 levels after irradiation increases over the 10^{15} cm^{-2} to 10^{16} cm^{-2} fluence range, i.e. there is an increase in the density of EL2 and EL12. Contrary to general perception of damage of semiconductors on nuclear irradiation, we observe decrease in the density of EL2 and EL12 of SI-GaAs on electron irradiation at lower fluence levels.

It is recognized that the EL2 and EL12 defects in the forbidden energy band limit the use of GaAs semiconductor on high speed application. Consequently, there has been much work related to the understanding of these traps. One method of introducing traps in a rather controlled manner is through radiation with light nuclear particles. Electron radiation is more convenient and economical. Borkovskaya et al [5] proposed that certain defects, such as the Frenkel pair, can disappear if as a result of the radiation an interstitial atom returns to its proper lattice site. In our work, we observe the decrease of the EL2 and EL12 defects, moreover, the increase of EL3 and EL6 defects at lower fluences. Since the major effect of irradiation is the creation of vacancies and interstitials, which in turn lead to the EL2 and EL12 etc.. The identity of these traps is still being debated [11]. The candidates are an isolated arsenic at gallium site (As_{Ga}) or As_{Ga}-As_i [11] and $As_{Ga}V_{As}V_{Ga}$ [12]. According to $As_{Ga}V_{As}V_{Ga}$ model proposed by Zou [12], the formation of EL2 defect can be expressed as

$$As_{AS} + (V_{Ga})_2 = As_{Ga}V_{As}V_{Ga}{}^+ \text{ (or } As_{Ga} + V_{Ga}V_{As}) + e^- \tag{1}$$

As shown in Eq.(1) both As_{Ga} and $As_{Ga}V_{As}V_{Ga}$ can be formed from $(V_{Ga})_2$, which are expected to be the dominant vacancy species at high temperature in LEC GaAs crystals grown from an As-rich melt [13]. At lower fluences, the EL2 defect can be dissociated. Reaction (1) is proceeding toward the direction of dissociation. Consequently, EL2 density is decreased, and EL6 and EL3 which are simpler complex defects are increased at room temperature. At higher fluences, 10 MeV electrons result in the creation of high density of V_{As}, V_{Ga}, $(V_{Ga})_2$, and As_i etc. Reaction (1) is proceeding toward the direction of formation of EL2 and EL12 traps.

The resistivity measurements were carried out by using Hall effect at 300 K. We observe obvious increase in the resistivity of SI-GaAs on 10 MeV electron irradiation at about 10^{15} cm^{-2} fluence level. The increase in the resistivity ranges from 5% to 80%. It is found that the resistivity of SI-GaAs not only is determined by EL2 and EL12 levels, but is affected by EL6 and EL3 levels etc.. In our samples irradiated at 1×10^{15} cm^{-2} fluence, the increase of EL2 and EL12 defects is not apparent, however, the decrease of EL6 and EL3 defects is remarkable. The decrease of EL6 and EL3 defects benefit the increase of the resistivity of SI-GaAs.

Conclusions

In conclusion, we report the change in density of EL2 and EL12 of SI-GaAs by varying 10 MeV electron irradiation fluences. At lower fluences, we observe the decrease in density of EL2 and EL12 traps and the increase in density of EL6 and EL3. It appears likely that the dissociation of EL2 and EL12 defects occurs at lower electron irradiation fluences. Whereas the results are contrary at higher fluences. Choosing

reasonable irradiation fluence,the resistivity of undoped SI-GaAs can be raised.

References

[1] G. M. Martin , A. Mitonneau and A. Mircea , Electron Lett. **13**, No.7, 191(1977)

[2] D. V. Lang , L. C. Kimerling and S. Y. Leung , J. Appl. Phys. **47**,No.8, 3587(1976)

[3] D. Stievenard , J. C. Bourgoin and D. Pons , Physica **116**B, No. 1-3, 394(1983)

[4] N. K. Goswami, R. C. Newman, and J. E. Whitehouse, Solid State Commun. **40**, No. 4, 473(1981)

[5] O. Yu Borlovskaya, N. Y. Dmitruk, V. G. Litovchenko and O. N. Mishchuk, Sov. Phys. Semicond. **23**, No.1, 129(1989)

[6] S. R Blight and H. Thomas, J. Appl. Phys. **65**, 215(1889)

[7] D. V. Lang, J. Appl. Phys. **45**, No.7, 3022(1974)

[8] P. Omling, P. Silverberg, and L. Samuelson, Phys. Rev., B**38**, No.5,3606(1988)

[9] G. M. Martin, E. Esteve, P. Langlade, and S. Makram-Ebeid, J. Appl. Phys., **50**, No.10, 2655(1984)

[10]F. D. Auret, W. R. Leitch, and L. S. Vermaak, ibid **59**, No.1, 158(1986)

[11]K. Krambrock, J. M. Spaeth, C. Delerue, G. Allan, and M. Lannoo, Phys. Rev., B, **45**, No.3, 1481(1992)

[12]Yuanxi Zou, 1982 Gallium Arsenide and Related Compounds(Inst. Phys. Conf. Ser., No.63, 185(1981)

[13]R. H. Logan, and D. T. Hurle, J. Phys. Chem. Solid **32**, 1793(1971)

A STUDY OF ANNEALING BEHAVIOR OF EL2 AND EL6 GROUPS IN SI-GaAs

Wu Fengmei, and Zhao Zhouying*
Department of physics, Nanjing University, Nanjing, 210093, China
*Nanjing electronic Devices Institute, Nanjing, 210016, China

ABSTRACT

We present annealing behavior for EL2 and EL6 groups as dominant deep levels in semi-insulating GaAs using Photo Induced Transient Spectroscopy (PITS) measurement. During rapid thermal annealing, a relation has been identified between EL2 group at 0.79 and 0.82 eV and EL6 group at 0.24, 0.27 and 0.82 eV below the conduction band. It is found that they may be close in structure, and belong to the EL2 and EL6 groups, respectively. In rapidly annealed samples, the quantity of all defects in the EL2 group increases, while that in the EL6 group decreases. However, by furnace annealing at 950°C for 5 hours, some of the defects in the EL2 group break up, and the quantity of all defects in the EL6 group increases. It is suggested that the EL2 group and EL6 group are related in their microscopy structures. We then discuss a relation between the two groups and their origins.

1. INTRODUCTION

Deep defect levels are important and very often determine the recombination properties and the resistivity in semi-insulating (SI) GaAs. Recently, there have been shown that deep traps are also responsible for persistent currents observed frequently in SI-GaAs[1-3]. The point defects and especially the EL2 and EL6 defects have been studied extensively using various characterization techniques and theoretical calculations to determine the atomic structures of the defects. From these studies, many models were presented. The EL2 and EL6 defects are suggested to be $As_{Ga}V_{As}V_{Ga}$[4-6], $As_{Ga}As_i$[7,8] and $V_{Ga}V_{As}$[9], $As_{Ga}V_{Ga}$[10]. Some recent reports proposed that there is a relation between EL2 and EL6 defects[9-12]. According to these reports, the atomic structure of EL2 and EL6 is assumed to be $As_{Ga}V_{As}V_{Ga}$ and $V_{Ga}V_{As}$, respectively. Despite an enormous worldwide interest in these centers, a microscopic identification and explanation for their behaviors have not been provided so far.

In this paper we report the annealing behaviors of the EL2 group and EL6 group in the undoped LEC semi-insulating GaAs by rapid thermal annealing (RAT) and normal furnace annealing. This work emphasizes that there is a direct relation between EL2 and EL6 groups in their microscopic structures.

2. EXPERIMENT

Good-quality commercial liquid-encapsulated Czochralski (LEC) SI-GaAs was used in this study. They were labeled as grown sample A and sample B annealed at 950°C for five hours. The wafer was cut into small pieces of approximately $5\times5mm^2$ which served for PITS measurement[12]. In order to take the PITS spectra, two ohmic contacts were made on each sample. They consisted of 0.5mm diameter spots sintered at 400°C for 5 minutes under H_2 atmosphere. Before fabricating ohmic contacts, the surface layers of 0.5 μm thickness were

chemically etched in order to remove the thermally damaged layers.

The A samples were annealed by the rapid thermal process at 500℃-800℃ for 10 seconds under N_2 atmosphere. The rate of elevated temperature was 100℃/s. The PITS measurement was performed with a BIO-RAD DL4600 deep level transient spectroscopy system equipped to EG&G company 181 model current preamplifier. The wave length of pulse light is 850nm, the width 4 ms. 6V voltage was applied between two ohmic contacts. PITS temperature scan was from 77k to 400K. Changing rate windows, we obtained a series of PITS curves.

The essential feature of PITS is the ability to set an emission rate window so that the measurement apparatus responds only when it sees a transient with a rate within this window. Thus, if the emission rate of a trap is varied by varying the sample temperature, the instrument will show a response peak (the peak intensity is proportional to trap concentration) at the temperature where the trap emission rate is within the window. If we take the $Ln(e_n/T^2)$ as a function of temperature, where e_n is electron emissivity, by plotting $Ln(e_n/T^2)$ vs. $1/T$, the activation energy E_a and the capture cross section of the defects can be determined.

3. RESULTS AND DISCUSSION

Fig.1 shows PITS signal for as-grown sample A and sample B annealed at 950℃ for five hours in our work. In Fig.1, PITS signal is represented by logarithmic coordinate, and the rate window is 20 s^{-1}. Eight PITS peaks are obvious in Fig.1. Their activation energy E_a is shown in table 1. Because of the difficulty in separating hole traps and electron traps using PITS method, many workers[9,13] grow n-type LEC GaAs in order to perform DLTS measurements and then assume that defects present in n-type GaAs are also present in SI material.
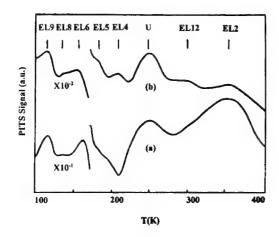

FIG.1. The PITS signal for SI-GaAs (a) sample A: as-grown
(b) sample B: annealed at 950℃, 5 h.

TABLE 1. The activation energy (E_a) on LEC SI-GaAs studied in this work.

Energy level	EL9	EL8	EL6	EL5	EL4	Uband	EL12	EL2
E_c-E_a(eV)	0.24	0.27	0.38	0.42	0.54	?	0.79	0.82

Two midgap levels EL2 and EL12 are the primary electron traps in SI-GaAs. U trap is composed of two close peaks. We could not resolve it sufficiently to measure its energy. The EL6 is also common electron trap in variant GaAs. From Fig.1 we observe a significant change in PITS signal intensity, the intensity of EL6 and EL9 defects is much larger than that of EL2 and EL12 defects after annealing at 950°C for 5 hours, but energy position is almost not changed. On the one hand, the density of the EL2 and EL12 defects in sample B is decreased compared with that in sample A. On the other hand, the density of EL6, EL8 and EL9 defects is increased.

Fig.2 shows the PITS spectra for SI-GaAs sample rapidly annealed (10s) according to various temperatures. In Fig.2 the U level splits apart into two peaks after 500°C annealing. It is noticeable in Fig.1(a) and Fig.2 that the intensity of EL2 and EL12 defects is increased and the intensity of EL6, EL8 and EL9 is decreased for RTA samples compared with those for as-grown crystal. This result is as contrasted with the change of Fig.1. It is important that there are variations for the intensity of these levels in Fig.2.
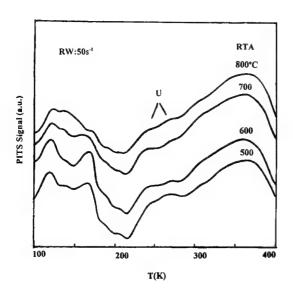

FIG.2. PITS signals of sample A annealed for 10 s according to the annealing temperature.

Fig.3 represents PITS intensity variation of the deep levels in SI-GaAs as a function of annealing temperature. From Fig.3 there are similar variation trends in PITS intensity between EL2 and EL12, or among EL6, EL8 and EL9. The density of EL12 and EL2 defects first increases and then gets saturated with increasing annealing temperature from 500℃ to 800℃. Weng et al. reports similar results[14]. For EL6, EL8 and EL9, the intensity of PITS signal reaches maxima at about 600℃, then reduces. The variation of the EL4 and EL5 defects is similar to that of EL6 defect. But their variation is not so obvious as that of the EL6 defect. It is plausible that EL4 and EL5 defects are the complex which is related to EL6 defect and some impurities[15].
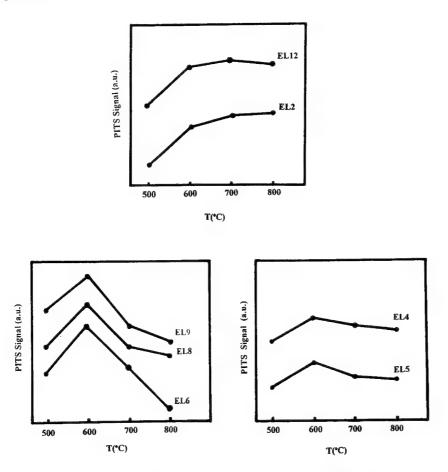
FIG.3. PITS intensity of the defects in SI-GaAs as a function of annealing temperature (RTA).

From these annealing experimental results, it can be proposed that the EL2 and EL12 defects may have similar atomic structures because of their close energy positions and similar annealing behaviors. They can be ascribed to EL2 group. For the same reason, the EL6, EL8 and EL9 defects are ascribed to the EL6 group. On the other hand. it can be seen that there is a direct relation between the EL2 group and EL6 group in their annealing process. After thermal treatment at less then 900℃, the density of EL6 group is reduced and the density of the EL2 group raised. However, after thermal treatment at above 900℃, the density of EL2 group decreases and the density of EL6 increases. It is possible that some of EL2 defect dissociates above 900℃. According to the above, structure of EL2 and EL6 may be $As_{Ga}V_{As}V_{Ga}$ and $V_{As}V_{Ga}$.

There is great strain force in LEC GaAs crystal grown from an As-rich melt. They promote the formation of the dislocation and the storage of total strain energy in cooling process[16]. A reduction in the total strain energy of a system should result from the formation of a defect complex, which will therefore be facilitated in the neighborhood of a dislocation where lattice distortion exists. During thermal process at less than 900℃, both As_{Ga} and $V_{As}V_{Ga}$ can move to form $As_{Ga}V_{As}V_{Ga}$ under the action of strain energy. Increasing annealing temperature, the density of the EL2 defect is toward saturation. In our experiment, above 900℃ temperature, especially long time annealing, $As_{Ga}V_{As}V_{Ga}$ dissociates to form As_{Ga} and $V_{As}V_{Ga}$. The EL6 may have the $V_{As}V_{Ga}$ structure. In Fig.3 after RTA at 600℃ both EL2 and EL6 defects increase. It may be because of $V_{As}V_{Ga}$ multiplying during the movement of the dislocations[18]. The increase of the EL6 may be in excess of the decrease of EL6 due to forming the EL2 defect.

4. CONCLUSION

The technique of photo induced transient spectroscopy has been used to observe thermal behaviors of deep-level defects in annealed SI-GaAs. With isochronic rapid thermal annealing at temperatures ranging from 500℃ to 800℃, PITS signals of EL2 and EL12 strengthen first and then get saturated, and those of EL6、EL8 and EL9 reach maxima at 600℃ or so and then weaken. These indicate that they may respectively be close in structures and belong to EL2 and EL6 group. On the other hand, after RTA (lower than 900℃), the quantity of defects of the EL2 group increases, while that of the EL6 group decreases, compared with the case of as-grown samples. By furnace annealing, however, defects of the EL2 group decrease, while defects of the EL6 group increase. From the experiment, it can be seen that the EL2 group (EL2, EL12) and the EL6 group (EL6, EL8 and EL9) are related in microscopic structure. And it might be reasonable assuming that EL2 is $As_{Ga}V_{As}V_{Ga}$ and EL6 is $V_{As}V_{Ga}$.

REFERENCES

[1] U.V.Desnica, Rad.Eff.Def. Solid 111+112, 83 (1989).
[2] U.V.Desnica and B.Santic, J.Appl.Phys. 67, 1408 (1990).
[3] B.Santic, D.I.Desnica, B.G.Petrovic and U.V.Desnica,
     Solid State Commun. 74, 847 (1990).
[4] Zou Yuanxi, 1982 Gallium Arsenide and Related Compounds
     (Inst. Phys.Conf.Ser. 63, 185 (1981).
[5] J.F.Wager and J.A.Van Vechten, Phys.Rev. B35, 2330 (1987).
[6] G.Wang, Y.Zou, S.Benakki, A.Goltzene, and C.Schwab, J.Appl.Phys. 63, 2595 (1988).

[7]   D.Stievenard, X.Boddaert, J.C.Bourgoin, and H.J.Von Bardeleben,
       Phys.Rev. B41, 5271 (1990).

[8]   C.Delerue, M.Lannoo, D.Stievenard, H.J.Von Bardeleben, and   J.C. Bourgoin,
       Phys.Rev. B59, 2875 (1987).

[9]   Z.-Q.Fang, T.E.Schlesinger and A.G.Milnes, J.Appl.Phys. 61, 5047 (1987)

[10] M.Kuzuhara and T.Nozaki, J.Appl.Phys. 59, 3131 (1986).

[11] U.V.Desnica, D.I.Desnica and B.Santic, Appl.Phys.Lett. 58, 278 (1991).

[12] S.R.Blight and H.Thomas, J.Appl.Phys., 65, 215 (1989).

[13] D.C.Look, Semiconductors and Semimetals 19, 118 (1983).

[14] Y.M.Weng, S.Liu, X.F.Song, J. Ingrared and Millimeter Waves , 11, 27 (1992).

[15] A. Mircer, A. Mitonneau, L.Hollan and Briere, A., Appl.Phys., 11, 153 (1976).

[16] Logan, R.H. and Hurle, D.T.J., J.Phys.Chem.Solids, 32, 1793 (1971).

[17] Y.X.Zhou, G.Y.Wang, Rare Metals, 6, 81 (1987).

[18] Figielski, T., Wosinski, T. and Morawski, A., Journal Physique, 44, 353 (1983).

THE ELECTRIC FIELD MEASURING BY PHASE SELECTIVE PHOTOREFLECTANCE

J. S. Hwang*, W. Y. Chou*, S. L. Tyan*, Y. C. Wang*[a], H. Shen**, *National Cheng Kung University, Department of physics, Tainan, Taiwan. **U.S. Army Research Laboratory, Physical Science Directorate, AMSRL-PS-PB, Fort Monmouth, New Jersey 07703-5601

ABSTRACT

The built-in electric fields in a MBE grown δ-doped GaAs homojunction have been investigated by the techniques of photoreflectance and phase suppression. Two Franz-Keldysh oscillation features originating from two different fields in the structure superimpose with each other in the photoreflectance spectrum. By properly selecting the reference phase of the lock-in amplifier, one of the features can be suppressed, thus enabling us to determine the electric fields from two different regions. We have demonstrated that only two PR spectra, in-phase and out-phase components, are needed to find the phase angle which suppresses one of the features. The electric field in the top layer is $3.5 \pm 0.2 \times 10^5$ V/cm, which is in good agreement with theoretical calculation. The electric field in the buffer layer is $1.2 \pm 0.1 \times 10^4$ V/cm, which suggests the existence of interface states at the buffer/substrate interface.

1. INTRODUCTION

In recent years, the capability of confining in a very narrow region is of great interest for many device applications. The δ-function-like doped structures have received a great deal of interest as a means of obtaining two-dimensional electron gas (2DEG) system. The δ-doping technique represents the ultimate control of a dopant profile and certainly will play an important role in future quantum-electronic and quantum-photonic device research.

Modulation spectroscopy has become an important technique in characterization of bulk semiconductors, semiconductor thin films and heterostructures[1-5]. It provides an accurate method for determining the energy gap[1,2], quantum transition[1,4], built-in surface or interface electric field[6,7] as well as doping concentrations in these systems. Photoreflectance (PR) is a particularly useful tool for device characterization since it is non-destructive and contactless, requires no special mounting of sample, and can be performed in a variety of transparent ambients[2,4]. Recently, there has been a growing interest in the applications of PR to the investigation of real devices such as InGaAs/GaAs[5], and GaAs/GaAlAs[6,7] heterojunction bipolar transistors (HBT), and GaInP/GaAs heterojunctions[8].

Since modulation spectroscopy is an AC method representing the optical response of the system to the modulating parameter, there is also important information embedded in the temporal response, such as reference phase and modulation frequency. These parameters can also be used to separate mixed features. For example, Krystek et al.[9] have reported a frequency dependent study of PR signals from the collector and emitter regions of a GaAs/GaAlAs heterojunction bipolar transistor (HBT) and found the time constant of the emitter region is more than an order of magnitude greater than that of the collector region. Zhou et al.[10] have reported

275

a PR investigation of near interface properties in semi-insulation InP substrates and epitaxial grown InGaAs and InAlAs. By properly choosing the reference phase, they were able to separate Franz-Keldysh (FKO) features from exciton peaks. A similar method has been used by Lipsanen et al.[11] and Alperovich et al.[12].

In this report, PR was employed to investigate the built-in electric fields in a (100) δ-doped GaAs homojunction. There are two Franz-Keldysh oscillation features originating from two different fields existing simultaneously in the buffer layer and top layer of this structure. By properly selecting the reference phase, we exacted one of the features from the spectrum and thus determine both fields.

2. EXPERIMENT

The $\delta(N^+)$ structure used in this study was grown by molecular beam epitaxy (MBE)[12,13]. A 0.6 μm thick undoped GaAs buffer layer was fabricated on an undoped liquid-encapsulated Czochraski (LEC) <100> semi-insulated GaAs substrate. Next, a $\delta(N^+)$ doping layer of density 1.5×10^{13} cm^{-2} was grown on top of the buffer layer, and subsequently followed by a 200 Å thick undoped GaAs top layer. The host growth temperature was kept constant at T_s= 580 °C, except during the growth of the δ-doping layer when it was reduced to 450 °C. The thickness was determined by the growth conditions, the growth rate is 1 μm/hr.

A standard arrangement of photoreflectance apparatus[15] were used in this study. The probe beam consisted of a Xe lamp and a quarter meter monochromator combination. A He-Ne laser served as the pumping beam. In order to eliminate the photovoltaic effect[16], the probe beam was defocused on the sample and kept below 15 μW/cm^2 and the pump beam was kept below 20 μW/cm^2. The detection scheme consisted of an InGaAs photo detector and a lock-in amplifier. The modulated reflectance signals, ΔR/R, were processed by the lock-in amplifier and PC computer. All measurements were performed at room temperature (300 K) and at a modulation frequency of Ω_m=200 Hz.

There are two Franz-Keldysh oscillation features in the PR spectrum originating from two different electric fields existing simultaneously in the buffer layer and top layer of the sample. By properly selecting the reference phase of lock-in amplifier, we extracted one of the features from the spectrum and thus determine both electric fields.

3. THEORY

In PR, the surface electric field is modulated through the photo injection of electron-hole pairs via a chopped incident laser beam. The lineshape of the PR signal, ΔR/R, is directly related to the perturbed complex dielectric function. For a moderate electric field, the PR spectrum exhibits a series of oscillations, termed Franz-Keldysh oscillations (FKOs). A material's surface or interface electric field can be determined by the positions of FKO extrema, which are given by[7,17].

$$n\pi = (4/3)[(E_n - E_g)/\hbar\Omega)]^{3/2} + \Theta \tag{1}$$

where n, E_g, E_n and Θ are, respectively, the index of the nth extrema, the energy gap, the photon energy of the nth extrema and an arbitrary phase factor. The quantity, $\hbar\Omega$, is the electro-optical energy, defined as:

$$(\hbar\Omega)^3 = (e\hbar F)^2/2\mu \tag{2}$$

where e and μ represent, respectively, the electron charge and the reduced interband electron and heavy hole pair effective mass in the direction of electric field F, which was (100) in our study.

The PR modulation under a square wave pump is not between two finite electric fields, but rather a complex wave form[18]. The output from a lock-in amplifier is the fundamental harmonic response,

$$\frac{\Delta R(\Omega_m, \phi_{ref})}{R} = Re[e^{-i\phi_{ref}} \frac{2}{T} \int_0^T \frac{\Delta R(t)}{R} e^{-2\pi i \Omega_m t} dt] \tag{3}$$

where T is the period, ϕ_{ref} is the reference phase with respect to the phase of the chopped laser beam. $\phi_{ref} = 0$ and $\pi/2$ give the in-phase and the quadrature components of the lock-in amplifier output, respectively. Under small modulation, Eq. (3) can be simplified to

$$\frac{\Delta R(E, \Omega_m, \phi_{ref})}{R} = \sum_i L_i(E, F_i) \frac{1}{\sqrt{1 + 4\pi^2 \Omega_m^2 \tau_i^2}} \cos(\phi_{ref} - \phi_i) \tag{4}$$

where $L_i(E, F_i)$ is the lineshape at $\Omega_m = 0$ for signal from the ith region, F_i is the electric field, τ_i is the characteristic time constant, and ϕ_i is the phase delay given by :
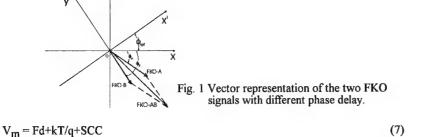
$$\phi_i = -\arctan(2\pi\Omega_m \tau_i) \tag{5}$$

If the time constants associated with various regions of the sample are different, Eq. (4) yields a different lineshape for the in-phase and out-phase signals. For example, a "slower" signal (larger τ_i) is more pronounced in the quadrature components, while a "faster" one is more pronounced in the in-phase component. Eq. (4) also shows the possibility of suppressing one of the features (from the ith region) by selecting ($\phi_{ref} - \phi_i$)= $\pi/2$ and to extract the other features (from the jth region) as long as $\tau_j \neq \tau_i$. It can be proven that

$$\frac{\Delta R(E, \Omega_m, \phi_{ref})}{R} = \frac{\Delta R(E, \Omega_m, 0)}{R} \cos(\phi_{ref}) + \frac{\Delta R(E, \Omega_m, \pi/2)}{R} \sin(\phi_{ref}) \tag{6}$$

where $\frac{\Delta R(E, \Omega_m, 0)}{R}$ and $\frac{\Delta R(E, \Omega_m, \pi/2)}{R}$ are the in-phase and the quadrature components of the lock-in output, respectively. Therefore, the output in a lock-in amplifier can be represented as a vector in the reference phase space. Illustrated in Fig. 1 is a vector representation of two signals (FKO-A and FKO-B) with different phase delay. The vector sum of them is shown by FKO-AB. Its projection on x (y axis) represent the in-phase (out-phase) signal. In a new reference phase frame (ϕ_{ref}) with OX' perpendicular to FKO-B, the projection of FKO-B on OX' is zero while FKO-A still has significant projection on OX'. Therefore, FKO-B can be extracted. It is

important to note that it is not necessary to take many spectra at different phases to find this angle (ϕ_{ref}). In fact, only two measurements (in-phase and quadrature) are enough. One can use Eq. (6) to generate a series of spectra at various angles, examine them, and pick one which suppresses one of the components. The surface potential barrier V_m can be determined from 19,20

Fig. 1 Vector representation of the two FKO signals with different phase delay.

$$V_m = Fd + kT/q + SCC \qquad (7)$$

where d, k, T, q and SCC are thickness of the undoped top layer, Boltzman constant, temperature, electron charge and the space charge layer correction term, respectively.

4. RESULTS AND DISCUSSION

Fig. 2 shows the band diagram of the (100) δ-doped GaAs structure. Two uniform electric fields F_A and F_B exist simultaneously in the buffer layer and in the undoped top layer, respectively. Shown in Fig. 3(a) is the in-phase PR spectrum from the sample. Two FKOs with different periods superimpose with each other in the spectrum. The quadrature component is plotted in Fig. 3(b). Although this spectrum still contains two superimposed FKOs, the short period oscillation is much less noticeable. Located in the vicinity of 1.42 eV is the excitonic feature. Comparing the in-phase spectrum with the out-phase spectrum, the excitonic feature has opposite signs in the two spectra. Shown in Fig. 3 (c) by a dashed line is a computer generated spectrum at ϕ_{ref}=67° using the in-phase and out-phase spectra of Fig. 3(a) and (b). In this case, the signal of the longer period FKOs disappears and the shorter period FKOs remains. Also shown in Fig. 3 (d) by a solid line is the experimental result from a re-scan at a phase angle of ϕ_{ref} =67° , which is in good agreement with the calculated lineshape. We designate this feature as FKO-A. Using the in-phase and out-phase spectra again, we found that FKO-A is suppressed at phase angle ϕ_{ref}=85°. In this case the longer period FKOs remain and we designate it as FKO-B. From the reference phase which suppressed FKO-A (FKO-B), we found that the phase delay for FKO-A (FKO-B) is ϕ_A = -5° (ϕ_A = -23°). The characteristic time constant for FKO-A and FKO-B were deduced from Eq. (5) to be 70 μs and 340 μs, respectively. These time constants are related to the limiting processes of discharge and recharge of the surface/interface states, such as thermoionic emission over the potential barriers, emission of charges from the surface/interface states/traps, etc. Since the density of the interface states in an MBE grown sample is typically less than the density of the surface states, we assign that fast process (FKO-A) to the buffer region, while the slower process (FKO-B) to the top undoped region. Plotted in Fig. 4 by triangle (squares) is the quantity $(4/3\pi)(E_n-E_g)^{3/2}$ as a function of index n for the related FKO-A (FKO-B). The solid lines are
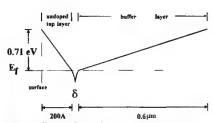
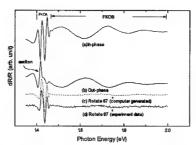**Fig.** 2 Illustration of the band diagram of the δ-doped GaAs sample.

Fig. 3 Room temperature photoreflectance spectra from the δ-doped GaAs sample. (a) in phase signal; (b) out phase signal;(c)computer generated spectrum at a phase angle of ϕ_{ref} =67°, (d) experimental result from a re-scan at the same phase angle.

least-squares fits to a linear function (Eq. (1)) which yield the value of $\hbar\,\Omega$ and hence the electric fields. The values deduced by Eq. (2) are $1.2\pm0.1 \times10^4$ and $3.5\pm0.2 \times10^5$ V/cm for FKO-A and FKO-B, respectively. The surface potential barrier V_m can be determined from Eq. (7) is 0.71 eV indicating that the surface Fermi level is pinned at the midgap, which is in good agreement with the reported values. From the field in the buffer layer, we calculated the Fermi level position at the buffer/SI-substrate interface and found it is at 0.75 eV below the conduction band edge. This position is lower than the Cr impurity level position (0.63 eV below conduction band) in the SI-substrate interface.
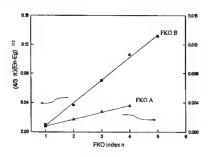
Fig. 4 The quantity $(4/\hbar)(E_n-E_g)^{3/2}$ as a function of index n. Triangle: FKO-A; square: FKO-B. The solid lines are least-squares fits to a linear function.

5. CONCLUSIONS

In conclusion, we have used the reference phase of the lock-in amplifier and phase suppression technique to resolve the two FKO features. We have demonstrated that only two PR spectra, in-phase and quadrature components, are needed to find the phase angle which suppresses one of the features enabling us to determine the electric fields from the two regions unambiguously. The electric field in the top layer is $3.5\pm0.2 \times10^5$ V/cm, which is in good

279

agreement with theoretical calculations. The electric field in the buffer layer is $1.2\pm0.1 \times10^4$ V/cm, which suggests the existence of interface states at the buffer/substrate interface.

ACKNOWLEDGMENTS

REFERENCES:

1. F. H. Pollak and O. Glembocki, in Proceedings of the Society of Photo-optical Instrumentation Engineers (SPIE, Bellighm 1988) Vol. **946**, p. 2 (1988).
2. N. Bottka, D. K. Gaskill, R. S. Sillmon, R. Henry, and R. Glosser, J. Electron. Mater. **17**, 161 (1988).
3. R. N. Bhattacharya, H. Shen, P. Parayanthal, F. H. Pollak, T. Coutts, and H. Aharoni, Phys. Rev. **B37**, 4044 (1988).
4. F. H. Pollak and H. Shen in Proceedings of the Society of Photo-optical Instrumentation Engineers (SPIE, Bellingham, 1989), Vol. **1037**, p. 16.
5. A. Badkashan, C. Durbin, A. Giordana, R. Glosser, S. A. Lambert, and J. Liu, in Nanostructure Physics and Fabrication, edited by M. A. Reed and W. P. Kirk (Academic, Boston, 1989). p. 485.
6. X. Yin, F. H. Pollak, L. Pawlowicz, T. O'Neill and M. Hafizi, Appl. Phys. Lett., **56**, 1278 (1990).
7. Michael Sydor, Neal Jahren, W. C. Mitchel, W. V. Lampert, T. W. Haas, M. Y. Yen, S. M. Mudare and D. H. Tomich, J. Appl. Phys. Vol. **67**, 7423 (1990).
8. J. S. Hwang, Z. Hang, S. L. Tyan, S. W. Ding, J. H. Tung, C. Y. Chen, B. J. Lee and J. T. Hsu, Jpn. J. Appl. Phys. Vol. **31**, L571 (1992).
9. W. Krystek, H. Qiang and F. H. Pollak, Proc. of the 21th international Symposium on Compound Semiconductor, Sen Diego, CA, Sept 1994.
10. W. Zhou, M. Dutta, H. Shen, J. Pamulapati, B. R. Bennett, C. H. Perry and D. W. Weyburne, J. Appl. Phys. **73**, 1266 (1993).
11. H. K. Lopsanen, and V. M. Airaksinen, Appl. Phys. Lett. **63**, 2863 (1993).
12. V. L. Alperovich, A. S Jaroshevich, H. E. Scheibler and A. S. Terekhov, Solid-State Electronics Vol. **37**, 657 (1994).
13. A. Y. Cho, Thin Solid Films, **100**, 291 (1983).
14. J. L. Shay, Phys. Rev. **B2**, 803 (1970).
15. H. Shen, P. Parayanthal, Y. E. Liu & F. H. Pollak, Rev. Sci. Intrum. 58(8), 1429 (1987).
16. H. Shen, M. Dutta, L. Fotiadis, P. G. Newman, R. P. Moerkirk, and W. H. Chang, Appl. Phys. Lett., **57**, 2118 (1990).
17. E. F. Schubert and K. Ploog, Jpn. J. Appl. Phys. , Vol. 24, L608 (1985). E. F. Schubert, A. Fischer and K. Ploog, IEEE Trans. Electron Device, Vol. **ED-33**, 625 (1986).
18. C. E. C. Wood, G. Metze, J. Berry and L. F. Eastman, J. Appl. Phys. **51**, 383 (1980).
19. J. S. Hwang, S. L. Tyan, W. Y. Chou, M. L. Lee, D. Weyburne, Z. Hang, H. H. Lin and T. L. Lee, Appl. Phys. Lett. **64**, 3314 (1994).
20. X. Yin, H. M. Chen, F. H. Pollak, Y. Cao, P. A. Montano, P. D. Kirchner, G. D. Pettit and J. M. Woodall, J. Vac. Sci. Technol. **A 10**, 131 (1992).

GROWTH AND CHARACTERIZATION OF GaAs EPITAXIAL LAYERS BY MOCVD

Mantu Kumar Hudait, Prasanta Modak and S.B.Krupanidhi*
Central Research Laboratory, Bharat Electronics, Bangalore-560 013, INDIA

* Materials Research Centre, Indian Institute of Science, Bangalore-560 012, INDIA

ABSTRACT

Device quality epitaxial layers of undoped GaAs were grown by MOCVD technique, on both semi-insulating and semi-conducting GaAs substrates with (100) orientation, offset by 2° towards (110) direction. Systematic variation of As/Ga was performed to gain an understanding of growth process, type of formation and other related physical properties. The films were characterized by using the variety of techniques, such as SEM, EDAX, HRTEM, XRD, and PL. Optical and electrical properties of undoped GaAs epilayers are presented with reference to the growth conditions and AsH_3/TMGa ratio. Photoluminescence measurements of GaAs epilayers were recorded at 4.2K and shows the emission of free exciton and confirmed their high purity. The dominant residual impurities in GaAs are presented by using PL. Finally, electrochemical depth profiling exhibited almost homogeneous background carrier distribution and excellent abruptness between the thin GaAs epilayer and substrate.

INTRODUCTION

Metal Organic Vapor Phase Epitaxy (MOVPE) is widely used for the epitaxial growth of GaAs and related III-V compounds and their heterostructures. In particular, the use of such high quality epilayers, an optoelectronic, microwave, and high speed digital circuits[1] has given very excellent results. In addition, this family(AlGaAs/GaAs) of compounds also promise number of interesting properties such as high mobility, resonant tunneling, and fractional Hall effect etc. Numerous attempts have been made for developing epitaxial layers of GaAs, AlGaAs and to apply the MOVPE layers to development of advanced devices ,such as, high electron mobility transistors (HEMTs)[2], multiple-quantum well (MQW)[2] and other electronic and optoelectronic devices. With all the success in the area of device development, the optimization process for obtaining high quality GaAs epilayers still remains unsolved. It has not been clearly understood what are the limiting factors that determine the layer quality. In order to achieve good performance of the device, high quality epitaxial layers are essential to satisfy the device requirements. Present paper reports the results from the growth and characterization of undoped GaAs epilayers and discusses a close process-property correlation.

EXPERIMENTAL

Undoped GaAs epitaxial layers were grown in a low pressure horizontal MOCVD reactor. The source materials were palladium-purified H_2, Trimethylgallium(TMGa) and Arsine(AsH_3, 100%). Both semi-insulating (Cr-doped) (100) GaAs and Si-doped n^+-GaAs (100) substrates misoriented towards [110] direction offset by 2°, were used for epitaxial growth process. Each substrates was thoroughly degreased and cleaned and given a brief 1:1:10 H_2O_2:H_2SO_4:H_2O to remove surface oxide and residual contamination. Prior to initiation of growth and after the temperature of the susceptor reaches 350°C, AsH_3 flow was initiated to avoid arsenic escape from the substrate and was maintained throughout the growth process. Once the desired temperature was reached, TMGa was introduced into the reaction chamber to initiate growth. The growth rate was linearly dependent on the flow rate of TMGa in the growth chamber. For reduced pressure growth, the exit of the reactor was connected to the high capacity vacuum pump. The pressure in the reactor tube was maintained at 100 Torr. After the completion of growth, the flow of TMGa was cut-off and AsH_3 flow was maintained until the temperature cooled below 350°C. The unspent reactants were cracked by using cracking furnace at a temperature of 800°C and the process gasses were allowed to go directly to the activated charcoal scrubber. The total flow rate was about 2.5 SLPM. The V/III ratios of the samples were varied from 21 to 80.

Photoluminescence (PL) measurements were carried out at 4.2K using a MIDAC Fourier Transform PL (FTPL) system. An Argon ion laser operating at a wavelength of 5145A° was used as a source of excitation. The exposed area was about 3mm². PL signal was detected by a LN_2 cooled Ge-Photodector whose operating range is about 0.75-1.9eV, whole resolution was kept at 0.5meV.

RESULTS AND DISCUSSION

The undoped GaAs epilayers were characterized in terms of structures, surface morphology, optical and electrical properties.

Surface Quality

The surface of epilayers is greatly influenced by the growth parameters, such as, pressure inside the reactor tube, growth temperature, substrate orientation, AsH_3/TMGa mole ratio[3] etc. In the case of growth on (100) oriented GaAs substrates, mirror-like surfaces as viewed by the naked eye can be obtained over a wide range of V/III ratios. But by using optical microscopic observation some of the samples shows the white spot on the surface, may be considered as hillocks. Since the temperature of the growth process was

kept at 700°C, the mirror-like surfaces, as viewed by naked eye on (100)GaAs was obtained.

Some of the samples were grown under constant AsH₃ flow rate, the stoichiometry of the samples was found to be unchanged, as observed by Energy Dispersive Analysis of X-rays (EDAX). The other sets of samples were grown by varying the AsH₃ flow rate while the TMGa flow rate kept constant. In this case the stoichiometry of samples was found to be changed. The thickness of each layer was varied by varying TMGa flow rate, and the typical growth rate was about $20A°/sec$. The thickness was measured by cross-sectional Scanning Electron Microscopy (SEM). Cross-sectional SEM (Fig.1) studies on undoped GaAs films exhibit a uniform smooth surface, a dense cross-section and a clear
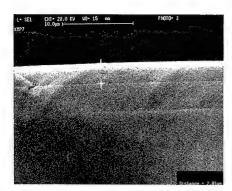
Fig.1: Cross-sectional SEM pattern of   Fig.2: Selective area diffraction pattern
        epi-GaAs film/substrate   of epi-GaAs film.

interface between the film and substrate. The compositional homogeneity of the films was quantified in terms of estimating the Ga/As ratio, using EDAX analysis. Results indicated a near stoichiometric Ga/As ratio, irrespective of the flow ratios of incoming gas precursors.

Besides conventional structural studies by using Double Crystal X-ray Diffraction (DCXRD), the epitaxial growth of the films was established by High Resolution Transmission Electron Microscopy (HRTEM) selective area diffraction studies, and the typical data is presented in Fig.2. It was observed by lattice indexing that our MOCVD growth layers of GaAs, in the present growth conditions, clearly exhibits epitaxial growth in (100) direction normal to the substrate surface. The film was further envisaged in terms of observing the lattice imaging by HRTEM, to visualize the atomic arrangement. The results are shown in Fig.3, for a typical film, which clearly exhibited a lattice for GaAs, consistent to give zinc blend structure.
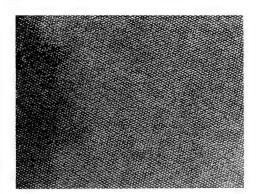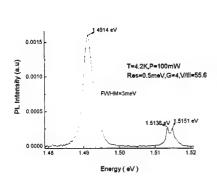
Fig.3: HRTEM lattice imaging of epi-GaAs film.

Optical Properties

The Photoluminescence (PL) spectroscopy is used for concerning the type, distribution of defects and impurity in a crystal. Typical photoluminescence spectra observed in the near band-edge region can be seen in Fig.4. Two characteristic photoluminescence bands were obtained from all the samples: the exciton complexes and the acceptor related transitions. In the exciton related region, these peaks are identified as the radiative recombination of a free exciton (FE) (1.5151eV), exciton bound to neutral donor $(D^°,X)$(1.5141eV),an ionized donor (D^+,X)(1.5133eV), and exciton bound to neutral acceptor$(A^°,X)$(1.5125eV). Since the emission due to the free exciton was observed from our samples, it confirmed their high purity[4,5].

The other photoluminescence bands were observed around 1.49eV(GaAs acceptor related region). The FWHM of this band was 3.0meV. Two of the more common impurities incorporated during the MOCVD growth of undoped GaAs epilayer are identified C and Zn[6]. The photoluminescence peaks at 1.490 eV and 1.4933eV(weak shoulder compared to peak intensity at 1.490eV at 4.2K) are due to the donor-to-acceptor transition (DA) and the conduction band-to-acceptor (also called free -to-bound, FB) transition, respectively. At very low temperatures(e.g.4.2K), the donor originated transition (DA) dominate over the conduction band originated transition (FB) and when the temperature is increased from 4.2K, DA pair intensity decreases rapidly because of the donor ionization energy.

To observe the effect of V/III ratios on impurity incorporation in GaAs epilayers, we have shown in Fig.5 the peak intensity of the($D^°A^°$) t transition due to carbon and the peak intensities of the $(D^°,X)$ and $(A^°,X)$ as a function of V/III ratios. From the figure it is seen that the intensities of the luminescence lines due to the $(D^°X)$, $(A^°X)$, and $(D^°A^°)$(C) are strongly dependent on the V/III ratios. The intensity of the $D^°A^°$(C) transition
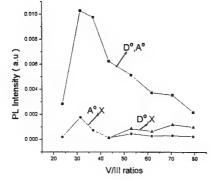
Fig.4: PL spectrum of MOCVD grown epi-GaAs film.
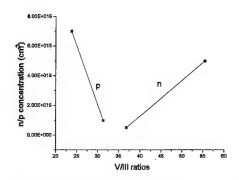
Fig.5: PL intensities of (D^oA^o), (A^oX); (D^oX) vs. V/III ratios

decreases with increasing V/III ratio, which is expected since C substitutes on As site as an acceptor. Nevertheless, the donor/acceptor exciton ratios increases with increasing V/III ratios indicating more donor incorporation and hence more n-type behavior. Therefore, the density of C atoms incorporated in epilayers is low under our growth conditions. Similar behavior was observed in GaAs films at 50Torr growth pressure.

Electrical Properties

Electrical characterization can give considerable information about the purity of the epitaxial layers. Such information is important for the growth process as well as the high quality epitaxial layers for device applications. Hall effect by Van der Pauw method was utilized to measure carrier concentration and mobility of the epitaxial films at room temperature. The measured carrier concentrations and room temperature mobilities of n-type and p-type samples are 10^{15} cm^{-3}, 4500cm^2/V-sec at V/III=55.6 and $7*10^{15}$ cm^{-3}, 400cm^2/V-sec (V/III=21), respectively. The electrical properties of GaAs epilayers vary with V/III ratios, as illustrated in Fig.6. At low V/III ratio, the sample is p-type and converts to n-type at higher ratios which is consistent with the literature[6] and also can correlate with PL spectra at 4.2K.

Electrochemical Capacitance-Voltage (ECV) profiler was used to determine the carrier concentration of undoped GaAs layers, type of formation and abruptness between the 3.5μm thin GaAs epilayer and substrate. The results are presented in Fig.7, which clearly establish an abrupt and unreacted interface, which is an essential requirement for

285
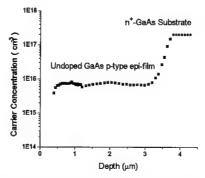
Fig.6: n or p (cm^{-3}) vs. V/III ratios.

Fig.7: ECV depth profiling of back ground impurity for MOCVD grown epi-GaAs film.

multilayer structure development, such as in heterostructure lasers, MQWs and optoelectronic devices.

CONCLUSION

Device quality epilayers of undoped GaAs were grown by MOCVD, with excellent smooth surface of n and p type films were successfully grown, by varying As/Ga mole ratios. Studies of photoluminescence at 4.2K indicates the emission of free exciton and confirmed the high quality of the films. Epitaxy was confirmed by HRTEM selective area diffraction and lattice imaging. Electrochemical depth profiling exhibited homogeneous background carrier distribution and excellent film/substrate interfaces.

REFERENCES

[1].   D.H.Reep and S.K.Ghandhi, J. Electrochem. Soc. **130** (1983), 675.

[2].   Timothy J. Drummond, William Ted Masselink, and Hadis Morkoc, Proc. IEEE, Vol.**74**, p.773,1986.

[3].   G.B.Stringfellow, *Organometallic Vapor- Phase Epitaxy: Theory and Practice*, San Diego, CA(Academic Press, 1989), p285.

[4].   Lorenzo Pavesi and Mario Guzzi, J. Appl. Phys. **75**,4779(1994).

[5].   V.Swaminathan, D.L.Van Haren, J.L.Zilko, P.Y.Lu, and N.E.Schumber, J. Appl. Phys. **57**, 5349(1985).

[6].   T.Nakanisi, J.Crystal Growth **68**(1994) 282.

FORMATION OF NEW SEMICONDUCTING Ge-Si-Fe ALLOY ON Si(100) AND ITS OPTICAL PROPERTIES

H.Chen, P.Han, X.D.Huang, L.Q.Hu, Y.Shi, Y.D.Zheng
Department of Physics, Nanjing University, Nanjing 210093, P.R.China

ABSTRACT

We report a new semiconducting Ge-Si-Fe alloy thin film grown on Si(100) by reactive deposition epitaxy(RDE) using high vacuum evaporation technique. AES and XRD results show that the new alloy can be regarded as a distorted β-FeSi$_2$ with the Ge participation. The direct band gap of the Ge-Si-Fe alloy was determined to be 0.83eV by optical transmission measurement, which means a red shift of band gap compared with that of β-FeSi$_2$ (Eg=0.87eV).

INTRODUCTION

Recently, there is an increased interest in the use of SiGe layered material for integration with Si technology [1],[2]. The SiGe system has the potential for high speed and optical devices which may compensate for deficiencies of conventional Si devices. But, the biggest problem with SiGe when it comes to optoelectronic application is its indirect band structure. As a result, it is not a efficient light emitter. At the same time, we have noticed a promising material β-FeSi$_2$ as a semiconductor with a direct band structure [3],[4]. The band gap was measured to be 0.87eV, which makes it an ideal candidate material for both source and detector devices in the 1.3-1.6um wavelength range. In addition, the fabrication procedure is compatible with the silicon-based microelectronic technology, which reveals its brilliant prospects in the optoelectronic industry.

So, the purpose for this work is based on such an idea that if we can combine the benefit of direct band structure of β-FeSi$_2$ with today's developed SiGe techniques, chance is good that a new silicon-based semiconductor with some encouraging characters would be obtained. In other words, since the lattice parameters of Ge atom are larger than those of Si atom, when some Si atoms in the β-FeSi$_2$ lattice structure are replaced with Ge atom, a certain kind of lattice distortion will take place, thus resulting in respective changes of β-FeSi$_2$ band structure and especially a shift of band gap following the way opened for GeSi system in the last decade.

EXPERIMENT

As we know, the conventional methods of fabricating β-FeSi$_2$ thin films are solid phase epitaxy(SPE) or reactive deposition epitaxy(RDE), which include iron deposition process on silicon substrate and a post annealing procedure. In order to form the Ge-Si-Fe alloy, the RDE process based on Si$_{1-x}$Ge$_x$/Si strain relaxed structure was attempted in our experimental work. During the solid phase reaction between iron layer and SiGe/Si structure, interfusion and recrystallization was supposed to take place at the same time to

form the new Ge-Si-Fe alloy on the silicon substrate. The whole process of Ge-Si-Fe alloy fabrication includes the SiGe strain relaxed layer preparation on Si substrate, iron deposition onto the SiGe layer and post annealing process.

In the first step, a strain relaxed SiGe layer was grown epitaxially on silicon substrate by LPCVD method. A very low pressure chemical vapor deposition system (RTP/VLP-CVD) has been employed in this step. The procedure details of the growth system have been described elsewhere [5]. Auger electron spectroscopy(AES) shows the SiGe layer has been successfully grown on Silicon substrate with the Ge content of 7%. In the second step, the SiGe/Si structure was loaded into a high vacuum evaporation system , where iron film was deposited onto it later on. During the deposition process, the SiGe/Si structure was kept at 450°C . In the last step, an in-situ post annealing process was carried out with the SiGe/Si structure kept at 700°C for 30min in the high vacuum evaporation system. After the annealing precess, ex-situ Auger electron spectra(AES) determined that the thickness of the Ge-Si-Fe alloy film grown on silicon substrate was about 1200Å .

For comparison, a (100)oriented silicon substrate was loaded into the evaporation chamber together with the SiGe/Si structure to grown β-FeSi$_2$ Thin film under the same process conditions as control sample.

RESULTS

X-ray diffraction(XRD) measurement was applied to investigate the structure character of the new Ge-Si-Fe alloy and β-FeSi$_2$. A comparison was made to show the difference. AES measurement gave the depth profiles of Si, Ge and Fe in the Ge-Si-Fe alloy. Finally, optical transmission measurement was also carried out to investigate optical properties of the new alloy.

The Ge participation in the Ge-Si-Fe alloy was testified by comparing the depth profiles
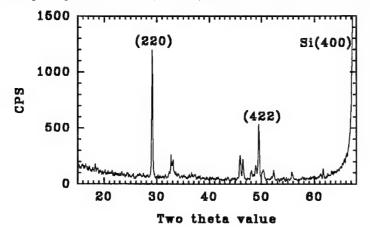
Fig.1 X-ray diffraction pattern for Ge-Si-Fe alloy thin film.
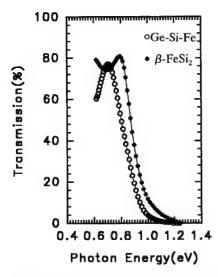
Fig.2 Optical transmission specta of Ge-Si-Fe alloy and β-FeSi$_2$ thin film

Fig.3 Absorption coefficient vs photo energy for Ge-Si-Fe alloy and β-FeSi$_2$ thin film

Fig.4 Absorption coefficient square vs photon energy for Ge-Si-Fe alloy and β-FeSi$_2$

of Ge-Si-Fe alloy and β-FeSi$_2$ thin films. The comparison shows that the two depth profiles are very alike and the sum of Si and Ge percentage in Ge-Si-Fe alloy is very close to the Si percentage in β-FeSi$_2$, which gives evidence of the Ge replacement. According to the comparison, about 2.5% Si atoms in β-FeSi$_2$ was replaced by Ge atoms, thus forming the new alloy.

XRD plot is shown in fig.1. It gives a set of diffraction peaks of Ge-Si-Fe alloy. The diffraction peaks are almost the same as those arising from β-FeSi$_2$ [6] thin film. Based on the XRD results and AES as well, it's natural for us to suggest that the distortion caused by the Ge replacement is so small that the changes of lattice parameters of β-FeSi$_2$ can't be detected by the XRD analysis due to the very low content of Ge in alloy film. For convenience, we continue to use the Miller indices of β-FeSi$_2$ to represent the

289

diffraction peaks of the Ge-Si-Fe alloy. Among the peaks, (220) peak is the most prominent one, sharp and intense, which implies a good crystal quality. The second most intense peak is (422) peak. Other weak peaks include (331), (400), (041), (511), (113), (024) and (600) peak, which can not be identified one by one in the figure due to the space limitation.

Since the Ge-Si-Fe alloy thin film on silicon substrate has been regarded as slightly distorted β-FeSi$_2$ thin film according to AES and XRD measurement, an expression can be given to represent the new Ge-Si-Fe alloy. That is:

$$\beta\text{-FeSi}_{2-x}\text{Ge}_x$$

Optical transmission spectroscopy technique was employed to study band structure of the Ge-Si-Fe alloy thin films in the range of 0.6-1.2eV. Fig.2 shows the transmission spectra of Ge-Si-Fe alloy and β-FeSi$_2$. Both Ge-Si-Fe alloy and β-FeSi$_2$ thin film exhibit a strong absorption, while the absorption edge of Ge-Si-Fe alloy is lower than that of β-FeSi$_2$. This result shows that Ge-Si-Fe is a new semiconducting material with the band gap a few meV lower than that of β-FeSi$_2$. The onset of absorption just below 0.6eV is due to extrinsic transitions involving defect states within the forbidden energy gap [6]. Absorption coefficient of Ge-Si-Fe alloy and β-FeSi$_2$ in fig.3 is deduced from the transmission data. A strong increase of absorption coefficient up to 10^5cm^{-1} can be observed, which is consistent with the existence of a direct optical gap of the new alloy. In order to estimate the energy gap of Ge-Si-Fe alloy and to confirm the direct band nature of both β-FeSi$_2$ and Ge-Si-Fe alloy, plots of the absorption coefficient square versus the photon energy were made in Fig.4, which yield straight lines with the intercepts indicating the direct band gap of 0.83eV for Ge-Si-Fe alloy and 0.87eV for β-FeSi$_2$.

CONCLUSION

In short, a new semiconducting material Ge-Si-Fe alloy thin film has been achieved by using reactive deposition epitaxy(RDE) on SiGe strain relaxed layer. The new Ge-Si-Fe alloy exhibits exciting direct optical absorption near 0.83eV in the optical transmission measurement, which means a red shift of band gap compared with that of β-FeSi$_2$ thin film. It is suggested that by changing the content of Ge in the alloy, Ge-Si-Fe alloy with desired energy gap can be formed, following the way opened for GeSi system several years ago. It offers new choice for silicon-based optoelectronic device engineers to "tailor" the optoelectronic properties to the need. The first step has been taken to study the formation and properties of the new alloy in our research work, further investigation is quite necessary about the role of Ge atoms in the new alloy, the kinetics of fabrication process and the potential prospect of application.

REFERENCES

[1] S.S.Iyer, G.L.Patton, J.M.C.Stork, B.S.Meyerson and D.L.Harame, "Heterojunction

Bipolar Transistors Using Si-Ge Alloy," IEEE Trans. Electron Devices, vol.36, no.10, pp.2043-2064, 1989

[2] Kang L.Wang and R.P.G.Karunasiri, "SiGe/Si electronics and optoeletronics, "J.Vac.Sci.Technol.B, vol.11(3), pp.1159-1167,1993

[3] N.Cherief, C.D'Anterroches, R.C.Cinti, T.A.Nguyen Tan and J.Derrien, "Semiconducting silicide-silicon heterojunction elaboration by solid phase epitaxy," Appl.Phys.Lett. vol.55, no.16, pp.1671-1673,1989

[4] J.Alvarez, J.J.Hinarejos, E.G.Michel, G.R.Castro and Miranda, "Electronic structure of iron silicides grown on Si(100) determined by photoelectron spectroscopies," Phys.Rev.B, vol.45, 14042-14051,1992

[5] P.Han, L.Q.Hu and R.H.Wang, "Strain relaxed $Si_{1-x}Ge_x$ layers using x step graded structure grown on (100) Si by RRH/VLP-CVD," 21st International Conference of the Physics of Semiconductors vol.1, pp.843-846, 1992

[6] M.C.Bost and J.E.Mahan, "Optical properties semiconducting iron disilicide thin films," J.Appl.Phys. vol.58, no.7, pp.2698-2703, 1985

A STUDY OF LOW-TEMPERATURE GROWN GaP BY GAS-SOURCE MOLECULAR BEAM EPITAXY

W. G. Bi, X. B. Mei, K. L. Kavanagh, and C. W. Tu
Department of Electrical and Computer Engineering, University of California, San Diego, La Jolla, CA 92093-0407, U. S. A. wbi@sdcc3.ucsd.edu
E. A. Stach and R. Hull
Department of Materials Science and Engineering, University of Virginia, Charlottesville, VA 22903-2442, U. S. A.

ABSTRACT

We report the effects of growth conditions on the strain and crystalline quality of low-temperature (LT) grown GaP films by gas-source molecular beam epitaxy. At temperatures below 160 °C, poly-crystalline GaP films are always obtained, regardless of the PH_3 low rate used, while at temperatures above 160 °C, the material quality is affected by the PH_3 flow rate. Contrary to compressively strained LT GaAs, high-resolution X-ray rocking curve measurement indicates a tensile strain of the LT GaP films, which is considered to be due to P_{Ga} antisite defects. The strain is found to be affected by the PH_3 flow rate, the growth temperature, and post-growth annealing. Contrary to LT GaAs, no P precipitates are observed in cross-sectional transmission electron microscopy.

INTRODUCTION

Semiconductors grown at low temperature (LT) possess several unique features which are useful for optoelectronic device applications. For example, GaAs grown at ~ 200 °C and annealed at high temperature exhibits high resistivity, short carrier lifetime, and high mobility [1-5]. These properties are desirable for field-effect transistors, photodetectors, ultrafast switches, and other device applications [6-8]. On the other hand, LT InP is highly conductive, which has been utilized in n-type modulation doping in InP-based heterostructures without using an extrinsic dopant (e.g., Si) [9,10]. Little work, however, has been reported on LT GaP. Recently, Ramdani et al. [11] reported that LT GaP films are semi-insulating. Studies by He et al. [12] indicate that excess phosphorus of 0.6 ~ 2 at. % can be incorporated in LT GaP films. In this paper, we report a systematic study on the growth condition dependence of the crystalline quality, strain, and excess P in LT GaP.

EXPERIMENTAL

The samples were grown in a modified Varian GEN-II molecular beam epitaxy (MBE) system which can handle group-V hydrides. Pure PH_3 thermally cracked at 950 °C was introduced into the growth chamber through an injector. Elemental Ga was used as the group-III source. Epi-ready (100)-oriented GaP:S substrates were used. After thermal cleaning at 650 °C, the substrate temperature was lowered to 140 ~ 350 °C under an overpressure of P_2 before growth. The growth rate was 1 μm per hour. The PH_3 flow rate used was in the range of 0.6 ~ 4 sccm. Reflection high-energy electron diffraction (RHEED) was used to monitor the growth mode. Ex-situ annealing was performed in forming gas (15% H_2 and 85% N_2). High-resolution X-ray rocking curve (XRC) was recorded using a Philips four-crystal X-ray diffractometer. A

Cambridge 360 scanning electron microscope (SEM) was used. Cross-sectional transmission electron microscopy (XTEM) photographs were taken using a JEOL 2000FX operated at 200 kV and a JEOL CM30 operated at 300 kV. The samples were prepared using standard mechanical thinning and ion-milling techniques.

RESULTS AND DISCUSSION

The dependence of the growth mode of LT GaP films on growth temperature (140 °C ~ 300 °C) and PH$_3$ flow rate (0.6 sccm ~ 3.8 sccm) is shown in fig. 1. At temperatures below 160 °C, LT GaP is poly-crystalline, independent of PH$_3$ flow rate, while at temperatures above 160 °C, it is single-crystalline when the PH$_3$ flow rate is less than a certain value. Above that value,
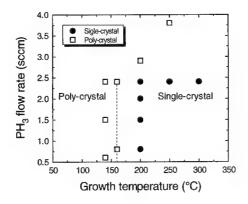
Fig. 1 Growth condition dependence of the crystalline quality of LT GaP.

GaP is poly-crystalline. Fig. 2 shows SEM images of GaP grown at 200 °C with a PH$_3$ flow rate of (a) 0.8, (b) 2.4, and (c) 3.0 sccm. We can see that at this growth temperature a smooth surface morphology (b) can be obtained only within a certain range of PH$_3$ flow rate. At lower PH$_3$ flow rate the surface consists of apparently Ga-rich droplets (a) or at higher flow rate it is P-rich (c). This is similar to the observations of LT-InP [13].
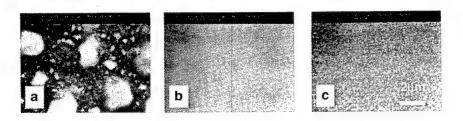
Fig. 2 SEM images of GaP grown at 200 °C with a PH$_3$ flow rate of (a) 0.8, (b) 2.4, and (c) 3.0 sccm. The maker represents 2 µm.

Fig. 3 shows X-ray (400) rocking curves of 2.0-μm-thick GaP films grown at 200 °C with a PH_3 flow rate of 2.4 sccm or 1.5 sccm. The latter shows only one diffraction peak, while the former shows two peaks. One is from the GaP substrate, and the other from the LT-GaP film. In order to determine which peak is that of the LT film, the epilayer was etched in a solution of $H_2SO_4:H_2O_2:H_2O$ (8:1:1) at 60 °C for 2 min.. The XRC of the etched film is shown in fig. 3 as a dotted line. The intensity decrease of the peak located at the larger angle, after part of the epilayer was etched off, clearly demonstrates that it is the peak of the LT-GaP film. From this we know that the lattice constant of the LT-GaP is smaller than that of normal GaP by 0.02%. This is different from LT-GaAs, where a lattice expansion was observed [14, 15]. The reason is considered to be due to atomic size difference. For LT III-V, the lattice constant change is mainly due to the incorporation of excess group-V species. In the case of LT-GaAs, since As atoms are bigger than Ga atoms, As_{Ga} antisite defects will cause lattice dilation. For LT-GaP, on the other hand, as P atoms are smaller than Ga atoms, P_{Ga} antisites should result in lattice contraction. Our result, however, is contrary to that of Ramdani et al. [11], who claimed a lattice expansion of LT-GaP. We do not understand this discrepancy except we note that the X-ray linewidths of their substrate and epilayer are very broad. The XRC full width at half maximum (FWHM) of our GaP film is 18 arcsec, indicating high crystalline quality even though the growth temperature is low. This is further confirmed by XTEM observations discussed below.
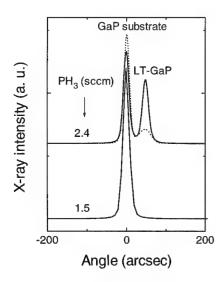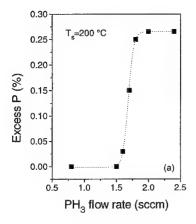
Fig. 3 (400) XRCs of GaP films grown at 200 °C with a PH_3 flow rate of 2.4 sccm or 1.5 sccm. The dotted line is the result of the sample (PH_3=2.4 sccm) after part of the epilayer was etched away.

The excess P in the LT-GaP is plotted as a function of substrate temperature T_s and PH_3 flow rate in fig. 4 (a) and (b), respectively. The excess P was determined from strain-free lattice constant of LT GaP derived from XRC (400) and (511) reflections [16]. From the figures we can see that at a given T_s, the excess P in GaP depends on the PH_3 flow rate, i.e., for PH_3 less than 1.5 sccm no excess P was detected, while for PH_3 in the range of 1.6 ~ 2.0 sccm, the excess P increases with PH_3 flow rate. At a fixed PH_3 flow rate, lowering the growth temperature leads to
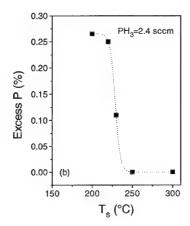
Fig. 4 Excess P in LT GaP as a function of (a) PH$_3$ flow rate and (b) growth temperature.

an increase of the excess P in LT GaP films. Further increase of PH$_3$ or decrease in T$_s$ will result in polycrystalline film.

Fig. 5 shows XRCs of the sample grown at 200 °C with a PH$_3$ flow rate of 2.4 sccm and annealed at different temperatures. Here the annealing time at each annealing temperature is 15 min. From the figure, we can see the trend that increasing the annealing temperature leads progressively to a reduction and elimination of strain in the epilayers. This behavior is similar to annealed LT-GaAs, where a complete restoration of the lattice constant was obtained and was attributed to the redistribution of excess As and the formation of As precipitates[15], but it is different from that of Ramdani et al. [11], who observed only a 30 arcsec reduction in the X-ray peak separation upon annealing.
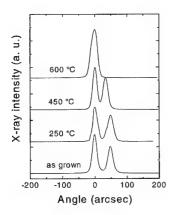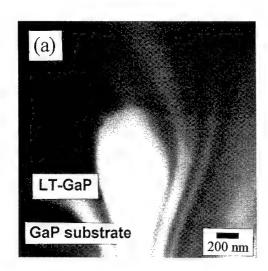
Fig. 5 XRCs of a LT GaP annealed at different temperatures. The film was grown at 200 °C with a PH$_3$ flow rate of 2.4 sccm.
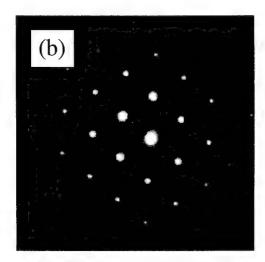
Fig. 6 (a) (110) XTEM image and (b) diffraction pattern of an annealed GaP film grown at 200 °C with a PH₃ flow rate of 2.4 sccm. The annealing temperature is 600 °C, and the annealing time is 1 hr.

Figs. 6 (a) and (b) are a cross-sectional TEM image and diffraction pattern, respectively, of the sample annealed at 600 °C. Due to excess P, the LT GaP shows a contrast from the substrate, which makes it possible to distinguish the LT GaP epilayer from the substrate. From

the figures we can see a high degree of crystalline perfection of the LT GaP film. However, no precipitates are observed. This could be due to the smaller amount of excess P incorporated (~ 0.26%) as compared with that of excess As in LT GaAs (~ 1%) [17,18].

SUMMARY

In summary, we have studied the effects of substrate temperature and PH_3 flow rate on the crystalline quality, strain, and excess P in LT GaP films. At T_s lower than 160 °C, LT GaP is poly-crystalline, independent of PH_3 flow rate, while at T_s higher than 160 °C, the crystalline quality of LT GaP depends on PH_3 flow rate. XRC results reveal a tensile strain in LT GaP films, possibly due to P_{Ga} antisite defects. The strain and the excess P increase as the PH_3 flow rate increases, but decrease as the annealing temperature increases. XTEM observation of a sample annealed at 600 °C indicates high-quality single-crystalline LT GaP, but no P precipitates are detected.

ACKNOWLEDGMENT

REFERENCES

1. R. A. Puechner, D. A. Johnson, K. T. Shiralagi, D. S. Gerber, R. Droopad, and G. N. Maracas, J. Cryst. Growth 111, 43 (1991).
2. F. W. Smith, A. R. Calawa, and C. Chen, IEEE Electron Device Lett. EDL-9, 77 (1988).
3. M. R. Melloch, K. Mahalingam, N. Otsuka, J. M. Woodall, and A. C. Warren, J. Cryst. Growth 111, 39 (1991).
4. A. C. Warren, N. Katzenellenbogen, D. Grischkowsky, J. M. Woodall, M. R. Melloch, and N. Otsuka, Appl. Phys. Lett. 58, 1512 (1991).
5. F. W. Smith, H. W. Le, V. Diadiuk, M. A. Hollis, A. R. Calawa, S. Gupta, M. Frankel, D. R. Dykaar, and T. Y. Hsiang, Appl. Phys. Lett. 54, 890 (1989).
6. F. W. Smith, Mater. Res. Soc. Symp. Proc. 241, 3 (1992).
7. U. K. Mishra, R. M. Kolbas, Mater. Res. Soc. Symp. Proc. 241, 159 (1992).
8. S. Gupta, G. Mourou, F. W. Smith, and A. R. Calawa, Mater. Res. Soc. Symp. Proc. 241, 205 (1992).
9. W. M. Chen, I. A. Buyanova, A. V. Buyanov, W. G. Bi, and C. W. Tu, this volume.
10. I. A. Buyanova, W. M. Chen, A. V. Buyanov, W. G. Bi, and C. W. Tu, unpublished.
11. J. Ramdani, Y. He, M. Leonard, N. EI-Masry, and S. M. Bedair, Appl. Phys. Lett. 61, 1646 (1992).
12. Y. He, N. A. EI-Masry, J. Ramdani, S. M. Bedair, T. L. McCormick, R. J. Nemanich, and E. R. Weber, Appl. Phys. Lett. 65, 1671 (1994).
13. B. W. Liang, Y. He, and C. W. Tu, Mater. Res. Soc. Symp. Proc. 241, 283 (1992).
14. M. Kaminska, Z. Liliental-Weber, E. R. Weber, T. George, J. B. Kortright, F. W. Smith, B. Y. Tsaur, and A. R. Calawa, Appl. Phys. Lett. 54, 1881 (1989).
15. A. C. Warren, J. M. Woodall, J. L. Freeouf, D. Grischkowsky, D. T. Mcinturff, M. R. Melloch, and N. Otsuka, Appl. Phys. Lett. 57, 1331 (1990).
16. W. G. Bi, F. Deng, S. S. Lau, and C. W. Tu, J. Vac, Sci. Technol. B13, 754 (1995).
17. F. W. Smith, C. L. Chen, G. W. Turner, M. C. Finn, L. J. Mahoney, M. J. Manfra, and A. R. Calawa, Proc. IEEE Int. Electron Devices Meeting (IEEE, New York, 1988), p. 838.
18. M. Kaminska, E. R. Weber, Z. Liliental-Weber, R. Leon, and Z. U. Rek, J. Vac. Sci. Technol. B7, 710 (1989).

ATOMIC FORCE MICROSCOPE CHEMICALLY INDUCED DIRECT PROCESSING

B. N. SHIMBO, S. KOMAROV, B. J. VARTANIAN, Y. OKADA, J. S. HARRIS, Jr.
Solid State Laboratory, Stanford University, Stanford, CA 94305

ABSTRACT

Interest in room-temperature operable quantum effect devices has created a need for simple and inexpensive nanofabrication techniques. By applying a bias to a conductive AFM tip, we have succeeded in fabricating narrow (~30 nm) oxide lines on a variety of metal and III-V semiconductor substrates. The effects of different drawing parameters such as tip bias, translation speed, ambient atmosphere, and substrate doping on line quality were explored.

INTRODUCTION

There is a growing interest in quantum effect electronic devices whose features are noticeable at room temperature. The primary fabrication requirement for such devices is uniform dimensions on the order of 10 nm. Crystal growth methods such as molecular beam epitaxy provide monolayer control in the vertical direction, but techniques for controlling lateral dimensions remain limited. Although optical, x-ray, and e-beam lithography processes may approach these small dimensions, they will only do so at great cost. Furthermore, once patterns have been lithographically defined, conventional etching techniques both damage surfaces and fail to provide sufficient dimensional uniformity. We seek a simple and inexpensive method for fabricating nanometer-scale devices.

The scanning tunneling microscope's (STM) capability for surface modification was realized shortly after its development as a tool for microscopy. The STM has been used to oxidize fine lines in Si for use as etch masks [1]. Additionally, in an ultra high vacuum STM system, Si oxide linewidths as narrow as 1 nm have been reported [2]. The atomic force microscope (AFM) became an attractive candidate for similar work because, unlike the STM, it allows for independent control over the tip-substrate spacing and the writing voltage. AFM-induced oxide lines have been used as etch masks to create Si MOSFETs [3] and side-gated FETs [4]. On a Ti substrate, room temperature-operable single-electron transistors with 15 nm features have also been fabricated [5]. One aspect that made this project unique was that AFM-generated oxides were used as integral parts of the device, and not just as a step in the fabrication process.

EXPERIMENT

By applying a voltage to a conductive AFM tip, we create an intense, localized electric field at the substrate. We believe that there are two processes working in parallel that lead to oxidation, anodization through a thin film of water adsorbed to the surface of the substrate [6], and field-enhanced oxidation that helps ionized water molecules diffuse through existing oxide to the substrate surface [7].

Using a Digital Instruments AFM with doped silicon tips, we have succeeded in drawing oxide lines on GaAs, AlGaAs, InGaAs, Ti, and NiAl substrates. We have conducted an investigation of the drawing parameters of tip voltage, translation speed, ambient atmosphere, and substrate doping. A computer script directed the AFM to draw pairs of 1 μm-long lines, one left-to-right, and another right-to-left, at tip voltages from 4 - 12 V. Cross-sectional measurements of line width and height were taken at three different points on the lines. The full line pattern was drawn for tip translation speeds ranging from 0.1 - 1.0 μm/sec. Ambient atmosphere effects were tested by placing a small drop of warm water on one corner of the substrate to increase the local humidity. The influence of doping was tested by drawing

patterns on two GaAs substrates, the first undoped and the second Si-doped to 5×10^{17} cm^{-3}.

RESULTS

The results agreed well with physical intuition. As shown in Figure 1, higher tip voltages resulted in wider and thicker oxide lines, with the difference being more prominent at lower writing speeds. The higher voltage likely enhanced both the anodization and ion diffusion processes. Figure 1 also shows how faster writing speeds led to thinner lines, as the tip spent less time over the oxidizing areas. The more humid atmosphere also resulted in wider and thicker lines, as shown in Figure 2. Increasing the water concentration around the tip likely provided a larger supply of oxidation reactants. Finally, the AFM image of Figure 3 demonstrates that increasing the conductivity of the substrate surface through increased doping led to thicker, more continuous oxide lines.
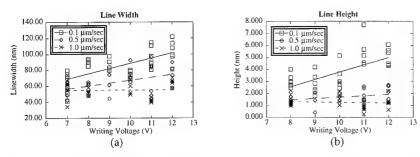
Figure 1. The effect of AFM tip voltage and tip translation speed on line width (a) and height (b). Both line width and height increase with higher tip voltages and slower translation speeds.
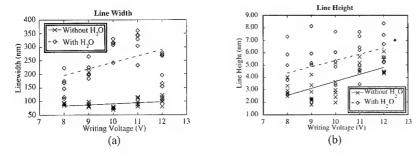
Figure 2. The effect of the ambient atmosphere on line width (a) and height (b). Both line width and height increase in a more humid atmosphere.

(a)   (b)
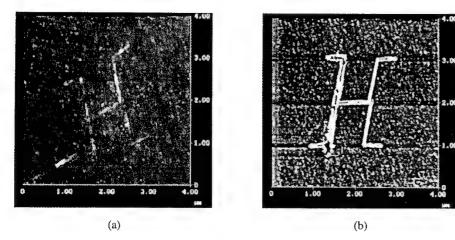
Figure 3. AFM images showing the effect of substrate doping on oxide lines drawn on an
undoped GaAs substrate (a) and a GaAs substrate Si-doped to 5×10^{17} cm^{-3} (b). The higher
substrate conductivity appears to improve oxide line continuity and increase line width and
height.

As can be seen from the spread in the data, the line width and height often varied over a
wide range. Inhomogeneous substrate surfaces are a likely culprit and we are investigating
different surface preparation schemes to smooth and passivate the substrate prior to AFM
oxidation.

CONCLUSIONS

We have used an AFM to draw narrow oxide lines on a variety of metal and III-V
semiconductor substrates, and explored the effects of a number of drawing parameters.
Though lines as narrow at 30 nm have been produced, the lines are not yet sufficiently narrow
nor controlled. Rurther optimization of drawing parameters will be required before the system
is fully suitable for nanofabrication.

ACKNOWLEDGEMENTS

REFERENCES

1. J. A. Dagata, J. Schneir, H. H. Harary, J. Bennett and W. Tseng, J. Vac. Sci. Technol. **B
   9**, 1384 (1991).
2. J. W. Lyding, T.-C. Shen, J. S. Hubacek, J. R. Tucker, and G. C. Abeln, Appl. Phys.
   Lett. **64**, 2010 (1994).
3. S. C. Minne, H. T. Soh, Ph. Flueckinger and C. F. Quate, Appl. Phys. Lett. **66**, 703
   (1995).
4. P. M. Campbell, E. S. Snow and P. J. McMarr, Appl. Phys. Lett. **66**, 1388 (1995).
5. K. Matsumoto, M. Ishii, K. Segawa, Y. Oka, B. J. Vartanian and J. S. Harris, Appl.
   Phys. Lett. **68**, 34 (1996).
6. H. Sugimura, T. Uchida, N. Kitamura and H. Masuhara, Jpn. J. Appl. Phys. **32**, **L**553
   (1993).
7. Y. Ejiri, M. Yasutake and T. Hattori, *Ext. Abstr. 1994 Int. Conf. Solid State Devices and
   Materials, Chiba, 1994* (Business Center for Academic Societies Japan, Tokyo, 1994) p.
   606.

Cl$_2$-BASED ECR ETCHING OF InGaP, AlInP AND AlGaP

J. Hong*, J. W. Lee*, S. J. Pearton*, C. Santana*, C. R. Abernathy*,
 W. S. Hobson** and F. Ren**
*University of Florida, Gainesville FL 32611
** Lucent Technologies Bell Laboratories, Murray Hill NJ 07974.

ABSTRACT

High microwave power (1000W) Electron Cyclotron Resonance (ECR) Cl$_2$/Ar plasma produce etch rates for In$_{0.5}$Ga$_{0.5}$P, Al$_{0.5}$In$_{0.5}$P and Al$_{0.5}$Ga$_{0.5}$P of ~1um/min. at low pressure (1.5mTorr), moderate rf power levels (150W) and room temperature. Addition of Cl$_2$ into Ar makes much smoother etched surface morphology as well as increasing the etch rate. All parameters, including microwave power, chamber pressure and rf power increase the etch rate of these alloys. Especially, there is at least a minimum rf power in order to get much higher etch rate with increasing microwave power. AlGaP in Cl$_2$/Ar discharges has lower etch rates than InGaP or AlInP, which is similar to the results based on CH$_4$/H$_2$/Ar plasma chemistries. The Cl$_2$/Ar chemistry enables smooth, high-rate etching without the need for polymer addition and thus simplifies the processing.

INTRODUCTION

The InGaAlP materials system is gaining in importance for photonic and electronic devices such as the commercially significant 600-680 nm light-emitting diodes (LEDs) and lasers and high electron mobility transistors (HEMTs).[1-20] In particular (Al$_x$Ga$_{1-x}$)$_{0.51}$In$_{0.49}$P lattice matched to GaAs is an extremely useful alloy since the direct bandgap can be varied from 1.9 eV for the ternary In$_{0.49}$Ga$_{0.51}$P to ~2.3 eV for (Al$_{0.66}$Ga$_{0.34}$)$_{0.51}$In$_{0.49}$P.[1,17] A lot of attention has been focused on growth (and ordering) of InGaP and AlInP for use in the visible LEDs and vertical cavity surface emitting lasers,[1,21] while InGaP/GaAs heterojunction bipolar transistors and HEMTs have shown numerous advantages over comparable AlGaAs/GaAs devices particularly because InGaP has lower impurity contents and surface recombination velocities.[8-12,19]

Several recent publications have reported on development of selective and non-selective wet chemical etches for InGaP, AlInP and AlGaP, [22-24] implant doping and isolation[25,26], and ohmic contact technology.[27] Less attention has been paid to the development of dry etching for these alloys. The CH$_4$/H$_2$ plasma chemistry provides smooth etching of all III-V semiconductor at slow rates (< 500Å min^{-1}), but the more aggressive Cl$_2$-based discharges are generally not suitable for In-containing materials unless sample heating above ~150 °C is employed to enhance desorption of the InCl$_3$ etch product.[28] Previous work has reported that ternary and quaternary materials in this system can be etched in Cl$_2$/CH$_4$/H$_2$/Ar discharges.[29] A recent report on use of BCl$_3$/N$_2$ high ion density plasmas demonstrated etch rates approaching 1um min^{-1} for InGaP at 100 °C, showing that efficient ion-assisted sputtering conditions can reduce the temperature required for etch product desorption.[30] In this paper we show that a simple Cl$_2$/Ar plasma chemistry produces smooth, high-rate (> 1um min^{-1}) etching of InGaP and AlInP under high ion density conditions. Much lower rates are obtained with AlGaP, which appears to correlate with the higher average bond strength in this material. This suggests that thin pseudomorphic AlGaP

EXPERIMENTAL

Latticed matched layers of undoped $In_{0.49}Ga_{0.51}P$ and $Al_{0.5}In_{0.5}P$ were grown on semi-insulating GaAs by both Metal Organic Chemical Vapor Deposition (MOCVD)[31] or Metal Organic Molecular Beam Epitaxy (MOMBE),[32] using trimethylindium, trimethylamine alane, triethylgallium and phosphine. Layers of $Al_{0.5}Ga_{0.5}P$ were grown on Si substrates by MOMBE - since there is substantial lattice mismatch at this composition , the films contained threading dislocations at densities of 10^9 - 10^{10} cm^{-2}. The area around these defects did not show any preferential etching effects. There was also no measurable difference in etch rates of InGaP and AlInP grown by either epitaxial technique.

Samples were lithographically patterned with AZ5209E photoresist and etched in a load-locked Plasma Therm SLR 770 system. The samples are mechanically clamped to an rf-biased (13.56GHz), He backside cooled chuck held at 22^0C. The discharge is generated in a low profile Electron Cyclotron Resonance (ECR) electromagnet source operating at 2.45GHz. The upper magnet is run at 170A to produce the ECR condition , while the lower collimating magnet is operated at 40A. The microwave power was varied from 600-1000W, the rf power from 150-300W and the process pressure from 1.5-10 mTorr. Electronic grade Cl_2 and Ar were injected into the ECR source at a total flow rate of 15 standard cubic centimeters per minute (sccm). The near surface stoichiometry was measured by Auger Electron Spectroscopy (AES). Etch rates were obtained by stylus profilometry of the features after removal of the photoresist mask in acetone.

RESULTS AND DISCUSSION

Figure 1 shows the etch rates of the three materials as a function of Cl_2 composition in 1.5mTorr ECR discharges of Cl_2/Ar. The removal rates of InGaP and AlInP rise rapidly with increasing Cl_2 content before saturating at a mixture of $10Cl_2$/5Ar. We assume that above this composition the etching is no longer reactant limited. Selectivities of ~6 for InGaP and AlInP over AlGaP are obtained at high Cl_2 compositions. We observed that the threshold rf power for etching AlGaP (~100W) was higher than that for the other two materials (~40W) and this may be
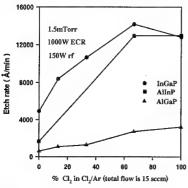
Figure 1. Etch rates of the ternary alloys as a function of Cl_2 percentage in 1.5mTorr, 1000W (microwave), 150W rf Cl_2/Ar discharges.
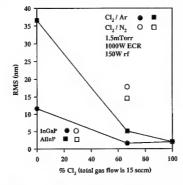
Figure 2. RMS roughness of InGaP and AlInP after etching in Cl_2/Ar or Cl_2/N$_2$, 1.5mTorr, 1000W (microwave), 150W rf discharges as a function of plasma composition

useful in situations requiring selectivity between InGaP and AlInP. A similar role is played by thin layers of InGaAs inserted between AlGaAs/GaAs when employing Cl_2-based plasma chemistries.[33] The rates are higher for InGaP and AlInP relative to AlGaP, corresponding to their melting points (1538K for InGaP, 2079K for AlInP, 2282K for AlGaP), which is a good indication of their average bond strengths.[34] If we take the binary bond strengths, and average them we obtain 51.1kCal mol^{-1} for InGaP, 49.6kCal mol^{-1} for AlInP and 53.4kCal mol^{-1} for AlGaP.[35] Since the volatilities of the etch products for AlGaP should be on average higher than for the In-containing materials, we conclude that the etch rate for AlGaP is limited by the initial bond breaking that must precede formation of the chlorine etch products.

Very smooth morphologies were obtained for the high Cl_2-content conditions. The dependence of RMS roughness on Cl_2-to-Ar content in 1.5mTorr, 1000W(microwave), 150W rf discharges is shown in Figure 2. There is a clear improvement in morphology at the higher Cl contents where near equi-rate removal of both the group III etch products and PCl_3 occurs. Note also that when N_2 was substituted for Ar, the morphologies of both InGaP and AlInP were significantly worsened.

While these high ion density conditions produce stoichiometric surfaces, a lowering of the Cl_2 content, or an increase in rf power (and hence ion energy) can tip the balance between the rates of etch product removal. For example, Figure 3 shows AES surface scans (top) and depth profiles (bottom) from an InGaP sample etched in a $2Cl_2/13Ar$, 1.5mTorr, 1000W (microwave)
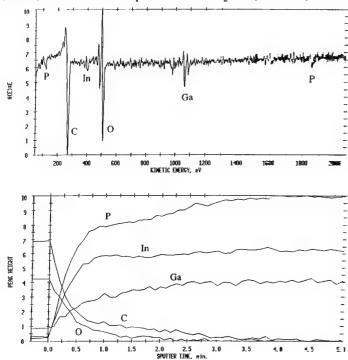
Figure 3. AES surface scan (top) and depth profile (bottom) from InGaP etched in a 1.5mTorr, 1000W (microwave), 300W rf discharges of $2Cl_2/13Ar$.

discharge with 300W of rf power. Note that both the P and Ga do not reach their bulk values until deeper into the sample relative to the In signal, suggesting they are preferentially lost under these conditions. The sputter rate in the profile of Figure 3 was ~60Å min^{-1}, so the depletion extends to ~200Å. The RMS roughness increases from 1.58nm for a sample etched in a 10Cl$_2$/5Ar, 1000W, 150W rf discharge to 8.7nm when the rf power was increased to 300W.

As the microwave power, and hence ion flux , is increased at fixed plasma pressure, composition and rf power, then the etch rates of all these materials increase (Figure 4). This is typical of ECR plasma processes and results from the faster sputter rates at higher ion fluxes. The InGaP continues to increase in rate, while those of the other two level-off for these conditions. At higher Cl$_2$ concentrations, the AlInP and AlGaP rates also continue to increase with higher microwave power. Thus the total ion-to-chlorine radical ratio can dramatically shift the etch rates, and also the surface morphology and stoichiometry. The ion density in the plasma increases from ~4×10^{10} cm^{-3} to ~3×10^{11} cm^{-3} between 600-1000W microwave power based on interferometry performed at 35GHz.[36] As previously reported by Ren et. al.[30] the morphology improves significantly with microwave power in InGaP and AlInP because the enhanced sputter rate prevents formation of a thick InCl$_3$ selvedge layer which can poison the surface and produce slow, rough etching. At an optimum ion/neutral flux ratio the InCl$_3$ is sputtered away at the same rate it is formed, maintaining a smooth stoichiometric surface. If the ion flux becomes too high, preferential loss of P (and Ga) will occur, producing rough etching.

The pressure dependence of etch rates for the three ternary alloys is shown in Figure 5 for fixed plasma power and composition. As more chlorine neutrals are supplied to the surface at higher pressure the rates increase monitored by optical emission, and since the ion density decreases due to the reduced microwave coupling efficiency, then the morphologies are observed to undergo a rough-to-smooth transition for AlInP and InGaP at $\geq$ 5mTorr. We believe this is the reason for the difference in behavior from Figure 1,where the rates also increase with Cl$_2$ partial pressure. We ascribe these results to the balance between formation and removal of the least
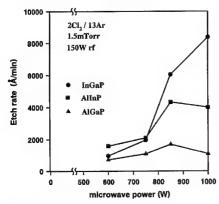

Figure 4. Etch rates of the ternary alloys in 2Cl$_2$/13Ar, 1.5mTorr, 150W rf discharges, as a function of microwave power.
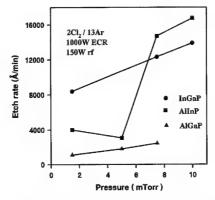
Figure 5. Etch rates of the ternary alloys as a function of pressure in 2Cl$_2$/13Ar, 1000W (microwave), 150W rf discharges.

volatile etch product, $InCl_3$. For more Cl_2-rich plasma compositions, it is not necessary to increase pressure, as discussed earlier. The small dip in etch rate for AlInP at 5mTorr is outside the experimental error and may be related to the higher Cl_2-coverage reducing the etch product removal rate. The InGaP etch rate is less sensitive to this effect.

CONCLUSION

A simple Cl_2/Ar plasma chemistry produces fast, smooth etching of InGaP and AlInP under ECR conditions, while the rates for $Al_{0.5}Ga_{0.5}P$ are significantly lower. Since the volatility of the products for the latter material are high it is logical to conclude that the high bond strengths reduce formation of these chlorides and hence lead to the slow removal rates. The ion/neutral ratio controls both the etch rates and morphologies for InGaP and AlInP, with the best results when formation of a thick $InCl_3$ reaction layer is avoided. The fact that Cl_2/Ar can efficiently etch In-containing III-V materials means that it can be employed as a universal etchant for compound semiconductors.

ACKNOWLEDGEMENT

REFERENCES

1. J. M. Kuo, Thin Solid Films **231**, p. 158 (1993), and references therein.
2. M. J. Hafich, H. Y. Lee, T. E. Crumbaker, T. J. Vogt, P. Silvestre and G. Y. Robinson, J. Vac. Sci. Technol. B **10**, p. 969 (1992)
3. K. Ozasa, M. Yuri and H. Matsunami, J. Cryst. Growth **102**, p. 31 (1990)
4. Y. J. Chan, D. Pavlidis, M. Razheghi and F. Omnes, IEEE Trans Electron. Dev. ED-**37**, p. 2141 (1990)
5. J. M. Kuo, and Y. J. Chan, J. Vac. Sci. Technal. B **11**, p. 976 (1993)
6. M. J. Mondry and H. Kroemer, IEEE Electron. Dev. Lett. EDL-**6**, p. 175 (1985)
7. M. O. Watanabe and Y. Ohba , Appl. Phys. Lett. **50**, p. 906 (1987)
8. W. Liu and S. K. Fan, IEEE Electron. Dev. Lett. EDL-**13**, p. 510 (1992)
9. S. L. Delage, M. A. DiForte-Poisson, H. Blanck, C. Brylinski, E. Chartier and P. Collot, Electron. Lett. **27**, p. 253 (1991)
10. W. Pletschen, K. H. Bachem and T. Lautybach, Proc. Mat. Res. Soc. Symp. Proc **240**, p. 493 (1992)
11. W. S. Hobson, F. Ren, J. R. Lothian and S. J. Pearton, Semicond. Sci. Technol. **7**, p. 598 (1992)
12. C.R. Abernathy, F. Ren, P. Wisk, S. J. Pearton and R. Esagui, Appl. Phys. Lett. **61**, p. 1092 (1992)
13. M. Ikeda, Y. Mori, H. Sato, K. Kaneko and N. Watanabe, Appl, Phys. Lett. **47**, p. 1027 (1985)

17. W. S. Hobson, Proc. Symp. Wide Bandgap Semiconductors and Devices (ECS, Pennington, NJ) pp. 26-42 (1995)
18. S. J. Groves, J. N. Walpole and C. J. Missaggia, Appl. Phys. Lett. **61**, p. 255 (1992)
19. A. W. Hanson, S. A. Stockman and G. E. Stillman, IEEE Electron. Dev. Lett. **14**, p. 25 (1993)
20. D.P. Bour, in Quantum Well Lasers , ed. P. S. Zory (Academic Press, NJ 1993) pp. 415-460
21. J. R. Lothian, J. M. Kuo, W. S. Hobson, E. Lane, F. Ren and S. J. Pearton, J. Vac. Sci. Technol. B **10**, p. 1061 (1992)
22. J. R. Lothian, J. M. Kuo, F. Ren and S. J Pearton, J. Electron. Mater. **21**, p. 441 (1992) 23. J. W. Lee, S. J. Pearton, C. R. Abernathy, W. S. Hobson, F. Ren and C. S. Wu, Solid State Electron. **38**, p. 1871 (1995)
24. S. J. Pearton, W. S. Hobson, J. M. Kuo, H. S. Luftman, A. Katz and F. Ren, Appl. Phys. Lett. **60**, p. 1318 (1992)
25. S. J. Pearton, J. M. Kuo, F. Ren, A. Katz and A. Perley, Appl. Phys. Lett. **59**, p. 1467 (1991)
26. F. Ren, J. .M. Kuo, S. J. Pearton and T. R. Fullowan, J. Electron. Mater. **21**, p. 243 (1992)
27. S. C. McNevin, J. Vac. Sci. Technol. B4, p. 1216 (1986)
28. F. Ren, W. S. Hobson, J. R. Lothian, J. Lopata, J. A. Caballero, S. J. Pearton and M. W. Cole, Appl. Phys. Lett. **67**, p. 2497 (1995)
29. W. S. Hobson, Mat. Sci. For. **148 / 149**, p. 27 (1994)
30. C. R. Abernathy, J. Vac. Sci. Technol. A11, p. 869 (1993)
31. S. Salimian and C. R. Cooper 111, J. Electrochem. Soc. **136**, p. 2420 (1989)
32. S. J. Pearton, T. Nakano and R. A .Gottscho, J. Appl. Phys. **69**, p. 4206 (1991)

PLASMA CHEMISTRIES FOR DRY ETCHING
GaN, AlN, InGaN and InAlN

S. J. Pearton[1], C. B. Vartuli[1], J. W. Lee[1], S. M. Donovan[1],
J. D. MacKenzie[1], C. R. Abernathy[1], R. J. Shul[2],
G. F. McLane[3] and F. Ren[4]

[1]University of Florida, Gainesville FL 32611
[2]Sandia National Laboratories, Albuquerque NM 87185
[3]Army Research Laboratory, Ft. Monmouth NJ 07703
[4]AT&T Bell Laboratories, Murray Hill, NJ 07974.

ABSTRACT

Etch rates up to 7,000Å/min. for GaN are obtained in $Cl_2/H_2/Ar$ or BCl_3/Ar ECR discharges at 1-3mTorr and moderate dc biases. Typical rates with HI/H_2 are about a factor of three lower under the same conditions, while CH_4/H_2 produces maximum rates of only ~2000Å/min. The role of additives such as SF_6, N_2, H_2 or Ar to the basic chlorine, bromine, iodine or methane-hydrogen plasma chemistries are discussed. Their effect can be either chemical (in forming volatile products with N) or physical (in breaking bonds or enhancing desorption of the etch products). The nitrides differ from conventional III-V's in that bond-breaking to allow formation of the etch products is a critical factor. Threshold ion energies for the onset of etching of GaN, InGaN and InAlN are $\geq$75eV.

INTRODUCTION

Dry etching proceeds by formation of etch products that are either spontaneously removed because of their gaseous nature, or can be ejected from the surface by ion-assisted processes such as sputtering. For III-V materials one can form chlorides, iodides, bromides, metalorganic or hydride species, and thus the basic etch chemistries are based on Cl_2, I_2, Br_2 or CH_4/H_2.[1] A table of the boiling points of various etch products is shown in Table 1.[2] From this data, one would expect to be able to rapidly etch GaN and related alloys in Cl_2 chemistries (with ion assistance for In containing alloys), I_2 chemistries, Br_2 chemistries (with ion assistance again to remove $InBr_3$) or CH_4/H_2, i.e. the normal plasma mixtures used for conventional III-V's such as GaAs.

However many different groups have reported low etch rates for GaN and the other III-N materials, with typical values of $\leq$1,000Å·min^{-1} under reactive ion etching conditions.[3-5] In higher ion density discharges, McLane et al. [6,7] and Shul et al.[8,9] have reported much faster rates, typically 3-5,000 Å·min^{-1} at moderate dc biases. The rates tend to peak around 1-3mTorr, and the fastest GaN etch rate obtained has been ~0.9µm·min^{-1} by the Sandia group using $Cl_2/H_2/Ar$ at high microwave (1000W) and rf (450W) powers.[10]

In this paper we show how different plasma chemistries, and in particular the ion current incident on the sample, can produce vast differences in GaN etch rates.

Table 1: Boiling Points of III-V Etch Products

Species	Boiling Point (°C)	Species	Boiling Point (°C)
$GaCl_3$	201	NCl_3	< 71
$GaBr_3$	279	NI_3	explodes
GaI_3	sub 345	NF_3	-129
$(CH_3)Ga$	55.7	NH_3	-33
		N_2	-196
$InCl_3$	600	$(CH_3)_3N$	2.9
$InBr_3$	> 600		
InI_3	210	PCl_3	76
$(CH_3)_3In$	134	PBr_5	106
		PH_3	-88
$AlCl_3$	183		
$AlBr_3$	263	$AsCl_3$	130
AlI_3	191	$AsBr_3$	221
$(CH_3)_3Al$	126	AsH_3	-55
		AsF_3	-63

EXPERIMENTAL

The etching was performed in either Plasma-Therm SLR 770 load-locked ECR systems, which are capable of operation in either an RIE mode (where only the lower electrode is rf powered) or in the ECR mode (where the microwave source and the lower electrode are both powered), or in a magnetron system where high ion densities are achieved through magnetic confinement of the discharge. Many different plasma chemistries have been employed, indicating HI/H_2, HBr/H_2, CH_4/H_2, Cl_2/H_2 and BCl_3, generally with additions of Ar to enhance the ion bombardment component. In some case N_2 or SF_6 was added to investigate the role of the additive gas.

The samples were generally grown by Metal Organic Molecular Beam Epitaxy (MO-MBE)[11], although other material grown by Metal Organic Chemical Vapor Deposition (MOCVD) was used in some instances. Under optimized growth conditions for the two techniques, the MOMBE material generally etches slightly (~10-15%) faster. This is probably an indication that its much lower growth temperatures (≤900°C for GaN) leaves more weak or defective bonds available for attack by the reactive neutrals in the plasma.

RESULTS AND DISCUSSION

We generally found that Cl_2-based discharges produced the fastest rates for GaN, with CH_4/H_2 having the slowest rates. The other plasma chemistries (BCl_3, HI and HBr) produced rates that were intermediate between these extremes.[12,13] As discussed previously it is necessary to add either H_2 or SF_6 to the Cl_2/Ar mixture in order to achieve the maximum etch rates, best morphology and to retain the stoichiometry of the near-surface.[14,15]

Figure 1 shows GaN and AlN etch rates in a 1.5mTorr, 0 or 1000W (ECR) plasma of $10Cl_2/5Ar$, as a function of rf power applied to the sample chuck. The rates are about a factor of 3 higher for the microwave-enhanced discharges and, are always higher for GaN relative to AlN. Since Table 1 shows that the volatility of the etch products are actually slightly higher for AlN, the rate-limiting step is the initial breaking of the group III-nitrogen bonds that must precede etch product formation. Further support for this idea comes from the fact that there is very little temperature dependence to the etch rates up to 300°C. If the rate-limiting step was etch product desorption then one would expect an exponential dependence of rate on sample temperature.
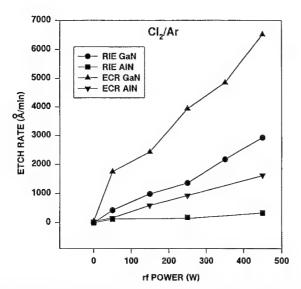
Figure 1. Etch rates of GaN and AlN in $10Cl_2/5Ar$, 1.5mTorr RIE or ECR discharges.

Figure 2 shows similar data for RIE and ECR etching of InN and InGaN. Note that the rates under RIE conditions are extremely low which is most likely due to the involatile $InCl_3$ etch product. Under ECR conditions there is more efficient sputter desorption and consequently much higher rates. Note that the rates are lower for InGaN, which again is consistent with the idea that bond-breaking is the critical step in these etch processes, since the average volatilities of the etch products for InGaN are actually lower than for pure InN.
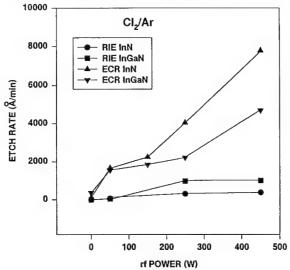
Figure 2. Etch rates of InGaN and InN in $10Cl_2/5Ar$, 1.5mTorr RIE or ECR discharges.

The dependence on rf power of GaN and AlN etch rates in $5CH_4/15H_2/10Ar$ discharges at 1.5mTorr is shown in Figure 3. The first thing to notice is that the rates are much lower for GaN compared to the Cl_2/Ar data. Secondly, the rates for AlN are similar for the two chemistries, suggesting again that bond-breaking is the main impediment to the achievement of faster rates. Once again ECR conditions produce much higher etch rates compared to RIE.
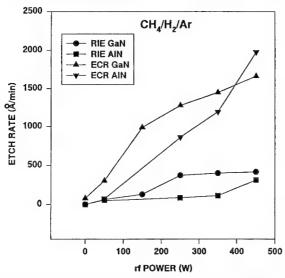
Figure 3. Etch rates of GaN and AlN in $5CH_4/15H_2/10Ar$, 1.5mTorr RIE or ECR discharges.

The most dramatic difference between ECR and RIE conditions was observed for $CH_4/H_2/Ar$ etching of InN and InGaN (Figure 4). The rates are negligible for both materials until very high rf powers in the RIE discharges, so that at moderate dc voltages one would be able to use InGaN or InN as an etch stop layer when removing GaN in $CH_4/H_2/Ar$. A similar result could be observed with AlN (Figure 3). Note also that the rates under ECR conditions are fairly similar to those obtained for InN and InGaN with Cl_2/Ar.

SUMMARY

The III-nitrides have slower etch rates than the more conventional compound semiconductors such as GaAs, GaP and GaSb. We have observed similar trends with the ternary compounds InGaP, AlInP and AlGaP. The average bond strength for AlGaP is higher than for the other two materials, and consequently it displays much lower etch rates in Cl_2-based plasma chemistries, even though the volatilities of the products are actually higher on average than for the InGaP and AlInP. We believe a similar explanation applies to the nitrides, because their etch products are volatile. The rate limiting step appears to be actually the initial bond-breaking which must precede etch product formation. Since the nitrides have high bond strengths, a high ion current is needed to enhance bond breaking and thus magnetically-enhanced discharges produce much higher rates than RIE conditions.
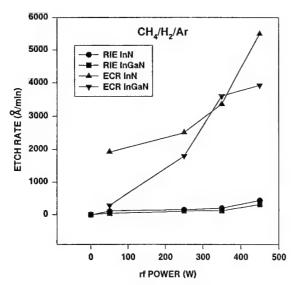
Figure 4. Etch rates of InGaN and InN in 5CH$_4$/15H$_2$/10Ar 1.5mTorr RIE or ECR discharges.

Acknowledgments

References

1. S. J. Pearton, Int. J. Mod. Phys. **8** 1781 (1994).
2. CRC Handbook of Chemistry and Physics (CRC Press, Boca Raton, FL 1990)
3. M. E. Lin, Z. F. Fan, Z. Ma, L. H. Allen and H. Morkoc, Appl. Phys. Lett. **64** 887 (1994).
4. I. Adesida, A. T. Ping, C. Youtsey, T. Dow, M. A. Khan, D. T. Olson and J. N. Kuznia, Appl. Phys. Lett. **65** 889 (1994).
5. S. J. Pearton, C. R. Abernathy, F. Ren, J. R. Lothian, P. Wisk, A. Katz and C. Constantine, Semicond. Sci. Technol. **8** 310 (1993).
6. G. F. McLane, L. Casas, S. J. Pearton and C. R. Abernathy, Appl. Phys. Lett. **66** 3328 (1995).
7. G. F. McLane, L. Casas, R. T. Lareau, D. W. Eckart, C. B. Vartuli, S. J. Pearton and C. R. Abernathy, J. Vac. Sci. Technol. **A13** 724 (1995).
8. R. J. Shul, S. P. Kilcoyne, M. Hagerott-Crawford, J. E. Rarmeter, C. B. Vartuli, C. R. Abernathy and S. J. Pearton, Appl. Phys. Lett. **667** 1761 (1995).
9. R. J. Shul, A. J. Howard, S. J. Pearton, C. R. Abernathy, C. B. Vartuli, P. A. Barnes and M. J. Bozack, J. Vac. Sci. Technol. **B13** 2016 (1995).
10. R. J. Shul (to be published).

11. C. R. Abernathy, J. Vac. Sci. Technol. A **11** 869 (1993).
12. S. J. Pearton, C. R. Abernathy and C. B. Vartuli, Electron. Lett. **30** 1985 (1994).
13. A. T. Ping, I. Adesida, M. A. Khan and J. N. Kuznia, Electron. Lett. **30** 1895 (1994).
14. S. J. Pearton. C. R. Abernathy and F. Ren, Appl. Phys. Lett. **64** 3643 (1994).
15. R. J. Shul, C. I. H. Ashby, D. J. Rieger, A. J. Howard, S. J. Pearton, C. R. Abernathy,C. B. Vartuli, P. A. Barnes and P. A. Barnes and P. Davis, Mat. Res. Soc. Proc. Vol. **395** (1996).

DRY ETCHING OF InGaP and AlInP IN CH₄/H₂/Ar

J. W. Lee, S. J. Pearton, C. J. Santana, E. S. Lambers and C. R. Abernathy
University of Florida, Gainesville FL 32611

W. S. Hobson and F. Ren
AT&T Bell Laboratories, Murray Hill NJ 07974

ABSTRACT

Electron Cyclotron Resonance (ECR) plasma etching with additional rf-biasing produces etch rates $\geq$ 2,500Å/min for InGaP and AlInP in CH₄/H₂/Ar. These rates are an order of magnitude or much higher than for reactive ion etching conditions (RIE) carried out in the same reactor. N₂ addition to CH₄/H₂/Ar can enhance the InGaP etch rates at low flow rates, while at higher concentrations it provides an etch-stop reaction. The InGaP and AlInP etched under ECR conditions have somewhat rougher morphologies and different stoichiometries up to ~200Å from the surface relative to the RIE samples.

INTRODUCTION

The ternary semiconductors InGaP and AlInP are becoming increasingly important in both electronic and photonic devices. In both high electron mobility transistors and heterojunction bipolar transistors InGaP can be employed as a replacement for AlGaAs.[1-5] The advantages of this substitution include reduced problems with oxidation, fewer deep level centers (especially of the DX center-type which leads to current-voltage collapse at low temperatures) and improved carrier confinement because of the larger valence band offset. Similar advantages accrue in employing InGaP cladding layers in 980nm strained InGaAs quantum well laser.[6] AlInP is less well developed but can also be used in a variety of both electrical and optical devices.[1] While a number of wet chemical etching solutions have been developed that are both selective and non-selective for these materials relative to GaAs,[2,7-9] much less work has been done on the dry etching of InGaP and AlInP. It is generally difficult to use Cl₂-based plasma chemistries for In-containing III-V semiconductors because of the relatively low volatility of InClₓ species, unless elevated etching temperatures can be tolerated.[10]

The other main plasma chemistry for III-V materials is based on CH₄/H₂, usually with addition of Ar to enhance sputter-induced desorption of the etch products.[11-13] The etch rates reported to date for InGaP and AlInP in CH₄/H₂/Ar are quite low, $\leq$400Å/min. The two main techniques employed have been reactive ion etching (RIE) and Electron Cyclotron Resonance (ECR) plasma etching. While the ion densities and plasma dissociation efficiencies in the latter technique are at least an order of magnitude higher than in RIE systems,[14] the reports to date have not fully exploited the capabilities of ECR reactors because only relatively low microwave powers were used.

In this paper we detail experiments on high ion density ECR plasma etching of InGaP and AlInP in CH₄/H₂/Ar. Etch rates $\geq$2,500Å/min with relatively smooth, stoichiometric surfaces can be obtained at 1000W of microwave power with additional rf biasing of the sample position. We have directly compared ECR and RIE techniques in the same reactor, and find the former has etch rates an order of magnitude higher. The CH₄/H₂/Ar plasma chemistry is non-selective for InGaAs

and AlInP, although one might expect that addition of a fluorine-containing gas would provide an etch-stop reaction when removing InGaP from an underlying AlInP layer.[11]

EXPERIMENTAL

The $In_{0.51}Ga_{0.49}P$ and $Al_{0.48}In_{0.52}P$ layers were grown lattice-matched to GaAs substrates by either Metal Organic Chemical Vapor Deposition (MOCVD)[6] or Metal Organic Molecular Beam Epitaxy (MOMBE).[16] The layers were typically ~1μm thick and were nominally undoped with n-type carrier concentrations of $\leq 10^{16} cm^{-3}$. In a few experiments we also used $Al_{0.5}Ga_{0.5}P$ epitaxial layers grown by MOMBE for comparison with the other two materials. Samples were lithographically patterned with AZ 5209E photoresist and etched in a Plasma-Therm SLR reactor. This is a load-locked system in which gases enter through electronic mass flow controllers into either an Astex 4400 low profile ECR source, or into a gas ring above the sample position. The CH_4 is injected into the gas ring because if it is cracked in the ECR source there is a prohibitive amount of polymer deposition within the chamber. The He back-side cooled sample electrode is powered with rf (13.56 MHz) power to induce a negative dc bias. The microwave power was varied from 0-1000W, while the rf power was changed from 0-300W, corresponding to dc biases of −15 to −325V. The process pressure was varied from 1.5-10mTorr, and standard gas flows of 5sccm CH_4, 15sccm H_2 and 25sccm Ar were employed.

The etch rates were obtained from stylus profilometry of the features after removal of the photoresist in acetone. Surface morphologies were examined by both scanning electron microscopy (SEM) and tapping mode atomic force microscopy (AFM), while the near-surface stoichiometry was measured by Auger Electron Spectroscopy (AES).

RESULTS AND DISCUSSION

Figure 1 shows etch rates for InGaP and AlInP in ECR $CH_4/H_2/Ar$ discharges at 1.5mTorr and 1000W of microwave power, as a function of rf power applied to the cathode. There is basically a linear dependence on power, suggesting that sputter-enhanced desorption of the etch
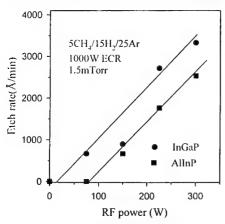
Figure 1. Etch rates of InGaP and AlInP in 5CH$_4$/15H$_2$/25Ar 1.5mTorr, 1000W microwave discharges as a function of rf power.
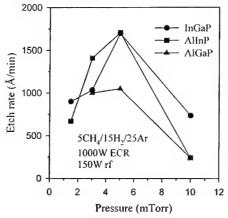
Figure 2. Etch rates of InGaP, AlInP and AlGaP in 150W rf, 1000W microwave 5CH$_4$/15H$_2$/25Ar discharges as a function of pressure.

products is one of the key factors limiting the etch rates. Note that there is a substantial threshold rf power required (~75W) before the commencement of etching of AlInP. Since this corresponds to an average ion energy larger than is present in an ECR-only discharge (typically ion energy ~15eV) this result suggests that, as in virtually every other situation we have encountered ion III-V materials processing, ECR etching without additional rf-biasing does not have any practical applications for patterning.[17] The results of Figure 1 also suggest the metalorganic Ga species formed in CH_4/H_2 discharges are more volatile than their Al counterparts, as reported previously under RIE conditions.[17]

The pressure dependence of etch rates at 150W rf, 1000W microwave are shown in Figure 2. There is a similar functional dependence for all three of the ternaries, with the etch rates peaking around 5mTorr. This is also a fairly typical result for ECR systems,[13] and results from a competition between the higher rates expected at higher pressures because of the increased neutral species density available, and the fact that the coupling efficiency of the microwave power to the discharge decreases at higher pressure. Note also that AlGaP has the slowest rates over the entire range of pressures investigated, indicating that the Ga products are less volatile than the In species.

The addition of N_2 to CH_4/H_2 discharges has recently been reported to provide smoother surfaces in reactive ion beam etching (RIE of InP).[18] We investigated the role of N_2 on InGaP etch rate, as shown in Figure 3 for 1000W microwave, 1.5 mTorr, 150W rf $CH_4/H_2/N_2/Ar$
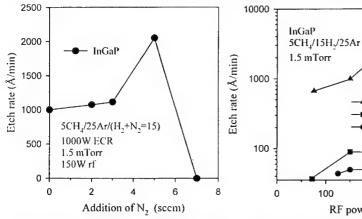
Figure 3. Etch rate of InGaP in 1000W microwave, 150W rf $CH_4/H_2/N_2/Ar$ discharges as a function of N_2 flow.
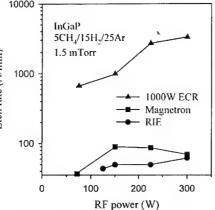
Figure 4. Etch rates of InGaP in 1.5 mTorr $CH_4/H_2/Ar$ discharges using three different techniques.

discharges. The CH_4 and Ar flows were held constant at 5 and 25 sccm, respectively, while the total $H_2 + N_2$ flow was fixed at 15sccm. The etch rate of InGaP initially increases with N_2 addition, which may be related to increased dissociation of CH_4 and H_2 by formation of NH_3 in the discharge. Above 5sccm N_2 flow, however, the etch rate decreases rapidly, and this could result from formation of nitride species on the semiconductor surface which have much higher sputtering thresholds than the corresponding phosphides. It has previously been reported that InGaN has much slower ion milling rates than InGaAs and other conventional III-V's.[19] This is a useful result from the viewpoint of producing selectivity when etching through to an InGaP

layer on which one wants to terminate the etch.

A direct comparison of etch rates for InGaP obtained with three different techniques is shown in Figure 4. In this case rf power is applied to the cathode, and either no ECR power and no magnets are used (i.e. RIE conditions), the lower magnet is operated and no ECR power is used (i.e. magnetron-like conditions), or ECR power is used and the magnets are operated (i.e. ECR conditions). Figure 4 clearly indicates the advantages of the ECR approach, with etch rates typically 10-30 times higher than for the other techniques. This is a result of the much higher ion densities and active neutral species concentrations, leading to a faster reaction and desorption rate at the InGaP surface.
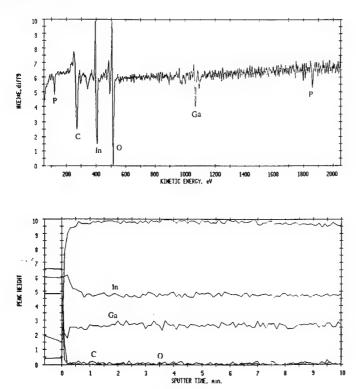
Figure 5 AES surface scan (top) and depth profile (bottom) from InGaP sample etched under ECR conditions.

AES surface scans and depth profiles from the same two samples are shown in Figure 5 (for ECR) and 6 (for RIE). There is a P and In deficiency to a depth of ~150Å-200Å in the ECR sample, based on our sputter rate calibration for the AES system. By contrast in the RIE sample the elemental profiles reach their bulk values within 25-50Å of the etched surface. In the case of AlInP, the near-surface of the ECR sample is again slightly deficient in P (and Al).
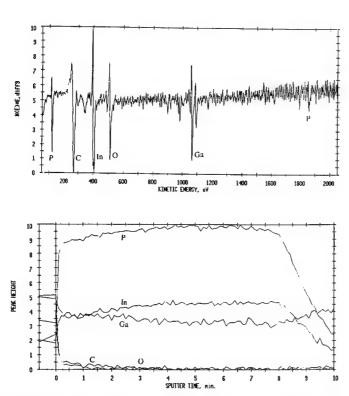
Figure 6 AES surface scan (top) and depth profile (bottom) from InGaP sample etched under RIE conditions.

SUMMARY AND CONCLUSIONS

The etch rates for InGaP and AlInP are much higher in ECR $CH_4/H_2/Ar$ plasmas, compared to conventional RIE conditions. The faster rates are accompanied by some deterioration of the surface morphology, and an alteration of the near-surface stoichiometry of both InGaP and AlInP. Depending on the specific application, one can improve surface smoothness by reducing the microwave power and accepting a lower etch rate. Addition of N_2 to the $CH_4/H_2/Ar$ plasma chemistry can either enhance the etch rate of InGaP, or at higher concentrations provide an etch-stop reaction. AlInP requires a threshold rf power to initiate etching and is removed at slower rates than InGaP.

ACKNOWLEDGMENTS

REFERENCES

1. J. M. Kuo, Thin Solid Films **231** 158 (1993).

2. J. R. Lothian, J. M. Kuo, F. Ren and S. J. Pearton, J. Electron. Mater. **21** 441 (1992).

3. F. Ren, Mat. Res. Soc. Symp. Proc. **300** 21 (1993).

4. C. R. Abernathy, J. Vac. Sci. Technol. **A11** 869 (1993).

5. F. Ren, J. R. Lothian, S. J. Pearton, C. R. Abernathy, P. W. Wisk, T. R. Fullowan, B. Tseng, S. N. G. Chu, Y, K. Chen, C. Yang, T. Fu, R. Brozovich, H. H. Lin, C. L. Henning and T. Henry, J. Vac. Sci. Technol. **B12** 2916 (1994).

6. W. S. Hobson, Mat. Res. Soc. Symp. Proc. **300** 76 (1993).

7. J. W. Lee, S. J. Pearton, C. R. Abernathy, W. S. Hobson, F. Ren and C. S. Wu, J. Electrochem. Soc. **142** L100 (1995).

8. J. W. Lee. S. J. Pearton. C. R. Abernathy, W. S. Hobson, F. Ren and C. S. Wu, Solid State Electron. (in press).

9. J. R. Lothian, J. M. Kuo, W. S. Hobson, E. Lane, F. Ren and S. J. Pearton, J. Vac. Sci. Technol. **B10** 1061 (1992).

10 R. J. Shul, R. P. Schneider and C. Constantine, Electron. Lett. **30** 817 (1994).

11. P. Collot and C. Gaonach, Semicond. Sci. Technol. $\underline{5}$ 237 (1990).

12. H. E. G. Arnott, R. W. Glew, G. Schiavini, L. J. Righb and A. Piccirillo, Appl. Phys. Lett. **62** 3189 (1993).

13. S. J. Pearton. W. S. Hobson, F. A. Baiocchi, A. B. Emerson and K. S. Jones, J. Vac. Sci. Technol. **B8** 57 (1990).

14 J. Asmussen, J. Vac. Sci. Technol. **A7** 889 (1989).

15. S. J. Pearton and W. S. Hobson, Appl. Phys. Lett. **56** 2186 (1990).

16. C. R. Abernathy, Mat. Res. Soc. Symp. Proc. **300** 3 (1993).

17. S. J. Pearton, Int. J. Mod. Phys. **B8** 1781 (1994).

18. J. R. Sendra and J. Anquita. Jap. J. Appl. Phys. **33** L390 (1994).

19. S. J. Pearton, C. R. Abernathy, F. Ren and J. R. Lothian, J. Appl. Phys. **76** 1210 (1994).

Passivation of Carbon Doping in InGaAs During ECR-CVD of SiNx

F. Ren, R. A. Hamm, R. G. Wilson*, S. J. Pearton** and J. R. Lothian

Lucent Technologies, Bell Laboratories, Murray Hill, NJ 07974, USA
*Hughes Research Laboratories, Malibu, CA 90265, USA
**University of Florida, Gainesville, FL 32611, USA

ABSTRACT

InGaAs (C) grown by gas-source MBE is found to contain significant concentrations 5 $\times$ 10^{18} cm^{-3} of hydrogen that is incorporated from the source gases. Subsequent deposition of ECR-CVD SiNx films as surface encapsulation produces additional hydrogen incorporation from the SiD_4/N_2 precursors, but actually reactivates C acceptors that were passivated in the as-grown InGaAs. Further thermal treatments produce substantial hydrogen in-diffusion from the SiNx film into the InGaAs, causing changes in sheet resistance and contact resistance. These processes simulate several steps in the formation of the base mesa of an InGaAs-based heterojunction bipolar transistor, and show how subtle changes in the temperature of these processes can affect subsequently device performance and apparent reliability.

Introduction

Heterojunction bipolar transistors in the InP/InGaAs and AlInAs/InGaAs systems have shown remarkably good dc, rf and microwave power performance[1]. In the GaAs/AlGaAs devices it has been shown that unintentional hydrogen passivated of the base dopant that occurs during epitaxial growth[2] or during subsequent device processing steps such as proton implant isolation alters the dc gain achieved[3]. Moreover, during operation of these devices, minority carrier injection causes de-bonding of neutral C-H complexes and an increase in effective base doping. This leads to a time-varying current gain as the electrically active C acceptor concentration slowly increases [2].

While most InGaAs-base HBTs have employed Be, Zn or Mg doping, there are advantages in the use of carbon due to its low diffusion coefficient and high solubility[4-6]. In self-aligned processing of these devices, a dry etch step to the base layer is often followed by deposition of a SiNx sidewall for passivation of the emitter-base junction periphery. The traditional source chemistry for this deposition is SiH_4/NH_3 or SiH_4/N_2, and there is a question of whether hydrogen from this plasma is incorporated into InGaAs (C) during this step. Subsequent annealing may also be carried out for ohmic content alloying or optimization of the resistance in implant-isolated regions. Therefore there is the possibility of further hydrogen in diffusion from the SiNx.

In this letter we show that atomic hydrogen is readily incorporated into InGaAs(C) during both SiNx deposition and subsequent annealing steps, but the sheet resistance of the InGaAs is a strong function of the process temperatures. We employ a SiD_4/N_2 plasma chemistry to allow for differentiation of the origin of hydrogen found in the InGaAs at various stages.

Experimental

The InGaAs was grown lattice-matched to semi-insulating (100) InP (Fe) substrates by gas-source MBE at 500 °C using triethyl indium, trimethyl gallium and AsH_3 as the source chemicals. The layers were ~0.5 µm thick. CCl_4 was used as the C-doping source-Hull measurements showed a p-type doping level of ~3 × 10^{19} cm^{-3} in the 0.2 µm thick upper layer grown on a 0.3 µm thick undoped buffer.

SiNx films were deposited in a Plasma-Therm SL 770 ECR system using 750W of 2.45 GHz power, a process pressure of 2 mTorr and 50W of no rf power applied to minimize the incident ion energy. Deuterium-substituted silane (SiD_4) was employed so that with isotope-selective SIMS measurements we could identify the origin of hydrogen species found in the InGaAs. The 1000 Å thick SiNx films were removed by CF_4/O_2 barrel etching after annealing for 5 min at temperatures up to 500 °C. Hydrogen depth profiles in the InGaAs were obtained from SIMS measurements using a Cameca system and a Cs^+ ion beam, while the electrical properties were obtained from TLM measurements using TiPtAu non-alloyed contacts.

Results and Discussion

Figure 1 shows SIMS measurements of C, ^{1}H and ^{2}H in the InGaAs for 3 cases. In the as-grown material (a), there is a significant hydrogen concentration whose profile follows that of the carbon, and therefore is assumed to result from formation of ~5 × 10^{18} cm^{-3} C-H neutral complexes by trapping of residual hydrogen from the metalorganics onto substitutional carbon. After deposition of the SiNx, and then removing if immediately afterward. Figure 1(b) shows that deuterium is incorporated into the top 1000 Å of the InGaAs. This clearly originates from the SiD_4/N_2 plasma. If the nitride film is annealed at 500 °C prior to its removal the deuterium is incorporated throughout the InGaAs layer, as shown in Figure 1(c).
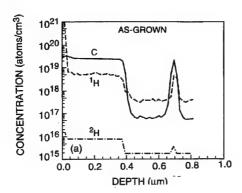
Fig.1. SIMS profiles of C, ^{1}H and ^{2}H in InGaAs, (a) as grown.
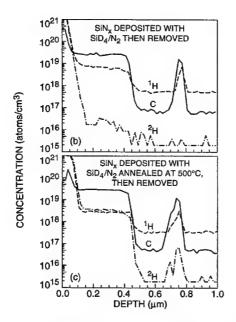
Fig.1. SIMS profiles of C, ^{1}H and ^{2}H in InGaAs, (b) after SiNx deposition
and then removal of the dielectric and (c) after SiNx deposition, annealing at 500 °C
and then removal.

Figure 2 shows the sheet resistance of the InGaAs as-grown, and after deposition with
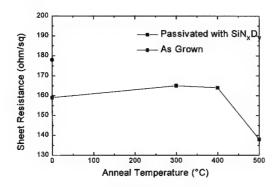SiN_4 and annealing at different temperatures.

Fig. 2. Sheet resistance of InGaAs (c) layer before and after SiNx deposition, as a
function of annealing temperature.

The deposition step actually decreases the sheet resistance, because the number of C acceptors reactivated by the annealing received by the InGaAs during this procedure is greater than the additional number passivated by the deuterium introduced. The reactivation can occur as a result of both the temperature increase, and by minority carrier injection during the initial exposure of the sample to the intense illumination from the ECR plasma [7]. Annealing up to 400 °C does not produce any major change in sheet resistance, but at 500 °C the reactivation of acceptors leads to a further ~10% decrease. This is despite the fact that there is a much higher total $^1H + {}^2H$ concentration under this condition. Above 400 °C reactivation of the acceptors becomes dominant, leaving C acceptors and hydrogen in an inactive form (probably molecules or larger clusters). Similar trends are observed in the contact receptivity, shown in log form in Fig. 3. The changes track those in sheet resistance, and therefore show that the variations result from the reactivating of the carbon dopiness.
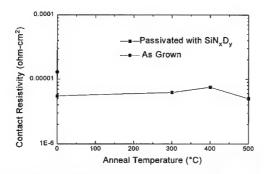
Fig. 3. Contact receptivity of TiPtAu on InGaAs (C) that was either as-grown, or had been deposited with SiNx that was subsequently removed after various annealing steps.

Since the gain of an HBT containing the InGaAs(C) base layer is inversely dependent on the base doping level, then our results show that the apparent gain will be determined by the exact temperature cycles undergone during processing. Importantly, if a significant density of C-H complexes remain in the completed device, one could expect to observe a time-dependent decrease in gain until reactivation of the C acceptors was complete.

ACKNOWLEDGMENTS

REFERENCES

1. See for example, InP HBTs: Growth, Processing and Applications, ed. B. Jalali and S. J. Pearton (Artech House, Norwood, MA 1995).

2. Ren, F., Abernathy, C. R., Chu, S. N. G., Lothian, J. R. and Pearton, S. J., "The Role of hydrogen in current-induced degradation of carbon-doped GaAs/AlGaAs HBTs", Solid State Electron 1995, Vol. 38 pp. 1137-1141.

3. Pearton, S. J., Abernathy, C. R., Lee, J. W., Ren, F. and Wu, C. S. "Comparison of H^+ and He^+ implant isolation of GaAs-based HBTs, J. Vac. Sci. Technol. B 1995, Vol. 13 pp. 15-18.

4. Hanson, A. W., Stockman, S. A. and Stillman, G. E. "InP/InGaAs HBTs with a C-doped based grown by MOCVD", IEEE Electron. Dev. Lett. 1992, Vol. 13, pp. 504-506.

5. Song, J. I., Hong, B. W. P., Palmstrom, C. J., Van\ der Gaag, B. P. and Chough, K. B., "Ultra-high speed InP/InGaAs HBTs", IEEE Electron. Dev. Lett. 1994 Vol. 15, pp. 94-96.

6. Gee, R. C. Chin, T. D., Tu, C. W., Asbeck, P. M., Lin, C. L., Kirchner, P. D. and Woodall, J. M., "InP/InGaAs HBTs grown by gas-source MBE with C-doped base", IEEE Electron Dev. Lett. 1992 Vol. 13 pp. 247-249.

7. Pearton, S. J., Corbett, J. W. and Stavola, M., "Hydrogen in Crystalline Semiconductors", (Springer, Heidelberg 1992).

MOVPE OF INP AND GAAS BASED OPTOELECTRONIC MATERIALS IN A MULTIWAFER PRODUCTION REACTOR USING TBA AND TBP EXCLUSIVELY

D. Schmitz, G. Lengeling, R. Beccard and H. Jürgensen

AIXTRON GmbH, Kackertstrasse 15 - 17, D-52072 Aachen, Germany

ABSTRACT

In this paper a study of the growth of GaAs and InP based materials using the alternative precursors TBAs and TBP is presented. For this purpose mass production multiple wafer reactors were employed. Both long-wavelength materials such as GaInAsP on InP and short wavelegth like GaInP and AlGaInP on GaAs are investigated. The results demonstrate that ther is no loss of material quality when using these novel precursors. In all cases growth temperatures and V/III ratios could be significantly lowered.

INTRODUCTION

After using the standard precursors arsine and phosphine in MOVPE for more than twenty years, there is a strong tendency today within the MOVPE production community to replace these highly toxic compounds by so-called alternative precursors. Among a variety of new precursors that have been developped in the last years, Tertiarybutylarsine (TBAs) and Tertiarybutylphosphine (TBP) have the highest potential to replace the hydrides completely. Many research publications already have demonstrated the suitability of these compounds to grow high quality III-V material. Additionally, devices manufactured from these layers reveal that there is no impact on the device performance when replacing the hydrides by TBP/TBAs. However, for many MOVPE users the decision to switch production completely to TBP and TBAs may still be difficult as long as it is not proven that *all* III-V materials can be grown with TBAs/TBP in the same class of reactors. The aim of this study is to demonstrate that these precursors can replace arsine and phosphine for the growth of all device structures in the Al-Ga-In-As-P system.

EXPERIMENT

In this study we want to show how TBAs and TBP can be used in different types of reactors which are all based on the same principle. The reactors used here are horizontal reactors of different size: AIX 200 for 1x2" wafer, AIX 200/4 for 1x4" or 3x2" and the AIX 2400 for 15x2" growth. All these reactors are operated at low pressure and have an optimized geometry to ensure laminar flow conditions and excellent uniformities of thickness and material composition. AIX 200 and 200/4 are reactors where the gas flows through rectangular-shaped liner tubes. AIX 2400 is a representative of the Planetary Reactor® family where the gas is injected in the middle of a rotating susceptor leading to a radial gas flow with decreasing velocity from the center to the edge. In all growth runs described here the group III precursors were trimethylgallium, trimethylindium and trimethylaluminium. In most cases hydrogen was used as the carrier gas; however, sometimes it was replaced by ultrapure nitrogen.

RESULTS

The materials that have been grown in these machines cover the entire range of III-V alloys in the Al-Ga-In-As-P system. Both InP-based materials like GaInAs and GaInAsP and GaAs based compounds like AlGaAs, GaInP and AlGaInP have beeen grown successfully using TBP and TBAs. Some typical examples of III-V compounds grown with these precursors and the basic growth parameters are listed in table I.

Reactor type	Material	T_{growth}	$p_{Reactor}$	V/III ratio
200	GaAs	650 °C	20-100	20-50
200	InP	610 °C	20-100	25
200/4	GaAs	650 °C	100	15
200/4	InP	610 °C	100	20-40
200/4	GaInAs	610 °C	100	40
200/4	GaInAsP	610 °C	100	40
2400	GaInP	675 °C	50-200	25
2400	AlGaInP	675 °C	50-200	25

Table I: III-V compounds grown with TBP/TBAs in AIXTRON reactors

There are two trends that are valid for all reactor types and all materials:

- For all materials lower growth temperatures can be chosen in comparison with standard processes using hydrides. Using these reduced temperatures, no loss of layer quality was observed.

- V/III ratios can be reduced significantly without any negative impact on the quality.

Both trends can be explained by the low thermal stability of TBP and TBAs compared to PH_3 and AsH_3. The high cracking efficiency leads to an increased effective P and As concentration at the substrate surface.

1. InP-based material

As a typical material to be grown in AIX 200 and AIX 200/4 systems, InP-based compounds shall now be discussed more in detail. As a basis material, InP was grown in these reactors. High quality layers could be obtained at total pressures between 20 and 100 mbar. While the standard growth temperature for the growth of InP with phosphine is 640 to 650 °C, it could be reduced to 610 °C when growing with TBP. At the same time the V/III ratio was lowered to 25 (PH_3: 150-250). The quality of the material grown this way was very good. 77K electron mobilities of more than 50.000 cm^2/Vs and carrier concentrations in the low $10^{14} cm^{-3}$ regime reveal the high purity of TBP-grown InP.

Using the same deposition temperature and the same reactor pressure, now GaInAs and GaInAsP were grown lattice matched to InP. Again a very low V/III ratio of only 40 was adjusted. Since the compositional homogeneity is an important issue in the fabrication of optoelectronic devices, now the uniformity of the TBP/TBAs-grown wafers was checked.

For industrial applications of InP based materials the uniformity of the layers is an important criterium. Today uniformities in thickness and composition in the percent range are necessary

for a reliable production of optoelectronic devices. The influence of using alternative precursors in combination with hydrides has been reported earlier /1/

First of all, the thickness uniformity of a quaternary layer is shown (layer grown in an AIX 200/4 system). Since the substrate was grown on a rotating susceptor, the uniformity pattern has a rotational symmetry. The maximum relative thickness deviation is below ±2% which is similar to conventionally grown material (Fig. 1).
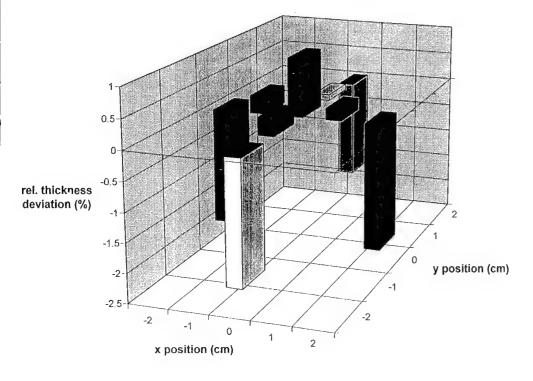

Fig. 1: Thickness uniformity of a 2" GaInAsP wafer

However, the thickness uniformity is not so much affected by the group V precursor since the growth rate is mainly determined by the total group III flux. The layer property which is much more influenced is the emission wavelength of the quaternary layer.

To investigate this, quaternary layers of different compositions were grown (nominal emission wavelength 1.1 and 1.55 μm). Fig. 2 shows the absolute wavelength of a quaternary layer measured by room temperature photoluminescence. The mean wavelength was 1.55 μm and the maximum deviation was ±1.5 nm. The same investigation was made for quaternary material with an emission wavelength of 1.1 μm (Fig. 3). Here a deviation of only ±1 nm was observed.
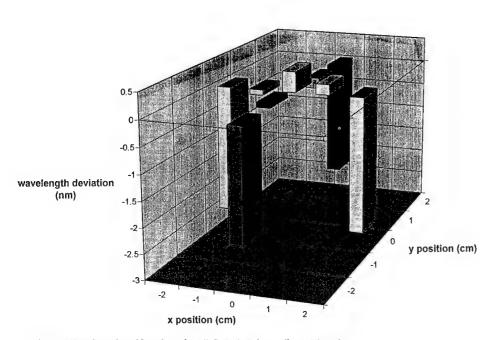
Fig. 2: Wavelength uniformity of a 2" GaInAsP layer (λ=1.55 µm)
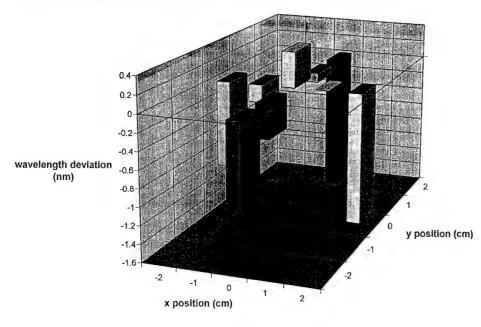
Fig. 3: Wavelength uniformity of a 2" GaInAsP layer (λ=1.1 µm)

The excellent uniformity indicates that TBP and TBAs have a more or less optimum cracking behaviour. The depletion profile along the gas flow direction must be very similar for both compounds. This seems to be much different from arsine and phosphine which have quite different decomposition characteristics.

2. GaAs based compounds

Most of the real mass products in the III-V sector are GaAs based. These are for example solar cells in the GaAs/AlGaAs system. But also the GaInP/AlGaInP system based on GaAs is gaining more and more importance. Devices manufactured from these compounds are for example HBTs or ultra-high-brightness-LEDs. These materials are grown in multiwafer MOVPE reactors. Since these devices are produced in high numbers, the consumption of hydrides (and thus the cost of scrubbing and gas monitoring) is very high. Thus there is a strong interest in replacing arsine and phosphine by TBP and TBAs.

TBP and TBAs have been investigated in AIXTRON Planetary Reactors®. Due to their sophisticated design, these reactors combine a high efficiency and excellent uniformities. The efficiency of the group III precursors is between 30 and 50%. However, due to the high thermal stability of the hydrides still rather high V/III ratios are used in the conventional process. By using TBP and TBAs a higher group V efficiency can be achieved together with reduced safety hazards.

As an example, the growth of GaInP using TBP shall be discussed here. Table II shows the basic growth parameters used in an AIX 2400 reactor with 15x2" capability.

GroupV precursor	PH_3	TBP
Growth temperature	700-750 °C	675 °C
Growth pressure	50-200 mbar	50-200 mbar
V/III ratio	100	25

Table II: Characteristical parameters for TBP- and PH₃-grown GaInP

Again the V/III ratio is much smaller compared to PH_3 grown GaInP. Even a further reduction of the TBP partial pressure may be possible; however, the lower limit was not investigated here. The growth of GaInP with TBP is diffusion controlled down to 625 °C (see Fig. 4). The low thermal stability compared to phosphine allows this reduction of the growth temperature. This is quite remarkable because also the V/III ratio is very low at the same time.
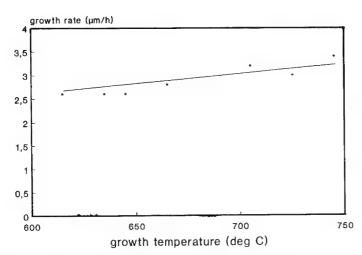
Fig. 4: Growth rate of TBP-grown GaInP vs. growth temperature

The uniformity of TBP-grown GaInP is also very good. The standard deviation of the GaInP emission wavelength was found to be below 1 nm on a 2" wafer grown in a multiwafer Planetary Reactor[®] (Fig. 5).
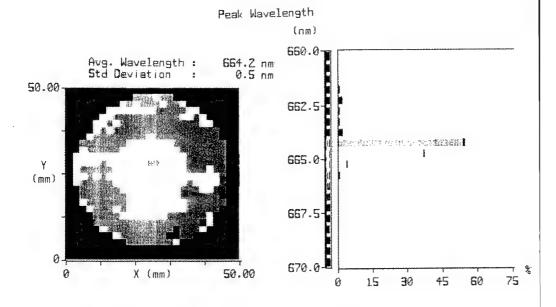

Fig. 5: PL wavelength uniformity of a 2" TBP-grown GaInP wafer

SUMMARY

This study shows that mass production processes for the fabrication of III-V materials can be switched completely to TBP and TBAs. The entire material system Ga-In-As-P can be grown without any loss of quality using TBP and TBAs not only in one reactor, but in a complete family of reactors. These reactors range from small-scale single wafer R&D reactors to multiwafer Planetary Reactor® systems. Both InP based and GaAs based materials could be grown with an excellent quality. Thus all growth processes for III-V devices - long and short wavelength lasers, LEDs, high speed transistors etc. - can be switched to TBP and TBAs. This will drastically reduce safety hazards and lead to processes that have advantages both from the ecological and economical point of view.

MBE GROWTH AND PROPERTIES OF HgCdTe LONG WAVE AND VERY LONG WAVE INFRARED DETECTORS

R. D. Rajavel, O.K. Wu and J.E. Jensen
Hughes Research Laboratories, Malibu, CA 90265

C.A. Cockrum, G.M. Venzor, E.A. Patten, P.M. Goetz, D.B. Leonard,
and S.M. Johnson
Santa Barbara Research Center, Goleta, CA 93117

ABSTRACT

In-situ doped p-on-n devices were grown by molecular beam epitaxy, and their structural, optical and electrical properties were evaluated. Significant progress has been made toward the growth of high performance HgCdTe devices by molecular beam epitaxy. Long wave infrared detectors operating at 9.9 μm at 78K exhibited a mean R_oA_o product of 1170 Ωcm^2 at 0-fov. Very long wave infrared detectors operating at 14 μm at 78K exhibited a mean R_oA product of 3.5 Ωcm^2 at f/2 fov. These values represent the state-of-the-art for molecular beam epitaxially grown HgCdTe detectors.

I. INTRODUCTION

Owing to the band gap tunability and other desirable material properties, HgCdTe alloys have been used for the detection of IR radiation from 1.3 μm to > 18 μm.[1] Liquid phase epitaxy (LPE) has been used for the commercial production of these HgCdTe detectors, and BLIP performance has been measured in these devices.[2] Owing to the flexibility offered by molecular beam epitaxial (MBE) growth, such as low temperature growth (< 200 °C), the capability to rapidly change the alloy composition, and the ability to tailor doping profiles in complex device structures, MBE has emerged as a promising technology for the growth of HgCdTe devices.[3,4] In this paper we report on the structural, optical and electrical properties of high-performance MBE-grown detectors that operate in the long wave infrared (LWIR) (8-12 μm) band, and the very long wave infrared (VLWIR) (> 14 μm) band.

II. EXPERIMENTAL PROCEDURE

Epitaxial growth of HgCdTe films by MBE was performed in a VG Semicon V-80 system, by using CdTe and elemental Te and Hg as the source materials.[5] The films were grown at a substrate temperature of ≈185 °C onto (211)B oriented $Cd_{0.96}Zn_{0.04}Te$ substrates at growth rates that ranged from 1.8-2 μm/hr. As is customary in the growth of narrow gap HgCdTe alloys, an overpressure of Hg was employed during growth.[5] The excess Hg re-evaporates from the surface, and the amount of Hg that is incorporated in the $Hg_{1-x}Cd_xTe$ film is determined by the magnitude of the incident tellurium flux. Hence the alloy composition (the Hg to Cd ratio) is dictated by the Te/Cd flux ratio, which is determined by the temperatures of the CdTe and Te effusion cells. For this study the beam equivalent pressures of Hg, CdTe, Te were $3-4\times10^{-4}$, 1.5×10^{-6} and 2.5×10^{-6} mBar, respectively. In this study the target composition of the base layer of the LWIR diode was x= 0.225 for operation at 10 μm at 78K, and that of the VLWIR diodes (x=0.204) was appropriate for the detection of 14 μm radiation at 78K. In and As were the donor and acceptor impurities, respectively. The compositions of the $Hg_{1-x}Cd_xTe$ films were

determined from infrared transmission measurements, using the empirical expression provided by Hansen, Schmit and Casselman.[6]

The p-on-n detector structures were grown by depositing ≈ 2 μm thick HgCdTe:As (cap) layer onto 6-8 μm thick HgCdTe:In (base) layers. The alloy composition of the As-doped p-type layer was a wider band gap material with x = 0.28 and 0.26 for the LWIR and VLWIR detector structures, respectively. The structural properties of the films were evaluated by x-ray rocking curve measurements, and a typical x-ray scan of a LWIR p-on-n structure is shown in Fig. 1. The peak occurring at the higher diffraction angle arises from the n-type base layer, while the other peak arises from the thin p-type cap layer. The x-ray rocking curve full width at half the diffracted intensity maximum (FWHM) of the base layer is typically < 40 arcsec., and that of the thinner cap layer is between 30-45 arcsec.

To determine the dislocation density in the base layer, the cap layer was first removed by a chemical etch. For LWIR layers grown on lattice matched substrates, the typical etch pit density is $\approx 5 \times 10^5$ cm^{-2}, and the values for the specific devices reported here are listed in Table 1. The etch pit density measured in the base layer was strongly dependent on the growth conditions, specifically the substrate temperature and the Hg/Te flux ratio employed for the growth of these layers. The 2 μm thick cap layers are not sufficiently thick to perform EPD measurements, however measurements performed on 6 μm thick cap layers exhibit etch pit densities in the $1-5 \times 10^6$ cm^{-2} range.
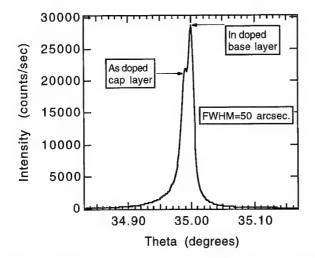
Fig. 1. X-ray rocking cure scan of a p-on-n LWIR device. The narrow rocking curves of the base and the cap layers attest to the high degree of the structural perfection.

The concentration of the As acceptor and In donor impurities were determined by secondary ion mass spectrometry (SIMS) measurements. The electrical activity of the acceptors at a concentration of 1×10^{18} cm^{-3} is estimated to be $\approx 60\%$, and that of the In

donors doped at $1-3 \times 10^{15}$ cm^{-3} is nearly 100%, based on Hall effect measurements, as reported previously.[7]

III. RESULTS AND DISCUSSIONS

LWIR Detectors

The p-on-n device structures were fabricated as mesa diodes. A test structure assembly with various detector structures including mini-arrays diodes were fabricated with the LWIR devices. The diode dimensions in the mini array were 28 μm x 38 μm. The test structure diodes were hybridized to a fan-out and tested in a dewar to evaluate the electrical and optical properties. Fig. 2 illustrates the spectral response of a typical diode with a steep cutoff at 9.91 μm. The mean $R_o A_o$ product of the diodes in the mini array was = 1170 Ωcm^2 at 0-fov and 389 Ωcm^2 at f/2 fov at 78K for wafer 1783. (Here $R_o^{-1} = (dI/dV)_{v=0}$, A_o is the optical area of the diode determined from spot scan measurements and A is the diode junction area. For these diodes the ratio A_o/A was 1.3) Similar results were also obtained for wafer 1784 that exhibited a cutoff of 9.88 μm at 78K. The results of these devices along with the material properties are listed in Table 1. The $R_o A$ values reported here are on par with the best grown by LPE, [2] and represent the state-of-the-art for MBE devices.[7]
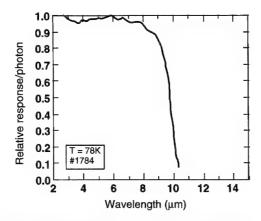
Fig. 2. Spectral response of a typical LWIR diode at 78K.

Table. 1. Properties of the MBE-grown LWIR diodes.

Wafer #	[In] in base layer (cm^{-3})	[As] in cap layer (cm^{-3})	EPD in base layer (cm^{-2})	$R_o A_o$ at 0-fov (Ωcm^2) at 78K	$R_o A_o$ at f/2 fov (Ωcm^2) at 78K	Cut-off at 78K (μm)
1783	2E+15	3E+18	1.4E+06	1170	389	9.91
1784	3E+15	3E+18	1.3E+06	605	505	9.88

VLWIR Detectors

The p-on-n VLWIR (λ_{co} = 14 μm at 78K) structures were also fabricated as mesa diodes and a 5x5 mini array of 50 μm x 50 μm diodes was hybridized to a fan-out and tested in a dewar. The detector cutoff of these diodes was 14 μm at 78K. The diodes exhibit a high degree of uniformity, and the distribution of the R_0A values (where A is the diode junction area) of the individual diodes is shown in Fig. 3. The mean R_0A at 78 K was 3.5 Ωcm^2 at f/2 fov and the standard deviation was 0.4 Ωcm^2.
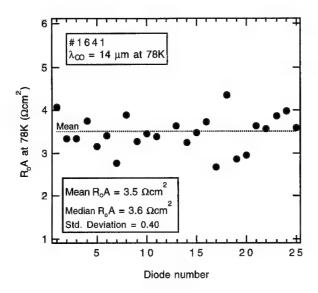
Fig. 3. Plot of the distribution of R_0A values in a 5x5 mini array of VLWIR diodes shows the high degree of performance uniformity in the mini array.

Fig. 4 shows the I-V characteristics of representative diodes from wafer 1641-A. These values are comparable to that reported in LPE-grown VLWIR diodes.[9] Previously, detector results for HgZnTe VLWIR diodes were reported by Patten et al.[10], however as detectivity measurements were not performed for the devices reported here, it is not possible to make a direct comparison between the two. Although 40 K spectral response measurements were not performed, the spectral response cutoff of these diodes is expected to be > 16 μm at 40K based on the temperature dependence of detector cutoff provided in Ref. 6.
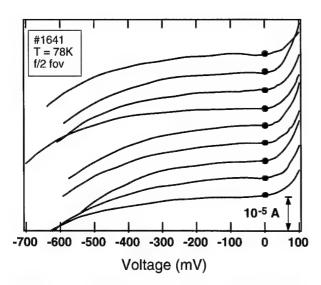
Fig. 4. I-V characteristics of representative VLWIR diodes measured at f/2 fov at 78K.

IV. CONCLUSION

In-situ doped p-on-n LWIR and VLWIR HgCdTe detectors structures were grown by MBE. X-ray rocking curve measurements showed that base and the cap layers exhibited a high degree of structural perfection with FWHM typically < 40 arcsec. Mini arrays of mesa diodes were fabricated and tested by hybridizing the detectors to a fan-out. Long wave infrared detectors operating at 9.9 μm at 78K exhibited a mean R_oA_o product of 1170 Ωcm^2 at 0-fov. Very long wave infrared detectors operating at 14 μm at 78K exhibited a mean R_oA product of 3.5 Ωcm^2 at f/2 fov. These values represent the state-of-the-art for molecular beam epitaxially grown HgCdTe detectors.

V. REFERENCES

1. D.A. Scribner, M.R. Kruer, and J.M. Killiany, Proc. IEEE, 79, 66 (1991).

2. T. Tung, L.V. DeArmond, R.F. Herald, P.E. Herning, M.H. Kalisher, D.A. Olson, R.F. Risser and S.J. Tighe, SPIE 1735, 109 (1992).

3. O.K. Wu, D.M. Jamba, G.S. Kamath, G.R. Chapman, S.M. Johnson, J.M. Peterson, K. Kosai, and C.A. Cockrum, J. Electron. Materials, 24, 423 (1995).

4. J.M. Arias, J.G. Pasko, M. Zandian, L.J. Kozlowski, R.E. DeWames, Opt. Engineering, 33, 1422 (1994).

5. O.K. Wu, D.N. Jamba, and G.S. Kamath, J. Crystal Growth, 127, 365 (1993).

6. G.L. Hansen, J.L. Schmit, and Y.N. Casselman, J. Appl. Phys. 53, 7099 (1982).

7. R. D. Rajavel, D.M. Jamba, O.K. Wu, J.A. Roth, P.D. Brewer, J.E. Jensen, C.A. Cockrum, G.M. Venzor, and S.M. Johnson, to be published in J. Electron. Materials

8. G.N. Pultz, P.W. Norton, E.E. Kruger and M.B. Reine, J. Vac. Sci. Technol. B9, 1724 (1991).

9. E.A. Patten, M.H. Kalisher, G.R. Chapman, J.M. Fulton, C.Y. Huang, P.R. Norton, M. Ray, and S. Sen, B9, 1746 (1991).

POLARIZATION CONTROL OF VERTICAL-CAVITY SURFACE-EMITTING LASERS BY TILTED-ETCHING OF CAVITY

HYE YONG CHU, BYUENG-SU YOO, MIN SOO PARK*, AND HYO-HOON PARK
Electronics and Telecommunications Research Institute, Yusong P.O. Box 106, Taejon 305-600, Korea, hychu@idea.etri.re.kr

ABSTRACT

We performed a polarization control method for vertical-cavity surface-emitting lasers by tilted-etching of the air-post. Circular laser posts were etched by tilting the substrate toward [110] or [1$\bar{1}$0] direction with an angle of $15^{\circ} \sim 20^{\circ}$ using reactive ion beam etching. For the laser devices with a diameter of $7 \sim 10$ μm, we observed outstanding selectivity of the polarization state. We found a dominant polarization perpendicular to the tilted direction. The maximum orthogonal polarization suppression ratio was about 25 dB. The selectivity of polarization in the tilted laser post devices is interpreted to be originated from the difference of optical losses of the two waves polarized to the [110] and [1$\bar{1}$0] directions.

INTRODUCTION

Vertical-cavity surface-emitting lasers (VCSELs) are considered promising light sources for applications in optical parallel processing, optical communications and optical interconnections. [1] The control of polarization for VCSELs is the most critical issue for polarization sensitive optical systems. In conventional VCSEL structure, the degenerate orthogonal polarization states with fundamental mode are observed at and above the threshold. In the absence of much stronger polarization selectivity, unstable polarization switching occurs and may result in an excess intensity noise by mode hopping. In the future optical interconnects, and so on, very low bit error rates are required. Thus, a stable polarization operation over wide current range is needed for low noise applications. Several attempts have been made to control the polarization of VCSELs. [2-6] A birefringent metal/dielectric polarizer on the top distributed Bragger reflector (DBR) [2] and the anisotropic gain medium of fractional-layer superlattice structure [3] were introduced. In particular, Choquette *et al* .[4] proposed anisotropic transverse cavity geometries for polarization control of VCSELs. They reported that an anisotropic transverse cavity like rhombus- or dumbbell-shaped has removed the two-fold polarization degeneracy and selected the dominant state of the polarization.

In this work, we propose a simple method for polarization control by tilted-etching of laser post for index-guided structure. This method can select a single dominant polarization state

---

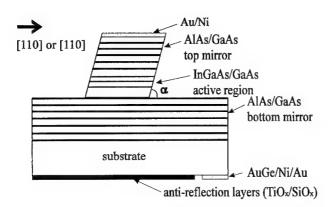*Visiting from the Department of Materials Science and Engineering, Korea Advances Institute of Science and Technology

Figure 1. Schematic diagram of a tilted-post VCSEL

with a perpendicular electric field to the tilted direction of the etched cavity.

EXPERIMENT

For this work, we used a periodic gain InGaAs/GaAs structure with a two-wavelength-thick cavity. The epitaxial structure was grown by metalorganic chemical vapor deposition. The top and bottom DBR mirrors consist of, respectively, 16 and 23.5 periods of AlAs/GaAs quarter
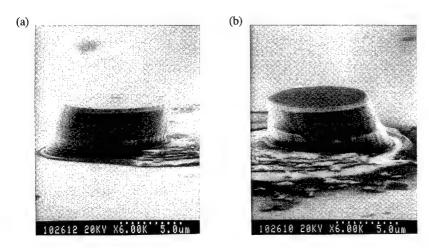

Figure 2. Scanning electron micrographs of VCSELs tilted toward (a) [110] and (b) [1$\bar{1}$0] direction with an angle of 20°.

wave stacks with $Al_{0.33}Ga_{0.67}As$ grading layers. The detailed laser structure was described in previous reports [7,8]. Tilted laser posts were formed using reactive ion beam etching (RIBE) with chlorine, by tilting the substrate toward [110] or [1$\bar{1}$0] direction with an angle of $15^{\circ} \sim 20^{\circ}$ against the ion-beam direction. The laser posts were etched through the active region, as shown in Fig. 1. Au (300 nm)/Ni (160 nm) was used as p-type contact and mask layers for RIBE. The back side of the as-grown epitaxial wafer was first polished and antireflection (AR) layers of TiO_x/SiO_x were deposited at 350 °C. For n-type contact on back side of the substrate, the AR layers on the edge of the sample were removed by reactive ion etching using CF_4 and He gases and then AuGe/Ni/Au layers were deposited. The n-type metal layers were alloyed by rapid thermal annealing. Figures 2(a) and 2(b) show scanning electron micrographs of VCSELs etched by tilting toward [110] and [1$\bar{1}$0] direction with an angle of 20°, respectively. The micrographs illustrate clearly the tilting of the laser posts, but the tilting angle of the posts is some smaller than the etching angle. Two orthogonal polarization characteristics of VCSELs were simultaneously measured using a polarized beam splitter. The emission spectra were measured using a monochromater with a resolution of 0.01 nm. The device characteristics were measured at room temperature without a heat sink.

RESULTS AND DISCUSSION

Figure 3 shows the light output power against current (L-I) characteristics measured under continuous wave (CW) operation for 10-μm-diameter devices with a tilted angle of 15°. The solid and dotted lines represent the devices with a cavity tilted toward [110] and [1$\bar{1}$0] direction, respectively. The polarization directions indicated by $\perp$ and $//$ represent perpendicular and parallel electric fields to the tilted direction of laser posts, respectively. We found that the light polarized perpendicularly to the tilted direction is dominant. This tendency was confirmed in the whole range of injection current and for almost all test devices with diameter of 7 and 10 μm. For the devices with a diameter of 10 μm, the orthogonal polarization
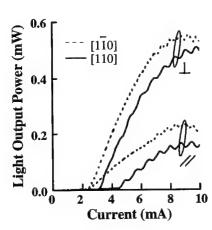
Figure 3. L-I characteristics for 10-μm-diameter VCSEL devices with a tilted angle of 15° toward [110] and [1$\bar{1}$0] directions.
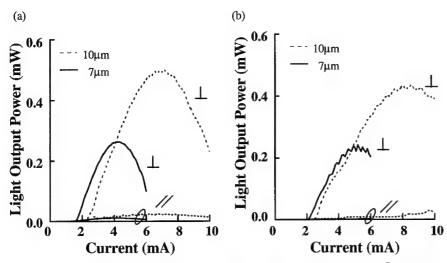
Figure 4.   L-I characteristics for tilted-post VCSELs toward (a) [110] and (b) [1$\bar{1}$0] directions
with an angle 20° for 7- μm- and 10-μm- diameter devices.

suppression ratio was around 4.5 ~ 15 dB. As the diameter of devices increased more than 15 μm, the polarization selectivity was reduced. The switching of polarization with bias current was observed for large devices with diameter ≥ 15 μm, indicating that the polarization selectivity of the tilted geometry is effective for smaller devices. The circularity of output beam was maintained although the cavity and waveguiding region were inclined.

The polarization characteristics are improved as the tilting angle increases. Figures 4(a) and 4(b) show the CW L-I characteristics of VCSELs with an angle of 20 ° tilted toward [110] and [1$\bar{1}$0] direction, respectively. The solid and dotted lines represent the devices with the diameter of 7 and 10 μm, respectively. The polarization characteristics were significantly improved compared those of 15 ° tilted devices and the orthogonal polarization suppression ratio was around 10 ~ 20 dB. As the diameter of the devices was decreased, the suppression ratio was generally enhanced. Most devices tilted toward [1$\bar{1}$0] direction showed stable polarization characteristics. However, a few devices tilted toward [110] direction showed an opposite polarization with a parallel electric field to the tilted direction or a switching characteristics between the two polarization directions. In conventional InGaAs VCSELs, a single dominant polarization to a specific <110> direction was usually observed. [4, 9]

In VCSELs with a vertically etched cavity, the linear transverse-electric polarization is randomly oriented in the plane of the active region [10] and the polarization direction can change with increasing the injection current. [9] For the lasers tilted toward [110] or [1$\bar{1}$0] direction, we expect that the reflection and/or deflection characteristics in the vertical resonance of the two polarized waves will appear differently depending on the direction due to the tilting of waveguiding surface. Thus, the tilted laser post can induce a difference in optical losses between the two directions.

Figures 5(a) and 5(b)   show the emission spectra of   VCSELs tilted toward   [110] and

344
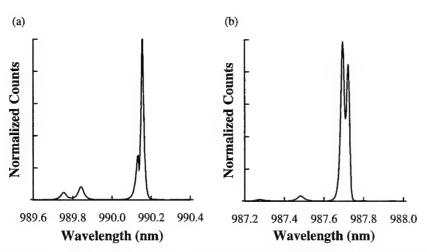
Figure 5   Emission spectra of VCSELs tilted toward (a) [110] and (b) [1̄10] directions with an
angle of 20° and a diameter of 10 μm.

[1̄10] directions with an angle of   20°   and a diameter of 10 μm, respectively. The spectra were
obtained under a current of the 1.1 times threshold current. The emission spectra were composed
of two peaks, corresponding to two degenerated orthogonal polarizations of the fundamental
mode. For the device tilted toward [110] direction, the dominant emission peak emerged at a
wavelength 0.025 nm longer than the weaker emission of the orthogonal state. However, for the
devices tilted toward [1̄10] direction, the dominant polarization state appeared at a wavelength
0.03 nm shorter than the orthogonal state. In our index-guided structure, we expect that a higher
optical loss should be induced in parallel surface of the tilted direction. Thus, the dominant
polarization state seen in Figs. 5(a) and 5(b) might appear along the directions with lower optical
loss. On the other hand, Fig. 5 shows that higher order transverse modes begin to lase
simultaneously, which are blue shifted about 0.3 and 0.2 nm from the dominant peak of
fundamental mode for [110] or [1̄10] direction, respectively. These behaviors can be explained
in terms of an amplified spontaneous emission.

CONCLUSION

We have proposed a simple polarization control method of VCSELs by tilted-etching of
the laser post toward [110] or [1̄10] direction. We found a dominant polarization with
perpendicular electric field to the tilted direction. For the laser devices with a diameter of 7~10
μm and a tilted angle of 15° ~ 20°, we observed outstanding selectivity of the polarization state.
Within this range of tilted angle, the polarization characteristics were improved as the tilting
angle is increased and device size decreased. The selectivity of polarization in the tilted-post
VCSELs can be attributed to the difference of optical losses of the two waves polarized to the
[110] and [1̄10] directions in the tilted cavity.

345

ACKNOWLEDGMENTS

REFERENCES

1. Y. H. Lee, J. L. Jewell, A. Scherer, S. L. McCall, J. P. Harbison and L. T. Florze, Electron. Lett. **25**, p.1377 (1989).
2. T. Mukaihara, N. Ohnoki, Y. Hayashi, N. Hatori, F. Koyama and K. Iga, IEEE J. Selected Topics in Quantum Electron. **1**, p.667 (1995).
3. A. Chavez-Pirson, H. Ando, H. Saito and H. Kanbe, Appl. Phys. Lett. **62**, p.3082 (1993).
4. K. D. Choquette and R. E. Leibenguth, IEEE Photon. Technol. Lett. **6**, p.40 (1994).
5. S. Jiang, Z. Pan, M. Degenais, R. A. Morgan and K. Kojima, Appl. Phys. Lett. **63**, p.3545 (1993).
6. J.-H. Ser, Y.-G. Ju, J.-H. Sin and Y. H. Lee, Appl. Phys. Lett. **66**, p.2769 (1995).
7. B.-S. Yoo, H.-H. Park, and E.-H. Lee, Electron Lett. **30**, p.1060 (1994).
8. H.-H. Park and B.-S. Yoo, ETRI J. **17**, p.1 (1995).
9. C. J. Chang-Hasnain, J. P. Harbison, G. Hasnain, A. C. Von Lehmen, L. T. Florez and N. G. Stoffel, IEEE J. Quantum Electron. **27**, p.1402 (1991).
10. C. J. Chang-Hasnain, J. P. Harbison, L. T. Florez and N. G. Stoffel, Electron. Lett. **27**, p.1067 (1991)

PROPERTIES OF H, O AND C IN GaN

S. J. Pearton[1], C. R. Abernathy[1], J. W. Lee[1], C. B. Vartuli[1], J. D. MacKenzie[1],
F. Ren[2], R. G. Wilson[3], J. M. Zavada[4], R. J. Shul[5] and J. C. Zolper[5]

[1]University of Florida, Gainesville FL 32611
[2]AT&T Bell Laboratories, Murray Hill NJ 07974
[3]Hughes Research Laboratories, Malibu CA 90265
[4]US Army Research Laboratory, RTP NC 27709
[5]Sandia National Laboratories, Albuquerque NM 87185

ABSTRACT

The electrical properties of the light ion impurities H, O and C in GaN have been examined in both as-grown and implanted material. H is found to efficiently passivate acceptors such as Mg, Ca and C. Reactivation occurs at $\geq 450°C$ and is enhanced by minority carrier injection. The hydrogen does not leave the GaN crystal until $>800°C$, and its diffusivity is relatively high ($\sim 10^{-11} cm^2/s$) even at low temperatures ($<200°C$) during injection by wet etching, boiling in water or plasma exposure. Oxygen shows a low donor activation efficiency when implanted into GaN, with an ionization level of 30 - 40 meV. It is essentially immobile up to $1100°C$. Carbon can produce low p-type levels ($3 \times 10^{17} cm^{-3}$) in GaN during MOMBE, although there is some evidence it may also create n-type conduction in other nitrides.

INTRODUCTION

H, O and C are the most common residual impurities in III-V semiconductors. Hydrogen can form neutral dopant-hydrogen complexes and dramatically reduce carrier levels. Oxygen introduces a deep acceptor level in GaAs and in particular AlGaAs, while carbon is an efficient shallow acceptor in some materials and a donor in others.

In both Si and GaAs[1-4], injection of minority carriers either by forward biasing of a diode structure or illumination with above-bandgap light produces dissociation of neutral acceptor-hydrogen or donor-hydrogen complexes at temperatures at which they are normally thermally stable. While the details of the reactivation process are not clearly established, it is expected that for an acceptor A the reactions likely can be described by

$$(AH)° \leftrightarrow A^- + H^+ \qquad (1)$$
$$H^+ + e^- \leftrightarrow H° \qquad (2)$$

The neutral hydrogen most likely forms diatomic or larger clusters with other neutral or charged hydrogen species.[4]

RESULTS AND DISCUSSION

1. Hydrogen

There has recently been a lot of interest in the stability of hydrogen passivated Mg acceptors in GaN. Amano et al.[5] first demonstrated p-type conductivity in GaN (Mg) after an e-

beam irradiation process near room temperature and later Nakamura et al.[6] showed that simple thermal annealing at ~700°C also reactivated the Mg acceptors. It is clear that atomic hydrogen remaining in the GaN after growth by metal organic chemical vapor deposition (MOCVD) with NH_3 and $(CH_3)_3Ga$ precursors attaches to the Mg, forming neutral complexes. Currently all Mg-doped GaN grown by MOCVD is annealed under N_2 for 20–60mins at ~700°C to achieve the full level of p-type conductivity.[6] The mechanism for acceptor activation during the e-beam irradiation process has not been studied in detail to date. To establish that minority carrier enhanced debonding of Mg-H complexes in GaN is responsible for this phenomenon, we examined the effect of forward biasing in hydrogenated p-n junctions. We find that the reactivation of passivated acceptors obeys second order kinetics and that the dissociation of the Mg-H complex is greatly enhanced under minority carrier injection conditions.

The sample were grown an c-Al_2O_3 by MOCVD using a rotating disk reactor. After chemical cleaning of the substrate in both acids (H_2SO_4) and solvents (methanol, acetone), it was baked at 1100°C under H_2. A thin (≤300Å) GaN buffer was grown at 510°C, before growth of ~1µm undoped material, 0.5µm of GaN(Mg) with a carrier density of p~$1.5x10^{17}cm^{-3}$ after 700°C annealing and 0.3µm of GaN (Si) with a carrier density of $5x10^{18}cm^{-3}$. Some of the samples were hydrogenated by annealing under NH_3 for 30 mins at 500°C. This produces passivation of the Mg acceptors but has little effect on the Si donors.

Mesa p-n junction diodes were processed by patterning 500µm diameter TiAl ohmic contacts on the n-GaN by lift-off and then performing a self-aligned dry etch with an Electron Cyclotron Resonance BCl_3/Ar plasma to exposure the p-type GaN. E-beam evaporated NiAu was patterned by lift-off to make ohmic contact to the p-type material. The carrier profiles in the p-type layer were obtained from 10kHz capacitance-voltage measurements at room temperature. Anneals were carried out in the dark at 175°C under two different types of condition. In the first, the diode was in the open-circuit configuration, while in the second the junction was forward biased at 9mA to inject electrons into the p-type GaN. After each of these treatments the samples were returned to 300K for re-measurement of the net electrically active acceptor profile in this layer.

Figure 1 shows a series of acceptor concentration profiles measured on the same p-n junction sample, after annealing at 175°C under forward bias conditions. After the NH_3 hydrogenation treatment the electrically active acceptor density decreased from $1.5x10^{17}cm^{-3}$ to ~$6-7x10^{16}cm^{-3}$. If the subsequent annealing was carried in the open-circuit configuration there was no change in the carrier profile for periods up to 20hr at 175°C. By sharp contrast Figure 1 shows that for increasing annealing times under minority carrier injection conditions there is a progressive reactivation of the Mg acceptors with a corresponding increase in the hole concentration. After 1hr, the majority of these acceptors have been reactivated. Clearly therefore, the injection of electrons has a dramatic influence on the stability of the MgH complexes. The Mg reactivation has a strong dependence on depth into the p-type layer, which may result from the diffusion distance of the injected electrons prior to recombination. We rule out heating of the sample during forward biasing as being a factor in the enhanced dissociation of the neutral dopant-hydrogen complexes. The samples were thermally bonded to the stainless steel stage and the junction temperature rise is expected to be minimal (≤10°C). Moreover from separate experiments we found that reactivation of the Mg did not begin until temperatures above ~450°C under zero-bias conditions.

The reactivation kinetics were found to follow second-order kinetics, according to [3]:

$$d[N_A-N(t)]/dt = C[N_A-N(t)]^2 \qquad (3)$$

where N_A is the uniform Mg acceptor concentration in the non-hydrogenated sample, $N(t)$ is the acceptor concentration in the hydrogenated GaN after forward bias annealing for time t and C is a second order annealing parameter. C was found to be $4 \times 10^{-20} cm^3/s$
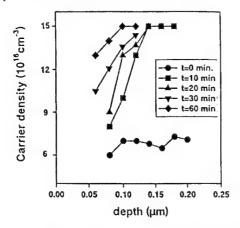

Figure 1. Carrier concentration profiles in hydrogenated GaN (Mg), after annealing for various times at 175°C under forward bias conditions.

The fact that the MgH complexes are unstable against minority carrier injection has implications for several GaN-based devices. Firstly, in a laser structure the high level of carrier injection would rapidly dissociate any remaining Mg-H complexes and thus would be forgiving of incomplete removal of hydrogen during the post-growth annealing treatment. In a heterojunction bipolar transistor the lower level of injected minority carriers would also reactivate passivated Mg in the base layer, leading to an apparent time-dependent decrease in gain as the device was operated.

We also investigated the susceptibility to hydrogen passivation of Ca acceptors in GaN. The Ca was implanted at a dose of $\sim 5 \times 10^{14} cm^{-2}$, and activated by annealing at 1100°C. The ionization level was found to be $\sim 169 meV$ from transport measurements. Samples were hydrogenated for 30 min at 250°C.

The initial H_2 plasma exposure caused a reduction in sheet hole density of approximately an order of magnitude, as shown in Figure 2. No change in electrical properties were observed in the He-plasma treated samples, showing that pure ion bombardment effects are insignificant and the chemical interaction of hydrogen with the Ca acceptors is responsible for the conductivity changes. Post-hydrogenation annealing had no effect on the hole density up to 300°C, while the initial carrier concentration was essentially fully restored at 500°C. Assuming the passivation mechanism is formation of neutral Ca-H complexes, then the hole mobility should increase upon hydrogenation. This was indeed the case. If the carrier reduction were due to introduction of compensating defects or impurities, then the hole mobility would decrease, which was not observed.

If the dissociation of the Ca-H species is a first-order process then the reactivation energy from the data in Figure 2 is $\sim 2.2 eV$ assuming a typical attempt frequency of $10^{14} s^{-1}$ for bond breaking processes. This is similar to the thermal stability of Mg-H complexes in GaN which we prepared in the same manner (implantation) with similar doping levels. In thicker, more heavily doped samples, the apparent thermal stability of hydrogen passivation is much higher because of

the increased probability of retrapping of hydrogen at other acceptor sites. This is why for thick, heavily doped ($p>10^{18}$cm^{-3}) GaN(Mg), a post-growth anneal of at least 700°C for 60min is employed to ensure complete dehydrogenation of the Mg. True reactivation energies can only be determined in reverse-biased diode samples where the strong electric fields present sweep the charged hydrogen out of the depletion region and minimize retrapping at the acceptors.
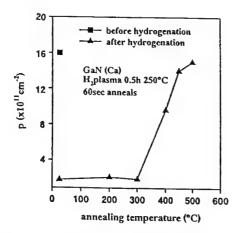

Figure 2. Sheet hole density at 300K in hydrogenated GaN(Ca) as a function of subsequent annealing temperature.

2. Oxygen

Oxygen is often assumed to be responsible for the background n-type doping in thin film GaN, although in bulk GaN it is more likely that nitrogen vacancies are responsible.[8]

Figure 3 is an Arrenhius plot of the resistance/temperature product of O-implanted GaN annealed at 1050°C along with data for an unimplanted and annealed (1100°C) GaN sample. For n-type conduction, an Arrhenius plot of the resistance/temperature product is thought to be more appropriate to account for the potential presence of two band conduction in GaN. O is seen to have an ionization level of 28.7meV. Using this value, the activation efficiency can be estimated to be only 3.6% for O ($n_S=5.9\times10^{12}$cm^{-2}) assuming $n_S\propto n_0\exp(E_a/kT)$. The low activation of O may be the result of the lighter O-ion not creating sufficient lattice damage, and therefore N-vacancies, for the O to occupy a substitutional N-site. This situation may be improved in the future by using a co-implantation scheme.[9] The low apparent O activation may also be explained by the existence of a second deep level for O in GaN that is associated with an oxygen complex. If this were the case, the electrons in the deep level would remain unionized at room temperature and not contribute to the measured electron density. Note that the unimplanted and annealed material has an activation energy for conduction of 335eV. The diffusivity of O in GaN was estimated to be $<2.7\times10^{-13}$cm^2/sec at 1125°C from SIMS measurements.
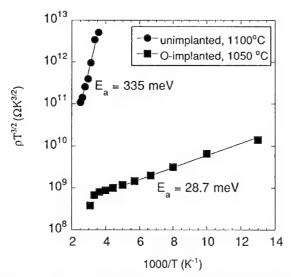
Figure 3. Arrhenius plot of resistance-temperature product for unimplanted GaN annealed at 1100°C and O-implanted GaN annealed at 1050°C.

3. Carbon

We have reported light ($p=3\times10^{17}cm^{-3}$) p-type doping of GaN with CCl_4 doping during MOMBE growth.[10] We have also observed that $In_XGa_{1-X}N$ and $In_XAl_{1-X}N$ films are invariably strongly n-type.[11] One reason could be nitrogen vacancies. Another possible explanation for the electrical behavior is the presence of unintentionally incorporated carbon. Though carbon has been shown capable of producing p-type GaN, the hole concentrations obtained have been limited to low ~$10^{17}cm^{-3}$ even though carbon levels are measured to be $10^{20}cm^{-3}$ or higher. It has been found in other III-V materials that the maximum hole concentration which can be obtained using carbon is related to the difference in bond strength between the group III-carbon case and group V-carbon sites. In the case of InP, the carbon actually sits on the group III site and acts as a donor resulting in n-type material. Based on this simple model, it is expected that carbon will be a donor in InN and high In concentration alloys (see Figure 4).[12] Thus at least some of the conduction observed in these ternary films may be due to carbon. Further, as the composition is reduced in In, the tendency for carbon to act as an acceptor rather than a donor increases, thus possibly explaining the reduction in electron concentration observed with increasing Ga or Al concentration. Clearly more work is needed in this area in order for the role of carbon to be fully understood.

We also implanted C into GaN and annealed at temperatures up to 1100°C, but did not obtain p-type conductivity. Based on the results to date we find that C probably displays amphoteric behavior in the nitrides, with acceptor formation under some conditions (MOMBE-grown GaN) and possible donor action in other cases (implantation in GaN; growth of In-containing alloys).
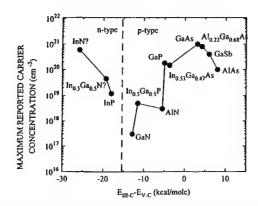
Figure 4. Maximum reported carrier concentrations for materials with various group III-carbon and group V-carbon bond strengths as a function of the difference between the two bonds.

CONCLUSIONS

In summary, we have shown that hydrogen passivated Mg acceptors in GaN may be reactivated at 175°C by annealing under minority carrier injection conditions. The reactivation follows a second order kinetics process in which the (MgH)° complexes are stable to $\geq$450°C in thin, highly-doped GaN layers. In thicker, more heavily doped layers where retrapping of hydrogen at the Mg acceptors is more prevalent, the apparent thermal stability of the passivation is higher and annealing temperatures up to 700°C may be required to achieve full activation of the Mg. Our results suggest the mechanism for Mg activation in e-beam irradiated GaN is minority-carrier enhanced debonding of the hydrogen. Hydrogen passivation of acceptors in GaN occurs for several different dopant impurities and that post-growth annealing will also be required to achieve full electrical activity in Ca-doped material prepared by gas-phase deposition techniques. The thermal stability of the passivation is similar for Ca-H and Mg-H complexes, with apparent reactivation energies of ~2.2eV in lightly-doped ($\sim 10^{17} \text{cm}^{-3}$) material. O behaves as an inefficient shallow donor when implanted in GaN, whereas C may play a significant role in the conductivity of ternary alloys.

ACKNOWLEDGMENTS

REFERENCES

1. I. Szafranek and G. E. Stillman, J. Appl. Phys. **68** 3554 (1990).

2. A. J. Tavendale, S. J. Pearton, A. A. Williams and D. Alexiev. Appl. Phys. Lett. **56** 1457 (1990).

3. A. W. R. Leitch, Th. Prescha and J. Weber, Phys. Rev. B. **44** 5912 (1991).

4. S. J. Pearton, J. W. Corbett and M. Stavola, Hydrogen in Crystalline Semiconductors (Springer-Verlag, Heidenberg 1992).

5. H. Amano, M. Kito, K. Hiramatsu and I. Akasaki, Jap. J. Appl. Phys. **28** l112 (1989).

6. S. Nakamura, N. Iwasa, M. Senoh and T. Mukai, Jap. J. Appl. Phys. **31** 1258 (1992).

7. M. Stavola, Mat. Sci. For. **148/149** 251 (1994).

8. S. K. Estreicher, Proc. Symp. Wide Bandgap Semiconductors and Devices, ed. F. Ren (Electrochem. Soc., Pennington NJ) Vol. **95-21** 78 (1995).

9. J. C. Zolper, R. G. Wilson, R. A. Stall and S. J. Pearton, Appl. Phys. Lett. (in press).

10. C. R. Abernathy, J. D. MacKenzie, S. J. Pearton and W. S. Hobson, Appl. Phys. Lett. **66** 1969 (1995).

11. C. R. Abernathy, J. D. MacKenzie, S. A. Bharatan, K. S. Jones and S. J. Pearton, Appl. Phys. Lett. **66** 1632 (1995).

12. C. R. Abernathy, Proc. Symp. Wide Bandgap Semicond. Devices, ed. F. Ren (Electronchem. Soc. Pennington NJ) Vol. **95-21** 1 (1995).

LONG WAVELENGTH SHIFTING AND BROADENING OF QUANTUM WELL INFRARED PHOTODETECTOR RESPONSE VIA RAPID THERMAL ANNEALING

D.K. Sengupta, W. Fang, J.I. Malin, H.C. Kuo, T. Horton, A. Curtis, N.F. Gardner, B. Flachsbart, W. Wohlmuth, D. Turnbull, S.L. Chuang, K. C. Hsieh, K.Y. Cheng, I. Adesida, M. Feng, S.G. Bishop, and G. E. Stillman

Department of Electrical & Computer Engineering, Center for Compound Semiconductor Microelectronics, University of Illinois at Urbana-Champaign, Urbana, Il-61801

ABSTRACT

A shift in the peak response wavelength and a broadening of the photoresponse spectrum is demonstrated for intersubband absorption in n-doped GaAs/AlGaAs multiple quantum well detectors following intermixing of the well and barrier layers during rapid thermal annealing. In general, a decrease in performance is observed for the RTA QWIPs when compared to the as-grown detectors. The peak absolute response of the annealed QWIPs is lower by almost a factor of four, which results in corresponding decrease in quantum efficiency. In addition, the noise performance results in a detectivity which is five times lower than that of QWIPs fabricated from as-grown structures.

INTRODUCTION

Infrared (IR) photodetection by intersubband absorption using GaAs/AlGaAs multiple quantum wells (QWs) grown on a GaAs substrate has recently become the subject of extensive investigations [1,7]. A detailed theoretical study of both linear and nonlinear intersubband absorptions has been reported [8]. The peak detector response can be adjusted to any wavelength in the 8-12 µm range by changing the quantum well width and depth. These quantum well detectors have a number of potential advantages with respect to HgCdTe detectors, including compatibility with the relatively mature GaAs processing technology, the possibility of monolithic integration with GaAs electronics and the potential to make uniform large area focal plane arrays[9,10]. Intermixing of the well and barrier layers during rapid thermal annealing (RTA)[11], can also be used to adjust the peak response to any value in the 8-12 µm wavelength range [12]. This tunability is of interest to IR detector applications as it would facilitate the fine tuning of the peak detector response of as-grown detector structures to a particular desired operational wavelength. The present article describes the effect of RTA on important operating characteristics of QWIPs such as the detector photoresponse, dark current characteristics, absolute responsivity, quantum efficiency, and detectivity.

EXPERIMENTAL DETAILS

GaAs/AlGaAs QWIPs were grown by solid source molecular beam epitaxy (MBE) on semi-insulating GaAs (001) substrates. The active region, sandwiched between two n-type (10^{18} cm^{-3}) GaAs layers, consist of 50 periods of 300Å undoped $Al_{0.25}Ga_{0.75}As$ barriers and 40Å Si (n ~ 10^{18} cm^{-3}) center-doped GaAs wells. The doping is confined to the center 20Å of the GaAs well. In all studies, prior to annealing, the samples were first degreased by tricholoethane, acetone and methanol rinse followed by a light surface etch using NH_4OH. A 1200Å SiO_2 encapsulant was then deposited by plasma enhanced chemical vapor deposition. The details of the process are described in Ref.[13]. The material quality and optical properties of the as-grown and annealed GaAs/AlGaAs MQW samples are investigated using cross-sectional TEM, PL, and infrared absorption measurements.

Quantum-well infrared detectors were fabricated from the as-grown and SiO_2-encapsulated RTA samples into 200µm circular mesas as described in Ref.[13]. All dark current, spectral response, and noise measurements on these as-grown and annealed QWIPs are performed with the detectors mounted on a stage in thermal contact with the cold end of a continuous flow helium cryostat. The dark current I-V

characteristics of the QWIPs are measured at various sample temperatures. The spectral response and noise measurements are performed at a sample temperature of 50K.

In order to obtain the absolute spectral response of the as-grown and RTA QWIPs, both blackbody and relative spectral response measurements are performed. The detectors are connected to an external bias circuit, and bias currents from 0.01µA to 1.37µA are supplied using a battery in series with a large resistor to provide a constant bias current.

The blackbody response measurement of the QWIPs is required to calculate their absolute response. The total absorbed optical intensity is determined by integrating the product of the normalized spectral response and the blackbody irradiance spectrum over wavelength. The peak absolute response is calculated from the absorbed optical intensity and the peak blackbody photocurrent. Once the peak absolute response is determined, the unity gain quantum efficiency can be calculated as shown in Ref.[13].

The noise measurements are performed at a temperature of 50K. The output noise voltage from the detector is amplified by an EG&G model 113 low noise pre-amplifier and measured with a Stanford model SR760 FFT spectrum analyzer. Both the detector and the pre-amplifier are powered by batteries to reduce the system noise, and all cables are of minimal length to reduce the parasitic capacitance. The noise spectral density is measured on the spectrum analyzer and divided by the pre-amplifier gain to find the true noise power spectral density at the detector. Once the absolute response and noise measurements are performed, the detectivity D^* (cm-Hz /W) can be calculated as shown in Ref.[13].

MEASUREMENTS

The cross-sectional TEM micrographs are shown in Fig. 1 for (a) an as-grown MQW and (b) an RTA MQW annealed at 850^0C for 30 seconds. A third micrograph, Fig. 1(c), shows the MQW structure after an anneal at 950^0C for 30 seconds. No defects or dislocations are observed in the as-grown MQW region, and the quantum wells (dark regions) are measured to be ~45 Å and the barriers (light regions) ~300 Å. A slight widening of the well width was observed in the 850^0C case and an almost complete intermixing in the 950^0C case, resulting in an effective well width of ~120 Å. The degree of layer intermixing is not uniform for each quantum well in the MQW stack, in fact, the wells at the top of the stack, near the surface of the SiO_2 encapsulant, are more disordered than the wells at the bottom of the stack. As will be discussed, this nonuniformity has a dramatic impact on the device performance of annealed quantum-well infrared detectors.

In Fig. 2, the 77 K PL spectrum shows a blue shift of 0.03 µm (65 meV) for the annealed QWIP structure in comparison to the as-grown structure. In addition, the RTA QWIP structure exhibits a reduction in luminescence intensity. This is attributed to the out-diffusion of Si dopant atoms from the well and is strongly dependent on the amount of disordering during the anneal. The room temperature intersubband absorption measurements are shown in Fig. 3. The absorption peak for the as-grown QWIP structure is measured to be 9.67 µm (128 meV), while the RTA QWIP shows a broader response with the absorption peak at 11.09 µm (112 meV), resulting in a red shift of 1.42 µm (16 meV). The broadened spectral response of the RTA structure is due to the nonuniform disordering within the MQW structure. Each well in the RTA structure has a slightly different potential profile and yields a slightly different spectral response. Therefore, the total spectral response, which is a summation of spectral responses from each well, should be broader.

We also note that the amount of energy shift of the intersubband transition in the conduction band is not in agreement with the interband energy shift, which should obey the 67/33 conduction band to valence band offset ratio for the AlGaAs/GaAs material system. This is due to the nature of the PL measurement and the depth dependence of the layer disordering during RTA. Since the pump light from the HeNe laser is strongly absorbed by GaAs, only the wells near the top of the MQW stack can be probed and measured for luminescence. Since these top wells have a larger amount of disordering and intermixing than the average well in the stack, the measured PL wavelength from the RTA MQW sample shows a much larger blue shift than expected.

The temperature-dependent dark current versus voltage (I-V) characteristics of the fabricated as-grown and RTA QWIPs are shown in Fig. 4. The dark current characteristics for the as-grown detector are in agreement with what is reported by several authors [14-19]. At low temperatures and low biases,
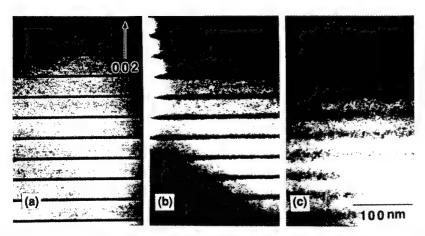
Fig. 1 Cross-sectional TEM of the (a) as-grown, (b) RTA (850°C, 30s), and (c) RTA (950°C, 30s) MQW structures.
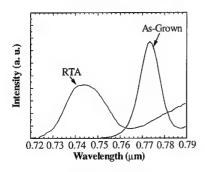

Fig. 2   Photoluminescence spectra at 77 K of the (a) as-grown and (b) RTA (850°C, 30s) MQW structure. A blue shift of 65 meV is observed.
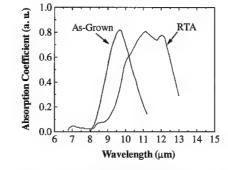

Fig. 3   Room temperature absorption spectra of the (a) as-grown and (b) RTA (850°C, 30s) MQW structure. A red shift of 16 meV is observed.
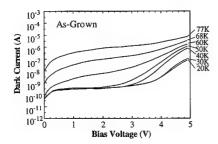

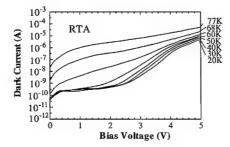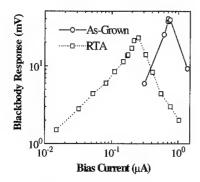Fig. 4 (a) Dark current versus bias characteristics as a function of temperature for the as-grown QWIP.

Fig. 4 (b) Dark current versus bias characteristics as a function of temperature for the RTA QWIP with cold shielding.

357
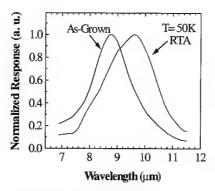
Fig. 5 Blackbody response of the as-grown QWIP (solid line) and the RTA QWIP (dotted line) at T = 50 K as function of biasing current.

Fig. 6 Normalized photoresponse of the as-grown QWIP and the RTA QWIP at T = 50 K. The response is measured for each QWIP biased to operate at its peak performance.

sequential tunneling through the barriers is dominant. At very low temperatures and intermediate bias, the as-grown detector exhibits a plateau in the dark current. At high temperatures and low biases, the dark current is dominated by thermionic emission of carriers from the wells and thermally assisted tunneling through the barriers. At high temperatures and high biases, Fowler-Nordheim tunneling is the dominant mechanism, with impact ionization observed at very high biases. At each temperature, the dark current of the RTA QWIP is higher than that of the as-grown detector, which adversely affects the noise performance of the RTA QWIP. At low temperatures both the as-grown and the RTA detectors exhibit a rapid increase in dark current at high biases. The onset of rapid noise increase occurs at a lower bias in the RTA detector than in the as-grown detector. At higher temperatures both the as-grown and the RTA detectors show a steady increase in the dark current as a function of applied bias. A lower effective barrier height of the RTA detector also explains the lower onset voltage for the rapid increase in the dark current in the RTA QWIP and the larger dark current.

In Fig. 5, we show variation of blackbody response for both as-grown and RTA quantum-well detectors with biasing current. The aperture was maintained at a width of 0.05". The blackbody response increases with current at low bias values until it reaches a maximum value and then decreases at higher currents. This maximum occurs at a bias current of 0.70 μA for the as-grown detector and at 0.25 μA for the RTA detector. The increase in the blackbody response with bias current at low biases occurs due to the increase in the detector voltage with applied bias. A larger voltage creates a larger field across the MQW region of the detector which results in a shorter carrier transit time, higher collection efficiency, and higher photoconductive gain. For larger current biases, however, the response actually decreases with increasing current. This may be attributed to a reduction in the intersubband absorption coefficient due to the large amount of dark current which populates the empty states in the higher subbands. Additionally, there exists a reduction of the intersubband absorption coefficient when the applied fields become large due to a reduced overlap integral of the MQW wave functions.

The spectral response and noise of the as-grown and RTA QWIPs were measured with each detector biased to operate at their peak blackbody response. In Fig. 6, we show the normalized photoresponse for both the as-grown and RTA detector. The peak response wavelengths measured are 8.8 μm for the as-grown detector and 9.6 μm for the RTA detector. Since the ground state is higher and the effective barrier height is lower in the RTA detector than in the as-grown detector, the peak response wavelength of the RTA QWIP experiences a long-wavelength shift[12], in agreement with the room temperature intersubband absorption measurement in Fig. 3.

RESULTS AND DISCUSSION

The peak absolute responses are calculated to be 0.571 A/W for the as-grown detector and 0.1557 A/W for the RTA detector from the blackbody and relative spectral response measurements,. The peak responsivity of the RTA QWIP is reduced by nearly a factor of four from the as-grown structure. The unity gain quantum efficiency is calculated from the absolute response. The peak quantum efficiencies are 8.11% for the as-grown detector as compared to 2.01% for the RTA detector. The four times reduction in quantum efficiency in the RTA QWIP is due primarily to its degraded peak responsivity and secondarily

its red-shift in the peak response wavelength. Although the broadened absorption spectrum of the SiO_2 encapsulated RTA detector can result in a reduced spectral response, we believe that the dominant reduction is a consequence of the out-diffusion of Si dopant from the well[12] and the increased dark current through the RTA MQW structure.

In Fig. 7, we show the voltage noise spectral density measured in the frequency range from 100 Hz to 10 kHz for both as-grown and RTA QWIPs biased to operate at their peak performance. As expected, the noise of the RTA detector is higher than that of the as-grown detector at all frequencies. This is attributed to the increase in the trapping-detrapping mechanism due to layer intermixing in the RTA structure. The noise spectra show 1/f dependence at low frequencies, and at intermediate frequencies, the spectra are dominated by the background G-R noise of the detector.
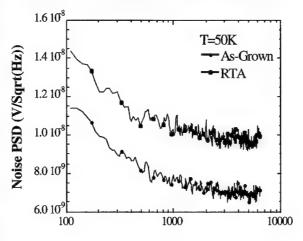
Fig. 7 Noise power spectral density of the as-grown QWIP and the RTA QWIP at T = 50 K. The QWIPs were biased to operate at their peak performance.

The detectivity D* for a peak wavelength of 8.8 μm, a chopping frequency of 500 Hz and a noise bandwidth of 1Hz is calculated to be 1.445×10^{10} cm-Hz$^{1/2}$/W for the as-grown detector as compared to 0.287×10^{10} cm- Hz$^{1/2}$/W at a peak wavelength of 9.6 μm for the RTA detector [13]. Due to the increased dark current and noise along with a decreased peak responsivity, the D* of the RTA QWIP is five times lower than that of the as-grown QWIP. This reduction in detectivity may still be acceptable for focal-plane array detector applications.[20]

CONCLUSION

We have demonstrated that RTA can be employed to both shift the operating wavelength of as-grown detectors to longer wavelengths and to broaden the response of quantum-well infrared photodetectors. The dark current of the SiO_2-encapsulated 850^{0}C RTA detector was higher at each temperature studied than that of the as-grown detectors. The spectral response and quantum efficiency were about a factor of four lower in the RTA QWIP. The overall reduction in the detectivity was a factor of five. The decrease of QWIP performance with RTA is attributed to the out-diffusion of dopant atoms during annealing and increased dark current. Rapid thermal annealing holds promise for adjusting the peak response of as-grown QWIP structures to a particular desired operating wavelength and also for

broadening their spectral response to be sensitive over a wider wavelength range in the important 8-12 μm atmospheric window. The use of RTA changes the well profile of a QWIP and peak wavelength, but the reduced detectivity indicates that this technique is limited for sensitive IR detectors. Recent advances in growth, complimented by innovative structures (random gratings and reflector layers) should offset any degradation in performance. This makes feasible integration of multiple-colored pixels.

ACKNOWLEDGMENTS

REFERENCES

1. L. C. West and S. J. Eglash, Appl. Phys. Lett. **46**, 1156 (1985).
2. B. F. Levine, A. Zussman, S. D. Gunapala, M. T. Asom, J. M. Kuo, and W. S. Hobson, J. Appl. Phys. **72**, 4429 (1992).
3. J. Y. Anderson and L. Lundqvist, Appl. Phys. Lett. **59**, 857 (1991).
4. B. K. Janousek, M. J. Daugherty, M. L. Bloss, M. L. Rosenbluth, M. J. O'Loughlin, H. Kanter, F. J. Deluccia, and L. E. Perry, J. Appl. Phys. **67**, 7608 (1990).
5. I. Grave, A. Shakouri, N. Kuze and A. Yariv, Appl. Phys. Lett. **60**, 2362 (1992).
6. E. Martinet, F. Luc, E. Rosencher, Ph. Bois and S. Delaitre, Appl. Phys. Lett. **60**, 895 (1992).
7. J. D. Ralston, D. F. G. Gallagher, P. Bittner, J. Fleissner, B. Dischler and P. Koidl, J. Appl. Phys. **71**, 3562 (1992).
8. D. Ahn and S. L. Chuang, IEEE. J. Quantum Electron. **QE-23**, 2196 (1987).
9. C. G. Bethea, B. F. Levine, V. O. Shea, R. R. Abbott and S. J. Hsieh, IEEE. Trans. Electron Devices **38**, 1118 (1991).
10. L. J. Kozlowski, G. M. Williams, G. J. Sullivan, C. W. Farley, R. J. Aderson, J. Chen, D. T. Cheung, W. E. Tennant and R. E. DeWames, IEEE Trans. Electron Devices **38**, 1124 (1991).
11. J. S. Major, F. A. Kish, T. A. Richard, A. R. Sugg, J. E. Baker and N. Holonyak Jr., J. Appl. Phys. **68**, 6199 (1990).
12. J. D. Ralston , M. Ramsreiner, B. Dischler, P. Koidl, M. Maier, G. Brandt, P. Koidl and D. J. As ,J. Appl. Phys. **71**, 3562 (1992).
13. D.K. Sengupta, W. Fang, J.I. Malin, A. Curtis, T. Horton, H.C. Kuo, D. Turnbull, C. H. Lin, K.C. Hsieh, S.L. Chuang, M. Feng, S. G. Bishop, and G.E. Stillman, Submitted to J. Elect. Mat.
14. K. K. Choi, B. F. Levine, C. G. Bethea, J. Walker and R. J. Malik, Appl. Phys. Lett. **50**, 1814 (1987).
15. E. Pelve, F. Beltram, C. G. Bethea, B. F. Levine, V. O. Shen, S. J. Hsieh and R. R. Abbott, J. Appl. Phys. **66**, 5656 (1989).
16. B. F. Levine, C. G. Bethea, G. Hasnain, V. O. Shen, E. Pelve, R. R. Abbott and S. J. Hsieh, Appl. Phys. Lett. **56**, 851 (1990).
17. K. K. Choi, B. F. Levine, R. J. Malik, J. Walker and C. G. Bethea, Phys. Rev, **B35**, 4172 (1987).
18. K. Brennan and Y. Wang, . Phys. Lett. **57**, 1337 (1990).
19. G. M. Williams, R. E. deWames, C. W. Farley and R. J. Anderson, Appl. Phys. Lett. **60**, 1324 (1992).
20. C. G. Bethea, B.F. Levine, V.O. Shen, R.R. Abbott, and S.J. Hseih, IEEE. Trans. Electron. Devices **38**, 1118 (1991).

The Effects of Base Dopant Outdiffusion on Low Frequency Noise Characteristics of AlGaAs/GaAs Heterojunction Bipolar Transistors

Y.C.CHOU AND G.P.LI
Department of Electrical and Computer Engineering, University of California, Irvine, CA. 92717
C.S.WU
Microelectronics Division, Hughes Aircraft Company, Torrance, CA 90505

ABSTRACT

The effects of base dopant outdiffusion on low frequency noise characteristics in beryllium-doped heterojunction bipolar transistors (HBT's) are investigated. The beryllium diffusion in HBT's are induced either by growth conditions or by forward-current stress. While an ideal 1/f noise characteristics is observed in HBT's without beryllium outdiffusion, a low frequency noise spectrum showing an anomalous hump is typically detected in HBT's with beryllium diffusion. An activation energy of 0.2 eV is extracted from the Arrhenius plot for the defect associated with this anomalous hump. While base current noise intensity (Sib) dependence on base current is in the range of $Ib^{1.3}$-$Ib^{1.5}$ for typical HBT's, its dependence changes to $Ib^{1.7}$-$Ib^{2.0}$ in devices with more beryllium outdiffusion. This implies that the recombination-generation current is dominant in HBT's with more beryllium outdiffusion. It is speculated that the higher and abnormal noise in devices with beryllium outdiffusion may be related to both an enlarged B-E junction space charge region and an accompanying increase of generation-recombination centers with beryllium outdiffusion process.

INTRODUCTION

Recently, beryllium dopant outdiffusion induced either during MBE growth or device forward current stress has been widely investigated in its effects on heteojunction bipolar transistors (HBT's) [1,2]. While beryllium outdiffusion is shown to cause Vbe shift and poses a device reliability threat [3,4], its effects on HBT low frequency noise (1/f noise) performance has not been studied. It is well known that 1/f noise in HBT's can limit the bandwidth and stability of circuit operation at high frequency [5,6]. The 1/f noise also causes phase noise in local oscillators and upconverts into the sideband noise around the RF carrier signal to degrade the noise performance [7]. Although a reduction in 1/f noise can be achieved in devices with AlGaAs passivation ledge or polyimide attributed to the reduction of surface recombination current in the extrinsic-base region [8,9], the effects of beryllium outdiffusion on HBT's 1/f noise are still not clear. To further improve the noise performance of HBT's for broad band circuit applications, it is essential to examine the noise sources originating from the emitter-base heterojunction. In this paper, we investigate the base dopant redistribution effect on low frequency noise characteristics in AlGaAs/GaAs HBT's. It is observed that both input base current noise intensity (Sib) and its exponent (α) dependence on base current (Ib^{α}) increase in devices with more Be outdiffusion.

EXPERIMENTS

The HBT's layers with a Be doping concentration of 1×10^{19} cm^{-3} in base layer and a compositionally graded layer on both sides of the emitter were grown by molecular beam epitaxy (MBE). The emitter geometry is 3x10 μm^2. HBT's with beryllium outdiffusion induced by forward-current stress at 70 KA/cm^2 , 200°C for 60 hours were used in this study. Inverted collector current ratio (R) measured at E-B junction reverse bias at 0/2 volt was used to indicate the amount of Be outdiffusion [10]. The higher the R value is, the more Be out diffuses in the HBT's. While HBT's with higher R values also have the higher Vbe turn-on voltage (measured at Ic=1 μA) as shown in Fig.1, the R ratio measurement does not suffer the same uncertainty caused by the device parasitic changes as in the Vbe shift measurement. The insert in Fig.1 is a typical U-shape characteristic of R curve as described in Ref.11. At low Vbe, the R ratio is governed by the reverse leakage current. At high Vbe, the series resistance dictates the R ratio value. In this paper, the bottom value of R ratio is used to indicate the amount of Be outdiffusion.
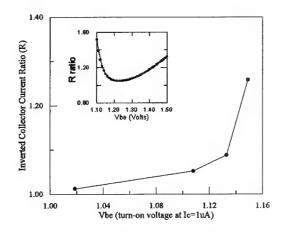
Fig. 1. Inverted collector current ratios in relation to the Vbe turn-on voltage
(The insert is a typical U-shape characteristics of R curve).

All the HBT's were mounted inside a 24-pin ceramic dual-in-line package to perform the DC characteristics and low frequency noise measurement. To minimize the noise from the power source and biasing circuit, a battery, metal resistors and wire wound potentiometers were used to provide the Vbe and Vce biases in the noise measurement. The whole biasing circuit was shielded by an aluminum box to measure the device noise. The collector current noise signal (Svc) was fed into a low noise transimpedance amplifier, whose low frequency noise was at least 10 dB lower than that from the devices. An HP3563A control system analyzer was used to acquire the amplified device noise spectrum. Each measurement was averaged 10 times and the noise spectra were normalized to a 1Hz resolution bandwidth. The Svc can be expressed as [9]:

$$Svc = R_L^2\beta^2(S_{ice}/\beta^2 + Sib) \tag{1}$$

The term S_{ice}/β^2 can be ignored because β is typically greater than unity. As a result, Svc can be transformed to an equivalent base current noise

$$Sib=Svc/(R_L^2\beta^2) \tag{2}$$

where R_L and β were load resistance and current gain, respectively. Sice is the associated noise spectrum of noise source current i_{ce} [9].

RESULTS AND DISCUSSIONS

HBT's with normal R value (≈ 1) exhibit an ideal 1/f noise characteristics in the measured frequency range (1Hz-100KHz) as shown in Fig.2. The corner frequency is beyond 1 MHz. However, higher R value devices show a noise spectrum deviating significantly from the ideal 1/f with an anomalous hump, whose center frequency is close to 10 KHz as shown in Fig.3. This anomalous noise spectra may be associated with the Be outdiffusion. Not only do we observe the Sib spectrum deviating significantly from the original ideal case, but the noise intensity also increases in higher R value devices. The noise intensity extracted at Ib=5 μA, f=10 Hz for as-processed HBTs is plotted as a function of their measured R value as shown in Fig.4 clearly showing a strong dependence of Sib on R. While R changes from 1.01 to 1.2, Sib shows one fold increase from 4×10^{-21} A^2/Hz to 4×10^{-20} A^2/Hz. Obviously, the low frequency noise is strongly affected by the base dopant outdiffusion.
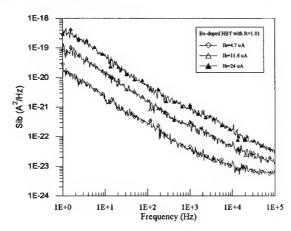
Fig.2 Input base current noise spectral density in HBT without Be diffusion (R$\approx$1.01) exhibiting the 1/f noise.

In order to examine the root cause of Sib increase in HBT's with higher R value, Sib measured at f=50 Hz was plotted as a function of base current (Ib). While Sib dependence on base current is in the range of $Ib^{1.3}$-$Ib^{1.5}$ for HBT's with R $\approx$1, it changes to $Ib^{1.7}$-$Ib^{2.0}$ in devices with more Be outdiffusion as shown in Fig.5. It is well known that Sib shows an exponent of 2 dependence on base current in the case of the surface recombination current dominant in base current and has an exponent of 1 dependence otherwise [12]. The higher exponent dependence on base currents implies that the low frequency noise of HBT's with higher R value may be dominant by the recombination-generation current. Normally, a Vbe increase of about 1.3 mV corresponds

to an approximate 1 Å Be out-diffusion from the heterojunction in HBT's [3]. From Fig.1, a displaced p-n junction in a distance of 93 Å can be estimated from devices with the R value of 1.12. Accordingly, one may speculate that the higher and abnormal noise in devices with Be outdiffusion may be related to both an enlarged B-E space charge region resulting in an increase in carrier recombination [12] , and an accompanying increase of generation-recombination centers with Be diffusion process.
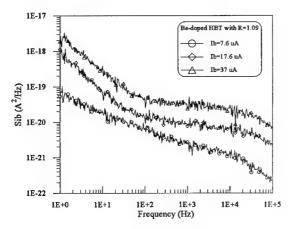
Fig.3 Input base noise current spectral density in HBT with Be outdiffusion (R≈1.09) exhibiting the anomalous noise characteristics.
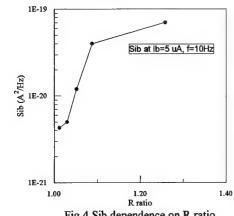
Fig.4 Sib dependence on R ratio.
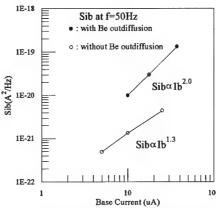
Fig.5 Sib dependence on base current in HBT's without and with Be diffusion.

The spectra in Fig.3 can be expressed as:

$$S_{ib} = \frac{A}{f} + \frac{B}{1 + (2\pi f)^2 \tau^2} \tag{3}$$

where the first term represents the ideal 1/f noise and second term is the generation-recombination noise. If the Ea is the activation energy of the trap center involved in the base current noise, the time constant τ of the Sib can be expressed as [13]:

$$1/\tau \propto T^2 \exp -Ea/KT \tag{4}$$

The time constant τ is simply determined from the -3dB characteristic frequency from the expression:

$$\tau = \frac{1}{2\pi f_p} \tag{5}$$

where f_p is the cutoff frequency of Lorentzian spectra. As a result, Ea can be extracted from the slope of Arrhenius plot. Fig.6 shows an activation energy of 0.2 eV extracted from the Arrhenius plot for the defect associated with the anomalous hump shown in Fig.3. D. Costa et al. [8] also reported an activation energy of 0.2 eV in the emitter-base junction in Be-doped AlGaAs/GaAs HBT's. DX center was identified as a possible candidate for the trap with an activation energy of 0.2 eV. In our case, it is not clear whether the Be diffusion leads to DX center formation. However, this trap is responsible for an increase in electron-hole pair recombination in the enlarged space-charge region of the emitter-base junction. Nevertheless, further investigation still needs to be done to identify the root cause of this anomalous trap.
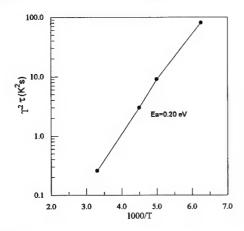
Fig.6 Arrhenius plot of activation energy of anomalous noise hump.

SUMMARY

We have conducted an investigation in the effects of base dopant outdiffusion on low frequency noise characteristics of Be-doped AlGaAs/GaAs HBT's. While normal devices exhibit an ideal 1/f noise characteristics, devices with Be outdiffusion show an anomalous noise hump with an activation energy of 0.2 eV. HBT's with a larger R value illustrating a Be outdiffusion case also show a larger Sib. While Sib dependence on base current is in the range of of $Ib^{1.3}$-$Ib^{1.5}$ for HBT's with R $\approx$1, it changes to $Ib^{1.7}$-$Ib^{2.0}$ in devices with more Be outdiffusion (R$\approx$1.09). The higher exponent dependence on base current implies that the low frequency noise of HBT's with higher R value may be dominant by the recombination-generation current.

REFERENCE

1. D.C. Streit, A.K. Oki, J.R. Velebir, K.S. Stolt and D. Umemoto, J. Vac. Sci. Technol., B10, 853(1992).

2. D.C. Streit, A.K. Oki, D.K. Umemoto, J.R. Velebir, K.S. Stolt, F.M. Yamada, Y. Saito, M. E. Hafizi, S. Bui and L.T. Tran, IEEE Electron Device Lett., 12, 471(1991).

3. M. E. Hafizi, L.M. Pawlowicz, L.T. Tran, D.K. Umemoto, A.K. Oki, M.E. Kim and K.H.Yen, Technical Digest of GaAs IC Symposium, 1990, p329.

4. O. Nakajima, H. Ito, T. Nittono and K. Nagata, Technical Digest of International Electron Device Meeting, 1990, p.673.

5. B. Hughes, N.G. Ferandez and J.M. Gladstone, IEEE Trans. Electron Devices, 34, 733(1987).

6. C.Y. Chen, J. Bayruns, R.J. bayruns and N. Scheinberg, Technical Digest of GaAs IC Symposium, 1988, p289.

7. H.J. Siweris and B. Schiek, IEEE Trans. Microwave Theory Tech., 33, 233(1985).

8. D. Costa and J.S. Harris, IEEE Trans. Electron Devices, 39, 2383(1992).

9. Tanaka, H. Shimawaki, K. Kasahara and K. Honjo, IEEE Trans. Electron Devices, 40, 1194(1993).

10. Y-H Chang and G.P. Li, IEEE Trans. Electron Devices, 40, 692(1993).

11. Y.C.Chou, G.P.Li, C.S.Wu, Peter Chu, C.K.Pao and T.C. Cisco, Proc. of Mat.Res.Soc.Symp.,378, 777(1995).

12. A.Van der Ziel, X. Zhang and A.H. Pawlikiewicz, IEEE Trans. Electron Devices, 33, 1371(1986).

13. C. Delseny, F. Pascal, S. Jarrix, G. Lecoy, J. Dangla and C. Dubon-Chevallier, IEEE Trans. Electron Devices, 41, 2000(1994).

TEMPERATURE DEPENDENCE OF THE OPTICAL ABSORPTION EDGE IN INDIUM PHOSPHIDE

M. BEAUDOIN, S.R. JOHNSON, A.J.G. DeVRIES, A. MOHADES-KASSAI, T. TIEDJE*

Advanced Materials and Process Engineering Laboratory and Department of Physics and Astronomy, University of British Columbia, 2355 East Mall, Vancouver, BC, V6T 1Z4

* Also Department of Electrical Engineering

ABSTRACT

Optical bandgap thermometry is a new method for measuring the temperature of semiconductor substrates. In this method, the temperature of the substrate is inferred from the wavelength of the onset of transparency of the substrate which is a measure of its bandgap. Common configurations of this technique are diffuse reflectance and transmittance. In order to calibrate these spectra to substrate temperature and to better understand the temperature dependence of the absorption edge, the transmittance spectra of semi-insulating InP:Fe and n-type InP:S substrates have been measured as a function of temperature in a tube. The width of the absorption edge (Urbach parameter) is found to increase linearly with temperature from 8.7 meV at room temperature to 15.7 meV at 595°C for semi-insulating InP:Fe while it remains independent of temperature at a value of about 21.5 meV for heavily doped $(6.5 \times 10^{18}$ cm$^{-3})$ InP:S. For InP:Fe, the temperature dependent part of the width is smaller than predicted by the standard theory where the width of the edge is proportional to the phonon population. The values of the Urbach parameter for InP:Fe are higher than those of semi-insulating GaAs which is attributed to the higher ionicity of InP.

INTRODUCTION

Optical bandgap thermometry [1-3] is a convenient non contact method for measuring substrate temperatures under ultra high vacuum conditions that overcomes some of the limitations of thermocouples and pyrometers. A common configuration used in molecular beam epitaxy is diffuse reflectance spectroscopy (DRS) where the wavelength for the onset of transparency of a substrate can be used to determine its temperature. The onset of transparency is related to the optical absorption edge which, in many semiconductors, is found to increase exponentially with photon energy [4-7]. This exponential edge, known as the Urbach edge, is a manifestation of the effect of structural and thermal disorder on the electronic properties of semiconductors [4,6-8]. In crystalline semiconductors, the characteristic width of the Urbach edge at high temperature is found to be proportional to the temperature [9] and is believed to be due to band tailing associated with disorder produced by thermal fluctuations in the crystal lattice [4,5,8]. Precise measurements of the temperature dependence of this absorption edge are required in order to develop calibration curves for various configurations of optical bandgap thermometry.

The temperature dependence of the optical absorption edge of semi-insulating InP:Fe and highly doped n-type $(6.5 \times 10^{18}$ cm$^{-3})$ InP:S 350 μm thick wafers is reported in this paper. The measurements were done in a tube furnace which allows for temperature determination to the high absolute accuracy desired for calibration of the DRS technique, in addition to a precise determination of the temperature dependence of the Urbach edge and optical bandgap. The

temperature dependence of the bandgap and Urbach edge are analyzed in terms of the structural and thermal disorder using a model based on the phonon occupation [5,7].

TEMPERATURE MEASUREMENT

In order to achieve the best possible absolute temperatures, the measurements are done in a radiation cavity where the wafers are in thermal equilibrium with their surroundings. The radiation cavity consists of two Ta baffles with optical access slits inserted on either side of the wafer inside a 7 cm diameter by 20 cm long tube, as shown schematically in Fig. 1. This radiation cavity is heated at the center of a 7 cm (2.75 in) diameter stainless steel tube in a tube furnace. The radiation cavity is light-tight as it fits snugly inside the stainless steel tube. The temperature is measured by two calibrated type-K thermocouples inserted in the middle of the radiation cavity with one thermocouple in contact with the edge of the sample and the other in contact with the center of the wafer. The temperature uniformity across the wafer was better than 0.5° as measured both by the thermocouples and by the optical transmission at different positions across the wafer.

The type-K thermocouples were calibrated against a highly accurate commercially calibrated Pt-Pt/Rh(13%) thermocouple by clipping both thermocouples to a holder. This is inserted in a crucible lightly packed with alumina powder and loaded in a furnace. Temperature measurements of both thermocouples were performed after the furnace temperature had stabilized. The measurements with the type-K thermocouple were 6°C higher than the "real" temperature at 600°C and within 1°C at room temperature. The intermediate temperatures scaled linearly with uncertainties of ± 1°C. The type-K thermocouples' possible drift with thermal cycling is not a problem here as the temperatures were kept below 650°C. These measurements are indicative of absolute accuracies in the temperature measurements of better than ± 6°C and possibly as good as ± 1°C.

During the temperature measurements, the tube is evacuated and filled with 10 mbar of Ar gas. Small chunks of As are placed on each side of the wafer in order to maintain a group V over pressure to offset the preferential evaporation of P at high temperatures. Each end of the stainless steel tube is capped with a Pyrex viewport in a 4.5 inch ConFlat flange, for optical access. A broad spectrum W-halogen lamp is placed at one end of the tube. The W filament of the lamp is focused on the sample through the optical access slits of the radiation shields using a 75 mm focal length lens. The sample is imaged onto an adjustable aperture at the other end of the tube with another 75 mm focal length lens. An optical fiber bundle is used to collect the light from the aperture to a monochromator and a liquid nitrogen cooled InGaAs detector where it is spectrally analyzed using standard lock-in detection. To minimize complications caused by light scattering the samples are polished on both sides.

OPTICAL ABSORPTION

The absorption coefficient α is determined by inverting the normalized transmittance spectra,

$$T = \frac{(1-R)^2 \exp(-\alpha d)}{1 - R^2 \exp(-2\alpha d)} \tag{1}$$

where T is obtained by dividing the measured light signal through the sample by the optical throughput of the system, d is the thickness of the wafer and R is the normal incidence reflectivity of the InP vacuum interface. $R = 0.29$ in the wavelength region of the InP absorption edge [10].

Because of the Kramers-Kronig, relations the spectral curve for the index of refraction shifts with the absorption edge and hence the reflectivity remains approximately constant at the absorption edge even though the temperature of the material is changing.

Figure 2 shows the measured absorption coefficient of InP:Fe and InP:S as a function of the photon energy for different temperatures. Both samples exhibit the exponential Urbach edge along with a weakly energy dependent subedge absorption region at lower energies. This subedge is much larger in the heavily doped InP:S sample and is attributed to phonon assisted interconduction band transitions [11]. On the other hand, the subedge absorption in the semi-insulating InP:Fe is due to deep levels associated with Fe related centers [12] at low temperatures while at higher temperatures absorption due to free carriers becomes important. The subedge absorption of InP:Fe at 204°C is lower than at either room temperature or 387°C. This behavior is not understood and no experiments have been performed to verify the reproducibility of this feature with other samples.

For the purposes of this paper, the absorption in the Urbach region can be described by the following expression [5]:

$$\alpha(h\nu) = \alpha_g \exp\left(\frac{h\nu - E_1}{E_0}\right) \tag{2}$$

where E_0 is the characteristic energy of the Urbach edge, E_1 is the extrapolated bandgap energy and α_g is the optical absorption coefficient at the bandgap energy. The extrapolated bandgap E_1 is close to the optical bandgap, E_g, but not equal to it because E_g is defined in a different way [13]. In order to determine E_0 from the data, it is first necessary to subtract the weakly energy dependent subedge absorption. This is accomplished by fitting a straight line to the absorption just below the exponential edge and subtracting it from the data. The resulting corrected absorption is then fitted by Eq. 2 from which both E_1 and E_0 are obtained [7]. For InP, the optical absorption in the vicinity of the bandgap is $\alpha_g = 11000$ cm^{-1} [13]. From this value of α_g, $E_1 = 1.354$ eV at 297 K which is slightly higher than the generally accepted value of 1.351 eV for E_g. For the
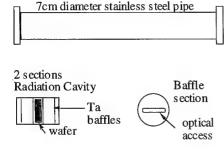
Figure 1: Schematic diagram of the measurement cavity. The wafer is mounted in a radiation cavity which ensures a uniform temperature.
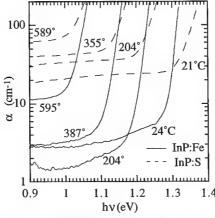
Figure 2: absorption coefficient of InP:Fe and InP:S at different temperatures.

higher temperature data, we obtain the bandgap from the room temperature offset between E_1 and E_g using $E_g(T) = E_1(T) - 0.003$ eV. The same procedure is used to analyze the InP:S data. The optical bandgaps and Urbach characteristic energies are shown in Fig. 3 for both samples. The optical bandgap is larger in n-type material due to partial filling of the conduction band [14].

TEMPERATURE DEPENDENCE

The width of the absorption edge is a manifestation of both thermal and structural, or "frozen-in", disorder in the material. In the standard theory for crystalline semiconductors, E_0 is proportional to a temperature dependent term proportional to the phonon population [4,8,9] which, in the Einstein single oscillator model, is given by:

$$E_0(T) = S_0 k\theta \left[\frac{1+X}{2} + \frac{1}{\exp(\theta/T)-1} \right] \tag{3}$$

where the dimensionless parameter X describes the structural disorder [5-7], θ is the Einstein temperature, T is the temperature and S_0 is a dimensionless constant related to the electron-phonon coupling. X should, in principle, be zero for a perfect crystal [5]. The temperature dependence of the bandgap is also proportional to the same phonon population [5,7]:
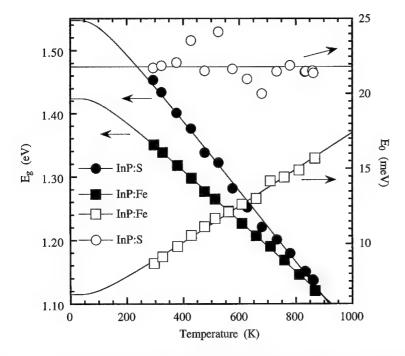
Figure 3: E_g and E_0 for InP:Fe and InP:S. The continuous lines are fits using a model based on the phonon occupation densities.

370

$$E_g(T) = E_g(0) - S_g k\theta \left[\frac{1}{\exp(\theta/T)-1} \right] \qquad (4)$$

where S_g is a dimensionless coupling constant. In Eq. 4, the effect of the zero point motion and the structural disorder is included in the zero temperature bandgap $E_g(0)$. Since both E_g and E_0 exhibit the same functional dependence on the phonon occupation, they are related via a proportionality constant G, called Cody's constant, and an Urbach focus energy E_f [5]:

$$E_g(T) = E_f - GE_0(T). \qquad (6)$$

The fits of Eqs. 3 and 4 are shown as continuous lines through the data in Fig. 3. A negative slope statistically consistent with zero is obtained when Eq. 3 is fitted to the data of InP:S. The resulting parameters obtained from the fits are reported in Table I.

DISCUSSION

The width of the absorption edge in the InP:S sample is dominated by fluctuations in the band edges caused by the Coulomb potentials of the ionized impurities and consequently is independent of temperature. On the other hand, the width of the absorption edge in the InP:Fe sample is dominated by thermal fluctuations at high temperatures. The phonon independent or structural disorder part of the width in InP:Fe is believed to be due to fluctuations in the band edges caused by the strain fields of point defects such as interstitial and substitutional Fe impurities.

Previously published results for semi-insulating and n-type GaAs [7] also showed that the temperature dependence of E_0 is weaker in doped material. The n-type GaAs sample studied had, however, a carrier concentration about three times smaller than the InP:S sample measured here. Here, as in the previous work [7], a non zero X has to be introduced to explain the data of the semi-insulating sample. The width of the edge in InP:Fe has a stronger temperature dependence than semi-insulating GaAs (S_0 of GaAs was 0.087 compared to 0.143 here) [7]. In general, the electron-phonon coupling constant S_0 increases with ionicity and is therefore expected to be larger in the more ionic InP sample [9].

The Einstein temperature obtained from the fits is in excellent agreement with the reported values of the Debye temperature for InP (the Einstein temperature is 0.75 times the Debye temperature).

CONCLUSION

The first measurements of the temperature dependence of the Urbach edge in InP:Fe and InP:S above room temperature are reported. For heavily doped InP:S (6.5×10^{18} cm^{-1}) the characteristic width of the Urbach edge is independent of temperature in the temperature

Table I: Parameters describing the temperature dependence of the absorption edge. For InP:S, both parameters S_0 and X have values consistent with 0 indicating that no temperature dependence is observed for E_0.

Parameter	InP:Fe	InP:S
$E_g(0)$ (eV)	1.424	1.547
$E_g(20°C)$ (eV)	1.351	1.454
$E_0(20°C)$ (meV)	8.7	21.7
$E_0(600°C)$ (meV)	15.7	21.4
θ (K)	269	269
S_0	0.143±0.003	-0.02±0.02
S_g	4.70 ± 0.04	6.56 ± 0.11
E_f (eV)	1.64±0.01	N/A.
X	3.0 ± 0.2	-94 ± 62

range from 20°C to 600°C while for semi-insulating InP:Fe, the Urbach width varies from 8.7 meV at room temperature to 15.7 meV at 595°C. The stronger electron-phonon coupling in InP compared to GaAs is attributed to the higher ionicity of InP. Finally, these accurate temperature measurements of the absorption edge in InP allow the development of calibration curves for optical bandgap thermometry.

ACKNOWLEDGMENTS

REFERENCES

1. E.S. Hellman and J.S. Harris, Jr., J. Cryst. Growth, **81**, 38 (1986).
2. S.R. Johnson, C. Lavoie, M.K. Nissen and T. Tiedje, US Patent 5,388,909 (1995).
3. D.M. Kirillov and R.A. Powell, US Patent 5,118,200 (1992).
4. S. John, C.H. Grein, Reviews of Solid State Science, **4**, 1-59 (1990).
5. G.D. Cody, *Semiconductors and Semimetals*, ed. by J.I. Pankove, Vol. 21B, Academic Press (1984).
6. M. Beaudoin, M. Meunier, T. Muschik, R. Schwarz, C.J. Arsenault, M. Beaulieu and O.Grimal, Can. J. Phys., **70**, 824 (1992).
7. S.R. Johnson and T. Tiedje, J. Appl. Phys., **78**, 5609 (1995).
8. W. Sritrakool, V. Sa-yakanit and H.R. Glyde, Phys. Rev. B, **33**, 1199 (1986).
9. M.V. Kurik, Phys.Stat.Sol.(a) **8**, 9 (1971).
10. *Handbook of optical constants of solids*, ed. by Edward D. Palik, Vol. 1, Academic Press (1985).
11. A.S. Jordan, J. Appl. Phys., **51**, 2218 (1980).
12. R. Fornari and J. Kumar, Appl. Phys. Lett., **56**, 638 (1990).
13. Sadao Adachi, *Physical Properties of III-V Semiconductor Compounds, InP, InAs, GaAs, GaP, InGaAs and InGaAsP*, John Wiley & Sons (1992).
14. T.S. Moss, Proc. Phys. Soc. (London) **B76**, 775 (1954); E. Burstein, Phys. Rev., **93**, 632 (1954).

W, WSi$_x$ AND Ti/Al LOW RESISTANCE OHMIC CONTACTS TO InGaN, InN AND InAlN

C.B. Vartuli*, S.J. Pearton*, C.R. Abernathy*, J.D. MacKenzie*, R.J. Shul**, J.C. Zolper**, M.L. Lovejoy**, A.G. Baca** and M. Hagerott-Crawford**
*Department of Materials Science and Engineering University of Florida, Gainesville FL 32611
**Sandia National Laboratories, Albuquerque NM 87185-0603

ABSTRACT

W, WSi$_{0.44}$ and Ti/Al contacts were examined on n$^+$ In$_{0.65}$Ga$_{0.35}$N, InN and In$_{0.75}$Al$_{0.25}$N. W was found to produce low specific contact resistance ($\varrho_c \sim 10^{-7}$ $\Omega \cdot$cm^2) ohmic contacts to InGaN, with significant reaction between metal and semiconductor at 900 °C mainly due to out diffusion of In and N. WSi$_x$ showed an as-deposited ϱ_c of 4x 10^{-7} $\Omega \cdot$cm^2 but this degraded significantly with subsequent annealing. Ti/Al contacts were stable to $\sim$ 600 °C ($\varrho_c \sim 4$x10^{-7} $\Omega \cdot$cm^2 at $\leq$600 °C). The surfaces of these contacts remain smooth to 800 °C for W and WSi$_x$ and 650 °C for Ti/Al. InN contacted with W and Ti/Al produced ohmic contacts with $\varrho_c \sim 10^{-7}$ $\Omega \cdot$cm^2 and for WSi$_x$ $\varrho_c \sim 10^{-6}$ $\Omega \cdot$cm^2. All remained smooth to $\sim$ 600 °C, but exhibited significant interdiffusion of In, N, W and Ti respectively at higher temperatures. The contact resistances for all three metalization schemes were $\geq 10^{-4}$ $\Omega \cdot$cm^2 on InAlN, and degrades with subsequent annealing. The Ti/Al was found to react with the InAlN above 400 °C, causing the contact resistance to increase rapidly. W and WSi$_x$ proved to be more stable with $\varrho_c \sim 10^{-2}$ and 10^{-3} $\Omega \cdot$cm^2 up to 650 °C and 700 °C respectively.

INTRODUCTION

Recently much progress been made in the processing of the III-V nitrides and their ternary alloys, resulting in nitride-based blue/UV light emitting and electronic devices.[1-8] The III-nitrides pose a problem however in the development of low resistance ohmic contacts because of their wide bandgaps. Most of the work done in this area has been focused on n-type GaN. Au and Al single metal contacts to n$^+$ GaN and non- alloyed Au/Ti and Al/Ti were found to have contact resistances of $\sim 10^{-3}$ to 10^{-4} $\Omega \cdot$cm^2.[9-13] Lin et. al.[14] reported the lowest contact resistance to n$^+$ GaN, with Ti/Al contacts after annealing at 900 °C for 30 sec in a rapid thermal annealer ($\varrho_c = 8$x10^{-6} $\Omega \cdot$cm^2). They suggested the formation of a TiN interface as important in the formation of the low resistance contact. W was found to produce low resistance ohmic contacts to n$^+$ GaN ($\varrho_c \sim 10^{-4}$ $\Omega \cdot$cm^2) with little interaction between the semiconductor and the metal up to 800 °C[15]. WSi$_x$ on n$^+$ GaN was found to be stable to 800 °C as well, with a contact resistance of $\sim 10^{-5}$ $\Omega \cdot$cm^2.[16] Graded contact layers to GaN have been formed with both InN[17] and InGaN with WSi$_x$.[16] Ohmic contacts to InN have also been investigated, with non-alloyed Ti/Pt/Au producing specific contact resistance $\varrho_c = 1.8$x10^{-7} $\Omega \cdot$cm^2.[19] Graded

373

In$_x$Ga$_{1-x}$As/InN contacts have also been used on GaAs/AlGaAs heterojunction bipolar transistors, with ϱ_c as low as $5 \times 10^{-7} \, \Omega \cdot cm^2$.[20] Ohmic contacts to the nitrides have been reviewed previously by Smith and Davis.[21]

For high temperature electronics applications, or for high reliability, we would like to employ refractory metal contacts such as W and WSi$_x$. Moreover, the contact resistance could be reduced if lower bandgap In-containing alloys (or InN) were used as contact layers on GaN, much as the case with InGaAs on GaAs. However the In-based nitrides are less thermally stable than GaN, and we need to establish the trade off between better contact resistance and poorer temperature stability.

In this paper we report the results of W, WSi$_{0.44}$ and Ti/Al contacts deposited on n$^+$ In$_{0.65}$Ga$_{0.35}$N, n$^+$ InN and n$^-$ In$_{0.75}$Al$_{0.25}$N. The electrical, structural and chemical stability of these contacts were examined after anneals up to 900 °C, using Transmission Line Method (TLM) measurements, Scanning Electron Microscopy (SEM) and Auger Electron Spectroscopy (AES). We find that InGaN allows achievement of excellent contact resistances, with stability up to ~ 600 °C for W metalization.

EXPERIMENTAL

The InGaN, InN and InAlN samples were grown using Metal Organic Molecular Beam Epitaxy (MO-MBE) on semi-insulating, (100) GaAs substrates in an Intevac Gen II system as described previously.[22,23] The group-III sources were triethylgallium, trimethylamine alane and trimethylindium, respectively, and the atomic nitrogen was derived from an ECR Wavemat source operating at 200 W forward power. The layers were single crystal with a high density (10^{11} - 10^{12} cm^{-2}) of stacking faults and microtwins. The InAlN and InGaN were found to contain both hexagonal and cubic forms. The InN, In$_{0.65}$Ga$_{0.35}$N and In$_{0.75}$Al$_{0.25}$N were highly autodoped n-type (~10^{20} cm^{-3}, ~ 10^{19} cm^{-3} and 8×10^{18} cm^{-3} respectively) due to the presence of native defects.

The samples were rinsed in H$_2$O:NH$_4$OH (20:1) for 1 min just prior to deposition of the metal to remove native oxides. The metal contacts were sputter deposited to a thickness of 1000Å in the case of W and WSi$_{0.44}$, and then etched in SF$_6$/Ar in a Plasma Therm reactive ion etcher (RIE) to create TLM patterns. For the Ti/Al contacts, 200Å of Ti and then 1000Å of Al was deposited, and the TLM pattern formed by lift off. The nitride samples were subsequently etched in Cl$_2$/CH$_4$/H$_2$/Ar in an Electron Cyclotron Resonance (ECR) etcher to produce the mesas for the TLM patterns.[24] The samples were annealed at temperatures from 300 to 900 °C for 15 sec under a nitrogen ambient in a RTA system (AG-410). TLM measurements were performed at room temperature, and the results used to calculate the specific contact resistances. SEM was used to examine the surface morphology of the contact both before and after annealing, and AES depth profiles were acquired for selected samples to determine the amount of interdiffusion during annealing.

RESULTS AND DISCUSSION

The contact resistance for W, WSi_x and Ti/Al ohmic contacts to InGaN as a function of annealing temperature is shown in Figure 1. All contacts had similar contact resistance as deposited, $\sim 2\text{-}4\times10^{-7}$ $\Omega \cdot cm^2$. After a 600 °C anneal, the W contact improved slightly, while the Ti/Al contact was stable, and the WSi_x contact resistance increased by an order of magnitude. Above 600 °C, the Ti/Al contacts degraded rapidly, and the WSi_x continued to degrade, while ϱ_c for both samples increased up to $\sim 10^{-5}$ $\Omega \cdot cm^2$ at 900 °C. The W contact resistance increased to the as deposited value at 700 °C, but dropped steadily as the temperature increased. The error in these measurements was estimated to be ±10 % due mainly to placement of the probes. The widths of the TLM pattern spacings varied slightly due to processing, (maximum of ± 5 %) as determined by SEM measurements, which were taken into account when calculating the contact resistances. These results show that W is an attractive choice for low resistance stable contacts on InGaN. The surfaces of the as deposited contact metals were relatively smooth. The W was still quite smooth even after 900°C anneal, while the Ti/Al had significant pitting at the lowest anneal of 500 °C even though the contact resistance did not degrade until ≥ 600 °C.
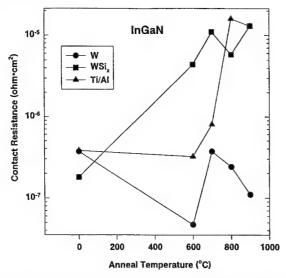
Figure 1. Contact resistance for W, $WSi_{0.44}$ and Ti/Al ohmic contacts to InGaN as a function of annealing temperature.

In Fig. 2 AES depth profiles of InGaN contacted with W before and after a 900 °C anneal are shown. As-deposited samples show some diffusion of W into the sample. After annealing however there was a large out diffusion of In and N. The In has only diffused about 500 Å into the W, showing a sharp peak in concentration at that point. Though much smaller amounts of N have diffused out, it also had a peak in concentration at that

point. The Ga remained stable, consistent with results that found GaN to be stable with W to high temperatures.[15] There is not significant diffusion of W after annealing emphasizing the excellent thermal stability of these contacts.
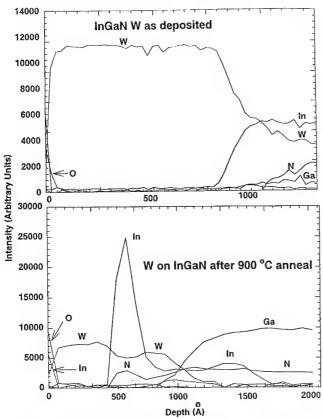
Figure 2. AES depth profiles of InGaN contacted with W before (top) and after a 900 °C anneal (bottom).

The contact resistance for ohmic contacts of W, WSi_x and Ti/Al to InN as a function of annealing temperature is shown in Fig. 3. Because of the lower thermal stability of InN, these contacts were annealed between 300 °C and 500 °C. As deposited samples again had similar contact resistances, $\sim 2x10^{-7} \Omega \cdot cm^2$. WSi_x contacts showed the most degradation at low temperature, with the resistance rising a factor of 5 after 300 °C annealing and then remaining constant. Ti/Al deviated little from initial values, although there was severe pitting on samples annealed at 500 °C while W resistance began to degrade at 500 °C.

In Fig. 4 the contact resistance is shown for W, WSi_x and Ti/Al ohmic contacts to InAlN as a function of annealing temperature. As-deposited Ti/Al had the lowest contact resistance on this material, $\varrho_c \sim 1x10^{-4} \Omega \cdot cm^2$. The contact resistance rose to $\sim 2x10^{-2} \Omega \cdot cm^2$ after a 500 °C anneal, and continued rising with annealing temperature. WSi_x was

stable at 500 °C at ~ 1×10^{-3} $\Omega \cdot cm^2$, but degraded rapidly above that. W had the highest initial contact resistance, (ϱ_c ~ 1×10^{-2} $\Omega \cdot cm^2$) but the resistance remained relatively constant until the 900 °C anneal where it began rising. The W on InAlN remained smooth until 800 °C, and then begins to form hillocks, as did the WSi_x contact at 700 °C. The Ti/Al began pitting at 400 °C. As will be seen in subsequent figures, the pitting in the
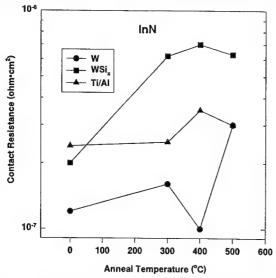
Figure 3. Contact resistance for ohmic contacts of W, WSi_x and Ti/Al to InN as a function of annealing temperature.
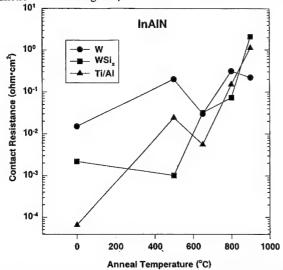
Figure 4. Contact resistance for W, WSi_x and Ti/Al ohmic contacts to InAlN as a function of annealing temperature.

Ti/Al contacts was due to diffusion of the Al through the Ti into the sample. Hillocks appear to be formed from diffusion of In from the nitride sample into the contact layer.

AES depth profiles of Ti/Al contact on InAlN as-grown and after a 550 °C and 900 °C anneal are shown in Fig. 5. In the as grown, a small out diffusion of In through the Ti/Al contact and onto the surface was detected. The interfaces were still well defined. After anneal the In had diffused out significantly, with a peak in concentration
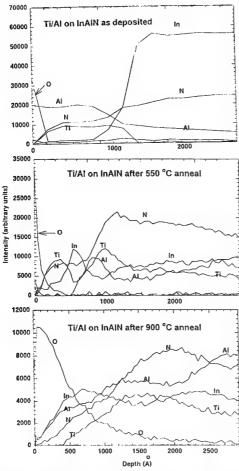
Figure 5. AES depth profile of Ti/Al contact on InAlN before (top) and after a 550 °C (middle) and 900 °C anneal (bottom).

again at about 500 Å from the surface. N and Al also diffused to a large extent and were lost from the surface, though it is not clear to what extent the Al diffused from the contact or the nitride sample. Ti was redistributed as well, both into the nitride sample and into the Al contact. After the 900 °C anneal the Ti has diffused throughout the sample. The In and N have migrated completely through the contact layer, and a large amount of Al has been lost from the surface.

Figure 6 shows AES depth profiles of InAlN contacted with WSi_x, as-grown and after 550 °C anneal. As-deposited, the interface was about 200 Å wide, with minimal interdiffusion of all components. After anneal W and Si were found throughout the nitride sample, with the N reaching approximately 500 Å in the contact layer, and In diffused into the contact layer with a peak concentration approximately 500 Å from the surface.
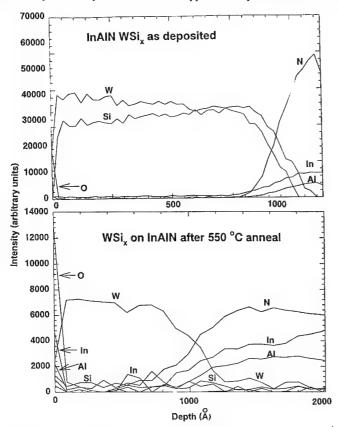
Figure 6. AES depth profiles of InAlN contacted with WSi_x before (top) and after a 900 °C anneal (bottom).

CONCLUSION

W, WSi_x and Ti/Al were found to produce low resistance ohmic contacts on n^+ InGaN and InN. W contacts proved to be the most stable, and also gave the lowest resistance to InGaN and InN, $\varrho_c < 10^{-7}$ $\Omega \cdot cm^2$ after 600 °C anneal, and $1x10^{-7}$ $\Omega \cdot cm^2$ after 300 °C anneal, respectively. Significant diffusion of In, N and Al, as well as Ti and W were found after anneal. The contact resistance stability varies for each material and degraded at temperatures > 400 °C on InN, ≥ 500 °C on InAlN and ≥ 600 °C on InGaN. W contacts remained smooth at the highest anneal temperatures. We are currently measuring the conduction mechanism in these contact structures in order to further elucidate their properties.

REFERENCES

1. S. Nakamura, M. Senoh, and T. Mukai, Jpn. J. Appl. Phys. **30**, L1708 (1991).

2. S.C. Binari, L.B. Rowland, W. Kruppa, G. Kelner, K. Doverspike, and D.K. Gaskill, Electron. Lett. **30**, 1248 (1994).

3. M.A. Khan, M.S. Shur, and Q. Chen, Electron. Lett. **31**, 2130 (1995).

4. M.A. Khan, J.N. Kuznia, A.R. Bhattarai, and D.T. Olson, Appl. Phys. Lett. **62**, 1248 (1993).

5. S. Nakamura, M. Senoh, and T. Mukai, Appl. Phys. Lett. **62** 2390 (1993).

6. I. Akasaki, H. Amano, M. Kito, and K. Kiramatsu, J. Lumin. **48/49**, 666 (1991).

7. S. Nakamura, M. Senoh, N. Iwasa, and S. Nagahama, Appl. Phys. Lett. **67**, 1868 (1995).

8. J.C. Zolper, A.G. Baca, R.J. Shul, R.G. Wilson, S.J. Pearton and R.A. Stall, Appl. Phys. Lett. **68**, 166 (1996).

9. J.S. Forsei and T.D. Moustakas, Appl. Phys. Lett. **62** 2859 (1993).

10. M.A. Khan, T.N. Kuznia, A.R. Bhattaraia and D.T. Olson, Appl. Phys. Lett. **62** 1786 (1993).

11. S. Nakamura, T. Mukai and M. Senoh, Jpn. J. Appl. Phys. **30** L1998 (1991).

12. S.C. Binari, L.B. Rowland, W. Kruppa, G. Kelner, K. Doverspike and D.K Gaskill, Electron. Lett. **30** 1248 (1994).

13. S. Nakamura, M. Senoh and T. Mukai, Appl. Phys. Lett. **62** 2390 (1993).

14. M.E. Lin, Z. Ma, F.Y. Huang, Z.F. Fan, L.A. Allen and H. Morkoe, Appl. Phys. Lett. **64** 1003 (1994).

15. M.W. Cole, D.W. Eckart, T. Monahan, R.L. Pfeffer, W.Y. Han, F. Ren, C.Yuan, R.A. Stall, S.J. Pearton, Y. Li and Y. Lu, J. Appl. Phys. (in press).

16 A. Durbha, "Study of Ohmic Contacts on Gallium Nitride Thin Films" Master thesis.

17. M.E. Lin, F.Y. Huang and . Morkoc, Appl. Phys. Lett. **64** 2557 (1994).

18. F. Ren, C.R. Abernathy, S.N.G. Chu, J.R. Lothian and S.J. Pearton, Appl. Phys. Lett. **66** 1503 (1995).

19. F. Ren, C.R. Abernathy, S.J. Pearton and P.W. Wisk, Appl. Phys. Lett. **64** 1508 (1994).

20. F. Ren, C.R. Abernathy, S.N.G. Chu, J.R. Lothian and S.J. Pearton, Appl. Phys. Lett **66** 1503 (1995).

21. L.L. Smith and R.F. Davis, in Properties of Group III Nitrides, ed. J.H. Edgar, EMIS Datareview (INSPEC, London 1994).

22. C.R. Abernathy, J. Vac. Sci. Technol. A **11** 869 (1993).

23. C.R. Abernathy, Mat. Sci. Eng. Rep. **14**, 203 (1995).

24. R.J. Shul, S.P. Kilcoyne, M. Hagerott-Crawford, J.E. Parmeter, C.B. Vartuli, C.R. Abernathy and S.J. Pearton, Appl. Phys. Lett. **66** 1761 (1995).

381

TEM STRUCTURAL CHARACTERIZATION OF NM-SCALE ISLANDS IN HIGHLY MISMATCHED SYSTEMS

S. RUVIMOV*# and Z. LILIENTAL-WEBER
Lawrence Berkeley National Laboratory, MS 62-203, Berkeley, CA 94720, # ruv@mh1.lbl.gov

N.N. LEDENTSOV*, M. GRUNDMANN and D.BIMBERG,
Technische Universität Berlin, Hardenbergstr.36, D-10623, Berlin

V.M. USTINOV, A.YU. EGOROV, P.S. KOP'EV, and Zh.I. ALFEROV,
A.F. Ioffe Institute, Politekhniczeskaya 26, 194021, St.Petersburg, Russia

K. SCHEERSCHMIDT, and U. GÖSELE
Max-Planck-Institut für Mikrostrukturphysik, Weinberg 2, D-06120 , Halle/S, Germany

* on leave from A.F. Ioffe Institute, Politekhniczeskaya 26, 194021, St.Petersburg, Russia

ABSTRACT

Transmission electron microscopy has been applied to study the ordering in size and shape of InAs quantum dots and in their lateral distribution. InAs islands were grown by MBE on GaAs substrates at different As-pressures and growth temperatures. Experiments with growth interuption support the theoretical predictions concerning equilibrium island size, shape and arrangement. The stability of the equilibrium dot arrays to changing of growth conditions was studied by varying the deposition temperature, arsenic pressure or growth interruption time. Significant deviation from the optimal As-pressure towards both the lower and higher values was shown to supress the formation of InAs dots resulting either in mesoscopic InAs clusters or 2D corrugated islands. Energy benefit due to the strain relaxation at island edges explains the experimental results better than kinetic consideration.

INTRODUCTION

Spontaneous formation of self-organized nm-scale islands -quantum dots (QDs)- has been reported for the InAs-GaAs system.[1-2] It has been shown that coherently strained (In,Ga)As islands grown by MBE on (001) GaAs substrates allow attainment of a high level of quantum confinement. The islanding is usually considered as a 2D-3D morphology transformation after deposition of 1.7-2 monolayer-thick InGaAs layer (Stranski-Krastanow mode) resulting from either elastic relaxation of the misfit strains[3,4] or kinetics of strain-induced surface roughness.[5,6] Periodic arrays of 3D strained islands were theoretically predicted[7] for a highly lattice-mismatched heteroepitaxy by taking into account the stress relaxation at facet edges and strain-induced renormalization of the surface energy. There is a quite narrow window in growth conditions to produce uniform quantum dots[2,8] that was sometimes considered as an indication of kinetically limited growth.[5,6] However, kinetics is shown to be efficient in providing strain relaxation even through formation of mesoscopic islands.[2] Thus, any role of kinetics in the islanding seems to be secondary. The growth conditions (growth temperature, partial pressures, substrate miscut) are also expected to influence surface reconstruction and, hence, surface energy and stability of an equilibrium island array. Therefore, the study of stability of an equilibrium island array to changes in the growth conditions is a key point in understanding the driving forces for islanding.

In this paper the results of a TEM study of InAs quantum dot arrays grown by MBE at various deposition temperature, arsenic pressure and growth interruption on vicinal (001) GaAs substrates are reported.

EXPERIMENTAL

Samples were grown by molecular beam epitaxy (MBE) using an EP1201 system. After oxide desorption, a 0.5 μm-thick GaAs buffer layer was grown at 600°C, before the substrate temperature was reduced to desirable values (T_d) and the desired amount of InAs was deposited. The nominal thickness of the deposits was varied from 2 to 4 monolayers (ML). The growth rate was about 0.08 nm/s for InAs. The normal arsenic pressure p_0 of $(2-3)10^{-6}$ Torr was varied in the range from $1/6$ p_0 to 5 p_0. The growth temperature is typically 480 °C being varied from 450 to 550°C to study the stability of QD formation. After the deposition of the In-containing layer, two GaAs cap layers of 5 nm and 40 mn in thickness were subsequently grown at T_d and at 600 °C, respectively. In a number of the samples, two cladding superlattices (SL) of (2 nm $Al_{0.3}Ga_{0.7}As$ /2 nm GaAs)n were grown on both sides of the In-containing layer which is inserted into a 14 nm-thick GaAs quantum well.

Transmission electron microscopy (TEM) was carried out using JEOL JEM1000 and JEM4000EX microscopes. Both plan view and cross-sectional specimens were prepared for TEM studies. Low temperature photoluminescence (8 K) was used to characterize the luminescence properties of the dots in the samples under consideration.

RESULTS AND DISCUSSION

Equilibrium size and shape of nm-scale islands

Scattering in size and shape for quantum dots reported by different groups raises important questions about equalibrium the geometry of small islands grown in epitaxial systems exhibiting the Stranski-Krastanow growth mode. At a certain critical thickness (~1.7 ML), 3D islands are formed on the initially 2D InAs coverage or (wetting layer) to decrease the strain energy caused by the high lattice-mismatch between InAs and GaAs (7%). This results in the energy reduction due to the difference between the total energies of the system before and after relaxation. Total energy decreases for critical island size because the increase of surface energy is less than the decrease of strain energy due to islanding.
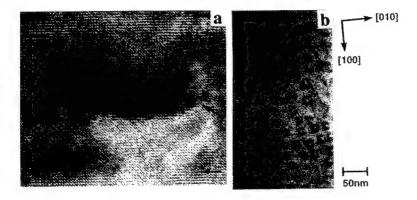
Fig.1   InAs quantum dots in GaAs: HREM cross-sectional image of single QD (a) and plan view TEM micrograph of quantum dot array (b)

Finite element analysis shows that the top of the islands is elastically relaxed while strain is concentrated at the bottom of the island. Therefore, maximum energy gain due to the relaxation occurs for pyramidal-shaped islands. It is about 60% of the total energy of a pseudomorphic strained layer for an angle of side facet of 45°. For comparison, a facet angle of 5° corresponds to the energy gain of only 8%. This also suggests that formation of coherent pyramid-like islands is more energy favorable than that of truncated pyramids as the material at the top of pyramid is relaxed to the greatest extent. The maximum strain is located at the edges and corners of the island. The wetting layer is in biaxial compression.

Under appropriate growth conditions the pyramid-like shape of islands can be maintained during the subsequent deposition of GaAs. A typical HREM image of an InAs quantum dot is shown in Fig.1a. Pyramid-like InAs island with 14 nm in base length and 7 nm in hight is embedded in the GaAs active layer which is in between two cladding superlattices of (2 nm $Al_{0.3}Ga_{0.7}As$ /2 nm $GaAs)_{10}$. Strain-induced contrast significantly influences the image, but the pyramidal shape of the island is still visible. A correspondent plan view image of this heterostructure is shown in Fig.1b which demonstrates an ordering of the islands in both shape and size. Each island has a square base and they are locally arranged in a two dimensional square lattice with main axes along <100> crystallographic directions. The square base of the island can be understood by taking into account elastic anisotropy of the cubic GaAs substrate which has lowest stiffness along <100> and <010> crystallographic directions. Repulsive interaction of islands via the strained substrate results in their tendency to order. In addition, the ordering in size leads to high uniformity of quantum dot arrays due to reduction of surface energy of island facets caused by volume strain relaxation. Thus, it can be energetically favorable for strained 3D system to keep the characteristic size of the island because it reduces the total surface energy. According to our calculations, the total energy of the system has a minimum for particular size which depends on material parameters.[7]
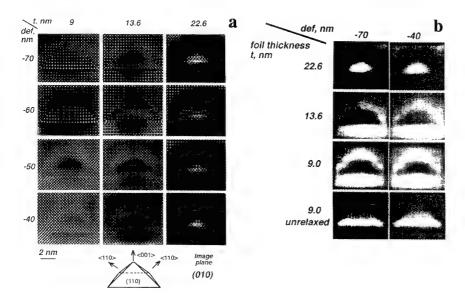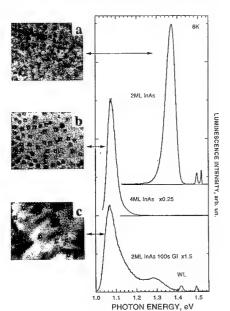
Fig.2.   Simulated HREM (a) and bright-field TEM images (b) of pyramidal InAs dot in GaAs in cross-sectional foil.

<u>TEM/HREM imaging of quantum dots</u>

While AFM suffers from the possibility of dot shape modification during cooling, TEM enables us to study laser structures and to compare directly structural and luminescence properties of QDs. However, strain-induced contrast strongly affects the dot image on TEM micrographs, and optimization of imaging conditions is required to visualize a true shape and size of the quantum dots. Molecular Dynamics calculations have been applied to model the atomic displacement field of an InAs island and GaAs matrix. The calculations were carried out using the CERIUS program package (Molecular Dynamics Inc., Cambridge) detailed elsewhere.[9] A pyramid-like InAs island was chosen having a base length a of 6 nm. The total number of atoms in the model is $2 \cdot 10^4$. The atomic displacement field has then been used for simulations of HREM images at different foil thicknesses and defoci shown in Fig.2a. One can see that an increase of foil thickness significantly affects the image due to strain-induced contrast so that the true size and shape of the island can hardly be resolved at foil thickness larger then 2a. Besides, the island contrast is clearly seen at a certain defoci range (60-70 nm for the JEOL 4000EX microscope with $C_S=1$ mm) where the chemical contrast difference is most pronounced. Detuning from these optimal imaging conditions will result in the over or under estimation of QD size. Conventional TEM images of QDs are affected by strain even more strongly. Fig.2b shows calculated bright-field images taken at symmetrical Laue orientation for the same model. Contrast depends on foil thickness, but is independent on defoci. Even for thin foils, the shape of the dot can hardly be resolved. However, the size of the dot can be determined if the thickness of the foil is not larger then 2a. Similar results were carried out for plan view imaging.

<u>Experiments with growth interruption</u>

Fig.3 shows PL spectra and plan-view TEM images of the samples with 2 ML (a, c) and 4 ML InAs (b) deposited at 480°C with standard ~$2 \cdot 10^{-6}$ torr arsenic pressure (P_{As}).
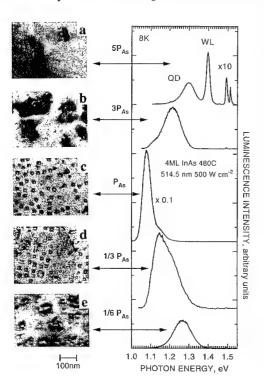
No growth interruptions were introduced in cases (a) and (b). Sample (c) was deposited with submonolayer (0.3 ML InAs) growth cycles separated by 100 s long growth interruptions. Dots formed after the critical layer thickness is just exceeded are small, mostly do not show well resolved crystalline shape, and exhibit large size dispersion. Smaller size of the dots in the case of the 2 ML sample agrees well with a strong shift of the corresponding PL line towards higher photon energies.

Fig.3. Plan-view bright-field TEM images and PL spectra of InAs quantum dots corresponding to 2 ML (a,c) and 4 ML (b) coverage without (a,b) and with (c) growth interruption.

Since the shape of the dots is different for 2 ML and for 4 ML InAs depositions one might question the existence of an equilibrium shape of the dots. We have found that the introduction of a growth interruption 40 s (10 s) after the InAs is deposited is enough to let the dot reach its equilibrium size for 2.5 ML (3 ML) InAs deposition. Large clusters and dislocations do not appear in this case. With very long growth interruptions (sample c) one can even force 2 ML dots to reach the equilibrium size. For this interruption time (10 min total) the wetting layer starts to decompose, resulting in appearance of large clusters. However, the size of the dot approaches the equilibrium size (see Fig. 3 c) and the PL peak coincides in energy with 4 ML InAs PL peak at ~1.1 eV. Thus, the growth interruption experiments confirm the equilibrium nature of the dot array.

Influence of As-pressure and deposition temperature on the formation of quantum dots

Fig. 4 demonstrates the influence of arsenic pressure on dot formation and of PL spectra (4 ML InAs, no growth interruptions). At optimal arsenic pressure of $p_0 \sim 2 \cdot 10^{-6}$ torr and growth temperature of 480 °C (Fig. 4 c) equilibrium dots of high density ($\sim 5 \cdot 10^{10}$ cm^{-2}) are formed. The dot array is stable in the range of ± 50% of the arsenic pressure fluctuations (growth window).

Increase in As pressure by a factor of 3 ($3p_0$) results in dramatic changes of the growth mode (Fig. 4 d). The size of the dots reduces dramatically and a high concentration of large ($\sim$500-1000 Å) relaxed InAs clusters appears. Accordingly the PL peak shifts towards shorter wavelengths due to increased carrier confinement energies in small coherent InAs dots. Further increase in arsenic pressure ($5 p_0$, Fig. 4, e) even completely suppresses the dot formation and only macroscopic InAs clusters can be resolved on the featureless InAs wetting layer. PL emission is dominated by the wetting layer ($\sim$1.5 ML InAs) peak at low temperatures and no dot emission may be resolved at 300K. The integral intensity of PL strongly degrades in agreement with the formation of large relaxed (dislocated) islands.

Fig.4.Plan-view bright-field TEM images and PL spectra of InAs quantum dots corresponding to different As-pressure: $5p_0$ (a), $3p_0$ (b), p_0 (c), $1/3p_0$ (d) and $1/6p_0$(e).

Reduction of arsenic pressure influences the dots in a different way. As shown in Fig. 4 b ($1/3 p_0$), the dots undergo local "melting" and macroscopic 2D InAs islands appear. The lateral

size of remaining dots is weakly affected. Further reduction in arsenic pressure ($1/6p_0$, Fig. 4 a) results in practically complete disappearance of dots in favor of macroscopic 2D InAs islands. For these growth conditions which are close to "virtual surfactant epitaxy", the RHEED pattern is streaky. No macroscopic 3D InAs clusters are formed in this case. The PL peak shifts towards higher energies and broadens as the InAs arrangement resembles a highly nonuniform corrugated 2D layer. However, the integral PL intensity strongly drops, as it was the case for the growth at high As pressure.

We emphasize that both low and high arsenic pressures result in macroscopic surface structures (~1000 Å). For the highest arsenic pressure, InAs clusters are separated by 0.2 - 1 µm. This indicates that growth kinetics do not play any important role, particularly not for equilibrium dots having a size of ~120-140 Å and a typical separation of 250-350 Å. Moreover, we have found that the RHEED pattern converts from spotty to streaky within several seconds if the As flux is interrupted and 0.15 ML of pure indium is deposited even after the 3D dots are formed (4 ML InAs deposition under the optimal As pressure).

An increase of substrate temperature from 480 °C to 520 °C keeping the arsenic pressure at p_0 results in an increase of the lateral size of the dot to ~180 Å and in a strong decrease of dot density (down to $\sim 1.5 - 2 \cdot 10^{10}$ cm^{-2}). The dot lateral shape (well-defined square) is not affected. Large clusters appear locally. PL peak position shifts slightly (~30-50 meV) towards higher energy with respect to PL line for 480 °C growth indicating that the increase of the lateral size is compensated by the reduction of the dot height and the facet angle.

In conclusion, our results suggest the modification of surface reconstruction with the changes of growth conditions which lead to a change of the facet surface energy. Since the stability of the equilibrium dot array strongly depends on the facet surface energy we can expect that significant change in growth parameters influences the stability of the dot array. Thus, energy benefit due to the strain relaxation at the island edges and strain-induced renormalization of the surface energy are the driving forces responsible for quantum dot formation.

AKNOWLEDGEMENT

REFERENCES

1. L. Goldstein, F. Glas, J.Y. Marzin, M.N. Charasse, and G. Le Roux, Appl. Phys. Lett. **47**, 1099 (1985)
2. N.N. Ledentsov, M. Grundmann, N. Kirstaedter, J. Christen, R. Heitz, J. Böhrer, F. Heinrichsdorff, D. Bimberg, S.S. Ruvimov, P. Werner, U. Richter, U. Gösele, J. Heydenreich, V.M. Ustinov, A.Yu. Egorov, M.V. Maximov, P.S. Kop´ev and Zh.I. Alferov, *Proc. of the 22nd International Conference on the Physics of Semiconductors*, Vancouver, Canada, 1994, D.J. Lockwood, ed. (World Scientific, Singapore, 1995), vol. **3**, 1855
3. S. Guha, A. Madhukar, and K.C. Rajkumar, Appl.Phys.Lett. **57**, 2110 (1990)
4. D.J. Eaglesham and M. Cerullo, Phys.Rev.Lett. **64**, 1943 (1990)
5. C.W. Snyder, B.G. Orr, D. Kessler, and L.M. Sander, Phys.Rev.Lett. **66**, 3032 (1991)
6. B.G. Orr, D. Kessler, C.W. Snyder, and L. Sander, Europhys.Lett. **19**, 33 (1992)
7. V.A. Shchukin, N.N. Ledentsov, P.S. Kop´ev, and D. Bimberg, Phys. Rev. Lett. **75**, 2968 (1995)
8. S. Ruvimov, P. Werner, K. Scheerschmidt, U. Gösele, J. Heydenreich, U. Richter, N.N. Ledentsov, M. Grundmann, D. Bimberg, V.M. Ustinov, A.Yu. Egorov, P.S. Kop´ev, and Zh.I. Alferov, Phys.Rev. **B 51**, 14766 (1995)
9. S. Ruvimov and K. Scheerschmidt, Phys. St. Sol. (a) **150**, 471 (1995)

GROWTH OF EPITAXIAL GaN FILMS USING ZnO BUFFER LAYER BY PULSED LASER DEPOSITION

T. F. HUANG, E. TUNCEL, J. S. YEO* AND J. S. HARRIS JR.
Solid State Electronics Laboratory, CIS 126, Stanford University, CA 94305.

*Department of Materials Science and Engineering, Stanford University, CA 94305

ABSTRACT

GaN films and ZnO buffer layers have been deposited on c-cut sapphire substrates by pulsed laser deposition (PLD) employing a KrF laser ($\lambda = 248$ nm). The influence of the deposition parameters, such as substrate temperature and gas pressure during growth, have been studied. GaN films grown above 700 °C are single crystalline and the full width of half-maximum (FWHM) of the GaN (0002) peak decreases to 0.37° as the growth temperature increases to 800 °C. The optimum growth pressure for GaN is determined to be 0.01 torr N_2. The optical transmission below the bandgap of the GaN film grown at this pressure is over 85%.

INTRODUCTION

GaN is a III-V direct band gap semiconductor with enormous potential for optoelectronic device applications in the blue, violet and near-ultraviolet spectra. High quality GaN films have mostly been prepared by metal-organic vapor phase epitaxy (MOCVD)[1, 2] and molecular beam epitaxy (MBE).[3] A great deal of research has been done in understanding the growth kinetics and the properties of the GaN films grown by these two techniques. Recently, Nakamura[2] has successfully demonstrated a blue laser diode from III-V nitride materials.

Compared to the MOCVD and MBE techniques, pulsed laser deposition (PLD)[4,5] is a relatively new growth technique used widely for the growth of oxide thin films, such as ferroelectrics and superconductors. There has been very little III-V nitride growth[6] using the PLD technique. However, several advantages of the PLD approach for depositing high quality thin films make it interesting to study III-V nitrides grown by PLD. The congruent ablation achieved with short UV-laser pulses allows deposition of a multicomponent material by employing a single target. This advantage makes PLD very suitable for growing muitilayer structures sequentially in the same chamber and investigating the effect of various buffer layers. The growth rate of PLD can be varied from 0.1 Å/sec to 1μm/hr through adjusting the repetition rate of the laser, which is useful for both atomic level investigations and thick buffer layer growth. Moreover, the strong nonequilibrium growth conditions of PLD may allow a much broader range of metastable materials to be grown, including introduction of higher dopant concentrations and alloy compositions that phase segregate.

In this paper, we have investigated the optimum growth conditions for ZnO buffer layers and GaN films. ZnO is chosen as a buffer layer because of the smaller lattice mismatch of 2% between ZnO and GaN compared to other substrates.[7]

DEPOSITION CONDITIONS

ZnO and GaN films have been deposited on c-cut sapphire substrates using the pulsed laser deposition (PLD) setup described previously.[8] A KrF excimer laser operating at a wavelength of 248 nm, a pulse duration of 20 ns and laser fluences ranging from 3.0 - 5.0 J/cm^2 was used. The laser repetition rate was 5 Hz and the target-substrate distance was varied from 4 to 6.5 cm. Light yellow ZnO targets were prepared by pressing and sintering ZnO powder of 99.999% purity at 1100 °C for three hours. ZnO films were deposited in an oxygen partial pressure of 0.01 torr between 400 and 650 °C. A pressed pellet of dark gray GaN powder with 99.9% purity was used as a target. A range of substrate temperatures between 400 and 800 °C and nitrogen partial pressure of 10^{-4} - 0.45 torr were investigated for GaN growth. The target was rotated to ensure uniform ablation and the substrate was rotated to enhance the temperature and thickness uniformity during deposition.

RESULTS

ZnO/sapphire

From x-ray diffraction studies (θ-2θ, ω, ϕ scans), the ZnO films are single crystalline at the growth temperature of 400-650 °C despite the high lattice mismatch between ZnO and sapphire. The epitaxial relationships are ZnO[0001]//Al$_2$O$_3$[0001] and ZnO[10-10]//Al$_2$O$_3$[[11-20]. The optimum growth temperature is 550 °C with a FWHM of ZnO (0002) peak of 0.35°. Figure 1 is the photoluminescence (PL) spectra of the ZnO film grown at 550 °C. The film is excited by He-Cd laser at 77K. The near-band-edge (NBE) emission peak appears at 3.34 eV with the FWHM of 89 meV.
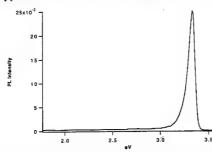
Figure 1: 77K photoluminescence spectra of the ZnO film grown at 550 °C

GaN/sapphire

The influence of two essential deposition parameters, substrate temperature and nitrogen partial pressure on the properties of GaN films have been studied. We examined a wide range of growth temperature from 400 to 800 °C in a nitrogen partial pressure of 0.01 torr N2. As shown in Figure 2, the films deposited under 400 °C were found to be

essentially amorphous, with no sharp XRD peaks of GaN. Between 400 and 600 °C, the films gradually became crystalline and are mainly c-axis oriented. Above 700 °C, the films are single crystalline with strong GaN(0002) peaks. From ϕ scans, the epitaxial relationship between GaN and sapphire, GaN[10-10]//Al$_2$O$_3$[11-20], is found to be the same as the relationship of ZnO/Al$_2$O$_3$. Only six (11-22) peaks are observed during 360 degree scan, indicating single crystal GaN films.
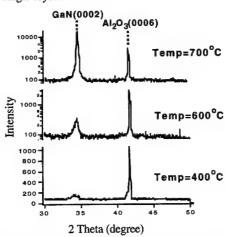
Figure 2: X-ray 2θ-scans of GaN on sapphire indicating the effect of the substrate temperature on crystallinity

In order to optimize the growth temperature, the FWHM of GaN (0002) peaks for the films grown between 675 to 800 °C were measured by x-ray ω scans. As shown in Figure 3, the FWHM is 0.58° for the films grown below 725 °C and the values decrease with increasing temperature. At 800 °C, best crystallinity is obtained with a FWHM of 0.37°. This tendency suggests the crystalline quality is greatly improved at higher temperature growth.
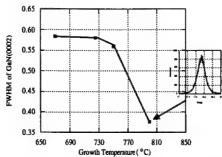
Figure 3: FWHM of GaN(0002) peaks vs. growth temperatures

The dependence of crystalline quality, in terms of the FWHM of GaN (0002), on the nitrogen pressure during growth was investigated for the films deposited at 725 °C with nitrogen pressures varying from 10^{-4} to 0.45 torr. As shown in Figure 4, films grown over a broad nitrogen pressure range of 10^{-4}-0.2 torr exhibit sharp GaN(0002) peaks in 2θ scans and the values of FWHM of GaN(0002) peaks are between 0.58° and 0.63°, indicating that the crystalline quality of GaN films does not strongly depend on the nitrogen pressure. At a nitrogen pressure of 0.45 torr, no GaN peak is observed at any target-substrate distance. As a result, the nitrogen pressure of 0.45 torr is the upper pressure limit for GaN growth by PLD.
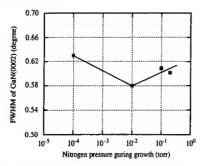
Figure 4: FWHM of GaN(0002) peaks vs. nitrogen pressure during growth

While the nitrogen pressure has relatively small effect on the mechanical properties, it appears to have a very strong effect upon the optical and electronic properties. The color of the films grown at 10^{-4} torr is gray while the films grown in the range of 10^{-2} torr are more transparent. As the growth pressure increases to 0.45 torr, the films become yellowish and there are more particulates on the surface of the films. The transmission spectrum of GaN films grown at 725 °C under different nitrogen pressures are taken between the wavelengths of 180 nm to 3200 nm. Figure 5 is the maximum transmission (%) of the films vs. nitrogen pressure during growth. The GaN film grown at 0.01 torr nitrogen has the highest transmission of 87% and the transmission drops to approximately 60% at higher or lower nitrogen pressure. Therefore, we conclude that adding nitrogen gas with the order of 0.01 torr can improve the optical properties GaN films.
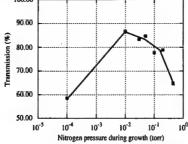
Figure 5: The maximum transmission of GaN films vs. nitrogen pressure during growth

GaN/ZnO/sapphire

A thin ZnO film with a thickness of 15 nm was deposited at 550 °C at 0.01 torr oxygen pressure as a buffer layer. After pumping out oxygen, GaN is sequentially grown at 750 °C under 0.01 torr nitrogen pressure. Figure 6 shows a θ-2θ pattern for a GaN/ZnO/sapphire multilayer structure. The theoretical 2θ position of GaN(0002) is only 0.183° from the ZnO(0002) peak, thus the peaks of both films are not resolved in this scan. From the rocking curve analysis, the FWHM of GaN(0002)/ZnO(0002) is found to be 0.51°. Phi scans of the GaN(11-22) and Al$_2$O$_3$(11-23) peaks are shown in Figure 7. The GaN films grown on ZnO/sapphire is rotated 30° with respect to the sapphire substrate.

Figure 6: X-ray 2θ-scan of GaN grown at 750 °C under 0.01 torr nitrogen pressure on ZnO/sapphire
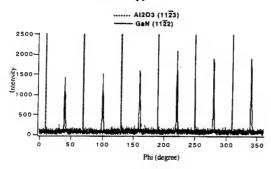
Figure 7: X-ray phi scans on the (11-22) plane of GaN and the (11-23) plane of sapphire

The transmission spectra of the GaN/ZnO/sapphire multilayer is given in Figure 8. The interference fringes mainly come from the GaN film, since the ZnO film is too thin to produce interference fringes. A steep fall-off at 368 nm gives an estimated band-gap energy for GaN at 3.37 eV. Taking n = 2.35 for GaN, the thickness (t) of the film can be estimated to be 420 nm from the relationship $t=1/2n\Delta$, where n is the refractive index and Δ is the fringe period. The corresponding growth rate of GaN is approximately 0.12 Å/pulse.
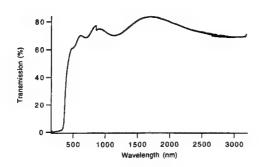
Figure 8: The transmission spectrum of the GaN film between 180 nm and 3200 nm

CONCLUSIONS

Single crystalline ZnO layers are grown on a c-cut sapphire substrate by PLD at a temperature of 550 °C and oxygen partial pressure of 0.01 torr. From the PL measurement at 77K, near-band-edge emission is observed at 3.34 eV with a FWHM of 89 meV.

Substrate temperature and nitrogen partial pressure are found to be critical for the growth of GaN films on sapphire substrates by PLD. Below 400 °C, the films are amorphous but the crystallinity is greatly improved with increasing substrate temperature. Single crystal GaN films are obtained above 700 °C. The FWHM of GaN(0002) peak decreases with increasing temperature and 0.37° is obtained for a film grown at 800 °C and 0.01 torr nitrogen. From the transmission spectra, the optimum nitrogen pressure during growth appears to be at 0.01 torr. For growth pressures as low as 10^{-4} torr, the GaN films are of poor quality. For the films grown at 725 °C under a nitrogen pressure of 0.01 torr, greater than 80% transmission is obtained At 0.45 torr, the films are yellow with more particulates on the surface of the films .

At 750 °C and 0.01 torr nitrogen, a single crystal GaN film was grown on a sapphire substrate with a thin ZnO buffer layer. The transmission spectra estimates the band-gap energy of 3.37 eV and the thickness of 420 nm for the GaN film, which corresponds to the growth rate of 0.12 Å/pulse.

REFERENCES

1 S. Nakamura, T. Mukai, and M. Senoh, Appl. Phys. Lett. 64, 1687 (1994)
2 S. Nakamura et al., Jpn. J. Appl. Phys. (1996)
3 D. B. Oberman, H. Lee, W. K. Gotz and J. S. Harris, Jr., J. Cryst. Growth 150, 912 (1995)
4 J. Cheung and J. Horwitz, MRS Bulletin, Feb. 1992
5 Rajiv K. Singh and J. Narayan, Phys. Rev. B 41, 8843 (1990)
6 R. D. Vispute, J. Narayan, Hong Wu, K. Jagannadham, J. Appl. Phys. 77, (1995)
7 T. Detchprohm, K. Hiramatsu, H. Amano, I. Akasaki, Appl. Phys. Lett. 61, 2688 (1992)
8 S. Schwyn Thony, K. E. Youden, J. S. Harris Jr. and L. Hesselink, Appl. Phys. Lett. 65, 2018 (1994)

THEORETICAL STUDY OF InAsSb/InTlSb SUPERLATTICE FOR THE FAR INFRARED DETECTOR

S. Iyer*, S. Chowdhury-Nagle*, J. Li*, and K.K. Bajaj**
*Dept. of EE, North Carolina A&T State University, Greensboro, NC 27411, iyer@ncat.edu
**Department of Physics, Emory University, Atlanta, GA 30322, phskkb@physics.emory.edu

ABSTRACT

We propose a novel superlattice (SL) $InAs_ySb_{1-y}/In_xTl_{1-x}Sb$ lattice matched to InSb for a potential application as an infrared detector material in the 8-12 μm wavelength range. We report on the results of energy band calculations for this SL using the modified Kronig-Penney model. Our preliminary calculations indicate that $InAs_{0.07}Sb_{0.93}/In_{0.93}Tl_{0.07}Sb$ would exhibit a type-I SL with conduction band offset of 34 meV and valence band offset of 53 meV at 0K. Due to the lack of accurate information on material parameters, namely, energy offsets and effective masses of InTlSb, these were estimated by comparison with the behavior of HgCdTe system. The theory predicts three heavy hole subbands and one partially confined electron in the 30Å $InAs_{0.07}Sb_{0.93}$/100Å $In_{0.93}Tl_{0.07}Sb$ SL. The band gap of the SL was computed to be 0.127 eV (9.7 μm). It is expected that this SL will allow improvements in the InTlSb epilayers' structural quality as it will be sandwiched between higher quality zincblende InAsSb layers.

INTRODUCTION

There is currently an increasing research interest for a III-V based semiconductor materials as an alternate candidate to HgCdTe for long wavelength (8-12 μm) infrared detectors. One possible series of alloys based on InSb, where the lattice could be dilated by heavier elements such as Bi and Tl, are being considered as potential material systems. Alloying with Bi has posed severe problems in the growth due to the equilibrium alloy miscibility for Bi concentration necessary to achieve narrower band gap [1]. Alloying with Tl is reported [2] to exhibit similar miscibility problem , however the concentration of Tl required to go beyond 10 μm is comparatively smaller. Preliminary work [3,4] on the growth of these alloys by MOCVD are quite encouraging. Hence, of the two, Tl appears to be a more promising element for alloying.

Though the material parameters for TlSb are not well established, the available data and the preliminary calculations of the band structure [5] strongly suggest a marked similarity between HgTe/CdTe and TlSb/InSb systems. Here we propose a new InAsSb/InTlSb superlattice structure on InSb substrate. Many of the physical parameters needed for the computation of hetrostructure such as band offsets and effective masses were estimated from the comparison of the above two alloy systems.

Our preliminary calculations indicate that the proposed structure would exhibit a type I superlattice. The subband structures in $InAs_ySb_{1-y}/In_xTl_{1-x}Sb$ system were calculated by using the modified version of Kronig-Penney model developed by Cho and Prucnal [6] where Bastard's boundary condition was adopted. Calculations have been made for the heterostructure compositions of $y = 0.07$ and $x = 0.93$, which corresponded to the band gap in the wavelength region of 10 μm.

ESTIMATION OF THE PHYSICAL PARAMETERS

In this section a brief review of the similarity between HgCdTe and InTlSb system is presented. The choice of the compositions constituting the superlattice, and the estimation of different parameters required for the energy band calculations of the InAsSb/InTlSb superlattice is described below.

Similarities Between HgCdTe and InTlSb System

Although TlSb has been predicted to slightly favor the CsCl over zincblende structure, alloys of InTlSb towards InSb corner of the phase diagram with Tl content less than 15%, are expected to exhibit a stable zincblende phase with a direct band gap at the Γ point [2,5]. TlSb with zincblende phase is predicted to exhibit a negative band gap. Chen et al. [5] calculated the band gap using local density approximation (LDA) which was found to be in good agreement with the estimated value obtained from tight binding calculations. The inversion to negative gap was found to be -1.5 eV, and the valence band offset in the InSb/TlSb system was predicted to be 20% of the band gap difference, which correlates well with that observed in HgCdTe system. The difference in the band gap between the two end binary compounds in the two alloy systems is also the same ~ 1.8 -1.9 eV. Chen et al. [5] also calculated the energy band structures for HgCdTe and InTlSb alloys at both compositions corresponding to an energy gap of 0.1 eV at zero temperature by using a hybrid psuedopotential tight-binding method. It was found that the two alloys have very similar band structures at this band gap, with similar band gap variation as a function of alloy concentration. Approximately linear shift in band gap with concentration has been predicted for both of these alloys [5]. Thus, all the available evidences suggest strong similarity in the electrical and optical properties of these two systems.

Composition and Thickness of the Epilayers

The composition of the InTlSb alloy was chosen for an energy gap corresponding to a wavelength of 10 μm. This composition corresponded to a Tl content of 7% which was estimated from the linear interpolation of the band gap from TlSb (Eg $_{TlSb}$ = -1.5 eV [2,5]) to InSb (Eg $_{InSb}$ = 0.236 eV).

The thickness of the well (In$_{0.93}$Tl$_{0.07}$Sb) and the barrier (InAs$_{0.07}$Sb$_{0.93}$) were calculated so that the entire superlattice is lattice matched to InSb. The thickness of the well and the barrier were thus determined to be 100 Å and 30 Å, respectively.

The Effective Mass

The effective mass variations with band gap are predicted to be similar for both Hg$_{1-x}$Cd$_x$Te and In$_x$Tl$_{1-x}$Sb [5]. The effective mass in HgCdTe decreases with x up to a zero band gap, thereafter increases linearly with composition shift towards CdTe [7]. The zero band gap composition in InTlSb was thus predicted to occur at x = 0.884. We assume that the effective mass of InTlSb alloy interpolate linearly between the end points x = 0.884 and x = 1. Thus the effective mass at the desired composition of x = 0.93 was determined (m*/m = 0.0139 at 0K). This calculated electron effective mass in InTlSb is very close to that of InSb. Hence, the hole effective mass in InTlSb has been assumed to be the same as that of InSb.

Band Offsets

Finally, the band offsets were determined from estimating the band offsets of the two individual alloys with respect to InSb independently as discussed below and thereby calculating the band offsets between the two desired alloy system.

The valence band maximum of $InAs_{0.13}Sb_{0.87}$ has been reported [8,9] to be 47 meV lower than that of InSb. Assuming that the same fraction of the band gap decrease will be accommodated by the valence band offset in $InAs_{0.07}Sb_{0.93}$/InSb system, the latter is determined to be 29 meV with the valence band maximum of $InAs_{0.07}Sb_{0.93}$ being lower. The valence band offset of InTlSb/InSb is small ~ 20% as per the predictions of Chen et al. [5] and hence the conduction band offset should account for the most of the band gap difference. The valence band maximum of $In_{0.93}Tl_{0.07}Sb$ was thus determined to be 24 meV above that of InSb. As the transitivity property is a common feature and well proven for this class of materials, the valence band offset between $InAs_{0.07}Sb_{0.93}$ and $In_{0.93}Tl_{0.07}Sb$ was estimated to be approximately 53 meV.

Figure 1 illustrates the energy positions of the these two alloys with respect to InSb. As is evident from Fig. 1, InAsSb/InTlSb energy band should be a type I configuration.

Although these are just estimates on the band offsets of $InAs_{0.07}Sb_{0.93}$/$In_{0.93}Tl_{0.07}Sb$, we believe that the nature of the superlattice will remain unaltered and the basic conclusion derived thereof will remain valid. Further, HgCdTe/CdTe superlattice with similar band gaps is also type I superlattice.
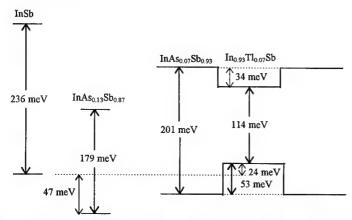
Fig. 1. Energy levels of the conduction and valence bands of the different alloys relative to InSb.

RESULTS

Modified Kronig-Penney formalism [6] with only one boundary condition (Bastard's) at the substrate epilayer interface has been used for the subband energy calculations. This formalism yields envelope wave function corresponding to the minimum and maximum energies of each band. The computations of the band edges by this method are considerably simpler and in the case of GaAlAs/GaAs superlattice, it has been shown [6] to yield results in good agreement with those obtained by conventional Kronig Penny model.

As shown in Fig. 2, calculations on InAsSb/InTlSb superlattice yielded confinement of the first three heavy hole subbands. These subbands were located at 4.9 meV, 19.1 meV and 40.6

meV respectively, deep in the valence band, with a corresponding increasing band width of 0.09 meV, 4.1 meV and 11.2 meV. Only partial electron confinement was obtained in the conduction band with the minimum energy of 7.7 meV. The resultant energy gap of the superlattice thus determined was 127 meV corresponding to 9.7 μm in wavelength.

Due to the presence of high quality InAsSb layers in this lattice matched SL, it is expected that the structural quality of the system should be superior to that of bulk InTlSb, as latter is reported [10] to be a difficult material to grow. Though our focus was on the wavelength close to 10 μm, wavelength over somewhat wider region could be achieved in principle, by varying the layer thickness and the composition of the alloys.

InAs$_{0.07}$Sb$_{0.93}$

In$_{0.93}$Tl$_{0.07}$Sb
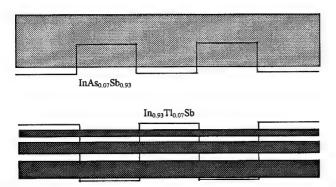
Fig. 2. Conduction and valence subband profiles of the InAsSb/InTlSb type I superlattice.

CONCLUSIONS

In conclusion, InAsSb/InTlSb SL lattice matched to InSb is predicted to exhibit a type I energy band configuration, a desirable result. The SL band gap falls well into the 8-12 μm infrared wavelength region. Three valence subband confinements and a partial conduction subband confinement have been predicted in this SL.

ACKNOWLEDGMENTS

REFERENCES

1. A.J. Noreika, W.J. Takei, M.H. Francombe, and C.E.C. Wood, J. Appl. Phys. 53, 4932 (1982).
2. M.V. Schilfgaarde, A. Sher, and A.B. Chen, Appl. Phys. Lett. 62, 1857 (1993).
3. P.T. Staveteig, Y.H. Choi, G. Labeyrie, E. Bigan, and M. Razeghi, Appl. Phys. Lett. 64, 460 (1994).
4. Y.H. Choi, C. Besikci, R. Sudharsanan, and M. Razeghi, Appl. Phys. Lett. 63, 361 (1993).
5. A.B. Chen, M.V. Schilfgaarde, A. Sher, J. Electron. Mater. 22, 843 (1993).
6. H.S. Cho and P.R. Prucnal, Phys. Rev. B 36, 3237 (1987).

7. P.W. Kruse in <u>Semiconductors and Semimetals</u>, edited by W. Beer, Academic Press, New York, 1981, p. 9-10.
8. S.R. Kurtz, Mater. Res. Soc. Symp. Proc. 216, 163 (1991).
9. S.R. Kurtz and R.M. Biefeld, Phys. Rev. B 44, 1143 (1991).
10. C.E.C. Wood, A. Noreika, and M. Francombe, J. Appl. Phys. 59, 3610 (1986).

SURFACE PASSIVATION OF GaAs-BASED PHEMT BY HYDROGEN ION IRRADIATION

Song S. Shi*, Ying-lan Chang**, Evelyn L. Hu*, and Julia J. Brown***
*Center for Quantized Electronic Structures (QUEST) and Department of Electrical and Computer Engineering, University of California, Santa Barbara, CA 93106, stone@engrhub.ucsb.edu
** Hewlett -Packard Laboratories, Palo Alto, CA 94303-0867
*** Hughes Research Laboratories, Malibu, CA 90265

ABSTRACT

Surface passivation is a key issue in compound semiconductor device technology. The high density of surface states on unpassivated surfaces can lead to excessive non-radiative recombination at the surface, affecting optical devices, or provide leakage and low-field breakdown in electronic devices. Our previous studies on low energy, low-dose hydrogen ion treatment carried out at room temperature showed long-term improvement in the optical properties of near surface quantum wells. We have accordingly applied this process to GaAs-based pseudomorphic HEMTs (PHEMT) in order to improve their power performance. Although our process is designed so that the hydrogen reactions are confined to the surface of the substrate, a critical factor in the success of this treatment is the extent of in-diffusion of the hydrogen, and the possibility of dopant passivation. PHEMT structures were hydrogenated at various conditions and both Hall mobility and carrier density were monitored. For a low hydrogen ion dose (3×10^{16} cm^{-2}) at 80 eV energy, some degradation of Hall mobility and carrier density was noted after the treatment, but full recovery of both parameters was achieved after a 400°C thermal anneal. Much higher hydrogen doses resulted in severe degradation of mobility and carrier density, which were only partially recovered after thermal anneal. Measurements on actual PHEMT devices showed an approximately 15% decrease in the transconductance, and in addition, a 60% decrease in the gate-to-drain leakage current after irradiation with 80 eV hydrogen ions at a dose of 3×10^{16} cm^{-2}. The decrease of the leakage current indicates that passivation is taking place. The decrease of the transconductance suggests that hydrogen may be diffusing into the regions of the dopants. Optimization of the hydrogenation parameters should allow leakage reduction without sacrifice of transconductance.

INTRODUCTION

GaAs-based pseudomorphic HEMTs (pHEMTs) have been pursued for both low noise and high power device applications. The device has met with limited success as a power device, largely due to irreproducible high gate-drain breakdown voltages [1] and "power slump" phenomena [2]. Both of these effects have been attributed to the presence of surface states[2,3] which change the potential between gate-drain and gate-source electrodes. Although a variety of wet and gas-phase passivation treatments have been proposed and demonstrated , the results of such treatments have generally been short-lived and difficult to reproduce [4,5].

Our earlier studies of hydrogen ion passivation involved luminescence measurements of undoped, near-surface quantum wells such as that shown in the inset of Figure 1. Our assessment of passivation was linked to the enhanced photoluminescence of the hydrogen ion treated-QW1. Such an enhanced luminescence was found to be stable over a period of 3 years[6, 7]. Based on numerous studies of those structures, using *in situ* Auger [8] and Temperature Programmable Desorption (TPD)[7], we believe that the role of the hydrogen ions is to react with excess arsenic in the material, removing it in the form of arsine. Such excess arsenic can form As_{Ga} antisite defects, with characteristic energies situated mid-bandgap. The antisite defects are likely to be responsible for the degradation of pHEMT devices[3]. Since the hydrogen should desorb from the material with the excess As, effective passivation *should not require* that the hydrogen remains

bound to the surface of the semiconductor; this provides hope for longer-term stability of the passivation process and its applicability to passivation of devices. This paper describes such an application of the hydrogenation process to fabricated GaAs-based pHEMT devices and device structures.

EXPERIMENT and RESULTS

Optimal hydrogen ion dose

A critical determinant for successful hydrogen passivation is the amount of hydrogen being introduced into the sample. Too low a dose may not be sufficient for removal of the As antisite defects, leaving the surface unpassivated; exceeding the optimal hydrogenation dose may introduce excess hydrogen into the material structure, which can lead to a degradation of material quality. This is evident from Figure 1, which plots the normalized luminescence intensity of a near-surface quantum well as a function of hydrogenation dose. The peak intensity first rises, then declines, with the maximum luminescence observed for a hydrogen ion dose of 3×10^{16} cm^{-2}. Data like these were used to determine the appropriate hydrogen ion dose to be used in the actual device passivation.
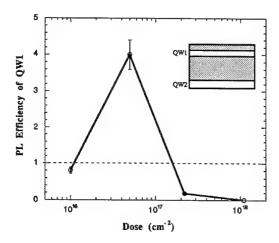
Figure 1. Normalized PL efficiency vs. hydrogen ion dose. The PL intensity for upper 70Å QW1 (see the inset) is normalized to that of deep, 100Å QW2. That value is subsequently divided by the normalized intensity for a reference sample (as-grown). That is, we plot $[I_{QW1}/I_{QW2}]^{hydrogenated}/[I_{QW1}/I_{QW2}]^{ref}$ as function of hydrogenation dose.

Hydrogenation of pHEMT Devices

The pHEMT structure used in this work is shown in Figure 2. The structure is a double δ-doped $Al_{0.24}Ga_{0.76}As/In_{0.15}Ga_{0.85}As/GaAs$ heterostructure grown by MBE. The room temperature

Hall sheet charge and mobility were measured to be 2.0×10^{12} cm^{-2} and 7,800 cm^2/V-s, respectively. The gate recess process was performed by a two-step non-selective etch process using a citric acid-based etchant; the 0.25 µm gates were then formed by e-beam lithography and deposition of Ti/Pt/Au metalization. A source-drain spacing of 3 µm and channel recess width of 1.5 µm were found to result in the best combined dc and RF performance for application as microwave power amplifiers [9].

| n+ GaAs (50Å) |
| AlGaAs (350Å) |
| Spacer AlGaAs (25Å) |
| Channel InGaAs (150Å) |
| Spacer AlGaAs (25Å) |
| Buffer Layer |
| GaAs Substrate |

Si δ Doping
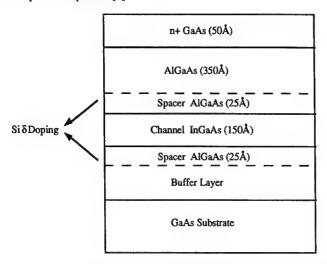
Figure 2. Schematic Drawing of Pseudomorphic HEMT Structure. Al mole composition of all AlGaAs layer is nominally 0.24 and In mole composition in the InGaAs channel is nominally 0.15.

Hydrogenation was carried out in a load-locked hydrogenation chamber with a base pressure of a few times 10^{-8} Torr. The pressure in the chamber rises to 6.5×10^{-4} Torr after introduction of hydrogen gas with a flow rate of ~25 sccm. Hydrogen ions are generated using a Kaufman type ion source, operated at 80 eV with typical beam current density ~ 40 µA/cm^2. The hydrogen ion dose attaining the sample surface was measured through a Faraday cup. All hydrogenation was carried out at room temperature. Device parameters for a typical device, before and after hydrogenation at a dose of 3×10^{16} cm^{-2}, are summarized in Table 1. We note the reduction in transconductance and maximum source-drain current. However, there is also a significant drop in gate-drain 'leakage' current, I_{gd}, that is, the reverse current at a fixed

Hydrogenation	G_m (ms/mm)	I_{max} (mA)	I_{gd} (µA)
Before	345	15.7	-1.10
After	334	14.0	-0.25

Table 1. Summary of characteristics of pHEMT devices before and after hydrogenation at a dose of 3×10^{16} cm^{-2}.

bias (-15V). On the average, the transconductance is reduced by ~20% and the maximum source-to-drain current by ~15%, while the gate-drain current is reduced by as much as ~60%. The

hydrogen treatment has therefore been successful in reducing the leakage current of the device, but apparently also introduces an undesirable reduction in transconductance and I_{ds}.

Hydrogenation of pHEMT Device Structures

In order to better understand these results, and how to improve them, we carried out a series of experiments on device *structures*, rather than the fully-fabricated devices; van der Pauw patterns fabricated into the pHEMT material were used to monitor the mobility and carrier concentration before and after the hydrogenation treatment. Figure 3 shows those date for structures irradiated at 3×10^{16} cm^{-2} (the conditions used for the devices) and at the much higher
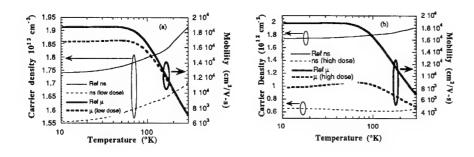
Figure 3. Carrier density and mobility of pHEMT structure vs. temperature prior to and after hydrogenation at different doses (a: 3×10^{16} cm^{-2}; b: 1.1×10^{18} cm^{-2}).

dose of 1.1×10^{18} cm^{-2}. Mobility and carrier density both decrease after hydrogenation, with a more severe decrease at the higher dose. Annealing the samples at 400°C for 5 minutes in a forming gas ambient, restores both mobility and carrier density for the low dose hydrogenation, while at high dose, only the mobility is fully recovered. These data are shown in Figure 4. For hydrogenation at low dose, although the electron mobility (μ) drops slightly at low temperatures,
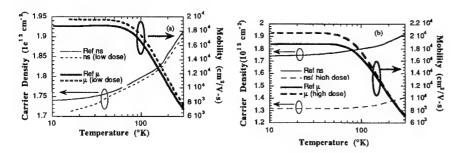
Figure 4. Annealing effects on carrier density and mobility of the hydrogenated pHEMT structure. The hydrogen ions exposures for (a) and (b) are 3×10^{16} cm^{-2} and 1.1×10^{18} cm^{-2}, respectively.

the dependence of μ on temperature remains flat. Ionized impurity scattering produces a greater degradation on the mobility at lower temperatures. The fact that the mobility does not further degrade at low temperatures suggests that the hydrogen ions may have penetrated into the material, located primarily in the region of the δ-doped layer, but not in the InGaAs channel itself. Those hydrogen ions may passivate the Si donors and cause a reduction in the number of carriers made available to the channel. Such a reduction in donor activity upon exposure of n-type bulk GaAs to a hydrogen plasma has been well studied, and it has been found that donors can be reactivated by annealing at temperatures as low as ~400°C [10]. These data motivated our choice of 400°C as the annealing temperature, and our post-annealing results accord well with the earlier studies. On the other hand, the degradation of carrier density and mobility are more severe in the high dose case $(1.1 \times 10^{18} \text{ cm}^{-2})$. The continued decrease in mobility at low temperatures indicates the importance of impurity scattering, perhaps due to H interstitials present in the channel itself.

Posthydrogenation Anneal of the Devices

Posthydrogenation anneal of the actual devices was carried out at 400°C for 5 minutes in a vacuum system of ~mTorr with nitrogen ambient in the hope of restoring the electrical characteristics of the devices without losing passivation effect on the surface. Although the transconductance of the device improved, I_{gd} also returned to its pre-hydrogenation value. Earlier studies of the thermal stability of the hydrogenation treatment showed that at 400°C annealing temperature, a degradation in the passivation (i.e. degradation in luminescence) appeared after only a few seconds annealing. The loss of the surface passivation effect may be attributed to the in-diffusion of oxygen or other impurities (present in the poor annealing ambient) through the overlaying oxide layer [7]. There may be reappearance of As_{Ga} antisite defects as a result of oxidation of the underlying substrate instigated by this in-diffusion of oxygen and creation of the other impurity defect states. Both the in-diffusion and oxidation could be facilitated by the elevated temperature. Ultimately, this could be addressed through the proper choice of a capping material for anneal.

DISCUSSION and CONCLUSIONS

These initial experiments on pHEMTs clearly show that hydrogen ion treatment can produce a significant reduction in surface leakage. The issue to be addressed is achieving the proper balance between surface passivation and prevention of hydrogen in-diffusion into the material which can produce reduced mobility and carrier density. Capping the substrate during the post-hydrogenation anneal may provide one solution. Optimizing the hydrogenation process to minimize hydrogen at the outset provides other avenues to explore. The in-diffusion of hydrogen has been found to be greatly enhanced by plasma radiation [11]; shortening exposure the time, using a larger ion current (to maintain the equivalent dose) may be a strategy that will limit hydrogen penetration into the substrate.

Pearton *et al.* have found that a shallow n^+ layer inhibits the in-diffusion of deuterium in GaAs during plasma exposure[12]. A carefully designed structure with a proper placement of a Si δ-doped layers near surface should circumvent this in-diffusion problem without sacrificing device's performance.

In summary, we have found that gate-drain reverse leakage current of pHEMT devices is reduced by approximately 60% after irradiation with low energy (80 eV) hydrogen ions at a dose of $3 \times 10^{16} \text{ cm}^{-2}$. The inadvertent reduction of the transconductance and maximum source-drain current (to less degree, about 15%-20%) was correlated with reduced carrier density and mobility due to deactivation of Si dopants in the top δ-doped layer by hydrogen, as evidenced in Hall measurements of the pHEMT structure. The exact distribution of hydrogen ions in the device remains to be elucidated and the Secondary Ion Mass Spectroscopy (SIMS) measurement of

deuterated sample is currently being pursued. We believe that it is possible to determine conditions in which reduced device leakage can be obtained without an accompanying reduction in transconductance and I_{ds}.

ACKNOWLEDGMENTS

REFERENCES

[1] J. C. Huang, G. S. Jackson, S. Shanfield, A. Platzker, P. K. Saledas and C. Weichert," *IEEE Trans. Microwave Theory and Techniques*, vol. 41, pp. 752-759, 1993.
[2] J. C. Hwang, "Gradual degradation under RF overdrive of MESFETs and PHEMTs," *Proceedings of GaAs IC Symposium* , pp. 81-84, 1995.
[3] S. H. Wemple, W. C. Niehous, H. Fukui, J. C Irvin, H. M. Cox, J. C. Hwang, J. V. DiLorenzo and W. O. Schlosser, "Long-term and instantaneous burnout in GaAs power FET's: Mechanisms and solutions," *IEEE Trans. Electron Devices, vol.* ED-28, pp. 834-840, July, 1981.
[4] C. J. Spindt and W. E. Spicer, "Recent attempts to passivate Gallium Arsinide using sulfur," *Proceedings of the Twelfth State-of-Art Program on Compound Semiconductors (SOTAPOCS XII) and the Symposium on Superlattice Structures and Devices*, vol. 90-15, pp. 3-19, 1990.
[5] R. N. Nottenburg, C. J. Sandroff, D. A. Humphrey, T. H. Hollenbeck and R. Bhat, "Near-ideal transport in an AlGaAs/GaAs heterostructure bipolar transistor by $Na_2S \cdot 9H_2O_2$ regrowth," *Appl. Phys. Lett.*, vol. 52, pp. 218-220, 1988.
[6] Y.-L. Chang, I.-H. Tan, Y.-H. Zhang, J. Merz, E. Hu, A. Frova, V. Emiliani, "Luminescence efficiency of near-surface quantum wells before and after ion-gun hydrogenation," *Appl. Phys. Lett.* vol. 62, pp. 2697-2699, 1993.
[7] Ying-lan Chang, Sang I. Yi, Song Shi, Evelyn L. Hu, W. H. Weinberg, and James L. Merz, "Long-term and thermal stability of hydrogen ion passivated AlGaAs/GaAs near-surface quantum wells," *J. Vac. Sci. Technol.* vol. B 13, no 4, pp. 1801-1804, 1995.
[8] Ying-lan Chang, Wolf Widdra, Sang I. Yi, James Merz, W. H. Weinberg, and Evelyn Hu, "Study of surface stoichiometry and luminescence efficiency of near-surface quantum wells treated by hydrogen ions and atomic hydrogen," *J. Vac. Sci. Technol.* vol. B 12, no 4, pp. 2605-2609, 1994.
[9] J. J. Brown, J. Josefowicz, A. E. Schmitz, M. Thompson and C. E. Hooper, "Atomic Force Microscopy Structural Analysis for the Development of a Manufacturable HEMT Gate Recess Etch Process," *GaAs Manufacturing Technology Conference*, pp. 171-174, 1995.
[10] Y. Chung, D. W. Langer, R. Becker and D. Look, "Modification of surface characteristics in GaAs with dry process," *IEEE Trans. Electron Dev.*, vol. 32, pp. 40-44, 1985.
[11] E, Yoon, R. A. Gottscho, V. M. Donnelly, and H. S. Luftman, "GaAs surface modification by room-temperature hydrogen plasma passivation," *Appl. Phys. Lett.* 60, 2681-2683, 1992.
[12] S. J. Pearton, W. C. Dautremont-Smith, J. Lopata, C. W. Tu and C. R. Abernathy, "Dopant-type effects on the diffusion of deuterium in GaAs," Phys. Rev. B 36, no 8, pp. 4260-4264, 1987.

A DEFECT MAP FOR DEGRADATION OF InGaAsP/InP LONG WAVELENGTH LASER DIODES

S.N.G. CHU, S. NAKAHARA*

AT&T Bell Laboratories, 600 Mountain Ave., Murray Hill, NJ 07974, * Breinigsville, PA 18031

ABSTRACT

We summarize the characteristic defect structures associated with gradual-degradation, rapid-degradation, catastrophic (mirror-facet) optical damage (COD), electric static discharge (ESD) and electric overstress (EOS) damages to provide a defect-map for device failure mode analysis. The generation mechanisms of these lattice defects are discussed which pinpoint the weak links in the device structures.

INTRODUCTION

Degradation of photonic devices during operation occurs at the weak links of the device structure[1-18]. These weak links are usually associated with the structural imperfections of the materials constituting the device. In principle, a laser diode consists of an active semiconductor region surrounded by passive structures of semiconductor, metal and dielectric materials such as current blocking structure, ohmic contacts, wire and die bonding, dielectric isolation and heat sink to provide electrical and thermal conduction to the active region of the device. Degradation of these structures deteriorate the device performance and often results in permanent damage inside the active region. Characteristic defect structures are generated by different degradation mechanisms. A careful failure mode analysis (FMA) of degraded devices reveals the characteristic defect structures inside the damaged active region and thereby identifies the possible degradation mechanism. In this study, we summarized the various types of crystalline defects associated with five commonly known degradation mechanisms for semiconductor lasers, i.e. gradual-degradation, rapid-degradation, catastrophic (mirror-facet) optical damage (COD), electric overstress (EOS) and electric static discharge (ESD) damages, to provide a defect-map for identification of device failure modes.

EXPERIMENTAL

Laser diodes were stressed under various temperatures ranging from 25 to 125°C and current ranging from 20 to 400 mA for 24 -100 hrs. The optical power of the devices were monitor continuously as a function of time under constant operating current during stressing or vice versa.

407

The characteristics of the devices were measured and compared before and after stressing and optical degradation mechanisms were identified. The degraded devices were debonded from the header and the back side of the chip lapped to remove the metal contact following by a mirror surface polishing. The crystalline defects generated inside the active region of the lasers were first characterized by electroluminescence imaging and then by transmission electron microscopy. Both top and cross-sectional views of the active stripe were examined to obtain a precise picture of the defect generation mechanisms. A defect map for the various degradation mechanisms is then compiled for FMA uses.

RESULTS AND DISCUSSIONS

1.Gradual-degradation

Gradual degradation is one of the most commonly observed degradation mechanisms, where the optical properties of the laser degrade gradually with time during operation. Typically the devices show a combination of the following changes, an increasing in lasing threshold current, a decreasing in slope efficiency, peak power and peak power current, and a degradation in the p-n junction characteristics. Each of these changes can be due to several factors. To the first order, we correlate optical degradation with the defect structure generated inside the active region. A more general view of gradual degradation of laser diodes will be discussed elsewhere[19].

There are basically four types of the dislocations generated inside the active region during gradual degradation. They are ½<100> sessile dislocation loops, ½<110> slip dislocations, ½<110> misfit dislocations, and for distributed-feedback buried heterostructure (DFB) lasers, dislocations may also generated at the grating waveguide interface which thread through the active layer and form complicated dislocation structure due to non-radiative recombination assisted dislocation climb. We will discuss each cases separately in the following.

I. ½<100> Sessile Loops.

The ½<100> extrinsic sessile dislocation loops are usually generated at the active stripe sidewall interface (SWI) or bottom interface [1,2]. These loops grow rapidly into the active region during devices purging by continuous condensation of self interstitials onto the extra plane of dislocation loops. Detailed trace analysis confirmed that the Burgers vectors of the {100} loops are a/2<100>, where a is the lattice constant, and the loops were extrinsic in nature [2]. Figure 1 shows an example of such <100> types dislocation loops.
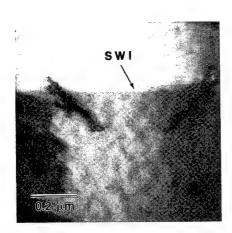
Figure 1. TEM micrograph of a topview of degraded active region (lower part) of a 1.3 μm wavelength buried heterostructure, bulk active, Fabry-Perot laser diode showing a/2<100> sessile dislocation loop originated at the sidewall interface (SWI) and grown into the active stripe.

Under electroluminescence imaging, the loops reveal as <100> darkline defects oriented at 45° with respect to the [011] oriented active stripe, and darkspot defects lying in the (100) growth plane. Since {100} planes are not slip planes in a zincblende structure, the {100} dislocation loops can be grown only by dislocation climb. The presence of these extrinsic loops therefore indicates that there are excess interstitials inside the active region. The growth of the loops are expected to stop when the interstitials are exhausted and hence the associated optical degradation will be saturated. Indeed this has been observed in a stepped-purging test where the gradual degradation process saturates when the {100} loops stop growing [3].

II. ½<110> Slip Dislocation

60° dislocations with Burgers vectors a/2<110> and slip planes {111} are the commonly observed slip dislocations generated under stress in zincblende structure. These types of dislocations have been observed in as-grown laser structures containing strained layers. They are also be responsible for the gradual degradation during device purging test in devices containing strained active layer. As shown in Figure 2, they are generated at the active stripe sidewall interfaces and propagated along the {111} slip planes into the active region forming complex dislocation structures.

Figure 2. TEM micrograph of a topview of degraded active region of a 1.3 μm wavelength buried heterostructure, bulk active, Fabry-Perot laser diode showing complex a/2<110> slip dislocation loops originated at the sidewall interface and gliding on {111} slip plane into the active stripe.

Since the slip dislocations are driven by the internal and thermal stresses, once generated, they continue to propagate and multiply through dislocation interaction along the slip planes during device operation. The associated optical degradation of the devices therefore will not be saturated as long as the stresses are present. Detailed correlation with the optical degradation characteristics will be discussed elsewhere [19].

III. ½<011> Misfit Dislocation

Misfit dislocations of pure edge type generated at the bottom hetero-interface of active stripe during device purging test have been observed, which are shown in Figure 3(a) and (b) using two perpendicular diffraction vectors. The fact that only one set of the dislocations which is perpendicular to the ½<011> diffraction vectors is in contrast indicates that they are pure edge dislocations.

0.2 μm
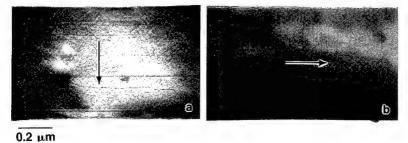
Figure 3. TEM micrographs of a topview of degraded active region of a 1.3 μm wavelength buried heterostructure, bulk active, Fabry-Perot laser diode taken under two perpendicular diffraction conditions showing a/2<011> pure edge misfit dislocations lying in the bottom interface of the active stripe. Arrows indicate diffraction vectors.

410

Since pure edge dislocations with Burgers vectors of ½<011> lying on the (100) plane are also sessile dislocations in zincblende structure, these misfit dislocations are more likely formed by condensation of point defects. Although it is possible to form such dislocations by interaction of two 60° slip dislocations gliding along two symmetric {111} slip planes through the following dislocation reactions,
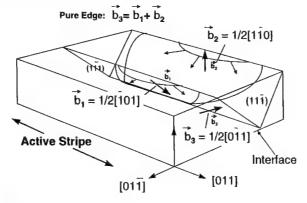
$$\tfrac{1}{2}[\bar{1}\,\bar{1}\,0] + \tfrac{1}{2}[101] \rightarrow \tfrac{1}{2}[0\,\bar{1}\,1] \tag{1}$$

and

$$\tfrac{1}{2}[\bar{1}\,10] + \tfrac{1}{2}[101] \rightarrow \tfrac{1}{2}[011], \tag{2}$$

as also illustrated in Figure 4, it is most unlikely that the intersection line of the two slip planes where the above reactions takes place will lie exactly at the interface. On the other hand, if reactions (1) or (2) took place, one expect to see some unreacted segments remaining on the {111} planes. However, no such segments were seen in Figure 3.
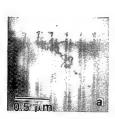
Figure 4. Schematic diagram of the dislocation reactions to form a/2<110> pure edge misfit dislocations at the bottom interface of the active stripe.

IV. Threading Dislocations in DFB Lasers

A DFB laser structure consists of a grown-in Bragg diffraction grating under the active stripe. The waveguide layer grown over the grating involves epitaxial growth over a corrugated surface. The waveguide/grating interface as well as the materials grown inside the grooves of the gratings usually contain a significant amount of strain due to changes in composition and growth rate over the multi-faceted grating surface. Under the accelerated aging condition, dislocations nucleate in the grating region and propagate up through the entire structure as shown in Figure (a) and (b). The segments of dislocation line which thread through the active region will further grow into

411

complex dislocation structures, see in Figure 5(b), due to climb of dislocations assisted by the strong non-radiative recombination of injected carriers in the active region.
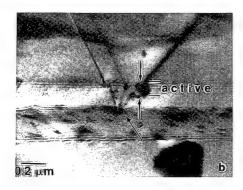
Figure 5. (a) TEM topview shown grating lines and dislocation nucleation from the bottom of the gratings, and (b) a tilted view of XTEM micrograph showing dislocations grown from the waveguide/grating interface and threading through the active region. The segment inside the active region further grown sideways due to nonradiative recombination assisted climb of dislocations.

2. Rapid Degradation

Rapid degradation involves massive generation of dislocations or even localized melting at the weak points inside the active stripe. It differs from COD which initiates at the mirror facet. In electroluminescence imaging, it often reveals as multiple dark sections along the active stripe as shown in Figure 6.
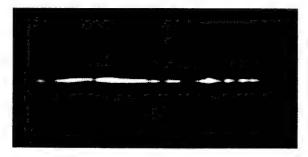
Figure 6. Electroluminescence imaging of heavily damage active region showing large dark section inside the lasing cavity. The length of the stripe is 250 µm.

The corresponding defect structure is shown in Figure 7. Massive dislocation tangles indicating a heavily damage region inside the active stripe.
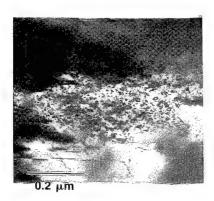
Figure 7. TEM micrograph of a topview of heavily degraded active region of a 1.3 μm wavelength buried heterostructure laser diode showing complex dislocation tangles associated with the rapid degradation.

3. Catastrophic Optical Damage (COD)

The classical COD initiates at the mirror facet interface and propagates along the lasing stripe into the center of cavity. It is believed that strong non-radiative recombination of injected carriers at the dielectric mirror/semiconductor interface results in a localized heating of the semiconductor in the vicinity of interface. The shrinkage of energy bandgap of semiconductor in the heated region leads to an absorption of laser light inside the cavity. This positive feedback of light absorption process thus trigger a catastrophic melt down of the semiconductor at the interface [14]. The melting process continues on the side of melt/solid interface facing the impinging laser light, while the back side of the melted region rapidly solidifies. The net effect is propagation of a melted region from the mirror facet into the center of the cavity. The epitaxial regrowth of semiconductor on the back side of melted region forms a tunnel of defective materials as shown in Figure 8.

413

Figure 8. TEM micrograph of a topview of melt track generated inside the active stripe due to COD. The mirror facet is on the left side.

Since the melt/solid interface scatters laser light inside the cavity, it reveals as a bright spot along the lasing stripe in electroluminescence imaging. The growth of melted region during COD can be monitored in real time as a bright spot moving along the lasing stripe from the mirror facet into the center of cavity. Sometime more than one bright was seen as shown in Figure 9.
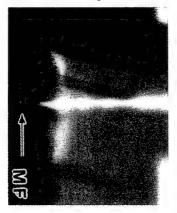
Figure 9. Electroluminescence imaging of melt droplet shown melting and regrowth process in real time.

Detailed TEM analysis confirms that the melted region lies on a (111)P plane in the shape of a circular patch. It is conceivable that the localized melting initiates on (111)P plane where the lattice spacing between the molecular layers is the largest.

4. Electrostatic Discharge Damage (ESD)

ESD usually regards electrostatic discharge in the kilovolt range [18]. A typical discharge voltage used in a human body model ESD test is around 5 kV. In electrostatic discharge damaged devices, an unique defect structure is generated inside the active stripe by a high transient current zapping through the weak spots of the active region. These weak spots can be p-n junction spikes, current leakage paths and spatial non-uniformity in electrical conductivity. The fact that the defect structure only generates inside the active region of a buried heterostructure indicates the activation process may involve both optical and electrical energies. Figure 10 shows the characteristic defect structure associated with ESD.

0.5 μm
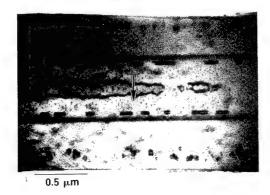
Figure 10. TEM micrograph of a topview of ESD generated characteristic defects inside the active stripe of a 1.3 μm wavelength buried heterostructure laser diode showing high density of small dislocation loops bounded by two parallel dislocations.

It consists of large dislocation loops filled with small loops. Depending upon the strength of electrical discharge, the large dislocation loops may further grow into long rectangular shape along the active stripe and reveals as two parallel dislocation lines lie symmetrically along the central axis of the cavity. In general, there are less damage outside the region bounded by the two parallel dislocation lines indicating that the current distribution during discharge is concentrated around the central axis of the active stripe. Furthermore, the damage occurs discontinuously along the length of the cavity as revealed by the electroluminescence imaging in Figure 11. Presumably these are the weak spots along the active stripe.
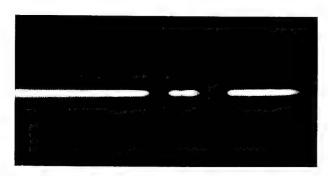
Figure 11. Electroluminescence imaging of a ESD damaged active stripe showing discontinuous dark sections.

5. Electrical Overstress Damage (EOS)

EOS covers a voltage range from few tenth to several hundredth volts. It can be regarded as a lower level ESD. The defect generation mechanism is believed to be similar to ESD but at a lower driving force. Therefore, the nature of the dislocation loops, as shown in Figure 12, are similar but much less in density in comparing to ESD. There are fewer and narrower long rectangular shaped dislocations with less tiny loops inside.

0.5 μm
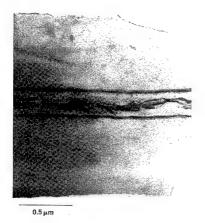
Figure 12. TEM micrograph of a topview of EOS generated defects inside an active stripe of a 1.3 μm wavelength buried heterostructure laser diode showing less damage than ESD.

CONCLUSIONS

We have summarized the major defect structure generated during device degradation either in accelerated purging test or under normal operation to provide a defect map for device failure mode analysis use. It is particularly useful for identifying system related problems such as EOS and ESD versus device degradation such gradual and rapid degradation and COD during normal operation.

ACKNOWLEDGMENTS

REFERENCES

1. S.N.G.Chu, S.Nakahara, M.E.Twigg, L.A.Koszi, E.J.Flynn, A.K.Chin, B.P.Segner, and W.D.Johnston, Jr., J.Appl.Phys., 63, 611(1988).
2. S.N.G.Chu and S.Nakahara, Appl.Phys.Lett., 56, 434(1990).
3. S.N.G.Chu, MRS Bulletin, Vol. XVIII, No 12, 43, December (1993).
4. S.N.G.Chu and S.Nakahara, Appl. Phys. Lett., 62, 917, (1993).
5. S.N.G.Chu, R.A.Logan, H.Temkin, J.Appl.Phys., 61, 2434(1987).
6. S.N.G.Chu, Mat.Res.Soc.Symp.Proc.Vol.184, 135(1990).
7. S.N.G.Chu, S.Nakahara, L.C.Luther and H.W.Krautter, J.Appl.Phys., 69,6974(1991)
8. O.Ueda, Mat.Res.Soc.Symp.Proc.Vol.184, 125(1990).
9. O.Ueda, J.Electrochem.Soc., 135, 11C(1988).
10. M.Fukuda, "Reliability and Degradation of Semiconductor Lasers and LEDs",Artech House, Boston, 1991,
11. U.Gangert, A.T.Briggs, A.R.Goodwin, and P.Charsley, Inst. Phys. Conf. Ser. 117, 581 (1991).
12. B.C.deCooman, C.W.T.Bulle-Lieuwma, J.A.dePoorter, and W.Nijman, J.Appl.Phys. 67, 3919(1990).
13. O.Ueda, K.Wakao, S.Kanija, A.Yamaguchi, S.Isozumi, and I.Umebu, J.Appl.Phys. 58, 3996(1985).
14. C.H.Henry, P.M.Petroff, R.A.Logan, and F.M.Merrit, J.Appl.Phys. 50, 3721(1979).
15. A.Jakubowicz, A.Oosenbrug, and Th.Forster, Appl. Phys. Lett. 63, 1185 (1993).
16. A.Dietzel, A.Jakubowicz, and R.F.Broom, Inst. Phys. Conf. Ser. No 146, 583(1995)
17. R.Hull, D.Bahnck, F.A.Stevie, L.A.Koszi, and S.N.G.Chu, Appl. Phys. Lett. 62, 3408(1993).
18. Y.Twu, L.S.Cheng, S.N.G.Chu, F.R.Nash, K.W.Wang, and P.Parayanthal, J.Appl.Phys.74, 1510(1993).
19. S.N.G.Chu, Lucent Technologies, Bell Laboratories, to be published.

ANALYSIS OF RADIATIVE RECOMBINATION AND OPTICAL GAIN IN GALLIUM NITRIDE-BASED HETEROSTRUCTURES

Petr G. Eliseev*, Vladimir A. Smagley, and Marek Osiński

Center for High Technology Materials, University of New Mexico, Albuquerque, NM 87131-6081

*on leave from P. N. Lebedev Physics Institute, Moscow, Russia

ABSTRACT

Threshold current density in GaN-based UV double-heterostructure lasers is predicted in the range of 2-4 kA/cm^2 using theoretical calculation of optimized heterostructure for various types of devices. Free-carrier (*FC*) and Coulomb-enhancement (*CE*) models are compared. Results are given for different combinations of effective masses. The minimum threshold current is not strongly influenced by the choice of effective masses. The *FC* model predicts lower than *CE* threshold in edge-emitting lasers, whereas the *CE* model predicts lower than *FC* threshold in thin VCSEL devices.

1. INTRODUCTION

Gallium nitride and related alloys AlGaN and InGaN are perspective optoelectronic materials emitting in the UV and in the visible spectrum. Optically pumped stimulated emission in GaN-related materials has been reported [1-9]. Recent demonstrating of electrically pumped diode laser [10] illustrates the present need for formulating the design guidelines for low-threshold GaN-based lasers.

In this paper, a theoretical analysis of radiative recombination and optical gain in bulk GaN is described. The influence of certain material parameters is estimated. Also, different interband transition models are compared. The analysis includes spontaneous emission spectra, optical gain spectra, radiative recombination rate in function of the carrier density N.

2. THEORETICAL MODELS

Optical gain in GaN and related materials has been recently calculated by several groups [11-20]. However, it is not clear to what extent the results may suffer from uncertainties associated with present poor knowledge of various material parameters. Here, we use a non-parabolic band model with several values of electron and hole effective masses (m_e/m_0 from 0.18 to 0.27 and m_h/m_0 from 0.8 to 1.6) and intraband relaxation times τ_{in} (from 26 to 500 fs). Two approaches are used, namely, *free-carrier* (*FC*) model, which is quite traditional for other III-V-compound based lasers, and *Coulomb-enhancement* (*CE*) model. This enhancement of the transition probability due to an electron-hole interaction can be more important in short wavelength laser materials than in GaAs [16, 19]. The radiative characteristics are calculated for bulk GaN using the conventional approach [21,22], which was already applied to GaN earlier [15,18]. The first step is to calculate the spectral distribution of the spontaneous emission rate $r_{sp}(E,N)$ by means of integration over the entire interband transition range. Here, E stands for the photon energy and N stands for the excess carrier density. The intraband relaxation is taken into account assuming the Lorentzian line broadening. In the traditional *FC* model, the transition matrix element is assumed to be independent of energy. Its estimate in terms of the optical transition strength parameter E_p is taken as $E_p \approx (m_0/m_e - 1)E_g$ [15]. For the wurtzite-type GaN, assuming $m_e = 0.22m_0$ and $E_g = 3.4$ eV, we obtain $E_p \approx 12$ eV, which is in a satisfactory agreement with recent theoretical calculations (13 - 14 eV) [23]. We neglect a weak anisotropy of E_p. The same approach is valid for zincblende-type GaN with an estimate of $E_p = 14.6$ eV, $m_e = 0.18m_0$ and $E_g = 3.2$ eV.

419

In the *CE* model, we include the energy dependence of the transition matrix element using a normalized correction factor $F(E)$. For the direct-bandgap semiconductor [24] it is equal to

$$F(E) = z \exp z \, / \sinh z, \tag{1}$$

where $z = \pi[Ry/(E - E_g)]^{1/2}$, $Ry = m_{red}e^4/2\hbar^2\varepsilon^2$ is an effective Rydberg energy, and $m_{red} = m_e m_h/(m_e + m_h)$ is the reduced effective mass. The value of Ry can be found from the free exciton binding energy, which is ~ 27 meV in GaN [25,26], or can be calculated using assumed effective masses. The factor $F(E)$ gives an enhancement of the transition probability just above the band edge. This is rather important for calculation of laser gain because of the involvement of these transitions in the stimulated emission process. Uncertainty of this calculation is associated with assumption of the same factor (1) in a wide range of carrier densities. At large N, carrier screening and other many-body effects can alter $F(E)$.

Integration of the spontaneous emission spectrum gives us the total radiative recombination rate $R_{sp}(N)$. The radiative component of the injection current follows immediately from the expression $j_{rad}(N) = edR_{sp}(N)$, where d is the active layer thickness. The spectral distribution of the material gain coefficient is expressed as follows [21,22]

$$g(E,N) = (\hbar^3\pi^2c^2/ n^2E^2)r_{sp}(E,N)\{1 - \exp[(E - \Delta F)/k_BT]\}, \tag{2}$$

where $\Delta F = F_e - F_h$ is the separation between the quasi-Fermi levels of electrons (F_e), and holes (F_h), respectively, k_B is the Boltzmann constant.

3. RADIATIVE RECOMBINATION COEFFICIENT AND LIFETIME

Radiative recombination coefficient $B = R_{sp}(N)/N^2$ is numerically calculated. Over a wide range of N, the following analytical approximation is found to describe very well the $B(N)$ dependence $B(N) = B_0/[1 + (N/N^*)^p]$, where B_0, N^* and p are fitting parameters. The coefficient B_0 is valid for the *bimolecular* regime of recombination at low carrier densities, whereas when N approaches N^* the recombination rate is close to linear. The radiative lifetime τ_{rad} of the excess carriers is determined as

$$\tau_{rad} = N/B(N) = [1 + (N/N^*)^p]/B_0N \tag{3}$$

and it decreases along with an increase in N. Provided that $p > 1$, the minimum lifetime is equal to $\tau_0[1 + (p -1)^{1/p}]$, where $\tau_0 = 1/B_0N^*$. The minimum is reached at $N = N^*/(p -1)^{1/p}$. Dependence of the τ_{rad} on N for *FC* and *CE* models is shown in Fig. 1.
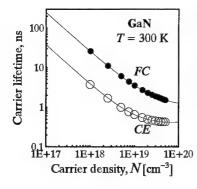
Fig. 1. Calculated radiative lifetime in GaN according to *FC* and *CE* models with following assumptions: electron effective mass is $0.27m_0$, hole effective mass is $0.8m_0$, broadening time is 500 ns, effective Rydberg energy is 27 meV. Points are obtained by numerical integration, curves are obtained using expression (3). Fitting parameters are given in text.

The approximation (3) is shown by curves. The value of p is found close to unity for FC model through the whole ranges of T and N (up to 5×10^{19} cm^{-3}). For the CE model, p changes from 1.247 at 100 K to 1.106 at 400 K. A minimum radiative lifetime, for example, at 300 K is 0.339 ns as it is predicted by the CE model at $N = 7.4 \times 10^{19}$ cm^{-3}. Near this point, $R_{sp}(N)$ is proportional to N rather than to N^2. Temperature dependence T^q is found for the calculated low-density co-efficient B_0 in the FC model where $q = -3/2$, whereas for the CE model a law $T^{-1.85}$ seems to be more adequate. Values of N^* in the CE model are also temperature-sensitive and N^* in-creases from 3.28×10^{18} cm^{-3} at 100 K to 1.86×10^{19} cm^{-3} at 400 K. The deviation from the bimol-ecular law is larger at low temperatures.

4. OPTICAL GAIN AND THRESHOLD CHARACTERISTICS

Spectral distribution of the material gain for a particular case of $N = 10^{19}$ cm^{-3} (CE model) is shown in Fig. 2. It is seen that the peak value is strongly influenced by the broadening time τ_{in}. In Fig. 3, it is demonstrated how a choice of effective masses influences the peak gain plotted versus N. This effect is seen also in Table 1 where the differential "effective cross-section" dg/dN is evaluated above the inversion threshold. In contrast, when the peak gain is plotted versus J_{nom}, the influence of the effective masses on the curve slope is rather weak as shown in Table 1 (the slope $\beta = dg/dJ_{nom}$ is the differential gain). There is a compensating influence of effective masses on the differential gain parameter β via the gain magnitude and via the carrier lifetime. As a result, the differential gain differs by a few percent only while the calculated gain cross-sections differ by a factor of ~2. The CE model predicts much higher B_0 and dg/dN than the FC model. The parame-ter β is sensitive to the value of the nominal current density.

Table 1. Calculated parameters in GaN for assumed effective masses at $\tau_{in} = 26$ ps.

Model	m_e/m_0	m_h/m_0	B_0, 10^{-11} cm^3/s	N^*, cm^{-3}	dg/dN, 10^{-16} cm^2	β, 10^{-2} cm.µm/A
FC	0.18	0.8	7.83	2.26×10^{19}	1.38 [a]	1.03 [c]
FC	0.22	0.8	6.18	2.18×10^{19}	1.23 [a]	1.02 [c]
FC	0.27	0.8	4.38	2.37×10^{19}	1.05 [a]	1.02 [c]
FC	0.27	1.6	1.80	5.0×10^{19}	0.66 [a]	0.98 [c]
CE	0.27	0.8	28.80	1.27×10^{19}	5.55 [b]	0.35 [c] 1.2 [d]

[a] at $N = 2 \times 10^{19}$ cm^{-3}; [b] at $N = 10^{19}$ cm^{-3}; [c] at $J_{nom} = 50$ kA/cm^{2}µm; [d] at $J_{nom} = 200$ kA/cm^{2}µm.
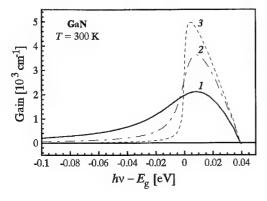
Fig. 2. Calculated spectra of material gain in bulk GaN according to the CE model with following assumptions: electron effective mass is $0.27m_0$, hole effective mass is $0.8m_0$, broadening time is 26 fs (line 1), 100 fs (line 2), and 500 fs (line 3); excess carrier density is 10^{19} cm^{-3}.
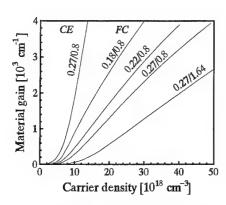
Fig. 3. Calculated material gain coefficient in bulk GaN at 300 K according to *FC* and *CE* models with assumption of effective masses as indicated, and of broadening time equal to 26 fs.

The modal gain is determined using a simplified model of the double heterostructure. The active layer is assumed to be sufficiently thin in order to neglect a non-uniformity of the carrier density across the layer. It was assumed also that 1) potential barriers between active medium and cladding layers are sufficiently high to neglect the carrier leakage over the barriers at both hetero-junction interfaces, 2) refractive index steps at both interfaces are efficient for an optical confinement. The index steps are not much influenced by carrier-induced depression of the refractive index. Such a confinement condition can be met in GaN/AlGaN or InGaN/AlGaN double heterostructures with the aluminum mole fraction in the AlGaN alloy of 0.10-0.15. For instance, according to [4], the refractive index step between GaN and $Al_{0.1}Ga_{0.9}N$ at the lasing wavelength of 370 nm is 0.19, therefore the step $\Delta\varepsilon$ is ~1 in this case. The modal gain is taken as

$$G(N) = \Gamma g(N) - \alpha_{in}, \tag{4}$$

where α_{in} is the total internal loss coefficient, Γ is the optical confinement factor. For the latter a simple approximation [27] may be used, $\Gamma = D^2/(D^2 + 2)$, where $D = (2\pi d/\lambda)\Delta\varepsilon$ is the dimensionless thickness of the waveguide layer, and λ is the free-space wavelength. The threshold current density is calculated from the condition of modal gain G balancing the external losses in the laser cavity. We use the lasing threshold equation $G = (1/2L)\ln(1/R_1R_2)$, where L is the cavity length, R_1 and R_2 are cavity end reflectivities. External losses are controlled by the cavity end reflectivity which in EE-laser equals to 0.21 for GaN/air interface. Thus, total optical losses in EE cavity are estimated as ~60 cm^{-1}. In VCSELs, the mirror reflection is to be higher by use of distributed Bragg reflectors. It is assumed as ~ 0.99.

An example of the modal gain curves calculated according to both *FC* and *CE* models is given in Fig. 4. The same effective masses and broadening times are utilized. At low current densities (< 5 kA/cm^2) the *FC* model predicts a steeper growth of the modal gain, and lower threshold for inversion from attenuation to amplification (~ 1 kA/cm^2 in the *FC* model and ~ 2 kA/cm^2 in the *CE* model). Then, along with the increase of the current density, the *CE* model predicts a steeper growth. Both curves are crossing near 8.5 kA/cm^2. Above this point the *CE* model gives higher mode gain. The lasing threshold is expected at lower currents in low-gain cavities (most of EE lasers) if the *FC* model is used. In high-gain cavities (short cavity VCSELs), the *CE* model predicts lower threshold currents. The calculated threshold current density (radiative component) for EE-lasers is shown in Fig. 5. In this example, the *FC* model predicts a minimum of ~2 kA/cm^2 at an optimal thickness of the active layer near 40 nm. The *CE* model predicts a little higher minimum threshold current density, ~4 kA/cm^2, at smaller optimum thickness of 12 nm.
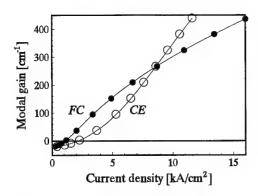
Fig. 4. Calculated modal gain in GaN-based double heterostructure with 30-nm thick active layer at 300 K according to *FC* and *CE* models. Assumptions: electron effective mass is $0.27m_o$, hole effective mass $0.8m_o$, $Ry = 27$ meV, broadening time is 26 fs, relative dielectric permittivity step is $\Delta \varepsilon = 1$, no carrier leakage and non-radiative recombination losses are included.

Similar calculations for the VCSEL predict monotonic lowering of j_{th} with a decrease of the active layer thickness. This again suggests that quantum-well structures are preferable. However, if we include some restriction on the cavity parameters, it is possible to analyze a thickness optimization for a certain combination of parameters. The idea is to minimize the length L in order to reduce the optical loss in the passive part of the vertical cavity. We assume $L = d + 2$ μm including passive layers and multilayer reflector at both cavity ends. The dependence of the threshold current density on the active layer thickness passes a minimum, as shown in Fig. 5. The *FC* model predicts a minimum of ~16.5 kA/cm² near $d = 0.1$ μm. It is interesting that the *CE* model predicts lower minimum, which is about 12.9 kA/cm² (with the broadening time $\tau_{in} = 26$ fs). This reflects the higher gain in the *CE* model at a stronger pumping.

In conclusion, the radiative recombination rate and optical gain are calculated in GaN assuming different theoretical approaches and different values of effective masses (spanning the range of available data). The radiative recombination rate can be described in a wide range of carrier density in a compact form with three or, in simple cases, with only two fitting parameters. It is
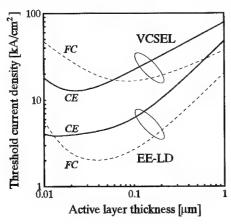
Fig. 5. Calculated dependence of threshold current density (radiative component) in GaN-based DH edge-emitting (EE) laser diodes and vertical-cavity surface-emitting laser (VCSEL) on the active layer thickness at 300 K according to *FC* and *CE* model. It was assumed: internal losses of 20 cm⁻¹, $R = 0.21$ in EE lasers and $R = 0.99$ in VCSELs.

shown that the choice of basic model and values of effective masses influences the gain and threshold characteristics, however, this influence is more pronounced in gain curves versus carrier density than in gain curves versus current density. The FC model predicts lower threshold current in low-gain cavities (compared to the CE model), while in high-gain cavities, for example, VCSELs with a thin active layer, the FC threshold current is higher than the CE one. Preliminary optimization of GaN-based double-heterostructures for laser action in the UV range is obtained with reasonable accuracy; the calculated material and modal gain characteristics are presented. The threshold current density 2-4 kA/cm^2 may be expected in such a structure at room temperature if nonradiative recombination losses could be reduced to a negligible level. Theoretical minimum for a threshold current density in double-heterostructure GaN-based VCSEL is estimated in the range of 12-16 kA/cm^2 at room temperature for a short vertical cavity with high reflectivities (99%) at both ends.

REFERENCES

1. R. Dingle, K. L. Shaklee, R. F. Leheny, and R. B. Zetterstrom, *Appl. Phys. Lett.*, 19 (9), 5-7, 1971.
2. H. Amano, T. Asahi, and I. Akasaki, *Jpn. J. Appl. Phys.*, 29 (2) L205-L206 (1990).
3. M. A. Khan, D. T. Olson, J. M. Van Hove, and J. N. Kuznia, *Appl. Phys. Lett.*, 58 (14), 1515-1517 (1991).
4. H. Amano, N. Watanabe, N. Koide, I. Akasaki, *Jpn. J. Appl. Phys.*, 32 (7b), L1000-L1002 (1993).
5. K. Yung, J. Yee, J. Koo, M. Rubin, N. Newman, and J. Ross, *Appl. Phys. Lett.*, 64 (9), 1135-1137 (1994).
6. S. T. Kim, H. Amano, I. Akasaki, and N. Koide, *Appl. Phys. Lett.*, 64 (12), 1535-1536 (1994).
7. M. A. Khan, S. Krishnankutti, R. A. Skogman, J. N. Kuznia, and D. T. Olson, *Appl. Phys. Lett.*, 65 (5), 520-521 (1994).
8. X. H. Yang, T. J. Schmidt, W. Shan, J. J. Song, and B. Goldenberg, *Appl. Phys. Lett.*, 66 (1), 1-3 (1995).
9. A. S. Zubrilov, V. I. Nikolaev, D. V. Tsvetkov, V. A. Dmitriev, K. G. Irvine, J. A. Edmond, and C. H. Carter, Jr., *Appl. Phys. Lett.*, 67 (4), 533-535 (1995).
10. S. Nakamura, M. Senoh, S. Nagahama, N. Iwasa, T. Yamada, T. Matsushita, H. Kiyoku, Y. Sugimoto, *Jpn. J. Appl. Phys.*, 35 (1B), Pt. 2, L 74-L 76 (1996).
11. D. Ahn, *J. Appl. Phys.*, 76 (12), 8206-8208 (1994).
12. C. Cooper, P. Rees, P. M. Smowton, and P. Blood, *Techn. Digest, CLEO '95, May 21-26, 1995, Baltimore*, 34-35 (1995).
13. T. Honda, A. Katsube, T. Sakaguchi, F. Koyama, and K. Iga, *Jpn. J. Appl. Phys.*, 34 (7A), 3527-3532 (1995).
14. S. Kamiyama, K. Ohnaka, M. Suzuki, and T. Uenoyama, *Jpn. J. Appl. Phys.*, 34 (7a), L821-823 (1995).
15. W. Fang and S. L. Chuang, *Appl. Phys. Lett.*, 67 (6), 751-753 (1995).
16. W. W. Chow, A. Knorr, and S. W. Koch, *Appl. Phys. Lett.*, 67 (6), 754 -756 (1995).
17. A. T. Meney and E. P. O'Reilly, *Appl. Phys. Lett.*, 67, no 20, 3013-3015 (1995).
18. M. Osiński and P.G. Eliseev, *SPIE Symp. "Photonics West'96", Conf. 2693*, San Jose (1996).
19. P. Rees, C. Cooper, P. M. Smowton, P. Blood, and J. Hegarty, *IEEE Photon. Techn. Lett.*, 8 (2), 197-199 (1996).
20. W. W. Chow, A. F. Wright, and J. S. Nelson, *Appl. Phys. Lett.*, 68, no 3, 296-298 (1996).
21. G. Lasher and F. Stern, *Phys. Rev.*, A, 133, 553-563 (1964).
22. S. L. Chuang, J. O'Gorman, and A. F. J. Levi, *IEEE J. Quant. Electron.*, 29 (6), 1631-1639 (1993).
23. M. Suzuki and T. Uenoyama. (to be published).
24. F. Bassani, G. P. Parravicini. Electronic states and optical transitions in solids. Pergamon Press, Oxford, 1975, 191-194.
25. B. Monemar. *Phys. Rev.*, B, 10 (2), 676-681 (1974).
26. T. Ogino and M. Aoki. *Jpn. J. Appl. Phys.*, 19 (12), 2395-2405 (1980).
27. D. Botez. *IEEE J. Quant. Electron.*, 17, 178-185 (1981).

TEMPERATURE DEPENDENCE OF THE ELECTRICAL TRANSPORT OF CARBON DOPED GaN

Wim Geerts[1], J.D. MacKenzie[1], C.R. Abernathy[1], S.J Pearton[1], and Thomas Schmiedel[2]
1. Department of Materials Science and Engineering / NHMFL, University of Florida, Gainesville, FL32611, USA.
2. National High Magnetic Field Laboratory, Tallahassee, FL32306, USA.

ABSTRACT

The temperature dependence of the Hall voltage and resistivity of highly carbon doped GaN were measured. From the sign of the Hall voltage, the material appears to be p-type. Charge transport takes place in an impurity band and the valence band. The effective activation energy as estimated from the maximum in the temperature versus Hall voltage relation is 10-30 meV.

INTRODUCTION

Research on GaN has been performed for more than sixty years [1]. The usefulness of the material in semiconductor devices, however, was for a long time limited by the absence of a good p-dopant. Since the discovery that Mg-doped GaN can be made p-type by a de-hydrogenation treatment [2], the field has flourished. The successful application of GaN in blue photonic devices [3,4] opened up several new markets for the compound-semiconductor industry. Within a short time span, new products are to be expected in the areas of illumination, information technology, and high contrast screens and displays.

The relative large ionization energy of Mg (~160 meV), makes it an inefficient acceptor at room temperature, with only 1 % of the acceptors ionized. It has been predicted on the basis of d-state relaxation effects that C may be a shallower acceptor than Mg, Zn and Be [5]. Carbon has become the most commonly used p-type dopant in GaAs and related materials because of its high incorporation efficiency and low diffusivity [6]. In this paper we report about the electric transport properties of carbon doped GaN.

Several investigations have been performed on carbon doped GaN. Pankove et al. measured the photoluminescence of carbon implanted GaN and found a large peak near 2.17 eV [7]. Ogino et al. doped GaN by adding carbon grains to the Ga boat [8]. They also found a large peak around 2.2 eV in the photoluminescence spectra and suggest that a carbon gallium-vacancy complex forms a deep acceptor level (860 meV) in their films. The exact origin of the photoluminescence spectra, however, is still under discussion [9]. Abernathy et al. prepared carbon doped GaN by the Metal Organic Molecular Beam Epitaxy (MOMBE) method [10]. Their films appear to be p-type and have excellent mobility values at room temperature relative to other p-GaN films [11].

EXPERIMENTAL PROCEDURE

The films were prepared by MOMBE in an Intervac Gen II system with a background pressure in the 10^{-7} Torr range. The samples were grown on 2" semi insulating (100) GaAs substrates. An Electron Cyclotron Resonance (ECR) N_2 (10-13 sccm) plasma source operating at 2.45 GHz and 200 Watt forward power provided the reactive nitrogen flux. High purity He was used as a transport gas for triethylgallium (TEG). The substrate temperature during deposition was 1000 Kelvin. Under these conditions the grown GaN appears to be p-type with a hole concentration of 2×10^{16} cm^{-3}. The p-type doping level was increased by adding CCl$_4$ to the growth chemistry during deposition. More details about the growth procedure can be found in reference [10]. Secondary Ion Mass Spectroscopy (SIMS) showed that the C-concentration exceeded 10^{18} cm^{-3}. The exact lattice positions of the carbon is not known. In other III-V's, carbon can occupy the group V site where it is a single acceptor, or forms C_{III}-C_V neutral pairs, or be in an interstitial site. Carbon donors have not been observed [6]. The difference in bonding energy between the C-III and C-V bond is for GaN much smaller than for example for GaAs [10]. This implies the difficulty for preferential incorporation of carbon on the V-sites and suggests a large sensitivity on the chemistry and physics of the deposition process [12]. Standard X-ray analysis indicated that the crystal structure was hexagonal. Table I gives an overview of the film parameters.

The transport properties were determined by Van der Pauw geometry Hall measurements [13] using alloyed (annealed at 700 K for 180 seconds) HgIn contacts. The ohmic behavior of the contacts was checked by measuring the I-V relation over several decades. The typical size of the samples and the contacts were 5x5 mm and 0.5x0.5 mm respectively. Measurements were performed for both directions of the current and for both directions of the field. The current was kept low in order to avoid heating of the sample. The electric field was also kept low in order to assure that impact ionization or Poole-Frenkel type of effects would not occur and influence the free carrier concentration. Corrections were made for the asymmetry of the samples but not for the contact sizes and not for the possible depletion effects near the surface and substrate interface. The latter, if present, is expected to be small because of the large carrier/doping concentrations and the absence of any Fermi-level pinning at GaN surfaces. In order to exclude any effects from parasitic conduction channels through the substrate, we determined the transport properties of the SI-GaAs we used. The following necessary conditions appear to be valid over the complete investigated temperature range:

$$(\rho_{film}/t_{film}) \ll (\rho_{sub}/t_{sub}) \qquad (1)$$

$$(t_{film} \cdot R_{Hfilm}/\rho_{film}^2) \gg (t_{sub} \cdot R_{Hsub}/\rho_{sub}^2) \qquad (2)$$

where: ρ is the resistivity, t is the thickness, R_H is the Hall coefficient, "film" refers to the GaN film, and "sub" refers to the SI-GaAs substrate.

The electrical properties at low magnetic field were measured by using an MPMS-5S Squid from Quantum Design. This system provides a convenient platform for applying a magnetic field (0-5.5 Tesla) and controlling the sample temperature (1.7-400K). A Keithley 220 programmable DC-current source and a Keithley 2000 multimeter (input impedance >50 Gohm) were connected by IEEE bus to the system computer. The whole setup was controlled via the External Device Control (EDC) option of the MPMS software.

Table I: characteristics of carbon-doped GaN films

layer thickness:	0.4 nm	deposition temp.:	1000 K
p(70 K):	$3.8\ 10^{17}$ [cm^{-3}]	μ(70 K):	46 [cm^2/V.s]
crystal structure:	α		

RESULTS AND DISCUSSION

From the sign of the Hall voltage it appeared that the GaN was p-type (hot probe measurements also indicated p-type conductivity). The temperature dependence of the Hall coefficient and the resistivity are presented in Fig. 1. Measurements were performed on two separate samples from the same wafer.

For low temperatures the electrical properties are almost independent of the temperature. This indicates the existence of a metallic impurity band [14]. For larger temperature the Hall voltage increases. This is not related to a decrease in carrier concentration, but is caused by the transition of electrons to states with a higher mobility. As the average velocity of these carriers is larger, a larger Lorentz field will cause a larger Hall voltage. The Hall voltage will no longer be inversely proportional to the carrier concentration. The occurrence of a maximum in the Hall voltage versus temperature curve has in fact been observed for a wide range of different semiconductors [15].

A maximum in the temperature dependence of the Hall voltage occur in all systems in which the mobility depends on the electron energy. A detailed analysis of this problem was given by Look in reference [16]. He distinguishes between single band effects and mixed band effects. The former have been calculated for the conduction band of intrinsic GaN by Rhode [17]. He found that the temperature dependence of the Hall factor shows a maximum of 1.25 near 400 K. Calculations on single band effects of the valence band have not been performed yet. The small spin orbit splitting (160 meV) [18], however, suggests a complicated temperature dependence of the Hall factor. Mixed band effects of unintentionally doped n-GaN have been investigated by Molnar et al. [19]. They calculated the mobility of carriers in the impurity band and conduction band from the electrical transport data. Similar to them, we calculated the mixed band effects of our p-GaN. The results suggest that the carbon doped GaN is heavily compensated. The ratio between the mobility in the impurity band and that in the valence band was approximately a factor 10. More details can be found in [20].
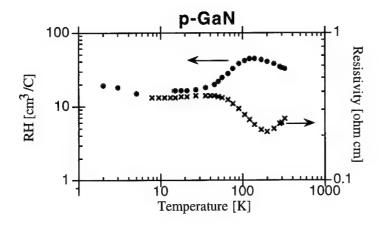
Fig. 1: Hall voltage and resistivity as a function of the temperature for p-GaN.

Several general calculations have been performed on the temperature dependence of the electric transport properties of heavily doped semiconductors [21, 22]. Fukuyama et al. [23] calculated the mobility as a function of the Fermi level and impurity concentration for heavily doped semiconductors. They found that the mobility in the impurity band hardly depends on the impurity concentration or compensation of the material. This is in contrast with the large change of mobility in the conduction band as a function of the donor concentration. Similar effects are expected for p-type material: i.e. we anticipate a low mobility which depending on the acceptor concentration is separated from the valence band by an energy interval in which carriers have a lower (or zero) mobility and state density. Using their results Saitoh [21] calculated the temperature dependence of the Hall voltage. Figure 2 gives a summary of his calculation. The ratio of the maximum Hall voltage over the Hall voltage at low temperature versus the temperature for which this maximum occurs (which is related to the ionization energy for a single acceptor) is plotted for several values of the compensation (K) and the relative impurity concentration (c0 is the concentration for which the impurity band merges the valence band). The investigated GaN had a maximum of log(Rmax/R(T=0))=0.5 at 130 Kelvin (see Fig. 1). This value was used to determine the value of the activation energy, ΔE, from Fig. 2. In [20] we found that the ratio of valence band and impurity band mobility was approximately a factor 10. According to Fig. 2 of reference [23], this corresponds to relative impurity concentration, c/c0, of 2.5. Extrapolating the results of Fig. 2 and taking into account the large noise on this data, results in

Maximum in Hall-voltage versus Temperature curve
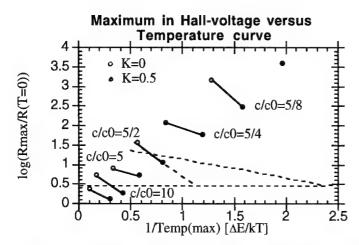
Fig. 2: *Position of the maximum in the Hall voltage versus temperature curve for several values of the relative impurity concentration (c/c0) and the compensation (K).*

an activation energy, ΔE, somewhere in the interval 10-30 meV. This is in agreement with the value reported in reference [20]. We emphasize that this is not the ionization energy of a single well-defined acceptor, but the effective activation energy of conduction in a heavily compensated system.

CONCLUSIONS

The temperature dependence of the Hall voltage and resistivity of highly carbon doped p-GaN was measured. Both resistivity and Hall data show characteristics of two-band conduction. At low temperature charge transport mainly takes place in the impurity band, while at higher temperatures also the valence band forms a conduction path. The effective activation energy estimated from the maximum in the Hall voltage curve was 10-30 meV. Although this value is not expected to be very accurate, it is definitely much lower than the 860 meV suggested by the photoluminescence results of Pankove [7] and Ogino et al. [8]. The high carbon concentration [12] and the relative low carrier concentration at low temperatures, suggest that the material is highly compensated [20]. This may be related to the small thermodynamic advantage to incorporate C on a V-sites over III-site incorporation [10,12]. Improvements may be expected with better control of the carbon incorporation during growth. In the current material, carbon can be incorporated from a number of sources including the metalorganic precursors in addition to the CCl_4.

The role of carbon as a dopant was not addressed in this paper and has to be solved in the future. It is not clear at the moment whether or not carbon directly

acts as an acceptor or that it forms a complex with a defect or vacancy which can create a hole in the valence band. Although the electrical properties are excellent of C-doped GaN [11], the currently grown material appears to have less favorable optical properties [8]. A systematic study to produce C-doped GaN with a smaller yellow band luminescence is desirable.

ACKNOWLEDGMENTS

REFERENCES

[1] W.C. Johnson, J.P. Parsons and M.C. Crew, J. Phys. Chem. 36 (1932) 2651.
[2] H. Amano, M. Kito, K.Hiramatsu, and I. Akasaki, Jpn. J. Appl. Phys. 28 (1989) L2112.
[3] S. Nakamura, T. Mukai, and M. Seno, Jpn. J. Appl. Phys. 30 (1991) L1998.
[4] Shuji Nakamura, Masayuki Senoh, Shin-ichi Nagahama, Naruhito Iwasa, Takao Yamada, Toshio Matsushita, Hiroyuki Kiyoku, and Yasunobu Sugimoto, Jpn. J. Appl. Phys. 35 (1996) L74.
[5] S. Strite, Jpn. J. Appl. Phys. 33 (1994) L699.
[6] see for example C.R. Abernathy, Mat. Sci. Eng. Rep. R14 (1995) 203.
[7] J.I. Pankove, J.A. Hutchby, J. Appl. Phys. 47 (1976) 5387.
[8] Toshio Ogino and Masaharu Aoki, Jpn. J. Appl. Phys. 19 (1980) 2395
[9] T.A. Kennedy, E.R. Glaser, J.A. Freitas, Jr., and W.E. Carlos, M. Asif Khan, D.K. Wickenden, J. Electron. Mat. 24 (1995) 219.
[10] C.R. Abernathy, J.D. MacKenzie, and S.J. Pearton, W.S. Hobson, Appl. Phys. Lett. 66 (1995) 1969.
[11] Properties of group III-Nitrides, D.K. Gaskill, L.B. Rowland, and K. Doverspike, pp. 108, (edited by James H. Edgar, London, 1994).
[12] S.J. Pearton, C.R. Abernathy, J.W. Lee, C.B. Vartuli, J.D. MacKenzie, R. Ren, R.G. Wilson, J.M. Zavada, R.J. Shul and J.C. Zolper, Mat. Res. Soc. Symp. Proc. 430 (1996).
[13] L.J. van der Pauw, Philips Research Report 13 (1958) 1.
[14] G. Bush and H. Labhart, Helv. Phys. Acta. 19 (1946) 463.
[15] C.S. Hung and T.R. Gliessman, Phys. Rev. 79 (1950) 726.
[16] Electrical characterization of GaAs materials and devices, David C. Look (John Wiley and sons, Chichester, 1989).
[17] D.L. Rode, Phys. Stat.. Sol. b 55 (1973) 687.
[18] Masakatsu Suzuki and Takeshi Uenoyama, to be published in Solid State Electronics 39 (1996).
[19] R.J. Molnar, T. Lei, and T.D. Moustakas, Appl. Phys. Lett. 62 (1993) 72.
[20] Wim Geerts, J.D. MacKenzie, C.R. Abernathy, S.J. Pearton, and Thomas Schmiedel, Electrical transport in p-GaN, n-InN and n-InGaN, submitted to Sol. State Electr.
[21] Motohiko Saitoh, J. Phys. Soc. Jpn. 29 (1970) 1470.
[22] Hiroyuki Shiba, Kunishiko Kanada, Hiroshi Hasegawa, and Hidetoshi Fukuyama, J. Phys. Soc. Jpn. 30 (1971) 972.
[23] Hidetoshi Fukuyama, Motohiko Saitoh, Yasutada Uemura, Hiroyuki Shiba, J. Phys. Soc. Jpn. 28 (1970) 842.

PARAMETRIC STUDY OF COMPOUND SEMICONDUCTOR ETCHING UTILIZING INDUCTIVELY COUPLED PLASMA SOURCE

C. CONSTANTINE[1], D. JOHNSON[1], C. BARRATT[1], R. J. SHUL[2], G. B. McCLELLAN, R. D. BRIGGS[2], D. J. RIEGER[2], R. F. KARLICEK, JR.[3], J. W. LEE[4] AND S. J. PEARTON[4]

[1]PLASMA THERM IP, St. Petersburg FL 33716
[2]Sandia National Laboratories, Albuqureque NM 87185
[3]EMCORE Corporation, Somerset NJ 08873
[4]University of Florida, Gainesville FL 32611

ABSTRACT

Inductively Coupled Plasma (ICP) sources are extremely promising for large-area, high-ion density etching or deposition processes. In this review we compare results for GaAs and GaN etching with both ICP and Electron Cyclotron Resonance (ECR) sources on the same single-wafer platform. The ICP is shown to be capable of very high rates with excellent anisotropy for fabrication of GaAs vias or deep mesas in GaAs or GaN waveguide structures.

INTRODUCTION

Inductively coupled plasma (ICP) etching offers an attractive alternative dry etching technique.[1,2] The general belief is that ICP sources are easier to scale-up than ECR sources,[3] and are more economical in terms of cost and power requirements. ICP plasmas are formed in a dielectric vessel encircled by an inductive coil into which rf-power is applied.[4-8] A strong magnetic field is induced in the center of the chamber which generates a high-density plasma due to the circular region of the electric field that exists concentric to the coil. At low pressures (≤ 10 mTorr), the plasma diffuses from the generation region and drifts to the substrate at relatively low ion energy. Thus, ICP etching is expected to produce low damage while achieving high etch rates. Anisotropic profiles are obtained by superimposing a rf-bias on the sample to independently control ion energy.

In this paper we report the first etching results for GaAs and GaN in an ICP tool. It is found that ICP sources are capable of producing the extremely high rates needed for producing via holes on 4"Φ GaAs substrates, and have the high ion density needed to obtain high etch rates for strongly bonded material such as GaN, where the rate-limiting step is usually the initial bond breaking that must precede etch product formation. GaN has a bond energy of 8.92 eV/atom, compared to 6.52 eV/atom for GaAs,[9] and the low rates reported with reactive ion etching are due to the low rate of bond breaking in RIE discharges.

EXPERIMENTAL

A typical ICP system (Plasma Therm 790 series) is shown schematically in Figure 1. Power at 2MHz is inductively coupled into the plasma volume to create a high ion density ($\geq 10^{11} cm^{-3}$) discharge, while the sample sits on a He backside-cooled, rf (13.56MHz) powered chuck, which controls the ion energy. This is a prototypical single-wafer, high density system, in

431

which there is separate control of ion density (via the ICP power) and ion energy (via the rf biasing of the sample position). We directly compared the performance of the ICP and ECR sources, by placing them on a Plasma Therm SLR 770 platform that is designed for an ECR source.
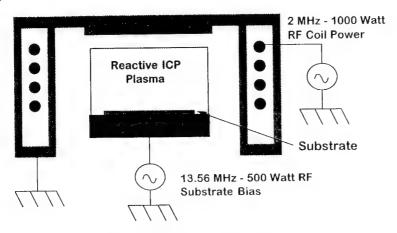
Figure 1. Schematic of ICP reactor.

The principle of the ICP source operation is shown schematically in Figure 2. The electric field produced by the coils in the horizontal plane induces an oscillating B field in the vertical plane, trapping electrons and producing high ionization and excitation efficiencies without leakage of the electrons to the chamber wall. Therefore, as in an ECR source, the ion density is high while the induced self-bias on the cathode is low.

Inductively Coupled Plasma
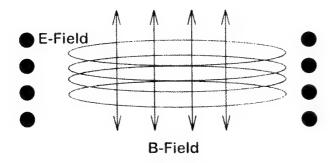
Figure 2. E- and B-field configurations in ICP.

RESULTS AND DISCUSSION

The self-bias developed on the sample chuck was measured as a function of applied rf power on the SLR 70 platform with the ICP or ECR (Astex 4400 low profile source) sources in place. Figure 3 shows that these self-biases are almost identical when the high density sources are not powered.
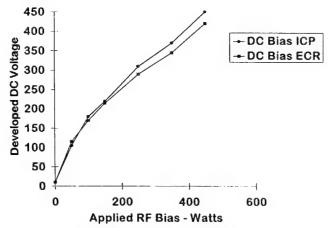
Figure 3. DC self-bias as a function of rf power in an ECR and ICP reactor.

As the ICP power is increased and hence the plasma density increases, there is a suppression of the cathode self-bias, as shown in Figure 4. Therefore it is possible to achieve very high ion densities while retaining low acceleration voltages. This is an important result when considering the etching of device structures where mask integrity or ion-induced damage can be an issue, such as in III-V semiconductor structures like heterojuction bipolar transistors or laser diodes.[10,11]
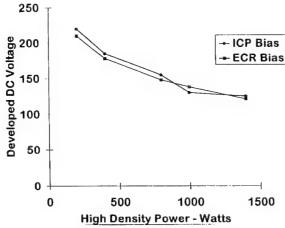
Figure 4. DC self-bias as a function of ECR or ICP power.

There was basically no dependence of self-bias on process pressure with either high density source, as shown in Figure 5. Thus both sources have a wide operating pressure, although the coupling efficiency of microwaves to the ECR plasma decreases above ~10 mTorr. It is expected that the ICP is capable of higher pressure operation and thus the cost of ownership should be lower because one can employ smaller pumps. This is a major consideration for manufacturing processes, where multiple reactors may be needed to produce a sufficiently throughput of wafers.
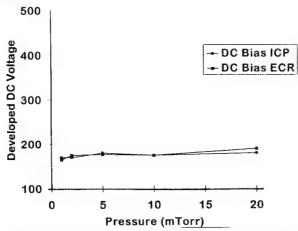
Figure 5. DC self-bias a function of pressure in an ICP tool.

For controlled rate etching of GaAs/AlGaAs for HBT mesas or laser diode waveguides, BCl_3 plasma chemistries are attractive since they are non-selective for GaAs over AlGaAs for BCl_3 or BCl_3/Ar. If a fluorinated gas such as SF_6 or SiF_4 is added to the chemistry , then it is possible to achieve high selectivities (>200:1) for GaAs over AlGaAs.[12,13] These etches are highly anisotropic even at moderate rf bias, in part because the BCl_X residues aid in sidewall protection. Figure 6 shows the GaAs etch rate and selectivity over photoresist at 750W or ICP power. The rate is controllable between 25-450 nm/min for fixed ICP power and rf powers between 50-350W. The selectivity over resist varies from 1-5.

The etch uniformity measured on 2"Φ GaAs wafers was strongly dependent on ICP power, as shown in Figure 7, which displays etch rate and uniformity percentage as a function of the ICP power. The rf chuck power up to 1000W (maximum rate ~500 nm/min) and decreases at 1500W , which may be due to one or both of the following factors: either sputter-enhanced removal of the chlorine neutrals before they can react with the GaAs surface, or a further decrease in self-bias at very high ICP powers. Note however that the uniformity degrades rapidly over 750W of ICP power. This effect is still under investigation, and it is not clear if this is due to non-uniform suppression of the self-bias or non-uniformities developing in the discharge itself.
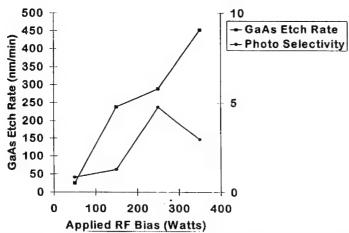
Figure 6. GaAs etch rate and selectivity over resist in a BCl_3 ICP discharge with 750W ICP power, as a function of rf chuck power.
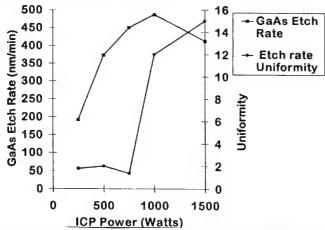
Figure 7. GaAs etch rate and uniformity in a BCl_3 discharge with 150W rf chuck power, as a function of ICP power.

If necessary the etch rate can be increased by addition of Cl_2. Figure 8 shows the dependence of etch rate on discharge composition at 1000W ICP power and 350W rf power. The etch rate of GaAs stays above ~2.3 μm/min for BCl_3 percentages ≤ 25%. The uniformity of etching is better than 5% for BCl_3 percentages above 50%. This may be due to the well-known efficiency of BCl_3 for removing the native oxide on III-V materials. For Cl_2-rich discharges the breakthrough of this oxide may be non-uniform, and with such a high etch rate, the overall etch rate uniformity suffers.
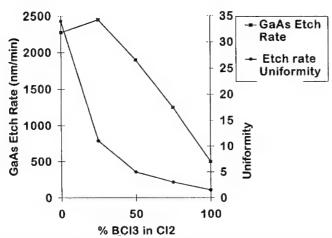
Figure 8. GaAs etch rate and uniformity in BCl_3/Cl_2 discharges with 1000W ICP power and 350W rf power, as a function of plasma composition.

Figure 9 shows the pressure dependence of GaAs etch rate and selectivity over photoresist for pure BCl_3 discharges (1000W ICP power, 350W rf power). The selectivity is between 3-6 over the pressure range 1-20 mTorr. The maximum in etch rate around 2-3 mTorr is also typical of ECR processes[14] and is related to an absence of ion collisions and recombination at low pressures.
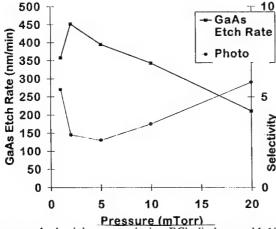
Figure 9. GaAs etch rate and selectivity over resist in a BCl_3 discharge with 1000W ICP power and 350W rf power, as a function of pressure.

A scanning electron micrograph (SEM) of features etched into GaAs with 750W ICP power, 100W rf power, 2 mTorr BCl_3 discharge (40 sccm of gas) is shown in Figure 10. The photoresist mask has been removed. The etch rate under these condition is 230 nm/min, and the surfaces are smooth with anisotropic sidewalls. The resist mask generally showed facetting at its edge, but the GaAs sidewalls were very smooth and straight. This is a critical requirement for

laser mesas or waveguides where any sidewall roughness will lead to scattering of light as it traverses the stripe, and hence to a decreased optical output.[15,16]
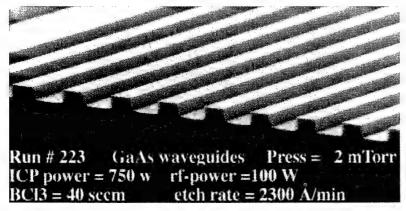
Figure 10. SEM micrograph of features etched into GaAs with a 750W ICP BCl$_3$ discharge.

As mentioned earlier, addition of Cl$_2$ to BCl$_3$ can produce high rates for GaAs and related alloys. A benchmark for backside via-hole processes is to achieve an etch-rate of greater or equal to 4 μm/min for 4"Φ GaAs wafers. For this process one will require both high ICP and rf power, and active wafer cooling (i.e. clamping to the He backside cooled chuck. the sidewalls must be relatively anisotropic and smooth because they will be plated with metal to complete the through-wafer via.[17,18]

Figure 11 shows the pressure dependence of GaAs etch rate and photoresist selectivity in 25%Cl$_2$:75%BCl$_3$ discharges at 750W ICP power as a function of rf power (5 mTorr pressure). There is little dependence on rf bias, since the etching is not strongly desorption-limited under these conditions, but the rate does increase from ~1 μm/min at 50W rf to 1.7μm/min at 350W, and the selectivity decrease from ~3.8 to ~2.
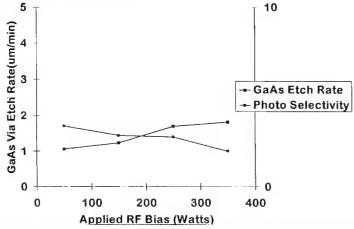
Figure 11. GaAs etch rate and selectivity over resist in a 1:3 Cl$_2$:BCl$_3$ discharge with 750W ICP power as a function of rf chuck power.

The GaAs etch rate and selectivity over photoresist is shown in Figure 12 as a function of ICP power. Once again the etch rate increases over the range 250–1000W from ~0.8 μm/min to ~1.3 μm/min as the ion and neutral density both increase at higher power. The selectivity over photoresist is in the range 2-3 over this set of conditions.
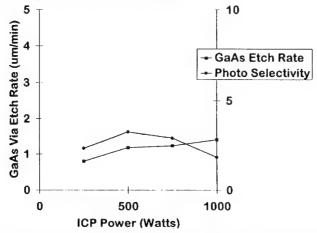
Figure 12. GaAs etch rate and selectivity over resist in a Cl_2/BCl_3 discharge as a function of ICP power.

As etch rate of slightly higher than 4 μm/min was achieved and 10 mTorr pressure, as shown in Figure 13. The selectivity is still only 3-5, which is barely sufficient for a typical 75μm etch depth with 12–16μm of resist. In these applications a Ni mask has proven effective.
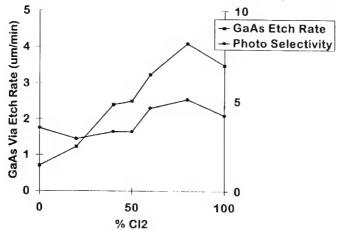
Figure 13. GaAs etch rate and selectivity over photoresist as a function of Cl_2 composition in a 750W ICP, 250W rf BCl_3/Cl_2 discharge.

As expected, the etch rate depends strongly on process pressure since the chemical component is enhanced at higher pressure. The neutral density is $3x10^{14}$ cm^{-3} at 10 mTorr, and with a gas such as Cl_2 a higher pressure should increase the etch rate. This is confirmed by the

data in Figure 14, where the GaAs etch rate is seen to increase from 0.8 µm/min at 2 mTorr to 2.3 µm/min at 20 mTorr. An extremely anisotropic GaAs via-type feature is shown in the SEM micrograph of Figure 15. This was produced with a 80%Cl_2:20%BCl_3, 10mTorr, 750W ICP, 250W rf discharge. Note the excellent sidewall morphology, even in the absence of a photoresist mask.
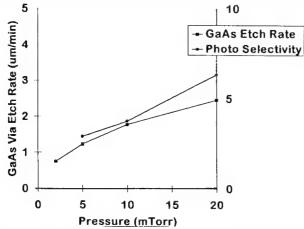
Figure 14. GaAs etch rate and selectivity over resist as a function of pressure in BCl_3/Cl_2 ICP discharges.

Run # 230
GaAs Via
Ni mask
Pressure = 10 mTorr
ICP power = 750 w
rf-power = 250 W
Cl2 = 32 sccm
BCl3 = 8 sccm
Depth =105 µm
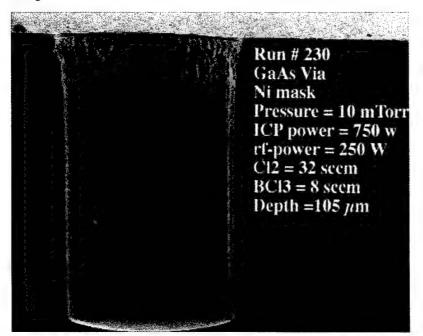
Figure 15. SEM micrograph of feature etched into GaAs using a 4:1 Cl_2:BCl_3, 750W ICP, 250W rf discharge.

RIE-lag is relatively minor in this low pressure tool, as shown in the SEM micrograph of Figure 16, which has closely-spaced via-type features (diameter of 20 or 60 µm) that were etched under the same conditions as the previous figure. There is a 10–15% lower effective etch rate in the smaller features due to the difficulty in getting reactants into, and etch products out of, these vias. This type of difference is typical of that reported previously for ECR-etched vias.[18] The anisotropy and smoothness of the sidewalls can be controlled by careful control of pressure, rf power and $Cl_2:BCl_3$ ratio.
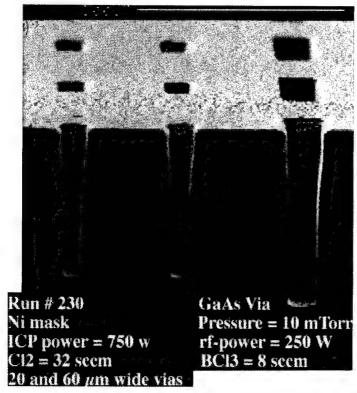
Figure 16. SEM micrograph of feature etched into GaAs using 4:1 $Cl_2:BCl_3$, 740W ICP, 250W rf discharge.

As mentioned previously the difficulty in finding practical wet etch solutions for GaN has placed a strong emphasis on developing dry etching methods. ECR etch rates up to an order of magnitude faster than for RIE are typical.[19-22] We have employed 22.5 sccm Cl_2, 2.5 sccm H_2, 5 sccm Ar, 1 mTorr pressure, 500W ICP power, 150W rf power (dc bias of ~190V) discharges for etching of MOCVD grown GaN. Figure 17 shown the rf power dependence of GaN etch rate. The increase at higher powers can be attributed to enhanced sputter desorption of the etch products. The root-mean-square roughness as measured by atomic force microscopy remained fairly constant at ~2 nm ($10 \times 10 \mu m^2$ analysis area).
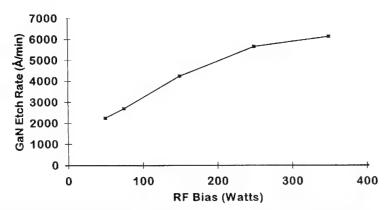
Figure 17. GaN etch rate as a function of rf power in a 00W ICP $Cl_2/H_2/Ar$ discharge.

The dependence of GaN etch rate on ICP power is shown in Figure 18. Since the rf power was held constant at 150W, the self-bias decreased at higher ICP powers. The etch rate initially increased due to a higher density of reactive species, but beyond ~500W, the rate falls off somewhat due either to lower ion energies or sputter desorption of the reactants at the surface prior to reaction. Etch rates as a function of pressure are shown in Figure 19. During these runs the rf power was again held constant at 150W, resulting in an increase in self-bias at higher pressure. The GaN etch rate increased up to ~5 mTorr due to an increased reactant supply, and remained constant beyond that, as expected. Once again the RMS surface roughness remained essentially constant over the entire pressure range investigated.
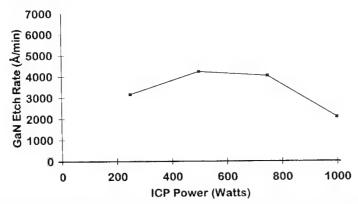
Figure 18. GaN etch rate as a function of ICP power in a 150W rf $Cl_2/H_2/Ar$ discharge.

A comparison of ICP and ECR etch rates as a function of percentage Cl_2 in $Cl_2/H_2/Ar$ is shown in Figure 20. The rates increase in both cases as the $Cl_2:H_2$ ratio increases, due to the higher reactive chlorine density. The ICP rates are slightly higher for the ICP source at the same source power, rf power and pressure, indicating a slightly higher plasma density for the former. An SEM micrograph of a GaN sidewall produced by ICP etching with a 5 mTorr, 500W ICP, 150W rf, $Cl_2/H_2/Ar$ discharge at room temperature is shown in Figure 21. The etch rate was ~6900 Å/min under these conditions, and produced smooth, vertical sidewalls.

441
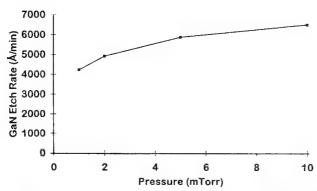
Figure 19. GaN etch rate as a function of pressure in a 500W ICP, 150W $Cl_2/H_2/Ar$ discharge.
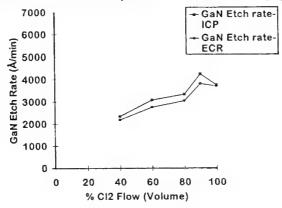
Figure 20. Composition of GaN etch rates in ICP or ECR $Cl_2/H_2/Ar$ discharges under the same conditions, as a function of Cl_2-to-H_2 percentage.

SUMMARY AND CONCLUSIONS

An ICP source has proven to be as effective tool for high ion density etching of GaAs, GaN and related materials in applications ranging from waveguide mesa formation to via holes. In basically all respects the ICP appears to perform as well as an ECR source under the same conditions, and has lower cost of ownership and should be scaleable to larger diameter while retaining excellent uniformity.

ACKNOWLEDGMENTS
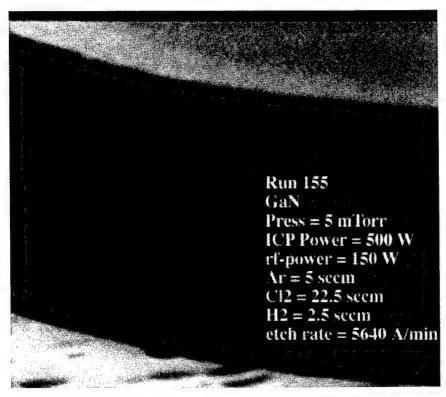
Figure 21. SEM micrograph of feature etched into GaN using a 5 mTorr, 500W ICP, 150W rf Cl₂/H₂/Ar discharge.

REFERENCES

1. see for example, High Density Plasma Sources, ed. O. A. Popov (Noyes Publications, Park Ridge NJ 1996).

2. M. A. Lieberonan and R. A. Gottscho, in Plasma Sources for Thin Film Deposition and Etching, ed. M. H. Francombe and J. L. Vossen, Physics of Thin Films Vol. 18 (Academic Press. San Diego 1994).

3. J. Asmussen, J. Vac. Sci. Technol. A **7** 883 (1989).

4. J. H. Keller, M. S. Barnes and J. C. Forster, 43rd Ann, Gaseous Electronics Conf. Champaign-Urbana, Ill. Oct. 1990, Abstract NS-S.

5. J. W. Denneman, J, Phys. D., Appl. Phys. **23** 292 (1990).

6. J. Amorion, H. S. Maciel and J. P. Sudano, J. Vac. Sci. Technol. B **9** 362 (1991).

7. F. F. Chen, J. Vac. Sci. Technol. A **10** 1389 (1992).

8. R. W. Boswell and D. Henry, Appl. Phys. Lett. **47** 1095 (1985).

9. W. A. Harrison, Electronic Structures and Properties of Solids (Freeman, San Francisco, 1980).

10. R. J. Shul, M. E. Sherwin, A. G. Baca and D. J. Rieger, Electron Lett. **32** 70 (1996).

11. R. J. Shul, D. J. Rieger, A. G. Baca, C. Constantine and C. Barratt, Electron.. Lett. **30** 85 (1994).

12. S. J. Pearton, Int. J. Mod. Phys. B **8** 1781 (1994).

13. F. Ren, T. Fullowan, C. R. Abernathy, S. J. Pearton, P. Smith, R. Kopf and J. R. Lothian, Electron. Lett. **27** 1054 (1991).

14. S. J. Pearton, F. Ren, T. Fullowan, A. Katz, W. S. Hobson, U. K. Chakrabarti and C. R. Abernathy, Mat. Chem. Phys. **32** 215 91992).

15. C. Constantine, R. J. Shul, C. T. Sullivan, M. B. Snipes, G. B. McClellan, M. J. Hafich, C. T. Fuller, J. R. Mileham and S. J. Pearton, J. Vac. Sci. Technol. B **13** 2025 (1995).

16. R. J. Shul, C. T. Sullivan, M. B. Snipes, G. B. McClellan, M. J. Hafich, C. T. Fuller, C. Constatine, J. W. Lee and S. J. Pearton, Solid State Electron. **38** 2047 (1995).

17. C. Constantine, C. Barratt, S. J. Pearton, F. Ren, J. Lothian, W. Hobson, A. Katz, L. W. Yang and P. C. Chao, Electron. Lett. **29** 984 (1993).

18. S. J. Pearton, F. Ren, A. Katz, J. Lothian, T. Fullowan and B. Tseng, J. Vac. Sci. Technol. B **11** 152 (1993).

19. I. Adesida, A. Mahajan, E. Andideh, M. A. Khan, D. T. Olson and J. N. Kuznia, Appl. Phys. Lett. **63** 2777 (1993).

20. S. J. Pearton, C. R. Abernathy and F. Ren, Appl. Phys. Lett. **64** 2294 (1994).

21. R. J. Shul, S. P. Kilcoyne, M. Hagerott-Crawford, J. E. Racmeter, C. B. Vartuli, C. R. Abernathy and S. J. Pearton, Appl. Phys. Lett. **66** 1761 (1995).

22. R. J. Shul, A. J. Howard, S. J. Pearton, C. R. Abernathy, C. B. Vartuli, P. A. Barnes and M. J. Bozack, J. Vac. Sci. Technol. B **13** 2016 (1995).

AUTHOR INDEX

SUBJECT INDEX

power, 107
precipitates, 293

quantum
  dots, 119, 133
  wells, 171
QWIPs, 203, 355

Raman spectroscopy, 39
RBS, 81
RDE, 373
recombination velocity, 81
resistivity, 263
RHEED, 99
RIE, 153
RTA, 269, 355

Schottky diode, 257
selective area epitaxy, 125
SiC, 153, 251
single mode emission, 75
SiN_x, 321
solid phase regrowth, 221
stability, 107

strain, 119, 125, 171
stress, 119
surface stabilization, 99

TDMAA, 15
TEM, 53, 81, 221
tertiary
  butylarsine, 3, 327
  butylphosphine, 3, 327
threshold current, 53
tilted etching, 335
transistors, 3
TRR, 221

Urbach parameter, 367

VCSELs, 53, 75, 81, 341
V/III ratio, 189
VPE, 189

wafer fuse, 63, 165
WDM arrays, 63
wide bandgap, 153